Heat, Fluid, and Sample Control in Point-of-Care Diagnostics

Joshua Ronald Buser

A dissertation
submitted in partial fulfillment of the
requirements for the degree of

Doctor of Philosophy

University of Washington

2016

Reading Committee:
Paul Yager, Chair
Barry Lutz
Wendy Thomas

Program Authorized to Offer Degree:
Bioengineering

University of Washington

Abstract

Heat, Fluid, and Sample Control in Point-of-Care Diagnostics

Joshua Ronald Buser

Chair of the Supervisory Committee:

Professor Paul Yager

Bioengineering

Point-of-care diagnostics have transformed healthcare workflow, perhaps most notably in the wide-reaching impact of home pregnancy tests. Lateral flow strips are simple and inexpensive, but limited in their application to relatively simple diagnostic tasks. Nucleic acid amplification assays on the other hand are more accurate and sensitive, but currently restricted to use in well-equipped laboratories due to reliance on external supplies, power, and trained users. The Multiplexable Autonomous Disposables for Nucleic Acid Amplification Tests in Limited Resource Settings (MAD NAAT) Project, led by Paul Yager, uses instrument-free, disposable,

paper-based fluidics for multiple pathogen detection with DNA/RNA. The end goal is to create a sample in, answer out isothermal nucleic acid amplification device simple enough for untrained users, with low enough cost to enable wider use of nucleic acid testing. My contributions to this project, combining to form my thesis, include advances in sample preparation for nucleic acid amplification, isothermal chemical temperature control, and fluid transport in paper microfluidics. Progress in these subject areas will help advance the development of nucleic acid tests and other advanced assays compatible with point-of-care usage.

1 Table of Contents

2 Acronyms

1DPN: One-dimensional paper network

2DPN: Two-dimensional paper network

μPAD: Microfluidic paper analytical device

ACP: Achromopeptidase

AIDS: Acquired immune deficiency syndrome

ANOVA: Analysis of variance

ART: Antiretroviral therapy

ARV: Antiretroviral

ASSURED: Affordable, sensitive, specific, user-friendly, rapid and robust, equipment-free, and deliverable to end users

ASTM: American Society for Testing and Materials

ATCC: American Type Culture Collection

BSA: Bovine serum albumin

BSL: Biosafety level

CFU: Colony forming unit

CI: Confidence interval

CPA: Cross priming amplification

CV: Coefficient of variation

DARPA: Defense Advanced Research Projects Agency

DI: Deionized

DSC: Differential scanning calorimetry

DNA: Deoxyribonucleic acid

ELISA: enzyme-linked immunosorbent assay

ESI: Electronic supplementary information

FDA: US Food and Drug Administration

gDNA: Genomic DNA

GF: Glass fiber

HDA: Helicase-dependent amplification

HIV: Human immunodeficiency virus

IAC: Internal amplification control

iSDA: Isothermal strand displacement amplification

IHME: The Institute for Health Metrics and Evaluation

LAMP: Loop-Mediated isothermal amplification

LCD: Liquid crystal display

LF: Lateral flow

LFT: Lateral flow test

LOC: Lab on a chip

LOD: Limit of detection

LRS: Low-resource settings

LSAMP: Lewis Stokes Alliance for Minority Participation

MAD NAAT: Multiplexable Autonomous Disposables for Nucleic Acid Amplification Tests in Limited Resource Settings

MRE: Meal ready-to-eat

MS: Manuscript

MRSA: Methicillin-resistant *Staphylococcus aureus*

MSSA: Methicillin-sensitive *Staphylococcus aureus*

MSSE: Methicillin-sensitive *Staphylococcus epidermidis*

MT: Mid-turbinate

MW: Molecular weight

NA: Nucleic acid

NAA: Nucleic acid amplification

NAAT: Nucleic acid amplification test

NASA: US National Aeronautics and Space Administration

NC: Nitrocellulose

NI: National Instruments

NIH: National Institutes of Health

NINA: Non-Instrumented Nucleic Acid amplification platform

NNIN: National Nanotechnology Infrastructure Network

NSF: National Science Foundation

NTC: No template control

NTUF: Washington Nanotech User Facility

OD: Optical density

PAD: Paper analytical device

PBS: Phosphate buffered saline

PBST: Phosphate buffered saline with Tween 20

PCB: Printed circuit board

PCM: Phase change material

PCR: Polymerase chain reaction

PDMS: polydimethylsiloxane

pDNA: pyranosyl DNA

PEG: Polyethylene glycol

PEM: Proton exchange membrane

PES: Polyester

PFGE: Pulsed field gel electrophoresis

PMMA: Poly(methyl methacrylate)

POC: Point of care

PPM: Porous polymer monolith

PS: Patient sample

PUR: Polyurethane

PVC: polyvinylchloride

PVP: Polyvinylpyrrolidone

qPCR: Quantitative polymerase chain reaction

RPA: Recombinase Polymerase Amplification

RPM: Revolutions per minute

RSV: Respiratory syncytial virus

RT-PCR: Reverse transcriptase polymerase chain reaction

RNA: Ribonucleic acid

SDA: Strand displacement amplification

SDS: Sodium dodecyl sulfate

SE: Standard error

SEM: Scanning electron microscopy

SIAO: Sample in, answer out

SNM: Simulated nasal matrix

SP: Sodium polyacrylate

SPE: Solid phase extraction

TB: Tuberculosis

TEAB: Triethyl ammonium bicarbonate

TSB: Tryptic soy broth

US: United States

UV: Ultraviolet

UW: University of Washington

WHO: World Health Organization

WRC: Water retention curve

3 Summary: Heat, fluid, and sample control in point-of-care diagnostics

Point-of-care diagnostics have transformed healthcare workflow, perhaps most notably in the wide-reaching impact of home pregnancy tests. Lateral flow strips are simple and inexpensive, but limited to relatively simple diagnostic tasks. Nucleic acid amplification assays are more accurate and sensitive, but currently restricted to use in well-equipped laboratories due to reliance on external supplies, power, and trained users. During my time with the Yager lab, I have been involved with the Multiplexable Autonomous Disposables for Nucleic Acid Amplification Tests in Limited Resource Settings (MAD NAAT) Project from its early stages.

Figure 1: MAD NAAT device. Swab sample obtained from the patient is inserted in the device. The automated assay quantifies nucleic acid sequence of interest. After some time, the cell phone quantifies assay signal. Graphic by Paul Yager.

The MAD NAAT device uses disposable, paper-based fluidics for instrument-free multiplexed pathogen detection with DNA/RNA. The end goal is to create a sample in, answer out isothermal nucleic acid amplification device simple enough for untrained users, with low enough cost to enable wider use of nucleic acid testing.

The device operational sequence begins with transfer of sample *via* swab into a temperature-controlled lysis tube where pathogens are lysed and nucleic acids released. After a set time, lysate flows to the amplification zone, driven by the capillary pressure of the hydrophilic porous media used in the device, rehydrating dehydrated amplification reagents along the way. Temperature is then controlled for nucleic acid amplification. After a set time,

amplified sample is released into the detection zone, where specifically amplified nucleic acid sequences bind with an immobilized test line, forming a colorimetric signal, and are detected optically by a smartphone.

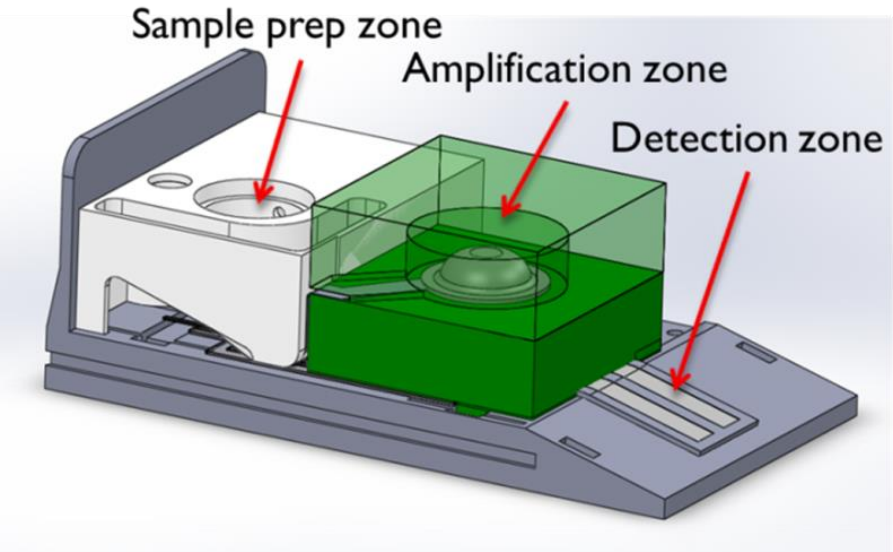

Figure 2: MAD NAAT device overview. The swab is inserted into the sample prep zone where pathogens are ruptured and DNA released. The amplification zone is temperature controlled for nucleic acid amplification. Amplified sample then flows through the detection zone, where the amplified sequence binds to an immobilized reagent and a colorimetric test line appears. Graphic by Josh Bishop.

I have been most heavily involved with three main areas of the project:

1) **Fluid transport:** necessary parameters to predict and control flow rates are not available in the current literature, so we developed a technique to measure them
2) **Isothermal temperature control**: a recurring requirement in MAD NAAT device
3) **Sample preparation**: including cell rupture and nucleic acid release

Three of the four aims of my thesis are centered on these subjects, with a fourth aim comprised of applications of the first three aims.

My thesis begins with a background section comprised of a book chapter on point-of-care diagnostics for low resource settings, and concludes with the integrated MAD NAAT paper.

Manuscripts completed during my PhD timeframe for which I am a contributing author and do not fit within the main thesis arc are included as appendices.

4 Overview of thesis sections

4.1 Background

The need for point-of-care testing is outlined in detail in a book chapter written by myself, Dr. Carly Holstein, and Dr. Paul Yager. This chapter is included as the Background section of this thesis.

4.2 Aim 1) Fluid flow in paper microfluidics: parameter measurement and flow modeling

Parameters necessary for predicting flow behavior in paper microfluidics are unavailable in the literature, and existing characterization techniques are limited. Here we develop novel characterization techniques, measuring and reporting relevant parameters for a wide array of paper microfluidic materials. Using these parameters in flow models has uncovered a near omnipresent partially-saturated flow regime which precludes the usage of the widely accepted flow rate models for paper microfluidics. This aim applies geological flow models to paper microfluidics for partially saturated flow.

Main deliverable: Publication: Parameter measurements & flow equations ***MS in prep.***

4.3 Aim 2) Isothermal temperature control using chemical heaters

NAAT-based devices require precise heating and temperature control. For the MAD NAAT device, we developed non-electrical temperature control systems using chemical heaters. This effort included quantitative modeling of the chemical heater system primary components, exothermic chemical power supply quantifications, composite phase change material research

and development, along with integrated system geometry optimizations for use with two-dimensional paper microfluidics. This work was completed in collaboration with PATH.

Main deliverable: Publication: Comprehensive chemical heater development ***Published***

4.4 Aim 3) Develop an electromechanical sample preparation methodology for hard-to-lyse pathogens compatible with point-of-care deployment

Here, a portable audio source-powered electromechanical sample preparation technique was developed which is capable of releasing DNA from a range of bacteria, including hearty Gram-positive *Mycobacterium marinum*, a *Mycobacterium tuberculosis* analogue. A second publication, which Dr. Erin Heiniger is primary author, compares the AudioLyse to other point-of-care compatible lysis techniques (see Appendix for full text).

Main deliverable: Publication 1: Initial data and optimization parameters. ***Published***
Publication 2: Comparison to other POC lysis techniques ***Published***

4.5 Aim 4) Utilize the techniques developed in Aims 1-3 to design and build integrated systems

These projects were completed in collaboration with multiple researchers; see the related sections for author lists and contributions.

Sub-aim 4.1: Non-electric sample preparation heater ***Published***

Sub-aim 4.2: Large volume samples using paper microfluidic physics ***Published***

Sub aim 4.3: Paper microfluidic hydrogen fuel cells ***Published***

4.6 Integrated MAD NAAT

The MAD NAAT project over the last five years has been quite productive, and the work presented in the four aims of my thesis has contributed to this effort. One milestone our team is proud to have reached is an integrated sample-to-result nucleic acid test, described in the manuscript (Dr. Lisa Lafleur is primary author) included in this section.

4.7 Appendices

Manuscripts highlighting work where I was a contributing author, but not the main author, during my PhD have been included as appendices.

4.8 Future directions

The fluids work could enable a new set of design principals for paper microfluidics, partial saturation likely affects all aspects of paper microfluidics from reagent patterning, drying, and subsequent assay steps. The chemical heaters, both lysis and amplification, are being incorporated into a fully integrated electricity-free version of the MAD NAAT device. The mechanical lysis work will likely be incorporated into future projects within the Yager group.

4.9 Publications during PhD

Peer-Reviewed Manuscripts

1. *In preparation:* JR Buser, J Atwood, RP Gallagher, G Kimpel, PC Kauffman, BR Lutz, and P Yager. Nothing is saturated: Corrected assumptions and necessary parameter measurements for flow prediction in paper microfluidics.
2. *In preparation:* **JR Buser***, SA Byrnes*, CE Anderson, P Kauffman, JD Bishop, MH Wheeler, P Yager. The P-switch: A pressure-based system for controlling flow and automating assays in paper microfluidics.
3. *Submitted:* JP Esquivel, **JR Buser**, CW Lim, Carlota, S Rojas, P Yager, N Sabate. Single use water-activated paper-based hydrogen fuel cells for disposable applications.
4. *In preparation:* S Dharmaraja, I Andrews, **JR Buser**, SA Byrnes, PC Kauffman, LK Lafleur, N Panpradist, BJ Toley, B Lutz. Capillary-controlled sequential delivery in a lateral flow strip: the 1-D paper network (1DPN).
5. *In preparation:* CE Anderson, **JR Buser**, EM Strauch, PD Ladd, R Marzan, D Baker, P Yager. Automated detection of viral surface proteins using computationally designed affinity proteins in a two-dimensional paper network.
6. *In preparation:* S Schmidt, **JR Buser**, BR Lutz, DM Ratner. Serologic phenotyping using silicon photonic biosensors and capillary driven networks.
7. LK Lafleur, JD Bishop, EK Heiniger, RP Gallagher, MH Wheeler, PC Kauffman, E Kline, X Zhang, **JR Buser**, BH Toley, S Kumar, SA Byrnes, PD Ladd, BR Lutz, P Yager. A rapid, instrument-free, sample-to-result nucleic acid amplification test. *Lab on a chip,* 2016, **16**, 19, 3777-3787.
8. EK Heiniger, **JR Buser**, L Mireles, X Zhang, PD Ladd, BR Lutz, P Yager. Comparison of point-of-care-compatible lysis methods for bacteria and viruses. *J. Microbial Methods,* 2016, **128**, 80-87.
9. **JR Buser**, X Zhang, SA Byrnes, PD Ladd, EK Heiniger, MD Wheeler, JD Bishop, JA Englund, BR Lutz, BH Weigl, P Yager. A disposable chemical heater and dry enzyme preparation for lysis and extraction of DNA and RNA from microorganisms. *Analytical Methods,* 2016, **8**, 2880-2886. **Front cover**
10. **JR Buser***, S Diesburg*, J Singleton, D Guelig, JD Bishop, C Zentner, R Burton, P LaBarre, P Yager, BH Weigl. Precision chemical heating for diagnostic devices. *Lab on a chip*, 2015, **15**, 23, 4423-4432. **Back inside cover**
11. **JR Buser**, A Wollen, EK Heiniger, SA Byrnes, PC Kauffman, PD Ladd, P Yager. Electromechanical cell lysis using a portable audio device: enabling challenging sample preparation at the point-of-care. *Lab on a chip*, 2015, **15**, 9, 1994-1997.
12. SA Byrnes, JD Bishop, L Lafleur, **JR Buser**, B Lutz, P Yager. One-step purification and concentration of DNA in porous membranes for point-of-care applications. *Lab on a chip*, 2015, **15**, 12, 2647-2659.
13. BJ Toley, JA Wang, M Gupta, **JR Buser**, LK Lafleur, BR Lutz, E Fu, P Yager. A versatile valving toolkit for automating fluidic operations in paper microfluidic devices. *Lab on a chip*, 2015, **15**, 6, 1432-1444.

14. KG Shah, D Guelig, S Diesburg, **JR Buser**, R Burton, P LaBarre, R Richards-Kortum, B Weigl. Design of a New Type of Compact Chemical Heater for Isothermal Nucleic Acid Amplification. *PloS One*, 2015, **10**, 10, e0139449.
15. N Panpradist, BJ Toley, X Zhang, SA Byrnes, **JR Buser**, JA Englund, BR Lutz. Swab sample transfer for point-of-care diagnostics: characterization of swab types and manual agitation methods. *PloS one*, 2014, **9**, 9, e105786.
16. BJ Toley, B McKenzie, T Liang, **JR Buser**, P Yager, Elain Fu. Tunable-delay shunts for paper microfluidic devices. *Analytical chemistry*, 2013, **85**, 23, 11545-11552.

Conference Proceedings

1. JP Esquivel, **JR Buser**, FJ del Campo, S Rojas, P Yager, N Sabate. Disposable hydrogen fuel cells for powering next-generation lateral flow devices*. Solid-State Sensors, Actuators and Microsystems (TRANSDUCERS),* 2015.
2. SA Byrnes, **JR Buser**, EK Heiniger, PC Kauffman, PD Ladd, P Yager. A Novel method to control flow in paper microfluidics for rapid processing of large volume samples. *MicroTAS,* 2015, 1308-1310.
3. J Singleton, C Zentner, **JR Buser**, P Yager, P LaBarre, BH Weigl. Instrument-free exothermic heating with phase change temperature control for paper microfluidic devices. *SPIE MOEMS-MEMS*, 2013, 86150R.
4. S Dharmaraja, L Lafleur, SA Byrnes, PC Kauffman, **JR Buser**, BJ Toley, E Fu, P Yager, B Lutz. Programming paper networks for point of care diagnostics. *SPIE MOEMS-MEMS*, 2013, 86150X.

Book Chapters

1. **JR Buser***, CA Holstein*, P Yager. Microfluidic Diagnostics for Low-resource Settings: Improving Global Health without a Power Cord. *Book chapter of Microfluidics for Medical Applications*, 2014, 151-190.

*Contributed equally

4.10 Patent applications

1. **JR Buser,** SA Byrnes, EK Heiniger, JD Bishop, P Yager. Pressure-based control of fluid volumes and associated devices, systems, and methods. US non-provisional patent application. April, 2016.
2. **JR Buser**, JD Bishop, MH Wheeler, P Yager. Phase change valve and fluidics devices. US Provisional Patent Application 62/120,985. February, 2015.
3. **JR Buser**, A Wollen, EK Heiniger, SA Byrnes, PC Kauffman, P Yager. Systems for cell lysis and associated devices and methods. US non-provisional patent application. January, 2015.
4. JD Bishop, **JR Buser**, PC Kauffman, LK Lafleur, M Li, MH Wheeler, P Yager. eMADNAAT. U.S. Provisional Patent Application No. 62/030,371. July, 2014.

5. JP Esquivel, MN Sabate Vizcarra, FJ Del Campo Garcia, **JR Buser**. Dispositivo con capacidad de reaprovechamiento de hidrogeno y pila de combustible para reaprovechamiento de hidrogeno. Spanish Patent Application no. P201430145. February, 2014.
6. JD Bishop, **JR Buser**, SA Byrnes, S Dharmaraja, E Fu, J Houghtaling, PC Kauffman, S Kumar, LK Lafleur, T Liang, BR Lutz, BJ Toley, MH Wheeler, P Yager, X Zhang. Sequential delivery of fluid volumes and associated devices, systems, and methods. International Patent Application PCT/US2014/012618. January, 2014
7. **JR Buser**, LK Lafleur, BR Lutz, J Singleton, MH Wheeler, P Yager, C Zentner, X Zhang. Device for the rapid lysis of bacteria compatible with point-of-care use. US Provisional Patent application no. 61/867,950. August, 2013
8. **JR Buser**, J Singleton, BH Weigl, P Yager, C Zentner. Instrument-free exothermic heating with phase change temperature control for paper microfluidic devices. US Provisional Patent Application 61/755,066. January, 2013.

4.11 Posters and presentations

1. **Buser JR**, Heiniger EK, Mireles L, Wollen A, Kauffman PC, Yager P. (2015) *Gordon Research Conference.*
2. **Buser JR**, Diesburg SP, Guelig D, Singleton J, Yager P, LaBarre P, Weigl B. (2015) *Gordon Research Conference.*
3. Diesburg SP, **Buser JR,** Guelig D, Singleton J, Yager P, LaBarre P, Weigl B. (2015) *Gordon Research Conference*
4. Singleton J, Guelig D, **Buser J**, Burton R, Edeh O, Hawkins K, Weigl B, LaBarre P. (2014) *Clinical Chemistry Oakridge*
5. Singleton J, Guelig D, **Buser J**, Burton R, Edeh O, Hawkins K, Weigl B, LaBarre P. (2014) *IEEE GHTC*
6. Byrnes SA, Bishop J, Lafleur L, **Buser JR**, Li B, Olsen C, Lutz B, Yager P. (2014) *MicroTAS*
7. Byrnes SA, Bishop J, Lafleur L, **Buser JR**, Li B, Olsen C, Lutz B, Yager P. (2014) *Oral presentation at BMES*
8. Yang J, **Buser JR**, Fu E. (2013) *BMES*
9. **Buser JR**, Kimpel G, Kauffman P, Toley BJ, Yager P. (2013). *Gordon Research Conference.*
10. **Buser JR**, Kimpel G, Kauffman P, Fu E, Lutz B, Yager P. (2012) *BMES*

5 Introduction: The Need for Diagnostics in Low-resource Settings

This introduction is adapted from[1]*:*

JR Buser, CA Holstein, and P Yager. "Microfluidic Diagnostics for Low-resource Settings: Improving Global Health without a Power Cord." *Microfluidics for Medical Applications*: 151.

5.1 Importance of Diagnostic Testing

The ability to diagnose a patient quickly and accurately is of paramount importance in the management of most diseases, as the appropriate treatment cannot be administered until the cause has been identified. In the developed world, accurate diagnosis can often be achieved, especially in hospitals and large clinics where sophisticated equipment and trained laboratory staff are available[2]. In these settings, the available infrastructure supports advanced diagnostic procedures such as the enzyme-linked immunosorbent assay (ELISA) and nucleic acid amplification (NAA) assays such as polymerase chain reaction (PCR). Additionally, bacterial culture remains widely used for microbe identification, epidemiology, and drug resistance testing[3]. While diagnostics account for only about 1.6% of total Medicare expenditures in the US, an estimated 60–70% of medical decisions are based on their results[4], highlighting the role of diagnostics as an extremely valuable, and cost-effective, tool in medicine.

5.2 Limitations in Low-resource Settings

In low-resource settings, such as those found in many developing countries, clinics are equipped with only minimal infrastructure, often lacking consistent electricity and refrigeration, and do not have access to highly trained personnel[3]. The lack of these resources and, often, the lack of rapid and effective transportation also make it difficult to establish a cold chain, which is required for transport of many diagnostics that use aqueous reagents[5]. Additionally,

laboratories that are fortunate enough to possess diagnostic equipment often cannot support the required maintenance schedules, leaving much advanced equipment in an unmaintained and unusable condition[6]. For these reasons, performing expensive, sophisticated laboratory testing is usually not possible in resource-poor areas of the world, often leaving clinics without the means for accurate diagnosis. This is especially unfortunate, since treatments are often available, if only the diagnosis could be made[3], [7].

Overall, there is an urgent need for affordable diagnostics that can be used at the point of care (POC) of the patient. Diagnostic techniques utilized in high-income regions are often resource-intensive, requiring climate controlled usage and storage, calibration, reliable electrical power, and trained personnel. The POC, from a global health standpoint, is often lacking these amenities[6]. The fact that diagnostic tests for prevalent diseases are not available in formats compatible with low-resource settings not only contributes to lowering the quality of life in these areas, but also results in compounded health problems, such as incorrect treatments and increased drug resistance[3]. To guide the development of diagnostic devices for low resource settings, the World Health Organization (WHO) compiled the ASSURED criteria, stating that devices should be Affordable, Sensitive, Specific, User-friendly, Rapid and robust, Equipment-free, and Deliverable to end users[8]. The ability to manufacture high-performance diagnostics inexpensively would lower one of the critical barriers to their adoption in clinics across the globe, thereby increasing access to accurate diagnostic information. This would, in turn, improve disease management, individual patient outcomes, and potentially public health outcomes[7], [9], [10].

5.3 Scope of Section

The goal of this section is to provide the reader with a concise and holistic assessment of the need for and use of microfluidic diagnostics in low-resource settings. Since comprehensive review articles already exist on the topic of point-of-care diagnostics[9], [11], our goal is not to review all microfluidic technologies in detail, but instead to offer an overview of the field to highlight both the successes of and opportunities for microfluidic diagnostics in global health. This overview intentionally incorporates our own perspective on these issues, including an emphasis on paper-based microfluidics, which we view as an important and rapidly growing component of the microfluidics field with significant potential to revolutionize diagnostic testing in low-resource settings. Most importantly, we aim to provide a useful context with which to think about the development of microfluidic diagnostics. To do so, we first categorize and describe the different types of diagnostic testing that are needed in low-resource settings. We then provide an overview of the major types of microfluidic diagnostics that are being pursued for global health applications, which we broadly categorize into channel-based microfluidics and paper-based microfluidics. Finally, we break down the diagnostic tests into many of the components that must be considered, and ideally integrated, when developing a diagnostic test for use in low-resource settings. In this section, we highlight microfluidic technologies that have addressed these aspects particularly well, in addition to pointing out areas that are rife for microfluidic innovation.

5.4 Types of Diagnostic Testing Needed in Low-resource Settings

There is a good deal of diagnostic testing underway today to improve and maintain the health of individuals in low-resource settings in venues ranging from large hospitals in urban settings, to small clinics in villages and rural homes by itinerant healthcare workers. However, there is a substantial outstanding need for more and better testing, at a manageable cost. The most

imperative types of testing comprise the diagnosis of disease, including the identification of drug-resistance, and monitoring of therapy. Additionally, tests that can determine the quality of drugs used for treatment and identify counterfeits would help improve health in the developing world. Finally, tests that can detect environmental contaminants related to health issues are also needed in resource-poor settings.

5.5 Diagnosing Disease

The ability to identify the cause(s) of a given patient's disease is the most pressing diagnostic need everywhere. Diseases caused by pathogens are top contributors to the global burden of disease, due to the high prevalence of infectious diseases in parts of the developing world[12], [13]. For example, the 2010 Global Burden of Disease study led by the Institute for Health Metrics and Evaluation ranks lower respiratory infections, diarrhea, HIV/AIDS, and malaria in the top ten causes of global disease burden, accounting for an estimated 337 million DALYs (disability-adjusted life years) in total[12], [13]. All four of these infectious diseases can have multiple pathogenic causes, including an array of viruses and bacteria for lower respiratory infections and diarrhea[12], [13] and several different strains of the specific pathogens for malaria (five different species of the Plasmodium parasite[14]) and HIV/AIDS (two different types of HIV, each with multiple sub-types[15], [16]. Diagnostic tests that can detect and identify specific disease-causing pathogens from biospecimens are therefore of extreme importance for managing a patient's disease and getting him/her on the correct path to treatment. While infectious diseases afflict many parts of both the developed and developing worlds, no region is more severely impacted than sub-Saharan Africa, where infectious diseases are still the leading causes of disease burden[12], [13], as illustrated in Figure 3. The resource-poor areas of

sub-Saharan Africa therefore present a unique intersection of the need for infectious disease diagnostics and tight design constraints that is well suited for low-cost microfluidic technologies.

Point-of-care testing would be invaluable for the diagnosis, treatment, and epidemiological strategy for a variety of infectious agents, but tuberculosis (TB) represents a prime example of a disease that is widely globally prevalent and in need of better diagnostic testing. According to the WHO, roughly one third of the world's population is infected with TB. While most of these cases are dormant, the WHO estimates that there were 1.3 million deaths from TB and 8.6 million new cases of TB in 2012 alone[17], indicating the severity of this disease. A recent report from UNITAID on the TB diagnostic technology landscape outlines the current status of TB testing along with unmet needs[18]. The illustration in Figure 4, reproduced from that report, highlights laboratory capacity for TB diagnostics in resource-limited settings, along with the types of testing performed at each level of the health system. This figure highlights a huge problem and area of need: there are currently no suitable TB diagnostics available at the peripheral level of health systems, where 60% of the patients are seen[18].

Like many other infectious diseases, diagnosing TB early in the disease progression and providing effective treatment is critical to patient outcome and for controlling spread of the disease. Sputum smear microscopy and culture are the conventional diagnostic technique, with drug susceptibility testing performed on cultures, but results often take weeks[17]. Failing to test for drug resistance can lead to inappropriate treatments, prolonged disease, increased mortality, and increased drug resistance (discussed in detail next). More timely and specific detection of TB can be achieved using nucleic acid amplification (NAA) assays, but much of the technology required to perform these assays has not traditionally been functional in low-resource settings, where diagnostics must be portable and operable without advanced training.

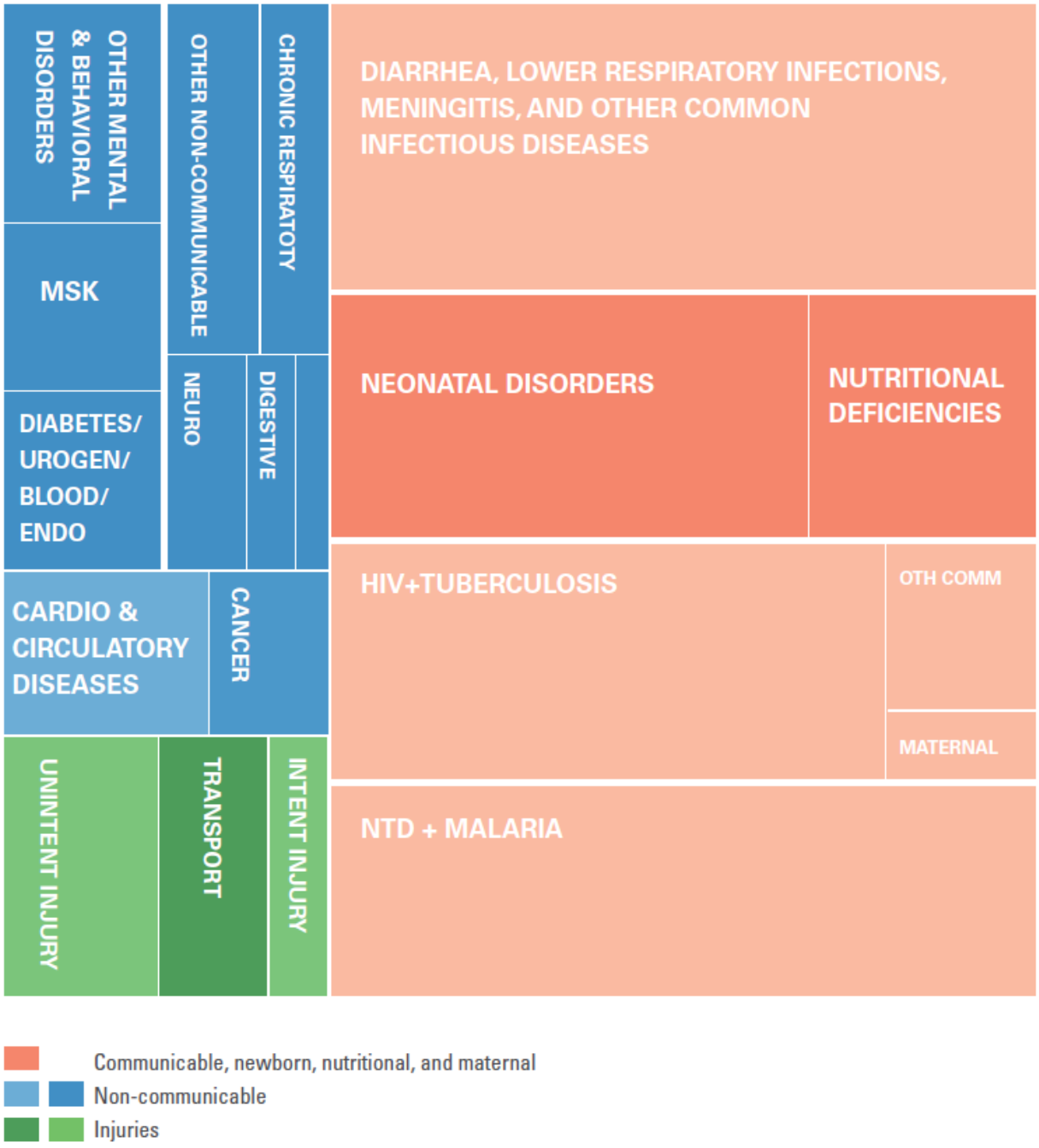

Figure 3: Illustration of the relative contributions of various diseases and causes to disease burden (quantified in DALYs) in sub-Saharan Africa in 2010. Infectious diseases, including HIV, TB, and malaria, are the major contributors to disease burden in this region. Reprinted from the 2010 Global Burden of Disease report[12]. (Institute for Health Metrics and Evaluation, The Global Burden of Disease: Generating Evidence, Guiding Policy, University of Washington, Seattle, WA, IHME, 2013.)

In addition to pathogen detection, the ability to determine whether or not a given pathogen is resistant to drugs used for treatment is critical to both managing a patient's disease effectively and monitoring the prevalence of such drug-resistance for public health purposes. Drug resistance is a major consideration when choosing the treatment for a patient's disease, since it is critical to know if the infecting pathogen will be resistant to the drug of choice. Diagnostics that cost less than the difference between potentially ineffective, cheap drugs and efficacious, more expensive drugs are critical for implementing effective patient management[3]. Further, limiting the use of effective second-line drugs helps to keep the pathogens from developing resistance to these drugs, preserving them as treatment options for a longer period of time[3]. Finally, tests for drug-resistant pathogens could also be used to monitor a region for drug-resistance, which can be an important public health strategy[3]. For these reasons, monitoring drug resistance is a critical effort in the control of prevalent infectious diseases such as malaria, TB, HIV, and bacterial infections[3].

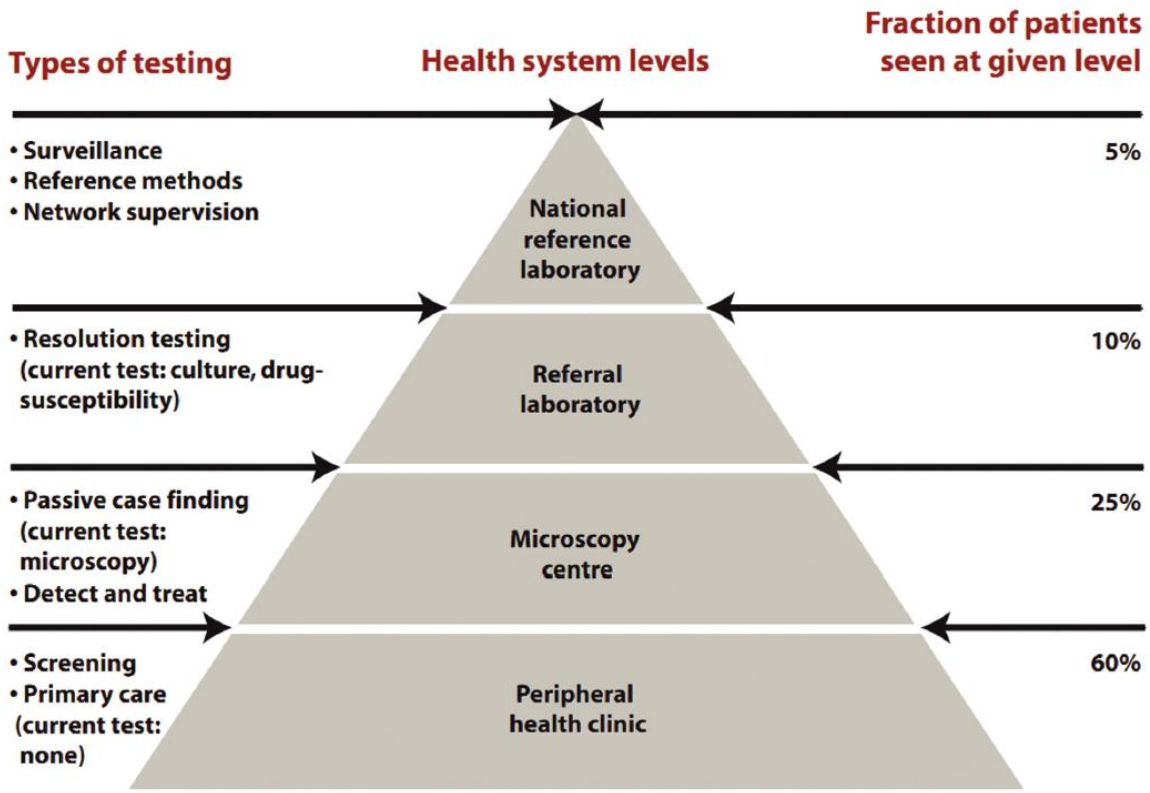

Figure 4: Pyramid representation of the fraction of TB patients seen at the four different levels of typical health systems in resource-poor countries and the types of diagnostic testing available at each level. Most notably, there is currently no TB diagnostic test available for use at the peripheral level, where the majority of TB patients are seen. Reprinted from UNITAID–Tuberculosis diagnostics technology landscape report[18].

Finally, as infectious diseases are controlled in the developing world, lifetimes increase. Consequently, chronic diseases such as diabetes and cancer increase, generating a need for low-cost diagnostic tests for these non-infectious (also called non-communicable) diseases as well. According to the 2010 Global Burden of Disease report, mortality due to chronic diseases has increased 30% since 1990 for people worldwide, reflecting a global shift in disease burden from infectious to non-infectious diseases[12], [13]. As shown in Figure 5, non-communicable diseases actually account for the majority of disease burden (DALYs) in most countries across the globe, including many developing countries[12]. The one major exception is the sub-Saharan

region of Africa, in which infectious disease remains the major contributor to disease burden[12], [13], as discussed above.

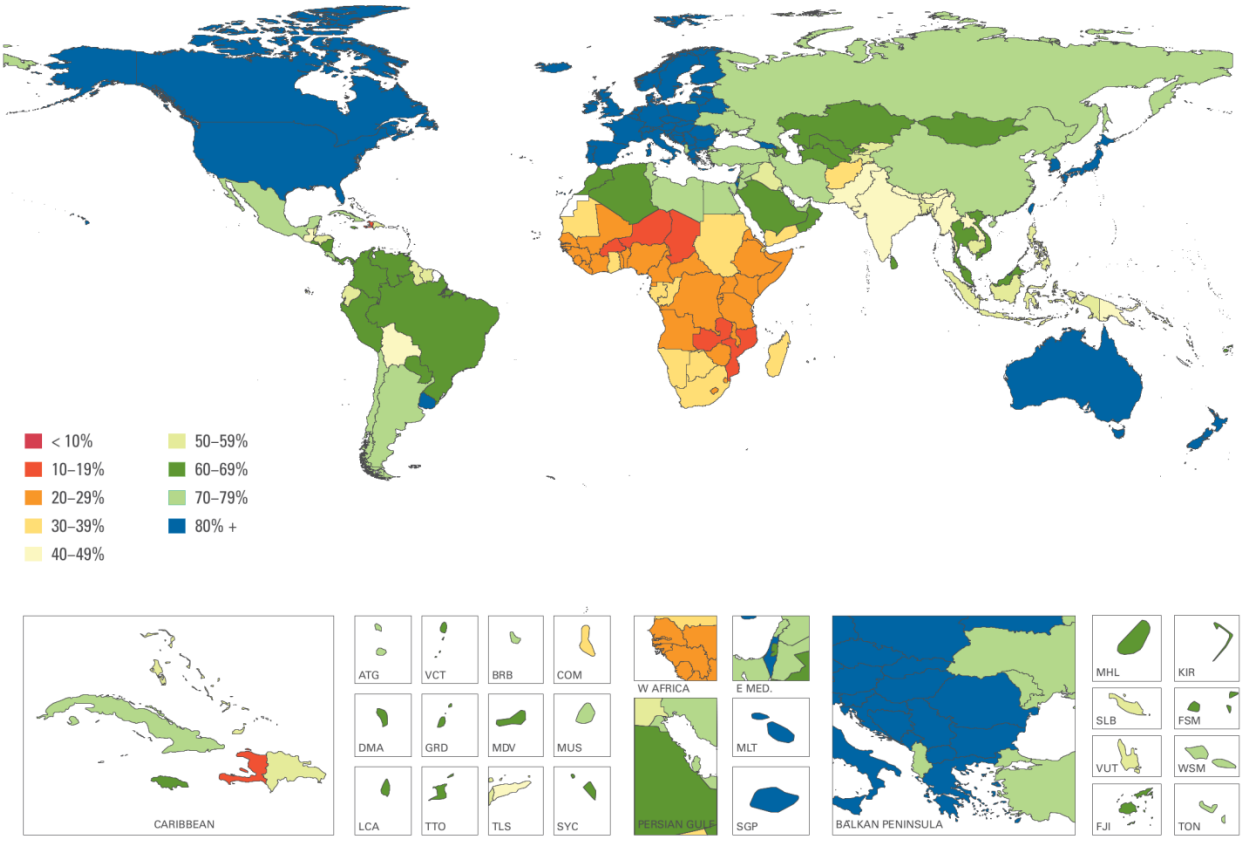

Figure 5: Percentage of disease burden due to non-communicable diseases in 2010, by country, quantified in terms of DALYs. In most countries, non-communicable disease is the major cause of disease burden. Reprinted from the 2010 Global Burden of Disease report[12]. (Institute for Health Metrics and Evaluation, The Global Burden of Disease: Generating Evidence, Guiding Policy, University of Washington, Seattle, WA, IHME, 2013.)

Diabetes represents one prominent and growing chronic disease worldwide, experiencing a 69% increase in global disease burden over the past 20 years[12]. Monitoring blood glucose levels through point-of-care test strips is a common practice for the management of diabetes, and will be discussed further later in this section. The diagnosis of diabetes represents a distinct and important area of diabetes testing in need of better point-of-care options, especially for use in the developing world[19], [20]. In particular, diabetes diagnostics that detect glycated hemoglobin

(HbA1c) have grown in popularity in the developed world, but are still widely unavailable in the developing world[20]. Glycated hemoglobin is considered to be a more convenient and robust biomarker for diabetes than blood glucose, since blood glucose levels fluctuate day-to-day, while HbA1c is more stable, representing the average blood glucose content of the patient over the previous 8 to 12 weeks[20]. Because of the robust nature of HbA1c as a diabetes biomarker, the patient does not need to fast prior to the test, making the diagnostic process much more convenient[20]. These advantages of HbA1c are magnified in the developing world, where access to healthcare is often already limited and inconvenient, making HbA1c tests an important area of need in global health diagnostics. Additionally, gestational diabetes – or diabetes that occurs during pregnancy–is another area in need of better diagnostic testing, due to the severity of complications that can arise for both mother and baby and to the lack of appropriate screening methods for low-resource settings[21]. One approach, under development by Weigl and colleagues at PATH, is to screen for glycated albumin using a lateral flow test[21]. This type of low-cost, microfluidic diagnostic offers much more convenience and ease-of-use than traditional glucose challenge tests, which require fasting, venous blood draws, and laboratory analysis[21].

5.6 Monitoring Disease

In contrast to diagnosing a new disease, monitoring a patient's existing disease is critical for the management of many long-term illnesses. In these circumstances, the need for tests to be inexpensive is even more crucial, since the test must be repeated many times during the duration of the patient's condition. Monitoring can be used to help control the patient's health and determine when medication is needed, as is the case for diabetes. Alternatively, monitoring can be used to evaluate a patient's response to treatment, which is typically done for HIV patients on

anti-retroviral therapy, and could be applied to compliance with the long-term course for treatment for tuberculosis.

For diabetes management, monitoring blood glucose levels is crucial for enabling patients to manage their disease, as they can know when to adjust their sugar intake or administer insulin to maintain a safe blood glucose level. Although chronic diseases like diabetes were once referred to as ‘‘diseases of affluence’’[8], diabetes incidence has increased in the developing world over the last few decades, with 80% of diabetics now living in low- and middle-income countries[22]. The 2010 Global Burden of Disease study highlights this change, showing that diabetes rose from the #21 global disease burden rank in 1990 to the #14 position in 2010, experiencing a 69% increase in DALYs during this time[12], [13]. Glucose monitoring devices have fundamentally changed the lives of diabetics in the developed world, allowing them to reduce or eliminate the development of devastating consequences of uncontrolled blood glucose. Consequently, it is no surprise that these devices lead the way in terms of commercial volume for point-of-care tests, given the prevalence of the disease and the need for multiple daily measurements. According to Gubala *et al.*, nearly 10^{10} glucose test strips are manufactured per year, with some production lines producing 10^{6} test strips per hour[9]. While glucose monitoring devices and test strips are fairly low-cost and translatable to the developing world, these low-resource settings carry their own unique challenges that remain to be addressed. In particular, the lack of doctors, health centers, and healthcare workers in remote areas of the developing world make it difficult for patients to connect with healthcare providers to review their blood glucose data and to obtain testing supplies in some cases[23]. For these reasons, combined with the prevalence of diabetes in the developing the world, the WHO seeks to promote improved methods for the diagnosis, surveillance, and control of diabetes in low- and middle-income

countries[19], [23]. Incorporating mobile health technology to connect patients to doctors would be one important step to helping patients manage their disease, and enabling continuous glucose monitoring for patients in these regions would be an even greater feat[23].

Disease monitoring is also an important process for patients infected with HIV, as proper monitoring of HIV treatment is key to optimal disease management and prognosis[24]–[27]. A key component of treatment monitoring is regular testing of HIV viral load[24]–[28], which represents the level of circulating virus in the blood. Since HIV is highly mutagenic, it commonly evades treatment regimens by mutating into drug-resistant forms, which can then resume viral replication[29]. By monitoring for an increase in a patient's viral load over time, clinicians can determine when treatment is failing and therefore when to switch the patient to an alternative drug regimen[24]–[28].

While HIV viral load testing is commonplace in the developed world, its current use is severely limited in low-resource settings[24]–[27]. This disparity is particularly problematic because the majority of global HIV prevalence is in low- and middle-income countries[30]. More specifically, the WHO estimates that of the 34 million people living with HIV in 2010, 30 million were in low-resource countries[31]. The unfortunate lack of viral load testing in these countries stems from the inappropriate nature of current testing methods for low-resource settings. The most common viral load test, by far, is nucleic acid testing by PCR to measure the number of copies of HIV RNA present in a blood sample. Since PCR requires sophisticated equipment, highly trained personnel, and specialized rooms and workflow to prevent contamination, it can only be performed in the highest-level laboratories and hospitals in developing-world countries[26], [27]. One proposed solution has been to collect samples as dried blood spots and send them to a reference laboratory for testing[26], [32], but this approach is

considered to be infeasible in many low-resource settings[26]. Furthermore, even if such reference laboratory testing can be accomplished logistically, the turnaround time (on the order of weeks) is prohibitively long, causing patients to be lost to follow up[25], [26]. Current alternatives to PCR-based viral load testing, such as the reverse transcriptase activity assay and the heat-denatured p24 antigen assay, represent improvements in point-of-care viral load testing, but are still not considered to be perfect solutions due to poor usability and reproducibility[27], [33], [34].

There is therefore tremendous need for a POC test for HIV viral load that can be used in low-resource settings[24]–[27], [30]. In fact, in a recent report on the global AIDS epidemic, UNAIDS touts the development of POC diagnostics as one of the five pillars of its ‘‘Treatment 2.0’’ plan to simplify and increase access to HIV treatment[30]. While previous unavailability of drugs for antiretroviral therapy (ART) in the developing world may have stagnated the search for low-cost HIV viral load tests, these drugs are becoming increasingly available[24], [25], [27], [30], [31]. From 2004 to 2009, access to antiretroviral (ARV) drugs increased 13-fold in low- and middle-income countries[30], and currently 6.6 million HIV-infected individuals in these countries are receiving ART[31]. While there are still nearly 10 million more people in low- and middle-income countries in need of ART[30], [31], the ever increasing number of patients receiving therapy necessitates POC tests for monitoring treatment adherence and efficacy[26], [27]. If anything, the limited supply of ARV drugs in low-resource settings should prompt better treatment monitoring and viral load testing, since efficient use of these drugs is all the more critical[24], [25].

While CD4+ T-cell counting is also performed for monitoring of ART, viral load testing alone would represent a significant improvement in HIV disease management. The combination

of CD4+ T-cell and viral load monitoring would be ideal[28], [35], [36], but it is known that CD4+ T-cell monitoring alone is not sufficient to predict treatment failure[26], [35], [37], and many experts support the use of viral load testing alone, if a choice must be made between the two methods[24], [27], [37]. Overall, the development of a POC viral load test represents a logical first step toward low-cost ART monitoring.

Finally, in addition to treatment monitoring, HIV viral load testing is also used for the diagnosis of HIV in infants. Since maternally derived antibodies persist in babies until approximately 18 months of age, traditional diagnosis based on the detection of patient-derived anti-HIV antibodies is not suitable for young infants[25], [26]. Conversely, diagnosis by viral load testing is much easier in infants than in adults, since HIV-infected infants have extremely high viral loads ($> 10^5$ RNA copies/mL) compared to the low levels that can circulate in adults with latent infection (10^2–10^3 RNA copies/mL)[26], [38]. A low-cost diagnostic device for viral load testing would therefore be extremely useful for infant diagnosis and prompt disease management for these young children[25], [26]. Moreover, a qualitative test for determining a yes-or-no diagnosis of HIV for infants could represent an ideal entry point for POC viral load testing, since the detection limit required is much higher than that needed for quantitative treatment monitoring[25], [26].

5.7 Counterfeit Drug Testing

Another important area in need of better testing capabilities is the identification of counterfeit medicines. While counterfeit drugs are not unique to the developing world, they are much more prevalent in these regions than in the developed world due to the lack of regulatory oversight in developing countries[39], [40]. The absence of required active drug compounds, the introduction of erroneous active drug compounds, and the use of binder and filler materials are

all common problems found in counterfeit medicines[40]. Having devices available can detect the presence or absence of important compounds for a given drug would therefore offer an important tool in the fight against counterfeit drugs, which currently contribute to morbidity, mortality, and the waste of precious medical and financial resources[39], [40].

The Lieberman group at the University of Notre Dame has made significant strides in counterfeit drug testing, using paper-microfluidic devices. In a recent publication from this group, Weaver *et al.* describe their novel paper analytical device (PAD) platform for rapid field testing of drugs used for disease treatment[40]. In these PADs, the drug is swiped across the bottom of a device, and several distinct lanes perform chemical analyses of the drug that generate colorimetric signals, resulting in a ‘‘color bar code’’ that describes the quality of the drug[40], shown in Figure 6. In particular, the authors demonstrate PADs for the evaluation of β-lactam-based antibiotics and anti-TB drugs that can identify wanted and unwanted compounds with mostly high sensitivities and specificities, all within a matter of minutes[40].

Figure 6: Example of a paper analytical device (PAD) developed by the Lieberman group for counterfeit pharmaceutical testing, in this case for TB drugs[40]. Reprinted from Anal. Chem., 85(13), 6453–6460. Copyright 2013, American Chemical Society.

5.8 Environmental Testing

Detecting a substance of interest in, not a patient, but in environment samples provides unique challenges in handling highly variable, complex sample matrices[41]. The outbreak of cholera in Haiti following the already devastating 2010 earthquake highlights the power of water-borne contaminants to affect large sections of a population. Between October 2010 and December 2012, the number of cholera cases in Haiti exceeded 630,000, killing over 7,900 people[42]. In addition, nearly 30,000 cholera cases were recorded after spreading to the Dominican Republic and Cuba, killing over 400 more people[42]. Better methodologies for monitoring cholera contamination are needed for low-resource settings like Haiti to help implement prevention and care efforts[43]. One promising opportunity is the monitoring for *V. cholerae* O1 and

vibriophages, which have been shown to indicate a cholera outbreak one month in advance, providing an opportunity for the implementation of prevention measures[44].

Additionally, the biochemical, industrial, pharmaceutical, and medical industries have seen much growth in the past few decades. As a result, the amount of waste product from these industries has increased dramatically, increasing the need for the monitoring of environmental contaminants, preferably without the need for complex and expensive peripheral equipment[41]. Microfluidic systems may be able to address some of these needs, but will need to handle sample preparation from a wide variety of sample matrices while maintaining compatibility with the detection of a variety of contaminants, including microorganisms, hydrocarbons, herbicides, and toxic metals[41], as well as emerging contaminants such as Splenda, siloxanes (widely used in consumer products), and synthetic musks (widely used fragrance additives)[45]. The fact that many of these pollutants are only present at extremely low concentrations further complicates the problem, introducing the need for sample pre-concentration in many cases. The unique capabilities of microfluidic devices may enable low-cost monitoring of these and other pollutants, allowing studies to monitor both acute and chronic effects of how we as a species choose to interact with our environment.

5.9 Overview of Microfluidic Diagnostics for Use at the Point of Care

Currently, there are many POC diagnostic tests on the market and even more emerging through the research pipeline as the need for these tests becomes increasingly recognized. Current POC tests vary in type, cost, sophistication, and efficacy, leaving much room for improvement in most cases. The two major types of current POC diagnostics on the market are channel-based microfluidic tests and lateral flow tests. The emerging platform of paper-based microfluidic tests

offers another solution that can combine the automation capabilities of channel-based microfluidic platforms with the low cost of lateral flow tests.

5.9.1 Channel-based Microfluidics

Microfluidics refers to the use of systems that manipulate fluid through channels with at least one dimension less than 1 mm. Microfluidics date back to at least the 1970s[46], with an uptick in interest in the 1990s and the push toward ‘‘micro total analysis systems’’ (MicroTAS)[47]. These systems utilized defined channels fabricated in materials such as glass, PDMS, and plastic laminates, combined with external pumps to deliver fluid through the channels[48]–[50]. These microfluidic systems feature several attributes that are ideal for rapid diagnostic testing, including process automation, fast diffusion times, and the need for only small (microliter) sample volumes[2], [51]. For these reasons, several microfluidics-based POC tests have been developed. We refer to these channel-based microfluidic systems as ‘‘traditional microfluidics’’, as opposed to the paper-based systems.

5.9.1.1 Current Microfluidics-based Platforms

The GeneXpert from Cepheid has greatly aided the diagnosis of tuberculosis (TB), including drug-resistant forms[52]. The GeneXpert MTB/RIF test, endorsed by the WHO in 2010, utilizes microfluidics to perform nucleic acid testing of *Mycobacterium tuberculosis*, obtaining a result within two hours[53]. The GeneXpert system consists of a fairly sophisticated instrument that performs most of the testing functionality and disposable, one-time-use cartridges on which the testing reagents are stored[54]. While the GeneXpert has greatly increased the speed of TB diagnosis, reducing mean testing-to-treatment times from 56 to 5 days in one study[52], the instrument is too expensive and requires too much infrastructure (*e.g.* electricity) to be used in very remote settings. Even at special negotiated prices for low-resource countries, the instrument

still costs $17k, plus $10 for every one-time-use cartridge[55]. For these reasons, the GeneXpert is recognized as a solution primarily for centralized laboratories within developing countries[10], [56]. As of the third financial quarter of 2012, 4,660 modules and 1,482,550 cartridges had been sold, with half of the cartridge sales in South Africa. Unfortunately, this technology will not reach the 60% of patients at the peripheral level (see Figure 4), and according to Pantoja *et al.*, will require further funding increases and/or price reductions to be financially viable in low-income countries[57].

The iSTAT from Abbot Diagnostics is a portable analyzer of a panel of common blood analytes used for patient monitoring[10], [59]. This handheld device is based on a microfluidic format that couples the fluid flow to electrochemical detection systems for the measurement of blood chemistries and electrolytes[10], [59]. Despite its utility, the iSTAT is still too expensive for many low-resource settings and is rendered useless in settings where maintenance is not possible when it breaks

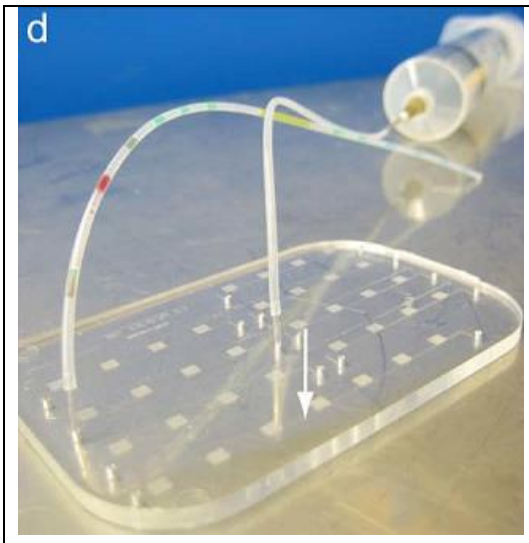

Figure 7: The ‘‘mChip’’ by Sia and colleagues, a low-cost, microfluidic replacement for ELISA testing[58]. Reprinted from Macmillan Publishers Ltd, Nature Medicine, 17, 1015–1019, copyright 2011.

Finally, the Sia group demonstrated the mChip (Figure 7), a great example of a low-cost microfluidic diagnostic system[58]. The mChip essentially performs the enzyme-linked immunosorbent assay (ELISA), but in a simple microfluidic format that includes an automated reader and comes at one-tenth of the cost of a traditional laboratory ELISA[58]. The Sia group used injection-molded chips from polystyrene and cyclic olefin copolymer, allowing for significantly reduced

cost compared to microfluidic chips created from polydimethylsiloxane (PDMS) via photolithography[58]. During field-testing in Rwanda, the mChip was able to simultaneously detect HIV and syphilis from 1 mL of whole blood with sensitivities and specificities comparable to laboratory ELISA[58]. To eliminate the need for pumps, the first version of the mChip utilizes a simple plastic syringe to drive fluid through the chip[58]. This creative approach is extremely low-cost, which is important for resource-poor settings, but the manual manipulation of reagents required by this method is not ideal, especially for untrained users. A more recent iteration of the mChip described by the Sia group addressed this issue by incorporating the fluidic handling into the handheld reader, creating a fully integrated portable device[60]. While much more user-friendly, this integrated mChip device is significantly more expensive (estimated <$1000), demonstrating a critical trade-off that exists for channel-based diagnostics.

5.9.2 Paper-based Microfluidics

Based on the continued need for low-cost, easy-to-use POC diagnostics, a new type of test has emerged: the paper-based diagnostic test. The use of paper in biological testing is actually a decades-old technique, most notably used in lateral flow test strips, which are discussed in detail later. The newly emerging paper-based diagnostic tests, however, are based on the concept of paper microfluidics–or Microfluidics 2.0[61]–which combines the simplicity of lateral flow tests with the sophistication of microfluidic-based tests to achieve an intermediate format that is highly suitable for POC use. The principles of paper microfluidics and current paper-based diagnostic platforms are discussed in later sections.

5.9.2.1 Principles of Paper Microfluidics

The hallmark of all paper-based diagnostic systems is the use of ‘‘paper’’ as the primary assay substrate. While paper in the literal sense refers to the everyday writing material made from

cellulose pulp, the paper microfluidics community broadly defines ‘‘paper’’ as any porous material that takes the form of a thin sheet[62]. This broad definition of paper will be used herein.

Paper is an ideal substrate for POC bioassays for many reasons. First, paper materials are generally inexpensive, allowing paper-based devices to be widely affordable and accessible[62], [63]. Second, paper is highly compatible with biological and chemical reagents and amenable to the storage of such reagents in dry form[62], [63]. These features enable long shelf lives for paper-based diagnostics, as have already been demonstrated by lateral flow tests[64]. Third, the porous structure of paper provides both a high internal surface area and short diffusion distances, allowing for high adsorptive capacity and fast reaction times, respectively[62], [63], [65]. Finally, and perhaps most importantly, paper affords the passive wicking of fluids by capillary action, eliminating the need for external pumps or power sources and thereby significantly reducing the cost of paper-based systems relative to their microfluidic counterparts[62], [63], [66].

5.9.2.2 The Ubiquitous Paper-based Diagnostic: The Lateral Flow Test

Lateral flow tests (LFTs) are the most ubiquitous commercially available point-of-care diagnostic. First gaining popularity in the 1980s for pregnancy testing[67]–[69], LFTs are now used for testing of many analytes, including disease markers in humans and animals, environmental and agricultural contaminants, drugs of abuse, and biowarfare agents[67], [68]. The widespread use of LFTs has propelled this technology into a $2.3 billion market, with pregnancy tests still comprising the largest market share[67]. In fact, 10 million lateral flow tests are manufactured each year for pregnancy testing alone[9].

A lateral flow test is based on a simple strip of porous membrane, typically nitrocellulose, which both allows fluid flow through the strip and serves as the substrate on which the detection reaction takes place[64], [68] (Figure 8). This porous strip is in contact with an absorbent pad on the distal end, which promotes wicking, and a series of sample and conjugate pads on the proximal end, where the assay begins. The conjugate pad contains dried detection antibody for the target analyte that has been conjugated to a visible label, typically gold nanoparticles. Two lines are pre-printed on the porous strip: 1) a test line containing antibody that specifically captures the target analyte of interest and 2) a control line containing antibody that captures excess gold-labeled detection antibody. To start the assay, the user simply applies the patient sample (usually blood, urine, or saliva) to the sample pad, which rehydrates the gold-labeled detection antibody and wicks through the porous membrane, allowing this antibody to bind the target analyte, if present. This antigen-antibody complex (if present) is then bound by the capture antibody at the test line, generating a pink color in this region due to the accumulation of gold nanoparticles. The control line also turns pink due to the binding of excess gold-labeled antibody, indicating that the test has functioned properly and the reagents have reached the end of the strip.

Due to their low cost and ease of use, lateral flow assays have found utility for diagnostic testing in both low-resource settings, such as clinics in the developing world and the battlefield, and POC settings in high-resource countries, such as doctor's clinics, emergency rooms, ambulances, and the home[3], [67], [70], [71]. In the developing world, lateral flow tests for infectious diseases such as malaria, influenza, and dengue fever have been important, yet imperfect, tools for the diagnosis of disease[72]–[74]. In the developed world, lateral flow assays have most commonly been used for at-home ovulation screening and pregnancy testing[67], but

are gaining increasing reach. For example, OraQuick[75], the first commercially available home HIV test, is now available in United States pharmacies without a prescription, and a preliminary study has found that usage of these at-home tests has resulted in decreased HIV transmission in a high-risk population[76].

Lateral flow tests have therefore played a significant role in establishing POC testing as a valid means of medical diagnosis, and the widespread success of lateral flow assays is undoubtedly related to their simplicity. Despite this success, LFTs often suffer from low sensitivity, as compared to gold standard laboratory-based tests[67], driving the need for more accurate POC tests.

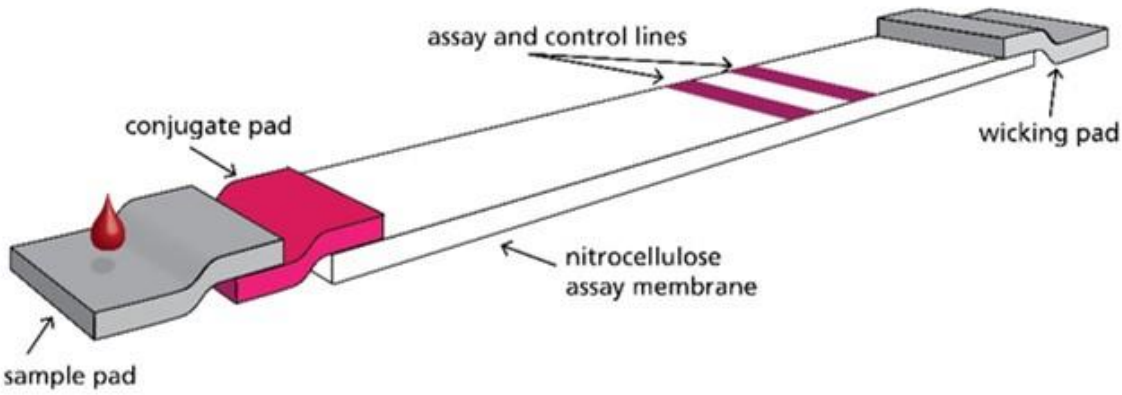

Figure 8: Illustration of a typical lateral flow test (LFT). Courtesy of Gina Fridley.

5.9.2.3 Current Paper-based Platforms

While paper chromatography, blotting assays, and lateral flow tests have existed for decades, the recent renaissance of novel paper-based diagnostic platforms began in the late 2000s with the work of George Whitesides' group[66], [77]. Recognizing the benefits of paper-based systems and their suitability for POC use, several different paper-based platforms and subsequent

iterations have since been developed. These platforms fall under two main categories: microfluidic paper analytical devices (μPADs) and two dimensional paper networks (2DPNs), as reviewed below. All platforms utilize some form of patterning to create flow channels in a porous medium that are hydrophilic relative to a hydrophobic barrier[63]. In general, paper-based microfluidic platforms are poised to bridge the gap between sophisticated channel-based systems and simple but less accurate lateral flow tests. While both channel-based microfluidic diagnostics and lateral flow tests can be highly effective for certain applications, we view paper-based diagnostics as the current platform that most widely fulfills the ASSURED criteria[8], as enumerated in Table 1.

5.9.2.3.1 Microfluidic Paper Analytical Devices (μPADs).

The original paper-based device of the paper resurgence was the microfluidic paper analytical device (μPAD), developed in the laboratory of George Whitesides[66], [77]. Basic two-dimensional μPADs feature a flow path consisting of a single inlet channel that diverges into multiple analyte channels, as shown in Figure 9A. These flow paths were initially created using photolithography to pattern hydrophobic channel barriers onto a cellulose substrate, a technique that was carried over from PDMS microfluidics[77]. Since then, most two-dimensional μPADs have been fabricated using wax printing to deposit the hydrophobic barriers that define the flow channels within the cellulose substrate[78]. Three-dimensional μPADs have also been developed (Figure 9B), created by the stacking of multiple layers of porous media (typically cellulose) and adhesive material[79]–[81]. The flow channels within each layer are designed to interact strategically with those of the other layers to achieve three-dimensional flow paths that fit compactly into a small material footprint.

Many examples of diagnostic tests have been developed using μPADs. These tests include the colorimetric detection of total glucose and protein in urine (*e.g.* urinalysis)[77], [79], the fluorescence-based detection of β-galactosidase using a fluidically activated battery[82], and the colorimetric detection of particulate metal in aerosols as a monitoring tool for occupational exposure[83]. μPADs have also been used in a liver enzyme test to monitor the health of patients who are taking combinatorial medications for HIV and/or tuberculosis[84], which is currently in field-testing[85]. Additionally, μPAD technology is continually being developed, and there is currently a large focus on incorporating printable electronic elements on μPADs[62], [86], [87]. Overall, the μPAD represents a useful paper-based platform, especially when multi-analyte detection is desired. However, demonstrations of μPADs to-date have been mostly limited to detection steps that employ simple, single-step chemical or enzymatic reactions.

Table 1: Comparison of the ability of three microfluidic diagnostic platforms to fulfill the ASSURED criteria. This assessment is based on each platform as a whole, while individual devices may vary in their characteristics. Overall, emerging paper-based microfluidic technologies seem best-suited to serve as diagnostics in low-resource settings.

	Channel-based microfluidics	Traditional lateral flow tests	Emerging paper-microfluidic platforms
	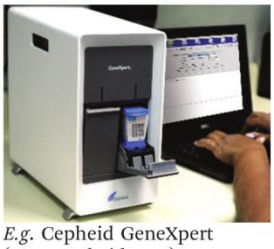 *E.g.* Cepheid GeneXpert (www.cepheid.com)	 *E.g.* Dengue NS1 Ag LFT (Courtesy of Yager Lab)	 *E.g.* 2DPN (Courtesy of Tinny Liang)
Affordable		✓	✓
Sensitive	✓		✓
Specific	✓		✓
User-friendly		✓	✓
Rapid & robust	✓	✓	✓
Equipment-free		✓	✓
Deliverable to end user		✓	✓

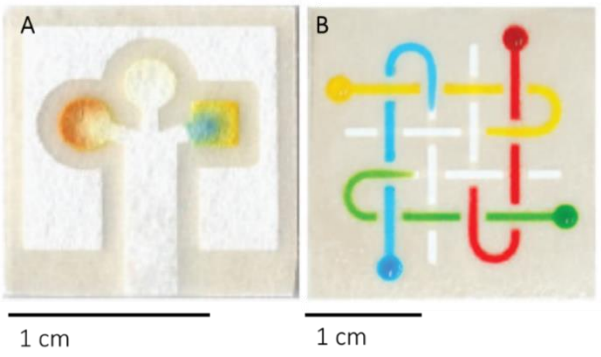

Figure 9: Examples of (A) two-dimensional[66] and (B) three-dimensional[79] μPADs. (A) Adapted from Anal. Chem., 82(1), 3–10. Copyright 2009, American Chemical Society. (B) Adapted from PNAS, 105(50), 19606–19611.

5.9.2.3.2 Two-dimensional Paper Networks (2DPNs).

Our own group in the Yager, Lutz, and Fu laboratories pioneered the development of the two-dimensional paper network (2DPN). This paper-based platform utilizes the shape and spatial arrangement of the paper substrate to control fluid flow and achieve automated, multi-step processing. These devices are made from porous nitrocellulose, in which flow paths are physically cut from the parent sheet, typically using a CO_2 laser cutter. This method represents a simple way to create flow pathways within the porous substrate and eliminates the need for patterning of additional materials to create hydrophobic barriers.

To date, our group has demonstrated many capabilities of 2DPNs. In particular, Fu *et al.* demonstrated that the timing of fluid delivery could be tuned based on the geometry of the network[88], [89]. Importantly, the use of multiple inlet legs and a single outlet leg allows for the delivery of multiple reagents over a given detection region (Figure 10)[89], [90]. This multiple input leg format has been used, in combination with a folding-activated card platform, to

demonstrate the chemical amplification of gold nanoparticle-based signal[91], the improvement in sensitivity of a lateral flow test for pregnancy[92], and the achievement of a malaria assay with sensitivity comparable to bench-top ELISA[93]. Additional tools have since been demonstrated by our group for use in 2DPN devices, such as mixing and dilution[94], flow visualization[95], and the use of sugar barriers to achieve timing delays without the expansion of the 2DPN footprint[89]. The Richards-Kortum group has also made significant contributions to the 2DPN platform, demonstrating a 2DPN folding card that performs isothermal amplification and subsequent detection of HIV DNA[96]. Finally, Apilux *et al.* recently demonstrated a nitrocellulose-based device for an automated ELISA[97]. Although these investigators employed inkjet printing of hydrophobic barriers, instead of laser cutting, the device utilizes the geometry of the paper network to control flow and achieve multi-step processing, making it a prime example of 2DPN technology. Overall, the 2DPN format is ideal for bioassays employing biological detection reagents and offers the advantage of multi-step processing, which can be used to achieve sample preprocessing, signal enhancement, and even simple rinsing to improve signal-to-noise ratios.

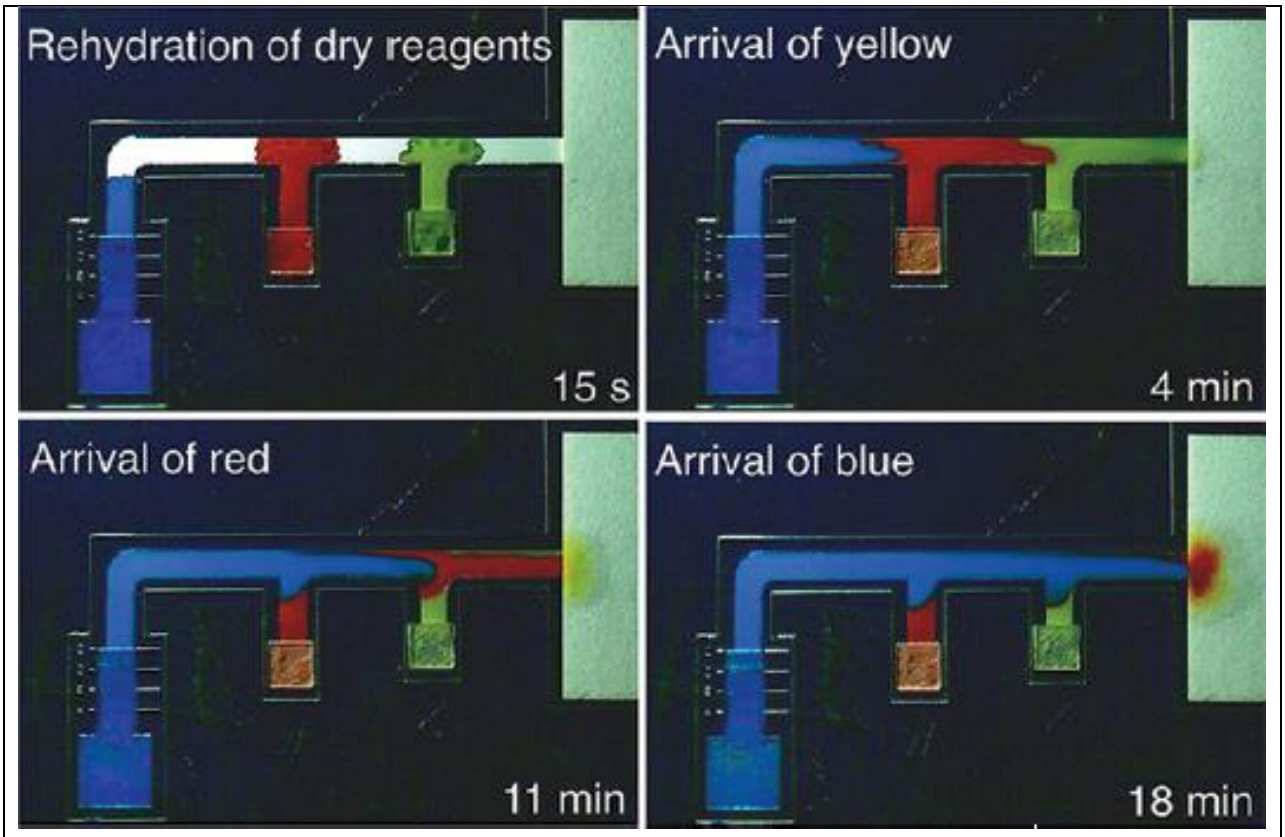

Figure 10: Demonstration of the multi-step reagent delivery afforded by 2DPNs[93]. Reprinted from Anal. Chem., 2012, 84(1), 4574–4579.

5.9.2.3.3 Other Paper-based Devices.

Since paper microfluidics is still a new and growing field, many opportunities for innovation still exist, both in terms of expanding the μPAD and 2DPN platforms and in regard to developing entirely new platforms. One prime example is the recent work of the Derda group demonstrating paper as a low-cost scaffold for cell culture[98] (Figure 11), proving that porous media can do more than provide capillary pressure to drive fluid flow. In this demonstration by Funes-Huacca *et al.*, hydrophobic inks are patterned onto sheets of paper, sandwiched between packing tape on one side and a PDMS membrane on the other. This setup provides a bacterial culture grown on the paper substrate with necessary gas exchange, but prevents evaporation of

the cell culture media. The authors went a step further, showing that the devices could be fabricated using simplified techniques amenable to the high school classrooms in which they were optimized. Based on retail pricing, Funes-Huacca *et al*. estimate that a simplified production facility could be set up for $1–2k. In addition, on-site production was demonstrated at the 1st annual Diagnostic Workshop in Nairobi, Kenya, highlighting the feasibility of paper-based cell culture in low-resource settings when culture-based diagnostic testing is required.

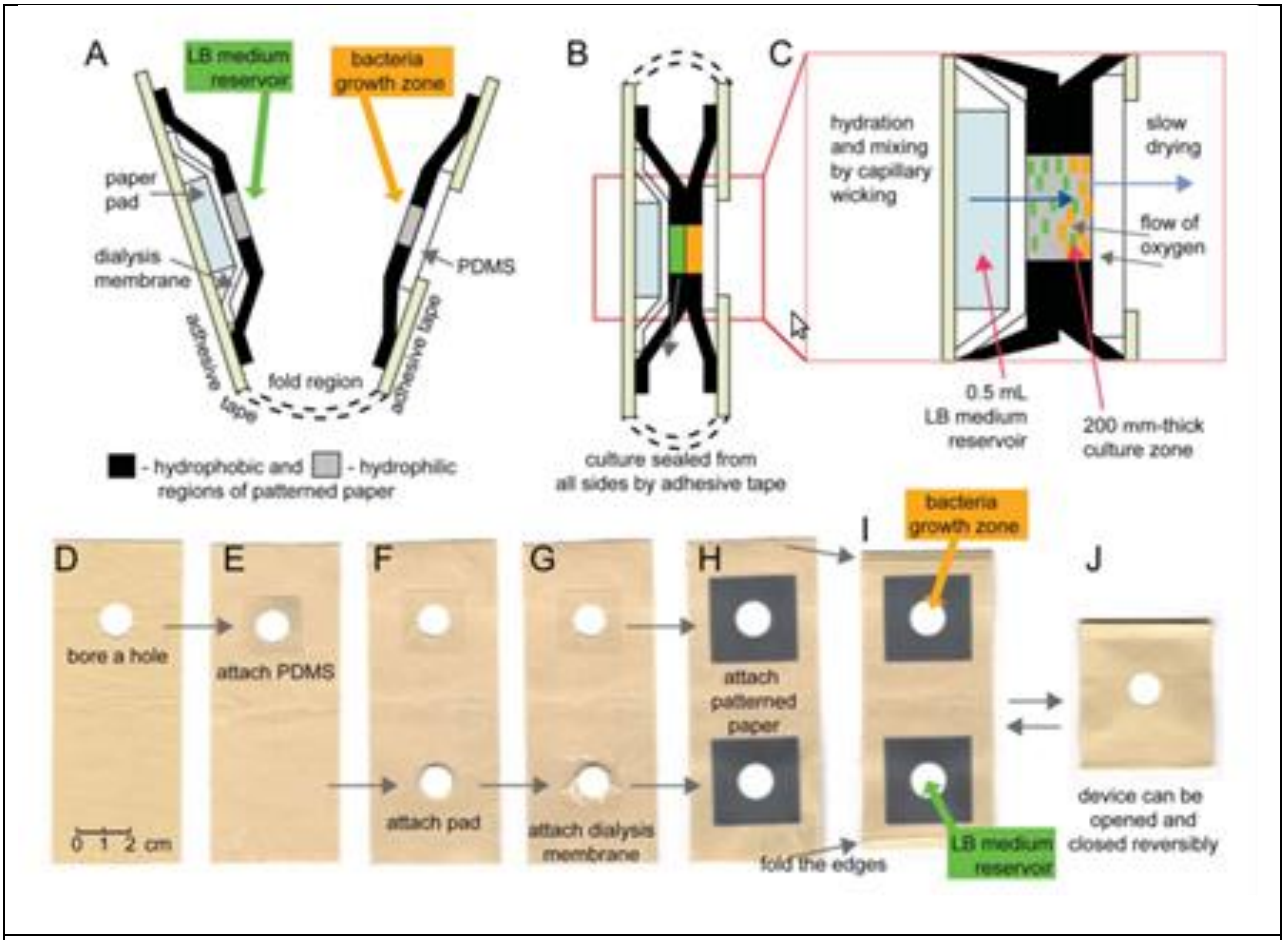

Figure 11: Paper-based cell culture, demonstrated by Funes-Huacca *et al*.[98] Reprinted from the Royal Society of Chemistry.

5.10 Enabling All Aspects of Diagnostic Testing in Low-resource Settings: Examples of and Opportunities for Microfluidics (Channel-based and Paper-based)

No matter the number of clever techniques developed by microfluidics focused academic groups and startup companies regarding fluid handling, signal detection, and fabrication, a successful diagnostic assay requires that the user transform a sometimes complex biological signal into a human-readable output[99]. Complicating this effort, many of the peripheral amenities (pipettes, clean water, reliable electrical power, etc.) common in higher-resource laboratories (including those in which these techniques are developed) are not available in the point-of-care. Additionally, even if appropriate diagnostics and supplies are available, adoption and scale-up can be hindered by economic, regulatory, policy-related, and user perception issues, along with cultural barriers[56]. The manufacturing and disposal of a diagnostic device must also be considered and designed for. Following is a non-comprehensive overview of some of the factors specially affecting point-of-care diagnostics in low-resource settings that should be considered by technology developers. Importantly, technologies that address and integrate all of these aspects will be best-suited for adoption and use in global health diagnostics.

5.10.1 Transportation and Storage of Devices in Low-resource Settings

Cold chain capacity and reliability is a well-known problem in vaccine delivery[5]. If the required reagents of a diagnostic assay require refrigeration, a reliable cold chain must be in place for a given region to have access to the diagnostic. The problems regarding temperature control do not stop when the supplies are delivered; communities are often not equipped or educated regarding best practices regarding storage of perishable reagents[100].

In the absence of a reliable cold chain, alternative approaches are necessary for keeping assay reagents functional. Storing reagents in anhydrous form on the device is one option, and can have the additional benefit of reducing the number of steps the assay user needs to perform[101]. The dried form of the reagent weighs less, and takes up less volume. Stevens *et al.*

show that anhydrous gold-antibody conjugates stored on a device in sugar matrices can be rehydrated after 60 days at elevated temperature while retaining 80–96% of their activity. The assay developed by Fu *et al.*[93] demonstrates that dried reagents can also be incorporated into a 2DPN comprised of glass fiber conjugate pads (within which the reagents are stored in a sugar matrix), a nitrocellulose section comprising the ‘‘legs’’ and detection region of the assay, and a cellulose wicking pad (Figure 12).

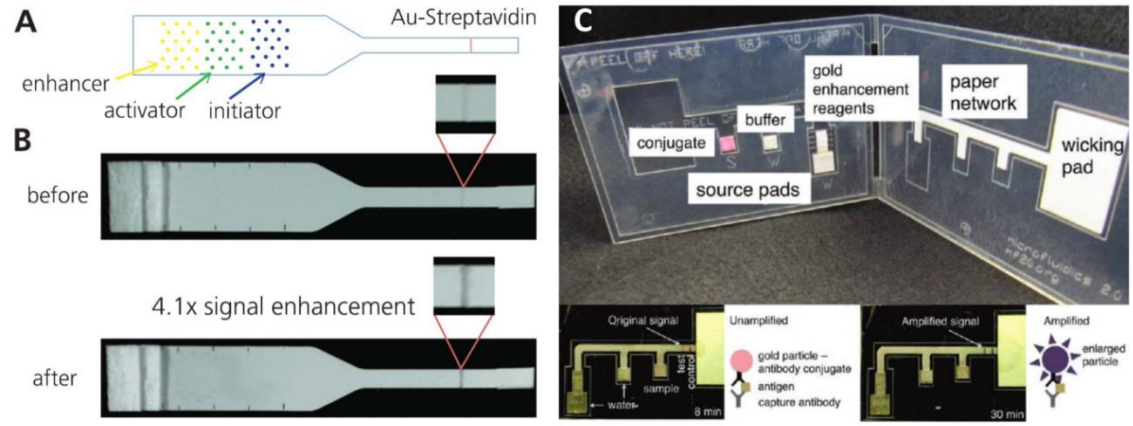

Figure 12: Dry reagent storage and rehydration. In both of these examples, reagents are stored in dried form and stabilized in a sugar matrix. On the left, reagents are stored directly on nitrocellulose membranes[102], whereas on the right, discrete glass fiber pads are used[93]. (A–B) Reprinted from the Royal Society of Chemistry. (C) Reprinted from Anal. Chem., 2012, 84(1), 4574–4579.

Storing reagents on separate pads from the nitrocellulose media used for the backbone of the assay requires additional parts and manufacturing steps. Fridley *et al.*[102] have demonstrated a methodology that eliminates some of these complexities while enabling precise control over reagent temporal and spatial release by preserving the reagents directly on the nitrocellulose membrane (Figure 12). Novel functions enabled by this format include the creation of uniform reagent pulses, mixing of rehydrated reagents, and tuning of temporal reagent delivery. A gold enhancement assay is demonstrated where gold enhancement reagents are sequentially combined to produce a 4.1x signal enhancement.

5.10.2 Specimen Collection

Specimen-collection strategies utilized in well-equipped clinics may not necessarily translate directly to lower-resource settings, and device performance is directly impacted by how samples are obtained. Cira *et al.* describe a device that only requires a single pipetting step to load the sample into multiple chambers[103] (Figure 13). The pressure differential used to drive the fluid flow through the device is provided by gas adsorbing properties of PDMS: the device contains multiple wells molded in PDMS, and is vacuum degassed after assembly. The user removes the device from its vacuum-sealed packaging, and pipettes a drop of sample onto the inlet port. The degassed PDMS then provides a negative pressure, pulling sample into each of the wells. These wells are pretreated with antibiotic and used to test for minimum inhibitory concentration of the antibiotic. Each self-loaded well holds roughly 1 mL. The device was shown by the authors to more closely mimic the protocol developed by the US Clinical Laboratory and Standards Institute more closely than its less automated counterparts.

Begolo *et al.* describe an additional automated sample collection device, which has the added capability of long-term stabilization of samples through desiccating in the presence of a stabilization matrix[104]. This microfluidic device is designed using the SlipChip-based methodology, which has repeatedly been demonstrated by the Ismagilov group to translate simple user steps into complex microfluidic channel switching[105], [106]. Briefly, this style of device is comprised of multilayer channels, and a one-dimensional ‘‘slip’’ action results in channel connections to be broken and established, rerouting any number of microfluidic channels in the process. The sample collection and preservation device described by Begolo *et al.* fills automatically, due to a pressure developed by the closure of the device lid after sample addition. After the automated filling of sequential fluid chambers, a pre-loaded desiccant dries the sample within the chambers. This methodology is shown by the authors to result in highly reproducible

sample volumes, and the preserved samples are shown to be recoverable with minimal degradation without refrigeration, demonstrating compatibility with environments beyond the reach of an established cold chain.

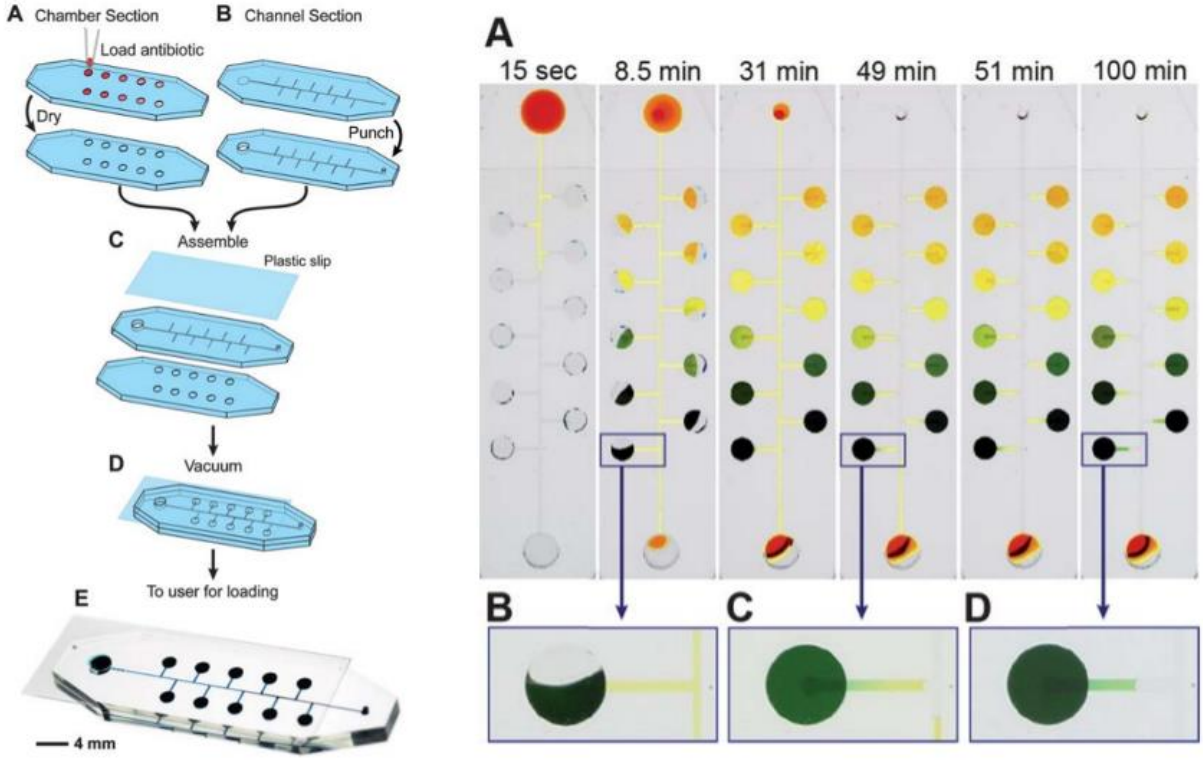

Figure 13: Sample collection demonstrated by Cira et al.[103]. After assembly, the device is vacuum-degassed and placed in a sealed package. The sample is drawn into the chambers by the negative pressure provided by the degassing. Reprinted from the Royal Society of Chemistry.

5.10.3 Sample Preparation

Blood, plasma, saliva, serum, sputum, stool, and urine are sample types from which clinically relevant analytes could be quantified. Before an analyte can be quantified, often the sample will need to be concentrated, filtered, or purified from substances (including proteins[107]) that may interfere with the assay[9]. Integrating these functions into the diagnostic device (rather than assuming the user has the time, knowledge, and amenities to prepare the sample before introducing the prepared sample to the diagnostic) is preferred. For example, Marshall *et al.*

demonstrate an integrated device capable of lysing cells through heating and purifying nucleic acids using isotachophoresis[108]. Cell lysis and DNA extraction kits (*e.g.* Qiagen) are often used in laboratories to prepare samples, but require centrifugation, heating steps, and quite a bit of waiting, making other methods of lysis and DNA isolation necessary for POC NAATs. The Klapperich group at Boston University demonstrated an on-chip sample preparation platform for lysis and DNA extraction of both Gram-negative and Gram-positive bacteria[109]. This platform utilizes a hybrid chemical/mechanical method of cell lysis, where a blood/bacteria suspension is first treated with a chaotropic buffer containing guanidinium thiocyanate (GuSCN), proteinase K, and detergents. GuSCN, used as part of the lysis buffer, is additionally necessary for the solid phase extraction, causing the DNA to preferentially bind to the silica particles. After extraction and rinsing, the bacterial nucleic acids are purified and ready for amplification.

As a more universal alternative to chemical techniques, which often require purification steps to keep from interfering with the DNA amplification, mechanical techniques inspired by bench-top bead beaters have been developed to lyse cells for nucleic acid amplification[110]. The OmniLyse cell lysis device currently being sold by ClaremontBio has been shown by Vandeventer *et al.* to have similar lysis capabilities to bench-top bead beaters[111]. Mechanical lysis methods like bead beating have the advantage of not using chemicals (for example, guanidinium thiocyanate salts) that need to be removed from the sample before subsequent assay steps, and also need to be safely handled and disposed of after completion of the assay; it is important to remember the disposal method of choice in many lower resource settings is incineration[3]. Benchtop bead beaters (Figure 14A) require electricity, and are quite heavy, making chemical lysis methods on the surface more desirable than mechanical means. The OmniLyse device shows that bead beater-like lysis efficiency can be accomplished with a very

small device, smaller than the three AA batteries used to power it (Figure 14B). The device consists of a small motor, plastic lysis chamber containing beads and a rotor, and a syringe used to pass the sample through the lysis chamber multiple times. A battery pack with an on/off switch powers the device, with one battery pack having sufficient energy to run many sequential samples. Though the manufacturer claim that ‘‘the kits can then be simply thrown away without any harm to the environment’’[112] is questionable, the disposal of alkaline batteries and other associated waste products may be simpler than agents such as chaotropic salts.

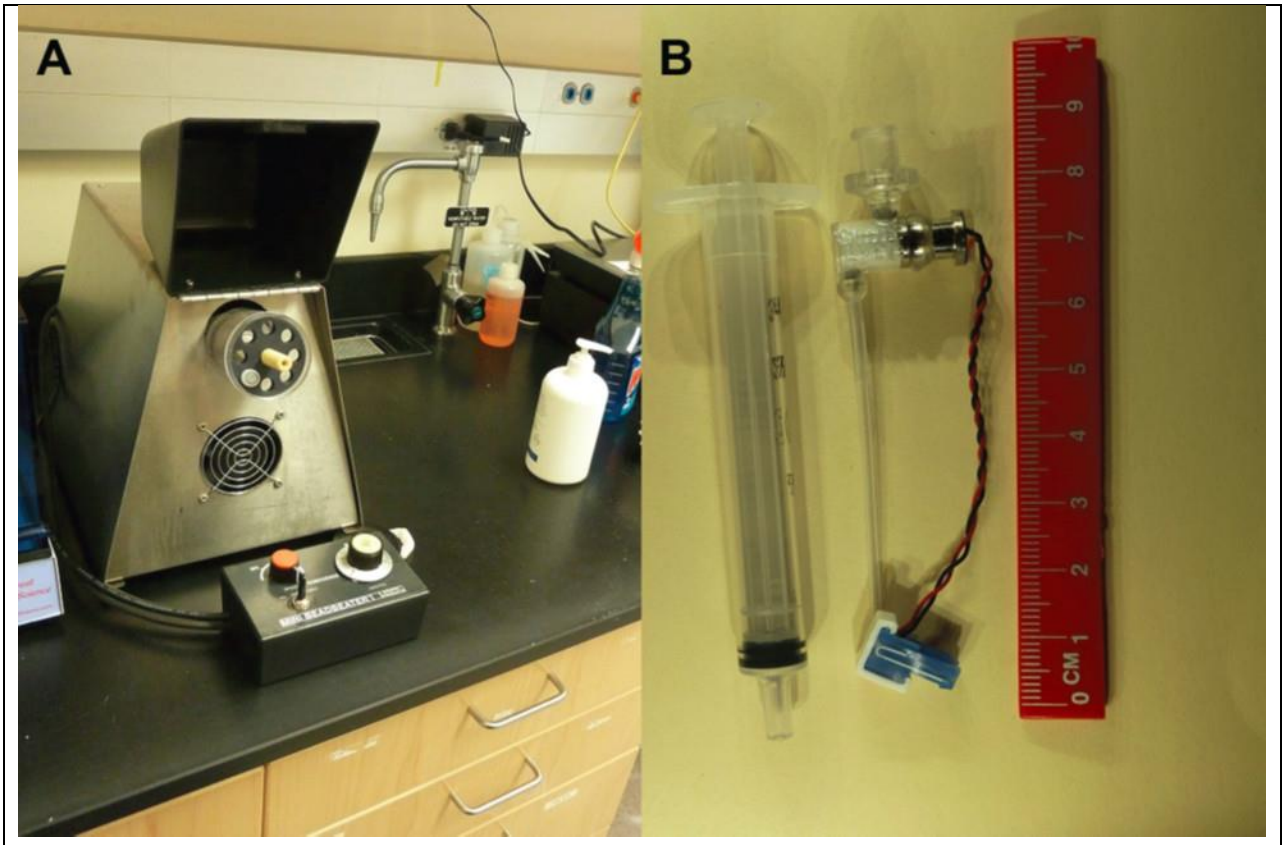

Figure 14: (A) Bench-top bead beater compared to (B) OmniLyse mechanical cell disruptor. These two devices, while being quite different in size, weight, and power requirements, were shown by Vandeventer et al.[111] to have similar efficacy in lysing *Bacillus subtilus* spores and *Mycobacterium bovis* BCG cells.

5.10.4 Running the Assay

A great number of assays have been developed which utilize microfluidic technologies, covered elsewhere in this section and in review articles. Rather than attempt to do all of these technologies justice within the confines of this section, the reader can refer to two comprehensive review articles which do a great job of covering microfluidic point-of-care diagnostics[9], [11]. This section will focus on some unique challenges of running diagnostic assays in lower resource settings, namely the lack of reliable electrical power, reagents, and supplies. Unlike in better-equipped laboratories, the technician cannot be expected to have a supply of pipette tips, sterilized water, and a 120 volt electrical receptacle.

Material compatibility with assay chemistry is perhaps no more complex than in nucleic acid amplification assays. Nevertheless, the potential value of a self-powered microfluidic device with the sensitivity and specificity of nucleic acid amplification in both low-resource settings and in the point-of-care in higher-resource settings explains the high level of interest in this technology. Rohrman *et al.* demonstrated isothermal Recombinase Polymerase Amplification (RPA) of HIV DNA in a paper and plastic device[96] (Figure 15).

Many assays, like the isothermal RPA demonstrated by Rohrman *et al.*, require precision temperature control. PATH has demonstrated several platforms for this purpose. The non-instrumented nucleic acid amplification (NINA) platform[113], [114] is designed to heat PCR tubes containing reagents for isothermal nucleic acid amplification, including isothermal loop-mediated isothermal amplification (LAMP) to the required 63°C. This device uses a reusable thermos-shaped double-walled container as an insulating shell. Tubes are placed into an aluminum block, where they are surrounded by phase change material (PCM) that melts at the target temperature of the assay. Energy for heating is provided by the exothermic reaction of

calcium oxide (CaO) and water. The authors show that this setup can retain 63°C for an hour under the conditions tested (see Figure 16).

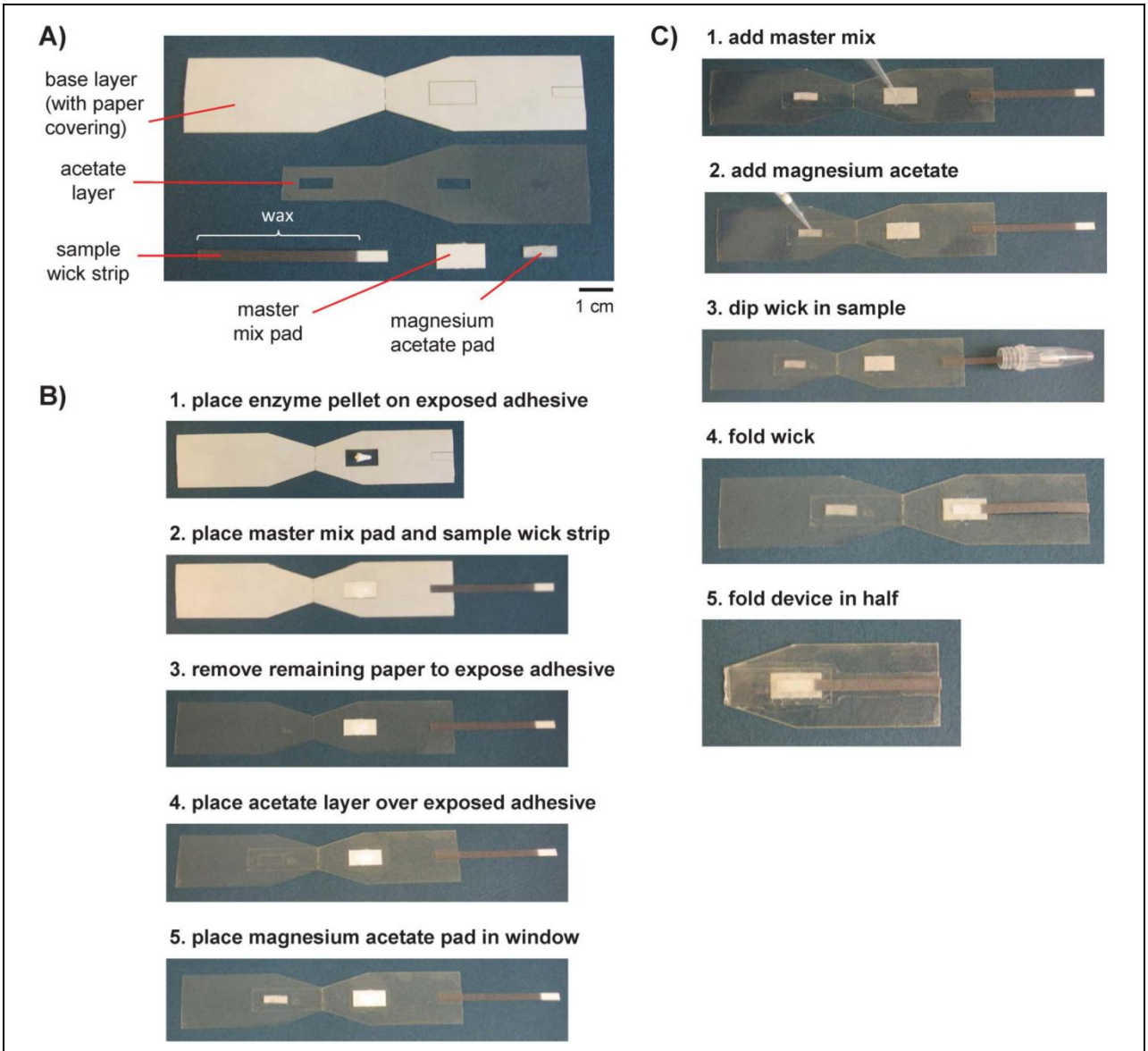

Figure 15: Isothermal nucleic acid amplification in porous media, demonstrated by Rohrman *et al.*[96] Here, the steps of the simple device construction and assay preparation are illustrated. Reprinted from the Royal Society of Chemistry.

A collaborative effort between PATH and our group at the University of Washington has produced a device[115] designed to heat reagents in a paper microfluidic format, which is optimized for a flat heated zone appropriate for reagents in a 2DPN. This prototype device was

designed to be integrated into a fully disposable device, dubbed the multiplexed analyte detection nucleic acid amplification test (MAD NAAT), and is currently being funded by the Defense Advanced Research Projects Agency (DARPA). The exothermic process chosen for this device is the reaction of a magnesium iron alloy and saline, the same fuel used in meal ready-to-eat (MRE) technology employed to provide heat meals away from the amenities of a kitchen. Shown in Figure 16, the fuel chamber is supplied saline by a blister pack located above. The temperature rise of the fuel is buffered by phase change material (PCM), providing a tightly controlled temperature to the sample region, which contains the assay reagents. Another chemical heater capable of heating without external power was developed by the Bau group at the University of Pennsylvania[116]. Here, the fuel chamber is provided water by a filter paper wick, which restricts the delivery of water and hence the reaction rate of the fuel. Temperature is again regulated using a phase change material, and the supplied heat is used to amplify *E. coli* DNA using LAMP.

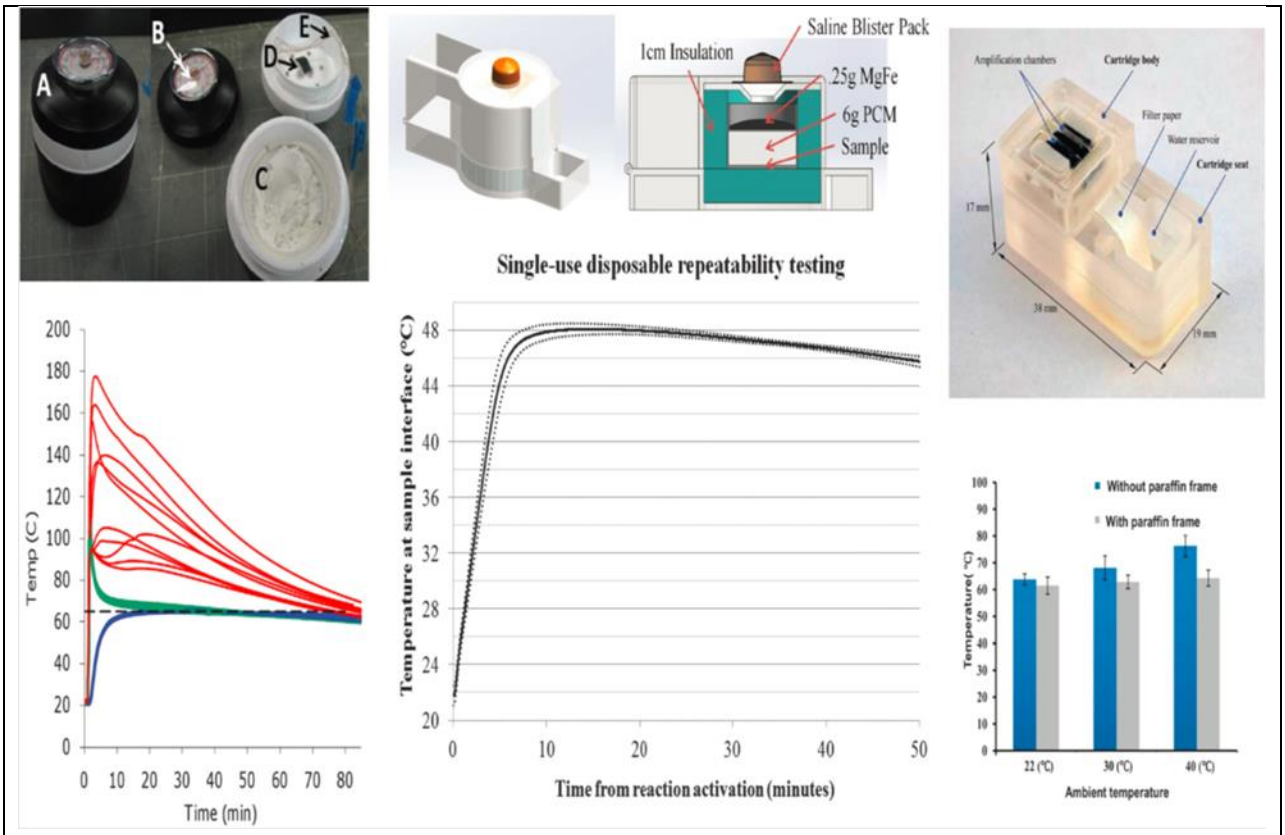

Figure 16: Comparison of different chemical heaters that can be used to implement point-of-care nucleic acid amplification assays. (LEFT) Thermos-based incubator demonstrated by LaBarre *et al.*[114] A: assembled incubator. B: incubator lid with integrated timer. C: Calcium oxide chamber provides heat from exothermic reaction with water. D: Assay tubes. E: thermocouple wires (not required for device operation, only for monitoring temperature). Temperature plot shows reliable achievement of a 63°C assay temperature (blue) over 10 replicate runs. Adapted from PLOS One. (CENTER) A single-use disposable design from Singleton *et al.*[115]. Isometric and cross-sectional views of device model. Temperature plot shows assay temperature average ± one standard deviation for 12 runs over time. Adapted from Singleton *et al.*, Proc SPIE, Microfluidics, BioMEMS, and Medical Microsystems XI, 86150R, 2013. (RIGHT) Cartridge heater from Liu *et al.*[116]. The addition of a paraffin phase change material regulates the assay temperature to 63 °C for three ambient temperatures. Reprinted from the Royal Society of Chemistry.

In developing world applications, the infrastructure necessary to provide external sources of electricity is often not present[6]. In addition to on-device commercially available batteries (AA, ‘‘button’’ Li-ion batteries, etc.), ‘‘fluidic batteries’’ can be constructed of galvanic cells incorporated into the device using paper microfluidic networks. Thom *et al.* showed that this type of power source can be used to power a ultraviolet light-emitting diode used to conduct an

on-chip fluorescence assay used for the detection of b–D-galactosidase[82]. Another great example of an on-chip power supply, demonstrated by Esquivel *et al.,* uses a microfluidic fuel cell[117]. Here, the authors demonstrate a micro direct methanol fuel cell, which has been incorporated into a microfluidic platform. In addition to providing electrical power, the CO_2 produced by the electrochemical reaction is utilized to provide a pressure for pumping liquids through the microfluidic channels.

5.10.5 Signal Read-out

The type of signal that is generated by an assay and the corresponding readout method require special attention by developers of diagnostics for low-resource settings. The first decision point is centered on whether the test needs to be quantitative (*i.e.* measures the amount of the target analyte present) or if it can be qualitative (*i.e.* determines whether or not the analyte is present at all). For many tests for infectious disease, the output can usually be qualitative, since the patient either does or does not have the given disease. For this reason, conventional lateral flow tests use qualitative evaluation of visual signal intensity to provide a simple yes-or-no answer. This type of read-by-eye signal can be achieved using any type of particle that absorbs light in the visible range of wavelengths, such as gold nanoparticles, latex beads, carbon black, or colorimetric enzyme substrates[118].

Tests that require a quantitative measure of the target analyte, such as glucose meters or HIV viral load tests, are necessarily more sophisticated than qualitative tests, and often require the use of an external reader to determine the result. A variety of methodologies exist to quantify signal intensity, and handheld readers[119] have been specifically designed to measure electrochemical, absorbance, reflectance, transmittance, fluorescence, or chemiluminescence signals. Not all quantitative tests require a reader, however. As an alternative to needing an

instrument to quantify signal, Pollock *et al.* have shown a multiplexed assay capable of reporting rapid, semi-quantitative measurement of two serum transaminases that are used to monitor for drug-induced liver injury[84]. Here, the authors optimize the device for users to ‘‘bin’’ the transaminase concentration into clinically relevant ranges visually using a color-reading guide. Multiple indicators for the same analyte can also be used to help the user visually determine analyte concentrations[120]. Additionally, quantification of analyte concentration through the use of fluidic timing elements that are incorporated into the device is another reader-less method that has been demonstrated[121]. Here, interaction of the analyte of interest and reagents patterned in the paper network cause a change in contact angle of the solution and pores of the paper network, which affects capillary flow rate. This flow rate can be compared to a reference and quantified, indicating analyte concentration.

Finally, cellular phones represent an increasingly useful tool to aid the read-out of both qualitative and quantitative assays. Cell phones have achieved extremely rapid market penetration in low-resource settings, which can largely be attributed to unreliable land-line infrastructure in these areas. In fact, Africa is now the second largest mobile phone market after Asia[11]. Phones equipped with cameras and fairly sophisticated processing capabilities are becoming increasingly present in low-resource settings, which could be a great asset for diagnostic tests.

Much interest has been shown in using mobile phone cameras for a variety of purposes in low-resource settings, from digitizing medical records (covered in the following section) to the quantification of diagnostic assays[122]. For cell phone-based diagnostics, it is important for the developer to determine whether it is most appropriate for the signal read-out algorithm to be performed on the phone itself, or for the phone to transmit the image to the cloud or other server

for remote analysis and subsequent notification of the result. While cell phones may provide the most utility for enabling quantitative assays, they can also be used to automate the read-out of qualitative assays and remove the error associated with manual user interpretation[119], [123], [124]. The cell phone also provides a useful means of connecting with the given health system as whole, which is discussed in the next section.

5.10.6 Data Integration into Health Systems

While achieving an actionable answer is the first order of business for any diagnostic test, integrating this data into the appropriate health system is an important next step, and one that is often overlooked by test developers. Connecting a diagnostic result with the health system can improve the management of a patient's condition, especially in remote areas where there is a lack of healthcare providers[23], [123], [124]. Integrating results of diagnostic tests into the health system is also important for epidemiological surveillance and effective public health management[123], [124].

A prime example of the need for better health systems integration is the state of medical records in the developing world. Physical paper forms remain an integral role in health systems data in low-resource settings, with this media being well understood, trusted, easy to use, and relatively low cost. The data contained within these paper records is not as easily aggregated, shared, or analyzed as digital data[125]. Digitizing paper forms is not a new design challenge, but the specialized systems that have been successful in developed regions are generally costly, and require maintenance and reliable electrical infrastructure. Recent work from the Open Data Kit team at the University of Washington demonstrates a smartphone application, ODK Scan (previously mScan), that uses computer vision to capture data from multiple-choice or bubble-format paper forms[125]. The authors used a low-cost stand fashioned from polyvinylchloride

(PVC) pipes and sheets of plastic, as shown in Figure 17, holding the smartphone steady and aligning it with the form. The ODK Scan software was demonstrated in this study to capture data with remarkable accuracy; even when the form was crumpled and filled out messily, accuracy was still over 80%. The accuracy of 19 other conditions tested was always over 90%, and usually (15/19) over 99%. Much data can be stored on a smartphone, which can be uploaded to a remote database when a network becomes available.

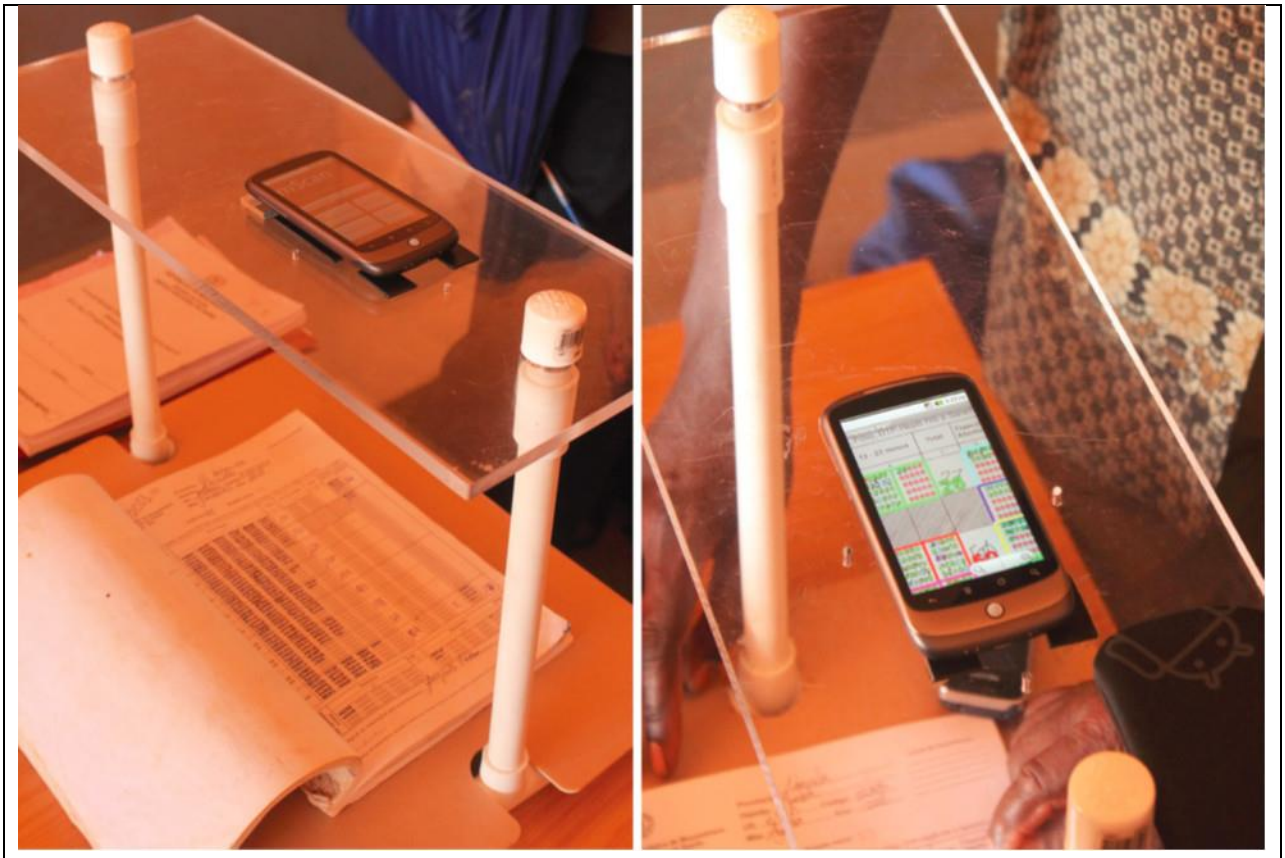

Figure 17: Medical record digitization using a mobile phone, demonstrated by Dell *et al*.[125] Image courtesy of Nicola Dell

Finally, the fully integrated version of the mChip from the Sia group[60] represents an excellent example of a microfluidic diagnostic system capable of communicating with the overarching health system. Not only does this device generate an HIV diagnosis from 1 mL of whole blood by automating an ELISA-type assay, but it also transmits the result to a cloud based

medical record system (Figure 18). This data integration allows the patient's data to be stored and accessed easily and enables the health system to track HIV incidence. While the device developed here is still fairly expensive (estimated <$1000) for some resource-poor settings, this work represents a great step forward for fully integrated diagnostic testing and may serve as a blueprint for other less expensive, potentially cellphone-based, systems.

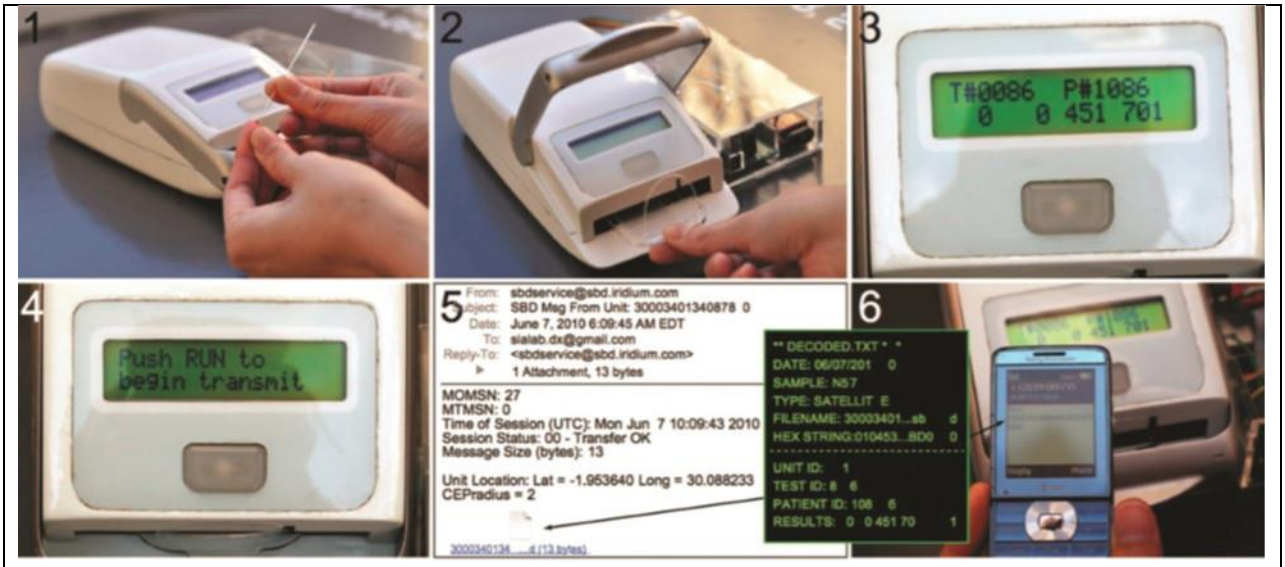

Figure 18: The fully integrated mChip system from the Sia group.[60]. This device plus- chip system performs ELISA-like diagnosis of HIV from 1 mL of whole blood and transmits the result to the patient's electronic health record stored on the cloud. Figure from Chin et al., Mobile Device for Disease Diagnosis and Data Tracking in Resource-Limited Settings, Clin. Chem., 2013, 59, 629–640. Figure reproduced from the American Association for Clinical Chemistry.

5.10.7 Disposal

Responsible design of diagnostics for any setting includes planning for disposal. Open outdoor incinerators are often utilized by hospitals in developing countries, and needle handling and disposal remain major challenges. Biosafety protocols, which protect workers and others in the community from infectious agents, are not always implemented[3]. Diagnostic devices need to be designed appropriately for the settings in which they will be used, and should minimize

waste[3]. Several representative images of disposal issues in low-resource settings are shown in Figure 19, highlighting the importance of planning for waste impact.

Figure 19: Photographs of medical waste in low-resource settings, presented in review by Yager *et al.*[3] (a) Medical waste in an open incinerator in Senegal (PATH). (b) Incinerator in Tanzania overflowing with medical waste (PATH). (c) Open incinerator in Nigeria (PATH). (d) Unsafe sharps disposal in a public waste dump in India (Mark Koska).

5.11 Conclusions

Many strides have been made in developing microfluidic technology in a way that could potentially improve the lives of people worldwide, but only a small number of lab-on-a-chip-based devices have been successfully commercialized[99]. The long-term impact of recently introduced instrumented systems like the Cepheid GeneXpert remains to be studied, but these

technologies are expected to greatly expand access to TB diagnostics to vulnerable populations. Success stories, such as the home pregnancy test and portable glucometers, illustrate the potential of low-cost, easy-to-use diagnostic technologies to be transformative. Future technologies under development, including more accessible point-of-care isothermal nucleic acid amplification assays, have the opportunity to expand the reach of microfluidics within global health. Creating standalone devices capable of these advanced assays requires that developers fully understand not only what it takes to transform a biological analyte into a human-understandable readout, but also the market and societal forces that will dictate whether such technology has a chance of being commercially viable. Finally, almost all microfluidic technologies being pursued for developing-world applications are also well-suited to tackle diagnostic challenges in the developed world, as low-cost, point-of-care testing represents a tremendously valuable capability in any country. Microfluidics-based diagnostics are therefore poised to improve health around the world, truly advancing the state of global health.

5.11.1 Acknowledgements

This introduction is adapted from[1]:

JR Buser*, CA Holstein*, and P Yager. "Microfluidic Diagnostics for Low-resource Settings: Improving Global Health without a Power Cord." Microfluidics for Medical Applications: 151.

*contributed equally to this work

6 Aim 1: Fluid flow in paper microfluidics: necessary parameter measurements and flow modeling

Fluid flow rate is critical in paper-based microfluidic devices, influencing interaction between flowing analyte and stationary capture reagents and device automation and timing. Parameters needed to predict flow rates in multiple-material porous networks are not available from manufacturers, resulting in a time-consuming guess-and-iterate approach to paper network design. In this work, porous media characterization techniques have been adapted to determine flow parameters critical to the operation of paper microfluidic devices. Membranes from several manufacturers were compared using a standardized protocol, and used to predict flow rates in multiple material porous networks. Using these parameters, in flow models has uncovered a near omnipresent partially-saturated flow regime which precludes the usage of the widely accepted flow rate models for paper microfluidics. Here, the goal is to adapt flow equations from hydrogeology for the use in paper microfluidic systems. Darcy's Law comes from the geological sciences, and is predictive for a subset of paper microfluidic systems where flowing sections of membrane are fully saturated. However, the majority of observed flow regimes are partially saturated, requiring more complex Richards equation modeling .

Main deliverable: Membrane parameter measurement and partial saturated modeling technique ***MS in prep.***

6.1 Background

Diagnostics comprise about 1.6% of total Medicare expenditures, yet an estimated 60–70% of medical decisions are based on their outcome[4]. While these numbers are for the US only, they highlight the notion that diagnostics are an extremely cost-effective tool in medicine. In the developed world, infrastructure exists to support advanced diagnostic procedures such as enzyme-linked immunosorbent assays (ELISAs), nucleic acid amplification tests (NAATs) like polymerase chain reaction (PCR), and bacterial cultivation, which remains widely used for microbe identification, epidemiology, and drug resistance testing[3]. These methods, in most current manifestations, require reliable electrical power, environmentally controlled laboratories staffed with trained personnel, and substantial equipment that often require regular maintenance and supply replacement. A cold chain must also be established for many diagnostics that use aqueous reagents, which is not so much a problem in the developed world, but is a very difficult challenge in much of the developing world[5].

In the developing world, much advanced equipment is in an unmaintained condition, or necessary infrastructure or supplies are unavailable, and advanced diagnostic procedures are unsupportable[6]. The tuberculosis (TB) diagnostic technology landscape recently published by UNITAID[18] indicates that there are currently no suitable TB diagnostics available at the peripheral level of healthcare, where 60% of the patients are seen. The fact that diagnostic tests for prevalent diseases are not available in formats compatible with low-resource settings not only contributes to a lower quality of life in those settings, but also results in incorrect treatments, potentially contributing to the emergence of drug resistant pathogens[3]. Enabling more complex diagnostics requires more advanced capabilities be incorporated into point-of-care devices.

Features like automated fluid sequencing, timing elements, and precision temperature control need to be built into diagnostic devices while keeping them inexpensive and simple to use[6]. Paper-based microfluidic devices have been shown to be capable of integrating these features and performing multi-step diagnostic procedures such as ELISAs and NAATs[93] [126] [96].

A parameter critical to the performance of paper-based microfluidic devices is the fluid flow rate, as it affects all time-dependent processes, for example the residence time of analyte with capture molecules, enzyme and other chemical kinetics, and device timing[93]. The Lucas-Washburn equation[127] has been used by our group[88], [90] and others[128] to describe the fluid flow rate in paper microfluidic devices. Unfortunately, this equation is based on assumptions that only hold for one-dimensional saturating flow in a single, homogenous porous membrane. The Lucas-Washburn equation cannot be used for prediction of fluid flow rate in multiple-material or two-dimensional porous membrane networks, heterogeneous membranes, or for partial-saturation flow regimes. Even the most simple lateral flow strips have at least two different porous membranes (nitrocellulose and a cellulose wicking pad).

Fortunately, Darcy's Law is of a form that can be used in two dimensions[129], and can be used for multiple porous membranes connected in series[88]. Darcy's Law defines the volumetric flow rate in porous media to be

$Q = \frac{\kappa A \Delta P}{\mu L}$	Equation 1

where flow rate (Q) is a function of membrane permeability (κ), cross sectional area perpendicular to flow (A), pressure difference between inlet and outlet (ΔP), viscosity of the flowing fluid (μ), and length of wetted membrane (L). Unfortunately, while Darcy's Law can be

used to model flow in multi-dimensional, multi-membrane porous networks, the permeability and capillary pressure parameters are not widely available, hindering its practical application.

The most common characterization performed by membrane manufacturers is capillary rise time, which is the number of seconds it takes for the fluid front to travel 4 cm from a fluid source in a constant width strip[130]. However, this characterization intertwines the permeability and capillary pressure parameters. These parameters can be separated for a capillary system by noting how high fluid rises under the influence of gravity. Unfortunately, for many porous membranes, the equilibrium height can be several meters, making the experiment slow and inconvenient. Likewise, many permeametry methods are limited in that they can only be applied to unbacked membranes[131]. Nitrocellulose membranes are often backed with a plastic sheet, onto which the membranes are cast during manufacturing, preventing measurement with this technique. Alternately, pore radius can be used to calculate permeability[129]. However, membrane pores have complex structure that is far from circular, so a radius is hard to define even if representative micrographs are available. Recent literature has estimated permeability based on the pore size provided by membrane manufacturers[129], or using only marginally related membrane types[88], but such estimates are uncertain at best.

Even if membrane parameters were fully characterized and reported by manufacturers, paper microfluidic device developers often need to modify the membranes in a variety of ways to run assays in a paper microfluidic format. Common modifications include blocking with proteins to prevent non-specific adsorption [51] and surface immobilization of capture molecules to enable test line reporting, and many such modifications involve steps that wash away proprietary additives used during membrane manufacturing. These modifications may change the capillary pressure, permeability, or other parameters of a membrane. Fortunately, the original apparatus

described by H. Darcy in 1856 can be adapted for the characterization of the membrane parameters used in Darcy's Law. We describe the adapted apparatus, its operation, and method for parameter determination in this work.

One more barrier to the practical application of Darcy's Law to paper microfluidic systems is the assumption of full saturation by the wetting front, which is often incorrect in realistic paper microfluidic systems. For instance, the geometry shown in Figure 20 results in the cellulose wicking pad only being ~60% saturated at the time the yellow dye solution is first visible throughout the entire pad. Luckily, this partially saturated flow regime is commonly encountered in hydrogeology, and so we turn to results in that field for a way forward.

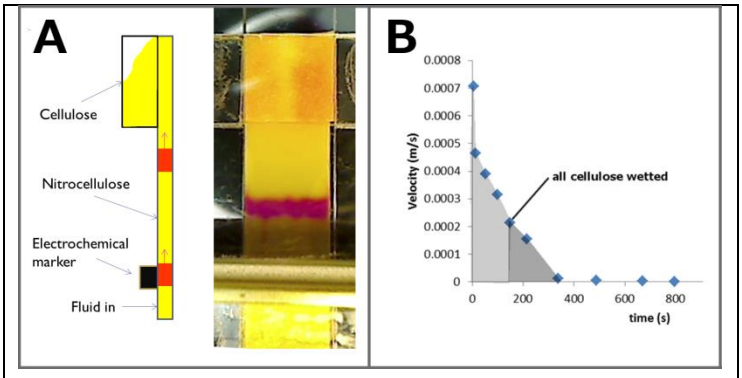

Figure 20: The wetting front does not fully saturate this paper microfluidic system. A: pH indicator and electrochemically-marked fluid bands[4] are used to visualize flow in a nitrocellulose membrane flowing into a cellulose wicking pad. Side view schematic (left). Top view of device (right) shows the setup when the full area of the cellulose is visibly yellow with pH indicator solution. B: Velocity quantification of marked fluid bands (pink). Fluid keeps flowing into wicking pad even after area is yellow, indicating the wetting front did not fully saturate the wicking pad. Only ~60% of the volume of the wicking pad was filled with the initial "wetting front" estimated by the area under the curve.

Buckingham[132] proposed that water flows more easily in porous substrates near saturation due to greater interconnection between pores. At decreased saturation these connections degrade, hindering fluid flow. Buckingham used this concept to rewrite Darcy's Law as

$$q = \frac{Q}{A} = -K(\theta)\frac{\partial \mathrm{H}}{\partial \mathrm{z}} \qquad \text{Equation 2}$$

where K is the hydraulic conductivity, θ is the volumetric water content, Q is

volumetric flux, A is the cross sectional area, q is the flux, and H is the total hydraulic pressure head defined as the sum of the matric suction and osmotic suction head (applicable in solute transport), and z is the gravitational head. Porous media permeability (ϰ) is related to hydraulic conductivity by

$\varkappa = K\frac{\mu}{\rho g}$	Equation 3

where μ is the dynamic viscosity, ρ is the density, and g is the acceleration due to gravity.

Richards later related changes in θ to changes in incoming and outgoing fluxes[133]. This equation, now known as the Richards Equation, provides a mathematical description of flow in partially saturated porous substrates, and is written

$\frac{\partial\theta}{\partial t} = \frac{\partial}{\partial z}\left[K(\theta)\frac{\partial H(\theta)}{dz}\right]$	Equation 4

Here, both the hydraulic conductivity and hydraulic pressure head are functions of the volumetric water content[133]. Several models have been proposed to describe unsaturated hydraulic conductivity as a function of the hydraulic head[134]–[137]. We used these models to estimate the hydraulic conductivity as a function of saturation from the measurement of the "water retention curve" (WRC) for a variety of porous membranes commonly used in paper microfluidic devices.

The WRC is a curve describing the pressure needed to remove fluid from a porous substrate of varying saturation. Procedures for measuring these curves in soils are well documented by the American Society for Testing and Materials (ASTM)[138]. We adopted the centrifugal methodology outlined in this standard, and apply it to different backed and unbacked membranes to obtain a WRC for each. The centrifugal method was chosen as it is particularly

convenient for a bioengineering laboratory where the required equipment is either already commonly used (centrifuge, balance) or can be readily adapted from commonplace supplies (spin columns). The overall concept of the centrifugal characterization method is relatively simple: a porous sample is first saturated with water, then centrifugation is applied at increasing speeds to determine the fraction of water removed from the sample for various rotational velocities. Using the rotational velocity and geometry of the centrifuge and sample holder, the amount of pressure working to remove fluid from the porous sample can be calculated.

Water retention curves can be fit to models using a variety of methodologies for the prediction of hydraulic conductivity as a function of saturation[134]–[137]. We used the SWRC Fit program[139] to fit the Van Genuchten and Brooks and Corey models to our data. The Van Genuchten model is widely used due to both its simplicity and superior fitting capabilities[139]. The suction head (h) is the measured pressure head calculated at each θ_i in Equation 5. The parameters θ_s, θ_r, n, and α were fit to WRC data with the Van Genuchten model, which is

$$\theta(h) = \theta_r + (\theta_s - \theta_r)[1 + (\alpha h)^n]^{\left(\frac{1}{n}-1\right)} \qquad \text{Equation 5}$$

After fitting the WRC data, hydraulic conductivity can be predicted as shown previously[137] using

$$K(\theta) = K_s \left(\frac{\theta - \theta_r}{\theta_s - \theta_r}\right)^{\frac{1}{2}} \left[1 - \left(1 - \left(\frac{\theta - \theta_r}{\theta_s - \theta_r}\right)^{\left(1-\frac{1}{n}\right)^{-1}}\right)^{\left(1-\frac{1}{n}\right)}\right]^2 \qquad \text{Equation 6}$$

Water retention curves were also fit with the Brooks and Corey model,

$\theta(h) = \theta_r + (\theta_s - \theta_r)\left(\frac{h_{bc}}{h}\right)^{\lambda} \quad h > h_{bc}$	Equation 7
$\theta = \theta_r + (\theta_s - \theta_r) \quad h \leq h_{bc}$	Equation 8

which has four fitting parameters: θ_r is defined as the residual water content, θ_s is the saturated water content, h_{bc} is the critical head and λ is a fitting parameter.

Once parameters such as porosity and saturated permeability are known for all membranes, and WRC data is available for the prediction of hydraulic conductivity as a function of saturation, the Richards Equation can be used to accurately model fluid flow in a partially saturated porous membrane network. A convenient implementation of the Richards Equation is found in the COMSOL Multiphysics Subsurface Flow module, which we used to validate our model against previously demonstrated paper microfluidic systems.

6.2 Materials and Methods

6.2.1 Porosity measurements

Membranes, stored in ambient laboratory conditions, were hole punched into 16 mm diameter circles, and dry membrane mass recorded. Water was introduced into each material by dipping an edge into a reservoir then wet membrane mass recorded. Water mass was calculated by subtracting dry membrane mass from wet membrane mass. Wet membrane volume was calculated using the wet membrane thickness and 16 mm diameter. Porosity was calculated by dividing water volume added to the membrane (calculated using the water mass) by wet membrane volume. Membrane water capacity was calculated by dividing the water volume by the area of the membrane (in the plane from which the membrane was cut).

6.2.2 Thickness measurements

Membrane thickness was measured optically. Membranes stored in ambient laboratory conditions were cut into 4 cm × 1 cm sections and stood on end, held in place with a tweezers, on a stereomicroscope (SMZ1500, Nikon, Tokyo, Japan). Membranes were then wetted with a pipette until saturated. An adjacent stage micrometer was used to calibrate the images, which were captured (Q Capture, Q Imaging, Surrey, BC, Canada) with a microscope camera (Retiga 1300i, Q Imaging). Captured images were opened in ImageJ (Rasband, W.S., ImageJ, U. S. National Institutes of Health, Bethesda, Maryland, USA, http://imagej.nih.gov/ij/, 1997-2014), where pixel width was calibrated to the stage micrometer, and membrane thickness was measured by drawing a line through the thickness of the membrane.

6.2.3 Wicking time measurements

The time required for fluid to imbibe four cm into an initially dry membrane was determined by submerging one end of a membrane into a large-capacity well containing deionized water. Time lapse images of imbibition were captured using a webcam, (Webcam Pro 9000, Logitech, Newark, CA), custom lighting setup, and HandyAvi (AZcendant, Mesa, AZ) software. Captured time lapse data were analyzed in ImageJ, tracking the imbibition front over time. The four-cm wicking time is measured by determining the time when the imbibition front reaches four cm from the reservoir.

6.2.4 Saturated permeability measurements

A constant pressure methodology for the characterization of parameters for membranes used in paper microfluidic systems was adapted from the original work of Darcy; the devices of Darcy and this project are highlighted in Figure 21.

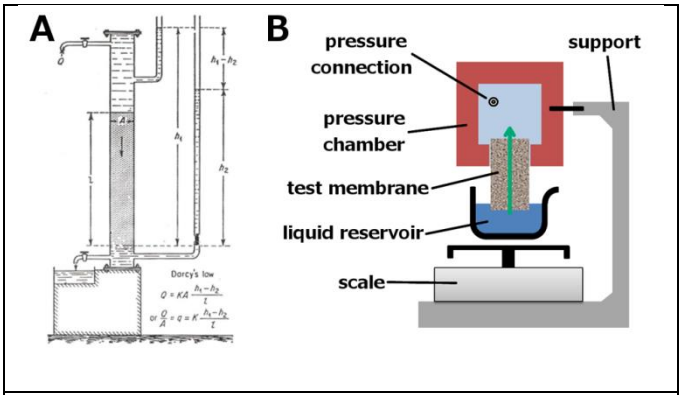

Figure 21: Measuring permeability. A: Darcy's apparatus[140] for measuring permeability of porous materials. A pressure gradient is created and measured across a saturated porous medium. Flow rate (Q) and hydrostatic pressure (h1-h2) are measured, and Darcy's law is used to calculate permeability. B: Permeability characterization schematic. The pressure chamber is supported by a clamp stand, and the inlet of the encapsulated membrane is submerged into water. The beaker containing the water is supported by a digital balance, which outputs values over time to a data logging program. Regulated negative pressure is applied to the pressure connection, and mass readings from the balance are communicated via a serial connection between the balance and a computer data logging program.

Membranes were cut on a CO_2 laser cutter (M360, Universal Laser Systems, Scottsdale, AZ) to 2 cm × 5 cm. Sections of cover tape (ARclad 7876, Adhesives Research, Glen Rock, PA) were also cut to 2 cm × 5 cm, and used to seal the exposed face(s) of the test membrane (Figure 22), which left only the four edges unsealed. After application of the cover tape, the two five-cm edges were sealed by manually dipping into molten wax (PureTemp48, Entropy Solutions, Plymouth, MN). This preparation left the two two-cm edges mostly open (Figure 22), with all other sides of the porous media sealed by either wax or cover tape. The cross-sectional area of the empty porous membrane was calculated from the membrane thickness and the distance between the wax-filled edges. The efficacy of the wax seal was confirmed in an experiment where three sides, instead of two, were sealed with wax. As expected, no flow was observed when the third, wax-sealed side was submerged in liquid even when negative pressure was applied to the fourth, unsealed side of the membrane (data not shown).

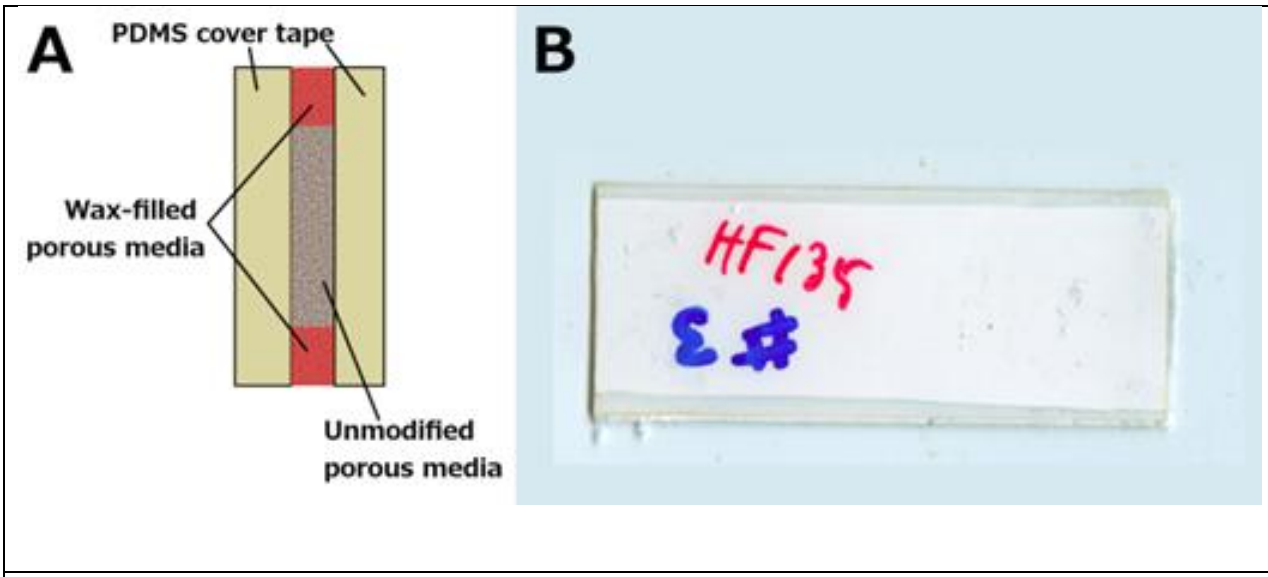

Figure 22: Membrane preparation for permeability measurement. A: Membrane encapsulation schematic, cross-sectional view. Membrane face (or both faces for a non-backed membrane) sealed with cover tape, and the long edges (top and bottom) sealed with wax. B: Photo of encapsulated membrane, top view. Wax penetration can be seen in the dark regions at the top and bottom of the membrane. The short edges (sides) are left open to serve as the fluid outlet and inlet, respectively.

Next, a pressure chamber was constructed to allow the application of negative pressure to one open end of the porous membranes (Figure 21). PMMA was laser-cut into two 6 cm × 6 cm × 0.2 cm thick sheets. Gaskets were created from ultra-soft polyurethane (8514K62, 30 Durometer, 3/16" thick, McMaster-Carr, Los Angeles, CA), with an opening to allow the insertion of the encapsulated porous membrane. To prevent crushing of the porous membrane, the gap between the acrylic plates was larger than the thickness of the encapsulated membrane. The area around the encapsulated membrane was gently packed with wax (Tacky Wax, Bard's, Mundelein, IL) for sealing. The pressure chamber was held together using paper binder clips. Negative pressure was applied to the pressure chamber via a 1/8" nipple embedded in one of the PMMA covers. Pressure gauges were calibrated as described in KH Head's Soil Laboratory Testing manual[141].

The pressure chamber was supported by a stand, and the free end of the membrane submerged into water in an open beaker, which rested on a digital balance (PGW 453e, Adam Equipment, Danbury, CT). This balance was connected to a computer with a terminal program (Terminal com port development tool, Bray, https://sites.google.com/site/terminalbpp/) and mass readings were collected at a sampling frequency of 5 Hz. The mass flow rate at a constant negative pressure from the beaker through the membrane and into the pressure chamber was then calculable using the measured mass loss over time from the beaker.

In order to use mass flow rate to calculate test membrane permeability via Darcy's Law (Equation 1), the following assumptions were made: 1) there was no contribution of capillary force after the membrane is wet; 2) the membrane was not crushed by cover tape, atmospheric pressure, or by the test fixture; 3) the wax seal solidified evenly and within 100% of the pores a measurable distance in from the strip edge; 4) no leaks occurred between the cover tape and membrane, and the cover tape did not otherwise affect flow rate; and 5) the membrane was not restricted at the pressure chamber inlet or outlet. The hydrostatic pressure of the vertical fluid column was subtracted from the applied pressure to calculate the pressure differential between the membrane inlet and outlet, and the membrane permeability was calculated using Darcy's Law (Equation 1).

6.2.5 Water retention curve measurements

Measuring the water retention curve for porous media is relatively straightforward, and various test methods are outlined in ASTM D6836-02(2008)e2: "Standard Test Methods for Determination of the Soil Water Retention Characteristic Curve for Desorption Using Handing Column, Pressure Extractor, Chilled Mirror Hygrometer, or Centrifuge"[138]. As mentioned

previously, we used the centrifugal method. Figure 23 shows the adapted apparatus for measuring materials used in paper microfluidics.

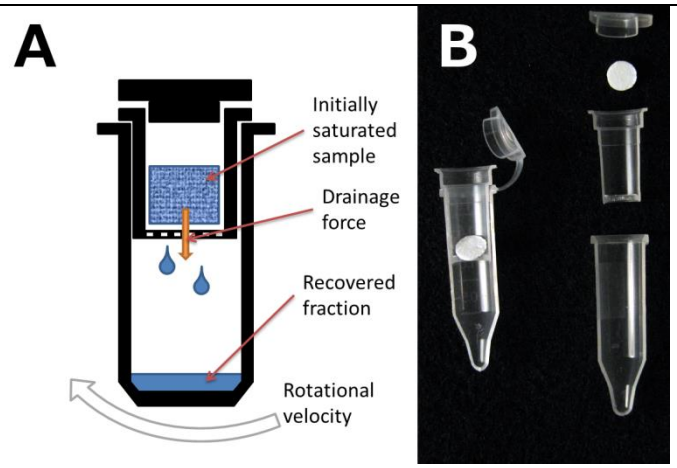

Figure 23: Centrifugal water retention curve apparatus. A: Device schematic. The porous media sample to be tested is first saturated with water, and then loaded into the filter portion of the spin column. The mass of the wet sample plus spin column is measured, and the loaded filter placed into the spin column. The loaded filter is spun at incrementally increasing rotational velocities, with the filter removed and the mass of the filter plus the partially drained porous sample measured at each velocity. B: Cross sectional views of assembled (left) and exploded (right) devices. The porous sample is the white disk, which sits perpendicular to the tube axis when the test is being run. Multiple disks of unbacked porous media can be stacked atop each other to increase the water volume to a more appropriate value for the sensitivity and accuracy of the balance being used.

A centrifuge (Sorvall Legend Micro 21, Thermo Fisher Scientific, Waltham, MA, USA) with a range of 300 to 14,800 RPM was used to measure matrix pressure as a function of saturation. To hold the test membrane and capture the water released due to the applied pressure, a centrifuge tube filter (Costar Spin X 8169, Corning Inc., Corning, NY, USA) was modified by removing the porous filter element with a tweezers.

6.2.6 Unbacked membrane preparation

Membranes with no water-impermeable polymeric backing were punched with a ¼" hole punch, stacked 4-5 high in the filter holder of the spin column, and the mass of the filter tube and dry membranes recorded. Water was added to each membrane by dipping an edge of the membrane

into a reservoir, after which the membranes were placed back into the filter holder and the mass of the membranes and filter holder recorded. The wet diameter and thickness of membrane punches were also recorded.

6.2.7 Backed membrane preparation

The membrane preparation procedure was modified for nitrocellulose materials with a water-impermeable polymeric backing. Membranes were cut into 5 cm × 10 cm strips. The dry mass of the membrane and filter tube were recorded, then each membrane was wetted using a pipette. Any water that had pooled on the surface of the membrane was wicked up carefully with a large-pore membrane such as a glass fiber. The wet strips were carefully rolled and inserted into the filter holder, and the mass of the filter holder and wet membrane recorded.

6.2.8 Time required to reach equilibrium

The minimum time needed to drain pores of a given size or larger at a specific angular velocity was determined for each membrane tested. A wetted sample of a membrane was loaded into filter tubes, which were placed into the centrifuge and spun at a single angular velocity for five minute intervals. After each interval we recorded the mass of the filter tube. Once the change in mass between runs at the same angular velocity became less than 1%, the total elapsed time at that speed was used in WRC experiments. For most membranes ten minutes was enough time for speeds of 300 to 1000 rpm. Higher than 1000 rpm, five minutes was sufficient for most membranes.

6.2.9 Water retention curve model fitting

WRC data was fit with the Van Genuchten and the Brooks and Corey models using the online nonlinear fitting program provided by Seki *et al.* [139]. Unimodal models were generated based on the means of the WRC data for each membrane at each centrifuge speed.

6.2.10 Finite element modeling of the Richards Equation

COMSOL (The COMSOL Group, Stockholm, Sweden) was used for simulations of fluid flow in partially saturated porous networks using the Richards Equation. The Subsurface Flow module was used for the calculation of fluid movement, and the Transport of Dilute Species in Porous Media module was used to visualize the progression of multiple fluids. Modeling parameters are described in Table 2 and Table 3 below.

Table 2: Richards Equation parameters used in COMSOL models

Membrane	θ_S	θ_R	α	n	l	P_0 [kPa]
8950	0.94351	0.020488	5.8799	2.9742	0.5	-21
8964	0.67257	0.0198	2.3813	4.0125	0.5	-21
HF075	0.93741	0.0512	0.4464	2.5151	0.5	-340
HF135	0.945	0.0473	0.2555	2.3521	0.5	-300
CF5	0.79502	0.1598	0.95955	2.2761	0.5	-70
CFSP223	0.93968	0.1359	1.4016	2.3178	0.5	-300

6.3 Results and Discussion

6.3.1 Permeability measurements

Membrane permeability was calculated using Darcy's Law along with the obtained data using the setup shown in Figure 21. Example data is shown in Figure 24 below.

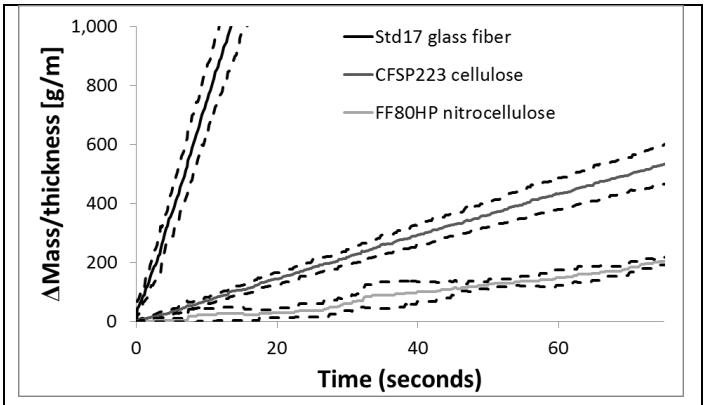

Figure 24: Example permeability characterization data. Fluid mass that has flowed into the membrane is plotted as a function of time. Data for each membrane type is linear, as expected. Mass is scaled to membrane thickness for plotting purposes. Solid lines are mean, dashed lines are ± one standard deviation, n=3.

Figure 24 shows the measured mass flow rate, which is proportional to the membrane permeability by Darcy's Law, in three types of porous membranes: Standard 17 glass fiber, CFSP223 cellulose, and FF80HP nitrocellulose. The glass fiber and cellulose data was almost perfectly linear, as predicted by Darcy's Law for a constant pressure applied over a constant length membrane. The nitrocellulose data was fairly close to linear, but contained fluctuations due to measurement error. This nitrocellulose has very low permeability and is very thin, which resulted in a low mass flow rate close to the limit of quantitation for the balance. This measurement error can be avoided with a more sensitive scale. Mass flow rate data were then converted to permeability as described above. The permeability, wet thickness, porosity, and four-cm wicking time for a wide range of membranes are given in Table 3.

Table 3: Measured membrane parameters

Membrane	Wet thickness wet [m]	Porosity [%]	Saturated permeability [m^2]	4 cm wicking time [s]
Nitrocellulose				
HF075	1.50×10^{-4}	76%	2.35×10^{-12}	89
HF135	1.60×10^{-4}	76%	5.50×10^{-13}	177
HF180	1.60×10^{-4}	75%	3.37×10^{-13}	201
FF80HP	1.01×10^{-4}	70%	6.73×10^{-13}	140
FF120HP	1.20×10^{-4}	70%	5.67×10^{-13}	163
Glass Fiber				
GR8964	5.20×10^{-4}	68%	7.73×10^{-11}	31
GR8950	3.30×10^{-4}	88%	1.92×10^{-10}	10
GF/A	4.20×10^{-4}	94%	1.41×10^{-12}	65
GF/B	9.30×10^{-4}	88%	1.54×10^{-12}	68
GF/C	4.00×10^{-4}	79%	8.27×10^{-12}	74
GF/D	1.40×10^{-3}	95%	1.32×10^{-11}	23
Standard 17	5.30×10^{-4}	91%	8.87×10^{-11}	22
Cellulose				
CFSP223	1.10×10^{-3}	72%	4.68×10^{-12}	47
GE CF5	1.40×10^{-3}	62%	1.09×10^{-12}	58

Overall, the membrane parameters we measured or calculated from measurements generally match up with expectations: membranes that visibly consist of large pores, like the glass fiber membranes Standard 17 and GR8950, have high permeability compared to membranes that visibly consist of small pores, like the nitrocellulose membranes. Cellulose membranes defy easy classification as their permeability varies greatly depending on type.

Interestingly, membranes from different manufacturers, which would seem nearly equivalent based on manufacturer specifications, can be quite different. For example, the nitrocellulose membranes Millipore HF075 and GE FF80HP have manufacturer-reported four-cm wicking rates of 75 and 80 seconds, respectively (6% difference). When compared directly using our method, the four- cm wicking rates are 89 and 110 seconds, respectively (21% difference). An even larger difference is observed in the permeability: HF075 is about two times more permeable than FF80HP, which would result in a flow rate about two times faster under an

equivalent pressure differential. These differences are likely due to the distinct pore structures of the membranes.

The nitrocellulose membrane HF135 also provides an interesting case study with respect to the historical use of permeability in the literature. In 2011, our group[9] published a flow model which used 1×10^{-12} m^2 as the permeability for HF135. Also in 2011, Mendez *et al.* used a value of 8.4×10^{-13} m^2 for the same membrane. The measured value falls in between at 5.5×10^{-13} m^2. The lack of published permeability values for membranes have led groups to use questionable calculations to obtain permeability values[142].

6.3.2 Capillary pressure vs saturation: water retention curves

With saturated permeability characterized, capillary pressure data is still needed to model fluid flow in porous media. The centrifugal method of water retention curve generation[138] was

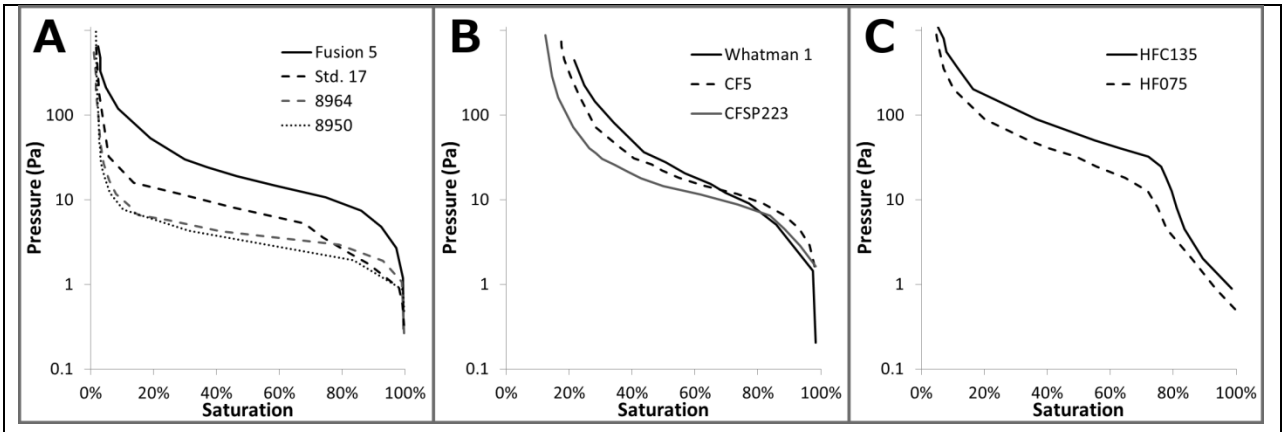

Figure 25: Water retention curve for glass fiber, cellulose, and nitrocellulose membranes. Plotted are experimental data means for the comparison of curves of different membranes. A: Glass fiber membranes. Fusion 5 has higher capillary pressure at all saturation levels. Standard 17 has higher capillary pressure than 8964 and 8950 for most saturation levels. 8964 has a slightly higher pressure than 8950. B: Cellulose membranes. Note that ~20% of the fluid was not recovered even at the highest centrifuge speed, indicating that a small fraction of the pores in cellulose are capable of withstanding very high suction pressures. The Whatman 1 filter paper has a higher capillary pressure for most saturation levels, followed by CF5 and CFSP223. C: Nitrocellulose membranes. HFC135 has a higher capillary pressure than HF075 for all saturation levels.

employed to characterize membranes. The mean of these data are plotted by membrane type in Figure 25 to compare membranes, with the full experimental data and model fits in Figure 26.

6.3.3 Hydraulic conductivity vs saturation: water retention curve-fitting

Using the SWRC fit program, water retention curve data was fit with Van Genuchten and Brooks and Corey models. Both models fit to the water retention curves reasonably well with R^2 values typically greater than 0.9. Data from water retention curve experiments along with both model fits are given in Figure 26 below.

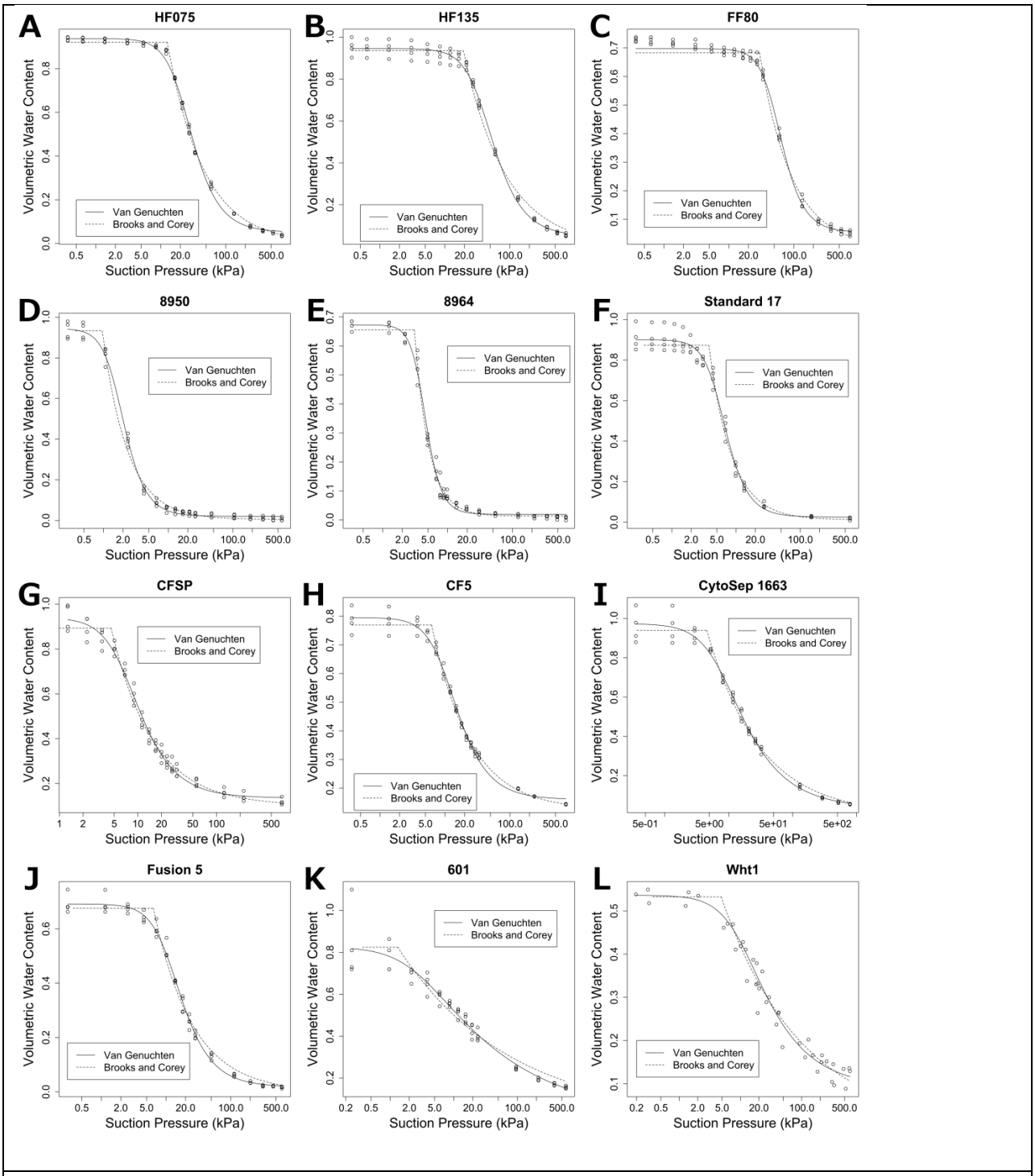

Figure 26: Water retention curve data and model fits.

6.3.4 Relative permeability vs. saturation

After fitting the WRC data with Equation 5, Equation 6 can then be used to plot relative permeability as a function of saturation. It can be seen that relative permeability drops off rapidly

as the suction pressure increases. Based on this, it would be expected that there may be a large pressure drop over a relatively short distance in the wetting front of a hydrating membrane.

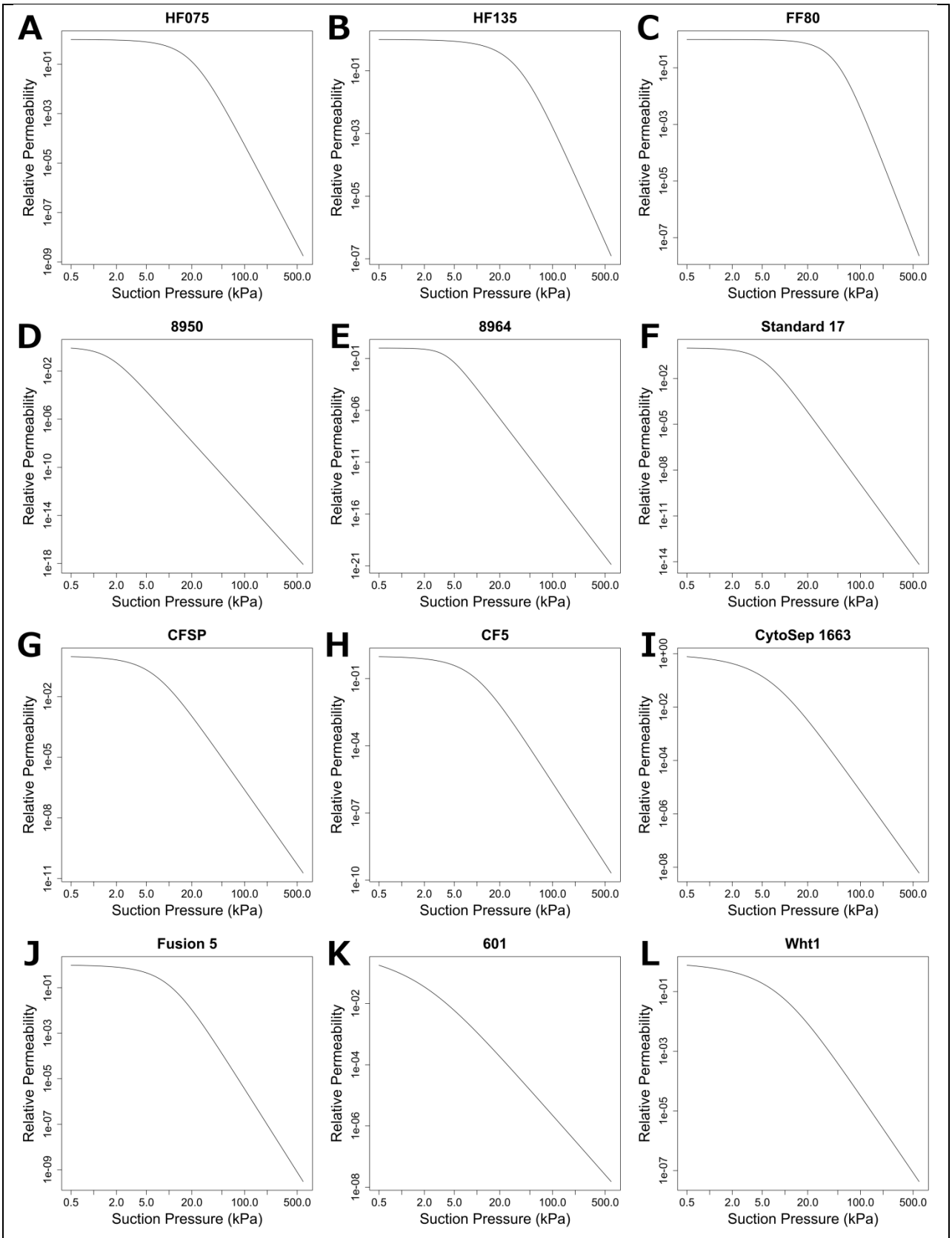

Figure 27: Calculated relative permeability vs suction pressure for selected membranes.

The parameters used for each of the Van Genuchten and Brooks and Corey model fits are given in Table 4 below.

Table 4: Water retention curve model fit parameters

	Van Genuchten				Brooks and Corey			
Membrane	θ_S	θ_R	α	n	θ_S	θ_R	h_b	λ
FF80	0.697	5.44E-2	0.189	2.94	0.683	2.35E-05	3.02	0.886
HF075	0.937	5.12E-2	0.446	2.52	0.921	6.71E-5	1.28	0.776
HF135	0.945	4.73E-2	0.256	2.35	0.936	1.07E-6	1.96	0.669
CF5	0.795	1.60E-1	0.960	2.28	0.769	0.124	0.634	0.730
CFSP223	0.940	1.36E-1	1.40	2.32	0.894	0.102	0.466	0.820
Whatman 1	0.536	8.97E-2	0.970	1.69	0.532	3.21E-6	0.492	0.333
8950	0.944	2.05E-2	5.88	2.97	0.933	4.87E-3	9.76E-2	1.120
8964	0.673	1.98E-2	2.38	4.01	0.656	1.37E-2	0.313	1.940
Standard 17	0.901	2.57E-2	1.79	2.91	0.874	1.20E-2	0.383	1.227
Fusion 5	0.692	1.83E-2	0.861	2.30	0.680	3.98E-7	0.649	0.723
CytoSep 1663	0.974	3.35E-2	1.29	1.78	0.940	6.98E-5	0.465	0.525
Ahlstrom 601	0.827	1.51E-6	3.72	1.32	0.825	1.85E-5	0.134	0.246

The Van Genuchten partial saturation models for various materials were then used in a COMSOL finite element implementation of the Richards Equation, simulating fluid flowing into a single material from a reservoir. The results shown in Figure 28 highlight correct predictions for fluid flow rate into nitrocellulose, glass fiber, and cellulose membranes.

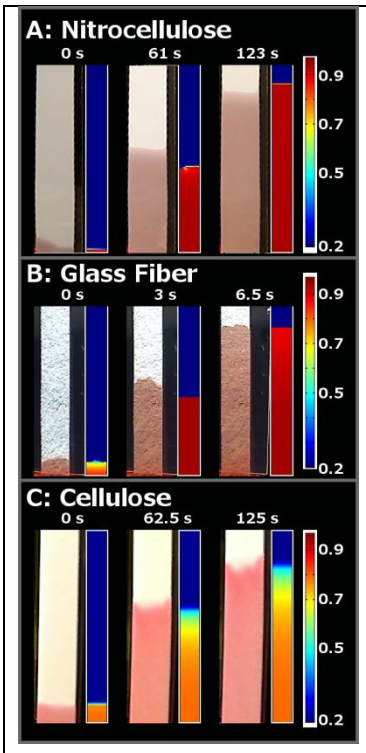

Figure 28: Experimental and modeled 4 cm wetting in various membranes. A: HF135 nitrocellulose. B: 8964 glass fiber. C: CFSP223 cellulose.

After confirming that the model produced realistic imbibition simulations for single material, simple geometry porous network, a more complex simulation was performed of a more complicated geometry device constructed from multiple types of porous media. In this simulation of a two-dimensional paper network, initially saturated glass fiber membranes drain into a nitrocellulose and cellulose network, delivering reagents sequentially to a test line, with the modeled results shown in Figure 29

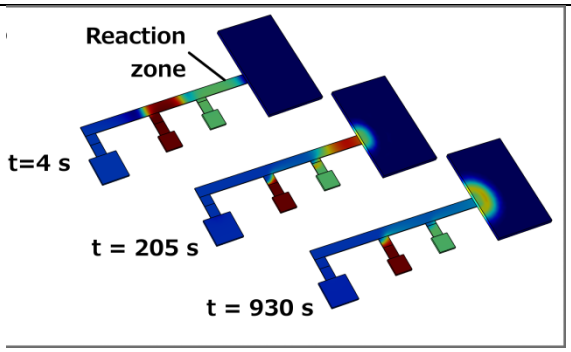

Figure 29: Modeling a realistic 2DPN device. Membrane parameters were used to model a realistic paper microfluidic device, where glass fiber squares drain into a multi-leg nitrocellulose network and cellulose wicking pad. Teal, red, and blue fluids are delivered sequentially through the reaction zone of the device.

6.4 Conclusions

Fluid flow is the fundamental operating principle of paper microfluidic devices. Paper microfluidic device development requires realistic models to help circumvent the time-

consuming optimization of membrane types, arrangements, and geometries, especially during concurrent optimzation of assay chemistries. Previous modeling techniques assumed that wetting fronts represented a boundary between dry membrane and wet, fully saturated membrane. Here, we have showed that this is not the case, that fluid flow is instead dominated by partially saturated flow, and that previous modeling techniques therefore do not yield realistic results.

We have presented an alternative approach to modeling partially-saturated flow in realistic networks of multiple porous membranes and described all of the membrane characterization test fixtures and protocols to measure or calculate the necessary model parameters. As paper microfluidic systems become more advanced, and perform more complex assays, models that accurately predict fluid movement, flow timing, and reagent delivery sequencing becomes more important. The techniques outlined in this manuscript can be adapted to any lab with basic equipment to allow vastly improved device design, enabling a more rigorous approach to paper microfluidic device design and optimization. The work presented here directly contributed to our understanding of the functionality of the p-switch, for which the operation cannot be explained by Darcy- or Washburn-based flow models. Future work on this topic will hopefully include exploration of the dynamic pressure distributions present in the wetting front of hydrating membranes.

6.5 Acknowledgements

Joel Atwood, George Kimpel, and Ryan Gallagher contributed greatly to the experimental work of this aim. Josh Bishop, Peter Kauffman, Barry Lutz, and Paul Yager provided much useful guidance in navigating the principals of partially-saturated fluid flow in paper microfluidics.

7 Aim 2) Precision heating in electricity-free diagnostic devices

NAAT-based devices require precise heating and temperature control. For the MAD NAAT device, we developed a non-electrical isothermal temperature control system using chemical heaters. This effort includes quantitative modeling of the chemical heater system, exothermic chemical power supply quantifications, composite phase change material research and development, along with integrated system geometry optimizations for use with two-dimensional paper microfluidics. This work was done in collaboration with PATH.

Decoupling nucleic acid amplification assays from infrastructure requirements such as grid electricity is essential to provide effective diagnosis and treatment at the point-of-care in low-resource settings. Here, we outline a complete strategy for the design of electricity-free precision heaters for isothermal nucleic acid amplification, or any other application requiring elevated temperatures, using low-cost components with better end-of-life disposal options than conventional batteries.

Main deliverable: Comprehensive chemical heater development ***Published***

The work presented in this aim is adapted from[126]*:*

J. R. Buser, S. Diesburg, J. Singleton, D. Guelig, J. D. Bishop, C. Zentner, R. Burton, P. LaBarre, P. Yager, and B. H. Weigl, *Lab Chip*, 2015, **15**, 4423–4432.

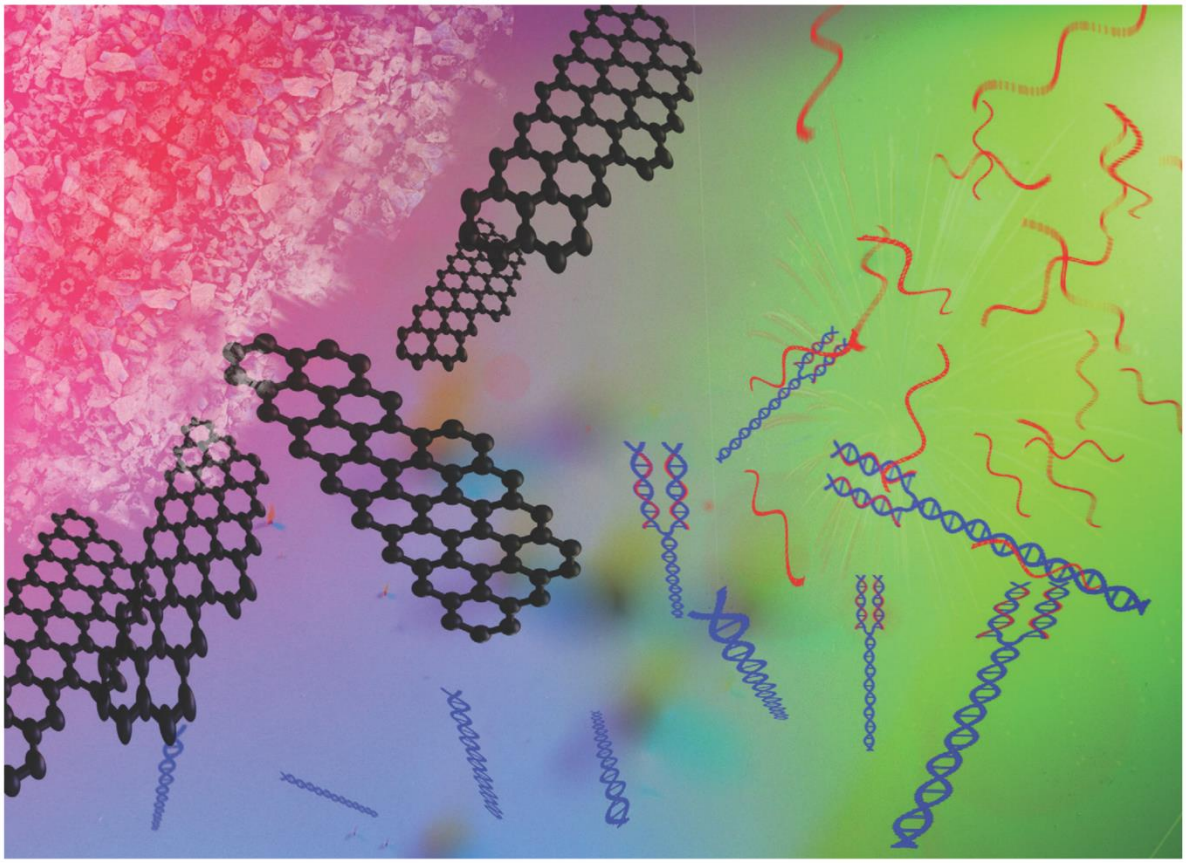

Featuring work from the Yager Lab at the University of Washington and PATH in Seattle, Washington, USA.

Title: Precision chemical heating for diagnostic devices

Electricity-free heaters are shown to be a viable alternative to conventional heating methods for isothermal nucleic acid amplification. A complete design strategy enables the design of precision chemical heaters for point of care use in low-resource settings.

As featured in:

See J. R. Buser *et al.*, *Lab Chip*, 2015, **15**, 4423.

ROYAL SOCIETY OF CHEMISTRY

www.rsc.org/loc

Registered charity number: 207890

Figure 30: This work earned us the inside back cover of Lab on a Chip

7.1 Introduction

Nucleic acid amplification tests (NAATs) have become essential tools for accurate, rapid diagnosis of infectious diseases[18], [143], [144]. This broad category of methods is, in many cases, replacing less sensitive protein-based tests for differential diagnosis of symptomatic patients, as well as for surveillance in elimination efforts where the disease burden may be very low. Despite demonstrated utility, many NAAT technologies can only be used in laboratories with significant infrastructure and capital equipment, and by users with extensive training. The required supplies, electrical power, and trained users are often unavailable in low-resource settings (LRS)[3], [18]. Decoupling NAAT diagnostics from these requirements could enable a new level of effective diagnosis and treatment at the point of care in LRS[6], [56], [145].

Isothermal NAATs are potentially simpler alternatives to traditional NAATs because they do not require an energy-intensive precision thermal cycler[96], [146]. These assays replicate target nucleic acid sequences at a single, constant temperature. To enable use of isothermal NAATs in the lowest resource settings, PATH[114], [115] and others[147]–[149] have demonstrated electricity-free approaches that employ exothermic chemical reactions coupled with a temperature-regulating phase change material (PCM) to process a sample at a precise temperature for an extended period of time. A useful phase change material must have an endothermic phase transition over a narrow temperature range centered at the temperature that one wishes to maintain. Devices using PCMs provide precision temperature control without requiring electricity, high levels of infrastructure, or large and expensive capital equipment. Development of such platforms is intended to meet the World Health Organization's recommended ASSURED guidelines for designing diagnostic tests that are affordable, sensitive, specific, user-friendly, rapid and robust, equipment-free, and deliverable to end-users[8].

Effective electric, portable NAAT devices are becoming available with the commercialization of new, more compact PCR device platforms[144], [150] such as the miniPCR mini8[151] and Ahram Palm PCR[152]. These portable platforms could enable NAATs in LRS if electricity is available for recharging batteries. However, even where an electric grid exists in LRS, service is often intermittent[2], and the intermittent supply of electricity for charging batteries may reduce productivity. Although the cost of these devices should continue to decrease, these devices are not appropriate for all LRS because of their reliance on grid electricity.

Although the ASSURED guidelines do not specifically require electricity-free solutions, there are settings in which advantages are apparent:

1. Where testing for extremely virulent pathogens (*e.g.* Ebola virus[153]) and where immediate incineration or decontamination of entire devices may be desired.
2. Where electrical grid infrastructure is nonexistent or cannot support rechargeable battery-powered devices.
3. Where supply chain management fails to support instrument maintenance and consumable inventories, and a non-instrumented, integrated device is needed.
4. Natural disaster scenarios where large sections of the population are cut off from electricity sources for long periods.
5. When disposal of batteries or electronics is a concern.

Robust, electricity-free isothermal NAAT devices show great promise for expanding molecular diagnostic methods into LRS. However, challenges exist when designing devices to specific isothermal NAAT temperature requirements, and in accommodating operation in uncontrolled ambient temperatures. As with electrical heating systems, system parameters can be adjusted to control the power source, temperature regulation, and integrated device performance. In this paper, we address these challenges and outline general design parameters.

Clearly, a point of care NAAT would ideally be small, fast, accurate, easy to use, and inexpensive—criteria that are often hard to meet at the same time. Under a grant from the

Defense Advanced Research Projects Agency, a team including the University of Washington, PATH, the ELITechGroup, and the GE Global Research Center have collaborated to develop a platform for the application of chemical heaters to isothermal NAATs. The grant is entitled Multiplexable Autonomous Disposables for Nucleic Acid Amplification Tests for Limited-Resource settings (MAD NAAT)[154]–[159]. One of the end-products of the project is a platform for an electricity-free, sample-to-result, point of care NAAT; the MAD NAAT platform takes a biological sample as input, prepares the sample by lysing the input cells using heat and enzymes, delivers the sample to a temperature-regulated zone for target nucleic acid sequence amplification, then delivers the amplicons to a lateral flow strip for readout. The precision heating requirements of the MAD NAAT project and the experience of the team with chemical heating applications have driven the development of the components, devices, and strategies presented in this paper.

Here, the requirements of the MAD NAAT device are used as the basis for discussion of:

1. General chemical heater design considerations.
2. Detailed design description of the chemical heater used in current MAD NAAT prototypes.
3. Experimental and computational results validating the MAD NAAT chemical heater as a stand-alone device, supporting an isothermal NAAT at varying ambient conditions.

We also highlight specific technical issues associated with implementation, and present an adaptable design process. That process combines engineering and finite element modeling, with the goal of enabling a design team working on similar problems to develop an optimized chemical heater.

7.2 General design considerations for chemical heaters

In the general design presented in this paper, a temperature-controlled chemical heater consists of an exothermic reaction thermally coupled with a temperature-regulating PCM,

surrounded by insulation. Figure 31 shows an exploded view of a generic chemical heater designed to incubate an isothermal NAAT.

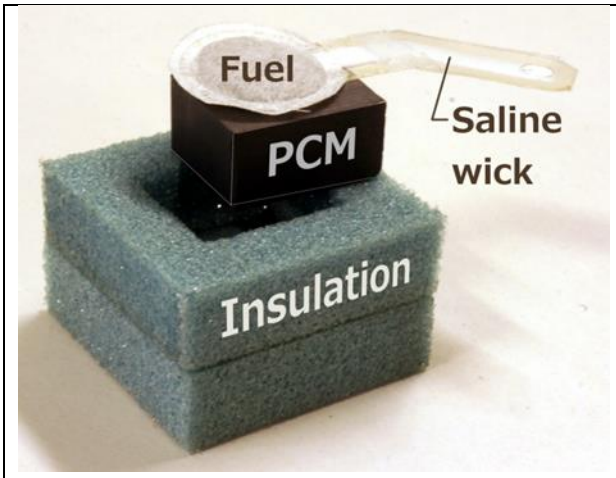

Figure 31: Precision heater designed for use with isothermal NAATs, partially disassembled view. The diagnostic assay sits beneath the PCM block within an appropriate cut-out in the insulation. Top insulation omitted for clarity. A NaCl solution is delivered to this type of power supply via a paper wick from a reservoir (not shown).

7.2.1 Assay Parameters

The design of a chemical heater is intrinsically tied to the assay for which it is designed, with critical assay parameters determining the fundamental heater specifications. The principal parameter is the optimal assay temperature, which defines the heater's nominal operating temperature. Another crucial parameter is the assay's tolerance to temperature fluctuation. Because biomolecular processes can have a narrow operating temperature range, relatively small temperature fluctuations can lead to large losses in assay sensitivity.

To achieve acceptable levels of sensitivity, the optimal temperature and associated tolerance should be quantified prior to design. This requires a series of experiments that vary the assay's temperature over a wide range. As an example, the MAD NAAT platform uses an isothermal strand displacement amplification[160], [161] (iSDA), which is an isothermal NAAT with an operating temperature and tolerance of ~51±4°C. This level of precision temperature control is easily achievable with a benchtop thermal cycler (see Figure 35). Variations in temperature can affect several aspects of assay performance, including efficiency and speed.

Two other assay parameters that are critical for defining heater specifications are (1) the maximum time it can take the sample to reach the operating temperature range (maximum warmup time) and (2) the minimum time the assay must be held in the operating temperature range (minimum holdover time). Both parameters should be defined relative to acceptable levels of overall assay sensitivity. Other important parameters that need to be considered include sample volume, sample format, size of the region to be heated, the range of environmental temperatures expected, and an acceptable volume for the entire heating system.

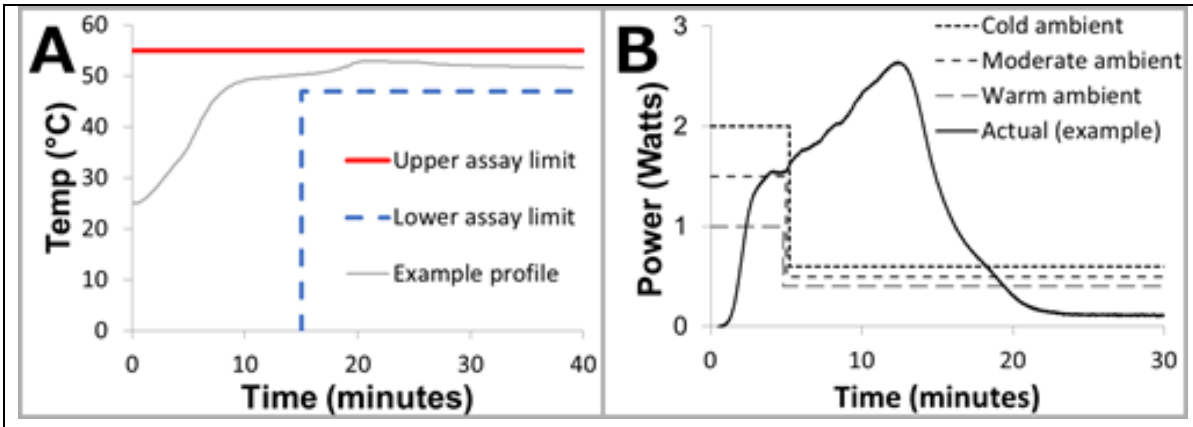

Figure 32: Desired assay temperature tolerances and power curves. A: Assay temperature specifications. The minimum assay temperature here is 47°C, and the temperature must warm up in 15 minutes or less, and hold for 25 minutes. To avoid permanently losing enzyme activity, this assay must never exceed 55°C. An example temperature profile is shown (grey line) that meets these specifications. B: Ideal power profiles to achieve isothermal heating for a range of ambient temperatures, along with an example power profile from a chemical power supply. Cold ambient conditions need more power to warm the system up, in addition to needing more power to account for steady-state heat losses. The non-ideal power profile requires that temperature be additionally regulated by other means (*e.g.*, PCM).

All of these parameters can have large implications regarding PCM choice, insulation requirements, device layout, and overall device size, as discussed in detail below. Assays which amplify effectively over a wide temperature range, experience the lowest possible susceptibility to performance loss as the system (sample and reagents) warms up to the operating temperature, and needs the shortest possible time for amplification are the simplest to design chemical heaters

for. Figure 32 shows the most important specifications related to temperature and time for a chemical heater given a specific assay.

7.2.2 Operating and environmental conditions

Although many diagnostic assays are currently used in temperature-controlled laboratories, fully realizing the advantages of testing at the point of care requires diagnostic devices that can accommodate a larger ambient temperature range. A design specification for ambient temperatures from 0 to 40°C is not unreasonable for LRS. However, designing a device for a larger ambient temperature range requires using a larger volume of insulation and PCM for a chemical heater.

Other environmental factors such as humidity levels, exposure to rain and wind, and shipping and storage conditions, can also affect the use of a chemical heater and should be considered at an early stage in the design process. Environmental factors can also dictate the need for either reusable or disposable designs. Table 5 shows the most basic information that should be known at the start of the design process, as well as the values specified for the MAD NAAT platform.

Table 5: Information needed for the design of a chemical heater for an assay application. These values are approximately those used for the MAD NAAT platform and are used for the example heater described in this paper.

Assay temperature and tolerance	51 ± 4°C
Ambient temperature range	15–30°C
Maximum warmup time	15 minutes
Minimum holdover time	25 minutes
Assay liquid volume	40 µl in porous media
Heated zone form factor	Flat 2 x 2 cm
Reusability/disposability	Disposable

7.2.3 Chemical heater components

Chemical heaters that can meet the previously cited requirements typically need two main components: (1) a chemical power source and (2) a PCM temperature regulator.

The power source provides heat at a predictable rate through an exothermic chemical reaction, and the PCM buffers the temperature by undergoing a phase change at a desired temperature. The power source and temperature regulator combine to form the integrated system. Design elements can be categorized as either affecting the two components or the integrated system, as outlined in Table 6.

Table 6: Parameters used to achieve desired assay temperature and other device specifications.

Power source
• Reaction chemistry, enthalpy of reaction, and reaction rate • Particle size, packing density, and surface area of solid reactants • Concentration of liquid/aqueous reactants • Supply modality and supply rate of liquid reactants • Geometry
Temperature regulator
• PCM phase change temp. range and latent heat capacity • Thermal conductivity • Geometry
Integrated system
• Containment of reactants and PCM • Insulation • Activation mechanism • User interface

7.2.3.1 Power source

The foundation of the chemical power source is the exothermic reaction chemistry. The choice of chemistry dictates the thermal output and modes of control. Generally, the power source should use chemistry with high energy density, safe peak temperatures, nontoxic by-products, and reagents with minimal shipping and disposal restrictions. Table 7 shows examples of some commercial applications of exothermic reaction chemistries.

The design of a chemical heater is greatly influenced by the parameters of the power source. For chemistries with solid reactants, parameters such as particle size, packing density,

chemical density, ratio of reactants, and reaction surface area will affect the thermal output. For chemistries with liquid reactants, parameters such as concentration and delivery rate will do the same. The geometry of the power source will also affect how the thermal output is delivered to the temperature regulator and sample, or is lost to the ambient environment.

Storage and activation of reactants influence the design of the integrated system. Reactants often have special storage requirements to maintain their integrity and must be kept separate prior to device operation. Because a controlled environment cannot be assumed in most LRS, storage needs should be understood and considered early in the design process. For example, water-reacting fuels must be kept from moisture, and iron-oxygen reactions must be prevented from contacting air during device manufacturing and storage.

Table 7: Existing commercial products that use exothermic reactions for heat. Battery estimated energy capacities (estimated from manufacturer datasheets) are listed for comparison.

Fuel	Reactants	Est. energy capacity	Sample consumer product
Calcium oxide	$CaO + H_2O$	1 kJ/g	Hot Can[A]
Calcium Chloride	$CaCl_2 + H_2O$	1 kJ/g	Rocket Fuel coffee[B]
Iron filings	$Fe + 3\ O_2$	30 kJ/g	HotHands hand warmers[C]
Sodium Acetate	$Na^+ + C_2H_3O_2$	0.3 kJ/g	Heat Wave hand warmers[D]
Magnesium Iron	$Mg\text{-}Fe + H_2O$	15 kJ/g	Field ration heaters for meals ready to eat (MREs)[E]
AA Alkaline battery[F]	Zn/MnO_2	0.4 kJ/g	Remote control
Lithium coin cell CR2032[G]	Li/MnO_2	0.7 kJ/g	Laser pointer

Table 7 Footnotes:
A: http://www.hot-can.com
B: http://www.rocketfuel.uk.com
C: http://www.hothandsdirect.com
D: http://www.bentgrassconcepts.com
E: http://www.luxfermagtech.com
F: http://data.energizer.com/PDFs/E91.pdf
G: http://data.energizer.com/PDFs/cr2032.pdf

Existing chemical heater design specifications can also affect the choice of chemistry. If a device is meant to be reusable, eutectic salts (*e.g.*, sodium acetate) may be a good fit[162].

However, some user steps may be required to renew the power source. By contrast, if the entire device or just the fuel pack is considered a consumable and a high power density is needed, a water reaction such as the galvanic corrosion of a magnesium-iron blend with saline may be a good fit.

Power sources other than exothermic chemical reactions are also possible. Sodium acetate solutions that have been supersaturated by cooling in the absence of nucleation sites are one example. The addition of a nucleation site causes exothermic crystallization of the salt. Although this power source may be desirable because it can be renewed by heating the sodium acetate solution (*e.g.*, the hand warmer application, see Table 7), it would require special design considerations. Example considerations include how nucleation will be triggered during the assay and how nucleation will be prevented during device construction, shipping, and storage.

The specific power source referenced in subsequent sections of this paper is the corrosion of mechanically alloyed particulate magnesium and iron (Mg-Fe) in the presence of saline. This Mg-Fe fuel and saline combination is a good fit for our application because it is easily stored, readily available, and inexpensive. It also allows for relatively straightforward activation mechanisms in an integrated chemical heater. Additionally, while electrical options are under consideration for powering MAD NAAT devices, Mg-Fe has a higher energy density than common inexpensive batteries (Table 7).

A model of the power source thermal output is necessary to accurately simulate the integrated device. This in turn enables more rapid system design iterations and optimization. A full system model describing the power output, chemistry, heat transfer, fluid dynamics, and phase change is, however, more complex than necessary to design a device. Instead, a power

profile for chemical heaters is measured using a simple test fixture, and then used in modeling, as outlined below.

7.2.3.2 Temperature regulator

The ideal source of heat for an isothermal assay would initially generate high power, to warm the sample from ambient to operating temperature, and then switch to low power to maintain the operating temperature in the face of inevitable heat losses to the environment (see idealized power profiles in Figure 32B). However, design and manufacture of this power source as its own chemical heater would require some or all of the following:

- Adjustable power output based on varying ambient temperatures
- Different reaction rates for the two power phases
- Variable timing and actuation of multiple reactions
- Active feedback controls

A more practical design couples a single exothermic reaction with non-ideal power output (*e.g.*, any of the chemistries shown in Table 7) to a PCM temperature regulation component to restrict the sample temperature to the nominal operating temperature range.

The optimal assay temperature will dictate selection of the PCM on the basis of its melting (or boiling) temperature. For instance, if the assay temperature range is ~47°C to ~55°C, a PCM that changes phase at 51°C has proven to be a good choice. The PCM must also have a narrow melting range that falls within the assay temperature range. The melting of a PCM can be monitored by many methods, including differential scanning calorimetry (DSC). Generally, on a plot of temperature versus heat input generated by DSC, a sharper-melting PCM is more effective at regulating temperature. Indeed, PCMs with similar peak melting temperatures may

have different melting ranges[163], in part because real materials have complex melting characteristics that depend on factors such as thermal history and chemical purity.

The thermal conductivity and latent heat capacity of the PCM are also critical to the design. A PCM with too little thermal conductivity will take too long to transfer heat from where it contacts the power source to the remote corners of its volume, resulting in increased warmup times and/or partial melting. Leaving a portion of the PCM unused for latent heat storage and release is wasteful. In practice, the thermal conductivities of many PCMs are too low for convenient chemical heater design -- an issue that is addressed by incorporating additives with high thermal conductivity[164]–[166], increasing the thermal conductivity of the resulting composite material. The use of aluminum wool and other shaped metals in PCM composites has been demonstrated[167]. However, in our experience it is difficult to produce void-free aluminum wool–PCM composites, resulting in inconsistent performance. The MAD NAAT device described in this paper uses graphene nanoplatelet powder (N008-100-P-10, Angstron Materials, Dayton, OH, USA). In our experience, the graphene–PCM composites are easier to cast reproducibly and produce a larger range of thermal conductivities.

The minimum volume of PCM required with a particular power source depends on the ambient temperature range specification. In the optimal case and at the maximum ambient temperature, almost all of the PCM would melt and the sample would meet the maximum tolerable assay temperature for the minimum holdover time. In the optimal case and at the minimum ambient temperature, the sample would meet the minimum tolerable assay temperature within the maximum warmup time and for the minimum holdover time.

A large number of PCMs are readily available[168] from chemical suppliers. These range from specifically designed fatty acid composites from manufacturers such as Rubitherm, RGEES, or Entropy Solutions to organic compounds such as lauric acid or paraffin waxes[169]. Room temperature liquids such as water, acetone, and methanol can also serve as liquid-to-gas PCMs. If a PCM with the desired peak melt or boil temperature does not exist, PCMs can be combined to shift the peak melt temperature[170]. However, this can often have undesirable consequences, such as a wider or bimodal melt or boil range, lower latent heat, or both. Fortunately, there are many available PCM options in a range of melt temperatures that do not require additional engineering (Table 8).

The current version of the MAD NAAT chemical heater uses PureTemp 53 PCM (PT53, Entropy Solutions, Plymouth, MN, USA) to maintain the assay temperature within tolerance. As another example, a LAMP-based isothermal NAAT system developed at PATH operates at 63°C[114]. At least two PCMs listed in Table 8 will provide that operating temperature. Additionally, a liquid-to-gas PCM is available because methanol boils near 63°C (depending on elevation).

Table 4: Commercially available solid/liquid PCMs along with manufacturer specifications. Melt temperatures and latent heat values obtained from manufacturer websites[171]–[173] or from other published values[169], [174].

Nominal melt temp [°C]	Name	Latent heat [J/g]
48	PureTemp 48	230
49	RT 50	168
49	Paraffin C20-33	189
53	PureTemp 53	225
53	Myristic acid	181
55	RT 55	172
55	Stearic acid	159
58	PlusICE A58	132
58	PureTemp 58	225
60	PlusICE A60	145
60	RT 60	144
61	PureTemp 60	220
61	Palmitic acid	200
62	PlusICE A62	145
63	PureTemp 63	206
64	RT 64HC	230
65	RT 65	152
68	PureTemp 68	198

7.2.3.3 Integrated heater system

A successful design for an integrated system balances the need for thermal performance with practical considerations. These include sample introduction to and extraction from the heated zone, along with power source and PCM storage and activation. The primary design consideration for an integrated system is the spatial arrangement of the system components and insulation. The chemical power source and PCM regulator components must be coupled to the sample in a way that maintains adequate thermal transfer between the power source and the PCM regulator, and between the PCM regulator and the sample, while maintaining adequate thermal separation between the power source and the sample. Additionally, the integrated system must be

insulated in such a way that the heater can provide adequate holdover time in the specified ambient temperature range.

The products of the power source chemical reaction also need to be considered. For example, the reaction of Mg-Fe with saline can rapidly reach the boiling point of the saline, and produces steam and hydrogen gas as by-products that need to be controlled. Proper handling of by-products is often required for safety, but other consequences of uncontrolled by-products, such as condensation in the sample zone, can also greatly affect thermal performance and device function.

At all stages of the design process, it is helpful to have working theoretical and finite-element thermal models of the integrated system. Such models enable effective iteration toward designs that provide adequate thermal performance in the least amount of space, among many other possible optimizations.

7.2.4 Deployment constraints

Additional design considerations can arise from deployment of the heater in a larger device. In some applications (*e.g.*, a heater for sample preparation), a heater should reach operating temperature as quickly as possible, whereas other applications may require a delay (*e.g.*, while waiting for an upstream process to complete). Two very different examples of successfully integrated chemical heater designs are (1) the NINA platform[113], [114], [175], and (2) the MAD NAAT platform[115], [154], [155], [157]. The NINA platform is optimized to provide incubation to assays in off-the shelf PCR tubes in a reusable vacuum thermos housing, but not integrated with other assay steps (*i.e.*, sample preparation, signal readout, whereas the MAD NAAT platform aims to integrate all assay steps and be disposable.

Many of the design considerations for the integrated chemical heater system apply to integration with a larger device. The specific arrangement of the chemical heater components within the larger device and with respect to the sample will continue to dominate thermal performance of the heater. The volume, geometry, and specific heat of other media being heated within the larger device are also important considerations. A chemical heater expected to heat a sealed PCR tube[114] will be designed much differently than one designed to heat a postage stamp-sized section of porous membrane with inlet and outlet connections to other porous membranes[115]. The form of the heated zone will also affect the insulation requirements, heat capacity, form factor, and eventual cost of the larger device insulation and enclosure. Other heating requirements, such as boiling for lysis during sample preparation, will also affect thermal performance of the chemical heater.

Finally, the use case for the larger device must be defined. If a reusable device is desired, where many assays are to be performed under a single chemical heater, it may be useful to design for robust, repeatable performance using insulating housings like a vacuum thermos[114] or Styrofoam box[149]. Alternately, a device meant to be fully disposable will likely use less expensive and more disposable materials and have a smaller form factor[115], [147], [148].

7.3 Materials and methods

7.3.1 Particle size reaction control, saline concentration reaction control

Reaction power output was quantified by monitoring temperature change in a vacuum thermos as a calorimeter. 1.00 grams of mechanically alloyed Mg with Fe fuel (Mg-Fe fuel A-131-325, Luxfer Magtech Inc., Cincinnati, OH, USA) were placed into the reaction vessel and reacted with 5 mL of 0.9% by mass saline solution delivered in a single bolus to the fuel bed. Temperature was measured at 1-second intervals using type T thermocouples and National

Instruments (NI) SignalExpress software and data acquisition hardware (NI cDAQ-9172 chassis and NI 9211 thermocouple input module, National Instruments Corporation, Austin, TX, USA). The bulk fuel was separated into particle size ranges of 50-55 μm each using a vibrating sieve shaker (Retsch GmbH model AS200, Haan, Germany). A similar calorimetry setup was used to measure the effect of saline concentration on the reaction rate. In this case, the Mg-Fe fuel total mass and particle size was constant using 1.00 grams of 300-355 μm Mg-Fe particles reacted with 5 mL of saline solution with varying percentages (0.6% to 1.4%) of NaCl to water by mass.

7.3.2 Chemical power source fuel pack construction

The fuel packs discussed throughout this paper were constructed with the wick either extending into the full circular section of the fuel pack, or lacking the circular extension and having the rectangular shape of the extended wick element protrude into the fuel approximately 10 mm (see Figure 37A). Wicks were cut from Standard 17 glass fiber (GF/Std17, GE Life Sciences, Piscataway, NJ, USA) using a laser cutter (M360, Universal Laser Systems, Scottsdale, AZ, USA) unless otherwise noted as a different porous medium. The circular tea bag enclosure was punched from four by five inch empty, heat-sealable tea bags (Empty Fillable Teabags, Muslin Bags, CA, USA) using a one inch diameter punch. The wick was then placed between two punched circles. With the wick enclosed, the two circles were heat sealed around the edge save for a 10 mm opening left open to load the Mg-Fe fuel using a lab-built impulse sealer making a 19 mm wide inner diameter circle for the fuel. The Mg-Fe fuel was measured by mass to ±0.001 g and loaded through the opening in the tea bag fuel pack. The opening in the fuel pack was then heat sealed using an additional custom element wired to the same impulse sealer.

7.3.3 Chemical power source wick geometry

In order to visualize the effects of wick geometry and liquid reactant delivery, fuel packs with Standard 17 wicks shaped as shown in Figure 37A were constructed as described in the

paragraph above. The rectangular part of the wick was 6 mm wide and 45 mm long as measured from the flat end of the wick to the intersection with the circular head (making the functional wicking length approximately 40 mm from the top of the saline well to the start of the fuel bed). The head diameter used was 19 mm. Reacting fuel packs were imaged using a thermal camera (SC655, FLIR Systems, Inc., Wilsonville, OR, USA) and a video created using the camera software (FLIR ExaminIR Max 1.30.0). Single frames at approximately the same time into the reactions were used for Figure 37B, C, and D to illustrate the difference in reaction rate and geometry.

7.3.4 Chemical power source test fixture

To determine the power output over time of the chemical power source, it is first necessary to quantify the thermal characteristics of the test fixture. The plotted line in Figure 33B represents the temperature recorded beneath the 3.5 cm diameter by 0.5 cm thickness cylinder machined from 6061 aluminum for a 0.8 W electrical heater power input. The electrical heater is composed of three parallel 10 ohm surface mount resistors (756-PWC2512-10RJI, Mouser Electronics, Mansfield, TX, USA), the composite heater having a resistance of 3.45 ohms. The power was set by voltage-limiting the electrical DC power supply (6612C, Hewlett Packard, Palo Alto, CA, USA) to 1.66 volts. The electrical heater sits in the location of the fuel pack in Figure 33A, affixed to the top of the aluminum cylinder with heat transfer tape (6838A12, McMaster-Carr, Elmhurst, IL, USA).

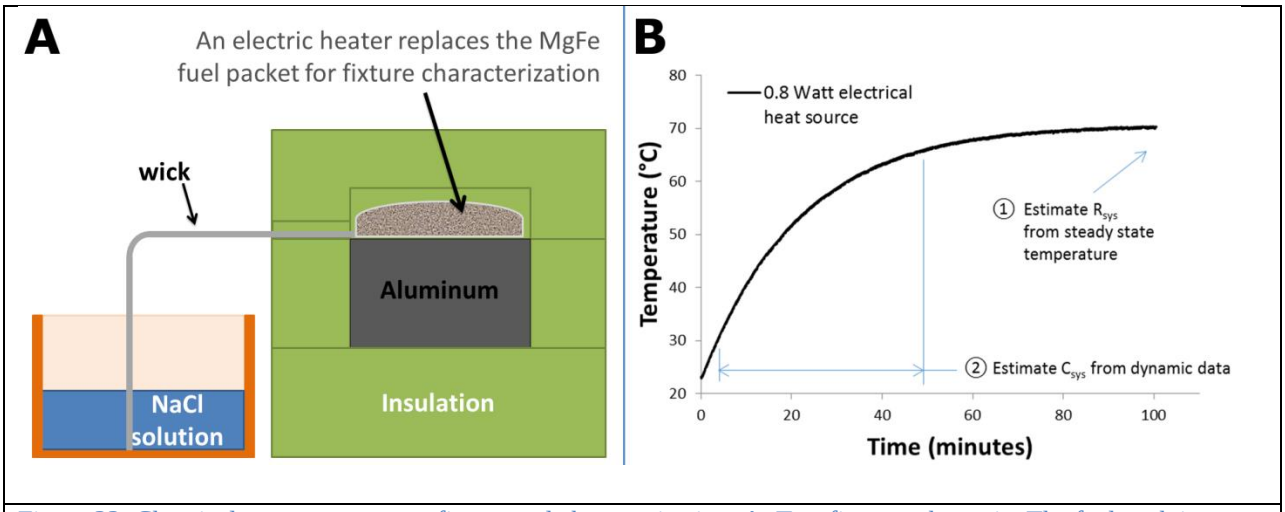

Figure 33: Chemical power source test fixture and characterization. A: Test fixture schematic. The fuel pack is supplied the NaCl solution via wicking from a reservoir and sits atop an aluminum block. The fuel pack warms the aluminum block, and temperature is recorded beneath the aluminum. The entire heater assembly is encased in an insulating shell. An electric heater replaces the fuel packet for test fixture thermal characterization. B: Temperature profile recorded beneath the aluminum block for a 0.8 W electrical power input. C_{sys} is estimated using the numeric model outlined below and the dynamic data. R_{sys} is estimated using the near-steady-state temperature data.

A section of 1.25 inch outer diameter by 0.125 inch wall thickness polymethylmethacrylate (PMMA) tubing (Part #8532K19, McMaster-Carr, Santa Fe Springs, CA, USA) was cut to 1.3 cm height to contain the fuel pack, and a 1.4 cm opening cut lengthwise to accept the wick enclosure. The wick enclosure was created with a 3D printer (Objet30 Pro, Stratasys ltd., Minneapolis, MN, USA and Rehovot, Israel) using the "high temperature" RGD525 material. The liquid reactant reservoir was also 3D printed, using the "transparent" RGD720 material. Fuel packs were constructed as described above. Insulation was machined in a 7.5 cm diameter by 7.6 cm height cylindrical shape split at 3.8 cm for assembly with cut-outs for the aluminum cylinder, PMMA tubing, and wick enclosure. Devices were constructed by first adhering a 36 AWG type T thermocouple (5SRTC-TT-T-36, OMEGA Engineering, Inc., Stamford, CT, USA) to the bottom-center of the aluminum cylinder, and then fitting the aluminum cylinder into the lower insulation in a cavity machined out of the PVC foam

(Part #9318K75, McMaster-Carr, Santa Fe Springs, CA, USA) of the same dimensions. The PMMA tubing was then centered and affixed on the top of the aluminum cylinder using double-sided DCM8 tape (DCM8, MBK Tape Solutions, Chatsworth, CA, USA) The wick enclosure was then lightly press fit into the opening in the PMMA tubing and placed over the liquid reactant reservoir. The fuel pack was then installed inside of the PMMA tubing on top of the aluminum cylinder, and the wick routed through the wick enclosure and bent downwards into the liquid reactant reservoir. Tape (Scotch Magic Tape 810, Scotch, 3M, St. Paul, MN, USA) was then used to cover the open sections of the wick enclosure to minimize evaporation. The top insulation was then installed. A 0.9% NaCl solution was added to the liquid reactant reservoir at time = 0 seconds, and thermocouple temperature data was recorded at 1 Hz using the NI DAQ.

Numeric model

To use the chemical power source test fixture to determine the power profile produced by a given fuel pack/wick combination, a simplified model of the system was devised. This system can be approximated by a thermal mass conducting heat through an insulating shell to an ambient temperature. A power input is applied to this thermal mass. The heat loss to ambient can then be written as:

$$P = \frac{T_{sys} - T_{amb}}{R_{sys}}$$	Equation 9

where R_{sys} is the system insulation value. Changing the temperature of the thermal mass requires

$$P = \frac{dT_{sys}}{dt} C_{sys}$$	Equation 10

where C_{sys} is the system thermal mass. The total power in to the system is then:

$$P = \frac{T_{sys} - T_{amb}}{R_{sys}} + \frac{dT_{sys}}{dt} C_{sys}$$	Equation 11

The R_{sys} term can be found by holding the power input constant and waiting for the system to reach a steady state where dT/dt = 0. Using the 0.8 W plot from Figure 33B, the temperature appears to be approaching a steady state value of ~80 °C (dT/dt = 0.) , R_{sys} is then:

$$R_{sys} = \frac{T_{sys} - T_{amb}}{P_{tot}}$$	Equation 12

The value of R_{sys} is then 75°C/W. C_{sys} can then be solved for:

$$C_{sys} = \frac{P_{tot} - \frac{T_{sys} - T_{amb}}{R_{sys}}}{\frac{dT_{sys}}{dt}}$$	Equation 13

Using the 0.8 W data with R_{sys} = 75 °C/W, gives C_{sys} = 0.3 [W-s/°C].

These R_{sys} and C_{sys} values were used in Equation 11 to solve for chemical power source power output in Excel (Microsoft, Redmond, WA, USA). dT_{sys}/dt was calculated for each time point using the 50th preceding and 50th following data point time and temperature. T_{sys} was measured using the on-device thermocouple, located beneath the aluminum cylinder. T_{amb} was measured using a thermocouple suspended in the laboratory air near the test fixture.

7.3.5 Finite element models

Models were created of the example heater using COMSOL Multiphysics (COMSOL Inc, Los Angeles, CA, USA) using the “Heat transfer in solids” module. Meshes were created using the software default with the mesh element size set to “Fine”. Phase change was modelled using the “Phase change heat transfer” model input. External boundaries were set to convective heat transfer with a 15 or 20 [W/m^2K] coefficient and ambient temperature of 21 or 23 [°C]. Power input for the integrated regulated heater was entered as

0*(t<60)+0.5*(t>60)*(t<120)+1.5*(t>120)*(t<180)+2.25*(t>180)*(t<300)+3*(t>300)*(t<420)+3.375*(t>420)*(t<540)+2.75*(t>540)*(t<600)+1.675*(t>600)*(t<720)+1*(t>720)*(t<840)+0.675*(t>840)*(t<1020)+0.125*(t>1020)*(t<1320)+0*(t>1320).

Table 8: Material properties used in finite element models

PVC Foam	Density	48.1 [kg/m^3]
	Thermal conductivity	0.033 [W/m-K]
	Specific heat	1,300 [J/kg-K]
PCM	Density	840 [kg/m^3]
	Specific heat	2,360 [J/kg-K]
	Ratio of specific heats	1
	Thermal conductivity	0.32, 0.6, 0.85, 1.5 [W/m-K]
	Latent heat of fusion	221, 206.5, 192, 172 [kJ/kg]
PMMA	Density	1,190 [kg/m^3]
	Specific heat	1,470 [J/kg-K]
	Thermal conductivity	0.18 [W/m-K]
Aluminum	Density	2,700 [kg/m^3]
	Thermal conductivity	238 [W/m-K]
	Specific heat	900 [J/kg-K]
Air	Density	COMSOL lookup table, 1.1 [kg/m^3]
	Thermal conductivity	COMSOL lookup table, 0.025 [W/m-K]
	Specific heat	COMSOL lookup table, 2000 [J/kg-K]
Fuel pack	Density	990 [kg/m^3]
	Thermal conductivity	0.58 [W/m-K]
	Specific heat	4,181 [J/kg-K]

Differential scanning calorimetry

Differential Scanning Calorimetry (DSC) was used to obtain latent heat values for PCMs used in the models. The DSC tests conducted using a microcalorimeter (Micro DSC VII Evo, Setaram Inc., Newark, CA, USA) confirmed changes in latent heat of PCM composites with varying amounts of graphene nanoparticle additive. For each sample, a conditioning cycle was run first to consolidate the powder and chips from the PCM composite. The conditioning cycle was run at a rate of 1.5°C/min from 30°C to 10-15°C above the nominal PCM melt temperature PCM. After conditioning, the sample was heated at a rate of 0.5°C/min from 30°C to 10-15°C above the

nominal PCM melt temperature. The sample was then held at that maximum temperature for 10 minutes and then cooled back down to 30°C at the same controlled rate of 0.5°C/min. Heat input during this ramp cycle was used to calculate latent heat and exact melt temperature. Figure 34 shows an example plot and software-computed latent heat and peak heat flow values for PureTemp 53 PCM with 10% graphene added.

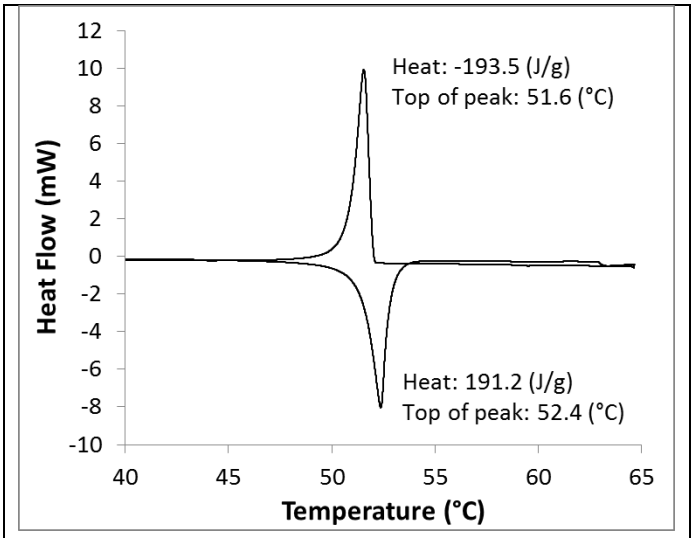

Figure 34: Example differential scanning calorimetry plot for 10% graphene in PureTemp 53 PCM. Latent heat and peak values are calculated by the software.

7.3.6 PCM casting

In general, for any final shape, the PCM casting process used is to heat the PCM, mix the composite components, cast, cool directionally, machine off the top, and cut to size if necessary. The PCM blocks used in test devices as well as the temperature regulator subsystem were cast using these steps. First, solid PureTemp 53 PCM (PT53, Entropy Solutions, Plymouth, MN, USA) was massed to ±0.01g. The PT53 was then melted in an oven at 80°C in a glass beaker covered with aluminum foil. After fully melted, graphene nanoplatelet powder (N008-100-P-10, Angstron Materials, Dayton, OH, USA) was similarly massed and introduced into the liquid PCM at a ratio of 20% graphene to total composite mass unless otherwise noted. Second, the composite was blended using a shear mixer (Model 1750, Arrow Engineering, Hillside, NJ, USA) for a minimum of 10 minutes at approximately 600 RPM. During mixing, the beaker was kept in a hot water bath regulated by a hot plate at 80°C. Third, a glass syringe, pre-heated in the 80°C oven, was used to transport the PCM composite to a similarly pre-heated, machined,

rectangular aluminum mold of the intended dimensions with removable end caps and an open top. In our case the mold was 20mm wide, 110 mm long, and 20 mm deep with approximately 3 mm thick sidewalls and a 30 mm thick bottom, allowing us to produce four 20x20x10 mm blocks per cast. Fourth, the filled mold was tapped on a table vigorously for one minute to remove entrained bubbles and air pockets in the corners of the mold. Fifth, the mold was placed in a cold water bath and the top was manually heated with a heat gun for 10 minutes to prevent the top from freezing. Heating the top and cooling the bottom allows the PCM composite to cool directionally from the bottom and sides while the liquid top can sink to avoid cavity formation during solidification. Sixth, the top of the cast stock is faced to the intended height using a jig machined to hold the cast PCM stock tightly and a router with a stand-off bit. After facing, the stock is cut into blocks of the intended length using a band saw. The blocks were then hand sanded more precisely to a consistent mass within 0.01g in order to control total PCM composite available for temperature regulation in each device.

Thermal conductivity

Thermal conductivity of materials was measured using a commercially available instrument (TCi, C-Therm Technologies Ltd., Fredericton, New Brunswick, Canada). Measurements were taken primarily of the PCM composite blocks.

Temperature regulator test fixture

The PCM composite was cast as described above and machined into a 20 x 20 x 10 mm block. The PCM block was fitted into a 3D printed four-sided shell, with a 5 mm thick aluminum bottom affixed with RTV silicone gasket adhesive (Blue RTV Silicone Gasket Maker 80628, Permatex, Hartford, CT, USA). This assembly was then fitted into a 65 x 65 x 29 mm insulation

block of two PVC foam layers with a cut-out in the center fitting the assembly. A type T thermocouple was attached to the bottom center of the aluminum plate. The bottom insulation was machined to 65 x 65 x 13 mm, and the top 65 x 65 16 x mm. A 0.5 kg weight was placed on top of the assembled device to avoid gaps between the foam layers. Before assembly, the device components were placed into an oven set to 80°C and allowed to equilibrate. The components were assembled warm (with the PCM melted), with (3) 10 x 10 x 10 mm PVC foam spacers holding the device off of the table and the weight off of the device. Temperature data was recorded from the thermocouple at a frequency of 1 Hz using the NI DAQ.

Integrated, regulated example heater

The integrated heaters are composed primarily of three layers of PVC foam with base dimensions 5.2 x 4.0 cm. Two layers of DCM8 tape seal the three layers together. The 12 mm high center layer is the temperature regulation subsystem. A cavity was punched into the middle foam layer to accommodate the PCM composite block (2.6 x 2.0 x 1.2 cm) placed directly into the foam. The RTV silicone gasket adhesive was again used in a ring on the foam around the PCM and under the top DCM8 tape layer to prevent PCM leakage during melting. A 6 mm deep, 25 mm diameter hole was machined into the lid as well as a 2 mm deep, 6 mm wide channel in the center of the long side of the lid. This channel acted as the wick inlet and the steam outlet for the system. A 1 mm deep 25 x 25 mm square was machined into the bottom foam layer to accommodate the assay hybridization chamber. A 0.5 mil Mylar layer was placed over the chambers and between the adhesive to facilitate removal of tested chambers. The fuel packs were produced as discussed in the chemical power source sections above. The single-piece GE Standard 17 material wicks in this case had a 6 mm wide rectangle wick extending 40 mm past the edge of the wick circle. 0.195±0.001 g of 355-400 µm particle size Mg-Fe fuel powder

was placed in the tea bag fuel encapsulation over the wick circle. Before placing the fuel pack onto the device a small rectangle of 2 mil Mylar was placed underneath to keep the adhesive layer from interfering with the wick fluidics.

This three layer foam stack was then set in a simple printed holder made of Objet "transparent" RGD720 material with a connected saline well. After introducing 5 mL of 2.0% by weight saline solution to the well and wick end, a printed lid was placed over the exposed wick without contacting it. The lid was necessary for running the devices in the environmental chamber (BTL-433, Espec, Hudsonville, MI, USA) to test the performance of an assay in the device at varied ambient conditions. The fans produce enough artificial convection in the chamber to drastically alter the flow properties of uncovered wicking materials due to evaporation (data not shown).

iSDA isothermal NAA assay

Four replicates of the isothermal NAAT (iSDA) reaction were prepared at a time for running inside four example heaters running simultaneously inside an environment chamber. Four replicates were run at ambient temperatures of 15, 22.5, and 30°C, for a total of 12 amplification results. Two replicates for positive and negative amplification controls were prepared at a later time for running inside a circulating-water-heated heat block set to 49°C. The iSDA reactions targeting the *ldh1* gene were assembled in four stages. 1) Molecular grade H_2O; K_2HPO_4 and KH_2PO_4 to 42.5 mM and 7.5 mM, respectively; dNTPs to 200 µM each; lateral flow probes; and primers (forward: 1000 nM, reverse: 150 nM, bumper: 50 nM) were added in that order and then the mix was vortexed. 2) 10^4 copies of methicillin-sensitive *Staphylococcus aureus* (MSSA) genomic DNA per reaction (ELITechGroup, Bothell, WA, USA) were added to the mix, and

then the mix was vortexed again. 3) 10 U of *Bst* 2.0 WarmStart DNA Polymerase (NEB, Ipswitch, MA, USA) and 0.64 µL per reaction of a modified Nt.BbvC1 (ELITechGroup) were added to the mix in that order and then the mix was vortexed again. 4) $MgSO_4$ to 3.75 mM was added to the mix and then the mix was vortexed again. All iSDA reactions were distributed in 40-µL volumes immediately after preparation to 14-cm diameter punches of Standard 17 glass fiber(GE Life Sciences). The reaction-loaded Standard 17 punches were then placed inside hybridization chambers (Cat. #70333-32, Electron Microscopy Sciences, Hatfield, PA, USA), which were then loaded into the appropriate example heater. Reactions were run in the heater(s) for 30 minutes, then the Standard 17 punches were extracted and spun at 13000 x g for 60 seconds in a collection tube. Lateral flow strips (ELITechGroup) were used to determine whether the amplification occurred, with 9.0 µL of each centrifuged sample mixed with 2.5 µL of 5x lateral flow buffer (3 M NaCl, 4% v/v PVP, and 4% v/v Triton X-100) and 1.0 µL of OD 10, 40-nm diameter, streptavidin-coated, gold nanoparticles (Innova Biosciences, Babraham, Cambridge, UK); added to a well in a deep-well plate; and wicked into a lateral flow strip attached to a cellulose waste pad.

Thermal performance analysis of a traditional tube heater

The temperature profile of a benchtop thermal cycler was characterized as a benchmark for thermal performance. A 1/32” hole was drilled into the cap of a 0.2 mL PCR tube (14230225, Thermo Fisher Scientific, Waltham, MA, USA). A 40 µL volume of water was added to each tube, and a type K thermocouple (5SC-TT-K-36-36, OMEGA Engineering, Stamford, CT, USA) was inserted through this hole so the thermocouple tip reached the bottom of the tube, and the thermocouple wire was taped into a groove cut into the tube cap. Instrumented tubes were loaded into the thermal cycler (MJ Mini, Bio-Rad, Hercules, CA, USA), and the thermal cycler set to

hold at 51°C. Temperatures were recorded at 1-second intervals using a data acquisition system (OMB-DAQ-54, OMEGA Engineering).

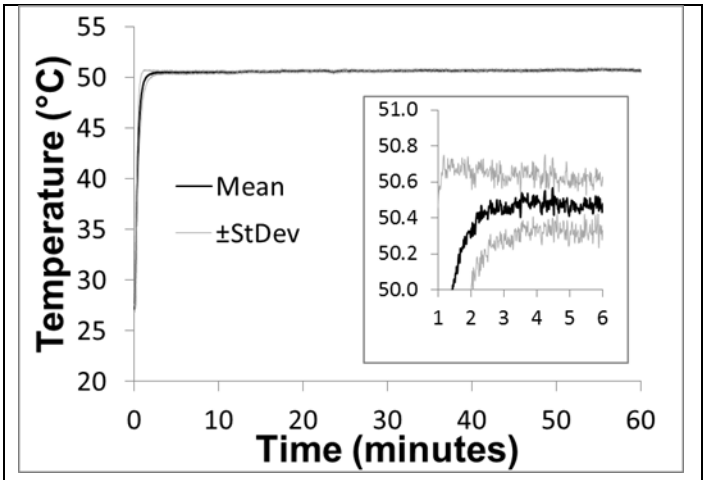

Figure 35: Sample temperature measured over time measured inside of a tube in a benchtop thermal cycler set to 51°C. The thermal cycler samples warm up to the lower assay limit (47°C) in less than one minute, and hold a stable temperature after ~2 minutes. The inset shows the standard deviation for the measured temperatures is quite small. The black line is the data mean, the grey lines are the mean ± one standard deviation, n=3.

7.4 Detailed prototype components

Prototypes of the chemical power source and PCM thermal regulator components have been designed according to the previously outlined criteria. These prototype components are used in the integrated MAD NAAT device, in the stand-alone NINA amplification platform, and as a prototype integrated chemical heater system, discussed in further detail below. The prototype chemical power source is the reaction of mechanically alloyed Mg-Fe powder with saline, and the prototype PCM thermal regulator consists of a PureTemp 53/graphene composite that is solid at room temperature.

7.4.1 Power source

Many variables can affect the performance of chemical power sources. A non-exhaustive exploration of selected variables for the Mg-Fe/saline reaction is outlined below. In all experiments, except for the calorimetry experiments, the Mg-Fe fuel was contained in a heat-sealed pouch made of paper tea bag material. Glass fiber porous membranes were used as wicks to deliver and meter saline solution to the fuel packs.

7.4.2 Particle size of solid reactants

Figure 36A shows how fuel particle size influences the time needed for the temperature inside a custom calorimetry device to reach 90% of the maximum observed. Smaller particles have a larger relative surface area for a given mass of Mg-Fe, allowing the reaction to proceed more vigorously. Consequently, more energy is released earlier in the reaction, resulting in faster warmup times.

Shorter warmup times may be desirable for many applications, but the trade-off is that fuel will be exhausted sooner, resulting in less energy being released during later stages of the heating process. This condition may require additional PCM to adequately buffer the temperature, storing energy early to keep the sample warm later. Balancing these factors is important for system optimization.

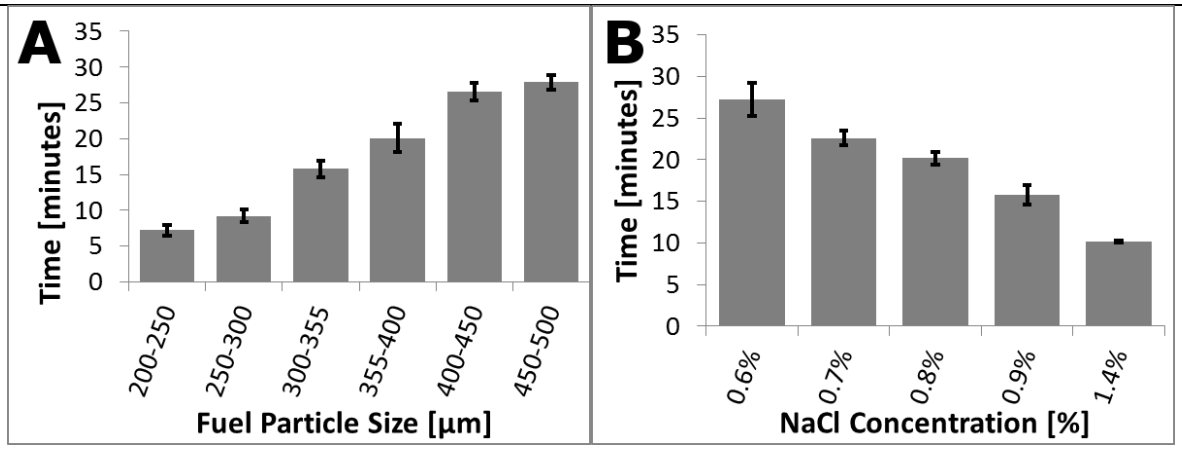

Figure 36: Exothermic reaction tuning. A: Mean time to reach 90% of the peak reaction temperature for various particle sizes of Mg-Fe fuel, n=6 minimum, error bars represent ± one standard deviation. B: Mean time to reach 90% of the peak reaction temperature is plotted for various saline concentrations. Reaction power output was quantified by monitoring temperature change in a lab-built calorimeter, n=4 minimum, error bars represent ± one standard deviation.

7.4.3 Concentration of liquid reactants

Figure 36B shows the warmup time for various saline concentrations. Increasing the concentration of NaCl resulted in shorter warmup times. Varying salinity over time may be desirable, but the trade-off is increased complexity of the saline delivery system. Nonetheless, this approach could decrease warmup time (high NaCl concentrations early) and extend holdover (low NaCl concentrations thereafter) with a slow, steady power output to match thermal loss to ambient surroundings and keep a stable operating temperature. Particulate NaCl can also be added to the fuel pack during assembly as a potential simplification of this approach. (Recent work from the University of Washington and PATH demonstrates a simple, ~95°C chemical heater for bacterial sample preparation in which particulate NaCl is added to the fuel[176])

7.4.4 Supply rate of liquid reactants

The volumetric flow rate of liquid reactant to the exothermic reaction also affects device warmup time. Delivering the liquid reactants through a wicking porous medium is a relatively simple means for continuously supplying the reaction with fluid. Conveniently, the principles of paper microfluidics[88] can be applied to chemical heater power supplies, metering the delivery of liquid reactants in the simplest case[148]. Lengthening or thinning the porous wick[148], or making it from a less permeable material, restricts liquid delivery and affects the power profile. Recent advances in paper microfluidics[157] could also be used to automate delivery of a series of reactants at varying concentrations, which could be used to create a bolus energy release (device warmup), followed by a period of lower power (temperature maintenance).

7.4.5 Chemical power source geometry

Geometric variations of the power source can have a large effect on power output and overall device performance. In addition to the width, length, and material of the saline delivery wick, the shape and coverage of the fuel bed by the wick (for more effective delivery of liquid reactants) is an important geometric consideration. Figure 37 shows a simple comparison of two

scenarios of wick overlap in the fuel bed, in which partial overlap resulted in uneven temperature distribution in the fuel pack. Furthermore, the shape and size of the compartment or material confining the fuel pack (which expands during reaction) can also affect reaction rate based on compaction of the fuel and access to the liquid reactant.

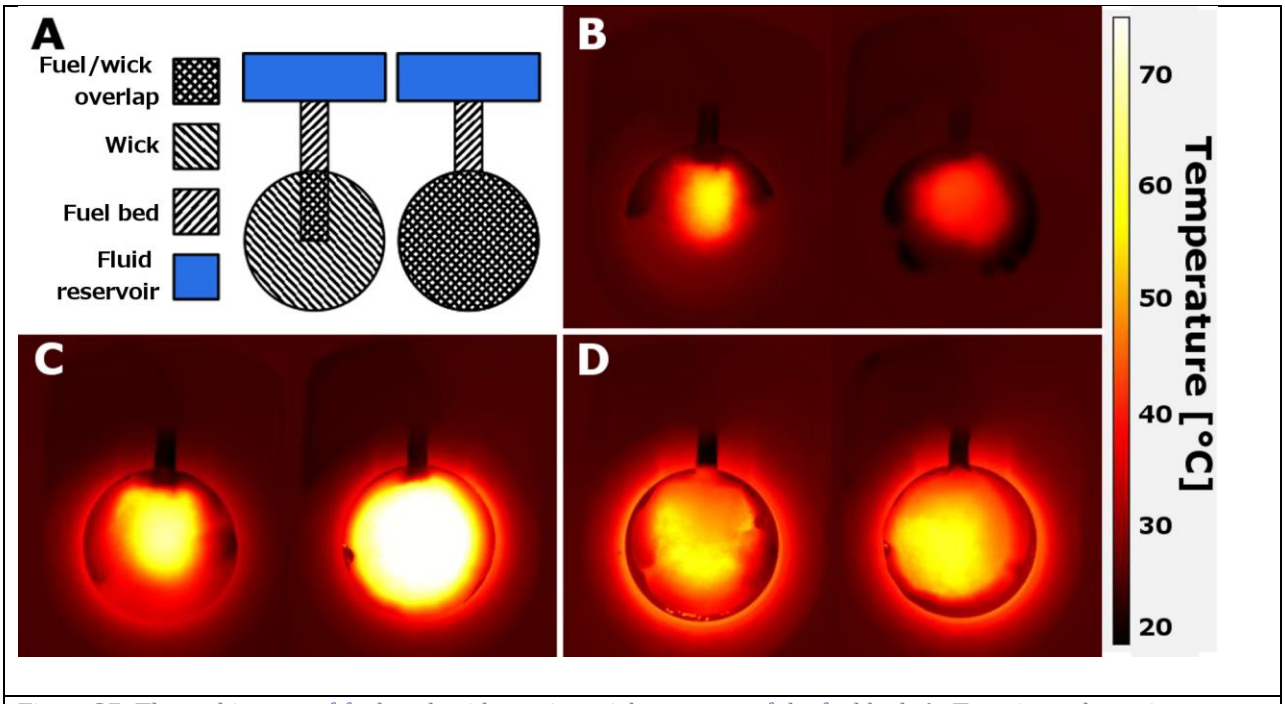

Figure 37: Thermal images of fuel pack with varying wick coverage of the fuel bed. A: Top view schematic comparing fuel pack construction. The partial extension wick (left) extends only a short distance into the fuel, whereas the full profile wick (right) covers the entirety of the fuel bed. B: Temperature at 2 minutes into the reaction. Both fuel packs are at elevated temperature, but the partial wick is at higher temperature where the wick directly contacts the fuel bed. C: Temperature at 5 minutes. The partial wick has a more uneven temperature distribution, whereas the full profile wick is at a more uniform, higher temperature. D: Temperature at 20 minutes. The partial wick may have a more uneven temperature distribution than the full profile wick, but the difference is difficult to distinguish.

7.4.6 Power source test fixture

A test fixture was constructed to characterize the chemical power source parameters such as fuel particle size and mass, saline volume, wick geometry, and fuel pack construction. The test fixture consists of an aluminum block, insulation, NaCl reservoir, and a cut-out for the chemical power source (see Figure 33). The method of characterization was to determine the power output

over time using the thermal characteristics of the test fixture (as determined with an electric heater). Temperature profiles measured within the test fixture were then converted to effective power profiles (efficiencies and losses due to non-ideal conductors and insulators are then taken into account by considering the effective power delivered as opposed to using total power output from the chemical reaction itself). Figure 38 illustrates the impact on temperature and power of varying the length and width of the saline supply wick. The resulting power profiles can be reproduced in a computational model and used to predict integrated device performance or simplified to step functions or average values and used in other, numerical calculations.

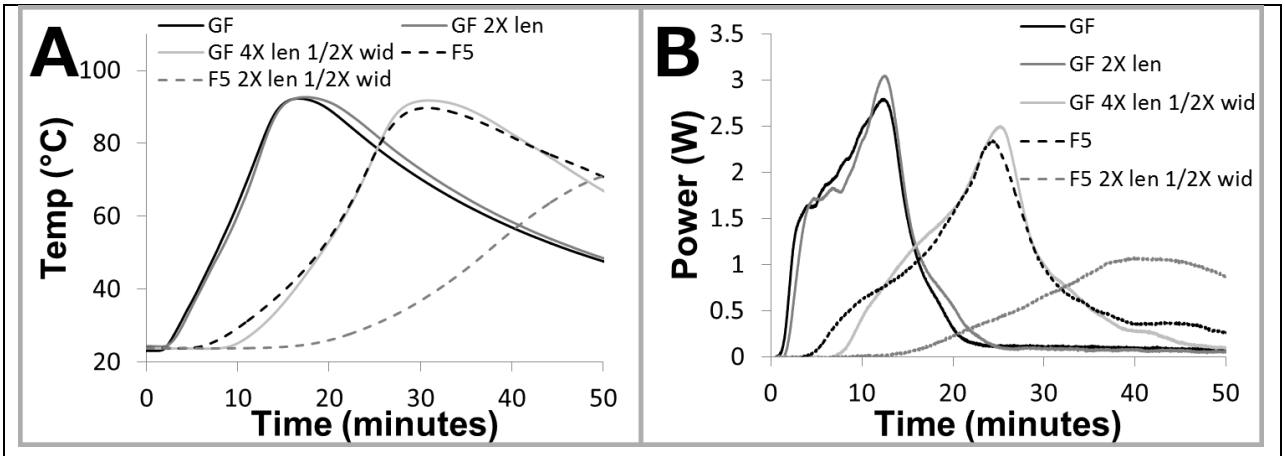

Figure 38: Data from chemical power source characterization test fixture. A: Experimental time vs. temperature for various saline supply wick geometries. Power sources utilizing both glass fiber (GF) and Fusion 5 (F5) membranes can be tuned using membrane length and width. B: Profiles from panel A converted to time vs. power using the numeric model.

7.4.7 Temperature regulator

For the MAD NAAT platform, the PCM temperature regulator was manufactured as a composite with graphene. As with the chemical power source, a PCM temperature regulator test fixture was constructed to test the performance of graphene-PCM composites and to validate phase change models.

Mixtures with a higher percentage of graphene were higher in thermal conductivity (Figure 39A). Although increased thermal conductivity is generally desirable, the trade-off is that a higher content of graphene in the mix means less PCM and less latent heat capacity (although recent work discusses the possibility of increased heat storage in certain materials due to graphene nanoparticle additives[166]). Increased graphene content decreased PCM latent heat

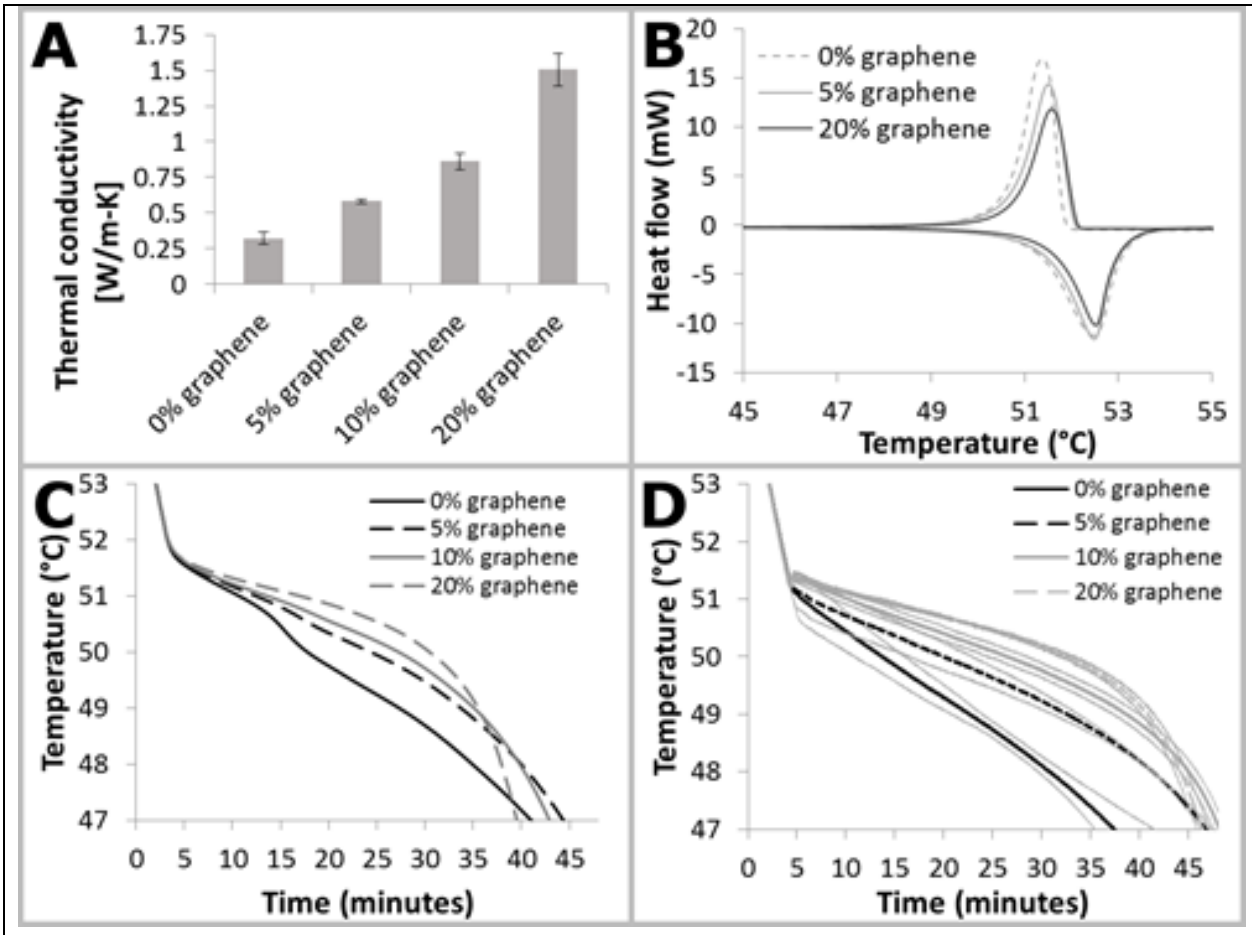

Figure 39: Graphene effect on thermal properties. A: Thermal conductivity of various percentage graphene by weight in PureTemp 53 PCM. Thermal conductivity increases when graphene is added. Data is mean ± standard deviation, n=6-8. B: DSC curves for graphene/PT53 PCM composites. Addition of graphene displaces PCM, resulting in a lower latent heat capacity of the composite (area under the curve in these plots). C: Modeled effect of varying graphene mass fraction. Lower graphene mass fractions have reduced holdover time. D: Experimental results for varying graphene mass fraction. A similar trend is observed as in the modeled results in panel C. Plotted is data mean ± one standard deviation, n=2-3.

capacity (Figure 39B), resulting in decreased holdover time (Figure 39C and D).

The manufacturing process developed for the prototype PCM temperature regulators resulted in repeatable thermal conductivity measurements. However, a gradient, where thermal conductivity increased from bottom to top, was observed in casts. Shear mixing time, location along the length of the casts, degassing by vacuum or other non-contact mixing means instead of tapping the mold, and the number of times the mold is tapped had little effect on conductivity.

Differences in graphene from the same manufacturer—such as differences in average platelet shape and grade—as well as in graphene from different manufacturers with similar nominal dimensions all affected the thermal conductivity of the PCM composite blocks. The batch-to-batch thermal conductivity coefficient of variation was approximately 3%, while the coefficient of variation due to machine error and test setup was about 0.1%.

Composite PCMs require adequate mixing to ensure the desired degree of homogeneity. Some protocols include degassing[164], though this has not been necessary in our experience. The mixture is heated above the melting temperature while shear mixing to prevent solidification of the PCM. After mixing, the PCM composite should be cast in a manner that controls the solidification process. PCM shrinkage during cooling can produce voids in the casting, potentially impacting device reproducibility. In addition, crystallization can introduce heterogeneity into the final cast PCM composite.

One method to control solidification is to cool the bottom of the mold (*e.g.*, in a water bath) while heating the open top of the PCM. This allows a controlled solidification process, where the first portion to solidify is the lower portion of the casting. As the casting cools from the bottom up, the remaining liquid PCM on the top lowers as the solidifying PCM below

shrinks, preventing voids from forming. This approach eliminates visible cavities and results in increased consistency (data not shown).

7.5 Validation of the prototype integrated chemical heater system

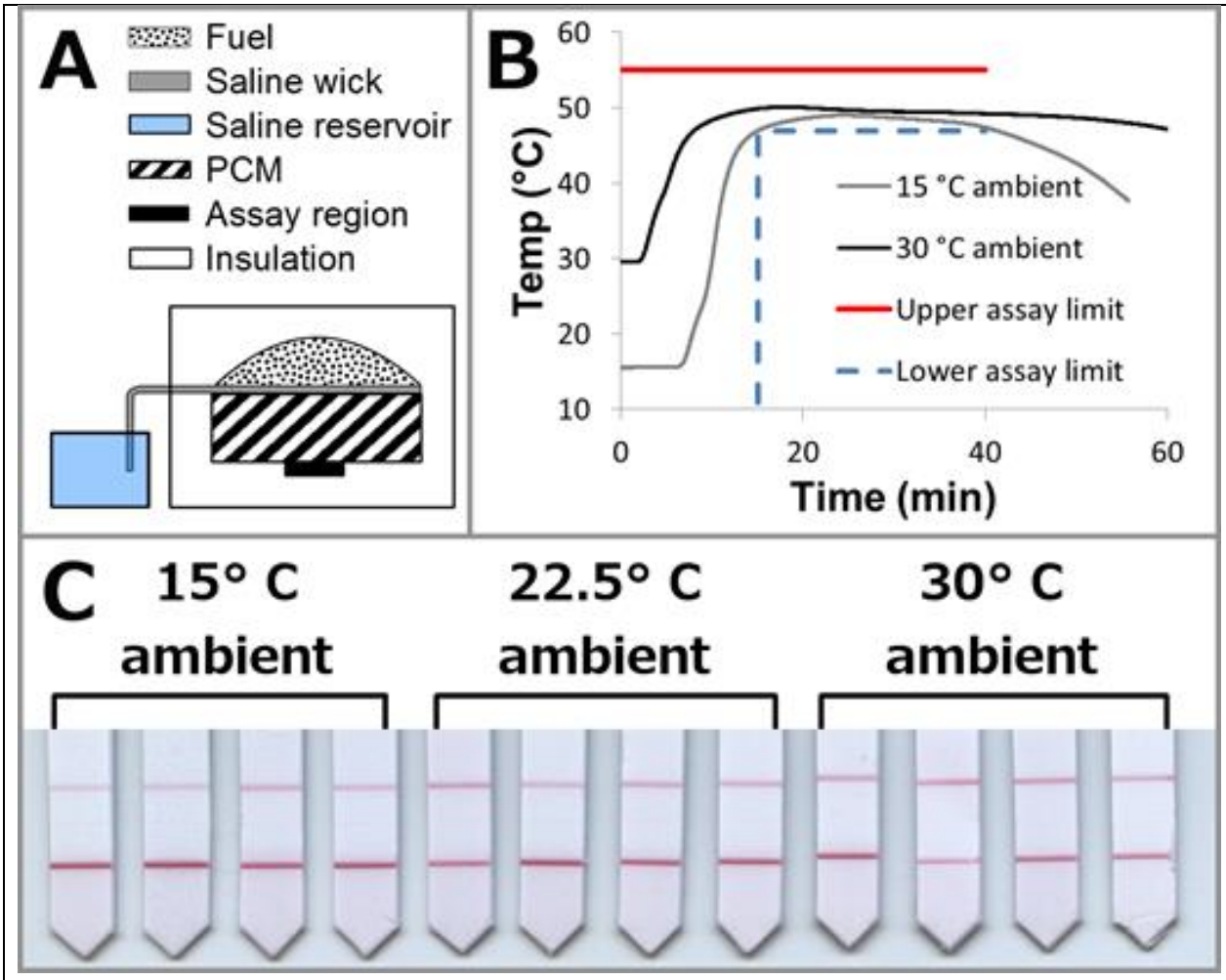

Figure 40: Integrated chemical heater. A: Device schematic (not to scale). The fuel pack sits atop a PCM block, under which is the heated sample zone. A shell of insulation surrounds this assembly, with cut-outs for the fuel pack, PCM, and sample zone. B: Prototype thermal performance. The temperature measured in the assay region is plotted for 15 and 30°C ambient temperatures. Plotted is the data mean, n=3. The assay upper and lower limits are also plotted to visualize device temperature and time requirements. C: Lateral flow detection of iSDA nucleic acid amplification in a prototype device at 15, 22.5, and 30°C ambient temperatures. Lower lines indicate presence of amplified product. Upper lines are biotin controls which bind the gold beads. Negative controls (not shown) indicate specificity of the reaction

After we constructed a prototype integrated chemical heater from the previously categorized components, the prototype heater performance was validated with an isothermal NAAT and against a finite element model of the system. Figure 40 illustrates the design of the prototype integrated chemical heater, along with its thermal and assay performance.

7.5.1 Prototype heater design and modeling

The following process was used to design the integrated chemical heater system:

1. Estimated the total fuel necessary for the assay.
2. Chose chemical power source geometry and designed an appropriate fuel pack.
3. Produced fuel packs and reacted them in a chemical power source test fixture similar to the final device to tune the power output profile.
4. Chose a PCM and additive and designed the PCM temperature regulator.
5. Integrated the chemical power source with the PCM temperature regulator.
6. Modeled the initial design and materials using COMSOL with phase change, as discussed in the Supplementary Information, for initial optimization of geometry for thermal transfer.
7. Completely built the initial design and tested it against performance targets (see Figure 32A). We iterated until the heater reached the thermal design goals, including performance at various ambient temperatures.

7.5.2 Prototype heater construction

For the prototype heater, placing the chemical power source above the PCM proved to be the most effective design (Figure 40), with assay region contacting the bottom surface of the PCM thermal regulator. Saline is delivered from the reservoir to the fuel pack using a porous wick. The fuel is encapsulated as previously described. This power source sits atop a 2.6 x 2.0 x 1.2 cm PCM composite temperature regulator. The insulation consists of sections of polyvinyl chloride (PVC) foam with cut-outs for the fuel pack, wick, PCM, and assay region. The individual PVC foam components are held together by a double-sided adhesive. As the reaction

proceeds, the fuel pack expands into a cut-out in the insulation lid. See Supplementary Information for construction details.

7.5.3 Prototype heater validation

The prototype heater held the sample within the assay tolerances for the required time (Figure 40B). To confirm that this prototype heater could meet the thermal requirements of the assay, iSDA amplification[160] was performed within the heater across a range of ambient temperatures. The assay was performed in porous media because the prototype design was intended for integration with a paper microfluidic device. While the level temperature control achieved by the chemical heaters is not as precise as a benchtop thermal cycler, the temperature profiles in the sample region were sufficient to perform iSDA in ambient temperatures ranging from 15°C to 30°C, as evidenced by the assay results shown in Figure 40C.

7.6 Conclusion

We have described a comprehensive approach and suite of tools that can be used to design chemical heaters for isothermal NAAT applications. Chemical heaters are especially appropriate where disposability or lack of electricity is a concern.

The use of test fixtures and models allows for evaluation of parameters such as fuel type, fuel particle size, reactant concentrations, fuel power output profile, PCM melt range, PCM thermal conductivity additives, and device geometry. These parameters then inform the design of an appropriate integrated chemical heater system.

If point-of-care diagnostics are to benefit from the use of precision chemical heaters for temperature control, additional studies will be needed regarding the stability of the magnesium iron fuel and phase change materials. Electric heaters are ubiquitous, and the electronics required

for precision temperature control are readily available. Additionally, mass manufacturing, along with the quality control procedures needed to ensure reproducibility, are very well established for electronic components. In our hands, the magnesium iron fuel and PCM composites have been fairly robust and straightforward to work with. However, quality control procedures will be needed for the scaling up of manufacturing processes. The robustness of these devices in transport to low-resource settings and in storage remains to be studied.

Our future work includes continued use of these tools to further the development and integration of the MAD NAAT sample-to-result isothermal NAAT platform and additional exploration into new ways to control temperature, such as the use of liquid-gas transition PCMs. Subsequent advances in the use of phase change to control temperature could yield smaller devices, more precise control, and lessened requirements for device insulation.

7.7 Acknowledgements

Funding was primarily provided by DARPA DSO HR0011-11-2-0007 to Yager, the UW Department of Bioengineering, and PATH. Heater development at PATH was also partially provided by NIH (R01EB012641) and NIAID (R01AI097038). The iSDA assay reagents were provided by ELITechGroup Inc. Molecular Diagnostics as a part of the DARPA grant. We thank John Ballenot at PATH for the editorial support during manuscript preparation. We also thank everyone in the Yager and Lutz labs and collaborators at PATH, GE Global Research, and the ELITechGroup who provided support and feedback. The funders had no role in study design, data collection and analysis, decision to publish, or preparation of the manuscript.

The work presented in this aim is adapted from[126]*:*

J. R. Buser, S. Diesburg, J. Singleton, D. Guelig, J. D. Bishop, C. Zentner, R. Burton, P. LaBarre, P. Yager, and B. H. Weigl, *Lab Chip*, 2015, **15**, 4423–4432.

8 Aim 3) Develop an electromechanical sample preparation methodology for hard-to-lyse pathogens compatible with point-of-care deployment

Here, an electromechanical sample preparation technique was developed which is capable of releasing DNA from a range of bacteria, including gram-positive *Mycobacterium marinum*, a *Mycobacterium tuberculosis* analogue. This mechanical cell disruption technique is powered by a portable audio source, and is inexpensive, highly portable, and nearly silent. This novel, robust cell rupture methodology uses a portable audio device, capable of recovering nucleic acids from gram-positive bacteria. The *Lab on a Chip* reviewers had very positive comments, leading the article to be classified by the journal as a "Hot Article".

Main deliverable: AudioLyse development and optimization parameters. ***Published***

The work in this aim is largely adapted from[158]*:*

J. R. Buser, A. Wollen, E. K. Heiniger, S. Byrnes, P. C. Kauffman, P. D. Ladd, and P. Yager, *Lab Chip*, 2015, **15**, 1994–97.

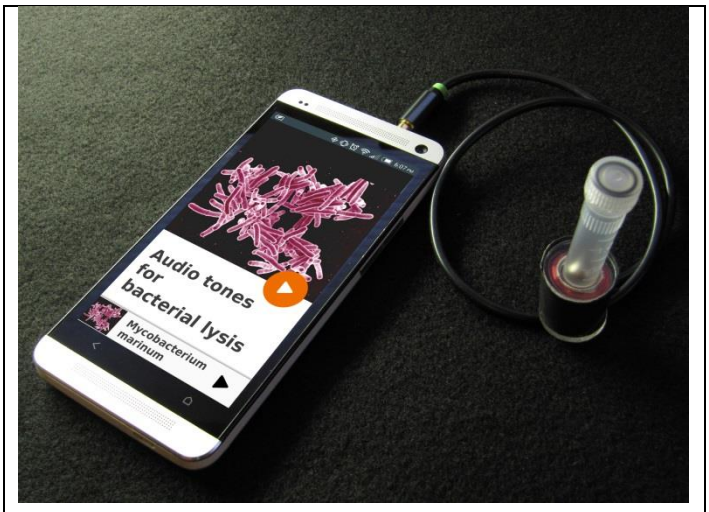

Figure 41: AudioLyse device. The headphone jack of a portable audio device (*e.g.* cell phone) excites an electromagnetic coil, spinning a magnet inside of a tube containing sample to be lysed. This spinning magnet causes pathogen cell rupture and consequent nucleic acid release.

Audio sources are ubiquitously available on portable electronic devices, including cell phones. Here we demonstrate lysis of *Mycobacterium marinum* and *Staphylococcus epidermidis* bacteria utilizing a portable audio device coupled with a simple and inexpensive electromagnetic coil. The resulting alternating magnetic field rotates a magnet in a tube with the sample and glass beads, lysing the cells and enabling sample preparation for these bacteria anywhere there is a cell phone, mp3 player, laptop, or other device with a headphone jack.

8.1 Background

Diagnosis is the first hurdle in disease management, expediting appropriate treatment in developed settings where sophisticated equipment and trained personnel are available. For example, in the US *in-vitro* diagnostic procedures represent about 1.6% of Medicare spending, yet influence 60-70% of medical decisions[4]. Nucleic acid amplification tests (NAATs) performed in the laboratory represent the pinnacle of sensitive and specific pathogen detection. Unfortunately, this state of the art is also expensive and complex, requiring infrastructure and instrumentation not available in all settings.

The lack of adequate diagnostics is especially troublesome in the case of tuberculosis (TB), which infects 1/3 of the world's population according to the WHO[17]. Sixty percent of

TB patients only have access to the peripheral level of the health system, where no suitable TB diagnostics exist[18]. Conventional TB diagnostics in lower-resource settings, mainly sputum smear microscopy and cell culture, lack the ideal specificity and timeliness. Also, required equipment isn't always available[18]. Microfluidic platforms have shown promise to enable the type of point-of-care devices that could bring NAATs directly to patients in lower resource settings, but sample preparation remains the weak link in microfluidics-based bioassays[177].

Existing microfluidic systems such as the Cepheid GeneXpert, consisting of sophisticated instrumentation into which a disposable cartridge containing the assay reagents is inserted, are capable of sample-to-result nucleic acid testing within two hours. While the GeneXpert has been shown to expedite TB treatment[52], due to cost and infrastructure requirements it remains primarily a solution for centralized laboratories. Therefore, further advances are needed in point-of-care sample preparation compatible with low resource settings and downstream NAATs.

Cell phones have provided a new tool used to interpret and communicate health data. In addition to telemedicine applications, cell phones have shown utility for applications including interpretation of diagnostic tests[40], [124], impedance measurements in microfluidic devices[178], and digitizing information originally recorded on paper forms[125]. If cell phones could also assist in sample preparation, NAATs may become more feasible to perform completely free of laboratory equipment.

If a low-cost point-of-care NAAT were available, not only could disease diagnostics be performed more rapidly, but also water and food safety could be evaluated quickly and inexpensively. The development of isothermal NAATs, such as loop-mediated amplification (LAMP) and recombinase polymerase amplification, is a large step towards enabling simpler

devices. These isothermal assays do not require precision thermal cycling, can be more robust against inhibitors than polymerase chain reaction (PCR)[179], and are compatible with paper-based microfluidics[96]. Low-cost precision isothermal heaters have been demonstrated that could enable point-of-care application of this type of assay[114], [115], [148]. Unfortunately, many low-cost point-of-care NAAT devices still rely on off-chip, instrumented sample preparation steps[177]. Mechanical lysis methods, such as bead beating, are desirable in that one can avoid the need to purify the sample from a chemical lytic agent before the downstream bioassay, but these methods traditionally suffer from relatively complex, user- and power-intensive instruments and protocols[180].

Many mechanical means of cell rupture have been demonstrated in the literature. Reports exist back to at least the 1960s of bacterial rupture due to compressive forces, Hughes *et al.* describe a press which crushes *Mycobacterium* with repeated hammer blows[181]. Cavitation , often induced *via* sonication, can also cause bacterial rupture[182]. In addition, other literature has demonstrated methodologies which rely on fluid shear to disrupt samples[183]. Lange *et al.*[184] showed a lower threshold of 1,800 Pa fluid shear for *Escherichia coli* cell disruption. According to Seltmann[185], the intact cell wall of gram-negative bacteria ruptures at ~5 atm compression, whereas gram-positive bacteria require up to 50 atm compression. The difference in mechanical thresholds of cell rupture between gram-positive and gram-negative bacteria can be explained by differences in the peptidoglycan layer of the cell wall.

A three-dimensional peptidoglycan network encapsulates the cell, and is largely accountable for the strength and rigidity of bacterial cell walls. The gram-positive cell wall is 15-30 nm thick, with the major component being highly-cross-linked peptidoglycan, which accounts for over 50% of the dry weight of the membrane. Gram-negative bacteria have an approximate

monomolecular layer of peptidoglycan, whereas gram-positive bacteria have peptidoglycan which is several layers thick. In addition to thickness differences between gram-negative and –positive bacteria, differences in the degree of crosslinking can also have mechanical consequences. In *E. coli*, about 50% of the peptidoglycan is crosslinked, which is considered relatively uncrosslinked. In some bacteria, up to 90% of the peptidoglycan is crosslinked. Crosslinking in gram-negative bacteria is usually non-covalent. Covalent crosslinking is usually observed for gram-positive. These differences in peptidoglycan layer, shown in Figure 42 below[186], result in gram-negative bacteria usually rupturing easier than gram-positive bacteria.

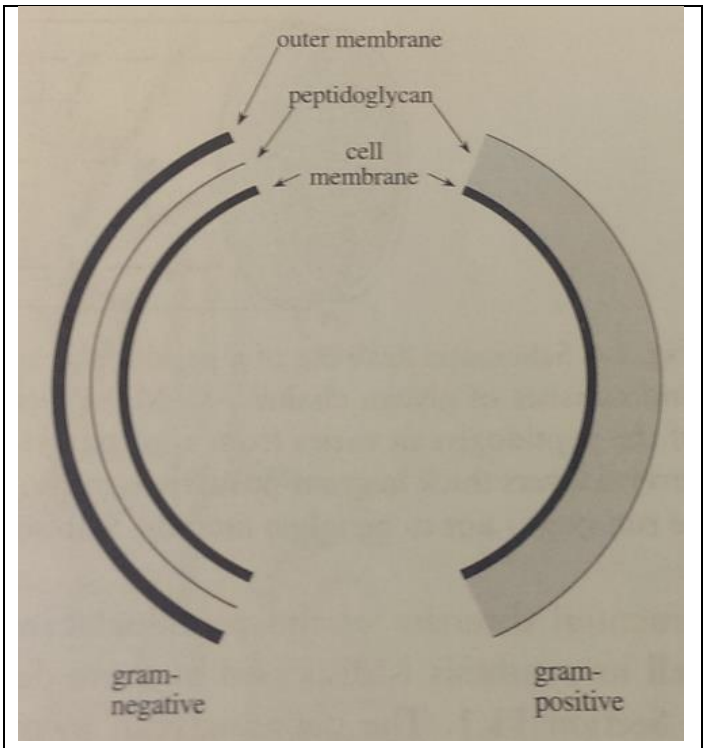

Figure 42: Gram negative and gram-positive cell walls. Gram-positive cells have a much thicker peptidoglycan layer, resulting in greater mechanical resilience. Image from [186].

Here we demonstrate lysis of two gram-positive bacteria—*Staphylococcus epidermidis* and a more difficult target *Mycobacterium marinum*—using a new form of highly portable, low-power, mechanical cell lysis. The choice of these bacteria is intentional, as analogues for important clinical targets: methicillin-resistant *Staphylococcus aureus* (MRSA) and *Mycobacterium tuberculosis*, respectively. Like other mechanical approaches, it does not introduce reagents incompatible with nucleic acid amplification. We believe this new apparatus could enable point-of-care NAATs for a wide range of organisms. At least one other group has demonstrated a low-cost mechanical lysis

method amenable to POC diagnostics[111]. What sets our device apart is that it is free from a device-specific power source: adequate power can be provided by the readily-available portable audio device signal. If one is already using a smartphone to quantify assay readout, the headphone jack of this same phone could power the sample preparation step. With the recent increase in the use of diagnostic interpretation aided by cell phones[9], which are fairly ubiquitous worldwide[124], this type of device may help close the loop in sensitive and specific pathogen detection in low resource settings. Here we show that the headphone jack of a low-cost mp3 player provides adequate power for this lysis methodology. The resulting DNA accessible for amplification after audio-powered lysis is compared to bead beating as a gold standard.

8.2 Material and methods

8.2.1 Bacterial culture

Staphylococcus epidermidis (strain Fussel ATCC 14990) was cultured in Tryptic Soy Broth (BD Bacto, Sparks, MD, USA) at 37°C, shaking (250 rpm). Overnight cultures were diluted 1:100 in fresh medium and grown to mid-log phase (OD_{600} = ~2). *Mycobacterium marinum* (Aronson ATCC 927) was cultured in Middlebrook 7H9 broth with ADC enrichment (BD Difco, Sparks, MD, USA) at 30°C, shaking (250 rpm) for 4-7 days. Cultures were diluted 1:100 in fresh medium and grown for 48 hours to mid-log phase (OD_{600} = ~1). After growth, cells were pelleted and resuspended in 1 volume Tris-EDTA (TE: 10 mM Tris-HCl, 1 mM EDTA, pH 8.0:Sigma-Aldrich, St Louis, MO, USA) buffer. Cells dilutions were also done in TE.

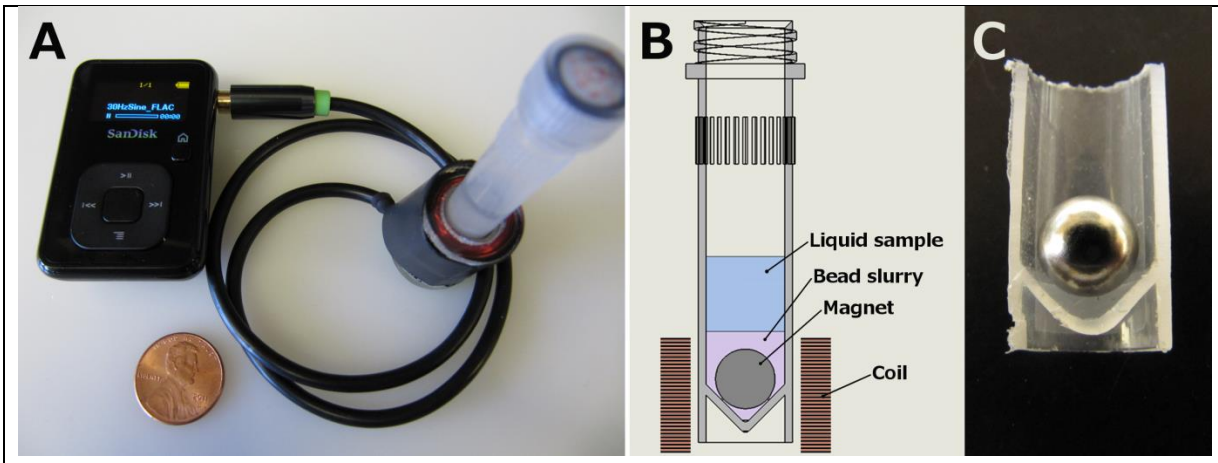

Figure 43: Overview of portable audio-powered electromagnetic cell lysis device. A: Sansa Clip mp3 player provides a 30 Hz sine wave signal to the coil using the headphone jack, US penny for scale. B: Schematic of tube showing user-added sample along with pre-loaded magnet and beads. C: Sectioned tube with magnet. The spherical magnet rides on the lower angled tube walls when the tube is vertically oriented. When provided an alternating magnetic field by the coil, the magnet rotates against the beads and the tube walls.

8.2.2 Audio-powered lysis

Device layout is highlighted in Figure 43. Coil bobbins were constructed from a hacksaw-excised well from a 24-well plate adhered to laser-cut acrylic upper and lower disks. The bobbin was wound with 490 turns of 32 AWG magnet wire, for a DC resistance of 11.4 ohms. The wound coil was soldered to a 1/8" stereo cable combining the left and right channels. The assembly was then wrapped with two turns of electrical tape around the circumference. Screw-top 2 mL O-ring tubes (02-682-558, Thermo Fisher Scientific, Waltham, MA, USA) were loaded with 100 µm glass beads (9830, Research Products International Corp., Mt. Prospect, IL, USA) and a ¼ inch NdFeB magnet (S4, K&J Magnetics, Inc., Pipersville, PA, USA). Sample was then added to the tubes, and the tubes loaded into the coils. The sample volumes tested were 800 µL, to match the bead beater protocol, along with 500 and 300 µL. A 30 Hz sine wave FLAC audio file was generated using Audacity 2.0.5†, and was played on the mp3 player (Sansa Clip+ 4 GB, SanDisk, Milpitas, CA, USA) at full volume with the equalizer set to maximize bass frequency response.

8.2.3 Bead Beater

800 µL samples were added to 2 mL O-ring screw top tubes (Fisher 02-682-558) with 800 mg of the 100 µm glass beads(9830, Research Products International Corp., Mt. Prospect, IL, USA). Tubes were loaded into the bead beater (Mini-Beadbeater-8, Biospec Products, Inc., Bartlesville, OK, USA), set to "homogenize", and run for (3) 1-minute cycles with a 1 minute pause between cycles.

8.2.4 qPCR

To quantify DNA recovery for *S. epidermidis*, qPCR was performed using primers designed against the *htrA* gene (FWD: 5'-GAG CGC ATA AGA CGT GAG AA-3', REV: 5'-TCT TCT TGT GTC AGC TTC TCT ATT-3'), and using Bioline SensiFAST SYBR No-ROX qPCR kit (Bioline USA Inc., Taunton, MA, USA). Samples (1 µL) from the bead beater or audio-powered lysis were used in 20 µL qPCR reactions run on a real-time PCR instrument (Rotor-Gene Q, Qiagen, Valencia, CA, USA) using: 95°C (3 min), 40 cycles of 95°C (5 sec), 54°C (10 sec), and 72°C (15 sec). Fluorescence data were collected during the 72°C step using the green channel. To quantify DNA recovery for *M. marinum*, qPCR was performed using the assay described by Jacobs et al., substituting the SensiFAST Probe No-ROX qPCR kit (Bioline USA Inc., Taunton, MA, USA) for the master mix used previously[187]. Samples were amplified as follows on a real-time PCR instrument (CFX96 Touch, Bio-Rad, Hercules, CA, USA): 95°C (5 min), followed by 40 cycles of 90°C (10 sec) and 60°C (20 sec). Fluorescence data were collected during the 60°C step using the green channel. Genomic DNA copy numbers were determined relative to standard curve analysis using purified DNA of known copy number using either the Rotor-Gene or Bio-Rad CFX software. Both assays are sensitive down to ~10 copies of the target sequence.

8.2.5 Statistics

A student t-test was performed on bead mass data (Figure 48A) and *M. marinum* data (Figure 49) in Excel (Microsoft, Redmond, WA, USA) for a single-tailed comparison assuming the data is homoscedastic. The 200 & 400 mg bead masses were grouped and compared separately to the 0 & 100 mg and 800 mg groups for both the 300 and 800 µL sample sizes.

8.2.6 Exploration of AudioLyse cell disruption mechanism

As mentioned earlier in this section, multiple types of mechanical perturbations have been shown to rupture bacterial cells. To explore the mechanism of cell rupture in the AudioLyse, calculations and experiments were performed to examine the effects of fluid shear, fluid pressure, and fluid mixing.

8.2.6.1 Fluid shear-driven rupture

Lange *et al.*[184] showed a lower threshold of 1,800 Pa fluid shear for *Escherichia coli* cell disruption. *E. coli* is a comparatively fragile gram-negative bacterium, gram-positive bacteria may need higher shear for cell disruption and nucleic acid release. To estimate the fluid shear present in the AudioLyse, some simplifying assumptions will be made: 1) a minimum gap of 100 µm (one bead diameter) between moving surfaces, 2) magnet rotation of 30 Hz, with no x-y translation, 3) no slip at contacting surfaces.

The beads translate in the direction of magnet rotation at half of the surface velocity of the magnet, assuming no slip at the magnet/bead and bead/tube wall interfaces. The fluid shear stress is calculated for the region between the magnet surface and the tube wall, near the glass beads separating the magnet from the tube wall. This region is approximated as Couette flow, with the fluid thickness approximated as the bead diameter. A schematic showing the simplified geometry is shown in Figure 44.

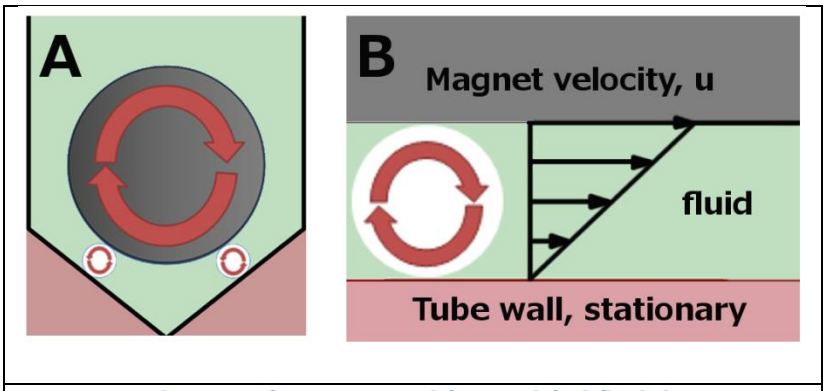

Figure 44: Schematic of geometry used for simplified fluid shear calculation, which is a 2D cross section through the center of the tube. A: The magnet (gray circle) is spaced from the angled tube walls by a 100 µm glass bead (white circles). The beads translate in the direction of rotation at half the surface velocity of the magnet assuming the magnet does not slip against the beads, and the beads do not slip against the tube wall. B: Couette flow, approximating bead and tube wall surface as parallel plates. In a Newtonian fluid, a linear velocity profile will be observed.

Calculating magnet surface velocity in this simplified system:

Magnet surface velocity (u):

$$u = Magnet\ circumference\ x\ frequency = \ pi * 0.25\ [in] * 25.4\ \left[\frac{mm}{in}\right] * 30\ [Hz]$$

$$= 598\ [\frac{mm}{s}]$$

Fluid shear rate (γ):

$$Fluid\ shear\ rate\ \gamma = \frac{u}{h} = \frac{0.6\ [\frac{m}{s}]}{1E-4\ [m]} = 6000\ [\frac{1}{s}]$$

Fluid shear stress (τ):

$$\tau = Shear\ rate\ x\ viscosity = \ \gamma\mu = 6000\left[\frac{1}{s}\right] x\ 1E-3[Pa\ s] = 6\ [Pa]$$

By these assumptions and calculations, fluid shear rate is over two orders of magnitude lower than the reported 1,800 Pa necessary to rupture gram-negative *E. coli* cells. Heartier bacteria such as gram-positive *Stapylococcus aureus* and *Mycobacterium marinum*, successfully disrupted in our experiments by the AudioLyse, will likely require higher shear stress than *E. coli* for disruption, and seem unlikely to be disrupted *via* this mechanism.

8.2.6.2 Pressure-driven rupture

According to Seltmann[185], the intact cell wall of gram-negative bacteria ruptures at ~5 atm compression, whereas gram-positive bacteria require up to 50 atm compression. To estimate the compressive pressure exerted on bacteria in the AudioLyse device, a simplified system is described. First, the downward force of the magnet (F_{magnet}) is estimated by subtracting the buoyant force ($F_{bouyancy}$) from the gravitational force ($F_{gravity}$). For the purposes of this estimation, the density of the glass bead/water slurry displaced by the magnet will be estimated as 1,800 kg/m^3 (common glass is 2,400-2,800 kg/m^3, water is 998 kg/m^3 @ 20°C). The magnet volume is $\frac{4}{3}\pi\, r^3$ = 1.3X10^{-7} m^3. The buoyant force exerted on the magnet is then:

$$F_{bouyancy} = \rho_f V_{disp} g = 1{,}800\ \left[\frac{kg}{m^3}\right]\ 1.3E-7\ [m^3]\ 9.81\left[\frac{m}{s^2}\right] = 0.0024\ [N]$$

And the downward force of the magnet is:

$$F_{magnet} = F_{gravity} - F_{bouyancy} = 9.8\ \left[\frac{m}{s^2}\right] 0.001\ [kg] - 0.0024\ [N] = 0.0074\ [N]$$

Assuming a packing density of 90% of beads (hexagonal packing) on the lower half of the magnet, ~6,500 beads would cover the bottom half of the magnet. For simplification, the projected area of the sphere will be used to estimate the amount of compressive pressure applied to the bacteria. Each bacterium is estimated to be 1 x 2 µm, with a cross sectional area of 2x10^{-12}

m^2. If each of the 6,500 beads were resting on a $2x10^{-12}$ m^2 bacterium, this would result in a compressive pressure of:

$$\frac{0.0074[N]}{6{,}500 * 2E - 12\ [m^2]} = 0.6\ [MPa]$$

Based on the 5 and 50 atm (0.5 and 5 MPa) rupture pressures for gram negative and positive bacteria reported by Seltmann, this estimation predicts that the static weight of the magnet alone is enough to rupture gram-negative bacteria. Given the conservative nature of the estimation of packing density, and load-bearing contact area, and zero x-y translation, it would not be surprising if the compressive forces present in the actual device were sufficient to rupture gram-positive bacteria.

Based on the fluid shear and compression estimations, crushing of the bacteria seems more likely in the AudioLyse than shear-driven rupture. This hypothesis will be tested *via* experiments where shear effects and compression effects are somewhat isolated.

8.2.6.3 Hydrodynamic pressure

Sonication techniques cause cavitation, and consequently cell rupture[182]. Other studies have shown that a system with similarities to the AudioLyse can achieve negative pressure-induced cavitation near a rolling sphere submerged in a viscous liquid[188]. If cavitation were present in the AudioLyse, it could be an additional cell rupture mechanism. For a first-pass exploration of the pressures present within the AudioLyse tube during operation, a two-dimensional cross section (similar to a journal bearing, Figure 45 below) will be used. For now, any bouncing of the magnet will be ignored. Journal bearings are used to support rotating radial loads, usually consisting of two cylinders. The outer cylinder, called the bearing, is the negative space into

which the inner cylinder, called the journal, is inserted. There is some clearance between the journal and bearing, which normally contains a liquid such as oil.

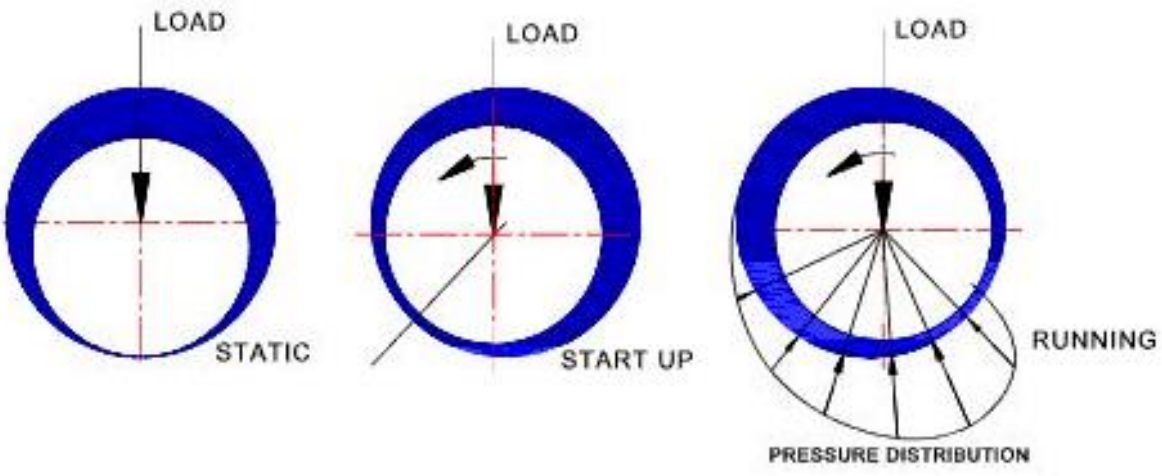

Figure 45: Journal bearing operational modes. Left: Static condition, journal is not rotating. Here, the surfaces of the journal and bearing are in contact. Center: Start up condition, boundary lubrication. Here, the fluid conditions may not allow for fluid pressures sufficient to separate the surfaces of the journal and bearing. Right: Running condition. Journal is supported by hydrodynamic fluid pressure, friction is reduced, and there is no surface-to-surface contact between the journal and the bearing. Figure from **http://www.brighthubengineering.com/manufacturing-technology/73568-hydrostatic-lubrication**

Similar generic operational modes to those shown in Figure 45 above are observed with the AudioLyse: the magnet at rest is centered at bottom of the tube. When an alternating magnetic field is applied, the static friction must be overcome to begin rotation. Once the magnet begins rotation it rotates at a constant velocity corresponding to the excitation frequency of the coil, confirmed using the back EMF of the coil generated due to the magnet rotating in the stationary coil[189]. To estimate the hydrodynamic pressure distribution in the AudioLyse, the mechanism of pressure generation in a journal bearing will be explored.

The journal and bearing are two solid surfaces separated by a fluid layer. To understand how this fluid layer opposes a radial load, Couette flow between two plates will be considered first (see Figure 44B). Here, the top plate is moving to the left, and the bottom plate is stationary.

If a vertical load were applied to the moving top plate, while the stationary bottom plate was held fixed, the top plate would move down, as no force opposes the downward force for parallel plates. If the plates are not parallel, however, fluid velocity gradients will cause pressure to be developed, shown in Figure 46 below.

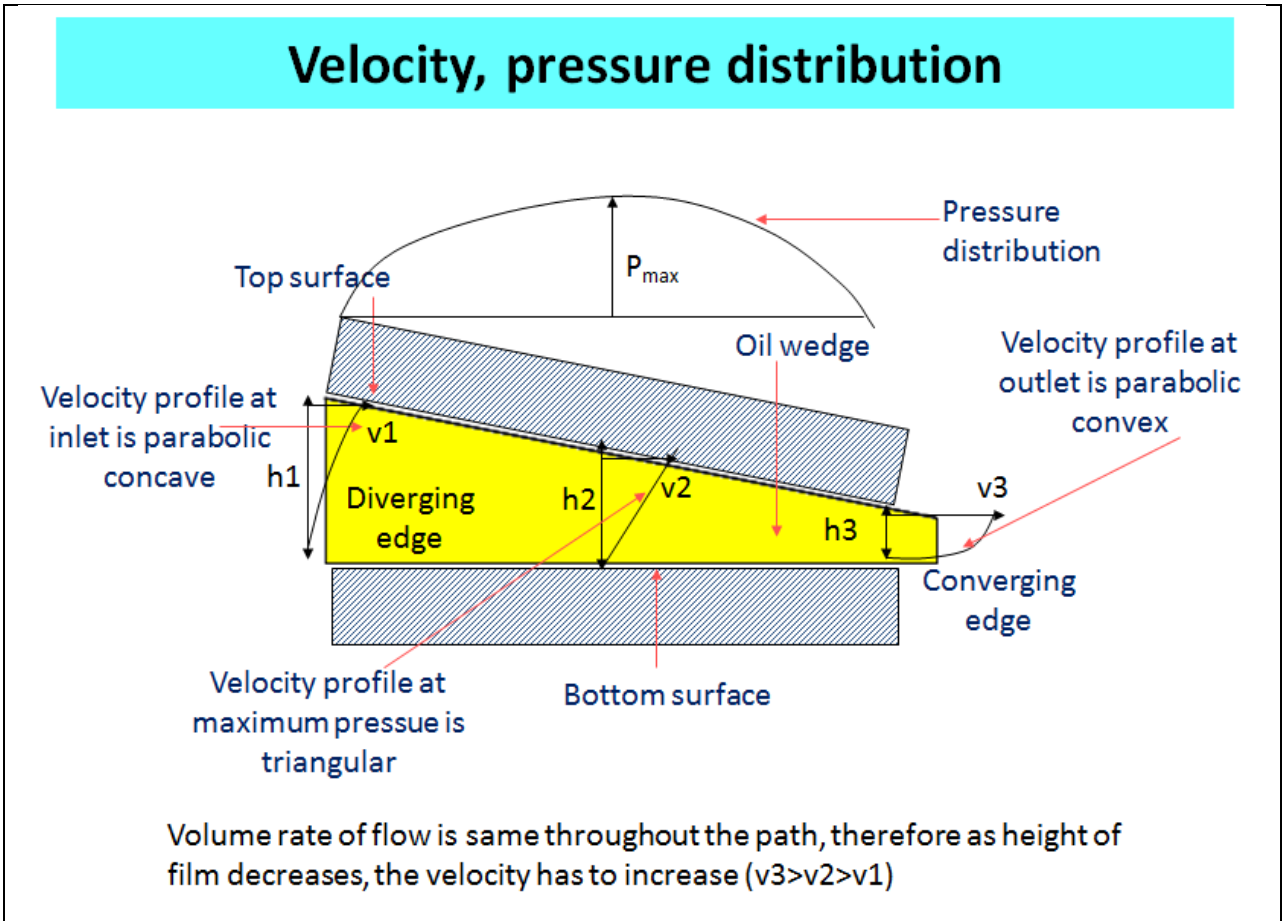

Figure 46: Pressure development between two non-parallel plates separated by a fluid channel. Due to the decreasing fluid thickness (h1>h3), assuming incompressible fluid, the average fluid velocity must increase moving from left to right. This velocity gradient results in a positive pressure, which is the source of the pressure that keeps a rotating journal separated from the bearing by a fluid layer. A negative pressure is also generated at the opposite side of the journal bearing (where these approximating plates would be diverging rather than converging), which explains the eccentric steady-state position of an operating journal bearing (see Figure 45). Image taken from http://web.iitd.ac.in/~rribeiro/MEL%20417%20Lubrication%20Lec%20100211.ppt.

8.2.6.4 Testing compression vs shear rupture via experimentation

To test the hypothesis that compressive forces are the primary mechanism of bacterial cell disruption, an experiment was designed to compare fluid shear effects and compressive force effects. The two experimental conditions are outlined below.

Isolated fluid shear effects: AudioLyse standard conditions with the magnet but minus beads. The hypothesized bacterial crushing zones at the bead/wall and magnet/bead interfaces have been removed in this experiment.

Isolated compressive force effects: AudioLyse conditions (including beads and magnet) attached horizontally to a rocking plate. The hypothesized high shear zone between the magnet and tube wall has been removed in this experiment.

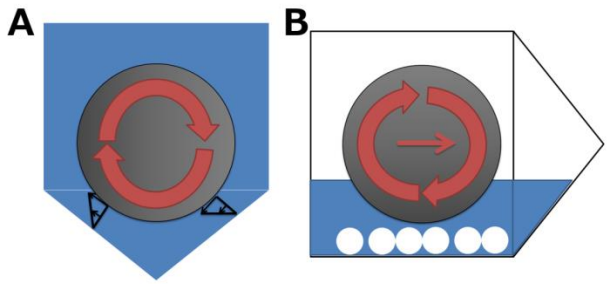

Figure 47: Comparing cell disruption due to fluid shear and compressive force. A: Schematic for experimental condition with exaggerated fluid shear effects. Without the beads, the magnet is expected to ride at the same level or lower in the tube, resulting in similar or higher fluid shear stress between the magnet and tube wall. B: Schematic for experimental condition with exaggerated compressive force. Tube is mounted horizontally on a rocking plate, which causes the magnet to roll back and forth. The fluid level is lower in the tube, resulting in less buoyant force on the magnet and higher magnet/bead, bead/wall, or magnet/wall compressive forces. The magnet rolls back and forth on the lower wall of the tube, with reduced fluid shear compared to standard AudioLyse conditions.

8.3 Results and Discussion

Figure 48 shows the dependence of lysis of *S. epidermidis* cells by the portable audio-powered device on bead mass, sample size, and processing time. The majority of amplifiable DNA is released in less than 10 minutes. Both bead and sample volumes were varied as a first-pass optimization for DNA recovery. A mass of 200-400 mg of glass beads achieves higher efficiency than

the other bead volume groups ($p<0.05$) for both 300 and 800 µL samples. Higher viscosities are interesting due to the potential of clinical applications with more viscous sample types, and for exploration of the underlying mechanism of cell rupture. A 30 Hz excitation frequency was found to produce reliable magnet rotation (starting from rest) even in samples as viscous as 50% glycerol (6 centipoise at 20°C, which was the highest viscosity tested).

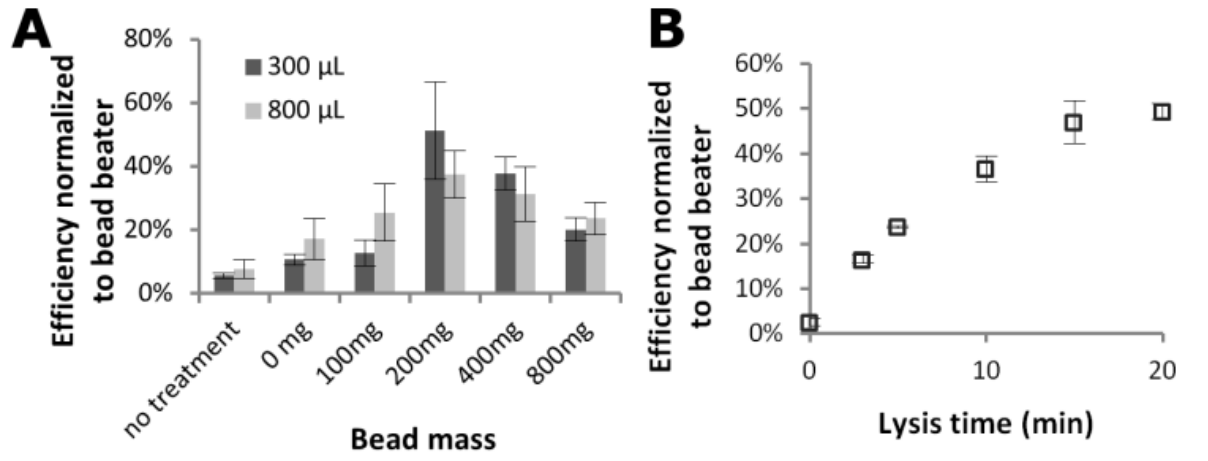

Figure 48: AudioLyse optimization for *Staphylococcus epidermidis*. A: Dependence of lysis efficiency on bead mass for 300 and 800 µL sample sizes. Amplifiable DNA quantified by qPCR, normalized to the bead beater computed copy number ($7.1x10^4$ copies/mL, 71 copies per PCR). Sample sizes of both 300 and 800 µL perform best with 200-400 mg beads. Data is mean ±1 standard deviation, n=3. B: Dependence of audio-powered lysis efficiency for *S. epidermidus* on total lysis time. Amplifiable DNA quantified by qPCR, normalized to the bead beater computed copy number ($3.6x10^4$ copies/mL, 36 copies per PCR) using a 800 µL sample size and 300 mg beads in the audio-powered device. Efficiency (as compared to bead-beater efficiency) plateaus near 50% at just over 10 minutes for the audio-powered device under these conditions. Data points are mean ± 1 standard deviation, n=3.

Mycobacterium marinum, a more difficult target to lyse, was chosen for study due to its similarity to the major pathogen *Mycobacterium tuberculosis*. The performance of the audio-powered technique is compared to that of a bench-top bead beater for a range of *M. marinum* concentrations in Figure 49.The audio-powered technique achieves appreciable lysis of *M. marinum* for all concentrations tested, with 10^4 cells/mL corresponding to an estimated maximum of 10 cells being transferred in the 1 µL sample used in the PCR. All non-zero input

copy concentrations were significantly higher than the 0 copy experiment ($p < 0.02$), including the 10^4 copy/mL input experiments. Thus, we have demonstrated that the portable audio-powered technique can be used as a sample preparation tool for DNA amplification for both *S. epidermidis* and *M. marinum*.

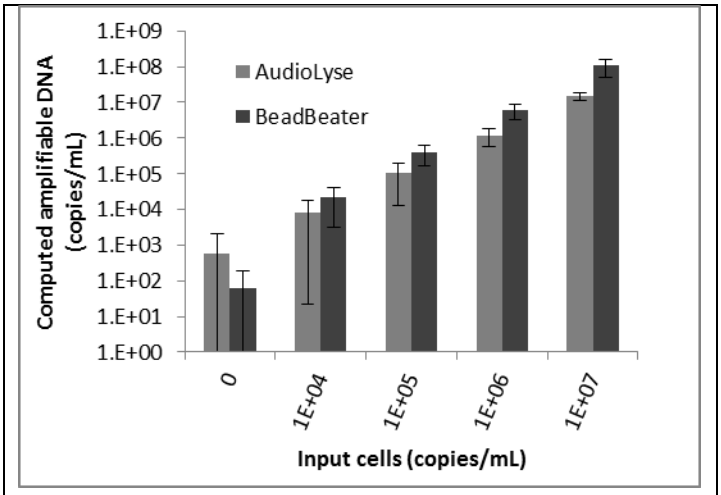

Figure 49: Amplifiable DNA quantified by PCR for varying input concentration of M. marinum cells. 500 µL sample size. 10^4 copies/mL corresponds to 10 copies per PCR quantification. Data points represent mean +/- 1 standard deviation. Minimum n=9 total spread across 3 different days.

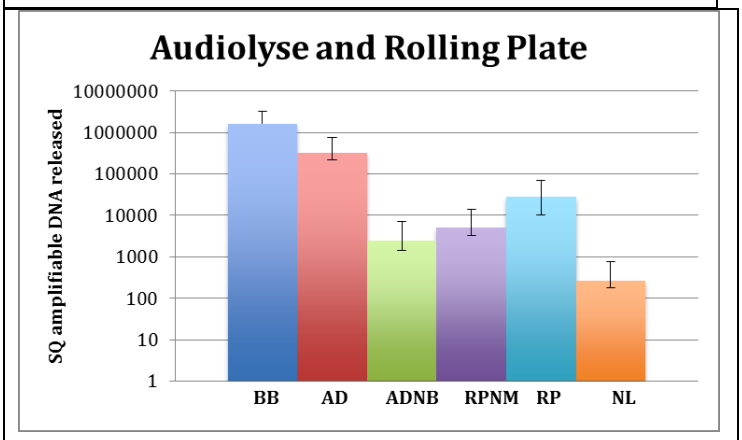

Figure 50: Exploration of lysis mechanism for AudioLyse. DNA recovery efficiency for bead beater (BB), AudioLyse (AD), AudioLyse without beads (ADNB), rolling plate without magnet (RPNM), rolling plate with magnet (RP), and no lysis (NL). The rolling plate with magnet (RP) outperforms the AudioLyse with no beads (ALNB), suggesting that fluid shear is less important for cell rupture than compressive forces.

Next, the mechanism of cell rupture was explored using the isolated fluid shear and isolated compressive force experiments described above, with results shown in Figure 50. The rolling plate with magnet (exaggerated compressive force, "RP") condition recovers more DNA than the AudioLyse without beads (exaggerated shear, "ALNM") condition, suggesting that the compressive forces may be more important than fluid shear for cell disruption in the AudioLyse. The rolling plate without magnet ("RPMN") condition confirms the magnet is necessary for improved DNA recovery, and the no

lysis control ("NL", stationary tube with no additives) confirms DNA is not made available without processing of some sort.

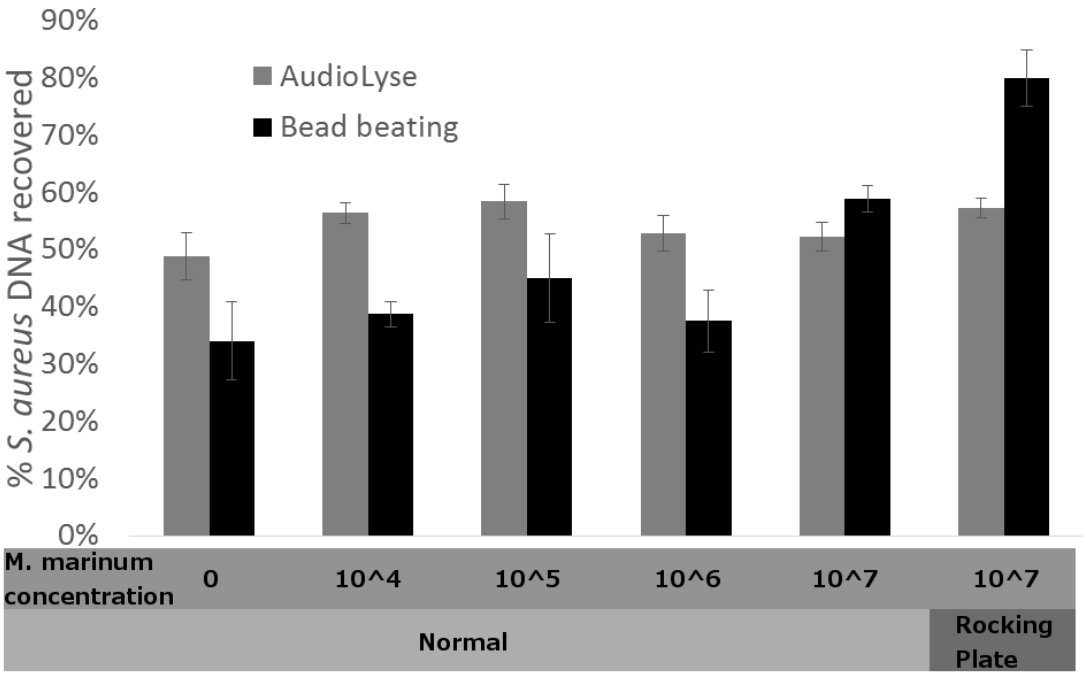

Figure 51: Potential DNA damage in bead beater and AudioLyse. Spiked *S. aureus* DNA recovery in the presence of *M. marinum* cells using AudioLyse, bead beater, and rocking plate techniques. Samples were run under normal AudioLyse and bead beater conditions, along with rocking plate versions of both. Between 50 and 60% of *S. aureus* genomic DNA was recovered using the AudioLyse across all *M. marinum* cell concentrations, similar to the "AudioLyse" rocking plate experiment (with beads and magnet). Less *S. aureus* genomic DNA was recovered using the normal bead beater conditions, suggesting that the cell rupture mechanism also could hinder the recovery of DNA. Interestingly, more DNA was recovered in the "bead beater" rocking plate experiment (with beads, no magnet), which supports that it is indeed the cell lysis mechanism, not DNA sticking to either the beads or tube walls, that yields reduced DNA recovery.

Cell rupture is necessary for the recovery of DNA. However, it is important that how the lysis technique affects the DNA is understood. Next, we explore at what efficiency DNA injected directly into either the bead beater or AudioLyse can be recovered. For this, *S. aureus* genomic DNA was spiked into a mixture with *M. marinum* cells in the AudioLyse device, bead beater, or

rocking plate, and recovery of the *S. aureus* DNA was quantified after processing in the AudioLyse device, with results in Figure 51.

In Figure 51, it can be seen that higher amounts of *S. aureus* DNA are recovered in normal AudioLyse operating conditions than normal bead beating conditions. The "AudioLyse" rocking plate experiments (with beads and magnet) recover a similar amount of DNA compared to the AudioLyse normal operating conditions. The "bead beater" rocking plate experiments (with beads, without magnet) recover more *S. aureus* DNA than the bead beater normal operating conditions, suggesting that no more than ~20% of the DNA loss is due to DNA sticking to either the glass beads or tube. Additional experiments will be performed which either increase (using centrifugal force) or decrease (by preventing magnet movement in the rocking plate experiments) the compressive effects of the magnet.

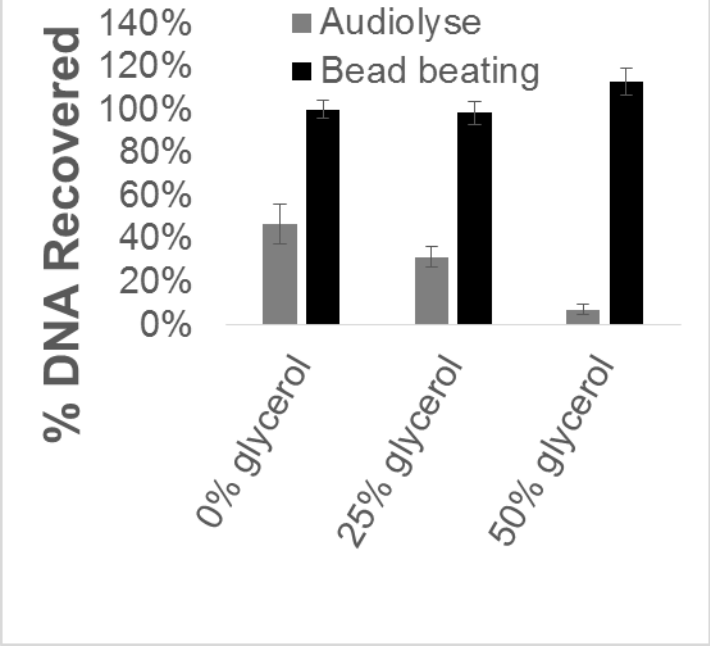

Figure 52: Glycerol affects DNA recovery from MSSA in AudioLyse. Increasing the glycerol concentration results in decreased DNA recovery. The bead beater does not appear to be affected by the higher viscosity and density glycerol solutions. The AudioLyse, on the other hand, shows reduced performance with increasing % glycerol. Results normalized to the bead beater with 0% glycerol.

8.3.1 Viscosity and fluid density effects on cell rupture/DNA recovery

Using more complex solutions than TE buffer is important for both clinical relevance of a sample preparation technique, and could yield valuable insight into the mechanism of cell

disruption. Experiments have shown decreased DNA recovery using the AudioLyse in solutions containing glycerol. Glycerol solutions are both more viscous and more dense (6 cP, 1.13 g/cc for 50% glycerol at 20°C) than water (1 cP, 1 g/cc at 20°C). Figure 52 shows that addition of glycerol differentially affects the AudioLyse method.

The glycerol hindering the AudioLyse performance, but not the bead beater performance, suggests that the mechanisms of cell rupture may be different in these techniques. Increases in viscosity could cause the shear stress to vary, while density differences could result in differences in magnet or bead buoyancy. In addition to viscosity and density cell rupture effects, a more viscous fluid could result in different convective flow patterns in the sample tube. This could affect convective mixing, and consequently cell rupture kinetics.

8.3.2 Exploration of convective patterns in AudioLyse

Convective mixing in the AudioLyse is expected to affect opportunities for any given bacterium in the sample to be ruptured. Changes in viscosity and fluid density were found to affect DNA recovery (Figure 52). This motivates a study in what convective patterns are present in the AudioLyse, and how changes in viscosity and density change the convective patterns.

To visualize fluid convection, glitter ("black licorice", Martha Stewart Crafts, New York, NY, USA) was added to the sample. When glitter is added to the water/bead solution, it aggregates and sticks to the walls of the tube. In order to use glitter to visualize fluid movement, 0.1% micro90 detergent was used to keep the glitter mobile. An initial experiment, shown in Figure 53 below, examines whether the micro90 affects the superficial movement of the beads, etc. in the operating AudioLyse. It should be noted that the glitter is much larger than bacteria, and may not necessarily move in the same as bacteria in the sample. Glitter was chosen simply as a particle to visualize fluid movement. The glitter used is denser than water, and consequently

settles, which may make it non-ideal for fluid movement visualization. Nevertheless, this glitter was used for a first-pass visualization of convective patterns present in the AudioLyse.

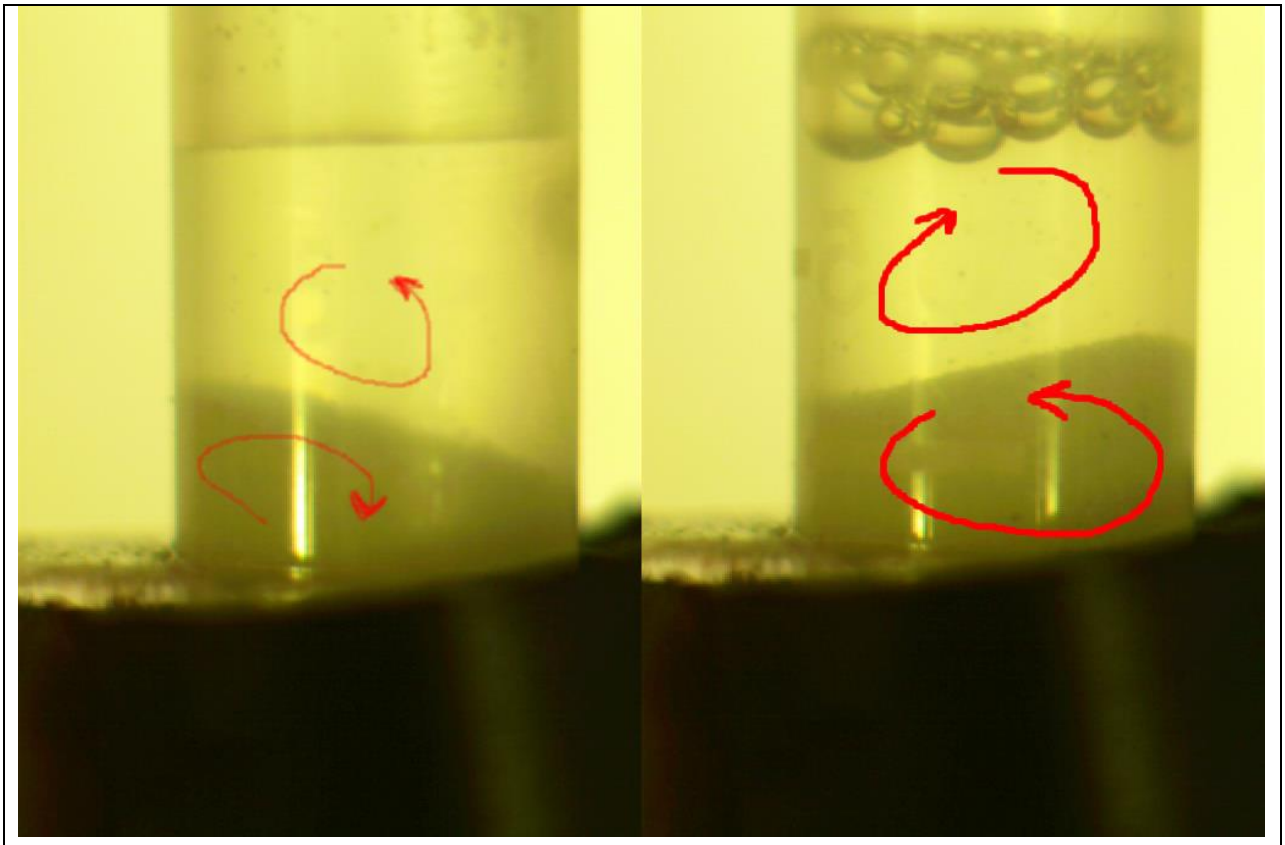

Figure 53: Comparing AudioLyse bead slurry movement with (right) and without (left) micro90 surfactant. The only superficial difference apparent in the videos was the presence of the bubbles at the top of the tube with the micro90, present due to vibration while the magnet, beads, micro90 and water were added.

Superficially, the only difference appears to be the formation of bubbles at the top of the solution, and it is not expected that the convective patterns in the fluid will be affected. The following experiments will use micro90 to keep the glitter mobile in the sample for flow visualization.

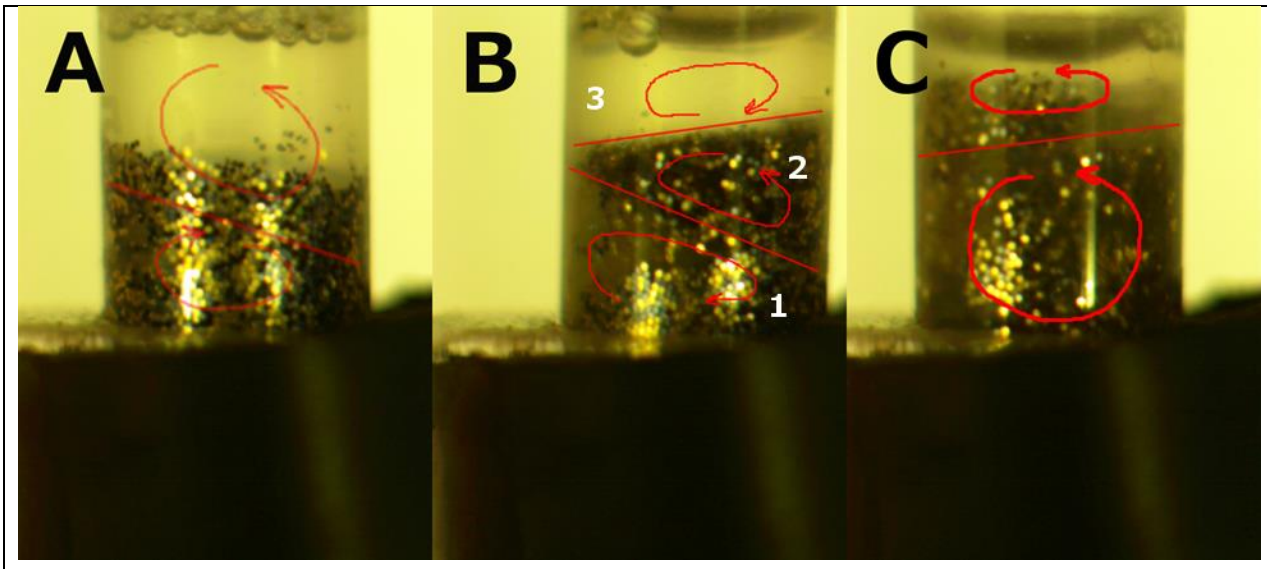

Figure 54: Comparing flow regimes with varied percent glycerol. Tube contains ¼"magnet, 250 mg of 0.1 mm glass beads, deionized H_2O, 0.1% micro 90, glitter, and a variable amount of glycerol. Glitter allows visualization of movement in the largely bead-free upper fluid zone. A: 0% glycerol. Bead slurry geometry and vortex regime in active device looks similar to without glitter. B: 25% glycerol. An additional fluid compartment seems to appear when glycerol is added: 1)beads+liquid+glitter, 2) liquid+glitter, and 3) liquid. Each fluid compartment appears to have counter-rotating vortices. The bead slurry (compartment 1) seems to ride up higher in the tube compared to 0% glycerol, potentially due to the increased fluid density. C: 50% glycerol. The bead slurry rides even higher in the tube. It is difficult to tell if the liquid-only portion of the fluid volume has a counter-rotating vortex or not, but it appeared in the video to be a part of the glitter+liquid vortex

8.3.3 Modeling hydrodynamic pressure distribution in the AudioLyse

Literature describes[188] cavitation in a lubrication flow separating a rolling sphere and a boundary. To examine whether the negative pressures necessary for cavitation are present in the AudioLyse, COMSOL is used to create a laminar flow model with a stationary, rotating magnet. For now, the assumption is made that the magnet is separated from the tube wall a distance of 100 µm, the bead diameter. This model was run for 10 seconds to allow the flow to fully develop. No slip conditions were assumed at the side and bottom tube walls. The top fluid/air boundary layer was set to pressure = 0, with no viscous stress. The circular magnet surface was set to 0.589 m/s tangential velocity, corresponding to the 30 Hz ¼" magnet rotation. Fluid properties were set to 8.9×10^{-4} or 3.56×10^{-3}Pa-s viscosity, 1000 kg/m^3 density.

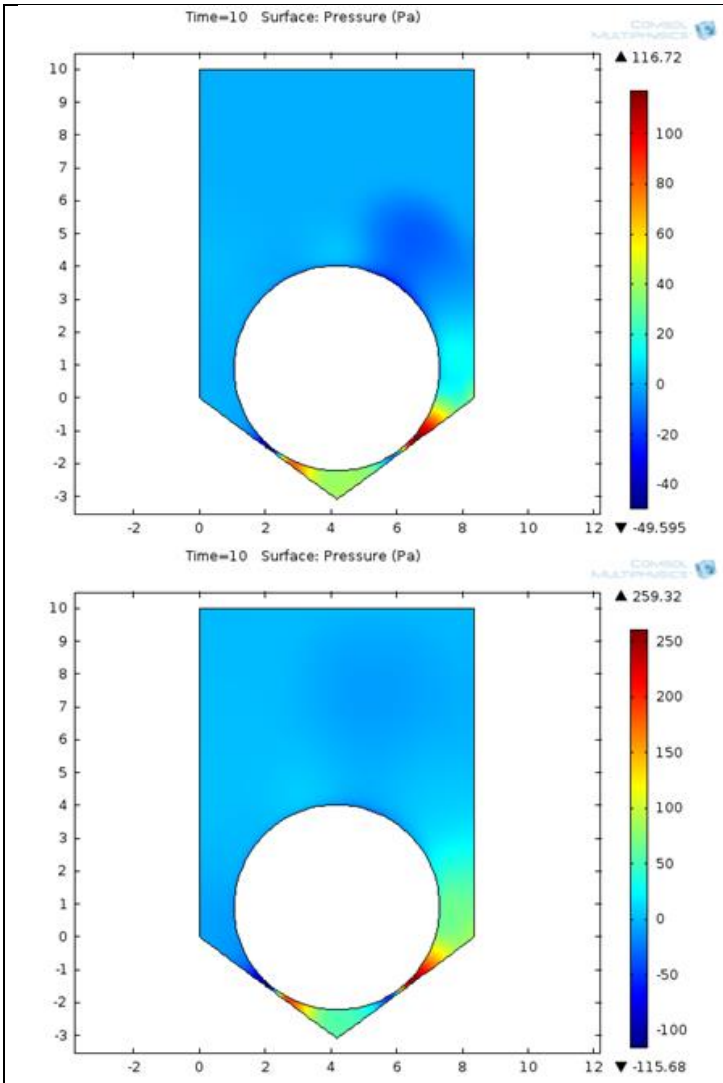

Figure 55: Modeled pressure distribution for top: water and bottom: 4x viscosity. The higher viscosity fluid has a larger predicted pressure variation, with a maximum of 250 Pa and minimum -100 Pa. The water model predicts ~110 Pa and -45 Pa.

For cavitation resulting from negative hydrostatic pressures to occur, the pressure must drop below the vapor pressure of water. This would require a pressure of 0.1 MPa below atmospheric pressure[188]. Looking at the pressure maps above, the predicted pressure is three orders of magnitude too small to achieve cavitation due to negative hydrodynamic pressure, assuming a stationary rotating magnet separated 100 μm from the tube wall. This analysis does not predict cavitation due to negative pressures developed by a rotating magnet not traveling in the x- or y-direction, assuming the fluid film thickness is the same as the bead diameter. Further analysis will be required to account for x/y translation of the magnet and impacts with the tube wall and/or beads.

8.4 Conclusions

The portable audio-powered device achieves 20-60% of the efficiency of the bench-top bead beater for various concentrations of *M. marinum* and *S. epidermidis*, while costing far less,

consuming just a small fraction of the electrical power, emitting far less audible noise, and being highly portable. This decreased lysis efficiency, compared to the bead beater, is balanced by the expansion in applicable settings. Whether this level of performance is sufficient depends on infection levels, sampling technique, and the associated assay sensitivity. Cell phones have expanded communication and medical capabilities in remote settings[11]. Additionally, portable audio devices have been shown capable of performing impedance measurements in microfluidic devices[178]. Now, in addition to using photo, voice, and text communication to transmit and interpret assay results, audio signals from a headphone jack can be used to power a device capable of retrieval of amplifiable DNA from some of the hardest-to-lyse bacteria in virtually any setting. The power requirements of this method are quite low. The mp3 player output of 1.6 V peak-to-peak when powering a coil with a 12 ohm impedance (11.4 ohms DC, 0.6 ohms inductive at 30 Hz) results in a power draw of 107 mW; ten minutes of lysis with this coil would account for just 0.18% of the capacity of a 2,700 mWh cell phone battery.

We expect further optimization of the sample volume and complexity, coil excitation frequency and duration, bead quantity and diameter, and other factors to lead to higher performance. Both *S. epidermidis* and *M. marinum* are difficult bacteria to lyse; performance with easier to lyse bacteria such as *E. coli* will likely be higher and testing is currently under way. Portable sample preparation could allow next generation point-of-care NAATs for bacteria such as *Mycobacterium marinum* and *Staphylococcus epidermidis* free from bench-top laboratory equipment.

What sets this device apart from other lysis techniques compatible with the point-of-care is freedom from additional power supplies (battery packs, etc.) and the potential of using the same peripheral equipment (cell phones) for sample preparation along with interpreting test

results. Academic medical laboratories can implement the methodology for very little cost. As shown here, less than $38 was spent for the mp3 player, magnet wire, cable, and bobbin materials per device, and less than $1 per assay for the screw-top tube, magnet, and beads. Further reductions in cost would be realized if quantities were scaled up or the device were optimized to reduce magnet size, bead volume, tube cost, etc. While clinical laboratories may find the noise of bench top bead beaters acceptable, a quieter technique such as demonstrated here may be more amenable to the point-of-care. Also, the inexpensive nature of the hardware makes it nearly disposable.

We are currently broadening the sample types tested using this technique, along with other lysis methods, for a wide range of bacteria and clinical sample types including blood, sputum, and nasal matrix. It is our expectation that this work will contribute to the next generation of portable nucleic acid amplification tests, including the multiplexable, autonomous, disposable nucleic acid amplification test (MAD NAAT) project[115], [155], [156], a collaborative effort including the Yager group at the University of Washington, PATH, the ELITech Group, and GE Global Research.

8.5 Acknowledgements

Major parts of this section of my thesis were taken from a recent publication from our group[158]. I would like to acknowledge and thank collaborators Alec Wollen, Dr. Erin Heiniger, Samantha Byrnes, Peter Kauffman, Lily Mireles, Dr. Paula Ladd, and Dr. Paul Yager for their contributions to the AudioLyse work.

9 Sub-aim 4.1: A disposable chemical heater and dry enzyme preparation for lysis and extraction of DNA and RNA from microorganisms

Sample preparation, including bacterial lysis, remains a hurdle in the realization of complete point-of-care tests for many pathogens. Here, we developed a sample preparation methodology for enzymatic lysis and sample heating for low-resource, point-of-care applications. We show an instrument-free chemical heater system for rapid lysis of a gram-positive bacterium (*Staphylococcus aureus*) and an RNA virus (human respiratory syncytial virus) using a dried lysis enzyme mixture (achromopeptidase) for S. aureus. After a lysis step (<1 minute), lysis enzymes are heat deactivated (<5 minutes) using a simple disposable chemical heater. We demonstrated that both DNA and RNA in the heat-treated sample could be directly amplified without purification, even in the presence of a clinically-obtained human nasal sample. This simple approach to dry enzyme storage and sample heating is adaptable to many applications where samples need to be lysed, including use in low-resource laboratories and in single-use or cartridge-based point-of-care diagnostic devices.

This sub-aim combines aspects of two of my main aims:

1. Harnessing the MgFe exothermic reaction for low cost, point-of-care chemical heaters. Here, no "conventional" wax phase change material was used, but the water used in the reaction boils. This work helped us develop our understanding of the reaction and sparked the idea of liquid PCMs that serve a dual purpose as both reactants and temperature regulators.
2. Many of the quantification techniques utilized for the AudioLyse application were already established, and quick to implement for the quantification of cell rupture and consequent DNA recovery here.

Here we have demonstrated a low cost, fast DNA extraction methodology that performs comparably to a bead beater for *S. aureus*, a relatively difficult-to-lyse bacterium. This method

uses dried reagents compatible with non-refrigerated storage, and doesn't require any additional infrastructure or external processing before nucleic acid amplification. The total cost of goods is very low, as we constructed the device from readily available Eppendorf tubes, paper towel, cotton balls, NaCl, and MgFe. As prepared, the only tools used were a knife, drill press, and scale. In addition to being a laboratory tool nearly anyone could build themselves, it would be relatively straightforward for a manufacturer of tubes to manufacture a tube for use without modification. We used the chemical heater here to deactivate an enzyme for direct usage in a downstream assay. Heat alone is sufficient to lyse many organisms, to perform heat-shock antigen-antibody dissociation, or to denature nucleic acid complexes or proteins. Many of these and other applications would be relatively simple to design chemical heaters for.

Main deliverable: Enzymatic DNA extraction for LRS… ***Published***

The work presented in this sub-aim is adapted from[176]:
J.R. Buser, X. Zhang, S.A. Byrnes, P. D. Ladd, E. K. Heiniger, M. D. Wheeler, J. D. Bishop, J. A. Englund, B. R. Lutz, B. H. Weigl, and P. Yager, Anal. Methods, 2016, 8, 2880–2886.

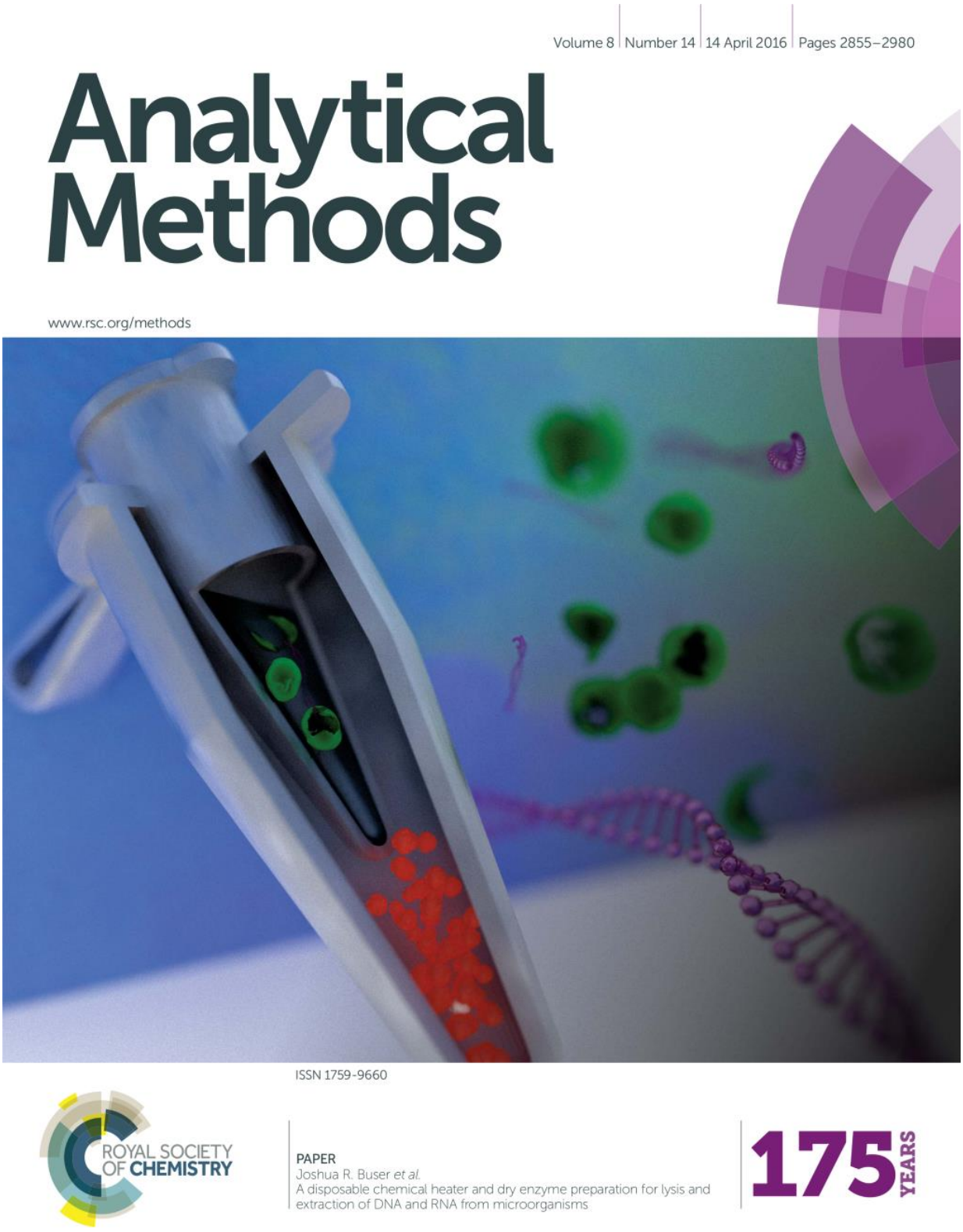

Figure 56: This work earned us the front cover of Analytical Methods

9.1 Introduction

According to the 2010 Global Burden of Disease study, four of the top ten causes of death world-wide are attributed to communicable diseases, which disproportionally affect low resource settings (LRS) [13], [190], [191]. Number four on the list is lower respiratory infections and number seven is diarrhea[190]. These infections have known and available treatments but often lack accurate diagnosis, especially in LRS where there is severely reduced availability of healthcare[192], [193]. In many settings, including the US and other developed countries, symptomatic diagnosis is commonly used by healthcare providers. Although symptoms are important, they can vary between individuals and are often shared by multiple infections. Diarrhea, for example, can be caused by viruses, bacteria, or parasites[194]–[197]. Each of these classes of pathogens require different treatments and within classes, treatments can vary due to different susceptibility to common drugs.

Antimicrobial resistance has been increasing around the world[198]; one method for curbing this trend is accurate molecular diagnosis which can lead to identification of specific pathogens and potential drug resistances. Methicillin-resistant *Staphylococcus aureus* (MRSA) is a significant pathogen causing hospital- and community-acquired infections in developing and developed regions[199], [200]; further advancement in diagnostics which can quickly identify methicillin resistance could aide in slowing the spread of this pathogen. Nucleic acid amplification tests (NAATs), which utilize a pathogen's DNA or RNA, are commonly used in pathogen identification: polymerase chain reaction (PCR) is a widely used example. The use of NAATs for disease diagnosis offers multiple advantages including increased sensitivity, the ability to multiplex, and epidemiological tracking of disease transmission and drift via nucleic

acid (NA) sequencing. These approaches, however, often require expensive equipment and highly trained personnel.

Integrated microfluidic systems, such as the Cepheid GeneXpert, provide sample-to-result diagnostics using disposable cartridges that contains the assay reagents. These cartridges are coupled with automated instrumentation to process the sample and perform the bioassay, and have been shown to expedite treatment for pathogens including *Mycobacterium tuberculosis*[52]. These systems, however, have significant cost, infrastructure, and maintenance commitments associated with them[57] and are most appropriate for use in well-equipped laboratories with reliable electricity. Significant advances in NAATs are still required for lower-resource settings[18].

Microfluidic bioassays have the potential to expand the reach of NAATs, but sample preparation, including pathogen lysis and nucleic acid extraction, remains an underdeveloped aspect of microfluidics-based bioassays, especially those designed for point-of-care use[177]. Many commercially available systems that are marketed for the point-of-care are often missing sample preparation components. In 2011, Niemz *et al.* evaluated 13 commercially available point-of-care NAAT-based systems. All of these systems include an expensive, non-disposable component that requires mains electricity and, likely, a service contract. Additionally, less than half of these include on-device sample preparation thereby increasing the overall time and costs required for operation and limiting their usability as truly point-of-care systems[144].

Enzymatic lysis has been shown to be effective in bacterial sample preparation. Some lytic enzymes are highly specialized for a specific cell type, such as lysostaphin which targets *staphylococcus* bacteria[201], while others are more generally applied. Lysozyme is a

commonly used and well understood lytic enzyme which cleaves the peptide-disaccharide linkage of peptidoglycans in bacterial cell walls causing them to denature[202]. Many gram-negative bacteria are insensitive to lysozyme because their thick outer membrane prevents the enzyme from interacting with the inner cell wall; additionally, some gram-positive bacteria, such as *S. aureus*, are also resistant to lysozyme treatment[203]. Achromopeptidase (ACP), purified from *Achromobacter*, was found to have bacteriolytic activity as early as the early 1970s[204]. Since then, it has been widely used for the lysis of lysozyme-resistant gram-positive bacteria such as *S. aureus*. Some MRSA diagnostic assays on the market use ACP for lysis and downstream real-time PCR for pathogen identification (e.g., the BD Gene Ohm MRSA test). Most of the assays employ ACP lysis at 37°C for 10-20 minutes, followed either by heat deactivation at a controlled temperature[205] or KOH deactivation[206].

Isothermal NAATs, such as loop-mediated isothermal amplification (LAMP) [114], [163] and recombinase-polymerase amplification (RPA)[162] have received much attention recently due to their simple heating requirements. In addition, isothermal NAATs have been demonstrated on paper microfluidic platforms[96], [146], [207]. Furthermore, paper microfluidics have been proven capable of automating multistep assays without external equipment[93]. Precise electricity-free heaters have been developed for these applications[114]: these are powered by exothermic chemical reactions and use phase change to regulate temperature. Our group has demonstrated the heating of flat-profile paper microfluidic networks using this technique[115], [126].

These technologies suggest GeneXpert-like molecular diagnostics are possible in low-cost, disposable devices[96], [146], though many existing isothermal NAAT-based diagnostics still rely on off-device sample processing steps that will not be available in all settings.

Fortunately, technologies are beginning to emerge that enable the operation of molecular diagnostics without the need for laboratory infrastructure[207], [208]. The multiplexable, autonomous, disposable nucleic acid amplification test (MAD NAAT) project[115], [126], [154]–[159] aims to create a comprehensive isothermal NAAT platform that takes a biological sample as input, lyses cells, amplifies nucleic acid sequences from the lysate, and provides visual readout of the assay results. Non-electric heating options allow for regulated, elevated temperatures optimal for bioassays in environments without the need for external electrical power or batteries[115], [126], [148], [163], [209]. A rapid, low-cost NAAT amenable to point-of-care diagnostics in lower-resource settings could significantly expedite identification of pathogens in people, food, and drinking water.

Here we demonstrate rapid lysis of a suspension of *S. aureus* using dry-stored ACP, followed by a rapid (<5 minutes) electricity-free heat deactivation step, the output of which can be tested directly using quantitative PCR (qPCR). In addition to lysis of *S. aureus* suspended in Tris buffer, we also demonstrate direct qPCR amplification of lysed *S. aureus* suspended in a human nasal sample. Further, human respiratory syncytial virus (RSV) virions suspended in human nasal sample are heat-treated without ACP and direct reverse transcriptase PCR (RT-PCR) used to quantify released RNA. In addition to the applications demonstrated, this methodology is easily adaptable to any assay that requires a temperature step at ~100°C.

The chemical heaters described here were produced from common laboratory supplies with minimal tooling and production steps and could be incorporated into more complex multi-step devices for sample pretreatment prior to a bioassay. This approach, when combined with advances in point-of-care nucleic acid amplification assays, could enable sample-to-result nucleic acid detection in lower-resource settings.

9.2 Materials and methods

9.2.1 Bacterial Culture

Staphylococcus aureus (strain RN4220 obtained from the Ferric Fang laboratory at the University of Washington) was cultured in Tryptic Soy Broth (BD Bacto, Sparks, MD, USA) at 37°C, shaking at 250 rpm. Overnight cultures were diluted 1:100 in fresh Tryptic Soy Broth and grown to mid-log phase (OD600 = ~2). Cells were spun down at 10,000 g for 3 minutes at 20°C after growth and resuspended in the same volume of Tris buffer (10 mM Tris, pH 8.0) or Tris-EDTA (TE: 10 mM Tris-HCl, 1 mM EDTA, pH 8.0) buffer. Cells dilutions used the same buffer.

9.2.2 Virus source and preparation

Human respiratory syncytial virus (RSV, laboratory strain obtained from the University of Washington Clinical Virology Laboratory) was cultured by the UW clinical virology laboratory. Virions were aliquoted at 10^6 RSV copies per microliter and stored at -80°C.

9.2.3 ACP lysis

S. aureus cell suspensions (OD600=2) were diluted in Tris or TE 1:1000 to ~10^6 cfu/mL. The cell suspension was added to tubes pre-loaded with ACP (20 U/µL stock, Sigma A3547) to a 3 U/µL (Lot 041M1380V) or 0.5 U/µL (Lot 031M1468V) final ACP concentration and mixed by gently pipetting up and down. Due to lot-to-lot variation of the ACP, 3 U/µL or 0.5 U/µL concentrations were used. The reaction was incubated at room temperature (20°C) or 37°C. ACP was deactivated by placing the tubes in a heating block (for experiments varying the heat deactivation time and temperature) or in the chemical heater (thermal profiles shown in Figure 59). Lysate tubes were briefly spun at 3000 g to pull condensation down from the tube walls before conducting qPCR.

9.2.4 ACP mixture dehydration

In a 0.2 ml PCR tube, 37% trehalose (TS1M-100, Life Sciences Advanced Technologies, St Petersburg, FL, USA) and 20 U/µl ACP were mixed together for a final trehalose concentration of 5% in the mixture and a final ACP concentration of 3 U/µl or 0.5 U/µL in the lysate (depending on the lot of ACP). The tubes were dried in a vacuum concentrator (miVac DNA, GeneVac, Stone Ridge, NY, USA) at 20°C for 1.5 hours, and then stored in a desiccator at 20°C. For cell lysis, the dried ACP was rehydrated with cell suspension following the protocol for 'ACP lysis'.

9.2.5 Chemical heaters

This type of heater is based on the exothermic reaction of a magnesium-iron alloy (MgFe) with a solution containing sodium chloride (NaCl). This approach is widely used to warm up portable meals[210] and is capable of releasing heat very quickly. The chemical heaters feature a tube-in-tube design: the outer heater tube contains the elements necessary for the exothermic reaction; the inner tube contains the dried ACP and sample. The outer heater tube consists of a modified 1.5 mL snap-cap tube (89000-028, VWR, Radnor, PA, USA), separated from the cap, cut to 26 mm height as measured from the conical end, and with a 0.5 mm hole drilled in the side to serve as a vent. The separated cap was drilled with a ¼" hole for insertion of the sample tube. A 3 cm x 3 cm square of paper towel (Kleenex C-fold towels, Kimberly Clark Professional, Roswell, GA) was inserted into the heater tube, followed by 120 mg of the solid MgFe fuel (Luxfer Magtech, Cincinnati, OH, USA), 70 mg of NaCl, and a portion of cotton ball (100% cotton, Kroger, Cincinnati, OH, USA). The modified heater tube was then fitted with the modified cap and pressed into a salvaged section of a Styrofoam shipping container. The heater was activated by adding 300 µL of deionized water through the ¼" hole, into which the sample tube (981005, Qiagen, Hilden, Germany) was then inserted. Caution should be observed: the MgFe reaction reaches 100 °C quickly and produces hydrogen and steam, which should vent from the vent hole.

Venting is critical to prevent pressure build-up and sample tube ejection. Sample temperature was measured with a type T needle thermocouple inserted into a hole drilled in the sample tube cap, recording temperature data over time with a data acquisition system (OMB-DAQ-54, Omega Engineering, Stamford, CT, USA).

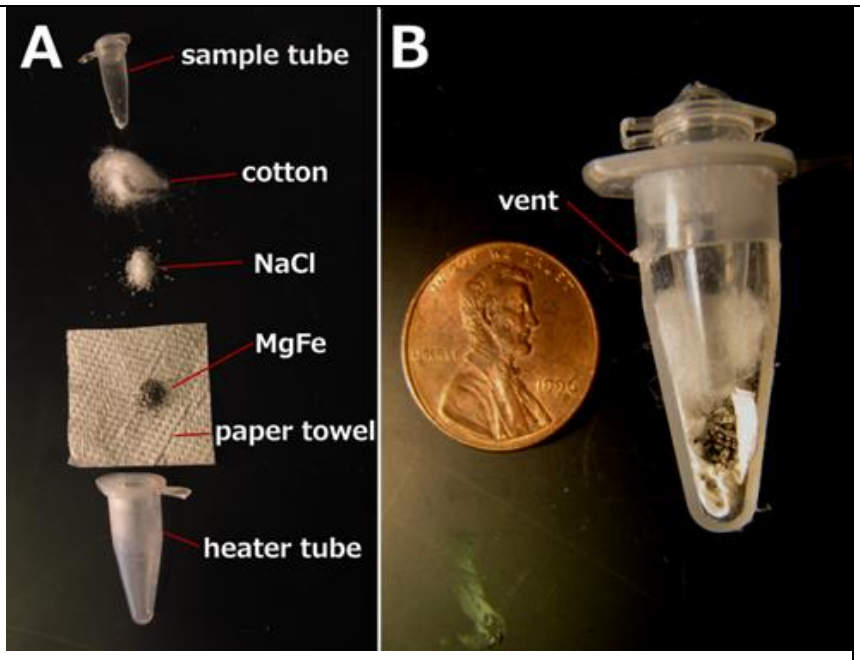

Figure 57: Device schematic. A: Exploded view. The paper towel was inserted into the heater tube, followed by the MgFe, NaCl, and cotton. Water was added to activate heating, after which the sample tube is inserted. B: Assembled sectional view. The MgFe corrosion reaction heats the sample tube. Hot gasses exit the vent upon device activation.

9.2.6 Bead Beater

Samples of *S. aureus* cell suspension (800 µL) were added to 2 mL O-ring screw top tubes (02-682-558, Thermo Fisher Scientific, Waltham, MA, USA) with 800 mg beads (9830, Research Products International Corp., Mt. Prospect, IL, USA). Tubes were loaded into the bead beater (Mini-Beadbeater-8, Biospec Products, Inc., Bartlesville, OK, USA), set to "homogenize", and run for three 1-minute cycles with a 1 minute pause between cycles.

9.2.7 qPCR

For quantification of *S. aureus* DNA, a commercially available qPCR kit (ELITech Group, Bothell, WA, USA) was used. Samples (2 µL) from the bead beater or ACP lysate were used in

20 µL qPCR reactions (Rotor-Gene Q, Qiagen, Valencia, CA, USA or CFX96 Touch, Bio-Rad, Hercules, CA, USA) using: 50°C hold for 2 minutes, 93°C hold for 2 minutes, 45 cycles of 93°C for 10 seconds, 56°C for 30 seconds, and 72°C for 15 seconds, ending with a final elongation step at 72°C for 5 minutes. Fluorescence data were collected during the 56 °C step using the orange channel. Genomic DNA copy numbers were determined relative to standard curve analysis using purified DNA of known copy number using the qPCR device software. The assay was sensitive down to ~10 copies of the target sequence.

9.2.8 qRT-PCR

For quantification of RSV RNA, UltraSense quantitative RT-PCR assay mix (Life Technologies, Carlsbad, CA, USA) was used with primer and probe sequences published previously[211]. The thermal protocol used was: 50°C hold for 15 minutes, 95°C hold for 2 minutes, 40 cycles of 95°C for 15 seconds and 60°C for 55 seconds using 20 µl reactions on a CFX96 Touch (Bio-Rad). Genomic RNA copy numbers were determined relative to standard curve analysis using control RSV RNA (American Type Culture Collection (ATCC), Manassas, VA, USA) of known copy number.

9.2.9 Clinical sample collection

Clinical samples were collected from patients following signed parental informed consent from January to March 2015 from pediatric patients with suspected influenza infection. Nylon flocked mid-nasal swabs were collected in the hospital or emergency department for influenza and RSV testing. Each swab was placed into 750 µl of phosphate buffered saline, 0.05% Tween-20, and 0.01% sodium azide. The diluted nasal swab sample was used for RT-PCR detection of influenza or RSV. Samples that were negative for either influenza or RSV were spiked with laboratory strains of RSV and MSSA to determine the impact of the sample composition on direct amplification assays. Seattle Children's Hospital Institutional Review Board approved the

sample collection and analysis of specimens. Written consent was obtained from a parent or legal guardian, as approved by the Seattle Children's Institutional Review Board, with paper copies given to parent and also maintained under secure storage by the research team.

9.2.10 Statistics

A Student's t-test was performed comparing 5- and 15-minute ACP data for 20 and 37°C (Figure 58A) in Excel (Microsoft, Redmond, WA, USA), comparing temperatures <= 70°C to 80-99°C (Figure 58B), comparing fresh and dried ACP results with 10^5 *S. aureus* cells, comparing performance of the thermal cycler and chemical heater for Tris buffer samples (Figure 60B), and comparing chemical heater and thermal cycler results for RNA recovery in Tris Buffer and human nasal sample matrix (Figure 61). Two-tailed comparisons were used, assuming the data were homoscedastic.

9.3 Results and discussion

As previously mentioned, NAATs that employ ACP lysis operated at 37°C for 10-20 minutes, followed by heat deactivation at a controlled temperature, have been demonstrated previously. Here, we compare ACP lysis at 20 and 37°C, for 5 and 15 minute incubations, followed by heat deactivation at 99°C. As shown in Figure 58A, the amount of recoverable DNA from *S. aureus* cells was similar for all conditions tested ($p>0.05$). No DNA was detected for either the fresh or dried ACP no-cell control. Figure 58B shows performance is dependent on the heat deactivation temperature, with temperatures less than 80 °C performing less well ($p<0.0001$). Lot 031M1468v ACP only recovered 57% of the amplifiable DNA compared to lot 041M1380v at 3 U/µL (activity units were reported by the manufacturer, $p=0.005$.) When lot 031M1468v was used at 0.5 U/µL, the resulting lysis performance was similar to 041M1380v at 3 U/µL ($p=0.10$). No difference in lysis efficiency was observed lysing cells in Tris or TE buffer ($p=0.45$). Heat

deactivation of ACP was also found to be robust, with times from one to ten minutes leading to similar performance.

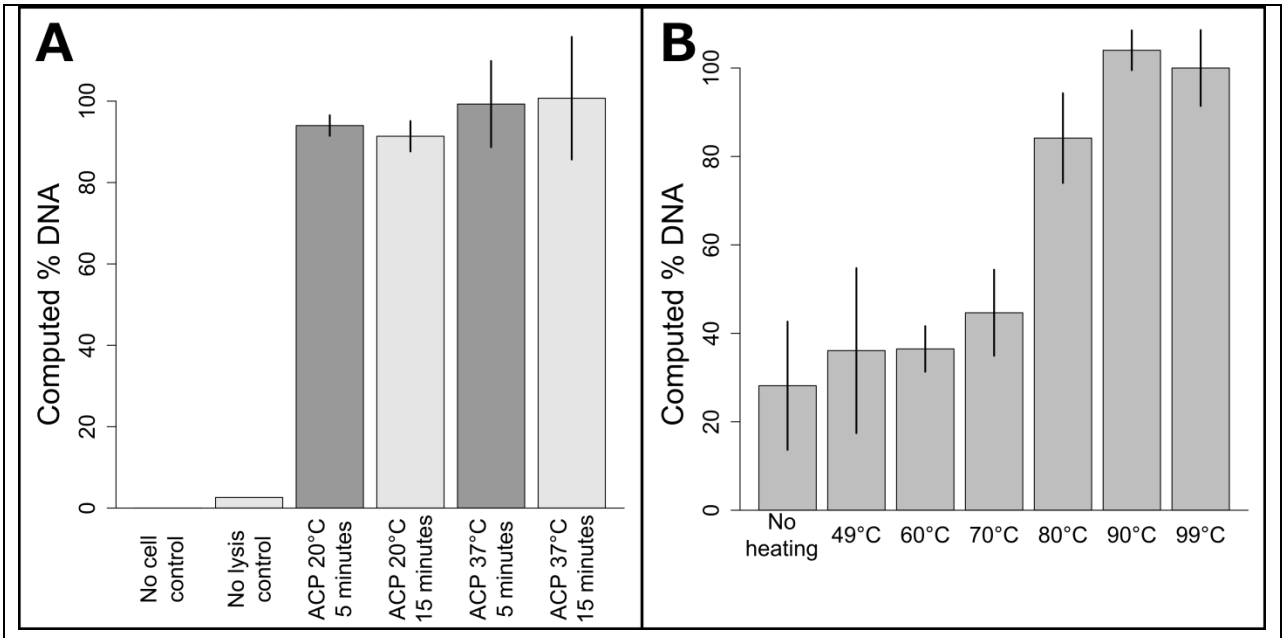

Figure 58: Optimization of ACP enzymatic lysis and heat-deactivation. A: Influence of varying ACP lysis time and temperature on DNA recovery. All ACP lysis conditions resulted in similar DNA recovery ($p>0.05$). The plotted data is the mean ± one standard deviation, with 37°C ACP 15 minute lysis set to 100%, n=3 for ACP lysis conditions, n=2 for no cell and no lysis controls. B: Comparison of heat deactivation temperatures for two minute ACP lysis at room temperature. Deactivation temperatures below 80°C reduced performance ($p<0.0001$). Data points are mean +/- one standard deviation, n=3. Data was normalized to the 99°C data, which was set to 100%.

Based on these data, a chemical heater was designed to heat the sample to over 80°C for over one minute from a range of initial ambient temperatures. Shown in Figure 59 are temperatures measured in the lysis tube for a heater run either in our laboratory or cold room, with time-temperature profiles adequate for ACP deactivation in both cases. The chemical heater reliably exceeds 80°C, and thereby deactivates the ACP enzymes in preparation for nucleic acid amplification, even in cold ambient conditions. The heater can be expected to reliably heat the samples in warmer ambient conditions due to the nature of the exothermic reaction.

Next, the enzymatic mixture was dried down into a form that can be stored easily and that can be rehydrated by the addition of the cell suspension. Fresh and dry ACP performs similarly at room temperature with a 5 minute 95°C deactivation step for 10^5 *S. aureus* cells (p=0.16.) No DNA was detected for either the fresh or dried ACP no-cell control. This dried ACP does not lose activity when stored for 4 months compared to fresh ACP (p=0.23).

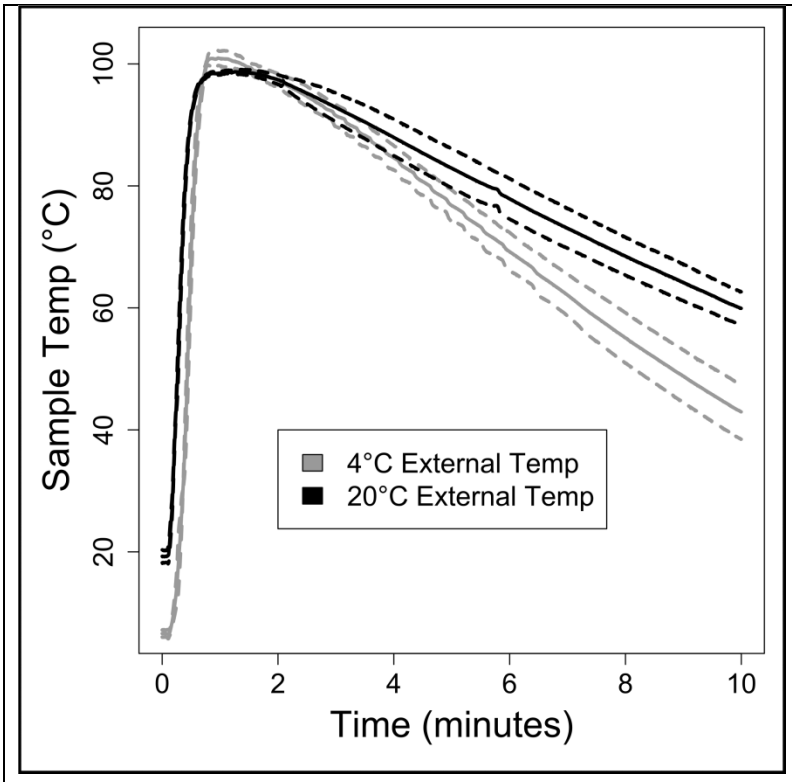

Figure 59: Chemical heater performance in varied ambient conditions. The chemical heater was run either in laboratory conditions (20°C) or in a cold room (4°C). The chemical heater was designed with enough MgFe fuel and NaCl to perform well even in cold ambient conditions. Solid lines are means, dotted lines are ± one standard deviation, n=3.

For lysis with dried ACP and the chemical heater, the device shown in Figure 57 was constructed by combining the separately-characterized chemical heater and dry ACP tube. *S. aureus* cells were lysed in the integrated device and the lysate was directly added to a PCR reaction for quantification of the *ldh1* gene. Mechanical cell disruption is effective for difficult-to-lyse microorganisms[144], bead beating was therefore chosen as a technique for comparison with the prototype devices. Figure 60A shows similar performance of the bead beater and the integrated device for each cell concentration tested. Figure 60B reports the amount of amplifiable

DNA recovered using ACP lysis with Methicillin susceptible *S. aureus* (MSSA) in Tris buffer with chemical heat deactivation or thermal cycler, and also chemical heat deactivation for MSSA spiked into a patient nasal sample. Here, chemical-heater-powered deactivation of ACP performs similarly to deactivation using the thermal cycler (p=0.16). The negative control shows very little target DNA is recovered when no MSSA is spiked into the patient sample. 1.5 U/µL ACP concentration was tested in addition to 0.5 U/µL, to check whether higher concentrations of ACP would be beneficial to account for the additional complexity of the human nasal sample matrix.

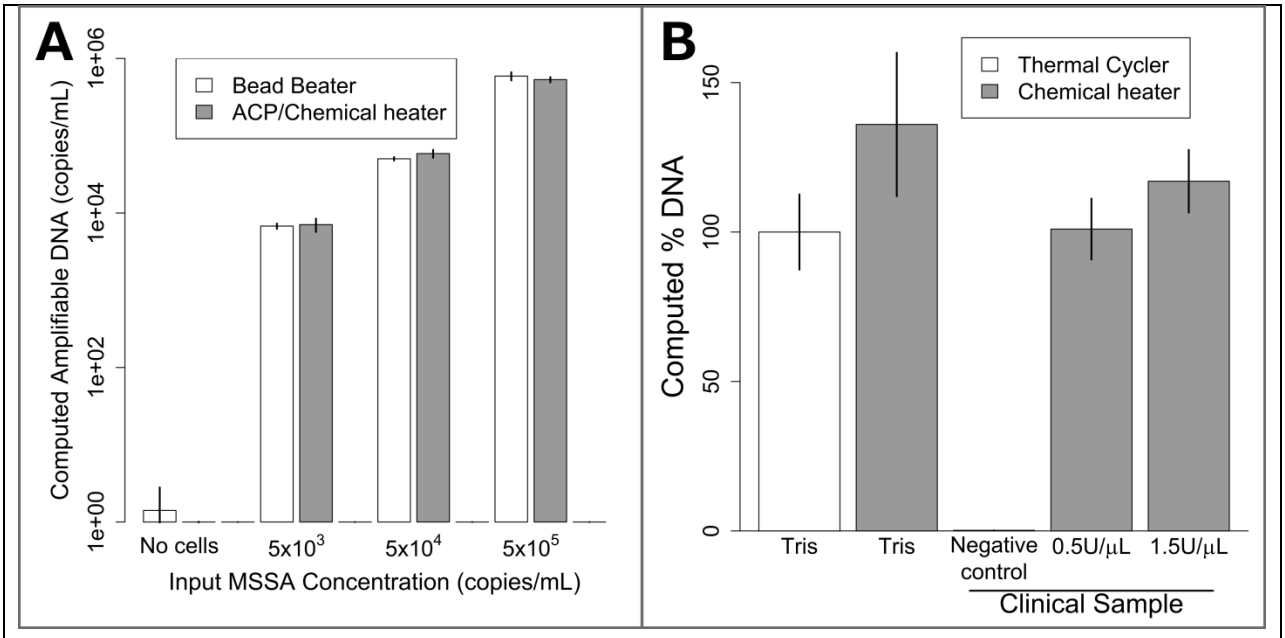

Figure 60: Lysis of MSSA with dry ACP and chemical heat deactivation in the device of Figure 57. A: Lysis of various concentrations of MSSA in Tris buffer. Bead beater DNA recovery is compared to dried ACP lysis at room temperature using a chemical heater for enzyme deactivation. The chemically-heated devices perform just as well as the bead beater for all concentrations tested. Data is mean ± one standard deviation, n=3. B: MSSA lysis using a conventional heater (thermal cycler) and chemical heat deactivation for samples in buffer and in human nasal sample matrix. Chemical heaters perform similarly (p=0.08) to thermal cycler-heated tubes for Tris samples. MSSA added to human nasal sample matrix was also successfully amplified, with no significant difference compared to the Tris buffer thermal cycler-heated data. The negative control shows DNA recovery when no MSSA is spiked in the clinical sample. The data were normalized to the Tris thermal cycler, which was set to 100%. Plotted is the mean ± one standard deviation, n=3.

With the chemical heater performing well for ACP lysis of bacteria, we wondered if it could also lyse RNA viruses. We selected RSV, an enveloped virus that contains a single segmented 15 kb genomic RNA fragment per virion[212]. We compared lysis of RSV virions in Tris buffer or in an RSV-negative human nasal sample matrix by a thermal cycler to chemical heaters. The thermal cycler and chemical heater performed nearly identically when RSV was in Tris buffer (p=0.94, Figure 61). When RSV was spiked at a known concentration into a clinical sample that previously tested negative, the thermal cycler and chemical heater performed similarly as well (p=0.62, Figure 61). Overall, we conclude that the chemical heater is also an effective tool for RSV lysis.

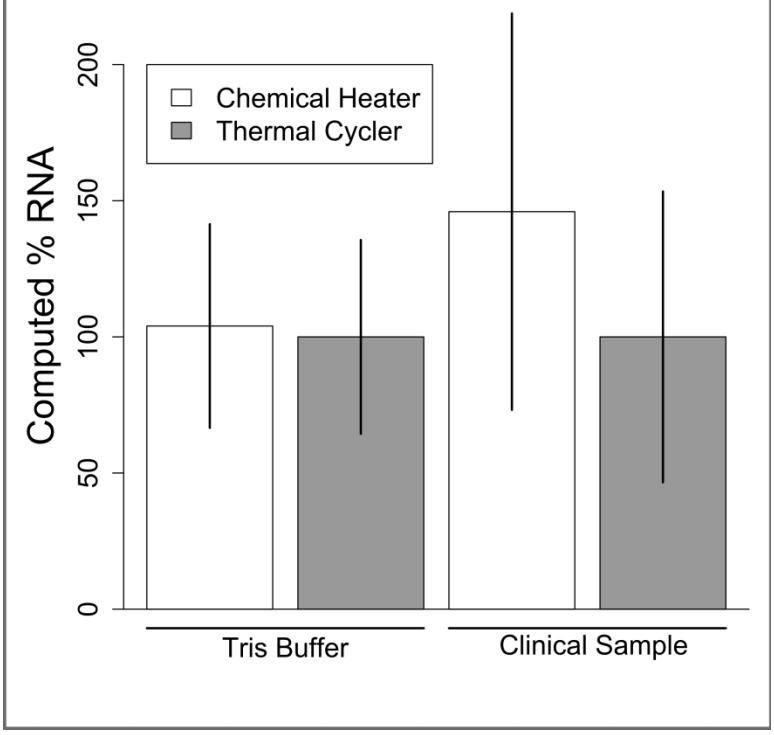

Figure 61: Lysis of RSV in Tris and human nasal sample matrix with thermal cycler and chemical heater heat deactivation. Equal concentrations of RSV in Tris buffer or human nasal sample matrix were lysed for 5 minutes then analyzed by qRT-PCR. Output is reported by percent amplifiable RNA, with thermal cycler data set to 100%. Data is mean ± one standard deviation, n=6 for Tris Buffer, n=5 for clinical sample.

9.4 Conclusions

Here we have demonstrated effective, rapid nucleic acid extraction from *S. aureus* and RSV. The method works in the presence of a clinically-obtained human nasal sample. *S. aureus* is a

relatively hard-to-lyse gram-positive pathogen, so these results highlight the robustness of the lysis method. RSV is a common childhood RNA virus, showing one potential application of the lysis method to a clinically-relevant diagnostic application. This method uses dried reagents compatible with non-refrigerated storage and a disposable chemical heat source for enzyme deactivation. No additional infrastructure or external processing was required before nucleic acid amplification. The total list price for the consumables (Eppendorf tubes, paper towel, cotton balls, NaCl, MgFe) used to construct the prototype heaters is less than $0.41. Purchasing these items at larger quantities will likely reduce the cost. The only tools used to build the prototype heater were a razor blade, a drill press, drill bits, a ruler, and a scale to weigh the components. In addition to being a laboratory tool that many could build themselves, it would be straightforward for a manufacturer to make modified tubes for this type of application.

This work was performed with low-resource clinical settings in mind; however, this method is a generic tool compatible with any process (lysis or not) that requires heat. Such processes include the use of proteinase K or NaOH for relatively quick cell lysis in limited-resource laboratory settings, animal facilities, or for environmental sample analysis. Heat alone is sufficient to lyse many organisms[213], to perform heat-shock antigen-antibody dissociation[214], or to denature nucleic acid complexes or proteins. This method is ideal for thermal lysis[215] of *E. coli* or other organisms that lyse at elevated temperature, which could enable quick screening of plasmid cultures.

We expect that this method and other sample preparation techniques in development by our group[155], [158], [159] will help enable the expansion of the next generation of point-of-care diagnostics assays to areas without access to traditional diagnostic infrastructure.

9.5 Acknowledgements

Buser, Zhang, Byrnes, Heiniger, Wheeler, Bishop, Lutz, Weigl, and Yager were supported by DARPA DSO/BTO HR0011-11-2-0007, awarded to Yager. Ladd was supported by NIH 1 R01 AI 096184-01 awarded to Yager. We would like to acknowledge Anne Cent of the molecular virology laboratory for providing a laboratory RSV virus strain for experimentation, along with the team at Seattle Children's who collected the patient nasal samples, including Kirsten Lacombe, Bonnie Strelitz, Alastair Murray, and Catherine Bull, as well as all of the patients and their families who participated in the study. We would also like to acknowledge Traci Kinkel from the Ferric Fang lab at the University of Washington for providing a laboratory strain of *Staphylococcus aureus*. We wish to thank Shichu Huang, Tinny Liang, both of the University of Washington and Elain Fu, now at Oregon State University, for their help in obtaining patient samples. We would also like to thank Sujatha Ramachandran for the helpful guidance regarding ACP dry storage. We thank everyone in the Yager and Lutz labs, and collaborators at UW, PATH, GE Global Research, and the ELITech Group for the support and feedback.

10 Sub-aim 4.2: Develop methodology for handling large samples using paper microfluidic physics

Nucleic acid-based diagnostics, such as the MAD NAAT device, have the potential to enable more sensitive and specific detection of many pathogens, including screening for drug resistance without needing time-consuming cultures. However, the current manifestation of the MAD NAAT device can only handle tens of microliters of input sample. In addition, the MAD NAAT device is currently relying on the lack of contaminants which may poison the downstream assay, as no purification step is currently integrated. This may hinder the ability of the MAD NAAT device to target urine-borne or water samples (which can be high volume) or blood-borne samples (which contain known PCR inhibitors such as immunoglobulin G and lactoferrin[216]).

To simultaneously increase the sample size which can be input to the device (sample concentration) and remove potential contaminants (sample purification), fellow PhD student Samantha Byrnes in the Yager group has been working on a chitosan-based methodology of nucleic acid purification, which can be capture and release DNA using changes in the solution pH. However, initial manifestations[159] (published in *Lab on a Chip*, included as Appendix) have relied on manual user steps and took a relatively long time to process larger-volume samples (25-30 minutes for 2 mL). Combining the work I've been doing studying the physics of capillary action in paper microfluidics with Samantha's nucleic acid concentration and purification work, we are able to both speed up the purification process and introduce a fluidic switch to redirect flow into a downstream assay region after an appropriate amount of purification time has passed.

Main deliverable: Publication 1: Large-volume NA purification ***MS in prep***

10.1 Background

During the last decade, a variety of valving techniques have been implemented for controlling fluid flow in porous networks. For example, materials can be embedded into a membrane to slow or delay flow. Noh *et al*. utilized varying concentrations of patterned wax to control fluidic timing in porous devices[217], [218]. Lutz *et al*. developed a different approach by embedding sugar barriers into porous membranes. Higher concentrations of sugars resulted in longer delays for fluid delivery[219]. The Yager, Lutz, and Fu groups have also designed methods for the sequential timed delivery of reagents through two-dimensional paper networks that rely on volume metering[90], [94], [95], [157]. Chen *et al*. developed a fluidic diode using a combination of hydrophobic and hydrophilic coatings to control direction and sequencing of fluid flow[220].

Although many of these systems effectively control fluid flow, they also share some limitations. For example, most of these methods are only able to turn flow on or off, but cannot do both. Additionally, many of these systems introduce an additional reagent (wax, sugar, etc.) into the primary fluid path. These reagents may interfere or completely inhibit sensitive downstream reactions such as nucleic acid amplification[221]–[223].

With these concerns in mind, Toley *et al*. developed valves that utilize fluid to actuate expanding elements. These elements are outside of the main fluid pathway and do not introduce additional reagents. These expanding valves can turn flow on or off and cause fluid diversion and redirection[154]. This system was able to achieve fluidic delays ranging from 5 seconds to 25 minutes with coefficients of variation of less than 9 %.

Recent publications have included reviews of additional valving for paper microfluidics including those detailed above[224]–[226]. Although effective, many these systems are limited to use with a maximum of a few hundreds of µLs of input sample. When processing large volumes such as urine or dilute blood, devices may need to manage up to 5-10 mL of volume. In a urine, for example, the first 5-10 mL contain the highest concentration of pathogen biomarkers[227].

In recent years, multiple groups have used isotachophoresis to concentrate pathogen biomarkers from complex samples[228]–[230], but these systems often use small sample volumes and involve multiple pre-processing steps, such as off-device centrifugation and sample dilution[231]. Additionally, isotachophoresis can be sensitive to high salt and white blood cell concentrations found in clinical samples[231]. Linnes *et al*. developed an integrated method for paper-based NA extraction coupled to in-membrane isothermal amplification to detect chlamydia[146]. Although effective, this device required multiple user steps and utilized only a small volume of urine, between 10 – 100 µL. We previously published on an in-membrane sample processing method that concentrated DNA from up to 2 mL of sample, but that system did not include any automation to enable development of an integrated device[159].

Alternatively, some samples require dilution prior to processing to reduce high concentrations of interfering species that may inhibit target detection[232] or restrict flow through paper[159]. Multiple groups have demonstrated paper devices that separate the input sample into multiple detection zones causing modest dilution, but there are only a few demonstrations of deliberate and automated dilution in porous-based devices. Osborn *et al* demonstrated a paper-based device capable of linear dilutions based on geometry[94] and Songjaroen *et al* designed a system that uses a wash step to dilute a sample on-device for blood

typing[233]. To date, there have not been any published reports of paper devices that automate a dilution series of a sample. The complexity of realistic samples – some which need concentration and others dilution – requires a reimaging of device design and fluid processing.

Many previous publications use simplified models to describe flow in paper microfluidic devices. The most commonly cited are the Washburn equation and Darcy's Law. The Washburn equation is limited to flow in one dimension while Darcy's Law can be used in multi-dimensional flows. Neither of these models, however, is fully representative of complex flow in porous media. For example, both Washburn and Darcy assume a fully saturating wetting front. In reality, the wetting front in a porous membrane is only partially-saturated and the degree of saturation depends on specific properties of the individual membranes such as the water retention curve. To accurately model these systems, a partially-saturated modelling technique is required. The Richards equation is widely used in hydrogeology to model partially-saturated flow through soil. A full description of the Richards equation for modelling flow in porous media along with characterization of commonly used membranes for paper microfluidics is covered in a separate manuscript in preparation by our group (see Aim 1, manuscript in prep, Buser *et al.* 2016).

Using this new insight, we have designed and developed multi-material porous networks to automate and control fluid flow in paper microfluidic devices. This simple-to-use system is demonstrated in two ways: (1) automated DNA extraction and concentration from mL-sized samples and, to our knowledge, (2) the first demonstration of automated dilution series in a paper-based device. Our system enables the integration and automation of complex, multi-step assays which would otherwise not be feasible with traditional paper microfluidic approaches.

10.2 Materials and Methods

10.2.1 Reagent preparation

All reagents were prepared with sterile molecular biology grade water (Fisher Scientific, Waltham, MA, USA). Low molecular weight chitosan oligosaccharide lactate (average MW 5000), Tris Base, MES, Achromopeptidase (ACP, A3547), 200 proof Ethanol, and Erioglaucine were purchased from Sigma Aldrich (St. Louis, MO, USA). Glycogen was purchased from Thermo Fisher Scientific (Grand Island, NY, USA). A 2 mg/mL solution of Erioglaucine was prepared in sterile water. A 20 U/µL solution of ACP was prepared in 10 mM Tris, pH 8. The 50 mM MES DNA wash buffer were prepared in sterile water and the pH was adjusted to 5. The 50 mM Tris DNA elution buffer was prepared in sterile water and the pH was adjusted to 9. De-identified human urine samples were provided by the Global Health STI Laboratory at the University of Washington Harborview Medical Center in Seattle, WA, USA. Urine sample pH and salinity was measured using a pH/conductivity meter. 40 nm InnovaCoat streptavidin gold conjugates were purchased from InnovaBiosciences (Cambridge, United Kingdom). Triethyl ammonium bicarbonate (TEAB) at 0.1 M and the biotinylated probe were supplied by ELITech Molecular Diagnostics (Seattle, WA, USA). The biotnylated probe consisted of the following sequence: 5'-TTTTTTTTTTTTTTTTTTTT-biotinTEG – 3' (T20-biotin). These reagents were diluted to 75 um of TEAB and 200 um of T20-biotin probe.

10.2.2 Device patterning and construction

All porous membranes and test card materials were cut using a CO_2 laser (Universal Laser Systems, Scottsdale, AZ). For the concentrator, Fusion 5 membranes (GE Healthcare Life Sciences, Niskayuna, NY) were patterned with chitosan and used as the primary network in the p-switch. The secondary network was comprised of 8964 glass fiber (Ahlstrom, Alpharetta, GA, USA). Test cards were made with 0.25 mm-thick Mylar backing with adhesive (10 mil AC Melinex, Fralock, Valencia, CA, USA) and cellulose wicking pads (CFSP223000 Millipore,

Millipore, Billerica, MA, USA) for waste fluid uptake. The Fusion 5 membrane was patterned with a 1% solution of low molecular weight chitosan solution prepared in 50 mM MES at pH 5. After patterning, the membranes were stored in a desiccator. For the diluter, nitrocellulose membranes (HF 135, GE Healthcare, Piscataway, NJ) were patterned with a T20-biotin probe at 200 uM in 75 uM TEAB using a piezoelectric printer (sciFLEXARRAYER S3, Scienion AG, Berlin, Germany). The solution was filtered using a 0.2-μm nylon membrane (VWR, Radnor, PA) at 8000g for 5 minutes prior to spotting. Test lines were created by 20 spots spaced 250 μm apart, with 30 droplets per spot. Each droplet was 450-500 pL. After spotting, membranes were UV treated for 8 minutes with a UV transilluminator (UltraLUM inc, Paramount, CA) at wavelength 300-310 nm and stored under desiccation before use.

10.2.3 Automated dilution using the p-switch

The calibration curve was generated using known concentrations of streptavidin gold (InnovaCoat Gold – 40 nm streptavidin gold conjugate, InnovaBiosciences, Cambridge, United Kingdom). Dilutions between 0-0.25 OD in a final volume of 40 μL were tested to determine the dynamic range for the system. The automated diluter was tested by applying 750 μL of gold nanoparticles diluted to OD 0.0625 in PBST+1%(w/v) BSA to the sample application portion of the fusion 5 pad. Once the entire membrane wet, the glass fiber base was placed into a well containing 3 μL of PBST and allowed to run until all buffer was used. All images were immediately scanned at 600 dpi and quantitative values were analyzed using the normalized pixel intensity across the test line.

10.2.4 Quantifying total Nucleic Acid in patient urine samples

Nucleic acids were purified from 500 μL of discarded urine samples by first harvesting intact cells *via* centrifugation at 13,000 xg for 3 minutes. The supernatant was saved in a separate tube and cells were resuspended in an equal volume of 10 mM tris at pH 8. Cells were then treated

with 10 µL of 20 U/µL ACP and incubated at room temperature for 2 minutes. Then, the suspension was heated to 95 ^{o}C for 5 minutes. Nucleic acids were purified from both the cell lysate and the supernatant by ethanol precipitation using 1/10 volume of 3 M sodium acetate (pH 5.2), 2x volumes of cold 100% ethanol, and 1/100 volume of 20 mg/mL glycogen. The solutions were mixed by inversion 10-12 times followed by incubation at -20 ^{o}C for 15 minutes. After incubation, the samples were centrifuged for 15 minutes at maximum speed: 21,000 g. The glycogen and nucleic acids formed a visible white pellet in the bottom of the tube. The supernatant was removed and the pellet was washed with 1 mL of 70% ethanol. The sample was mixed by inversion 10-12 times followed by centrifugation at maximum speed for 5 minutes. The supernatant was removed and the pellet air-dried for 10 minutes at room temperature. The pellet was then resuspended in 50 µL of sterile water with heating to 37 ^{o}C for 10 minutes. The concentration of nucleic acids was quantified using a Nanodrop (ThermoFisher Scientific, Grand Island, NY, USA).

10.2.5 qPCR for MRSA ldh-1 gene

DNA recovery was quantified with a qPCR kit for the *ldh*-1 gene provided by the ELITechGroup (ELITechGroup Molecular Diagnostics, Bothell, WA, USA). The 20 µL reactions were run on a Bio-Rad CFX real-time PCR instrument (Bio-Rad, Hercules, CA, USA) using the following protocol: 50°C hold for 2 minutes, 93°C hold for 2 minutes, 45 cycles of 93°C for 10 seconds, 56°C for 30 seconds, and 72°C for 15 seconds, ending with final elongation step at 72°C for 5 minutes. Fluorescence data were collected during the 56°C annealing step in the Texas Red channel. The qPCR results were analyzed using the automated threshold cycle (CT) value calculation in the Bio-Rad software (Bio-Rad, Hercules, CA, USA). This assay is sensitive down to ~10^{1} copies of the target sequence.

10.2.6 Large volume sample concentration using the p-switch

Devices were built as shown in Figure 63 with Fusion 5 glass fiber as the primary membrane and 8964 glass fiber as the secondary membrane. The waste pad was made from cellulose and the membranes were held in place by the adhesive layer of the Mylar backing.

The purification experiments were run as previously described[159], with the following changes. For these tests, 10 µL of fragmented MRSA gDNA (~$1x10^4$ – $1x10^5$ copies/µL) was diluted into 990-4990 µL of either buffer or discarded urine samples (Table S1) for a resulting concentration of ~$1x10^2$ – $1x10^3$ copies/mL. The full volume was then flowed through the device followed by 250 µL of wash buffer (50 mM MES, pH 5). 250 µL of the elution buffer (50 mM Tris, pH 9) was manually added to the secondary membrane.

After the secondary membrane was fully wet, the chitosan and elution sections of the device were removed and fluid was recovered by centrifugation at 10,000 g for 3 minutes. The amount of target DNA in the fluid from each membrane region was quantified by qPCR, correcting for volume recovered from the section.

10.2.7 Automating the p-switch through timed release of the secondary fluid source – the pinch valve

The secondary fluid source can be activated automatically, causing elution of the nucleic acid though the secondary membrane. For this purpose, a small leg of Fusion 5 membrane extends from underneath the cellulose waste pads, which wets once the cellulose pads reach saturation. This leg of Fusion 5 is in contact with a section of water-soluble paper, which dissolves on contact with liquid. This paper is holding closed a pinched section of silicone tubing that

prevents flow of the elution buffer. When the water-soluble paper dissolves, the pinch is released, allowing fluid to flow through the previously blocked tubing and into the inlet of the secondary membrane, activating elution through the chitosan-patterned portion of the p-switch.

10.2.8 Fully integrated system for concentrating DNA from mL-sized samples

Devices were built as shown in Figure 66 with Fusion 5 as the primary membrane and Alhstrom 8964 glass fiber as the secondary membrane. The waste pad stack was made from cellulose and the membranes held in place by the adhesive layer of the Mylar backing.

The fully automated purification experiments were run as described above with fragmented MRSA gDNA (~$1x10^4$ – $1x10^5$ copies) was diluted into 5 mL of buffer for a resulting concentration of ~$1x10^1$ – $1x10^2$ copies/mL. The full volume was added to the sample collection well and flowed through the device without a wash step. After the sample flow was complete, 300 µL of the elution buffer (50 mM Tris, pH 9) was automatically released to wet the secondary membrane, as described above.

After the secondary membrane was fully wet, fluid was recovered from the device by centrifugation at 10,000 g for 3 minutes. Recovery of target DNA was quantified by qPCR, correcting for elution volume.

10.2.9 Statistics

All statistics were run using the open-source statistical package R (64 bit, version 3.0.2)[234].

10.3 Results

10.3.1 The p-switch: Pressure-based valving in porous membranes

The use of porous materials for affordable diagnostics is partially driven by their automatic transport of fluids, removing the need for expensive operational equipment such as syringe pumps[94]. This fluid transport is driven by a pressure differential between a fluid source and the wetting front in the membrane, described here as the suction pressure. This simple relationship has been described previously in the literature[90], [94], [95]. More complex, multi-material networks, however, have not been well described.

When one membrane serves as a fluid source for a second membrane, the pressure differential at their intersection dictates fluid flow. For example, Figure 62A shows the water retention curve (WRC) for a nitrocellulose membrane (HF135, Millipore, Billerica, MA, USA). Wetting of the nitrocellulose membrane as modeled in COMSOL (Burlington, MA, USA) is shown in Figure 62B, with the wetting front advancing into the material from a fluid source located at the lower boundary. The modelled fluid pressure at 60s is shown in Figure 62C, along with the location of an overlapping secondary membrane, Ahlstrom 8964 glass fiber. The pressure along the vertical axis of the nitrocellulose membrane is plotted in Figure 62D. It can be observed that the fluid pressure at the junction is negative, ~11 kPa. A water retention curve for the 8964 membrane is shown in Figure 62E; at a suction pressure of 11 kPa, very little of the membrane is saturated. The practical implication of this is that the 8964 membrane will not pull significant fluid from the junction while the HF135 membrane is wetting, due to the pressure differential at the junction.

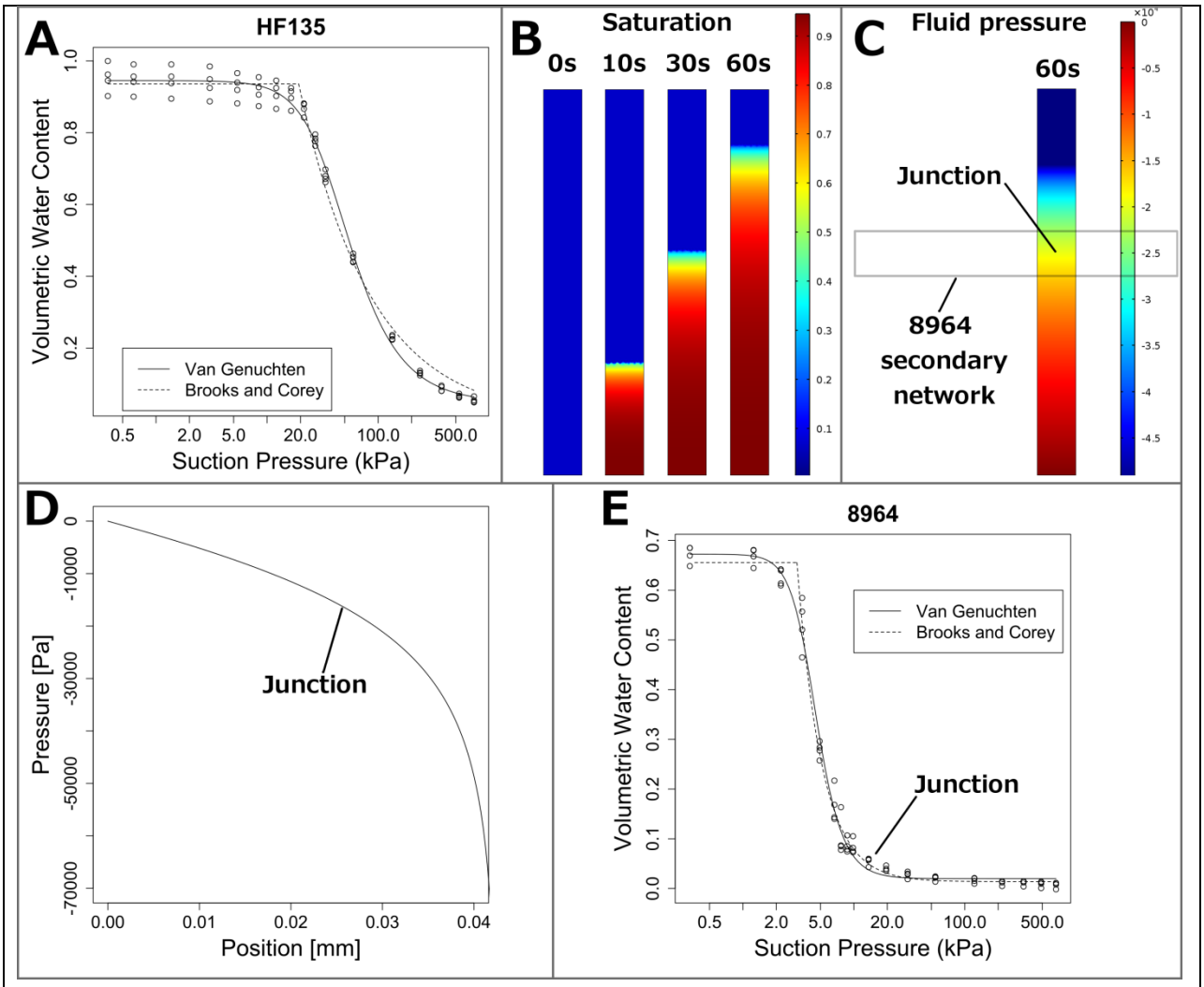

Figure 62: Explanation of p-switch operating principals. A. Water retention curve (WRC) for HF135 nitrocellulose. At lower levels of saturation, a larger suction pressure is generated. B. The WRC data along with the measured membrane permeability can be used to model flow with the Richards equation. Here, fluid is flowing into an HF135 membrane from a fluid source located at the lower boundary of the rectangle. The fluid front advances into the membrane as time goes on. C. The fluid pressure is displayed at the 60 second time point. A hollow rectangle is drawn where an 8964 membrane could be located to construct a junction. D. Fluid pressure is plotted as a function of vertical position, with 0 mm corresponding to the lower boundary of the rectangle. Fluid pressure starts as 0 at the fluid source, and decreases as a function of vertical position. The fluid pressure at the location of the 8964 junction is highlighted, around 11 kPa suction pressure. E. Water retention curve for 8964 glass fiber. At suction pressure of 11 kPa, very little of the 8964 membrane will wet. This means that the 8964 will not pull significant fluid from the junction while the HF135 is wetting.

Careful material selection allows predictable pressure differentials at material junctions and, therefore, controllable fluid flow and material wetting. Because this controllable valve is driven by pressure, we've named it the p-switch.

Figure 63A shows a device composed of multiple materials; the primary membrane is connected to a fluid source and a waste pad. This primary membrane is sandwiched between two pieces of the secondary membrane at the overlap region, Figure 63B. During wetting, the primary membrane will take up fluid, Figure 63C. The secondary membrane remains dry as the fluid flows through the overlap region. If an additional fluid source is connected to the secondary membrane, fluid can now flow through the overlap region.

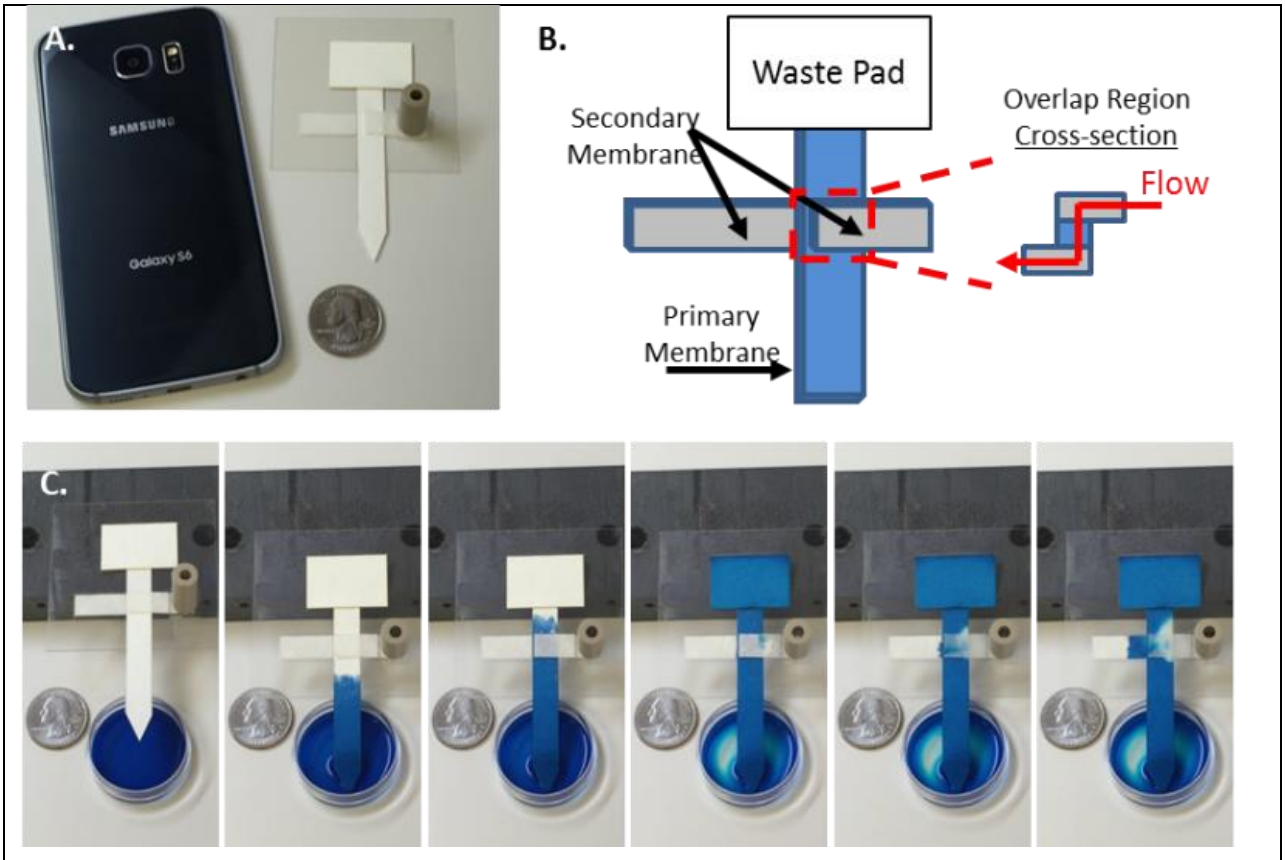

Figure 63: Demonstration of p-switch operation. A. Image of a simple p-switch device with a Galaxy S6 mobile phone and US quarter for scale. B. Schematic of p-switch device consisting of multiple materials and a cross-section of the junction. C. Images from a video showing fluid flow in a p-switch device.

10.3.2 Automated dilution using the p-switch

The p-switch enables automated on device dilution of a sample through the delivery of specific volumes of a sample across a series of test strips. Figure 64A shows the device designed for automated dilution, where the sample is applied to the primary membrane, named the sample pad. When the source pad is placed into a well containing running buffer, it carries varying volumes of the sample into the legs of each test strip. The increasingly smaller widths on each subsequent test leg led to the delivery of subsequently smaller volumes of the sample into each test strip, Figure 64B. The dilution factor on device was quantified using biotinylated gold nanoparticles that bind to a biotinylated oligonucleotide that is adsorbed onto a test line, Figure 64C. Utilizing a calibration curve the dilution factor across each test leg was calculated to be 0.8, 0.45, 0.24, and 0.1.

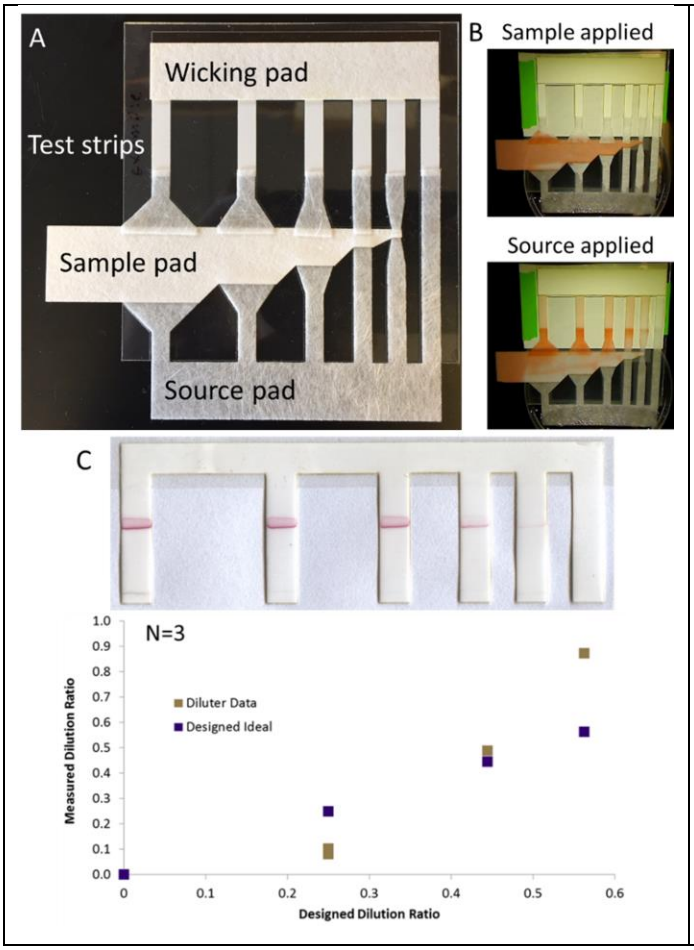

Figure 64: Paper-based automated dilution device using the p-switch. A. Device schematic of the automation dilution device, where the primary membrane is the sample pad, and the source pad is the secondary membrane to which running buffer is applied. B. Video stills of the dilution device using red dye C. Representative test lines and the calculated dilution factor for each leg of the automated diluter. Averages of N=3 are reported with error bars representing +/- one standard deviation.

10.3.3 Large volume sample concentration using the p-switch

We demonstrated an application of the p-switch for automated DNA extraction and concentration from large volume samples. Overall, the device recovered >80% of the target DNA spiked into discarded human urine, Figure 65.

Patient samples 08, 03, 02, and 05 have pH values at or below 6.8 and show high recovery of target DNA. These samples also had widely varying salinities: 11–214 mM. Patient samples 09, 01, and 04 had pH values above 7 resulting in poor capture and, ultimately, low recovery of target DNA. Patient sample 10 had a low pH (5.8), but did not result in a high recovery of target DNA. The amount of DNA remaining in the chitosan region after elution was less than 10% of the input for each sample (data not shown).

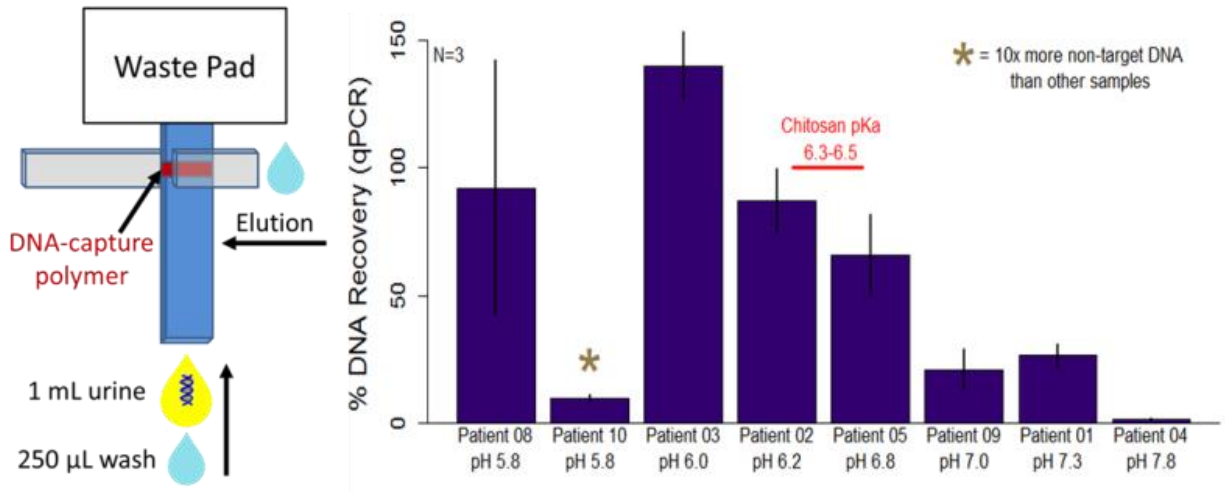

Figure 65: Application of the p-switch for in-membrane DNA purification and concentration from 1 mL of discarded human urine samples. The primary membrane is patterned with a DNA-capture polymer. Flow of the 1 mL urine sample through primary the membrane causes DNA to be captured by the polymer in the at the membrane junction. After a wash, an elution buffer is introduced to the secondary membrane causing the DNA to flow through the junction and into the elution region. Sample recovery was quantified with qPCR. Averages of N=3 are reported with error bars representing +/- one standard deviation. Generally, as sample pH increases, recovery of target DNA decreases.

These results were very promising, but still required multiple user steps: one to add the sample and a second, timed step to add the elution buffer. With this in mind, the next generation of this device was designed to appropriately time the automatic release of the elution buffer to the secondary membrane.

10.3.4 Automated processing of samples with the p-switch using the pinch valve

To enable device operation without user intervention, a release mechanism was added to the device to automatically deliver the elution buffer once the waste pad was sufficiently saturated with sample fluid, Figure 66.

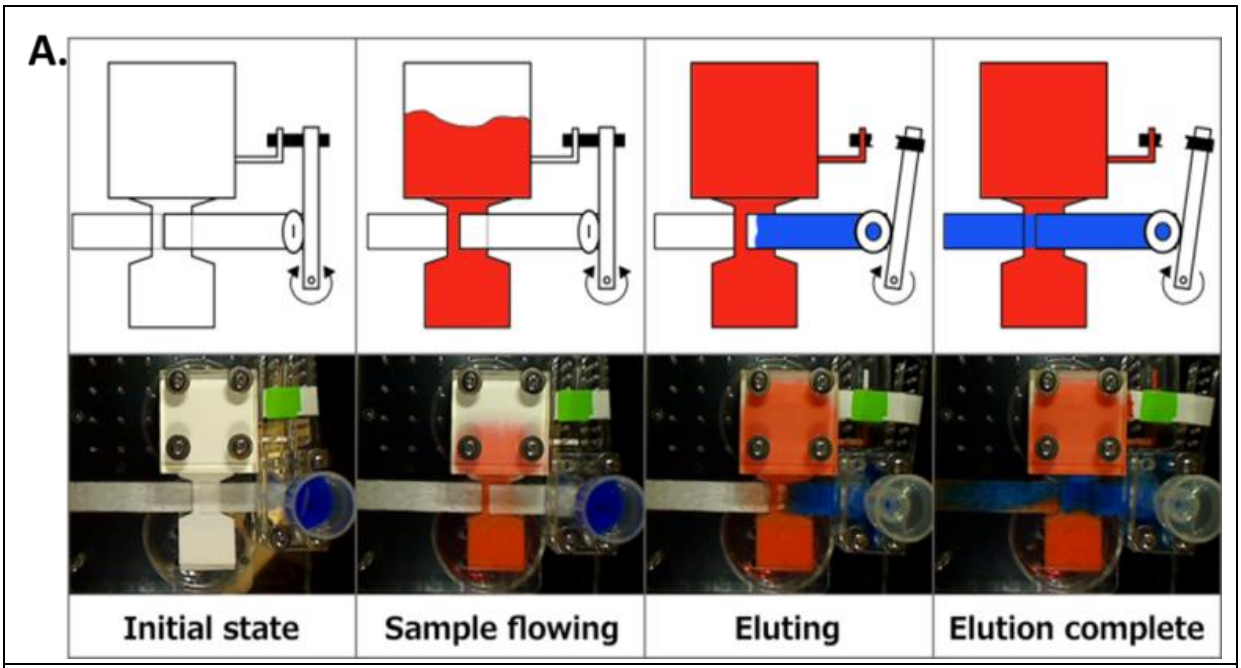

Figure 66. Automating the p-switch for the large volume sample concentration. Initially, the elution buffer well is full, but the tubing connecting the well to the secondary network is pinched closed. Once the sample (red) is added, it flows through the primary network into the waste pad. When the waste pad reaches a sufficient level of saturation, the activation leg wets a water-soluble paper, weakening it and causing the arm to release the pinch on the elution tube. When the pinch is relieved, the elution buffer (blue) flows through the junction and fills the secondary network.

10.4 Discussion

10.4.1 The p-switch: Pressure-based valving in porous membranes

Fluid flow through complex, multi-material networks is driven by material properties and pressure differentials at the junction of overlapping materials. The negative fluid pressure a material's wetting front is developed by the contact angle at the fluid/membrane/air interface and the pore structure. The fluid pressure at various levels of membrane saturation can be characterized and modelled dynamically using previously demonstrated methods (MS in prep, Buser *et al.* 2016). Briefly, a water retention curve (WRC) is generated using a laboratory centrifuge (Fisher Scientific, Waltham, MA, USA), recording fluid recovery from a saturated membrane sample at increasing speeds. The fluid pressure at each rotational velocity is

calculated ([138]) and the saturated fraction of the membrane pressure is plotted as a function of fluid pressure.

This WRC data is fit using the Van Genuchten technique and parameters related to WRC data along with membrane permeability, measured using previously demonstrated techniques (MS in prep Buser *et al.* 2016), are used in a Richards equation model implemented in the COMSOL subsurface flow module (Burlington, MA, USA). These measurements generate the data and models shown in Figure 62 with a single fluid source connected to a primary membrane in contact with a secondary membrane at a specified junction. Due to the membrane properties and the pressure differential at this junction, there is unfavorable pressure to sufficiently wet the secondary membrane, therefore preventing flow while the primary fluid pathway is wetting.

A second fluid source connected to the network at the secondary membrane, as shown in Figure 63C, will now cause this membrane to become more saturated with fluid. Higher saturation corresponds to a drop in the membrane suction pressure as described by the WRC. The change in the secondary membrane's pressure causes a more favorable differential at the junction allowing fluid to flow through the cross-section. This ability to control flow direction and wetting of multi-material networks enables the automation of complex assays in paper microfluidic devices.

10.4.2 Automated dilution using the p-switch

Serial dilution is one of the most commonly used laboratory techniques for a variety of molecular biology applications. The applications for serial dilution in a laboratory setting range from determining the binding kinetics of a binding interaction to sample preparation methods. Plastic microfluidic devices have been utilized for generating serial dilution series, however they require additional machinery to pump fluids throughout the entirety of the device. While paper

based diagnostics enable the delivery of more complex chemistries at the point of care, they have not previously been utilized for on device serial dilution coupled with detection of an analyte. As paper microfluidics utilize capillary action as the primary force for fluid flow, it is possible to further simplify these designs and enable their use at the point of care. Integration of on device serial dilution into a paper microfluidic device has the potential to increase the capabilities of traditional lateral flow assays to techniques that require dilution steps.

Here, we present proof of concept for on device dilution of both dye and streptavidin coated gold nanoparticles. By varying the area of each of the glass fiber sample legs in the diluter, it is possible to control the volume of a sample that is delivered across a test line, Figure 64. As compared to the anticipated signal, it was discovered that there are addition factors that affect the dilution ratio besides the area of the glass fiber transfer pad. The dilution ratio for each test leg was found to be further defined by the total area in the sample pad through which the source buffer runs. We anticipate that an automated dilution series can be integrated into a variety of devices that intend to complete complex chemistries required for laboratory based assays in an automated format.

10.4.3 Large volume sample concentration using the p-switch

As described previously, chitosan is a linear polysaccharide that electrostatically binds to DNA when the pH is below ~6.3-6.5, the pK_a of the primary amine[235], [236]. Above that pH, the amines are deprotonated and the electrostatic interaction is lost. Previously, we demonstrated chitosan's ability to capture and release DNA in porous membranes without any automation[159]. The work presented here demonstrates an automation of this assay using realistic patient samples.

Unsurprisingly, urine samples with pH values below the amine pKa show high recovery of target DNA while samples with higher pH values, show reduced recovery. The exception of this data is sample 10 which is an appropriate pH for DNA capture by chitosan, but showed very low DNA recovery.

We hypothesize that sample 10 had reduced recovery due to an overloading of the chitosan with non-target nucleic acids that are present from the patient sample. Patient 10 had 10x more non-target nucleic acids compared to the rest of the samples tested. Based on previous work, this amount of non-target nucleic acid is above the capacity of the chitosan patterned in this membrane.

10.4.4 Automated processing of samples with the p-switch using a pinch valve

In the automated concentration devices, the waste pad was in contact with a connecting arm made of Fusion 5 membrane. The connecting are contacted a water-soluble paper that restrained a plastic lever arm which was pinching closed tubing. This tubing connected the elution buffer to the secondary membrane. Once the waste pad was full, the connecting arm began to fill and wet the water-soluble paper which dissolved and released the lever arm and then pinch on the tubing. The open tubing then allowed elution buffer to flow into the secondary membrane, which is made of 8964 glass fiber. Flow of elution buffer through the junction eluted DNA captured on the chitosan and flowed it into the downstream region of the secondary membrane. The purified and concentrated sample was quantified by qPCR to determine recovery of target DNA.

10.5 Acknowledgments

This work was supported by a grant to Paul Yager from the Defense Advanced Research Projects Agency (DARPA) “Multiplexable Autonomous Disposable for Nucleic Acid Amplification Tests for LRSs” under Grant No. HR0011-11-2-0007.

We thank our colleagues Ryan Gallagher, Paula Ladd, and Erin Heiniger in the Yager Laboratory who provided valuable discussion and feedback on experimental design and analysis. We thank O. Soge Olusegun from the Global Health STI Laboratory at the University of Washington Harborview Medical Center for providing deidentified human urine samples. We thank collaborators from ELITechGroup Molecular Diagnostics for assistance with the supply of the qPCR assay. SEM imaging and sputter coating work was performed at the University of Washington Nanotech User Facility (NTUF), a member of the NSF-sponsored National Nanotechnology Infrastructure Network (NNIN).

11 Sub-aim 4.3: Disposable hydrogen fuel cells for powering next-generation paper microfluidic devices

This sub-aim was completed in collaboration with Dr. Juan Pablo Esquivel, a visiting scientist with the Yager group from Instituto de Microelectrónica de Barcelona, IMB-CNM (CSIC) in Barcelona, Spain. Juan Pablo started with our group working on methanol fuel cells previously demonstrated by his group[117], with the intention of using our expertise in paper microfluidics to optimize material choices and flow in the methanol fuel cells. We quickly realized that the MgFe reaction we have been using for chemical heater applications in the context of the MAD NAAT project could serve a novel purpose: the generation of on-device hydrogen for a paper-based H2 fuel cell. Previously, storage of hydrogen on-device was considered prohibitive and consequently paper-based hydrogen fuel cells had not been demonstrated.

This is an application combining aspects of two of my main aims:

1. Understanding and controlling flow in porous media. Here, KOH electrolyte solution needs to flow between the electrodes at a controlled rate. Additionally, the MgFe reaction needs NaCl solution delivered for the reaction, and needs to prevent hydrogen backflow.
2. The use of the exothermic fuel used in chemical heaters, here for the dual purposes of a convenient form of hydrogen production and heat for fuel cell optimal performance

Additionally, I designed and build the power converter electronics based on the Texas Instruments low power voltage converter chip (with much appreciated training and assistance from Peter Kauffman).

Electrical power enables enhanced functionalities in point-of-care diagnostics. This work presents the first paper-based hydrogen fuel cell, harnessing the hydrogen generated as a by-product of the exothermic reaction used for chemical heaters in point-of-care nucleic acid amplification devices. The electrical power produced by the fuel cell can be used for other assay applications including optical detection. The fuel cell delivers a maximum power of 16.5 mW

(66 mW cm^{-2}), which is sufficient to run an electronic pregnancy test that normally operates with a Li-ion battery.

The work presented in this sub-aim is adapted from[237]*:*
Esquivel JP, Buser JR, del Campo FJ, Rojas S, Yager P, and Sabaté N. (2015) Disposable hydrogen fuel cells for powering next-generation lateral flow devices. *Solid-State Sensors, Actuators and Microsystems Conference (TRANSDUCERS), 2015 18th International*

Main deliverable: Disposable hydrogen fuel cells… *Transducers* ***Published***

Secondary deliverable: Disposable hydrogen fuel cells… ***MS submitted***

Background

Rapid, portable diagnostics enable advanced medical testing at the point-of-care, but often lack desired quantitative capabilities[11]. In comparison, many instrumented diagnostic systems require electric power to perform different assay functions such as heating, moving fluids within the device (pumping, mixing, separating…), detecting analytes with a variety of working principles (electrochemical, optical…) or expressing the result to the user (through displays or wireless communications)[10], [52], [58]. However, these integrated systems often lack affordability and other characteristics necessary for use in lower-resource settings[8], [57].

Powering portable diagnostics with lithium-ion or alkaline batteries is common, but special disposal considerations must be considered. For instance, the Clearblue Digital Pregnancy Test (Swiss Precision Diagnostics GmbH) requires disassembly and battery removal before disposal, according to the manufacturer instructions[238]. After using this test, a user must also make a trip to the Household Hazardous Waste facility to dispose of the lithium-ion if they're here in Seattle[239]. The environmental risks of batteries also exist in lower resource settings where point of care diagnostics may be especially useful.

Alternative power sources that address the environmental implications are emerging in recent years, for example, printed batteries and other paper-based power sources like supercapacitors[240], [241], batteries[82], [242] and microfluidic fuel cells[243], [244]. These approaches have the advantages of slim form factors and scalable manufacturing, but still lack the necessary power density and energy capacity to fully replace lithium batteries.

In this work we present a paper-based hydrogen fuel cell. Compared to previous approaches, the present concept brings together the high power density typically delivered by

larger hydrogen fuel cells with the convenience of portable, disposable, inexpensive paper-based power sources.

Usually, hydrogen isn't considered for portable fuel cells due to storage and handling concerns. Here, we avoid this difficulty by using hydrogen generated in the magnesium-iron alloy corrosion reaction used for chemical heating in point-of-care nucleic acid amplification devices[115]. This eliminates the need for a pressurized gas canister. Further, we are generating usable electricity from what was previously a waste product of chemical heating devices.

Liquids in the paper-based hydrogen fuel cell we've designed are transported *via* paper microfluidics, so no external pumps are required. The device outlined in Figure 67 is capable of powering the previously mentioned Clearblue pregnancy test, designed to be powered by a lithium ion button cell battery. The Clearblue test performs optical detection of a colorimetric signal with LEDs, photodiodes, and a microprocessor, and displays test status and results on an LCD screen.

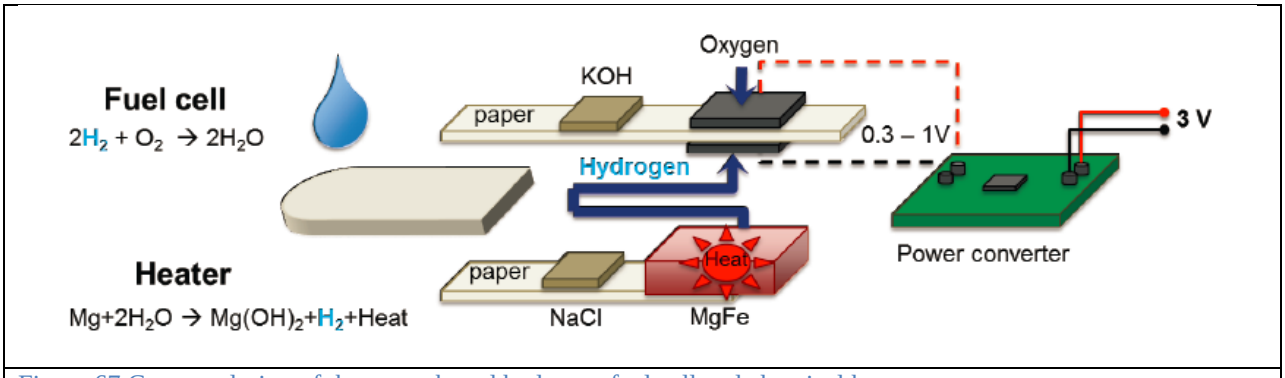

Figure 67 Concept design of the paper-based hydrogen fuel cell and chemical heater.

Materials and Methods

The device has two main subunits, a fuel cell and a chemical heater, and was fabricated using a combination of paper and laser-cut plastics. Assembly was done layer by layer using an alignment jig. Figure 68 shows a cross-section diagram of the device and its components.

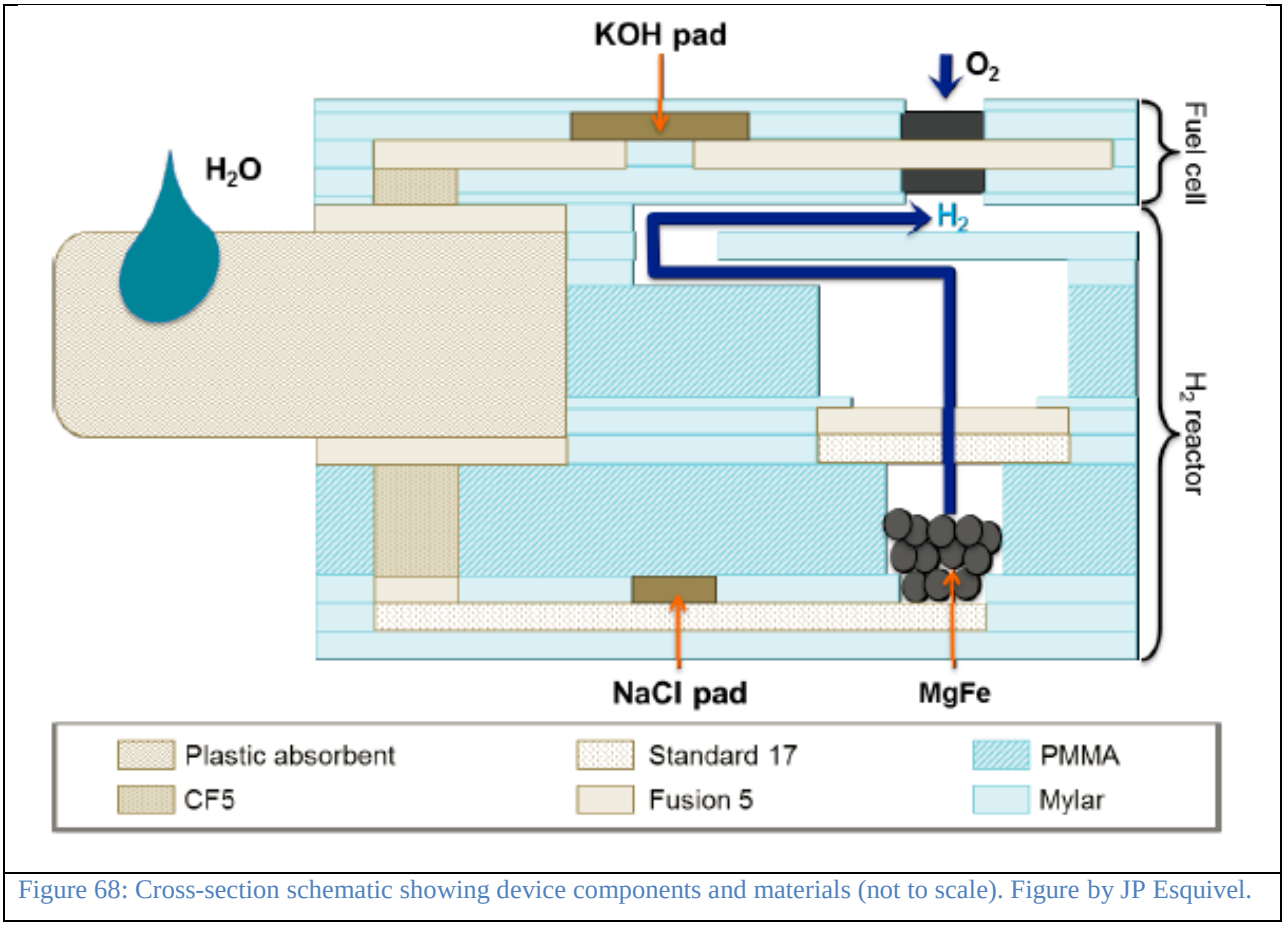

Figure 68: Cross-section schematic showing device components and materials (not to scale). Figure by JP Esquivel.

11.1.1 Fuel cell

The fuel cell core consists of a porous membrane placed between two porous carbon paper electrodes. The 5 mm wide porous membrane (Fusion 5, Whatman) wicks electrolyte between the electrodes when activated. Fuel cell electrodes were constructed from 5 mm wide carbon paper (Toray EC-TP1-060T). Catalyst layers were deposited by spray coating ink with a total metal loading of 1 mg cm-2 using 30 wt% PtRu/C (Pt/Ru 1/1 at:at; Johnson Matthey) on both electrodes. Fuel cell electrolyte was composed of 30 µL 10M KOH solution desiccator-dried in a cellulose (CF10, Whatman) strip, rehydrated when H_2O is applied to the device inlet.

11.1.2 Heater

The heater contained 30 mg of 400-450 μm MgFe particles (Luxfer Magtech). The top of the chamber was covered by a two layer gas separator of our design, composed of glass fiber membranes (Standard 17 and Fusion 5, Whatman) soaked with a windshield coating solution (Rain-X, ITW Global Brands) and dried. This gas separator allows exit of hydrogen while keeping liquids and solids contained in the heater chamber. Ten μL of 18 wt% NaCl was dried in glass fiber (Fusion 5, Whatman) to react with the MgFe fuel when H_2O is added to the device inlet.

11.1.3 Device operation

Addition of a liquid sample on a wicking pad activates the device, splitting to the heater and fuel cell. Capillary pressure avoids the need for external pumps or additional power to run any portion of the device. In the heater side, the sample dissolves the NaCl present in the storage pad, triggering the exothermic reaction when it reaches the MgFe stored in a chamber at the end of the strip. On the fuel cell side, the sample dissolves the KOH in the pad, which is used as electrolyte for the fuel cell. In contrast to other H_2/O_2 fuel cells with flowing electrolyte[245], the approach presented here produces the hydrogen *in situ*, harvests oxygen from air, and uses capillary pressure to deliver fluids.

11.1.4 Power converter

The Clearblue system was designed to run on 3V. A single hydrogen fuel cell can only achieve open circuit voltages around 1V. To avoid needing to stack fuel cells to increase output voltage, which would make fuel cell development more difficult, we designed and built a DC-DC power converter based on the ultra-low power Texas Instruments' BQ25504 chip. This chip is capable of stepping up voltages as low as 0.1 V up to voltage levels as high as 5.5 V. For this application, the converter has been configured to deliver an output voltage of 3 V. The converter circuit and

printed circuit board (PCB) layout was designed in Eagle (Cadsoft, Pines, FL, USA), and manufactured (Sunstone Circuits, Mulino, OR, USA).

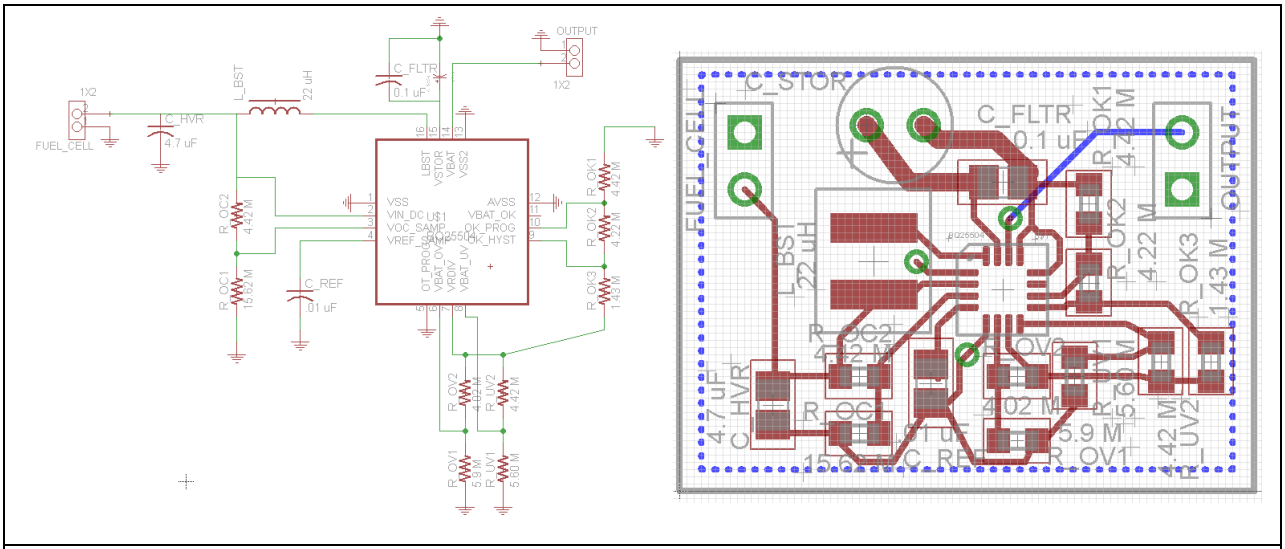

Figure 69: Power converter for paper-based hydrogen fuel cell. Left: Schematic. Right: PCB layout.

11.2 Experimental

We demonstrate here a paper-based hydrogen fuel cell capable of powering complex point-of-care devices, featuring microprocessors, liquid crystal displays (LCDs), and optical detection systems. For this purpose, an off-the-shelf commercial electronic pregnancy test was chosen to highlight our power source capabilities. The Clearblue Digital Pregnancy Test is a disposable lateral flow test system for the optical quantification of hCG hormone in urine. This device contains LEDs, photodiodes, electronics and an LCD to show the results of the test. Figure 70 shows the fuel cell, including power converter, next to a Clearblue pregnancy test.

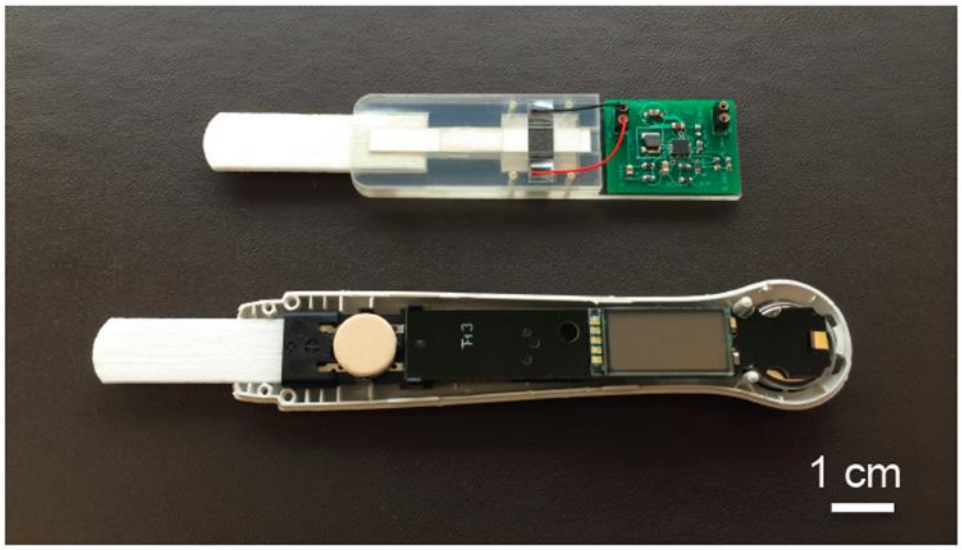

Figure 70: Picture of the integrated device (top) and a commercial electronic pregnancy test (bottom). Figure by JP Esquivel.

As shown in Figure 71, the fuel cell produces sufficient voltage and current to power the Clearblue digital pregnancy test. Plotted are the voltage output delivered by the fuel cell to the Clearblue after up-conversion and the current demanded by the pregnancy test. The voltage increases to 3.1 V quickly after adding the liquid sample to the fuel cell inlet. Around t = 150 s the pregnancy test is activated by adding PBS. The current draw of the test then increases to 13.5 mA, as LEDs used for quantification turn on. The converter voltage briefly drops down to 2.7 V and then returns to 3.1 V when the LEDs turn off and shows the result on the display. After this, the current needed by the test stabilizes at ~5 mA.

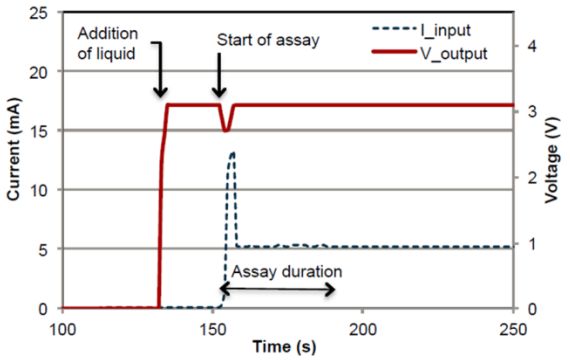

Figure 71: Voltage output from power converter and current input during a measurement of Clearblue digital pregnancy test. Figure by JP Esquivel.

This fuel cell has an open circuit voltage of 1.04 V, and a maximum power of 16.5 mW at 37 mA. Normalizing these values to the electrode area, this microfluidic fuel cell (0.25 cm^2) outperforms the coin battery (2 cm^2), yielding a maximum power density of 66 mW/cm^2, compared to the 30 mW/cm^2 of the CR1616 $LiMnO_2$ coin battery included in the Clearblue test.

11.3 Discussion

As shown above, this hydrogen fuel cell has the power to replace commercial Li-ion batteries for single use applications. This approach has advantages over other micro fuel cells, especially those which require pumps to drive electrolyte or reactants. The power density of this device is comparable to that of larger PEM hydrogen fuel cells, which is typically higher than that achieved by liquid fuels (*e.g.* methanol, ethanol, formic acid, glucose). The form factor of the fuel cell reported here was designed to suit for the Clearblue pregnancy test. However, it would be straightforward to customize shape and power output to fit the requirements of other applications.

Here, we have stepped up the voltage using a DC-DC power converter circuit. Alternatively, several fuel cells could be arranged in series to increase the output voltage. A two fuel cell stack we recently designed and tested has shown open circuit voltages up to 1.7V. We

have found these stacks give sufficient voltage to run LEDs and other electronic components without a DC-DC converter.

The cost of the devices is currently a bit higher than we'd like: the platinum in the electrodes represents the most expensive component (1 mg cm^{-2} Pt x 0.5 cm^2 x 0.247 $/mg Pt = $0.124 per fuel cell)[246]. JP Esquivel and our collaborators are currently exploring non-precious metal catalysts.

11.4 Conclusions

This disposable hydrogen fuel cell has the potential to fulfill power requirements of portable diagnostics with a lower environmental impact than other power sources, for little cost. In this work it has been shown how this type of power source could be integrated into an off-the-shelf commercial device, demonstrating that this technology is particularly suitable to make next generation of quantitative point-of-care testing without external power supplies or batteries.

11.5 Acknowledgements

Much of the work presented in this sub-aim is adapted from:

Esquivel JP, Buser JR, del Campo FJ, Rojas S, Yager P, and Sabaté N. (2015) Disposable hydrogen fuel cells for powering next-generation lateral flow devices. Solid-State Sensors, Actuators and Microsystems Conference (TRANSDUCERS), 2015 18th International

I would like to thank all of these coauthors, especially Dr. Juan Pablo Esquivel, without whom this work would not be possible for me. Peter Kauffman provided many hours of technical assistance regarding designing PCBs in Eagle, exporting appropriate CAM files, and ordering PCBs from Sunstone, along with providing general electronics mentorship. I would also like to thank Dr. Paul Yager and Dr. Bernhard Weigl for their valuable insight and guidance during this research.

12 MAD NAAT integrated device

This section of my thesis is presented in a largely unmodified form from our group's publication in Lab on a Chip, and covers the integrated electronic MAD NAAT device. This publication highlights how the work in my aims can come together to enable advanced point-of-care diagnostics. While this version does not utilize a chemical heater, instead relying on battery-powered electronics, there is ongoing work on a non-electric MAD NAAT that will hopefully be published in the next year.

A rapid, instrument-free, sample-to-result nucleic acid amplification test [247]

Lisa K Lafleur,[‡a] Joshua D Bishop,[‡*a] Erin K Heiniger,[a] Ryan P Gallagher,[a] Maxwell D Wheeler,[a] Peter Kauffman,[a] Xiaohong H Zhang,[a] Enos C Kline,[a] Joshua R Buser,[a] Sujatha Kumar,[a] Samantha A Byrnes,[a] Nicolaas MJ Vermeulen,[b] Noah K Scarr,[b] Yevgeniy Belousov,[b] Walt Mahoney,[b] Bhushan J Toley,[a] Paula D Ladd,[a] Barry R Lutz[a] and Paul Yager[a]

The prototype demonstrated here is the first fully integrated sample-to-result diagnostic platform for performing nucleic acid amplification tests that requires no permanent instrument or manual sample processing. The multiplexable autonomous disposable nucleic acid amplification test (MAD NAAT) is based on two-dimensional paper networks, which enable sensitive chemical detection normally reserved for laboratories to be carried out anywhere by untrained users. All reagents are stored dry in the disposable, and are rehydrated by stored buffer. The paper network is physically multiplexed to allow independent isothermal amplification of multiple targets; each amplification reaction is also chemically multiplexed with an internal amplification control. Total test time is less than one hour. The MAD NAAT prototype was used to characterize a set of human nasal swab specimens pre-screened for methicillin-resistant Staphylococcus aureus (MRSA) bacteria. With qPCR as the quantitative reference method, the lowest input copy number in the range where the MAD NAAT prototype consistently detected MRSA in these

specimens was ~5×103 genomic copies (~600 genomic copies per biplexed amplification reaction).

12.1 Introduction

The Yager laboratory and partners have engaged in multiple efforts to demonstrate that pathogen diagnosis can be moved out of centralized laboratories and into homes, primary care sites, and pharmacy clinics where the patients are actually located, both in the developed and the developing world. These efforts aim to reduce the cost of diagnostic tests and the time between sample collection and diagnosis, incentivizing healthcare systems to adopt a new technological platform. For large-scale adoption, however, clinical sensitivity and specificity standards must match those held by centralized laboratory evaluation. Nucleic acid amplification tests (NAATs) are the most sensitive approach to rapid pathogen detection, capable of finding just a few copies of a defined sequence of DNA or RNA in an appropriately treated biological sample. We report here on preliminary results of a collaboration aimed at making rapid NAAT diagnostics simple and accessible anywhere.

A low resource setting (LRS) can be considered any place where the tools commonly available in a sophisticated laboratory are not available to the end-user. However, diagnostic tests face similar challenges when used in health outposts in sub-Saharan Africa, clinics in rural Asia, or apartments in Seattle. Current instrumented systems are typically ill-suited to such settings because they can require laboratory training (e.g. for manual sample preparation and other steps), capital investment (e.g. up-front equipment and on-going maintenance costs), and specific infrastructure (e.g. cold storage, sterile conditions, clean running water, and electricity).

Some integrated NAAT platforms have reached the market recently (or will soon be on the market) that are specifically designed for use in venues that may be closer to LRSs[248]–[250]. These systems rely on instruments to make tests simple, and are therefore only appropriate for settings where the initial cost of instruments and continued upkeep are acceptable. NAAT kits that do not rely on instruments are commercially available, but are not fully integrated systems and therefore require many user steps[251]. A practical diagnostic solution for the user who lacks training, infrastructure, or both does not currently exist.

The ideal diagnostic would improve the sensitivity, but mimic the simplicity, of the most successful LRS platform: the lateral flow (LF) test or "rapid diagnostic test". The LF test eliminated the need for an instrument to carry out chemical detection, and the number of LF tests for detection of pathogens has grown continuously[252]. However, most LF tests are a linear arrangement of 4-5 paper components, and the only fluids are typically the sample and a flow buffer[253]. A major weakness of this format is that they only automate a limited number of assay operations.

It has been repeatedly demonstrated that the ability of porous materials to move fluids by capillary flow is a powerful diagnostic tool, beginning with glucose detection in the 1950s[11]. Since 2008, the Yager laboratory has been developing tools for designing, implementing, and characterizing automated microfluidic systems with porous materials. These two-dimensional paper networks (2DPNs) use geometry and porous material connectivity to automate complex fluidic operations, which minimizes the number of associated user operations[88], [89], [91]–[95], [102], [156], [254]. The goal is to allow an end user to introduce a sample (e.g., a nasal swab, urine, or blood) to a portable, autonomous diagnostic device. No instrument should be

necessary, with the possible exception of a cell phone camera to capture an image of the result for quantification or off-site transmission to a third party.

Other research is aimed at developing non-instrumented, point-of-care, autonomous NAAT systems for LRS applications. Various paper-based microfluidic formats have integrated some NAAT operations, but still use separate instrumentation for remaining operations (e.g. sample processing, heating, or reading the result) and none are autonomous sample-to-result systems[96], [207], [255]–[259]. Other point-of-care NAAT technologies have demonstrated useful features like digital NAAT[260] and chemical heating[114], but without integrated sample preparation.

The multiplexable autonomous disposable nucleic acid amplification test (MAD NAAT) is a platform that builds on existing research and other early demonstrations of useful approaches to a non-instrumented, point-of-care, integrated NAAT system[148], [175], [261]. The prototype reported here is the first demonstration of this platform. The disease target was methicillin-resistant *Staphylococcus aureus* (MRSA) and the molecular targets were two gene sequences. The first gene target, *ldh1*, is found in all *S. aureus* strains[262]. To discriminate methicillin-susceptible from methicillin-resistant *Staph* species, we targeted a second gene, *mecA*, which confers methicillin resistance and is found in *S. aureus* and other bacteria. In less than 60 min, the prototype performed sample processing, biplexed isothermal nucleic acid amplification, and LF detection of these targets without external instrument or user intervention.

12.2 Experimental

12.2.1 Patient specimens

Patient specimens were discarded and de-identified (human subjects protocol not needed) nasal swab specimens from adult patients who underwent MRSA screening at the Harborview Medical Center (Seattle, WA). Swab collection was performed with BD Liquid Amies Elution Swab sampling kit (Becton, Dickinson & Company, Franklin Lakes, NJ). Per hospital policy, screening is performed on adult intensive care unit and elective surgery patients. To reduce the concentration of salt in the Amies buffer and other nasal specimen interferents, samples were diluted to 1:100 for prototype tests, manual assays, and qPCR.

12.2.2 Freshly prepared reagents

12.2.2.1 Achromopeptidase (ACP) lysis

ACP (A3547, Sigma-Aldrich, St. Louis, MO) was used at a final concentration of 0.5 U µL-1 in 10 mM Tris-HCl (pH 8.0). In manual assays and qPCR, patient specimens were diluted from Amies buffer 1:10 into 10 mM Tris-HCl (pH 8.0) then further diluted 1:10 into 10 mM Tris-HCl with ACP (a final dilution of 1:100). After two minutes of room-temperature incubation, lysates were heated to 95°C for five minutes to deactivate the ACP and fragment the DNA[263] (S.A.B. manuscript in preparation).

12.2.2.2 Isothermal strand displacement amplification (iSDA)

The iSDA master mix was prepared in a reaction buffer (pH 7.6) consisting of 42.5 mM potassium phosphate, dibasic (P8584, Sigma), 7.5 mM potassium phosphate, monobasic (8709, Sigma), 3.75 mM magnesium sulfate (New England Biolabs, Ipswich, MA), 250 µM of each dNTP (New England Biolabs), 0.2 U µL-1 Bst 2.0 WarmStart DNA Polymerase (NEB), 1.6% v/v nicking endonuclease Nt.BbvCI (mutant strain, New England Biolabs), and target-specific primers: 500 nM forward, 250 nM reverse, 50 nM each bumper (Integrated DNA Technologies, Coralville, IA)[160].

12.2.2.3 Internal amplification controls (IAC)

An IAC was chemically multiplexed with each gene target. IAC templates for all assays used the same interior-sequence-matching probes for IAC detection (same for both assays) flanked by primer binding sites that matched the target sequence. This approach enabled co-amplification of the IAC using the target primers, eliminating the need to add extra primer sets for the IAC[264]. The IAC template used was a synthetic double-stranded DNA (Integrated DNA Technologies) to more closely mimic initiation from a double-stranded target. For each assay, the IAC template concentration was titrated to the lowest level that provided consistent IAC amplification in the absence of the target: 10^6 genomic copies for *ldh1* and 10^5 genomic copies for *mecA*. Sequences for iSDA primers, probes, and IAC templates for all assays are provided in Table 9.

Table 9: Isothermal strand displacement assay (iSDA) nucleic acid sequence designs for primers, probes, and internal amplification control templates.

	ldh1	***mecA***
Forward amplification primer (F) (CCTCAGC = nicking site)	5′–TAG AAT AGT CGC ATA CTT CCTCAGC ACA TCT CCT CGA ACT TTT T–3′	5′–CCA TTA TAC TAC CTG TCT CCTCAGC GGC AAA GAT ATT CAA CTA AC–3′
Reverse amplification primer (R) (CCTCAGC = nicking site)	5′–GCA TAA TAC TAC CAG TCT CCTCAGC CAA GCT ACG CAT TTT CAT T–3′	5′–TAG AAT AGT CAC TTA CTT CCTCAGC GCC ATA ATC ATT TTT CAT GTT–3′
Forward bumper primer (FB)	5′–AGG TAA TGG TGC AGT AGG T–3′	5′–GAT AAT AGC AAT ACA ATC GCA CA–3′
Reverse bumper primer (RB)	5′–CCA GCT TTC ACA CGA AC–3′	5′–GTG CTA ATA ATT CAC CTG TTT GA–3′
Capture probe (*pDNA[…]* = pyranosyl DNA)	4′–*pDNA*[TTTTTTTTC]–2′–HEG–5′–CAG TGT CTA AAT CAA TGA TG–hexanol–3′	4′–*pDNA*[CAAGAATC]–2′–HEG–5′–CTT TAG CAT CAA TAG TTA G–hexanol–3′

Biotin probe (A* = Super A®, ElitechGroup)	5′–CTA ATT CAT CAA CAA TGC–biotin TEG–3′	5′–GTT A*TA AAT A*CT CTT TTG A–biotin TEG–3′
Internal amplification control (IAC) (dsDNA template)	5′–AGG TAA TGG TGC AGT AGG TTC AAG CTA CGC ATT TTC ATT GAC CAG TTA CTT TAC GGA CCA CGT ACC GCA TTG GTA CAA GAT CTC AAA AAG TTC GAG GAG ATG TTG TTC GTG TGA AAG CTG G–3′	5′–GAT AAT AGC AAT ACA ATC GCA CAT GGC AAA GAT ATT CAA CTA ACG ACC AGT TAC TTT ACG GAC CAC GTA CCG CAT TGG TAC AAG ATC TCC AAC ATG AAA AAT GAT TAT GGC TTC AAA CAG GTG AAT TAT TAG CAC–3′

12.2.2.4 Lateral flow (LF) detection

Detection reagents were contained in all iSDA reactions in the following concentrations: 10 nM biotin probe, 20 nM DNA-pDNA (pyranosyl DNA) capture probe per target (*ldh1* or *mecA*), and 1.25 µL of 10 OD streptavidin-coated 40 nM gold nanoparticles (Innova Biosciences, Cambridge, UK). In manual assays, 8 µl of LF solution, comprising 1.875 M NaCl and 3.125% PEG 8000 (Hampton Research, Aliso Viejo, CA) in PBS, was added to 17 µL of iSDA amplicon product and mixed to yield final concentrations of 0.6 M NaCl and 1% PEG 8000. This solution was then allowed to flow up the LF strips.

12.2.3 Materials fabrication

Materials were fabricated on a CO_2 laser (VLS3.60, Universal Laser Systems, Scottsdale, AZ) or a 3D printer (Objet30 Scholar, Stratasys, Eden Prairie, MN), with exceptions noted below.

12.2.3.1 Porous materials

Standard 17 sheets (GE Healthcare Life Sciences, Pittsburgh, PA) were laser-cut into ‘Y’-shaped sample delivery pads and 2.5-mm by 20-mm amplification and detection reagent pads. Standard 17 was also razor-cut into 2.5-mm by 10-mm amplification valve pads from stock that had been striped with a 1.5-mm thick beeswax (Knorr Beeswax Products, Del Mar, CA) stripe 3 mm from the upstream end. Wax striping was done on a custom motorized stage with wax heated to 74°C. Cellulose sheets (C083, EMD Millipore, Billerica, MA) were laser-cut into 2-mm by 2.5-mm salt

pads and 5-mm by 12-mm waste pads. Cardboard-backed nitrocellulose sheets (FF80HP, GE Healthcare Life Sciences, Pittsburgh, PA) were striped with test lines (see below), laser-scored, then scissor-cut from the downstream end of the sheet into 2.5-mm x 23-mm LF strips.

12.2.3.2 Plastic materials

Several types of plastic were used in prototype fabrication. DuraWhitePlus (Stratasys) was 3D-printed to form the three housing pieces and the body of the lysis valve. Polymethyl methacrylate (PMMA; U.S. Plastic Corp, Lima, OH) was laser-cut to form the 0.06-in thick stages for heaters, "trays" to contain the 2DPN, elements for the lysis valve, and swab ports; and 0.098-in thick port blocks. Channels were created in the 2DPN trays by selectively ablating material with the laser. Prior to assembly, the PMMA pieces were power-washed with water (WaterJet, Stratasys) then dried in an incubator at 40°C for >1 hour. Mylar-backed, silicone adhesive tape (ARclad 7876, Valley Industrial Products, Huntington, NY) was laser-cut into pieces for lining the channels of, and adhering the port blocks to, the 2DPN trays. All silicone tape pieces were dried overnight in an incubator at 40°C before use. Polypropylene, 1-mL, Luer-Slip syringes (Henke-Sass Wolfe, Tuttlingen, Germany) were razor-cut to make the fluid introduction storage chamber and the sample chamber. Tygon E-3603 (1/32-in OD, Saint-Gobain, Paris, France) and platinum-cured silicone rubber (5/32-in OD, Saint-Gobain, Paris, France) tubing were razor-cut to 11 cm for fluid introduction and to 1.5 cm for the lysis valve, respectively.

12.2.3.3 Other materials

Wax blocks for lysis valves were fabricated from a mix of PureTemp 53 PCM (PT53, Entropy Solutions, Plymouth, MN) and 20% graphene nanoplatelet powder (N008-100-P-10, Angstron Materials, Dayton, OH) cast in silicone rubber molds, cured under a hot air gun, then allowed to cool to room temperature. Insulating foam inserts were razor-cut from discarded polystyrene

packaging to fill the negative space in the prototype housing when all components were assembled.

12.2.4 Dry reagent preparations

12.2.4.1 ACP dry reagent tubing

In prototypes, lysis reagents were stored dry in the fluid introduction tubing. A total of 80 U of ACP at a stock concentration of 20 U µL-1 in 10 mM Tris-HCl (pH 8.0) was mixed with 1 M trehalose (TS1M-100, Life Sciences Advanced Technologies) to a final concentration of 5% trehalose. The mixture was pipetted into the upstream end of the tubing allowed to dry for >16 hours in a desiccating environment. During prototype tests, the dried ACP was rehydrated with 160 µL of 10 mM Tris-HCl (pH 8.0) to a final ACP concentration of 0.5 U µL-1.

12.2.4.2 Combined amplification and detection dry reagent pads

In prototypes and manual assays, the amplification "master mix" and detection reagents for each target and IAC were stored together dry in amplification pads. The iSDA master mix and LF detection reagents were combined with 10% (w/v) trehalose (Life Sciences Advanced Technologies, St. Petersburg, FL) and 1% (w/v) PEG 8K (Hampton Research), which were added for stabilization during dry storage. The amplification pads were pre-blocked by soaking in 1% BSA and 0.1% Tween-20 for 1 hour, blotted dry, and dried in an incubator at 45°C overnight. The reagent mix (20 µL) was added to amplification and detection reagent pads. The pads were flash frozen in liquid nitrogen and dried for 2 h using a lyophilizer (FreeZone 4.5, Labconco, Kansas City, MO).

12.2.4.3 Internal amplification control dry reagent pads

In prototypes, IAC templates were stored dry in the sample delivery pads. The IAC templates for each target were combined with 10 mM Tris-HCl with and 5% (w/v) trehalose and 10 µL was dried in pads for >16 hours in a desiccating environment.

12.2.4.4 NaCl pads

In prototypes, salt for detection was stored dry in salt pads. A volume of 10 µL of 2.5 M NaCl was added to each salt pad, which were then flash-frozen in liquid nitrogen, and dried for 2h using a lyophilizer.

12.2.4.5 LF strips

In prototypes and manual assays, detection was performed on LF strips. The LF strips were striped (XYZ3050, BioDot, Irvine, CA) in ambient conditions (20-23°C, 40-60% RH is typical). The test lines were pDNA-T20 oligos striped at 400 µM in 50 mM TEAB at 0.3 µL/cm. The process control lines were T20-biotin oligos striped at 200 µM in 50 mM TEAB at 0.3 µL/cm. Striped LF strips were exposed to UV (~310 nm; TM-36 transilluminator, UVP, Upland, CA) for 7-8 min to cross-link the T20 to the LF strips.

12.2.5 MAD NAAT prototype assembly

Fluid introduction sub-assembly The fluid introduction sub-assembly was constructed from a syringe, with the barrel razor-cut to the 0.45-mL mark and the plunger razor-cut to be 2 mm longer; a female Luer-Slip to 1/32-in barb connector (Qosina, Ronkonkoma, NY); and Tygon tubing. The syringe was filled by pipette with 260 µL of 10 mM Tris-HCl (pH 8.0), with 100 µL dead volume. The syringe was then inserted into a connector with tubing attached.

12.2.5.1 Sample chamber sub-assembly

A sample chamber was fabricated from a syringe, which was razor-cut at both the 0.25 mL mark and halfway through the Luer-Slip fitting, then drilled with a 3/32-in hole at the 0.23-mL mark to accommodate the fluid introduction tubing. The sample chamber was mated to a silicone rubber tubing section using the modified Luer-Slip fitting. The tubing section was drawn through the lysis valve body and the valve was set with a graphene-wax block.

12.2.5.2 2DPN sub-assembly

The bottom of the 2DPN channels in the tray were lined with the aforementioned silicone adhesive inlays, onto which the porous material components were laid in order: amplification and detection dry reagent pads for each target, dry IAC sample delivery pad, dry salt pads, LF strips, amplification valve pads, and waste pads. After placement of these components, silicone adhesive overlay was used to seal the materials inside the tray. The wax valve was then pressed to make a full seal; pin-prick vent holes were created just upstream of the wax valve. A port block was bonded to the tray with silicone adhesive.

12.2.5.3 Housing and electronics sub-assembly

The housing of the device comprised three components: base, lid, and slide. A custom PCB control board was mounted to the housing base. The control board (Figure 72) contained an integrated microcontroller (ATmega328, Atmel, San Jose, CA) and wiring adapters for the lysis heater, lysis valve heater, amplification heater, and amplification valve heaters. The lysis heater was constructed from 9/32-in x 0.014-in aluminum tube stock (#8107, K & S Precision Metals, Chicago, IL) cut to a 12-mm length, wrapped in aluminum tape, instrumented with three thick film resistors (PWC2512-10RJI, Mouser Electronics, Mansfield, TX) and a thermistor (NB21N50104JBB, Mouser Electronics), and wrapped again in electrical tape. The lysis valve heater was made from a thick film resistor (PWC2512-10RJI, Mouser Electronics) wrapped in

Kapton tape (Dupont, Wilmington, DE) and was glued into the body of the lysis valve under the wax block zone.

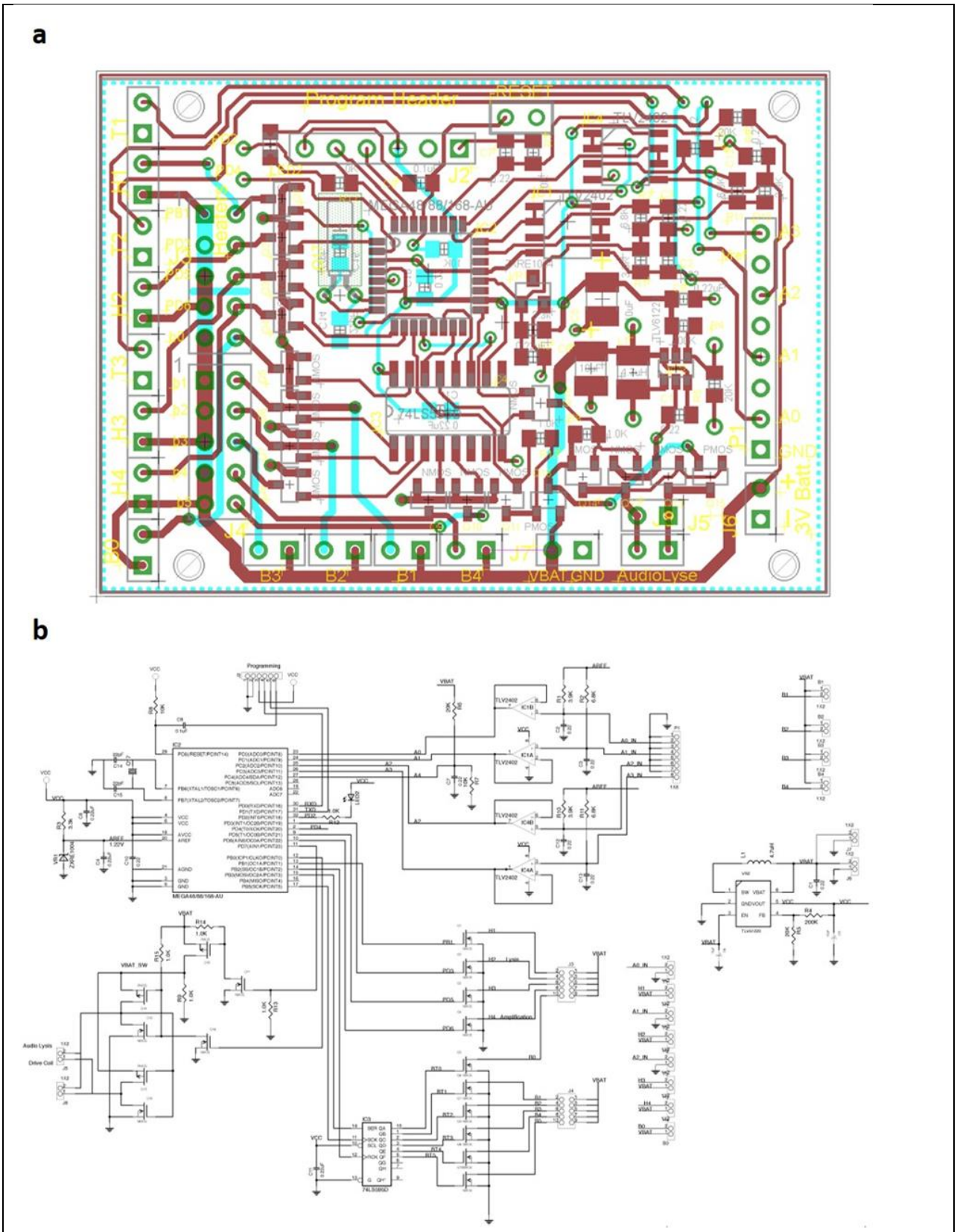

Figure 72: Control board design. (a) Layout for custom PCB. (b) Electronics schematic.

The amplification heater and amplification valve heaters were constructed from a custom PCB (Figure 73) and two more thick film resistors, respectively, aligned in the heater stage, all of which was wrapped in Kapton tape and mounted in the housing base. Two AA battery holders (BCAAPC-ND, Digikey, Thief River Falls, MN) were mounted in the housing base and connected in series to the control board, a contact switch (275-008, RadioShack, Fort Worth, TX), and a master slide switch (275-006, RadioShack).

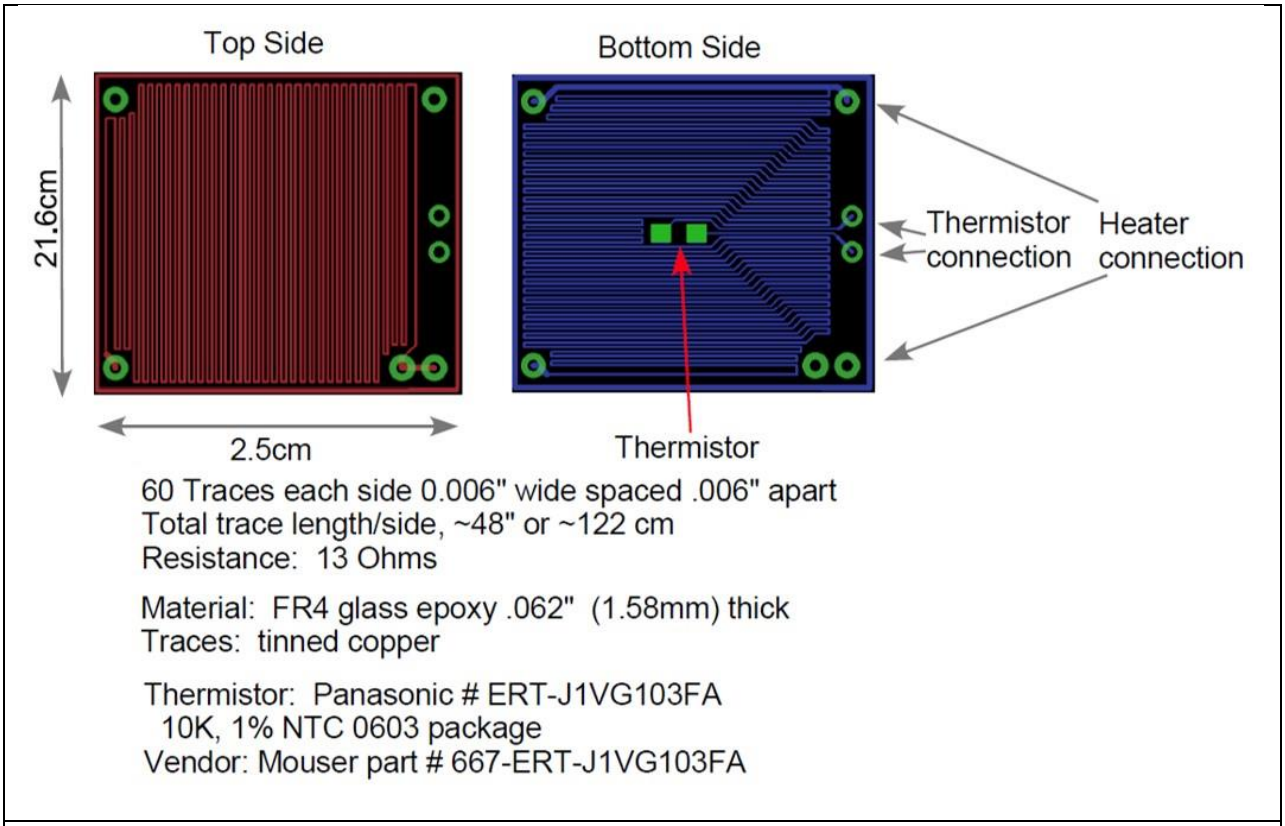

Figure 73: Amplification heater design.

12.2.5.4 Prototype device assembly

The fluid introduction sub-assembly and a swab port were clipped into the housing lid. The sample chamber was fitted with a lysis heater and the lysis sub-assembly was mated to the 2DPN sub-assembly by press-fitting the silicone rubber tubing below the lysis valve into the port block above the 2DPN. These two mated sub-assemblies were then snapped as one into the reusable

device sub-assembly. A polystyrene foam insulating insert was placed above the 2DPN and around the lysis heater before snapping the housing lid to the housing base. The housing slide was then mounted to the prototype to complete assembly.

12.2.6 Patient specimen tests

12.2.6.1 MAD NAAT prototype tests

For this version of our device, the volume of the sample chamber was fixed before the dilution factor from Amies buffer was determined. Therefore, patient specimens were diluted twice to achieve the target dilution of 1:100. First, a specimen was diluted from Amies buffer 1:8.6 by 10 mM Tris-HCl (pH 8.0). A polyurethane foam swab (Foamtec International, 19304613, Oceanside, CA) was immersed in the diluted specimen, rotated three times, and removed. The prototype was slid open to expose the swab port, with ~160 µL of 10 mM Tris-HCl (pH 8.0) forced into the sample chamber. The swab was inserted into the prototype, rotated ten times, and removed. These swabs transferred ~15 µL of sample when used as described[155], resulting in a sample input to the prototype with a total dilution of ~1:100. The prototype was closed to activate the test. Prototypes were run to completion (1 h), then disassembled and the 2DPN removed for imaging by scanner, which was used only as an assay development tool. An end-user would simply read the results at test completion, without disassembly.

12.2.6.2 Manual assays

ACP lysate was mixed with both IAC templates and allowed to flow into combined amplification and detection dry reagent pads placed in hybridization chambers (Electron Microscopy Sciences, Hatfield, PA). The chambers were sealed and incubated at ~50°C for 20 min. Following incubation, the reaction products were centrifuged at 2000 ×g for 1 min in a centrifugal filter

tube (0.22 µm Nylon centrifugal filters, VWR, Radnor, PA) and the resultant fluid was assessed via LF detection.

12.2.6.3 qPCR

Quantitative PCR (qPCR) for the *ldh1* and *mecA* genes was used as the reference method for estimating copy number from patient specimen samples. ACP lysate (1 µL) was quantified using the MRSA/SA ELITe MGB duplexed ldh1 and mecA qPCR assay. The input copy number estimate was calculated using the MAD NAAT prototype input volume (175 µL).

12.2.6.4 Image capture

All image capture was performed using a flatbed scanner (ScanMaker i900, MicroTek International, Cerritos, CA) in 48-bit-depth RGB mode at 600 dpi. Intensity profiles were generated for LF strips in both channels in each test using ImageJ 1.50g (NIH, Bethesda, MD). The green channel of each image was isolated, inverted, cropped to the detection zone, and straightened to the edges of the LF strips. Regions 50-pixels wide and 300-pixels long were overlaid at the longitudinal upstream end and lateral center of each LF strip in these transformed images, where the width dimension was chosen to eliminate edge effects and imperfect alignment and the length dimension was chosen to capture all four test lines and surrounding background. The average intensities across the width of each region were analyzed algorithmically using Mathematica 10.4 (Wolfram, Champaign, IL). Test lines were identified as local maxima in each intensity profile that survived a Gaussian blurring up to scale 6, had minimum sharpness 6, and had an intensity greater than 28% of the maximum. The background of each intensity profile was then estimated with a sixth-order polynomial fit to five background regions, the locations of which were fixed across all intensity profiles, and subtracted away. Background-subtracted intensity profiles were integrated within fixed-size regions, centered on

the local maxima, with values indicating the estimated relative intensity of the associated test line. The presence or absence of identified test lines within four signal regions, the location of which were fixed across all intensity profiles, indicated the results and the validity of each test. Occasional poor flow, depressions in the nitrocellulose that were introduced during their manufacture, and debris confounded this algorithm in eight cases. Occasional poor flow also contributed to a poor polynomial fit to the background, which resulted in some negative estimated intensity values.

12.3 Results

Our goal was to develop a rapid and accurate integrated diagnostic technology with a user experience that was as simple as a pregnancy test; the MAD NAAT prototype required only a single activation step. Results were reported as visible test and control lines that could be read by eye, or imaged with a cell phone camera for local processing or transmission to a remote location. The following results describe prototype development and subsequent repeated testing of four identical prototypes with samples from human nasal swab specimens.

12.3.1 Extremely simple user experience

The complete user experience for the MAD NAAT prototype comprised sample collection and introduction, test activation, and reading the result. Activation of the MAD NAAT prototype was a single, simple user step: sliding the housing closed (Figure 74). All other assay operations were automated.

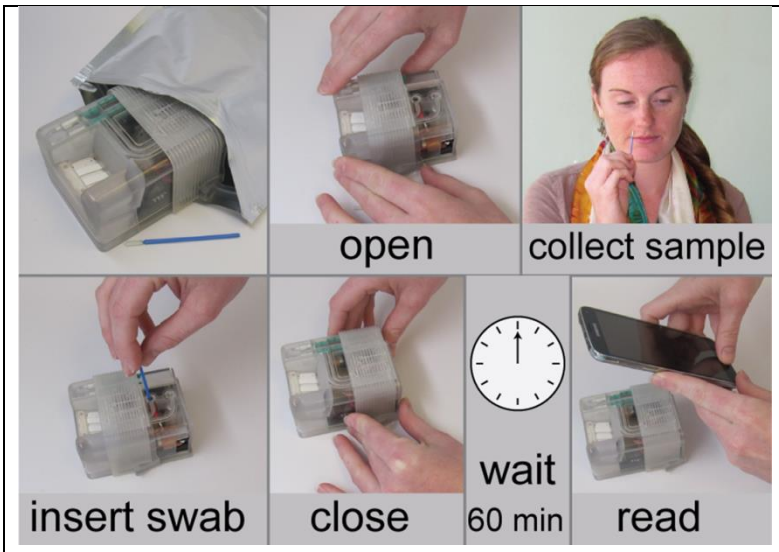

Figure 74: The MAD NAAT user experience: user steps required to operate the MAD NAAT prototype from upper left to lower right. The sample collection may be performed by the user or a healthcare provider, depending on the setting. Device closure is the single activation step required; all other assay steps are internal and automated. Results can be interpreted by eye or recorded and quantitatively analyzed with a cell phone camera.

12.3.2 Assay operations

NAATs contain three fundamental assay operations: 1) sample processing, 2) amplification, and 3) detection, all of which were automated in the MAD NAAT prototype (Figure 75). Reagents for these operations were stored dry and ready to use inside the device.

This first MAD NAAT prototype demonstration was performed on samples from human nasal swab specimens. A sample was collected with a swab and introduced to an open device by inserting the swab into a sample chamber containing buffer. Sample introduction was over 80% efficient (percentage of bacteria transferred from swab to sample chamber) for the swabs used, as measured using prepared samples in buffer and in simulated nasal matrix[155]. Sample processing was performed by incubating with an achromopeptidase (ACP) enzyme mixture for bacterial lysis, followed by heating for deactivation of enzymes incompatible with amplification (e.g. proteinases) and for bacterial gDNA fragmentation. ACP lysis followed by heating was previously found as effective as bead beating for release of amplifiable DNA from *S. aureus*[176] and other bacteria[265]. In addition, there was no statistical difference between the lysis performance of freshly prepared and dried ACP after 11 months of storage at ~23°C and

ambient humidity (106 ± 1.6% recovery of amplifiable DNA compared to freshly prepared, p = 0.26 [265]).

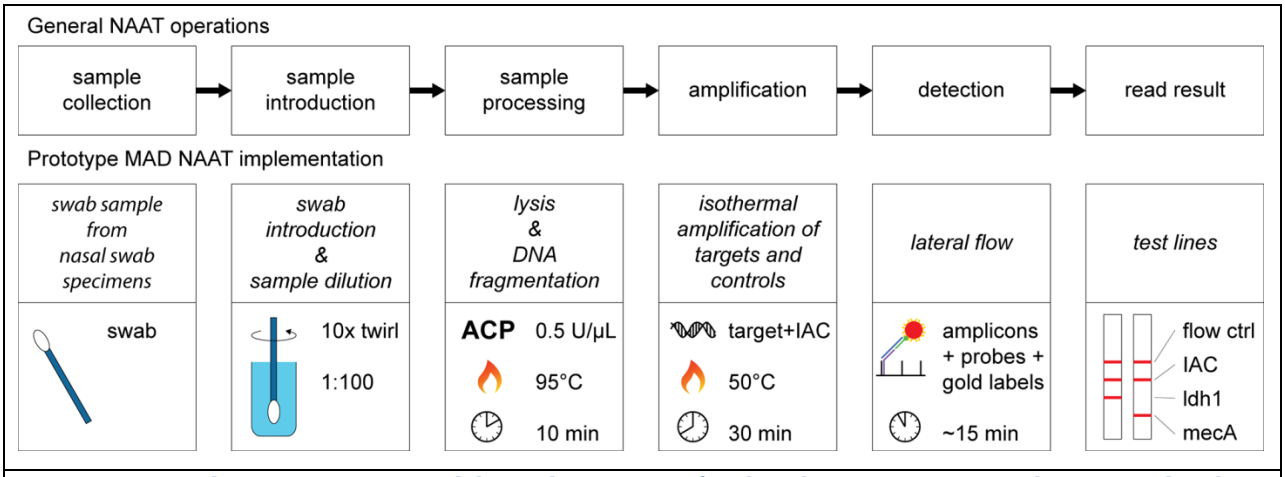

Figure 75: General NAAT operations and the implementation of each in the MAD NAAT. Swabs were used as the sample input for this prototype, which was tested with samples of human nasal swab specimens. The timing (and temperature where required) of each operation was chosen to maximize unit operation efficiency. Sample processing time (10 min) included heater warm-up and >5 min at 95°C for enzyme deactivation and DNA fragmentation. Amplification time (30 min) also included heater warm-up. Detection time was as fast as five minutes, but test line images were always captured after a total test time of 60 minutes.

We chose to develop MAD NAAT around isothermal strand displacement amplification (iSDA), a truly-isothermal method (no initial denaturation step) and one of the fastest isothermal amplification methods available (~$10^{10\text{-}12}$ fold from 10 target copies in ~10-30 minutes). In iSDA, amplification initiates by primer insertion during DNA "breathing," then proceeds to exponential amplification by repeated nicking, extension, and displacement of single strands[160]. The rules governing design and optimization of new iSDA assays is similar to that for strand displacement amplification (SDA), which is well-described in the literature[266]. The sequences for the *ldh1* and *mecA* primers and probes are provided in Table 9. We have found that combining iSDA with LF detection under ideal conditions can lead to sensitivity of <10 copies of target (Figure 76) and specificity against similar organisms (Figure 77).

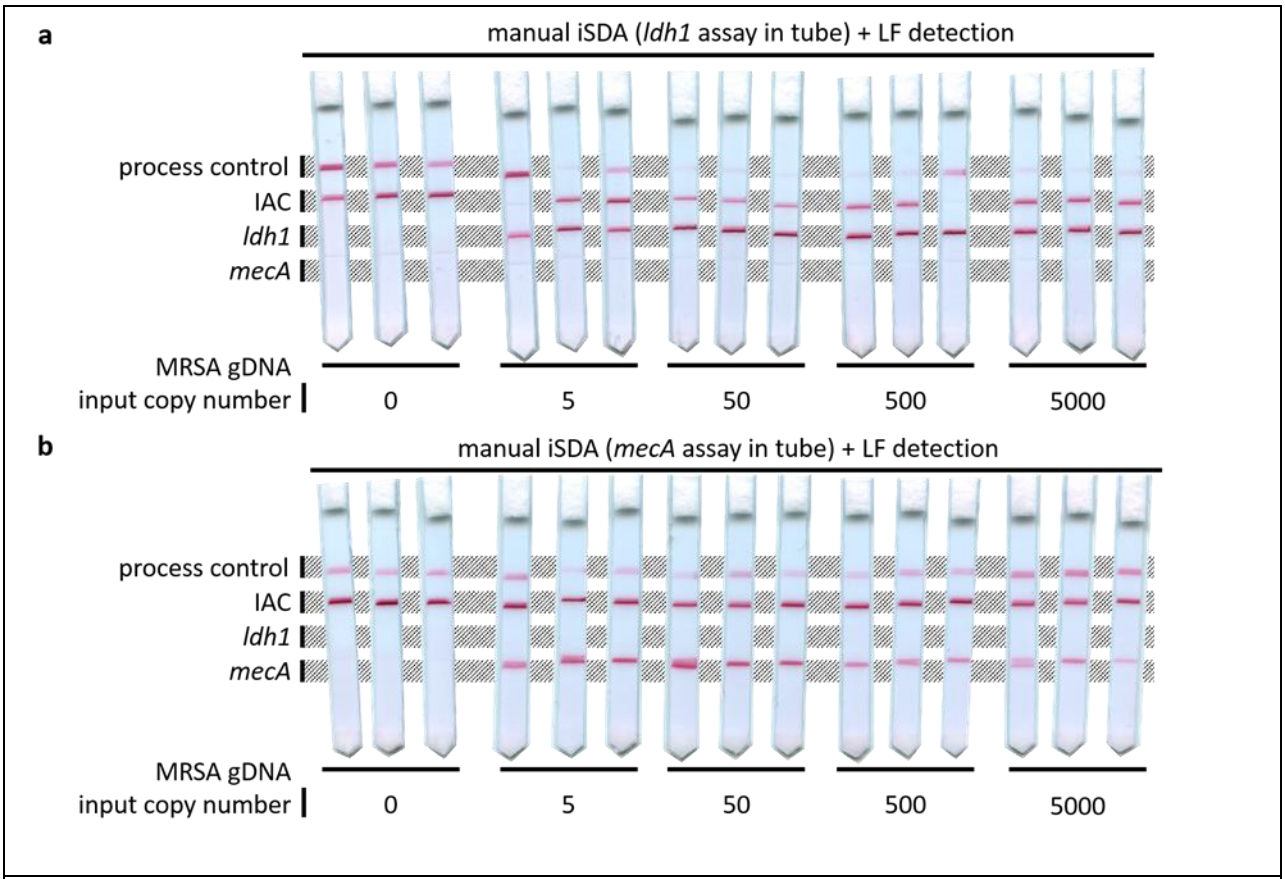

Figure 76: Manual iSDA and LF detection result for (a) ldh1 and (b) mecA assays at low copy numbers of MRSA genomic DNA (gDNA) template. Amplifications were performed in tubes. The results were mixed to salt and Tween-20 to final concentrations of 600 mM and 1% w/v, respectively, then allowed to flow on LF strips. The assay showed robust detection down to at least five copies.

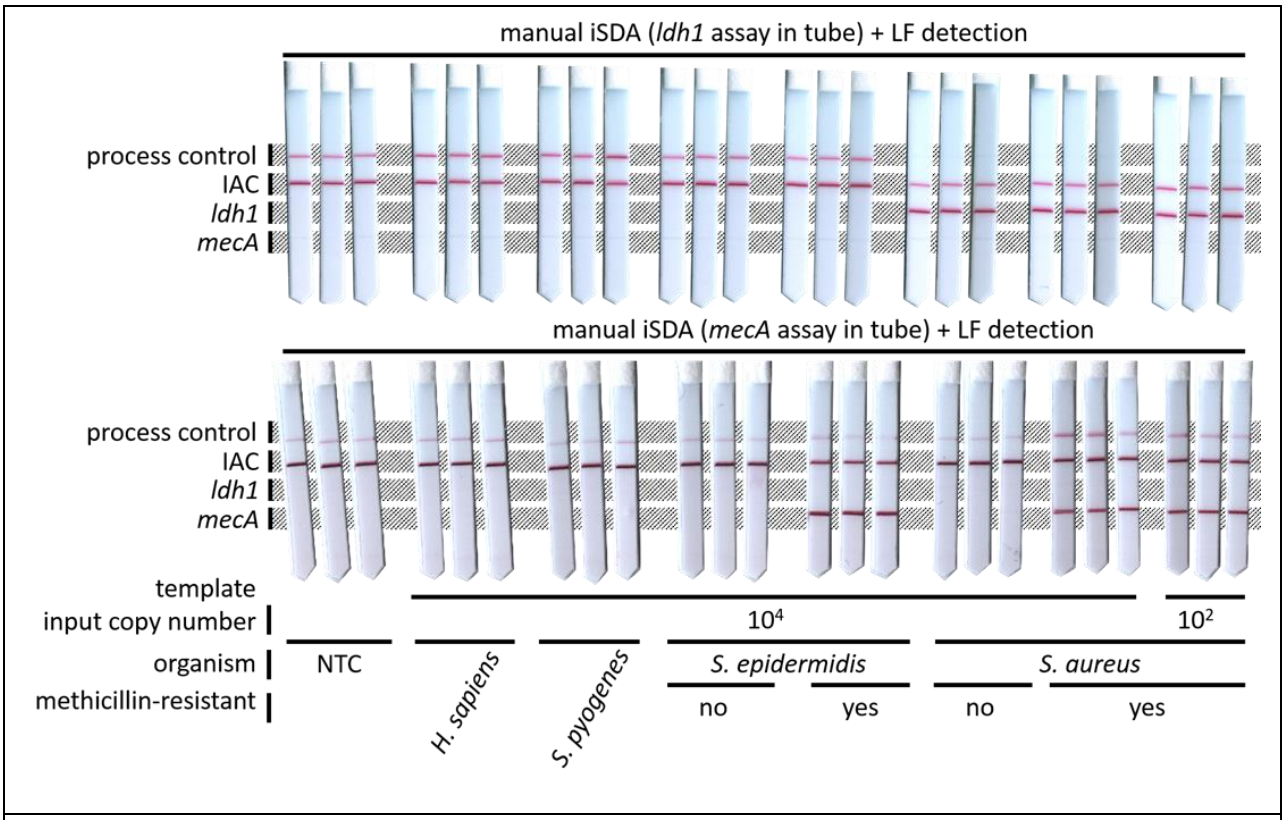

Figure 77: Manual iSDA and LF detection result for (a) *ldh1* and (b) *mecA* assays using no template (NTC); and 104 copies of human, *S. pyogenes*, methicillin-sensitive *S. epidermidis* (MSSE), methicillin-resistant *S. epidermidis* (MRSE), methicillin-sensitive *S. aureus* (MSSA), and methicillin-resistant *S. aureus* (MRSA) gDNA templates (left-to-right). Amplifications were performed in tubes. The results were mixed with salt and Tween-20 in PBS to final concentrations of 600 mM and 1% w/v, respectively, then allowed to flow on LF strips. The strips shown are the last each of a set of two *ldh1* and six *mecA* experiments. The previous experiments showed low-level signal on all nominally negative test lines, including in the NTC condition, and occasional IAC drop-outs in negative tests, which indicated invalid results. These errors were eliminated through use of new stocks of gold nanoparticles and IAC template, respectively. Across the 120 nominally negative conditions tested in the entire set of eight experiments, one NTC and one *S. pyogenes* template yielded a strong false positive, which may be indicative of contamination from five years of running these amplification assays in a single laboratory and open handling of amplicons for lateral flow detection and gel analysis.

LF detection used two probes as shown in Toley et al.[160]: one DNA probe with a triethyleneglycol linker and terminal biotin group to allow labeling by streptavidin-conjugated gold nanoparticles, and one chimeric DNA-pDNA probe to allow binding to complementary pDNA immobilized on the detection strip. The lyophilized, combined reagents for amplification and detection were shown to be stable for at least six weeks at ~23°C, and at least 15 days at

40°C, at 2-3% relative humidity (Figure 78). We have since demonstrated stability for longer times at elevated temperatures with similar stabilizers (S.K. manuscript in preparation). However, hybridization between complementary pDNAs required additional salt relative to iSDA to maintain test sensitivity over a range of ambient temperatures (Figure 79).

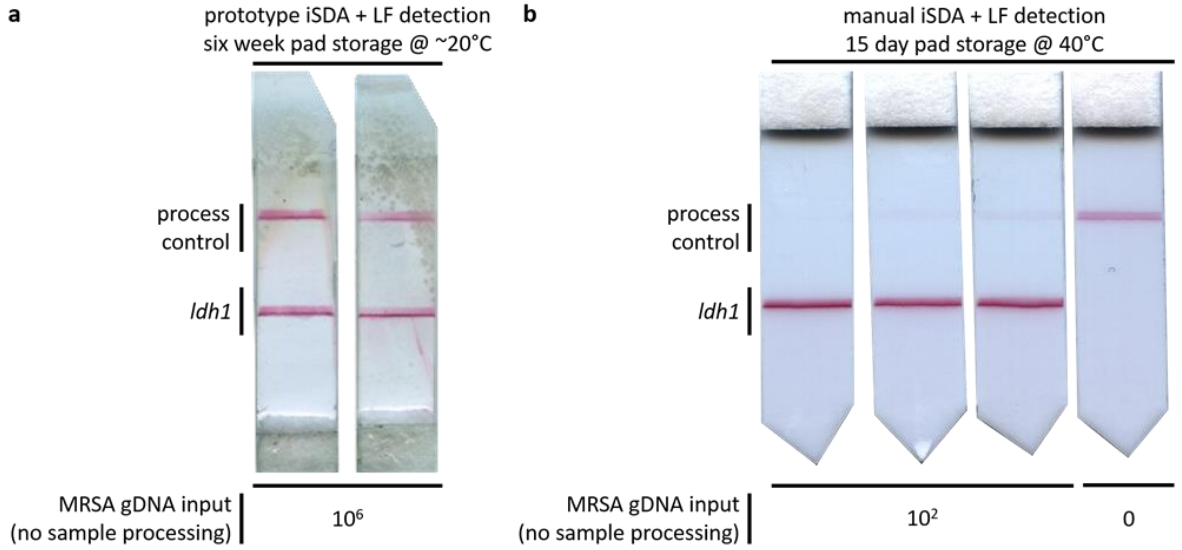

Figure 78: Detection results excerpted from dry storage study. (**a**) Prototype iSDA and LF detection on MRSA genomic DNA input using pads stored for six weeks at laboratory ambient temperature in desiccated conditions. Duplicate tests confirm dry reagent viability in these conditions through ldh1 amplification and detection functionality. (**b**) Manual assay tests on low input copy number MRSA genomic DNA using pads stored for 15 days at 40°C in desiccated conditions. Triplicate tests confirm dry reagent viability in these conditions through ldh1 amplification and detection functionality. Associated negative control indicates no contamination.

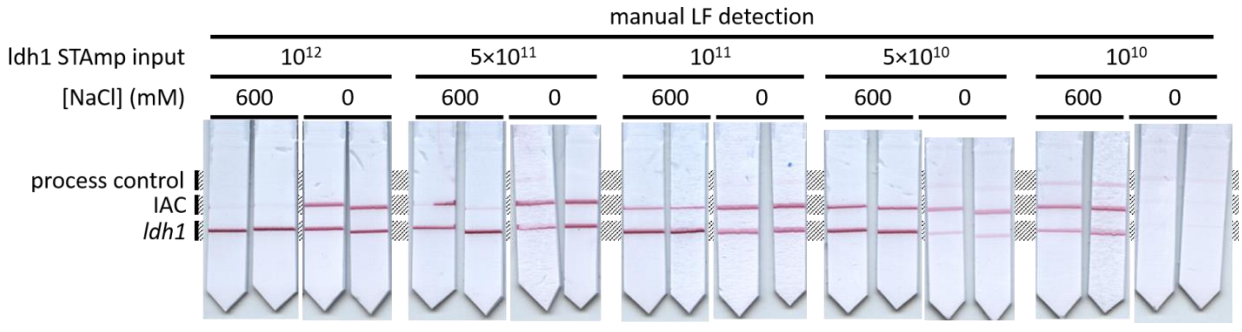

Figure 79: Detection results showing impact of salt condition on pDNA binding at ~20°C. A synthetic truncated amplicon (STAmp), which replicated the binding region of the amplicon output by the ldh1 iSDA reaction, was mixed with detection reagents with and without 600 mM NaCl, and allowed to flow on LF strips. Limit of detection was worse in the no-salt condition.

12.3.3 Internal fluid path

System operations were automated by creating a fluid path that managed sample introduction, sample processing, dry reagent reconstitution, multiplexing by routing to multiple isothermal amplification zones, amplification itself, and LF detection (Figure 81). Sample introduction and processing occurred in a sample chamber, which output lysate to a 2DPN after a valve operation. The 2DPN split the lysate and sequentially reconstituted internal amplification control (IAC) templates and dry master mixes (including primers, probes, and detection labels) into the lysate during flow into physically biplexed amplification zones. While chemical multiplexing (amplifying multiple targets in a single reaction) increases the complexity of assay development and typically decreases sensitivity of each target, physical multiplexing avoids these problems and allows for the amplification of both DNA and RNA targets on a single device (ESI Fig. S7[247]). After amplification, a second valve operation released both amplified lysate solutions, and the 2DPN reconstituted salt into them during flow into the detection zones.

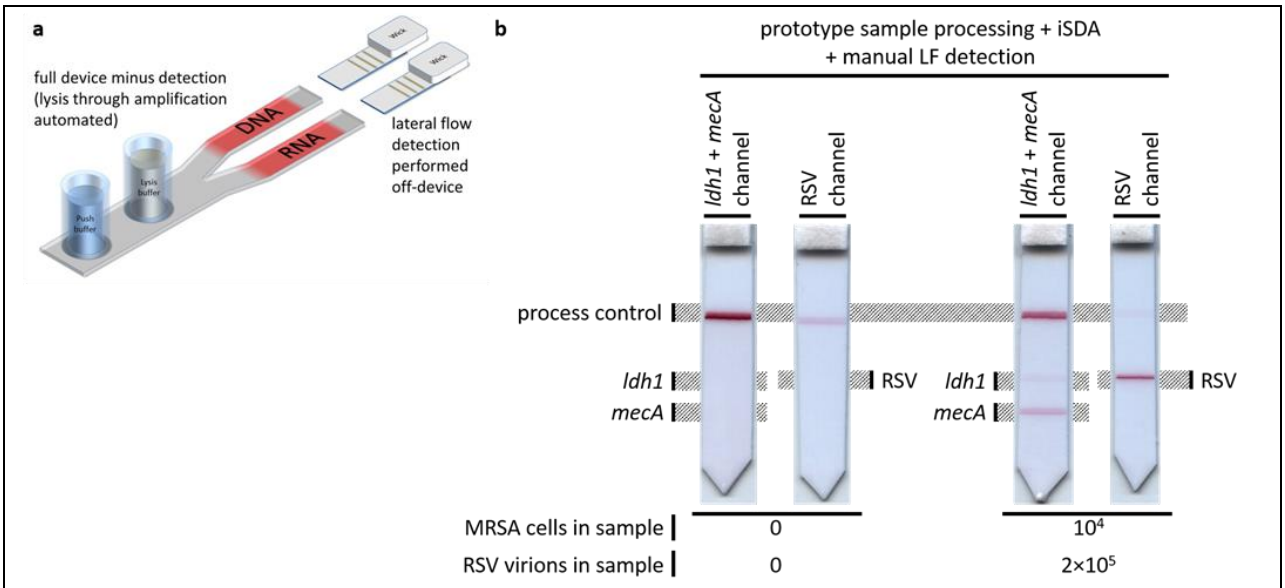

Figure 80: DNA and RNA detection in partial prototype test. (**a**) Cartoon of experimental setup. Sample introduction and processing, and amplification were performed on a prototype device. Amplification pads were then removed from the 2DPN and centrifuged at 10,000 ×g for 3 minutes. The resulting fluid was mixed to salt and Tween-20 to final concentrations of 600 mM and 1% w/v, respectively, then allowed to flow on LF strips. (**b**) Results show clean negatives, and positive amplification.

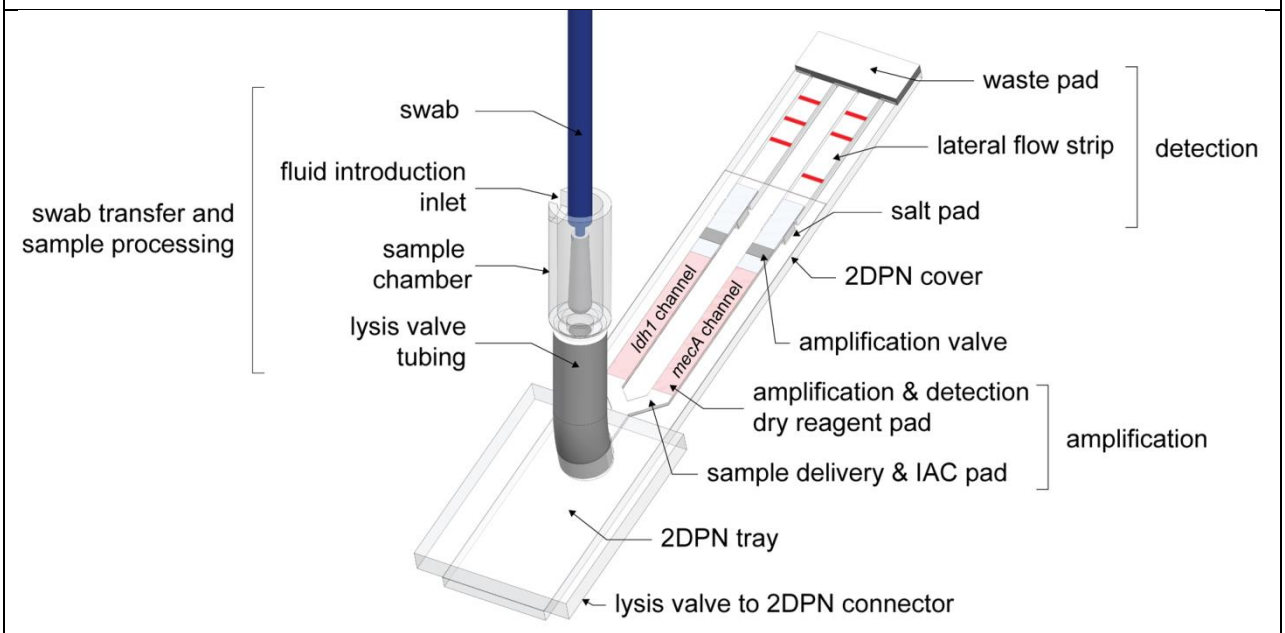

Figure 81: Fluid flow path of prototype. Sample introduction and processing are performed in a sample chamber. Processed sample is delivered by an automated valve (not shown) to a two-dimensional paper network (2DPN), where it is split into two physical channels (more channels are possible). Isothermal amplification and lateral flow (LF) detection with gold nanoparticles are also performed in the 2DPN. The LF strips are left uncovered to facilitate flash photography.

Each LF strip was striped with four capture lines. The target lines, one each for ldh1 and mecA, confirmed the presence in a sample of their respective targets and at sufficient concentrations. The IAC line confirmed that amplification of nucleic acids did occur in each channel and that the detection reagents rehydrated and flowed through the LF strip (independent of the presence of target lines). The process control line, which bound gold nanoparticles, confirmed that reagents were rehydrated and flowed to the end of the 2DPN. Note that a valid test result requires proof of amplification, i.e. either a test line, IAC line, or both in each LF strip.

12.3.4 Complete MAD NAAT prototype

The MAD NAAT system will ultimately be produced in the form of single-use disposables, but for prototype development we integrated single-use and reusable components. Using 3D-printed materials and inexpensive, microcontroller-based electronics enabled rapid prototyping of device components and programmable control over assay timing and temperatures. The prototype used feedback-controlled heaters at 95°C for sample processing and at 50°C for amplification, and open-loop heaters for valve actuation. While future prototypes will use lower cost components, such as an injection-molded housing, and will be fully disposable, in the current prototype any components that were single-use or could not be safely re-used (due to contamination from the sample or amplification products), such as fluid introduction parts, sample chamber, and 2DPN, were used once, then disposed (Figure 82A). All other supporting components, including the housing (Figure 82B) and electronics, heaters, and mechanical valve parts (Figure 82C) were reused. Two AA batteries powered the prototype.

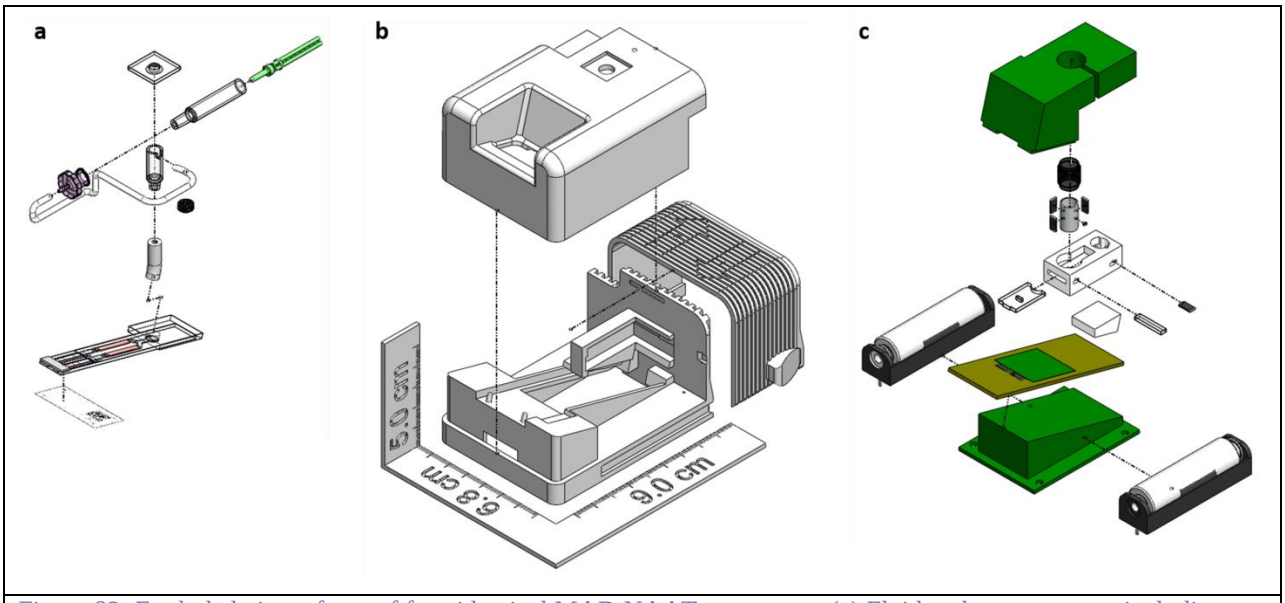

Figure 82: Exploded view of one of four identical MAD NAAT prototypes. (a) Fluid path components, including fluid storage and introduction syringe, sample chamber, and 2DPN. (b) Housing components: base, lid, and slider. (c) Supporting components, including electronics, valves, batteries, and insulation.

Autonomous operation required, in addition to dry reagents, on-device storage of a buffer, which was implemented with a syringe-based system. Opening the housing slider (Figure 82B) drove the plunger of the syringe, which delivered stored buffer through tubing containing dry lysis reagents into the sample chamber (Figure 82A). Closing the slider triggered a switch that activated the automated assay steps, after which no further user input was required.

Two styles of valves were developed for this system: a lysis valve that controlled flow from the sample chamber into the 2DPN and amplification valves that controlled flow from the amplification zones into the detection zones. Both valves used wax to create seals, and melting of that wax to release the seal. The sample chamber was connected to the 2DPN with flexible tubing pinched closed by a wax block. After the timed lysis step, a heater melted the wax, which released the pinch on the tube and delivered lysate to the 2DPN. The amplification valves were wax plugs pressed directly into the fluid pathway. After the timed amplification step, heaters melted the wax, allowing fluid to advance to the detection zone.

12.3.5 Sample-to-result demonstration with human nasal swab specimens

Prototype devices were tested using samples of discarded human nasal swab specimens from pre-surgical patients screened for MRSA colonization. Three types of tests were run to detect the presence of ldh1 or mecA gene targets in patient specimens (PS1, 2, etc.): the MAD NAAT prototype (e.g. Figure 84A), a manual analogue of the automated assay (e.g. Figure 84B), and qPCR. LF strips were used from the prototype and the manual assay, while the qPCR results were used to generate input copy number estimates based on a standard curve of gDNA from MRSA (Table 10, Figure 83).

Table 10: Testing of nasal swab specimens from 11 de-identified patients. Samples from nasal specimens were used as inputs to prototype devices, manual assays from the same dry amplification and detection reagents, and qPCR assays. The qPCR assays were used to estimate the copy number input to the MAD NAAT prototype in each sample. ND denotes a target was not detected by qPCR. Boxes with multiple results indicate replicates. Green and red boxes show agreement and disagreement, respectively, between iSDA results and qPCR. Positive detection of a gene target in any qPCR replicate meant all corresponding iSDA results needed to be positive for agreement. The lowest input level detected by the MAD NAAT system was ~3×103 (mecA from PS 4).

	ldh1				*mecA*		
Patient Sample #	**MAD NAAT prototype**	**manual assay**	**qPCR, genomic copies into MAD NAAT**		**MAD NAAT prototype**	**manual assay**	**qPCR, genomic copies into MAD NAAT**
PS 3	-	-	ND		-	-	ND
PS 2	-/-	-/-/+	ND / ND / 2×10^3		-/-	-/+/+	ND / 7×10^2 / 2×10^3
PS 4	+/-	-/-	ND / ND		+/+	+/+	3×10^3 / 1×10^4
PS 20	+	+/+/-	1×10^4 / ND / 5×10^3		-	+/+/+	1×10^4 / ND / ND
PS 17	-/-	-	ND		+/+	+	5×10^3
PS 14	-	-	2×10^3		+	+	1×10^5
PS 8	+	+	7×10^5		+	+	7×10^3
PS 1	+/+	+	5×10^5		+/+	+	6×10^5
PS 11	+	+	4×10^5		+	+	4×10^5
PS 29	+/+/+/+	+	2×10^6		+/+/+/+	+	1×10^6
PS 15	+	+	2×10^6		+	+	2×10^6

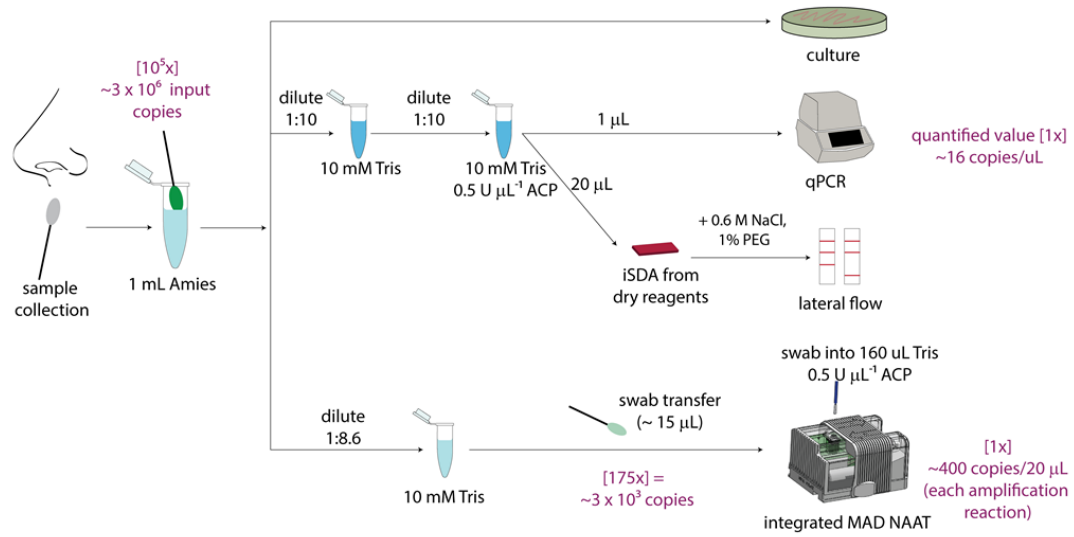

Figure 83: Illustration of methods for each patient specimen test. Green text tracks the calculations of estimated copy sensitivity. The ~16 copies uL-1 was quantified by qPCR for the lowest input where qPCR found target (PS4, mecA) and MAD NAAT showed this sample positive by LF detection. The MAD NAAT prototype held an input volume of 160 µL on-device buffer plus ~15 µL sample, and an amplification zone volume of 20 µL. That corresponded to a minimum detected value of ~3×103 input copies in the MAD NAAT prototype.

During testing, manual assays were performed with freshly prepared ACP, IAC template, and salt, but dry amplification and detection reagents, while prototypes contained all dry reagents. Although the prototype detected as few as 3×10^3 input genomic copies (PS4), complete agreement between data occurred for patient specimens with 7×10^5 genomic copies of *ldh1* (PS8) or above and with 5×10^3 genomic copies of *mecA* (PS17) or above. We therefore estimated the sensitivity of the MAD NAAT prototype to be about 5×10^3 input genomic copies, which corresponded to detection from ~600 genomic copies in each amplification reaction.

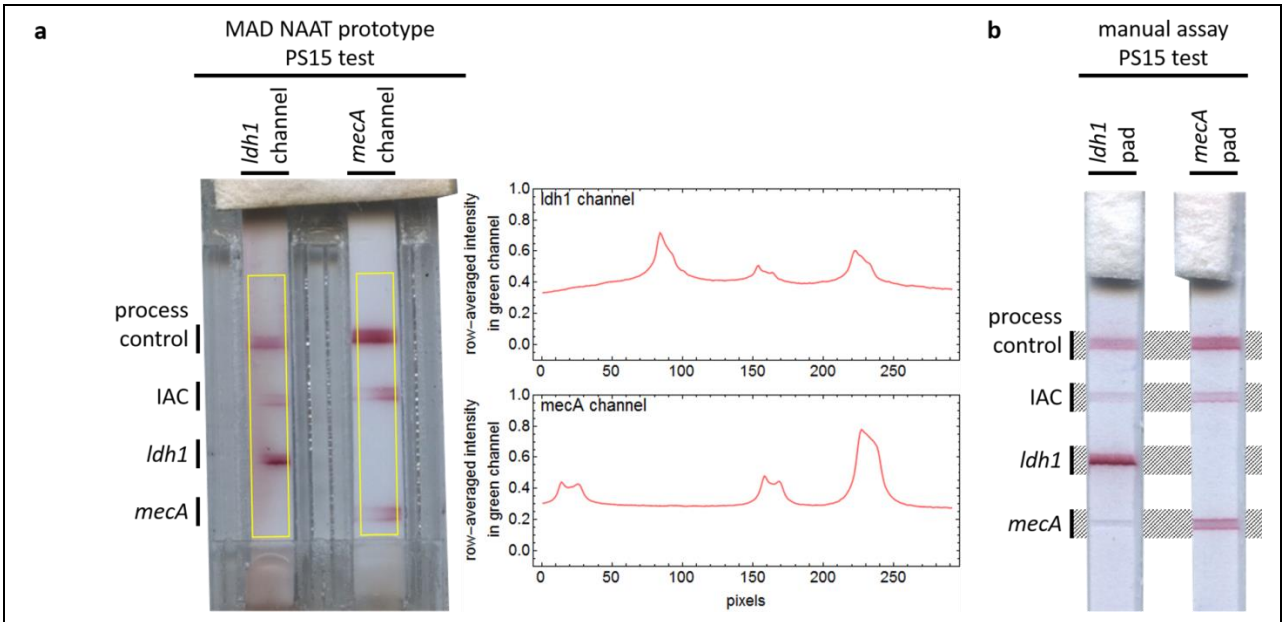

Figure 84: LF strip data for tests on a sample from PS 15, which was positive for MRSA. LF strips were 2.5 mm wide with four test lines spaced 3 mm apart. (a) MAD NAAT prototype test. Two channels amplified and detected *ldh1* with IAC (left) and *mecA* with IAC (right). Image analysis was conducted using regions of fixed size (yellow rectangles) to generate plot profiles for each channel. Non-uniform test lines and higher background in the prototype results are an artifact of valve operation, but they do not interfere with interpretation by eye or image analysis. (b) Manual assay test, which confirms results of MAD NAAT prototype test. Note that the left LF strip in the manual assay results shows a grey coloration, distinct from the red color of bound gold nanoparticles. It is a physical depression left during the striping process, not non-specific binding, and is not present in most of the strips.

In total, 33 integrated test runs were performed. Four tests did not run completely due to hardware failures unrelated to the chemical functions of the device operation (e.g. hand-soldered wire connections breaking due to wear from repeated use). Eleven other tests ran completely, but did not yield valid results due to under heating or overheating (e.g. lysis or amplification was

hindered, lysis or amplification valves did not operate properly), or poor flow conditions (e.g. evaporation from uncovered LF strips at a wetting front with high concentration of solute). These tests were ruled invalid due to missing both target and IAC lines on at least one LF strip. The ratio of valid to total completed (no hardware failure) tests yielded a success rate of 62%.

12.4 Discussion

We have demonstrated the first autonomous integrated sample-to-result NAAT system for the detection of bacteria from nasal swab samples designed to be fabricated as a complete disposable. While the prototype was not yet ready for full clinical trials, these initial results suggest that, with manufacturing refinement, MAD NAAT could be of great clinical value. The one-step activation of the autonomous MAD NAAT system combines the ease-of-use of many widely available point-of-care tests with the increased sensitivity and specificity of nucleic acid amplification. The dry reagents storage supports elimination of cold chain requirements during shipping or storage. Furthermore, the use of non-toxic materials and chemistries ensure user safety in a variety of conditions. These features make the MAD NAAT system well-suited for use in developed world settings as well as developing world LRS.

Other features of MAD NAAT demonstrate its utility as a diagnostic platform. For example, higher-order multiplexing could be implemented through additional amplification channels. Splitting the sample into more channels reduces the copy number of targets in each amplification reaction, but even a 10-fold split would still leave the copy number of targets far above the LOD of the system for many clinical targets. Additionally, the ACP lysis method is broadly applicable to many pathogen types and it works directly with iSDA.

The MAD NAAT prototype consistently detected bacterial inputs at a minimum of ~5×10^3 genomic copies and above, and the majority of the samples tested showed strong agreement between the MAD NAAT prototype and qPCR. Each of the biplexed amplification zones had an estimated sensitivity of ~600 genomic copies, and the estimated copy sensitivity from the original patient specimens was ~5×10^6 MRSA genomic copies. A wide clinical range for MRSA has been reported, with one study of 444 swab specimens yielding 3-1.5×10^7 CFU per swab with a geometric mean of 794 CFU per swab[267]. The estimated device sensitivity of ~5×10^6 genomic copies per swab do fall at the high end of that range, but the estimated amplification sensitivity of ~600 genomic copies falls below the clinically found geometric mean.

The human nasal swab specimens used for testing were all discarded clinical specimens that were stored in a high-salt buffer that inhibits ACP lysis[268], iSDA, and PCR. This collection artifact made the specimens incompatible with the MAD NAAT prototype, which was designed as a direct, sample-in device. Additional dilution was required to create a sample compatible with ACP lysis and iSDA, and to mitigate the effects of interferents from the human nasal specimens on amplification; this forced dilution step negatively impacted the sensitivity of our tests. However, our tests were largely successful anyway due to the abundance of MRSA in our positive specimens, for which our qPCR results indicate there were at least 10^6 genomic copies per original swab (prior to dilution).

Nonetheless, we are also developing new interferent depletion and target concentration mechanisms[159], anticipating their utility for other targets. Future patient specimen characterization on direct patient-to-device samples is expected to yield a better system sensitivity.

MRSA was a challenging first clinical target for demonstrating MAD NAAT, although it is a critically important target, particularly at the point-of-care. We chose MRSA because it posed two challenges: processing of a difficult-to-lyse, Gram-positive bacterium[269], [270] and incorporating detection of multiple targets. Although most commercial NAATs use a single target—the *SCCmec-orfX* junction—their specificity is decreased by *SCCmec* variants (false-negatives) and strains that have lost *mecA* but retain the *SCC-mec* flanking sequences (false-positives). The MAD NAAT prototype mirrored the approach of a commercial NAAT (MRSA/SA Elite MGB® Kit; ELITech Molecular Diagnostics, Puteaux, France) that instead measures the ratiometric quantity of *ldh1* to *mecA* gene targets. This approach has two advantages: high sensitivity due to the highly conserved sequence of ldh1, which is specific for clinical *S. aureus* isolates, and high specificity for MRSA over other *mecA*-containing species, due to the ability to measure equal quantities (within tolerance) of *ldh1* and *mecA*, indicating both genes were found in a single organism. The MAD NAAT prototype did not measure the ratiometric quantity of *ldh1* to *mecA*, which reduced test specificity but not sensitivity. The false-positive rate can be estimated by the co-colonization rate of methicillin-susceptible *S. aureus* (*ldh1* positive, *mecA* negative) with methicillin-resistant coagulase-negative *staphylococc*i (*ldh1* negative, *mecA* positive), which has been measured in nasal specimens at 3.4%[271].

This manuscript reports an important milestone in LRS NAAT technology: the first demonstration of a fully integrated, simple-to-use NAAT device, which detected two MRSA-related gene targets directly from samples of human patient swab specimens after a single activation step. Nonetheless, the MAD NAAT system is capable of more. Ongoing design improvements aim to 1) enhance reliability, sensitivity, and multiplexing; 2) reduce the time from sample introduction to results to ~30 minutes by amplification reaction optimization, dry

reagent reformulation, detection improvements, valve simplifications, and shorter heat-up times; 3) improve reproducibility of signal generation by reducing evaporation from LF strips; and 4) reduce part count and cost-per-device with a focus on manufacturability and marketability. In collaboration with Seattle-based non-profit PATH, we are also developing an electronics-free version of MAD NAAT with paper timing, fluidic valve actuation, and demonstrated chemical heaters[126], which combine to result in a device that is easily disposed, including through burning.

12.5 Acknowledgements

This work was supported by a generous grant from DARPA DSO/BTO--HR0011-11-2-0007, awarded to Dr. Paul Yager at the University of Washington. Subcontracts were awarded to Dr. Barry Lutz of UW Bioengineering, Dr. Janet Englund at Seattle Children's, Dr. Ferric Fang at UW Laboratory Medicine, Dr. David Moore at GE Global Research Center, Dr. Walt Mahoney at ELITechGroup, and Dr. Bernhard Weigl at PATH. All teams contributed materially to the concepts behind the design presented. Particular thanks are owed to Joel Atwood for manufacture of many parts, Mike Purfield for test and manufacture support, Lillian Mireles for patient sample test support, Dr. Fang for discarded nasal swab specimens from MRSA-screened patients, and to PATH for development of the graphene-impregnated wax.

13 Appendix: One-step purification and concentration of DNA in porous membranes for point-of-care applications

S. A. Byrnes, J. D. Bishop, L. Lafleur, J. R. Buser, B. Lutz, and P. Yager

This Appendix section is taken in a largely unmodified form from the manuscript[159]. I would like to thank primary author Samantha Byrnes and my other coauthors for involving me with the project.

13.1 Abstract

The emergence of rapid, user-friendly, point-of-care (POC) diagnostic systems is paving the way for better disease diagnosis and control. Lately, there has been a strong emphasis on developing molecular-based diagnostics due to their potential for greatly increased sensitivity and specificity. One of the most critical steps in developing practical diagnostic systems is the ability to perform sample preparation, especially the purification of nucleic acids (NA), at the POC. As such, we have developed a simple-to-use, inexpensive, and disposable sample preparation system for in-membrane purification and concentration of NAs. This system couples lateral flow in a porous membrane with chitosan, a linear polysaccharide that captures NAs via anion exchange chromatography. The system can also substantially concentrate the NAs. The combination of these capabilities can be used on a wide range of sample types, which are prepared for use in downstream processes, such as qPCR, without further purification.

13.2 Introduction

According to the WHO, the types of diagnostics used around the world have been shifting from traditional laboratory-based tests, such as ELISA and qPCR, to rapid test formats; the aim is to deliver diagnosis at the point-of-care (POC). From 1999 to 2009, the proportion of HIV rapid tests procured globally increased from ~35% to over 80%[272]. This trend reached a peak in 2007 with over 95% of procurements being of the rapid test variety[272]. Although this trend is encouraging, there is still a gap in the availability of accurate diagnostics for the POC.

According to the 2010 Global Burden of Disease study, four of the top ten causes of death world-wide are attributed to communicable diseases, which disproportionally affect low resource settings (LRS)[13], [190], [191]. Of these top ten, number four is lower respiratory infections and seven is diarrhea[13], [190], [191]. Each of these conditions can be caused by multiple pathogens; without a proper diagnosis, accurate treatment cannot be provided. In developed settings, these diagnoses are often performed through nucleic acid (NA) detection. The use of NA for disease diagnosis offers multiple advantages including increased sensitivity, the ability to multiplex, and epidemiological tracking of disease transmission and drift via NA sequencing. These approaches, however, are not available at the POC because they often rely on sample pre-treatment techniques that require expensive equipment and highly trained personnel.

Common methods of DNA purification used in both laboratory settings and tests designed for the POC often rely on one of three general mechanisms: solid-phase extraction, electrostatic interactions, or sequence-specific capture. One of the most widely used techniques is solid-phase extraction (SPE) with silica particles. Pioneering work by Boom *et al.* demonstrated a “rapid and simple” method for nucleic acid

purification using chaotropic agents, ethanol, and an acidic silica slurry. Their method cited a total assay time of less than one hour for greater than 50% recovery of DNA[273]. The current gold standard Qiagen kit utilizes a similar technique with silica particles embedded in a centrifugal filter for NA isolation from complex samples. Other common laboratory techniques rely on NA precipitation in the presence of solutions with high alcohol content[274]. Although these traditional methods are well characterized and reliable, they often require expensive laboratory equipment and highly trained laboratory technicians, limiting their availability in the developed and developing world to centralized facilities and hospitals.

Over the last 20 years, the field of microfluidics has aimed to address and overcome the gap between laboratory capabilities and POC systems through the development of single-use, plastic microfluidic chips[275]. There have been numerous publications about the wide range of applications for these chips including cell lysis and NA purification[215], [276], sample concentration[277], immunoassays[278]–[280], and NA amplification[281], [282]. Gubala *et al.* extensively reviewed many of these pioneering applications[9].

In the microchip format, NA purification for the POC often adapts techniques from traditional laboratory methods. For example, multiple groups have published on the use of SPE membranes in microfluidic devices[283]–[286]. The Klapperich group embedded silica particles in a porous polymer monolith (PPM) within microfluidic channels to combine DNA purification from complex samples with on-chip PCR[287]–[289]. The Bau group designed a sample-to-answer polycarbonate cassette with on-chip reagent storage for NA isolation using a silica membrane[290]. There has also been initial work

published on the use of sequence-specific capture for isolating NA targets in microfluidic chips[291], [292].

Another widely used technique for DNA purification in microfluidic devices exploits the negative charge of DNA molecules; DNA can associate with coated magnetic beads[293], [294], cationic polymers[295]–[297] or resins[298], and can be separated through electrophoretic methods[108], [228], [299]. The Landers group utilized chitosan, a cationic polymer, to selectively isolate NAs in a microchip from complex solutions[300]–[303]. Chitosan is a linear polymer comprised of linked sugar rings with a primary amine functional group on each monomer. Below its pK_a (6.3-6.5[235]) the amine is protonated, and the polymer becomes polycationic. At higher pH values, the amine is deprotonated and returns to an uncharged state. This charge reversal enables a controllable electrostatic attraction between NAs and chitosan at low pH values that can be reversed through a buffer exchange. Early work with the chitosan-NA interaction focused on NA compaction and delivery for gene therapy applications[236], [304], [305]. Although many of the above microchip-based systems show promise for translation to realistic POC systems, there is a drawback to their implementation due to the use of potentially expensive equipment for operation (*e.g.:* syringe pumps). Devices that require this type of equipment have limited usability in POC settings such as a patient's home or rural health clinics in the developing world. Due to these constraints, many groups have begun to focus on an alternative platform for diagnostics: porous membranes.

The use of porous membranes, or paper-based substrates, as a platform for bioassays dates back to the 1930s with the development of paper chromatography[306]–[308]. In the mid to late-1970s the home-based pregnancy test brought paper-based

diagnostics to the POC[309]–[311]. More recently, George Whitesides' group began patterning cellulose paper to simultaneously detect glucose and proteins in urine samples[77]. The field has also evolved beyond one-dimensional lateral flow systems to include two-dimensional paper networks (2DPN)[89], which offer advantages such as the ability to perform complex, multi-step processes[90], the sequential timed delivery of reagents[89], [102], and compatibility with various detection techniques[91]. Porous-membrane-based assays do not require mechanical pumps because capillarity wicks fluids into and through the paper[301]. These devices are also inexpensive, easy to manufacture, and disposable, making them ideal candidates for POC tests. Two recent reviews detail the use of porous membrane-based microfluidics for diagnostic devices[11] and the translation of multi-step processes from laboratory gold-standard techniques to paper-based systems[312].

There is still a significant gap in translating NA tests to paper platforms, especially those that may require NA purification and concentration. Mariella *et al.* noted that few paper-based devices have developed reliable solutions for the use of NA in paper-based formats[177]. Recent publications have detailed systems that isolate NAs using commercially available extraction membranes such, as FTA or Fusion 5[254], [313], or chromatography paper[146]. Although these membranes do selectively isolate NAs, they have only been demonstrated in conjunction with plastic microchips or require minimal equipment with multiple user steps.

Furthermore, sample concentration can be an additional critical step in the NA purification process, especially for environmental testing where only a few targets may be

present in large volumes (mL to L) of sample. As such, an ideal porous membrane-based NA purification system should also substantially concentrate the target.

In this work, a novel DNA purification and concentration system that uses the linear polysaccharide chitosan was developed in porous membrane substrates for POC applications. It is well known that surfaces can be modified with polymers to engineer or control surface properties such as charge[314], [315]; we've used these principles to investigate chitosan's interaction with two different porous membranes. Second, the capacity of different membranes for the polymer and polymer retention during lateral flow were measured. These steps provide a quantitative method for determining the capacity for DNA binding of chitosan-coated membranes. Finally, on the basis of this method, a system was developed and tested using porous membranes to simultaneous purify and concentrate DNA from complex samples containing high protein content, excess non-target DNA, and blood. Further, the purification system uses a novel, one-step, sequential reagent delivery mechanism developed in the Yager and Lutz labs[157], [316] that directly translates to a simple, one-step user experience; this further supports the feasibility of this system for use in POC applications.

13.3 Materials and Methods

13.3.1 Reagent preparation

All reagents were prepared with sterile molecular biology grade water (Thermo Fisher Scientific, Waltham, MA). Low molecular weight chitosan oligosaccharide lactate (average MW 5000), mucin from porcine stomach Type III, sodium chloride, Tris-HCl, and MES were purchased from Sigma Aldrich (St. Louis, MO). Pulse-field-certified agarose, sample loading dye, SYBR Gold gel stain, and DNA ladders were purchased

from BioRad (Hercules, CA). A 10x stock of TBE buffer was purchased from Thermo Fisher Scientific (Waltham, MA). Human genomic DNA (gDNA) was purchased from Promega (Madison, WI). The 50 mM MES DNA capture and wash buffers were prepared in sterile water and the pH was adjusted to 5. The 50 mM Tris DNA elution buffer was prepared in sterile water with red food coloring (Safeway, Pleasanton, CA) to track fluid flow; the pH was adjusted to 9. The simulated nasal matrix (SNM) was prepared as previously described[155]. Defibrinated sheep's blood was purchased from Hemostat Laboratories (Dixon, CA).

13.3.2 Device patterning and construction

All porous membranes and test card materials were cut using a CO_2 laser (Universal Laser Systems, Scottsdale, AZ). Untreated, backed, 5-10 µm pore diameter nitrocellulose (NC) membranes (FF80HP, GE Healthcare Life Sciences, Niskayuna, NY) and untreated, unbacked, 10-100 µm pore diameter glass fiber (GF) membranes (Standard 17, GE Healthcare Life Sciences, Niskayuna, NY) were patterned with chitosan. Test cards were made with 0.254 mm-thick Mylar backing with adhesive (10 mil AC Melinex, Fralock, Valencia, CA) and cellulose wicking pads (CFSP223000 Millipore, Millipore, Billerica, MA) for waste fluid uptake.

The nitrocellulose and glass fiber membranes were patterned with a low molecular weight chitosan solution prepared in 50 mM MES at pH 5 using a piezoelectric noncontact printer (SciFLEXARRAYER S3, Scienion AG, Berlin, Germany). After printing, the membranes were stored in a desiccator. Membranes patterned with fluorescently tagged chitosan were also wrapped in foil to protect them from light and photobleaching.

13.3.3 SEM of porous membranes

All images were collected using an FEI Sirion electron microscope and samples were Au/Pd sputter coated (SPI Module Control, Structure Probe, Inc., West Chester, PA, USA) with an estimated 12 nm Au/Pd. A 5 kV beam was used for imaging (Figure 85).

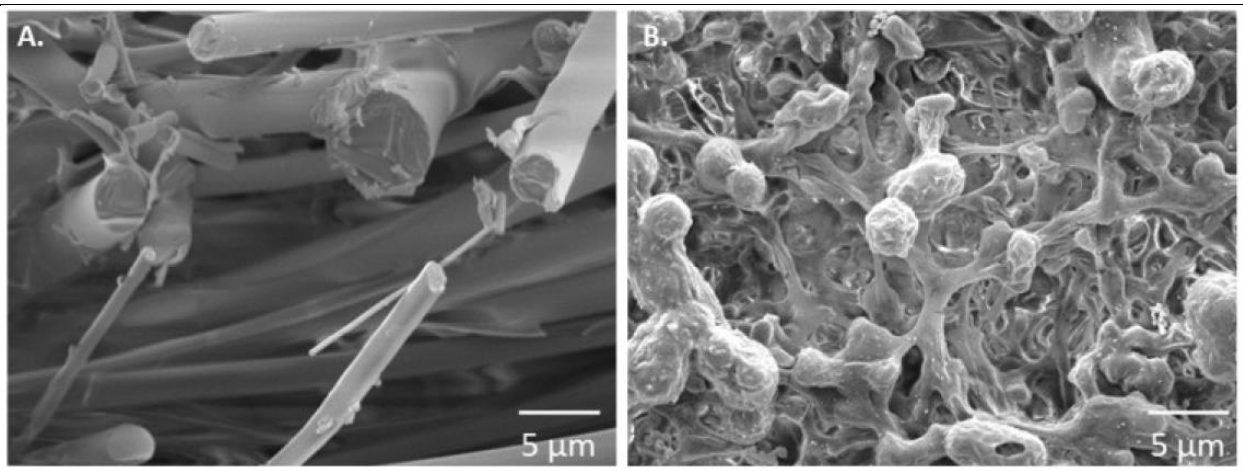

Figure 85: SEM images of glass fiber and nitrocellulose used to determine membrane surface area for polymer adsorption studies. SEM imaging and sputter coating work was performed at the University of Washington Nanotech User Facility (NTUF), a member of the NSF-sponsored National Nanotechnology Infrastructure Network (NNIN). A) Glass fiber. B) Nitrocellulose.

Using these images, membrane surface area was estimated by representing the features as spheres and cylinders to simplify calculations. The calculated surface areas per volume of nitrocellulose and glass fiber were 2.0 $\mu m^2/\mu m^3$ and 0.19 $\mu m^2/\mu m^3$, respectively. These calculated values are consistent within an order of magnitude with other published values[130], [317].

13.3.4 Fluorescent labeling of chitosan

Chitosan was fluorescently labeled using the commercially available 488 or 594 Amine-Reactive Dye Kit from Thermo Scientific (Logan, UT). Chitosan was dissolved in 50 mM MES at pH 5 to make a 1% w/v solution. After a one-hour incubation at room temperature with the amine-reactive dye, the chitosan was purified by precipitation using 5 M NaOH followed by centrifugation at 9400g for 3 minutes. The precipitated chitosan was re-dissolved in 50 mM

MES and the pH was adjusted to 5 to prepare it for reagent patterning. The solution was stored in the dark at 4 °C for up to one month.

13.3.5 Purifying and fluorescent labeling of DNA

All DNA was purified from freshly cultured methicillin-sensitive *Staphylococcus aureus* (MSSA, strain RN4220) bacterial cells. The DNA was purified using the commercially available Qiagen Gentra Puregene Kit (Qiagen, Valencia, CA) with a slightly modified protocol. During the lysis step, 50 µL of lysostaphin (100 µg/mL) was added with the recommended 1.5 µL of Lytic Enzyme Solution provided by the kit. Purified DNA was resuspended in 20 µL of sterile water and incubated for 20 minutes at 65 °C to complete resuspension. The final DNA concentration was calculated by qPCR (described below).

After purification, DNA was fluorescently labeled using the Alexa Fluor 488 or 594 ARES DNA Labeling Kit (Life Technologies, Carlsbad, CA) with a slightly modified protocol. During the initial nick translation step, the concentration of each of the dNTPs was 0.5 mM. After labeling, the final concentration of the fluorescent DNA was determined using qPCR for the *ldh*-1 gene.

13.3.6 Pulse field gel electrophoresis for DNA fragment size

Pulse field gel electrophoresis (PFGE, Fig. S2) was used to determine the fragment size of DNA both before and after purification with chitosan in-membrane. A 1.0% agarose gel was prepared in 0.5x TBE buffer and set overnight at 4 °C. Gels were run using the BioRad CHEF Mapper XA System (BioRad, Hercules, CA) in a cold room (4 °C) in 0.5x TBE running buffer. Agarose plugs containing the high molecular weight *S. cerevisiae* DNA ladder were loaded into the gel before submerging in running buffer. Liquid samples were added to the gel with sample loading

buffer. The "Auto-Algorithm" function was used with an input size range of 100 kbp to 2200 kbp. Gels were stained with 2x SYBR Gold in running buffer (limit of detection ~10^8 copies) for 20 minutes with shaking followed by 10 minutes of de-staining in DI water. Gels were imaged with the BioRad Gel Doc EZ System (BioRad, Hercules, CA).

13.3.7 qPCR for MSSA ldh-1 gene

DNA recovery was quantified with a qPCR kit for the *ldh*-1 gene provided by the ELITechGroup (ELITechGroup Molecular Diagnostics, Bothell, WA). The 20 µL reactions were run on a Rotorgene real-time PCR instrument (Qiagen, Valencia, CA) using the following protocol: 50°C hold for 2 minutes, 93°C hold for 2 minutes, 45 cycles of 93°C for 10 seconds, 56°C for 30 seconds, and 72°C for 15 seconds, ending with final elongation step at 72°C for 5 minutes. Fluorescence data were collected during the 56°C annealing step in the orange channel. The qPCR results were analyzed using the automated threshold cycle (CT) value calculation in the Rotorgene software (Qiagen, Valencia, CA). This assay is sensitive down to ~10^1 copies of the target sequence. The red dye or up to 0.5% blood in the elution buffer do not significantly interfere with the qPCR signal (Fig. S3[159]).

13.3.8 Chitosan interactions with porous membranes

13.3.8.1 Porous membrane capacity for chitosan

To determine the capacity of each membrane for chitosan, small punches (radius = 2.4 mm) were taken from sheets of nitrocellulose and glass fiber. These punches were filled to capacity for nitrocellulose and glass fiber, 1.81 or 7.56 µL, respectively, with varying concentrations of fluorescent chitosan in solution to produce different chitosan concentrations in the membranes. Here, chitosan concentration is defined as µg of chitosan per μm^2 of membrane surface area ($\mu g/\mu m^2$), assuming even coating on all surfaces. The membranes were placed in clear Petri

dishes and incubated in a dark chamber at 95% relative humidity for 24 hours to allow equilibration of chitosan adsorption to the membrane.

After incubation, the membranes were imaged wet to determine a baseline fluorescence signal for the input amount of chitosan. Next, the membranes were washed with 1x volume capacity of 50 mM MES at pH 5 and fluid was wicked away via a cellulose waste pad to remove unadsorbed chitosan. The membranes were re-wet with 50 mM MES at pH 5 and imaged a second time to track the loss in fluorescent signal. The loss of chitosan was measured as the difference between the baseline fluorescence and the post-wash fluorescence of the coated membranes. All fluorescence images were captured using an Axiovert fluorescence microscope (Zeiss, Thornwood, NY) fitted with a Retiga 1300i digital CCD camera (Quantitative Imaging Corporation, Surrey, BC, Canada). Images were taken with MicroManager software[318] using a 50 ms exposure and 2.5x objective.

Chitosan adsorption was calculated as the percent change in the integrated fluorescence intensity over the entire patterned region from pre- to post-wash conditions (Equation 14). These intensity values were measured using ImageJ[319].

$\%\ adsorbed = \frac{fluorescence_{postwash}}{fluorescence_{prewash}}\ x\ 100\%$	Equation 14

For both membranes, the chitosan concentrations tested ranged from 0 to 3.6×10^{-8} $\mu g/\mu m^2$. The upper limit of chitosan concentration for each membrane was bounded by the solubility of chitosan in buffer (50 mM MES, pH 5), the volume capacity, and the pore surface area of the membrane. Membrane capacity was determined by plotting the percent of chitosan adsorbed to each surface against the input chitosan concentration (in $\mu g/\mu m^2$) (Fig. S4C). These capacities were further verified by theoretical calculations based on the length of the chitosan

polymer and the membrane surface areas; see the *Supplementary Information*[159] (Fig. S4A and Fig. S4B) for the full calculations.

13.3.8.2 Chitosan retention in porous membranes during flow

To determine the retention of chitosan in each porous membrane during flow, a 2.5 mm long by 10 mm wide region of each membrane was patterned with fluorescent chitosan. Three concentrations were tested to determine if retention during flow was concentration dependent. The three tested concentrations for both membranes were based on the results of the previous adsorption studies. The concentrations in the patterned regions were $4.5x10^{-10}$, $8.9x10^{-10}$, and $1.3x10^{-9}$ µg/µm^2 for nitrocellulose and $8.9x10^{-10}$, $1.8x10^{-9}$, and $2.7x10^{-9}$ µg/µm^2 for glass fiber.

The patterned membranes were attached to 10 mil thick Mylar backing with adhesive (10 mil AC Melinex, Fralock, Valencia, CA) for ease of handling. An untreated cellulose pad (CFSP223000 Millipore, Billerica, MA), cut using the CO_2 laser cutter, was used as a waste collection reservoir. Before the initiation of flow, the chitosan regions on each membrane were wetted with 50 mM MES at pH 5 and excess unadsorbed chitosan were removed *via* wicking with a cellulose waste pad through the thickness of the membrane. This step was important to decouple the loss of chitosan due to incomplete adsorption to the membrane from the loss of chitosan during lateral flow.

To test chitosan retention during flow, two solutions were sequentially wicked through the membrane. These solutions were the DNA capture and elution buffers, which were selected to mimic an actual DNA purification experiment. The volume of the solutions was set to 2x the fluid capacity of the membrane (120 µL total for nitrocellulose and 500 µL total for glass fiber).

Dimensions of the patterned region and the fluorescence intensity of the chitosan were measured in ImageJ from uncompressed, time-lapse videos acquired using HandyAVI (AZcendant, Tempe, AZ, USA) in a humidified, light-tight box illuminated with two blue LEDs. Videos were captured using a web camera (Logitech, Fremont, CA) fitted with a 550 nm high-pass filter (FEL0550, Thor labs, Newton, NJ). The fluorescence intensity of the chitosan during flow was normalized to the initial wetted intensity to determine the percent of polymer retained in the membrane during flow.

13.3.9 DNA purification and concentration in porous membranes using chitosan

Chitosan is a linear polysaccharide with a primary amine functional group on every monomer. In solutions buffered below the polymer's pK_a, 6.3-6.5[235], the primary amine is protonated, resulting in a multivalent cationic polymer. In its protonated form, chitosan binds DNA and RNA *via* electrostatic interactions. When exposed to a solution above the pK_a, the primary amines are deprotonated and this electrostatic attraction is lost, resulting in release of nucleic acids (Figure 86).

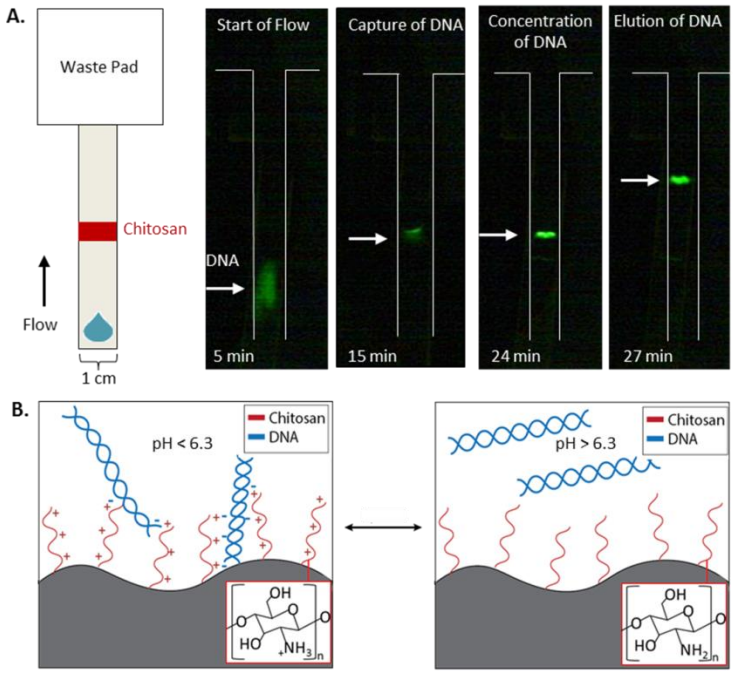

Figure 86: DNA purification in porous membranes using chitosan. A) Schematic and images from a purification experiment in nitrocellulose. The DNA (green) is initially seen as a smear. As it reaches the chitosan region, DNA stops flowing and becomes concentrated. Once DNA is eluted, it remains concentrated. B) Schematic of a membrane surface patterned with chitosan (red). In solutions with a pH below 6.3, the primary amines on each monomer become protonated and can bind DNA. When the pH is increased above the amine pK_a, the charge on the polymer returns to neutral and DNA is released. Note that the quantum efficiency of the label changes with pH and immobilization.

To evaluate the ability of chitosan to purify and concentrate DNA in paper, 60 x 10 mm membranes were patterned with chitosan in 50 mM MES at pH 5. The patterned region was set to an area 2.5 mm long by 10 mm wide to remain consistent with the chitosan retention experiments. Based on the capacity and retention experiments, the chitosan concentrations in nitrocellulose and glass fiber were set to 1.3×10^{-9} and 1.8×10^{-9} µg/µm^2 (± 5%), respectively.

13.3.9.1 Chitosan capacity for DNA and DNA concentration factor

Chitosan's capacity for DNA in both nitrocellulose and glass fiber was determined by increasing the concentration of DNA in the input sample until a decrease in the relative amount of DNA recovered was observed by qPCR. The range of input DNA concentrations tested in both membranes was between 1×10^5 copies (0.3 ng) to 4×10^8 copies (1200 ng) of fragmented MSSA DNA purified from cells. On average, the target DNA was less than 250-300 kbp long; larger DNA fragments are unable to flow through the pores of the membranes (Fig. S2[159]).

For these experiments, DNA was spiked into 100 µL of DNA capture buffer. This solution was wicked into the membrane, followed sequentially by 100 µL of wash and elution buffers for NC, and 250 µL of wash and elution buffers for GF to accommodate for the higher fluid capacity. These experiments were run in a humidified chamber to reduce effects from evaporation.

DNA was recovered post-elution by placing the membrane in a centrifugal filter tube (0.45 µm Nylon centrifugal filters, VWR, Radnor, PA) and centrifuging for 3 minutes at 10,000g (Fig. S6[159]). These elution volumes were measured and the target DNA concentration was determined by qPCR.

Concentration effects were measured by adding $1x10^5$ to $1x10^6$ copies (0.3 to 3 ng) of DNA into 100, 200, 500, 1000, or 2000 µL of capture buffer. These solutions were wicked through a membrane patterned with chitosan followed sequentially by either 100 µL for NC or 250 µL for GF of DNA wash and elution buffers. Post-elution, the DNA purification efficiency (% recovery) was quantified by qPCR. The concentration factor was calculated as the initial input volume divided by the measured elution volumes times the % recovery (Equation 15).

$Concentratrion\ Factor = \frac{Input\ volume}{Elution\ volume}\ x\ 100\%$	Equation 15

13.3.9.2 Recovery of DNA from complex samples

To determine the ability of a porous membrane pre-loaded with chitosan to purify DNA, approximately $1x10^5$ to $1x10^6$ copies of MSSA DNA was diluted into 100 µL of DNA capture buffer. The sample was wicked into the patterned membrane followed by wash and elution buffers, as described above. In addition to purification of DNA in water, the experiment was

repeated with 1 µg BSA, 0.1% w/v mucins, 1% w/v mucins, up to 1000x non-target human gDNA, and 1% or 10% SNM to mimic more complex solutions. The percent recovery for each sample was determined by qPCR. These experiments were run in a humidified chamber to reduce effects of evaporation.

13.3.9.3 DNA purification from blood samples

Nucleic acid purification using chitosan patterned in porous membranes was also used to purify and concentrate DNA from blood samples. Often, blood preparation procedures require multiple user steps and removal of blood components that can inhibit downstream amplification reactions, notably heme[320]. From 15 to 50 µL of defibrinated sheep's blood was spiked into sample volumes ranging from 100 µL to 2000 µL. These samples were wicked into porous membranes patterned with chitosan followed by sequential delivery of wash and elution buffers, as described above. The purified DNA was analyzed by qPCR. These experiments were run in a humidified chamber to reduce effects of evaporation.

13.3.10 Statistics

All statistics were run using the open-source statistical package R (64 bit, version 3.0.2)[234].

13.4 Results and Discussion

13.4.1 Chitosan interaction with porous membranes

13.4.1.1 Porous membrane capacity for chitosan

In this work, we aimed to demonstrate a simple, porous membrane-based device that purifies and concentrates DNA from complex samples. We started with determining the amount of chitosan available to bind DNA when patterned onto different porous

membranes. The amount of *available* chitosan should depend on its adsorption to the porous membrane.

For all concentrations tested in nitrocellulose, the amount of input chitosan that adsorbed to the membrane was above 90%, indicating that the membrane was not fully saturated with polymer. This same trend was not observed for glass fiber; at concentrations at or below $3.6x10^{-9}$ μg/μm^2, the percent of input chitosan adsorbed remained high. At concentrations above $3.6x10^{-9}$ μg/μm^2, the percent adsorbed dropped, indicating that the membrane capacity had been reached (Fig. S4C). These results are consistent with our understanding of the physical properties of these porous membranes; the high surface area of the nitrocellulose, with its small pores and features, provides a higher capacity (experimentally determined capacity: $3.3x10^{-8}$ μg/μm^2) for polymer adsorption than the coarser glass fiber (experimentally determined capacity: ~$5.4x10^{-9}$ μg/μm^2). This difference between nitrocellulose and glass fiber may be due to the way chitosan adsorbs to different surfaces. This data suggests that only a few monomers of the chitosan chain adsorb to nitrocellulose allowing more space for additional molecules to adsorb. In glass fiber, on the other hand, a larger fraction of the total polymer might bind to the surface restricting the space available for other molecules to bind (Fig. S4A[159]).

These empirical capacities were further supported by theoretical calculations that predict the chitosan capacity of nitrocellulose should be between $9.7x10^{-10}$ and $3.3x10^{-8}$ μg/μm^2. An adsorption capacity was not observed for the concentrations tested, up to ~$3.3x10^{-8}$ μg/μm^2, which is at the maximum of the theoretical range. Based on the theoretical calculations and empirically determined capacities, the chitosan coverage of the nitrocellulose surface was ~100%

of the theoretical geometric monolayer coverage (Fig. S4B[159]). For glass fiber, the theoretical capacity for chitosan should be between $9.5x10^{-10}$ and $3.2x10^{-8}$ μg/μm^2. The experimentally measured capacity for glass fiber falls within the lower range of the theoretical values and approximates to ~15% of the theoretical geometric monolayer coverage (Fig. S4B[159]). Using these conditions, there is a monolayer of chitosan coverage on the nitrocellulose surface and less than a monolayer on glass fiber surface. The upper limit of chitosan concentration tested for each membrane was bounded by the solubility of chitosan in buffer (50 mM MES, pH 5) and the volume capacity of the membrane.

13.4.1.2 Chitosan retention in porous membranes during flow

The total amount of chitosan available for DNA binding (Table 11) is determined by the amount patterned onto the membrane minus losses from incomplete adsorption, described above, and capillary flow, described below.

Table 11: Final chitosan concentration in each membrane after accounting for losses from incomplete adsorption and flow. *The "mean final concentration" is based on the average percent adsorbed and retained. **The "Range final concentration" is based on the standard deviations for the percent retained during flow.

Input Concentration (μg/μm^2)	% adsorbed	% retained	Mean final concentration* (μg/μm^2)	Range final concentration** (μg/μm^2)
Nitrocellulose				
$4.5 x10^{-10}$	89 %	83 %	$3.3x10^{-10}$	$3.3x10^{-10}$ – $3.4x10^{-10}$
$8.9x10^{-10}$	85 %	74 %	$5.6x10^{-10}$	$5.4x10^{-10}$ – $5.7x10^{-10}$
$1.3x10^{-9}$	91 %	71 %	$8.6x10^{-10}$	$8.3x10^{-10}$ – $9.0x10^{-10}$
Glass Fiber				
$8.9x10^{-10}$	79 %	89 %	$6.3x10^{-10}$	$5.4x10^{-10}$ – $7.1x10^{-10}$
$1.8x10^{-9}$	58 %	71 %	$7.3x10^{-10}$	$6.8x10^{-10}$ – $7.8x10^{-10}$
$2.7x10^{-9}$	40 %	82 %	$8.7x10^{-10}$	$8.1x10^{-10}$ – $9.4x10^{-10}$

After characterizing the membrane capacity for chitosan, the effects of capillary flow on chitosan retention were measured. The three tested concentrations for nitrocellulose were $4.5x10^{-10}$, $8.9x10^{-10}$, and $1.3x10^{-9}$ μg/μm^2 and for glass fiber were $8.9x10^{-10}$, $1.8x10^{-9}$, and $2.7x10^{-9}$ μg/μm^2. The concentrations vary in nitrocellulose and glass fiber due to the different surface areas of each membrane. These values were based

on high, medium, and low concentrations from the adsorption studies detailed above. Retention of chitosan in nitrocellulose is slightly concentration-dependent, with larger concentrations of patterned chitosan losing a higher percentage during flow (**Fig. 2A**[159]). For glass fiber, this trend is not observed. The loss of chitosan due to flow does not appear to be concentration-dependent (**Fig. 2B**[159]).

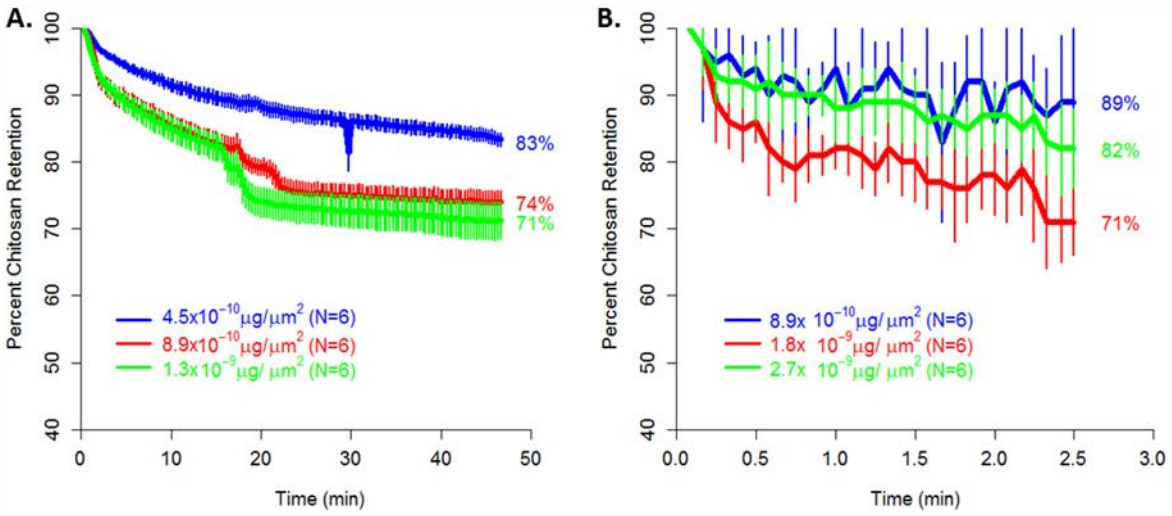

Figure 87: Chitosan retention during flow after accounting for losses due to incomplete chitosan adsorption. A) In nitrocellulose, retention during flow appears to be slightly concentration dependent. B) In glass fiber all three tested concentrations resulted in similar losses due to flow. The average retention (N=6) with +/- one standard deviation is plotted for each time point.

13.4.2 DNA purification and concentration in porous membranes using chitosan

13.4.2.1 Chitosan capacity for DNA and DNA concentration factor

Chitosan capacity for DNA in nitrocellulose and glass fiber was evaluated after optimizing adsorption and retention. The capacity for DNA in nitrocellulose was 1.9×10^6 copies of DNA/µg of chitosan (c/µg) (95% CI: 2.9×10^5 to 3.5×10^6 c/µg). The capacity for DNA in glass fiber was 9.9×10^6 c/µg (95% CI: 5.9×10^6 to 1.4×10^7 c/µg) (Figure 87).

These results are calculated using the mean final chitosan concentration from Table 11, which accounts for losses due to incomplete adsorption and retention. These data show that chitosan has a higher capacity for DNA in glass fiber than in nitrocellulose.

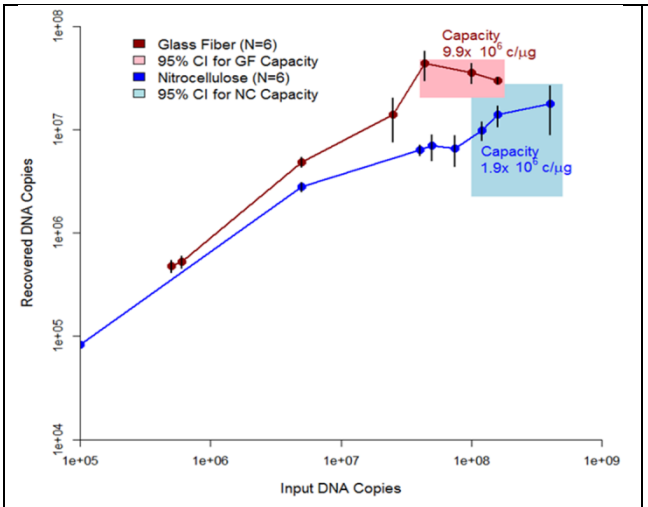

Figure 88: Capacity of chitosan for DNA in nitrocellulose (blue) and glass fiber (red) over a range of input concentrations (N=6 for each point) after normalization for membrane surface area. The capacity of chitosan for DNA is 1.9×10^6 c/µg (95% CI: 2.9×10^5 to 3.5×10^6 c/µg) in nitrocellulose and 9.9×10^6 c/µg (95% CI: 5.9×10^6 to 1.4×10^7 c/µg) in glass fiber.

The smaller pores (10 µm) and higher surface area per volume (2.0 $\mu m^2/\mu m^3$) of nitrocellulose adsorbs more chitosan than glass fiber; but these results indicate that only a proportion of the chitosan is available for DNA binding in nitrocellulose. The chitosan used in this study was small, ~5000 MW. This size may allow polymer to integrate into the smallest pore features of nitrocellulose, some of which may be inaccessible to large DNA fragments (100s kbp), causing a high membrane capacity for the chitosan and a lower than expected binding capacity for DNA. Further, chitosan may hinder convective transport in the smaller pore features (or block flow completely) in nitrocellulose, reducing or preventing flow of DNA-containing sample through these membrane regions. On average, the pore features in glass fiber are larger (10-100 µm) and the material has a lower surface area per unit volume (0.19 $\mu m^2/\mu m^3$) than nitrocellulose (2.0 $\mu m^2/\mu m^3$). This reduced surface area lowers the overall chitosan capacity of the membrane, but may allow more of the chitosan to be available for DNA binding.

Using these results, the calculated ratio of positive (chitosan) to negative (DNA) charges when the system has reached its maximum capacity for DNA indicates that there is less than a monolayer of nucleic acid bound to the chitosan in both nitrocellulose and glass fiber (Fig. S5[159]). These calculations assume that a full monolayer of DNA would equate to an equal ratio of charges at the DNA-chitosan binding capacity; see the *Supplementary Information*[159] for the full calculations. Further, these estimates and calculations assume all of the chitosan patterned in the membrane, after accounting for losses presented in Table 11, is available for DNA binding. More reasonably, only some percentage would be available because some of the polymer is interacting with the membrane surface, potentially rendering it unavailable for DNA binding. Additionally, both of these membranes have a range of pore size features and some fraction of the polymer may be trapped in the smallest of these features preventing it from interacting with DNA. Both of these scenarios further support the calculations that there is less than a monolayer of nucleic acid bound to the chitosan in each membrane.

To enable broader use of these methods, the DNA capacities of each membrane have been converted to other common units (Table 12). Using the membrane capacity for chitosan and the chitosan capacity for DNA, this method can be adapted to capture and concentrate DNA from a variety of samples based on the expected amount of total nucleic acids.

Table 12: Chitosan capacity in nitrocellulose and glass fiber.

*Assuming average DNA fragment size of $2.0x10^5$ bp.

**E. coli O157:H7, genome length $5.4x10^6$ bp.

***MSSA RN4220, genome length $2.8x10^6$ bp.

Capacity per µg chitosan	Nitrocellulose	Glass Fiber
copies DNA*	$1.9x10^6$	$9.9x10^6$
# bp*	$3.8x10^{11}$	$2.0x10^{12}$
ng DNA*	0.4	2.2
# *E. coli* bacteria**	$7.0x10^4$	$3.7x10^5$
# *MSSA* bacteria***	$1.4x10^5$	$7.1x10^5$

The maximum DNA concentration factors achieved with chitosan in nitrocellulose and glass fiber were 13.3x and 12.3x, respectively (Figure 88B). These results are based on the input sample volume and the purification efficiency of DNA since each membrane type yielded a specific elution volume.

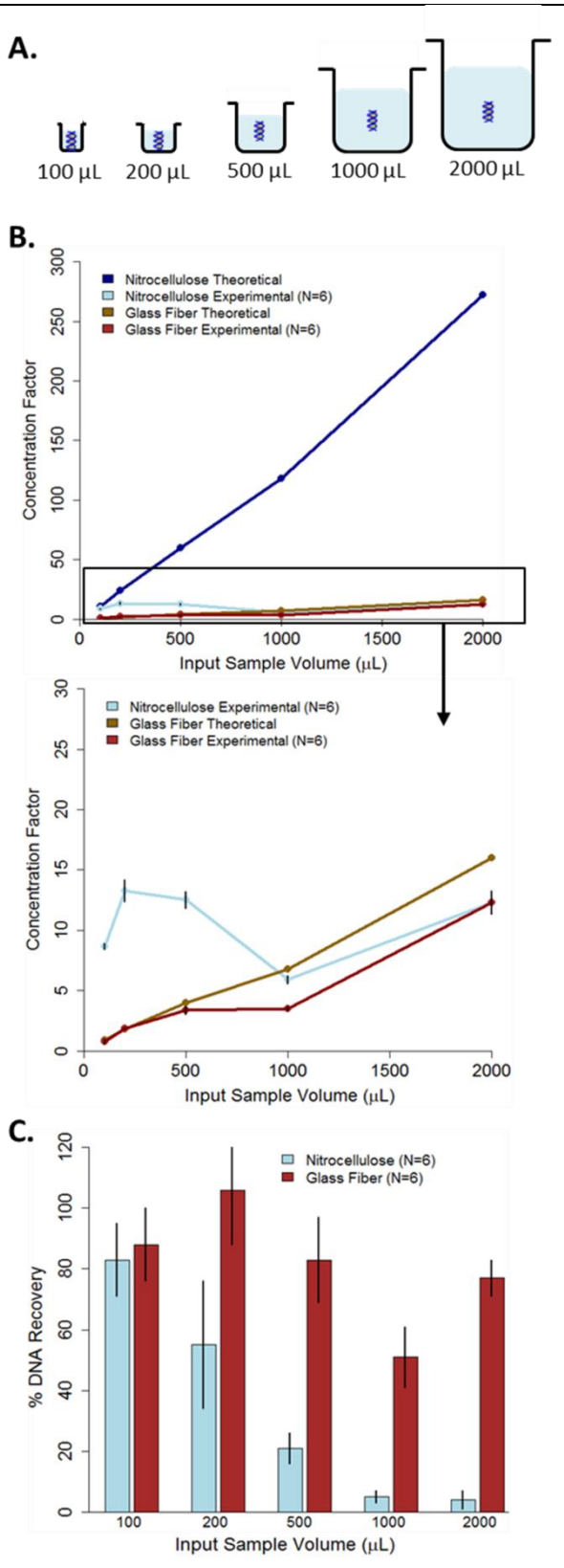

Figure 89: DNA concentration effects in nitrocellulose and glass fiber. A) Experimental schematic. B) Concentration factor from various input sample volumes. C) Corresponding recovery of DNA from various input sample volumes.

In nitrocellulose, which has a relatively homogenous pore size distribution, the interface between two sequentially delivered fluids is sharply defined. In this system, the wash and elution buffers have low and high pH values, respectively; the well-defined interface between the buffers under flow in nitrocellulose produces a sharp pH change (Fig. S6A[159]). When the interface reaches the chitosan patterned region, the rapid change from low to high pH deprotonates the chitosan quickly, and releases purified DNA in a concentrated plug (Fig. S6B[159]). In glass fiber, however, which has a relatively broad pore size distribution, the interface is poorly defined, which increases mixing between the two sequentially delivered buffers and causes a more gradual pH gradient to develop. When this gradient reaches the chitosan region, the gradual change from low to high pH deprotonates the chitosan slowly, resulting in a slower release (and therefore less concentrated plug) of purified DNA (Fig. S6C[159]). In nitrocellulose, DNA samples always eluted in 8 µL while for glass fiber, the elution volume was 100-150 µL.

In this system, which involves complex surfaces in porous membranes as well as in-flow binding, both concentration factor and percent recovery were independent of the starting DNA concentration in the sample within the ranges tested. Using the data presented in Figure 3, the corresponding elution volumes, and the resulting recovery percentages (data not reported here), we measured consistent concentration factors and percent recovery for input DNA concentrations ranging from $1x10^3$ copies of target per µL (c/µL) through $1x10^5$ c/µL where total input volume was set to 100 µL. These concentrations were below the saturation limit of the modified membranes' binding capacity for DNA (measured in Figure 88 and presented in Table 12). We have begun testing more dilute samples in larger input volumes and have preliminary data indicating this trend holds. That data will be the included in a future publication.

The theoretical concentration factor assumes 100% recovery of DNA. In nitrocellulose, DNA recovery decreased as the input sample volume increased (Figure 89C), likely due to the time it took to flow large volumes through the membrane. Wicking a 2000 µL sample, followed by 100 µL of wash and elution buffers, through nitrocellulose took over seven hours. This reduced recovery greatly reduced the actual concentration factors achieved in nitrocellulose. The same experiment in glass fiber only took 25 minutes and DNA recovery was independent of input sample volume in (Figure 89C). The long flow times required in nitrocellulose may exceed the chitosan/DNA off-rate which would cause bound DNA to prematurely release from chitosan and be lost to waste. The chitosan-DNA binding constant has been well studied and ranges from 10^9 to 10^{10} M^{-1} [321], [322], but, to our knowledge, the chitosan-DNA binding rates have not been published. There have been reported off-rates in the range of 3-5x10^{-2} s^{-1} [323], [324] for similar polycation-DNA interactions.

There are potential applications where concentration factor would matter less than purification but not necessarily recovery. For very dilute samples, such as urine, concentration factor would play a critical role to ensure enough pathogen nucleic acid is recovered for downstream analysis. Additionally, different infections present at a highly variable pathogen loads. For example, clinical studies have quantified active chlamydia infections in urine at 10^1–10^5 elementary bodies/mL[325], Ebola in serum at 10^3–10^9 RNA copies/mL[326], and influenza in nasopharyngeal wash at 10^3–10^7 TCID50/mL[327]. Each of these infections would benefit from a combination of both target purification and concentration. Specifically for infections that occur at low copy number or in dilute samples such as urine, concentration is especially important. Some of these samples would require the processing of larger volumes (mL instead

of µL) to ensure a sufficient number of pathogens for infection identification. The current approach, especially using nitrocellulose, is somewhat slow to process larger volumes and may result in decreased recovery (Figure 89C). The next iteration of this work will involve developing fluidic systems that can rapidly process large volumes in order to purify and concentrate targets from complex, dilute samples.

13.4.2.2 DNA purification from complex samples

We demonstrated the system's ability to purify DNA from complex sample types. Overall, this method was able to recover ~80% of the input DNA from most of the sample types tested (Figure 90).

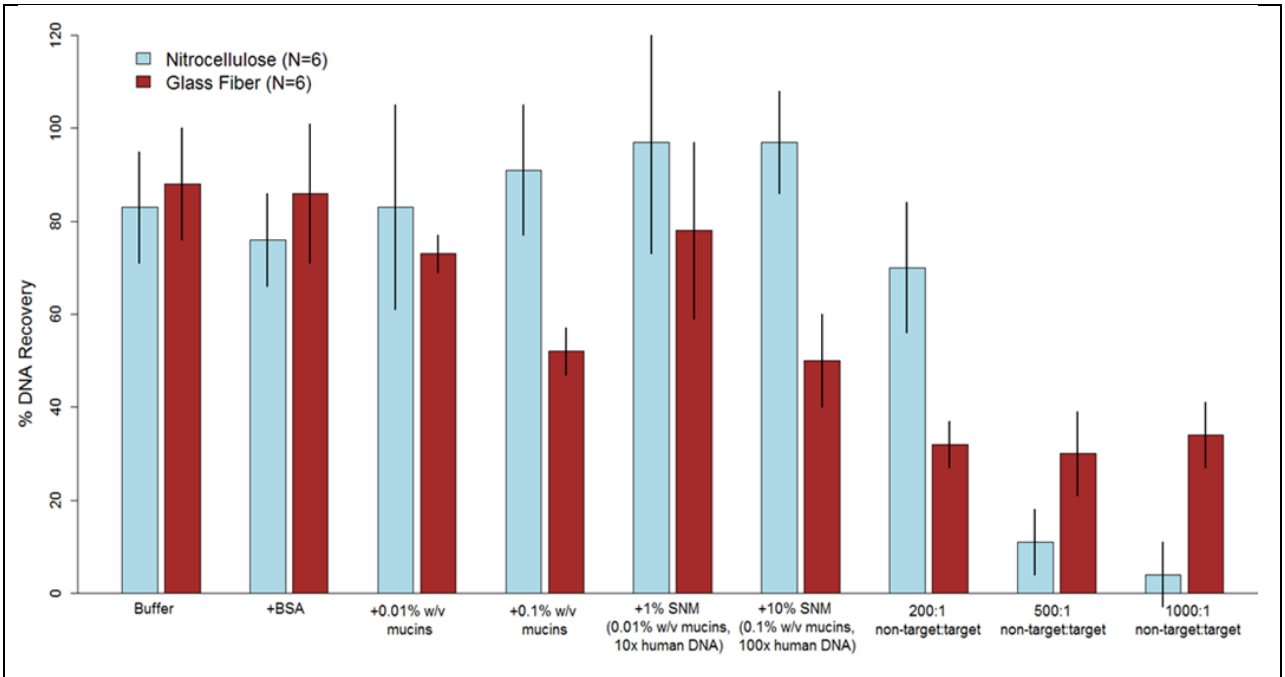

Figure 90: DNA purification in porous membranes by chitosan capture. Recovery of DNA in either nitrocellulose (blue) or glass fiber (red). The average of N=6 is reported with error bars representing +/- one standard deviation. Chitosan concentration at the capture line was $1.3x10^{-9}$ µg/µm^2 for nitrocellulose and $1.8x10^{-9}$ µg/µm^2 for glass fiber. Input DNA was between $1x10^5$ and $1x10^6$ copies of fragmented MSSA DNA. For SNM: 1% SNM contained 10:1 non-target to target DNA, 0.01% w/v mucins, 1.1 mM NaCl; 10% SNM contained 100:1 non-target to target DNA, 0.1% w/v mucins, 11 mM NaCl.

In both nitrocellulose and glass fiber, the recovery of target DNA was reduced when samples contained a non-target:target ratio of greater than 100:1. These data are slightly higher than the limits dictated by the capacity data above (~10:1 for nitrocellulose and ~20:1 for glass fiber). This discrepancy is likely a result of larger DNA fragments (greater than ~250 kbp) from the non-target DNA being too large to flow through the small pore features of the membranes. This size-exclusion effect is expected to be more severe in nitrocellulose than in glass fiber due to the differences in pore size distribution between the two membranes. This would suggest that some non-target DNA is essentially filtered upstream of the chitosan capture region rendering it unavailable to compete for binding. The data in Figure 5 support this assumption because at large non-target:target ratios of 200:1, there is a greater reduction in recovery for glass fiber than in nitrocellulose. At higher ratios, 500:1, the reduction in target DNA recovery is similar in both membranes. Recovery of target DNA in glass fiber with an extreme non-target:target ratio of 1000:1 was higher than expected.

The addition of mucins, to mimic nasal swab samples, reduced recovery of target DNA in glass fiber but not in nitrocellulose. Mucins are large protein aggregates (mass>10^6 Da) that are glycosylated with oligosaccharides that commonly form negatively charged side groups[328]. These negatively charged molecules can interact with positively charged chitosan, blocking the binding of DNA. These large aggregates may not pass through the small pores of nitrocellulose because DNA recovery is not affected by their presence in the sample. In glass fiber, however, the larger pores may allow these negatively charged aggregates to flow downstream and prevent DNA binding to chitosan, leading to reduced recovery as the concentration of mucins increases. When

both mucins and non-target DNA is present in samples (from simulated nasal matrix, SNM), DNA recovery remains high in nitrocellulose and decreases in glass fiber. Once again, the magnitude of this decrease is correlated to increasing concentrations of mucins. For applications containing mucins or high concentrations of non-target DNA, the chitosan-patterned region can be extended to increase the system's overall capacity.

DNA purification from blood samples

Blood preparation procedures often require many user steps to remove blood components that can inhibit downstream amplification reactions, notably heme[320]. The chitosan-based DNA purification system is able to rapidly purify target DNA from blood samples with only one user-step (Fig. S7[159]). The eluted samples were quantified by qPCR without further purification.

In both membranes, samples with lower blood concentrations resulted in higher recovery of DNA (Figure 91A). In nitrocellulose, recovery of target DNA from blood-containing samples was significantly inhibited and the flow rate of the sample through the membrane decreased as blood concentration increased. The reduced flow rate appeared to be a result of membrane clogging. For the sample containing 50% blood in nitrocellulose, only a small volume wicked into the membrane before flow stopped completely.

In glass fiber membranes, target DNA was purified from samples containing up to 50% whole blood but, as blood concentration increased, DNA recovery decreased. To verify this result, 50 µL of whole blood plus target DNA was diluted into increasing volumes of buffer. As blood concentration decreased, DNA recovery increased (Figure 91B).

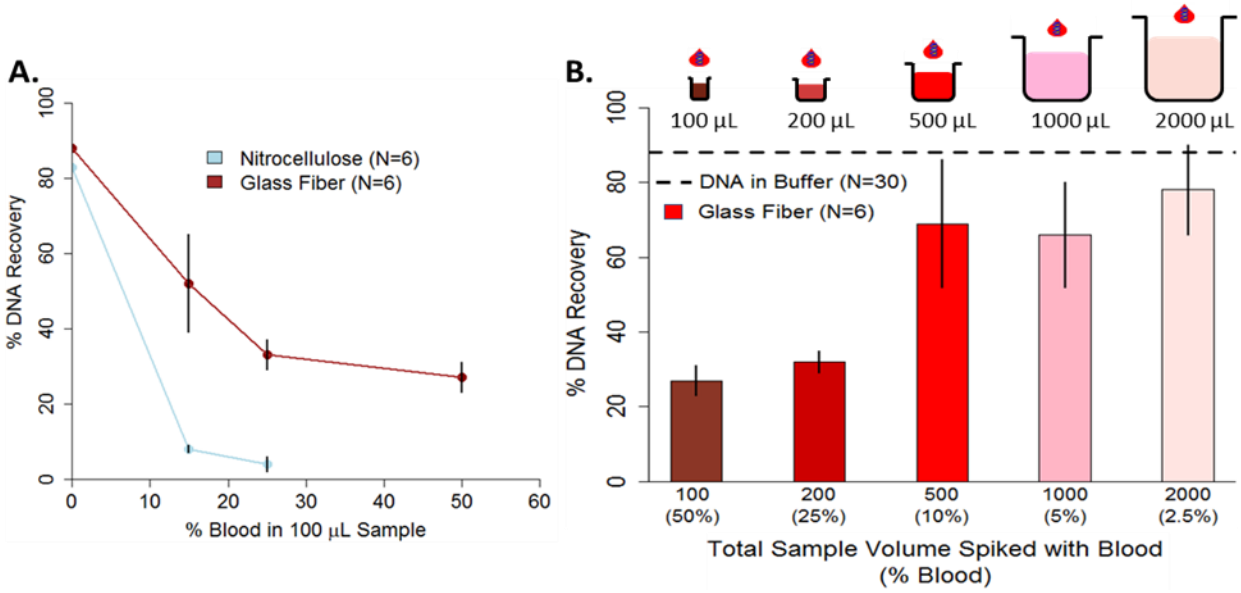

Figure 91: DNA purification in porous membranes from samples containing blood. The average of N=6 is reported with error bars representing +/- one standard deviation. Chitosan concentration at the capture line was $1.3x10^{-9}$ µg/µm^2 for nitrocellulose and $1.8x10^{-9}$ µg/µm^2 for glass fiber. Input DNA was between $1x10^5$ and $1x10^6$ copies of MSSA DNA. A) Increasing the percent of blood in a 100 µL sample reduced recovery in both nitrocellulose and glass fiber. The 50% blood sample in NC clogged the membrane preventing flow and therefore DNA purification. B) Diluting 50 µL of blood into increasingly large sample volumes improved recovery in glass fiber. For volumes larger than 200 µL, the recovery was similar to the "DNA in buffer" control.

For samples that were less than 25% blood, DNA purification efficiency is similar to the "DNA in buffer" control. This restored recovery is likely due to increased washing of the chitosan region to remove blood components that interfere with chitosan/DNA binding and not with the qPCR analysis. Based on the dilution factor of DNA eluted from chitosan in glass fiber (Fig. S5C[159]) and the sample volume used for qPCR (1 µL of the elution), the maximum amount of blood in a qPCR reaction would be less than 0.5%. For whole blood concentrations at or below 0.5%, qPCR is not inhibited (Fig S3B[159]).

13.5 Conclusions

Here we have demonstrated the first example of a system for the simultaneous purification and concentration of DNA from complex samples using chitosan and constructed entirely from porous membranes. First, the interaction of two porous membrane substrates with chitosan was characterized and a method to determine the adsorption capacity of these membranes for polymers was described. Next, to exhibit the broad applicability of this system, it was used to purify DNA from complex samples including those with high protein content, non-target DNA, and known amplification inhibitors such as blood. These samples are just a few examples of potential inputs that can be handled by this system. The choice of membrane provides the ability to control the sample processing time, volume, and concentration factor. Thus, large volume samples such as urine or contaminated environmental water could be rapidly processed with this system at the POC. This method can directly integrate with other paper-based point-of-care technologies such as in-membrane amplification[329] and detection. Further, this system is already well-suited for untrained end users via the use of automatic sequential reagent delivery[157], [316]. Future work will therefore demonstrate sample-to-result integrated systems that can rapidly and automatically process high input sample volumes in porous membranes.

13.6 Acknowledgements

This work was supported by a grant to Paul Yager from the Defense Advanced Research Projects Agency (DARPA) “Multiplexable Autonomous Disposable for Nucleic Acid Amplification Tests for LRSs” under Grant No. HR0011-11-2-0007.

We thank our colleagues Paula Ladd, Ryan Gallagher, and Erin Heiniger in the Yager Laboratory who provided valuable discussion and feedback on experimental design and analysis. We thank collaborators Barry Lutz and Nuttada Panpradist in the Lutz Laboratory at the University of Washington for providing useful discussions and materials for simulated nasal matrix. We thank collaborators Nicolaas Vermeulen and Boris Alabyev from ELITechGroup Molecular Diagnostics (previously Epoch Biosciences) for assistance with the supply of the qPCR assay and simulated nasal matrix. We thank collaborators David Moore, Cathryn Olsen, and Bing Li from GE Global Research for providing the porous materials and support on membrane selection. We thank our colleagues and members of the Yager Lab and Lutz Lab at the University of Washington. SEM imaging and sputter coating work was performed at the University of Washington Nanotech User Facility (NTUF), a member of the NSF-sponsored National Nanotechnology Infrastructure Network (NNIN).

14 Appendix: Comparison of point-of-care-compatible lysis methods for bacteria and viruses

Erin K. Heiniger, Joshua R. Buser, Lillian Mireles, Xiaohong Zhang, Paula D. Ladd, Barry R. Lutz, and Paul Yager

This appendix section is taken in a largely unmodified form from the manuscript[265]. I would like to thank primary author Dr. Erin Heiniger and my other coauthors for involving me with the project.

14.1 Abstract

Nucleic acid sample preparation has been an especially challenging barrier to point-of-care nucleic acid amplification tests in low-resource settings. Here we provide a head-to-head comparison of methods for lysis of, and nucleic acid release from, several pathogenic bacteria and viruses—methods that are adaptable to point-of-care usage in low-resource settings. Digestion with achromopeptidase, a mixture of proteases and peptidoglycan-specific hydrolases, followed by thermal deactivation in a boiling water bath, effectively released amplifiable nucleic acid from *Staphylococcus aureus, Bordetella pertussis,* respiratory syncytial virus, and influenza virus. Achromopeptidase was functional after dehydration and reconstitution, even after eleven months of dry storage without refrigeration. Mechanical lysis methods proved to be effective against a hard-to-lyse *Mycobacterium* species, and a miniature bead-mill, the AudioLyse, is shown to be capable of releasing amplifiable DNA and RNA from this species. We conclude that point-of-care-compatible sample preparation methods for nucleic acid tests need not introduce

amplification inhibitors, and can provide amplification-ready lysates from a wide range of bacterial and viral pathogens.

14.2 Introduction

In the modern clinical laboratory, detection of a myriad of pathogens with extreme sensitivity and specificity allows rapid diagnosis of disease and recommendations for treatment. However, these techniques are not always compatible with low-resource settings, or the point-of-care (POC). This disparity in technology availability affects not only health outcomes, but increases the burden of infectious disease in laboratory-poor areas of the developing world [2]. In order to narrow this divide, our group is developing the MAD NAAT (Multiplexable Autonomous Disposable for Nucleic Acid Amplification Testing) platform (Fig. 1A). The launch point for the MAD NAAT project was the use of two-dimensional networks of paper (2DPNs) to automate an isothermal nucleic acid (NA) amplification process, isothermal strand displacement amplification (iSDA) [160]. To enable full sample-to result NAAT automation, advances were required with regard to sample acquisition and transfer into the device [155], valving to automate and sequence the assay [154], [156], nucleic acid purification and concentration [159], isothermal nucleic acid amplification chemistry[160], and non-electric temperature-regulated heaters [115], [126], [209]. Most sample preparation techniques in the literature are predicated upon use in a laboratory. Point-of-care-compatible methods have previously been described in isolation; to evaluate nucleic acid preparation efficacy they must be compared head-to-head.

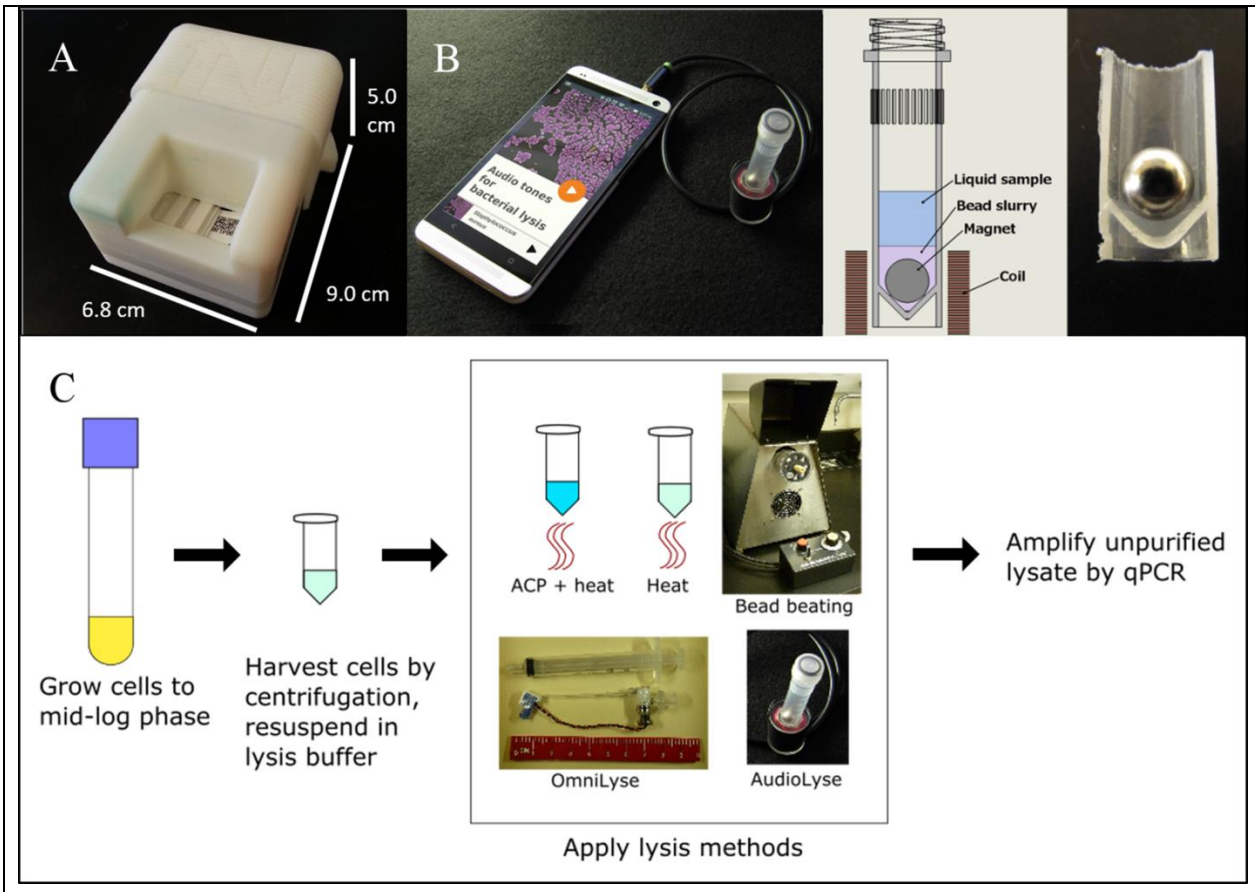

Figure 92: **Point-of-care-compatible lysis of a broad range of pathogens.** A) The MAD NAAT platform is a disposable instrument-free pathogen detection device currently being developed for point-of-care medical applications. To solve sample preparation hurdles for this device, we investigated a broad range of pathogen lysis methods. B) The AudioLyse device as used in previous work [158] C) The general lysis procedure followed in this work.

A sample preparation protocol must consider a number of constraints to be compatible with a lab-on-a-chip (LOC) device such as the MAD NAAT, informed by conditions found in the developing world where many of the mainstays of laboratory methods are absent [330], [331]. In these environments, trained personnel are rare. Electricity, and thus equipment such as refrigerators and centrifuges, may be unavailable or unreliable, and disposables such as pipette tips and centrifuge tubes may be cost-prohibitive. The same constraints are found in environmental monitoring and diagnosis of veterinary and plant diseases in the field. Currently available rapid diagnostics for non-human pathogens detect pathogen-specific antibodies or

antigens using immunochemistry [11]. Nucleic acid amplification tests are capable of low-copy detection, leading to greater sensitivity for the target of interest, but are often also more sensitive to inhibitors present in the specimen [332]. Currently, NAAT technologies for non-human pathogens are under development, but none is commercially available in a sample-to-result format [333], [334].

Constraints on diagnostics at the point-of-care are encompassed by the World Health Organization's ASSURED criteria: tests must be **A**ffordable, **S**ensitive, **S**pecific, **U**ser-friendly, **R**apid and robust, **E**quipment-free, and **D**elivered to those in need [330]. In order to meet these conditions for the MAD NAAT platform, we sought to develop a procedure to release amplifiable DNA or RNA from as broad a range of bacteria and viruses as possible, and allow direct input of lysed sample into the amplification reaction *without a purification step*. To meet, to the extent possible, the "user-friendly" ASSURED principle, we have also tried to minimize the number of user steps necessary for MAD NAAT, including sample preparation.

Lysis methods that use extreme pH, chaotropic salts, organic solvents, or detergents can interfere with subsequent nucleic acid amplification if these chemicals cannot be removed [270], [335]–[338]. Contaminant mitigation relies on purification using laboratory equipment (*e.g.* centrifuge), or drastically dilution of the sample, consequently reducing test sensitivity. We extensively considered the use of FTA paper, a product available from Whatman that was developed to capture and preserve nucleic acids from a variety of sample types, and has been used for prototype point-of-care NAATs [339]. However, we excluded FTA papers from this study because they must be washed before use in amplification reactions like iSDA [340], and thus were difficult to integrate into MAD NAAT. Remaining lysis techniques include **mechanical** lysis, **thermal** lysis, and **enzymatic** lysis.

Mechanical methods generally use grinding or shearing forces to lyse bacteria; they do not rely on chemicals that could inhibit nucleic acid amplification. A gold-standard mechanical method, bead beating, has been shown to release more DNA from hard-to-lyse microbes, including *S. aureus*, over other routine clinical laboratory techniques [341]. Point-of-care-compatible mechanical lysis methods evaluated in this study include the OmniLyse – a single-use, battery-powered miniature bead mill that has been shown to disrupt difficult-to-lyse bacteria and produce amplifiable DNA [111] – and our own laboratory's AudioLyse – a miniature bead mill that uses a portable audio device and electromagnetic coil to rotate a spherical magnet in a bead slurry, grinding the sample and causing lysis (shown in Figure 92B) [158].

Thermal lysis methods have been used to lyse bacteria, but often require the use of detergents such as Triton X-100 or SDS, or organic solvents such as phenol and chloroform [270], [338] which may inhibit nucleic acid amplification if not removed. Due to the constraints of our device, we chose to test boiling in a hypotonic solution free of these detergents and solvents as our thermal lysis condition.

Enzymatic lysis routinely utilizes proteinases (e.g., proteinase K) and/or lysozyme, but many important pathogens are resistant to these techniques. For example, *S. aureus*, our initial pathogen target in development of the MAD NAAT device, makes an enzyme—a peptidoglycan O-acetyltransferase, OatA—that determines its resistance to lysozyme [342]. We chose to test the broadly-applicable achromopeptidase (ACP), a cocktail of proteases and peptidoglycan-specific hydrolases [204], [343], [344]. Like other proteases, ACP is an inhibitor to downstream amplification. However, those components of ACP that affect both iSDA and PCR can be irreversibly deactivated at temperatures above 80°C [176]. A boiling water bath enables thermal deactivation of ACP without any other amenities. ACP activity can be stabilized by dehydration

in the presence of preservatives [176], and thus shipped worldwide in the absence of refrigeration. Prior to this work, it was unknown how tolerant ACP lysis would be to a range of conditions that might be present in an integrated device, such as exposure to varying ambient temperatures and duration of ACP enzyme deactivation by thermal deactivation allowable before DNA degradation began.

The three bacterial human pathogen targets tested represent a broad range of bacterial types. *Staphylococcus aureus* is a Gram-positive, opportunistic bacterial pathogen of great clinical relevance, especially in its methicillin-resistant form (MRSA) [345], [346]. *Staphylococcus* can be difficult to lyse compared to other bacterial species, in part due to its thick peptidoglycan cell wall, as is typical for Gram-positive bacteria [269], [270]. *Bordetella pertussis* is a Gram-negative bacterial respiratory pathogen, the causative agent of whooping cough, which takes 4-14 days to diagnose by cell culture, or a laboratory DNA purification and amplification method for diagnosis [347], [348]. Like all Gram-negative bacteria, *B. pertussis* has a cell wall protected from lytic enzymes by a lipid outer membrane, and consequently has lysis properties that are distinct from those of Gram-positive bacteria like *S. aureus.* *Mycobacterium marinum* has, like other mycobacteria, a unique cell wall structure, containing long-chain branched fatty acids and mycolic acids. This durable cell wall excludes lytic enzymes and makes *Mycobacterium* very difficult to lyse [349], [350]. In this study, we use *M. marinum* as a model organism for *Mycobacterium tuberculosis*, which causes a large portion of deaths worldwide, especially among HIV-infected individuals [331]. *M. marinum* was chosen because it has been used previously at our institution as a model organism for TB in fish pathogenesis studies [351], and because of its ease and speed of culture in our BSL-2 laboratory facilities [352].

Symptoms associated with bacterial infections often overlap those caused by viral infections, and MAD NAAT was designed to enable detection of both bacteria and viruses. Many common viral pathogens, such as respiratory syncytial virus (human RSV A) and influenza, contain RNA genomes. To ensure that the relatively rigorous conditions and enzymes needed to extract DNA from bacteria did not destroy RNA from easier-to-lyse viruses, integrity of amplifiable RNA targets introduced subsequent to the ACP lysis method was evaluated. Traditionally, RNA viruses are lysed using chaotropic salts or detergents, which require nucleic acid purification before amplification. A method enabling DNA and RNA assays for bacteria and viruses without purification would be hugely beneficial for integrated devices like MAD NAAT.

We performed a head-to-head comparison of point-of-care-compatible lysis methods for three diverse bacterial species and two viral species. Using these methods, DNA and RNA released from pathogens is quantified without purification. Furthermore, AudioLyse is evaluated for room-temperature release of RNA from bacterial cells, this work's primary DNA-releasing targets. The suite of lysis methods described here will be applicable to the development of a wide range of point-of-care diagnostic devices.

14.3 Materials and Methods

14.3.1 Bacterial growth

S. aureus (strain RN4220[353]) was cultured in Tryptic Soy Broth (BD Difco, Franklin Lakes, NJ, USA) at 37°C with shaking (250 rpm). Overnight cultures were diluted 1:100 in fresh medium and grown to mid-log phase (OD_{600} = ~2). *B. pertussis* (Moreno-Lopez ATCC 9797) was cultured in Stainer-Scholte (BD Difco) broth as described previously [354]. Cultures were grown for two days at 37°C with shaking (250 rpm), then diluted 1:100 in fresh medium, and grown 16-20 hours to mid-log phase (OD_{600} = ~1). *M. marinum* (Aronson ATCC 927) was

cultured in Middlebrook 7H9 broth with ADC enrichment (BD Difco) at 30°C with shaking (250 rpm) for 4-7 days. Cultures were diluted 1:100 in fresh medium and grown for 48 hours to mid-log phase (OD_{600} = ~1).

14.3.2 Virus source

Cultured RSV was obtained from the UW Clinical Virology Laboratory, Seattle, WA. Influenza A grown in embryonated chicken eggs was purchased from Virapur, LLC, San Diego, CA.

14.3.3 Lysis methods

The general lysis procedure used in this work is illustrated in Fig. 1C. Bacterial cell suspensions were diluted to OD_{600} = 0.02 in 10 mM Tris, pH 8.0. RSV virion concentration was determined by quantification of genomic RNA prior to dilution in TE buffer (10 mM Tris-HCl, 1 mM EDTA, pH 8.0). For the no-lysis negative control condition, the bacterium or virus was added to the qPCR reaction (described below) without further processing, quantifying the sum of extracellular DNA/RNA and DNA/RNA released by the denaturation step of the qPCR reaction.

For ACP lysis, ACP (20 U/µL, Sigma A3547) in TE buffer + 5% trehalose was added to 0.2 mL polypropylene tubes (Cat #951010006, Eppendorf North America, Hauppauge, NY, USA) and dried in a miVac (Genevac, Stone Ridge, NY, USA) for 1.5 hours. Dried-down tubes were stored in a desiccator (Cat #420721115, Bel-Art Scienceware, Wayne, NJ, USA) at room temperature for 1-15 days before use. Bacterial or viral suspensions (80 µL) were added to the dried ACP pellet to give a final concentration of 0.5 or 1.5 U ACP/µL. After gentle mixing by agitating the tube, the lysis reaction was incubated at 19°C (ambient room temperature) for 2 minutes unless otherwise noted. For incubation temperatures other than 19°C, tubes containing dried ACP and tubes containing cells to be lysed were equilibrated to the noted temperature using a digital heatblock (Cat #97043-610, VWR, Radnor, PA, USA) for 2 minutes before cells

were added to ACP and incubation began. ACP was deactivated by placing the tube in a boiling water bath (measured >95°C) for five minutes, unless otherwise noted. Previously, we have shown that temperatures above 80°C are sufficient for thermal deactivation of ACP used to lyse *S. aureus* cells [176].

Thermal lysis was performed by placing a tube containing cell suspension in a hypotonic buffer (10 mM Tris, pH 8.0) in a boiling (measured >95°C) water bath for five minutes, unless otherwise noted.

Bead beating lysis—used here as a gold-standard, positive control method—was performed by adding 800 µL cell suspension and 0.8 g of 0.1 mm sterile glass beads (Cat #11079101, BioSpec Products, Bartlesville, OK, USA) to a 2 mL screw-top tube (Cat #02-682-558, Fisher Scientific, Waltham, MA, USA). Tubes were agitated at maximum speed using a Mini-BeadBeater-16 (BioSpec Products, Bartlesville, OK, USA) for 3 cycles of 60 seconds on, 60 seconds off. Lysate was separated from the bead slurry by pipetting from above the settled beads. OmniLyse Cell Lysis Kits (Claremont Biosolutions, Upland, CA, USA) were used as directed by the manufacturer, manually drawing 500 µL cell suspension into and out of the device three times, at a rate of 500 µL per 30 seconds, for a total processing time of 1.5 minutes [111]. Construction of the OmniLyse retains glass beads within the bead mill, separating them from the lysate when liquid is ejected from the device. AudioLyse lysis was implemented using a 500 µL cell suspension with 250 mg 0.1 mm sterile glass beads and a ¼" diameter NdFeB spherical magnet (S4, K&J Magnetics, Inc., Pipersville, PA, USA) in a 2 mL screw-top tube as previously described [158]. A 30 Hz sine wave was supplied by an mp3 player (Sansa Clip+ 4 GB, SanDisk, Milpitas, CA, USA) for 10 minutes as previously described. Lysate was separated from the bead slurry by pipetting from above the settled beads and magnet.

14.3.4 Genome quantification

Amplifiable genomic DNA and RNA were quantified using real time quantitative PCR or RT-PCR. *S. aureus* DNA was quantified using the MRSA/SA ELITe MGB *ldh1* assay (ELITechGroup Inc. Molecular Diagnostics, Bothell, WA, USA). The thermal profile used was: 50°C hold for 2 minutes, 93°C hold for 2 minutes, 45 cycles of 93°C for 10 seconds, 56°C for 30 seconds, and 72°C for 15 seconds, ending with a final elongation step at 72°C for 5 minutes. *B. pertussis* DNA was quantified using the assay against IS*481* as described previously [347], substituting the Bioline SensiFAST Probe No-Rox kit (Bioline, Taunton, MA, USA) for the master mix used previously, using the thermal protocol: 95°C hold for 5 minutes, 40 cycles of 90°C for 10 seconds, and 60°C for 20 seconds. *M. marinum* DNA was quantified using a previously described assay against the 23S rDNA region [187], substituting the master mix with the Bioline SensiFast kit, and using the thermal protocol described above for *B. pertussis* quantification. All amplifications were run on a CFX96 (BioRAD, Hercules, CA, USA) and copy number values were generated by the CFX96 machine software from C_t using a standard curve of genomic DNA purified from lysates by ethanol precipitation and quantified using spectrophotometry (Nanodrop 1000, ThermoFisher, Waltham, MA, USA). Amplifiable DNA recovery for each experiment was calculated as a percentage of the copy number measured from the noted control sample.

RSV copy number was determined using the Ultrasense quantitative RT-PCR assay mix (Life Technologies, Carlsbad, CA, USA), the ATCC derived RSV genomic RNA (ATCC, Manassas, VA, USA), and primers and probe sequences published previously [211]. Influenza copy number was determined similarly, using the protocol developed by the UW clinical virology laboratory [355] and influenza A control RNA (a kind gift from PATH, Seattle, WA, USA).

14.3.5 Bacterial RNA quantification

In order to quantify RNA release from lysed bacterial targets, several strategies were employed. First, cells of *S. aureus* or *M. marinum* were lysed as described above, using the BeadBeater, the AudioLyse, ACP at 0.5 U/μL, and a "no-lysis" control (cells incubated in hypotonic 10 mM Tris pH 8.0 at room temperature). Unpurified lysates were then subjected to the following treatments: untreated samples (4 μL) were diluted in 7 μL 10 mM Tris pH 8.0. DNase I treatment consisted of sample (4 μL) combined with 10X DNase I reaction buffer (1 μL), DNase I (1 μL, Amplification Grade, Cat #18068015, ThermoFisher), and water to a volume of 10 μL. After a 15 minute incubation at room temperature (19-21°C), 1 μL 25 mM EDTA was added, and the sample was incubated at 65°C for 10 minutes to inactivate the DNase, as per the manufacturer's instructions. Mock-treated samples were prepared as for DNase-treated samples, substituting water for the DNase I enzyme solution.

Untreated, DNase-treated, and mock-treated lysates were quantified for nucleic acid (DNA + RNA) using the Ultrasense quantitative RT-PCR assay mix. Primers and probes for *S. aureus* and *M. marinum* were as described above for DNA quantification, at concentrations recommended by the Ultrasense manufacturer's protocol. This assay includes SuperScript III Reverse Transcriptase for cDNA generation and Platinum *Taq* DNA Polymerase for DNA amplification. To measure only DNA, the Ultrasense kit was modified by replacing the RT/DNA polymerase Enzyme Mix provided in the kit with Platinum *Taq* DNA Polymerase (Cat #10966018, ThermoFisher), used at 0.1 μL per 20 μL reaction (1 U).

14.3.6 Long-term ACP storage

ACP was dried as described above in a 0.2 mL PCR tube. Dried ACP tubes were stored at room temperature (19-20°C) under uncontrolled humidity for 11 months. Lysis efficiency was

measured by comparison to freshly-resuspended ACP lysis of *S. aureus* cells in Tris buffer, with amplifiable DNA quantified by qPCR, as described above.

14.3.7 Statistics

Statistics were performed using Excel (Microsoft, Redmond, WA, USA). Means and standard deviations were calculated using the AVERAGE and STDEV functions of Excel, respectively, for the array of values generated from at least three independent experiments. Standard error of the mean was calculated by dividing the standard deviation by the square root of n, the number of data points collected. Unless otherwise noted, n = 9 for all data points. P-values were calculated using the Excel TTEST function, assuming a two-tailed distribution and equal variance.

14.4 Results

Several point-of-care-compatible lysis methods were compared by quantifying release of amplifiable DNA or RNA from the chosen representative pathogens. Amplifiable DNA was normalized to the copy number obtained from the bead beating lysis condition (the reference, "gold-standard" method for mechanical lysis of recalcitrant organisms [356]). Table 1 shows that 0.5 U/μL ACP, followed by boiling water thermal deactivation, released amplifiable DNA from both the Gram positive bacterium *S. aureus* (90.4 ± 6.6%, $p=3.6 \times 10^{-10}$ vs. no-lysis control), as expected given previous literature, and from the Gram negative bacterium *B. pertussis* (89.4 ± 5.9%, $p=1.4 \times 10^{-10}$ vs. no-lysis control). ACP lysis did not release significant DNA from the mycobacterium *M. marinum* (0.42 ± 0.1%, p=0.79 vs. no-lysis control). Increasing the ACP concentration did not significantly improve the release of amplifiable DNA from *S. aureus* (p=0.66), or *M. marinum* (p=0.24).

ACP lysis was not predicted to be effective against Gram negative organisms due to the presence of the outer membrane between the environment and the peptidoglycan, which is presumed to be the primary target of ACP. The majority of *B. pertussis* lysis can be attributed to boiling thermal lysis (79.0 ± 5.8% vs bead beating, compared to 3.6 ± 0.6% for no-lysis vs bead beating). This 20-fold increase in DNA recovery by boiling lysis over the no-lysis condition is statistically significant ($p= 1.0 \times 10^{-6}$). Lysis of *B. pertussis* by boiling was not statistically different from lysis using 0.5 U/µL ACP (p=0.22). However, increasing ACP concentration to 1.5 U/µL increased DNA recovery from *B. pertussis* (104 ± 7.4% vs bead beating lysis, compared to 89.4 ± 5.9% in the 0.5 U/µL condition), distinguishing this condition statistically from boiling lysis (p=0.02). Lysis in a boiling water bath with hypotonic solution released seven times less amplifiable DNA from *S. aureus* than ACP/boiling deactivation lysis (12.1 ± 0.6%, $p=2.7 \times 10^{-9}$ vs. 0.5 U/µL ACP condition). Boiling lysis released almost 38 times less amplifiable DNA from *M. marinum* than did bead beating lysis ($p=3.6 \times 10^{-20}$ vs. bead beating condition).

The OmniLyse, which was previously shown to work well on *Mycobacterium bovis* [111], also worked well on *M. marinum* (41.2 ± 3.2%, $p=9.7 \times 10^{-10}$ vs. no-lysis control). The AudioLyse released a significant amount of amplifiable DNA from *M. marinum* (17.2 ± 2.6%, $p=9.8 \times 10^{-6}$ vs. no-lysis control) – approximately half as much as the OmniLyse.

Table 13: Comparison of DNA recovery between point-of-care lysis methods for selected bacterial pathogens. Organisms were lysed using a range of concentrations of ACP, boiling, OmniLyse, or AudioLyse. Results are reported as amplifiable DNA recovered, as measured by qPCR, normalized to bead beating as the control (± standard error of the mean). Sample size was n = 9 for all data points. P-values are given in the main text.

	No lysis	**0.5 U/µL ACP**	**1.5 U/ µL ACP**	**Boiling**	**OmniLyse**	**AudioLyse**
S. aureus	0.81 ± 0.12	90.4 ± 6.6	86.9 ± 4.2	12.1 ± 0.6	74.8 ± 2.5	41.3 ± 4.9
B. pertussis	3.6 ± 0.6	89.4 ± 5.9	104 ± 7.4	79.0 ± 5.8	39.5 ± 7.4	19.9 ± 4.9
M. marinum	0.37 ± 0.2	0.42 ± 0.1	0.30 ± 0.1	2.65 ± 0.2	41.2 ± 3.2	17.2 ± 2.6

ACP lysis released the greatest amount of amplifiable DNA from *S. aureus* and *B. pertussis*, though more ACP was required for ACP to outperform boiling lysis of *B. pertussis.* Amplifiable DNA release from *M. marinum* was low for ACP/boiling, and improved with the mechanical OmniLyse and AudioLyse methods. ACP lysis was investigated further due to its predicted ease of integration into point-of-care devices such as the MAD NAAT device (Figure 92A).

To extend the ACP shelf life in the absence of refrigeration, ACP was dehydrated in the presence of trehalose as a preservative. ACP can be stored in this dry form for up to 11 months without the loss of *S. aureus* lysis activity (106 ± 1.6% amplifiable DNA compared to the freshly-made control, p=0.26, n=2, data not shown). Figure 93A shows that after 2 minutes of ACP treatment at 19°C, 3 minutes of boiling is sufficient for maximum amplifiable DNA release from an *S. aureus* sample. Amplifiable DNA remained above 80% of maximum for boiling times from 3-30 minutes, with only a slight decrease below maximum at 30 minutes (86.8 ± 3.3%, p=0.01). However, a significant amount of amplifiable DNA is produced by the one-minute deactivation as compared to no-boiling deactivation (68.5 ± 2.3%, $p=1.5 \times 10^{-15}$). DNA purified by ethanol precipitation from a no-boiling control resulted in a much lower DNA recovery than from the ACP/boiling condition (9.6 ± 2.4%, $p = 4.1 \times 10^{-5}$ vs ACP/boiling condition, n = 3 data not shown). This suggests that while ACP is an amplification inhibitor, the boiling aspect of the ACP/boiling method is crucial for effective lysis and DNA recovery. Ambient temperature can vary widely in point-of-care settings without climate control, so the effect of temperature on the ACP digestion was quantified. Figure 93B shows that ACP effectively lyses *S. aureus* at a wide range of ambient temperatures.

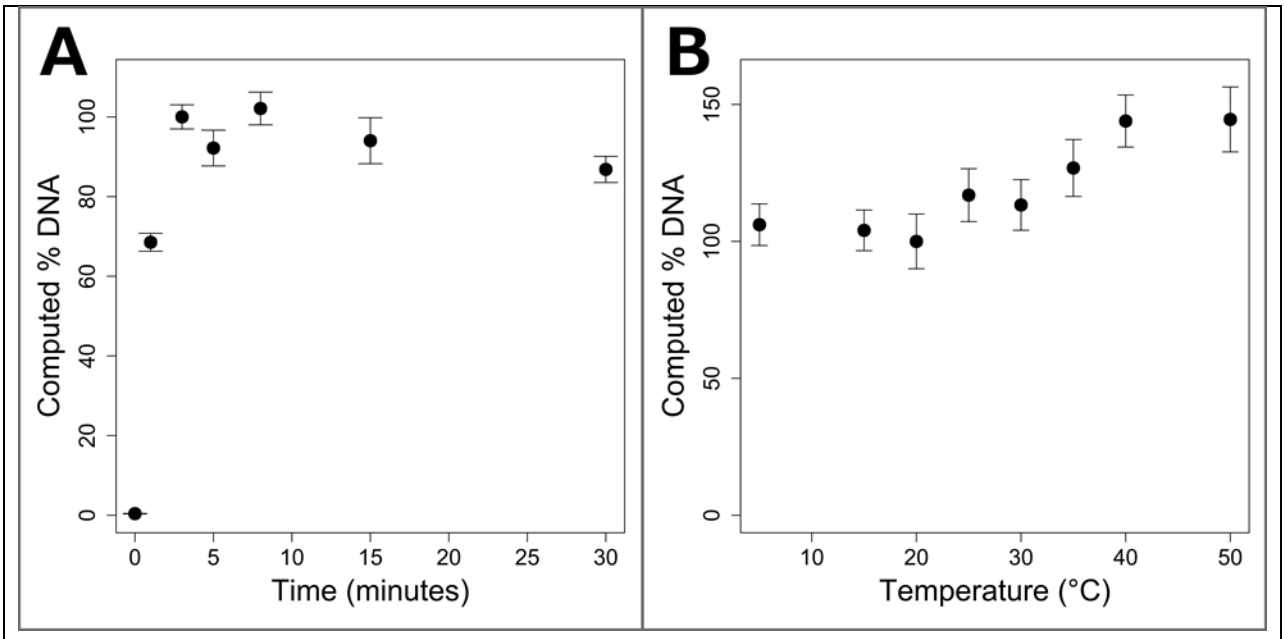

Figure 93: **Robustness of the ACP + boiling method.** A) DNA recovery as function of thermal deactivation time after ACP incubation at 19°C for two minutes. *S. aureus* samples were placed in boiling water for varying periods. DNA yields are reported as qPCR copy number normalized to the three-minute thermal deactivation (mean ± standard error of mean), n = 9. B) DNA recovery as a function of ACP incubation temperature. Incubations were performed for 2 minutes at various temperatures, followed by a 5-minute thermal deactivation in a boiling water bath (measured >95°C). DNA qPCR yields are normalized to the 20°C ACP incubation reported as mean ± standard error of the mean, n = 9. Statistical comparisons are described in the text.

In an effort to understand whether the ACP/boiling method could be applied to samples containing RNA viruses as well as bacteria, this lysis method was performed in the presence of one of two RNA viruses, RSV or influenza A. ACP treatment followed by thermal denaturation was expected to degrade the RNA template, as this was performed without addition of RNase inhibitors. However, quantitative reverse transcription coupled with PCR (qRT-PCR) revealed amplifiable product. When either virus sample was incubated with ACP for five minutes prior to 95°C thermal denaturation, there was significant amplifiable RNA from samples of both viruses (Figure 94). When 10,000 RSV virions (as measured by gRNA copy number of the stock) were treated with 12.5 units of ACP, an average of 7,500 RNA copies were detected in the 95°C denatured sample, representing 75% recovery (Figure 94, $p=3.78 \times 10^{-5}$ compared to no-

deactivation control). Similar recovery was seen for Influenza A, although the copy number was 2.5 times higher. Starting with 270,000 influenza A virions (as measured by gRNA copy number of the stock) and 12.5 units of ACP results in an average of 190,000 RNA copies, or ~70%, after thermal denaturation (Figure 94, $p=8.52 \times 10^{-4}$ compared to no-deactivation control). This result demonstrates that we can use a single lysis approach to identify the presence of both DNA and RNA in a sample.

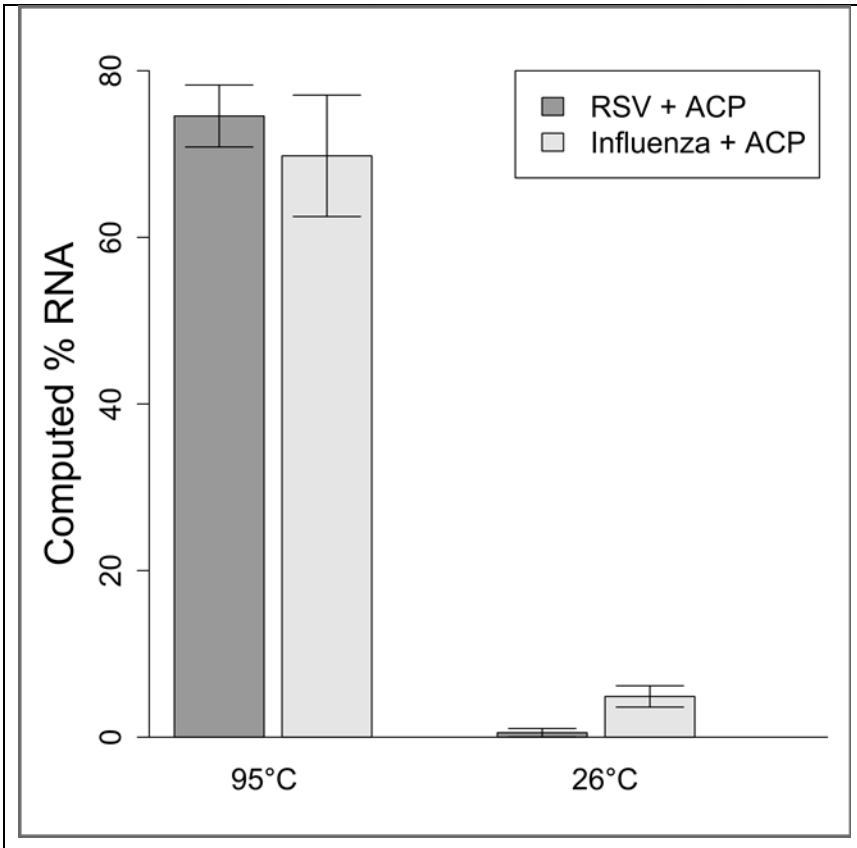

Figure 94: **Comparison of viral RNA recovery in the presence of ACP with and without 95°C thermal deactivation.** Each assay used 12.5 units of ACP with 10,000 RSV virons (as measured by gRNA copies, dark bars) or 270,000 influenza A virions (as measured by gRNA copies, light bars), respectively. Samples were incubated at 95°C or 26°C prior to direct qRT-PCR. Results normalized to input copy number, reported as mean ± standard error, n=3. Statistical comparisons are discussed in the text.

Since RNA was more stable in the presence of these lysis methods than expected, the amount of bacterial RNA released from *S. aureus* or *M. marinum* lysed with ACP, the BeadBeater, the AudioLyse, or a no-lysis control was quantified. Untreated, DNase-treated or mock-treated lysates were measured by qPCR, both in the presence and absence of reverse

transcriptase (RT). In the absence of RT, DNase-treated BeadBeater and ACP lysates for both species contained <1 % as many copies target DNA as the mock-treated lysates. The same low DNA recovery (<1% as many copies DNA as mock-treated) was true of the no-lysis control for *M. marinum*. DNase-treated lysates from the AudioLyse contained 8.6 ± 3.1% (*M. marinum*) or 8.2 ± 2.2% (*S. aureus*) as many copies as the mock-treated lysates. DNase-treated lysates from the *S. aureus* no-lysis control contained 46 ± 6.8% as many copies as the mock-treated lysates., Copy numbers measured in the presence of RT from the DNase-treated condition were adjusted by the copy number measured in the absence of RT (DNA copies remaining), to arrive at RNA copies present. RNA copy numbers were normalized to the bead beating condition, and are shown in Figure 95.

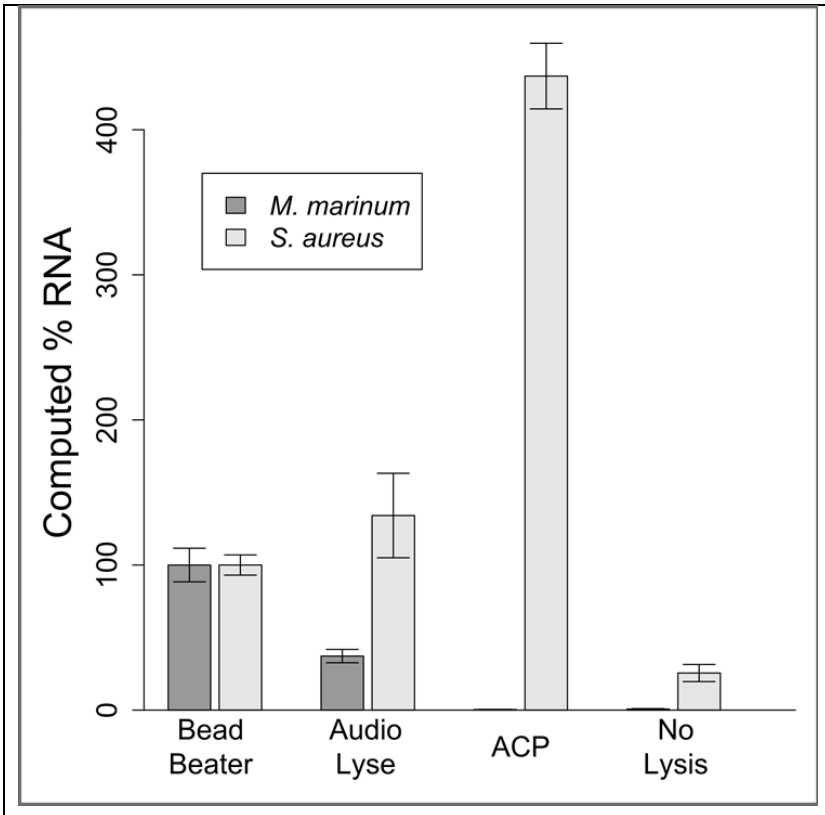

Figure 95: **RNA released from *S. aureus* or *M. marinum* using various lysis techniques.** Cell suspensions were lysed and copy numbers of RNA from *M. marinum* (dark grey bars) and *S. aureus* (light grey bars) were measured. All RNA values were normalized to that species' RNA-from-bead-beating value (set at 100%). Thin bars represent standard error of the mean, n = 9 for all data points, except the *M. marinum* no-lysis condition, where n = 8.

The RNA copy number recovered from AudioLyse-treated *M. marinum* was lower than that recovered from bead beating (37.2 ± 4.6%, p = 0.00012). ACP and no-lysis treatments resulted in very little recovery of RNA from *M. marinum* (0.4 ± 0.2%, $p = 2.1 \times 10^{-7}$ and 0.7 ± 0.3%, $p = 8.0 \times 10^{-7}$ vs bead beating, respectively). RNA copy level recovered from AudioLyse-treated *S. aureus* was roughly equivalent to that recovered from bead beating (134 ± 29%, p = 0.27), while that recovered from ACP lysis was roughly 4 times higher (437 ± 23%, $p = 1.7 \times 10^{-10}$). The no-lysis control for *S. aureus* showed an RNA copy number approximately $1/4^{th}$ as large as bead beating (25.6 ± 6.0%, $p = 4.3 \times 10^{-7}$).

14.5 Discussion and Conclusions

Identifying effective, easy-to-operate, and inexpensive methods of recovering amplifiable nucleic acids from bacteria, viruses and other pathogens in samples is an important step toward improving detection of them at the point-of-care or in the field. The optimum method would balance easy operation by untrained personnel, low cost, no reliance on laboratory equipment, and sufficient release of amplifiable DNA and/or RNA. We performed a head-to-head comparison of several methods of lysis, in order to evaluate their suitability for point-of-care sample preparation in low-resource settings.

In the course of this work, we used bead beating as a gold standard compared to all other methods. Because of the broad range of bacterial types used, we could think of no better common way to ensure disruption of the cell wall and cell membrane. It is possible that the DNA recovery efficiencies of the bead beater differ among the organisms tested. In order to answer this question, one would need to measure accurately the genome copies per colony forming unit (CFU), using the best possible lysis technique for each of the separate organisms, then relate that number to DNA copies per CFU from bead beating.

ACP lysis followed by heating to >95°C by boiling is effective for more bacteria and viruses than expected. Though ACP lysis has previously been shown effective for Gram-positive organisms, especially *S. aureus*, it was unknown whether the enzyme would work on a Gram-negative organism. Gram-negative bacteria like *B. pertussis* have an outer membrane that should protect the peptidoglycan cell wall from the peptidases that are the major components of ACP [343]. ACP/boiling deactivation lysis of *B. pertussis* using 0.5 U/µL ACP did not significantly increase amplifiable DNA recovered over the boiling lysis condition. However, increasing ACP concentration to 1.5 U/µL did result in a significant increase in amplifiable DNA recovery, suggesting that ACP participates in lysing *B. pertussis* when used at a high enough concentration. As ACP is a cocktail of enzymes including proteases [344], outer membrane perforation by ACP proteases may allow exposure of peptidoglycan to ACP peptidases, which degrade the bacterial cell wall and allow increased lysis. Increased lysis over the boiling condition caused by a sufficiently high concentration of ACP was also observed in preliminary experiments on the Gram-negative bacterium *Salmonella typhi* (data not shown).

The ACP plus boiling lysis protocol provides effective lysis from Gram-positive and Gram-negative bacteria over a range of temperatures and thermal deactivation times. As long as one can provide a thermal denaturation step >80°C (such as by boiling water), for at least 3 minutes, the method can release amplifiable DNA. The ACP incubation step can also be performed at a broad range of ambient temperatures. We would not have expected an enzyme from a mesophilic organism (*Achromobacter lyticus*) to be active at 5°C, as seen in Figure 93B. It is possible that the ACP enzymes retain some activity at 5°C, or that the transient intermediate temperatures while heating the sample to 95°C give the enzymes sufficient time to do their work. We do not have data showing exactly when in the process nucleic acids released or degraded.

Our group has shown thermal deactivation with a standalone disposable heater, and demonstrated ACP plus boiling amplifiable DNA recovery from *S. aureus* in the presence of patient nasal samples, confirming that this method can still function in the presence of a clinical patient sample [176]. We have also integrated an ACP plus boiling lysis into a standalone sample-to-result NAAT[247].

Based on work done with a similar organism, *Mycobacterium smegmatis* [350], we did not expect ACP to be effective for *M. marinum* lysis. This proved true in our hands, and we conclude that for *Mycobacteria*, mechanical methods such as OmniLyse and AudioLyse are the preferred point-of-care-compatible lysis techniques. The OmniLyse is difficult to multiplex (one pair of hands can only process one sample every 2 minutes or so) compared to the other methods. The AudioLyse does not require user intervention during the lysis operation, and may prove simpler to integrate into point-of-care diagnostic devices [158]. The AudioLyse was less efficient at lysing *M. marinum* than either the Bead Beater or the OmniLyse device. The Bead Beater is a large and powerful instrument running on mains electricity. The OmniLyse is battery powered, but uses a disposable rotary motor to agitate glass beads in a bead mill. Additionally, the entire sample is moved through the OmniLyse at a slow rate, giving all bacteria in the sample ample exposure to the site of grinding. We have observed mixing in the AudioLyse device, bringing portions of the sample into the area where grinding and lysis occurs, but we have performed only preliminary optimization of the mixing.

We have demonstrated that RNA can be amplified from minimally-processed virus-containing samples. Boiling virus releases RNA from within the viral capsid, making the RNA accessible to amplification enzymes. This result was surprising because RNA is believed to be much more thermally labile than DNA, and great care is generally taken when preparing RNA

samples in the clinic and laboratory settings [357], [358]. However, should the sample be moved quickly from lysis to amplification and detection, as could be the case in an integrated device, RNA degradation is less extensive than anticipated. Possibly, the boiling lysis processing inactivates endogenous RNases; this merits further investigation, as RNases are typically considered heat-tolerant. Much of our knowledge of RNase activity is derived from commonly-used RNase A, thermal denaturation of which is reversible [359]. We cannot rule out the possibility that proteases found in the ACP cocktail inactivate RNases, providing greater stability to the target RNA.

The AudioLyse device was used to prepare amplifiable RNA from two bacterial species as well. We noted that the AudioLyse performed comparably to the BeadBeater in RNA recovery from *S. aureus* and about 1/3rd as well as the BeadBeater in RNA recovery from *M. marinum*. This difference in performance between the two organisms could be explained by the difference in lysis efficiency, as was observed for DNA in Figure 1. There is a 4-fold difference in RNA recovery from *S. aureus* between the ACP/boiling condition and the BeadBeater condition, in contrast to the rough equivalence in DNA recovery. This result suggests that recovery of RNA from the BeadBeater is lower than the total number of RNA molecules present within the cells. This loss is perhaps due to destruction of RNA by elevated temperature in the BeadBeater. This highlights the potential importance of icing steps between bead beating cycles when targeting RNA for isolation. While the AudioLyse is half as good at releasing DNA from *S. aureus* as ACP/boiling, it is approximately 1/4th as good at releasing RNA. This two-fold difference between the DNA release efficiency and the RNA release efficiency may indicate some RNA destruction in the AudioLyse, but not to as great an extent as seen in the BeadBeater. Another explanation for the loss of RNA to both the AudioLyse and the BeadBeater could be the

differential adsorption of DNA and RNA to the silica beads [360]. Future work on RNA sample preparation using the AudioLyse will address methods to minimize this possible adsorption.

We have quantitatively compared several simple point-of-care-compatible lysis methods capable of releasing amplifiable nucleic acids from a wide range bacterial and viral pathogens. While the organisms chosen were all human respiratory pathogens or models thereof, their structural characteristics are different enough that we anticipate these results will be broadly applicable to non-pathogenic targets as well.

The methods used here do not inherently introduce amplification inhibitors not already in the samples, or deactivate added inhibitors (ACP enzymes) prior to amplification, and may allow us to move point-of-care technologies into the field more quickly than adoption of conventional laboratory methods or *de novo* development of other lysis techniques. It is inevitable that patient samples will introduce amplification inhibitors not assayed here. However, our group has already shown DNA detection of MRSA from ACP/boiling lysed patient nasal swab samples in the absence of purification [176]. We have also integrated this technique into a standalone sample-to-result NAAT[247]. For more challenging samples, such as blood and urine, we are developing paper network technologies to quickly and simply purify nucleic acids [159]. It is our hope that others may investigate the applicability of these lysis methods to their own microbial detection processes, whether for POC use or not. We have also shown a framework for considering what makes a lysis technique inherently point-of-care-compatible. We suggest that this or similar frameworks be used when designing sample preparation for diagnosis at the point-of-care. Coupling the sample preparation methods identified by this framework with low-power or power-free disposable amplification and detection devices could rapidly change how we diagnose disease in low-resource settings.

14.6 Acknowledgments

Our thanks to Nuttada Panpradist, Samantha Byrnes, and Alec Wollen of UW Bioengineering for initial work and helpful discussions. Thanks also to Walt Mahoney, Nicolaas Vermeulen, Boris Alabyev and Yevgeniy S. Belousov from ELITechGroup Inc. Molecular Diagnostics for supplying qPCR reagents. We thank our other collaborators at ELITechGroup Inc., at GE Global Research, and at PATH for their feedback and advice, as well as their generous donation of influenza A RNA. Thanks to the remaining members of the Yager Lab and the Lutz Lab at University of Washington. Finally, thanks to Claremont BioSolutions for their generous donation of a portion of the OmniLyse Lysis devices used for this work.

Heiniger, Buser, Zhang, Lutz and Yager were supported by DARPA DSO/BTO HR0011-11-2-0007, awarded to Yager. Mireles was supported by the Louis Stokes Alliance for Minority Participation (NSF #1410465). Ladd was supported by NIH 1 R01 AI 096184-01 awarded to Yager.

15 Appendix: A versatile valving toolkit for automating fluidic operations in paper microfluidic devices

Bhushan J. Toley, Jessica A. Wang, Mayuri Gupta, Joshua R. Buser, Lisa K. Lafleur, Barry R. Lutz, Elain Fu and Paul Yager

This appendix is taken in a largely unmodified form from the manuscript[154]. I would like to thank primary author Dr. Bhushan Toley and my other coauthors for involving me in this work.

15.1 Abstract

Failure to utilize valving and automation techniques has restricted the complexity of fluidic operations that can be performed in paper microfluidic devices. We developed a toolkit of paper microfluidic valves and methods for automatic valve actuation using movable paper strips and fluid-triggered expanding elements. To the best of our knowledge, this is the first functional demonstration of this valving strategy in paper microfluidics. After introduction of fluids on devices, valves can actuate automatically after a) a certain period of time, or b) the passage of a certain volume of fluid. Timing of valve actuation can be tuned with greater than 8.5% accuracy by changing lengths of timing wicks, and we present timed on-valves, off-valves, and diversion (channel-switching) valves. The actuators require ~30 μL fluid to actuate and the time required to switch from one state to another ranges from ~5 s for short to ~50 s for longer wicks. For volume-metered actuation, the size of a metering pad can be adjusted to tune actuation volume, and we present two methods – both methods can achieve greater than 9% accuracy. Finally, we demonstrate the use of these valves in a device that conducts a multi-step assay for the detection

of the malaria protein *PfHRP2*. Although slightly more complex than devices that do not have moving parts, this valving and automation toolkit considerably expands the capabilities of paper microfluidic devices. Components of this toolkit can be used to conduct arbitrarily complex, multi-step fluidic operations on paper-based devices, as demonstrated in the malaria assay device.

15.2 Introduction

Paper microfluidic devices enable the controlled movement of microliter quantities of fluids without pumps. Fluids in these devices move by wicking action, *i.e.*, capillary forces generated by the substrate porous materials. Because they do not require electricity or permanent instruments to operate, paper microfluidic devices present a promising platform for designing portable, low-cost, technically simple biochemical sensors[11], [66], [77], [361]. They provide an opportunity to conduct healthcare diagnostic assays in remote and low-resource settings, where constant electric supply and maintenance of sophisticated instruments is a challenge[312]. Several paper-based devices have been designed for conducting colorimetric analytical chemistries[40], [362]–[365] and lateral flow immunoassays[366]–[369]. The capabilities of paper microfluidics were enhanced by two major developments in the field – μPADs (microfluidic paper-based analytical devices) and 2DPNs (two-dimensional paper networks). μPADs, introduced by the Whitesides group in 2008, are 2D and 3D paper devices that distribute fluids from a common source to multiple detection zones and can be used for conducting multiplexed colorimetric assays[66], [77], [79], [80]. 2DPNs, introduced by our group in 2010, can be used to flow multiple fluids sequentially to a detection zone and enable conducting highly sensitive, signal-enhanced immunoassays in paper-based devices, thus transcending the

capabilities of conventional lateral flow immunoassays[88]–[93], [95] (here the term ‘paper’ is broadly used to represent porous materials, including nitrocellulose).

A major milestone in the development of any microfluidic platform will be when it can enable conducting a complete ‘sample-in-answer-out’ (SIAO) type diagnostic test in a portable device operable by an untrained user. SIAO tests typically involve multiple steps to carry out processes such as sample preparation, assay chemistry, and colorimetric detection. The flow control and automation capabilities of paper microfluidic devices are currently limited and such multi-step SIAO assays have not yet been conducted. As the flow-control capabilities of paper microfluidic devices improve, more complex, multi-step assays can be conducted. There is dire need of such low-cost technologies for conducting diagnostic tests in limited resource settings[370]. Currently, automatic multistep tests can only be conducted in expensive instruments, usually only available in sophisticated laboratories.

Valves are fundamental for enhancing the fluidic capabilities of any microfluidic platform. In paper microfluidic devices, valving is a challenge because valves must operate in absence of instrumented controllers and actuators. Several innovative strategies have been developed for paper microfluidic valving. Here, we refer to ‘valves’ as any method that can be used to control the flow rates of fluids in paper devices. Valves developed for paper microfluidics can be broadly classified into three categories based on the method used to control flow rates: a) those that use device geometry alone, b) those that make use of chemicals in the flow path, and c) those that use mechanical means to connect or disconnect channels. A brief review of these valving methods is presented next.

The simplest geometry-based flow control strategy is changing the width of channels[88], [89], [95]. Another method is changing the shape of a downstream wicking region[129]. Geometry-based methods of shutting flow off after a programmed volume of fluid flow have been developed. One method used source pads of different sizes that released a fixed volume of fluid[91], [93]. Another design used vertical paper legs of different lengths that disconnected from a fluid reservoir after passage of fixed fluid volumes[90]. Controlled flow-delay lines were created by using pads of porous materials as shunts[156]. Valves in the second category make use of chemicals in the flow path to alter flow rates. Controlled delays in fluid flow were obtained by depositing different amounts of sugar on paper channels[219]. Solid sugar blocked flow and flow resumed after sugar dissolved. Complementary to this, controlled flow shut-off was demonstrated by using dissolvable sugar[371] and dissolvable polymeric[372] bridges. In both cases, fixed fluid volumes flowed across the sacrificial bridges. Paraffin wax was used in one demonstration to alter the rate of fluid flow from a source to multiple target regions on a paper device[218]. Chen *et al.* developed paper microfluidic diodes that made use of surfactant to bridge a hydrophobic gap in the flow path[220], [373]. In another case, flow rate was controlled by electrowetting of a dielectric deposited on paper[374]. The third category of paper microfluidic valves involves mechanical means to connect or disconnect channels. Several of these require manual actuation[80], [375]–[377]. In one design, valves were actuated by electromagnets in response to the arrival of fluid at a certain location on the device[376].

In this article, we present a new strategy of valving and programming automatic valve actuation in paper microfluidic devices and demonstrate how it can be used to design a SIAO protein detection device that can be operated by an untrained user. Although some aspects of the valving strategy were presented in patents published in the early 1990's[378]–[380], the work

was apparently not needed for commercial lateral flow products at the time and was neither developed nor widely known in academia. Over the last few years, we have developed valving methods using a related strategy and have designed multiple functional valves. To the best of our knowledge, these are the first demonstrations of functional paper microfluidic valves using this strategy. The work described here was conducted in the context of two projects aimed at developing low-cost, rapid and sensitive infectious disease diagnostics using paper: one based on nucleic acid amplification and the other based on protein binding. Both projects use the wicking action of paper-like materials to move fluids with minimum ancillary equipment and conduct SIAO-type multi-step diagnostic assays in devices that can be operated by untrained users. In contrast to most other valves that enable a single fluidic operation, we present an entire toolkit of paper microfluidic flow-control tools that can be used to design multiple types of valves, *i.e.*, on-switches, off-switches, and flow-diversion switches. We also present a strategy to actuate these valves automatically after a chosen period of time or after the passage of a chosen volume of fluid. The valves fall under the category of mechanical actuation and use fluid-activated expansion of absorbent materials for actuation (expandable elements activated by pH of process fluids have previously been used for valving in conventional microfluidic devices[381], [382]). The design of these valves and all devices presented in this article is motivated by previously developed 2DPN devices in our group. The primary difference compared to 2DPNs is that, whereas all channels in a 2DPN reside on a single plane and stay connected throughout a test, the channels of devices presented here are placed at different heights and connect or disconnect during the course of the test, which makes these devices three dimensional. Three highly desirable characteristics of these valves are i) they do not require batteries or electricity to operate, ii) they do not introduce chemicals in the flow path, and iii) their actuation can be pre-

programmed so that user intervention is not required. Because it enables automation of multiple types of valves using a common set of fabrication processes, this toolkit enhances the capabilities of paper microfluidic devices and enables conducting SIAO tests in paper microfluidic devices. It is noteworthy that the initial patents on this core technology have now expired and these valves are available for use by all.

15.3 Results and discussion

15.3.1 Valving concept and classification of valves and actuation methods

The fundamental mechanism of valving utilized here is the displacement of one end of paper channels causing connection or disconnection with other channels, triggered by the arrival of fluid at the actuators. Actuation can be automated by designing geometries that control the arrival of fluid to the actuators. Expandable absorbent materials, such as hydrogels, sponges, or other porous materials (such as cellulose) constitute one class of actuators. Ideal actuators would be those that expand reproducibly and fast and have a high ratio of actuation displacement to volume of actuation fluid. Here, we tested two materials as actuators – compressed cellulose sponges and sodium polyacrylate (SP; a superabsorbent hydrogel used in diapers). We successfully built valves with both actuators. The expansion of compressed sponges was found to be faster and more reproducible than SP. All valves illustrated in this article use compressed sponges as actuators. For a comparison of the performance of sponges with SP, see ESI sections I and II[154].

The different types of valves presented here can be classified into two categories: those that can be programmed to actuate after a fixed period of time (branch A; Figure 96) and those that can be programmed to actuate after the passage of a fixed volume of fluid (branch B; Figure 96). These two types of valves use different fluid sources for actuation. Devices with timed

valves contain a timing fluid that flows in the timing channels, which is isolated from the process fluid that flows in the flow channels. Timing is controlled by the shape and length of the timing channel. On the other hand, volume metered valves are designed specifically to meter the flow of a process fluid. This is achieved by diverting the process fluid to a metering pad, which is connected to actuators. These valves do not require a separate actuation fluid. Three types of timed valves are presented: on-switches, off-switches, and diversion-switches (branches A1, A2, and A3, respectively; Figure 96). As illustrated in branches A1–A3 (Figure 96), when actuated, on-switches start flow, off-switches stop flow, and diversion-switches divert flow from one channel to another. The most practical application of an active volume-metered valve is a diversion-switch (volume-metered off-switches such as dead-end channels and limited volume fluid sources can be constructed in passive devices; volume-metered on switches cannot be constructed because there must be fluid flow before valve actuation). Two different designs of volume metered diversion switches are presented. As illustrated in branch B, Figure 96, both methods divert fluid flow from flowing into a metering pad to flowing downstream in the device. In one method, a paper channel is displaced to disconnect from the metering pad (branch B1; Figure 96), and in another method, the metering pad is displaced to disconnect from the paper channel (branch B2; Figure 96).

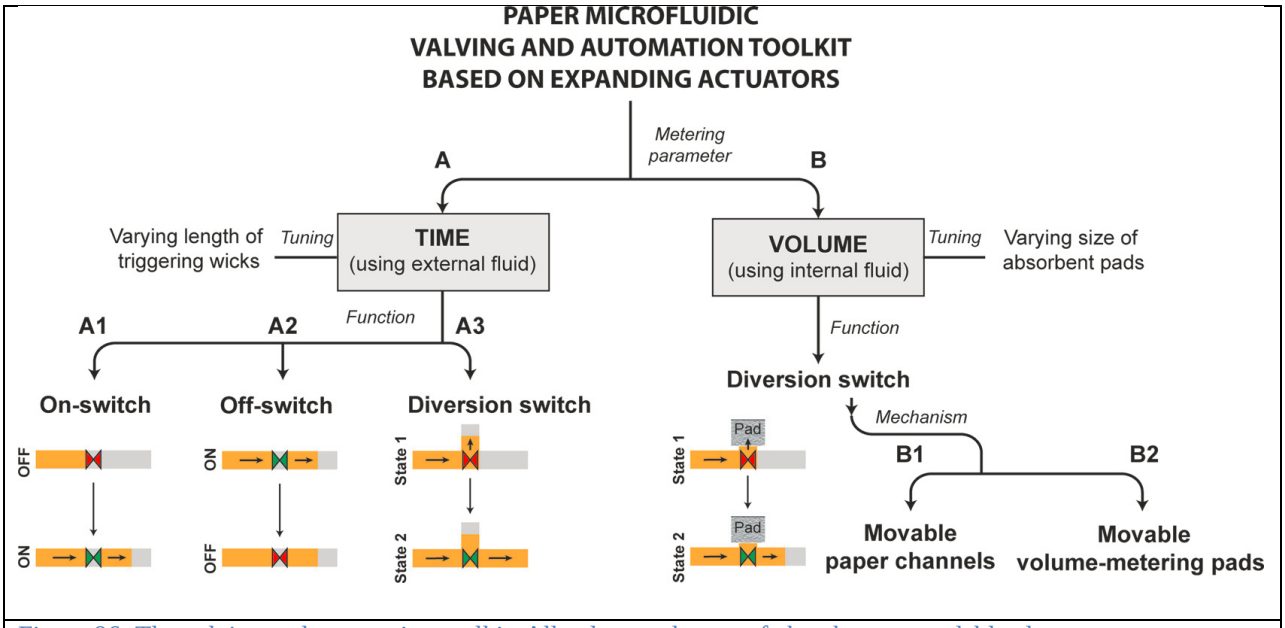

Figure 96: The valving and automation toolkit. All valves make use of absorbent expandable elements as actuators. Valves can be broadly classified into two categories – A. Those that actuate after a fixed period of time and make use of an external fluid for actuation, and B. Those that actuate after a fixed volume of fluid flow and make use of an internal process fluid for actuation. Time-metered valves consist of A1. On-switches that start fluid flow between two channels, A2. Off-switches that stop fluid flow between two channels, and A3. Diversion-switches that divert fluid flow from one channel to another. Volume-metered valves demonstrated here are diversion switches that use two different mechanisms: B1. Moving channels with fixed volume-metering pads, and B2. Fixed channels with moving volume metering pads.

15.3.2 Time-metered valves

Three types of valves that can be programmed to actuate after a certain period of time were designed. The valves are demonstrated here in absence of programmed timing first, focusing on the valving mechanism. An on-switch (branch A1; Figure 96) starts fluid flow when actuated. It consists of two collinear flow channels, channel A and channel B, placed at different heights with one end overlapping, but not touching (Figure 97A). Channel A is a cantilever channel, permanently secured to the surface at its left end, placed at a lower height than channel B. There is no initial contact between the two channels. The right end of channel A is attached to an impermeable fluid barrier, which is attached to the surface over a square cavity. This bond is not

permanent; it breaks when the actuator expands. The purpose of the bond is to secure the end of channel A before valve actuation. The cavity contains a compressed sponge actuator (Figure 97A). An actuation channel connects to the actuator from below (Figure 97A). When the actuating fluid reaches the actuator, the actuator expands, lifts the right end of channel A, and establishes its contact with channel B (Figure 97A; bottom panel). The impermeable barrier ensures that actuating fluid does not enter the flow channels.

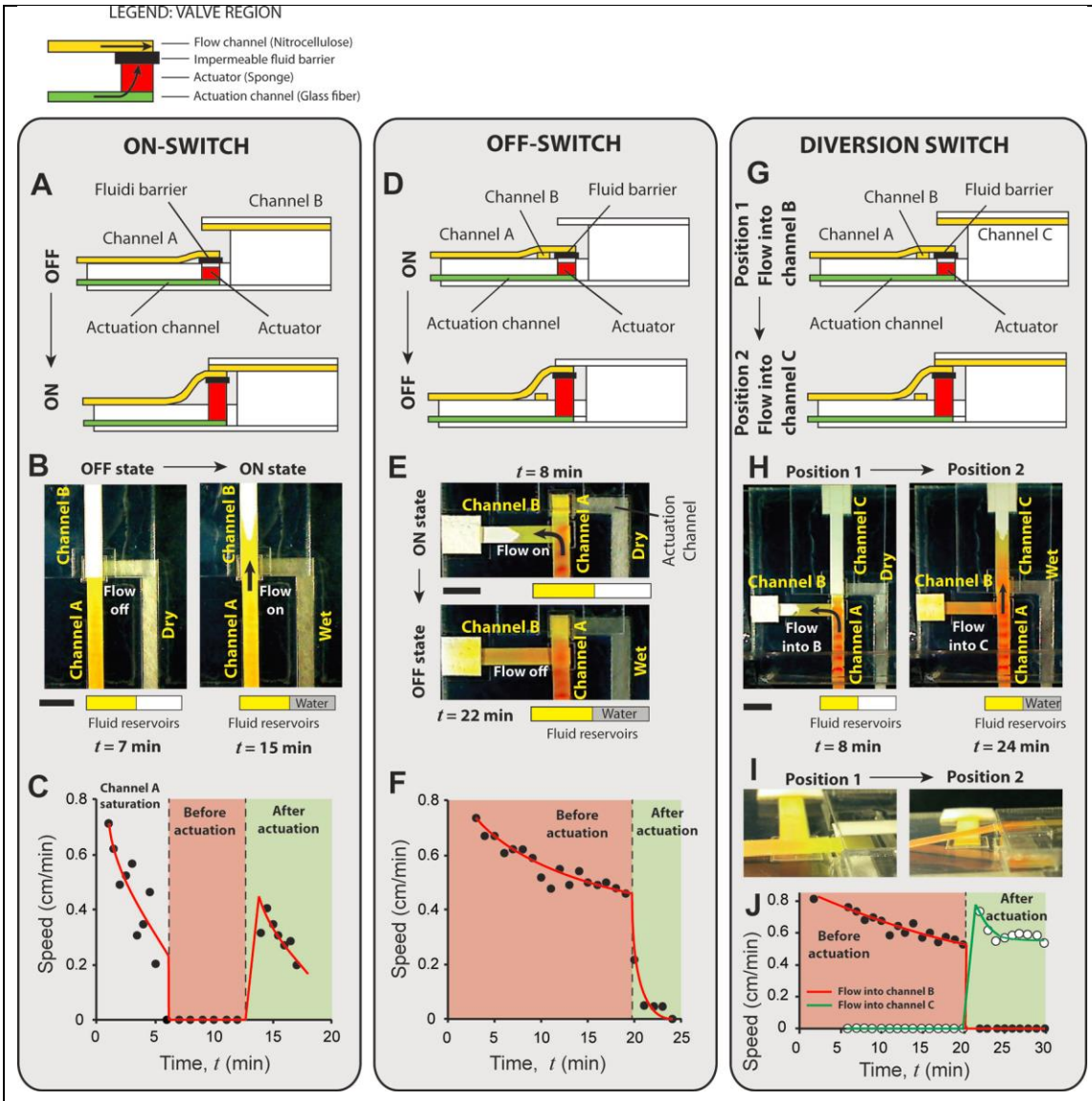

Figure 97: The three types of time-metered valves – on-switch (A–C), off-switch (D–F), and diversion switch (G–J). These valves consist of nitrocellulose flow channels (containing yellow fluid) and glass fiber actuation channels (containing water), separated by an impermeable fluid barrier (see legend). Water is added to the actuation channels manually after a certain period of time to actuate valves. A. Schematic of an on-switch. It consists of two flow channels, A and B, placed at two different levels. Upon actuation, one end of channel A lifts up to connect to one end of channel B. B. Images of the on-switch before and after actuation. C. Speed of the fluid front in the flow channels as a function of time shows the step increase in the flow speed on valve actuation. D. Schematic of an off-switch. It consists of two perpendicular flow channels, A and B, placed on one level and initially connected at one end. Upon actuation, channel A lifts up to disconnect from channel B. E. Images of the off-switch before and after actuation. F. Flow rate (linear velocity) as a function of time, as tracked by an electrochemical band marking setup, shows a rapid drop on valve actuation. G. Schematic of a diversion switch. It is a combination of an on-switch and an off-switch that diverts fluid flow from channel B to channel C. H. and I. Images of the diversion-switch before and after actuation. J. Flow rate (linear velocity) as a function of time shows a sharp drop for channel B and a sharp rise for channel C on valve actuation. All scale bars are 1 cm. In C, F, and J, curves were added to guide the eye.

We present one specific implementation of an on-switch in which channels A and B are made of 4.5 mm-wide plastic backed nitrocellulose (Figure 97B; Movie S1 in ESI[154]). The height difference between the channels is 1.5 mm, and they are oriented such that their nitrocellulose sides face each other. The actuation channel is also 4.5 mm wide and is composed of high permeability glass fiber. Glass fiber channels were selected over nitrocellulose or cellulose (filter paper) channels because they delivered fluid to the actuator faster, which enabled faster valve actuation. The actuator is a 4.5 mm square piece of compressed cellulose sponge, 2.3 mm tall, placed in a 5.6 mm square cavity, 2.5 mm deep. Channel A and the actuation channel were connected to fluid reservoirs. When a yellow process fluid (1 mg mL−1 solution of phenol red at pH 8) was introduced in channel A at time t = 0, it flowed toward the end of the channel until the channel was saturated (Figure 97B; left panel). As long as the actuation channel was dry, the sponge remained compressed, and there was no further flow in the flow channels (Figure 97B). Figure 97C shows the speed of the fluid front as a function of time. The reduction of flow rate from 0–5 minutes is a characteristic of wet-out flow, during which, fluid is imbibed into paper channels, and is explained by the Lucas–Washburn equation[88], [127], [383], [384], according to which the speed of the fluid front is related to time, t, as $t^{-0.5}$. In this example, channel A saturated at around 6 minutes after introduction of the process fluid, at which time, the flow rate became zero (Figure 97C; pink zone). The valve was held in this position for 5 minutes and then water was introduced in the actuation channel. The water reached the actuator at ~12.5 minutes and actuated the valve. Upon actuation, process fluid started flowing from channel A to channel B (Figure 97B; right panel). The step change in flow rate after valve actuation is seen in Figure 97C (transition from pink to green zone). The subsequent reduction in flow rate is due to wet-out flow (Figure 97C; green zone). The actuators are fast and reproducible. The time

required for the process fluid to enter channel B after the actuating fluid reached the actuator was 3–6 seconds (N = 6). The average time required for the process fluid to flow 1 cm into channel B after actuating fluid reached the actuator was 1.9 minutes with a standard deviation of 9 seconds (coefficient of variation (CV) = 8%; N = 6). This measurement excludes the variation in time required for the actuating fluid to flow through the actuation channel, thus, is a measure of the reproducibility of the actuator alone. Actuation time of these valves can be further reduced by reducing the size of the actuator, which will reduce the amount of fluid required for actuation. However, there is a lower limit on the size of the actuator below which the actuator may not generate enough force. While designing these valves, it must be ensured that an excess volume of actuation fluid is available because sponge actuators cease to expand if the supply of fluid is stopped prematurely.

The next type of valve is an off-switch (branch A2; Figure 96), which stops flow when actuated. It consists of two perpendicular channels, channel A (cantilever style) and channel B (Figure 97D). The two channels are placed at the same level. Where they cross, channel A makes contact with channel B placed under it, and extends slightly over channel B (Figure 97D). The overhanging section of channel A is attached to an impermeable fluid barrier, which is attached to the surface over a square cavity containing the actuator (Figure 97D). An actuation channel connects to the actuator from below. Upon actuation, the right end of channel A is lifted up and disconnected from channel B (Figure 97D; bottom panel). Similar to the on-switch demonstrated above, an off-switch can be constructed with two plastic-backed channels of nitrocellulose with their nitrocellulose sides facing each other. However, in order to use an electrochemical band marking setup18 to track fluid velocity over time, the top surface of channel A needed to be exposed. To satisfy this, in this implementation channel A was constructed of 4.5 mm wide

unbacked nitrocellulose (Movie S2 in ESI[154]). All other materials and dimensions were identical to the on-switch example. When a yellow process fluid was introduced into channel A, it flowed through channel A into channel B (Figure 97E; top panel). Flow was sustained by a cellulose wicking pad attached to the end of channel B (Figure 97E). Figure 97F shows the linear velocity of the fluid as a function of time as measured by tracking colored bands generated by the band-marking setup. The reduction in speed expected for Lucas–Washburn flow can be seen from 0–20 minutes (Figure 97F; pink region). After ensuring sustained flow from channel A to channel B (Figure 97F; pink zone), water was added to the glass fiber actuating channel at 19 minutes and reached the actuator at 20 minutes. Valve actuation stopped the flow of process fluid (Figure 97E; bottom panel and F; green zone). In all 5 repetitions, the velocity in channel A dropped to below 10% of the velocity at the time of actuation within 4 minutes. The slow bleed of flow after valve actuation was caused by unsaturated zones (dead volume) in channel A downstream the region where it crossed channel B and occurred after the two channels had disconnected. An alternate design, in which, the overhanging part of channel A is eliminated by moving the actuator upstream the intersection of channels, can eliminate this dead volume. The two channels can also be placed collinearly in this alternate design. However, we found that the design presented here facilitates better initial contact between channels.

A flow-diversion switch (branch A3; Figure 96) is a combination of an on-switch and an off-switch and diverts fluid flow from one channel to another when actuated. It consists of three channels – a source channel A (cantilever style), and two sink channels, B and C (Figure 97G). The design of this valve is identical to the off-switch, with the addition of a third channel, channel C (Figure 97G). Expansion of the actuator causes channel A to disconnect from channel B and connect to channel C (Figure 97G; bottom panel). Because channel A must make contact

with both channel B placed under it, and with channel C placed above it, it is imperative that channel A be made of an unbacked material. In the example presented here, channel A is made of unbacked nitrocellulose, while channels B and C are made of plastic-backed nitrocellulose, oriented such that their nitrocellulose sides face channel A (Movie S3 in ESI[154]). All other materials and dimensions are identical to the off-switch example presented above. When a yellow process fluid was introduced in channel A, it flowed through channel A into channel B, but not into channel C (Figure 97H; left panel). Water was then introduced into the actuation channel and reached the actuator at 20 minutes. After valve actuation, fluid stopped flowing into channel B and started flowing into channel C (Figure 97H; right panel). A representative side view of the valve shows the displacement of channel A between positions 1 and 2 (Figure 97I). The electrochemical band marking setup was used to measure fluid linear velocities. The step changes in flow rates between the two valve positions are seen in Figure 97J – flow rate in channel B drops to zero and flow rate in channel C rises from zero to a higher rate on valve actuation.

15.3.3 Programming timing of valve actuation

Time-metered valves can be programmed to actuate automatically by controlling the time at which actuation fluid arrives at the actuators, for example, by using serpentine actuation channels of different lengths. In these designs, fluids are simultaneously introduced into the flow channels and the actuation channels of valves. This simplifies the operation of such devices to a single user step of initial fluid addition. Figure 98A shows the automatic actuation of an on-switch with a pre-programmed time delay (Movie S4 in ESI[154]). The on-switch was constructed similar to the on-switch in Figure 97B, but with a 2.9 mm-wide serpentine glass fiber actuation channel (Figure 98A). A yellow fluid was introduecd in a reservoir at time, t = 0, which initiated simultaneous flow of the fluid in channel A and the actuation channel (Figure 98A; 1.5

min; note that the fluid appears darker in the thicker glass fiber channels compared to the nitrocellulose channels). Process fluid reached the end of channel A at 4.3 minutes and stopped (Figure 98A; 4.3 min). Note that fluid flowed faster through the actuation channel compared to the flow channel because of different material properties, for example, higher permeability of the actuation channel compared to the flow channel. At 10 minutes, the actuation fluid reached the actuator (Figure 98A; 10 min) and actuated the on-switch. At 13.5 minutes, the process fluid front can be seen in channel B (Figure 98A; 13.5 min). In 5 replicates of this design, the on-switch actuated at a mean time, t = 10.2 minutes, with a standard deviation of 42 seconds (CV = 6.9%; N = 5). Timed and reproducible valve actuation can thus be achieved. One implication of increasing the length or decreasing the width of actuation channels is that it increases the resistance imposed on the actuation fluid. This decreases the rate at which fluid is delivered to the actuators, which decreases the rate of their expansion. In these valves, the time required for fluid to enter channel B after the actuation fluid reached the actuators was in between 30–50 seconds, which was greater than 3–6 seconds for valves shown in Figure 97B. Assuming an infinite supply of fluid, valve actuation time can be tuned by changing the length of actuation channels. In order to determine the tunability and reproducibility of timing that can be achieved using glass fiber actuation channels, the time, tdelay, required for fluid to flow through different lengths, L, of glass fiber actuation channels was measured (Figure 98B). For five different channel designs, A–E (Figure 98B), time delays ranging from 4.1 min to 23.8 min were achieved with better than 8.5% accuracy (except design A; Figure 98B). See ESI† section IV[154] for details. Note that delays of the order of tens of minutes are necessary for conducting nucleic acid amplification assays[385] or protein detection assays requiring sequential delivery of multiple reagents[93], as we demonstrate below in an assay device.

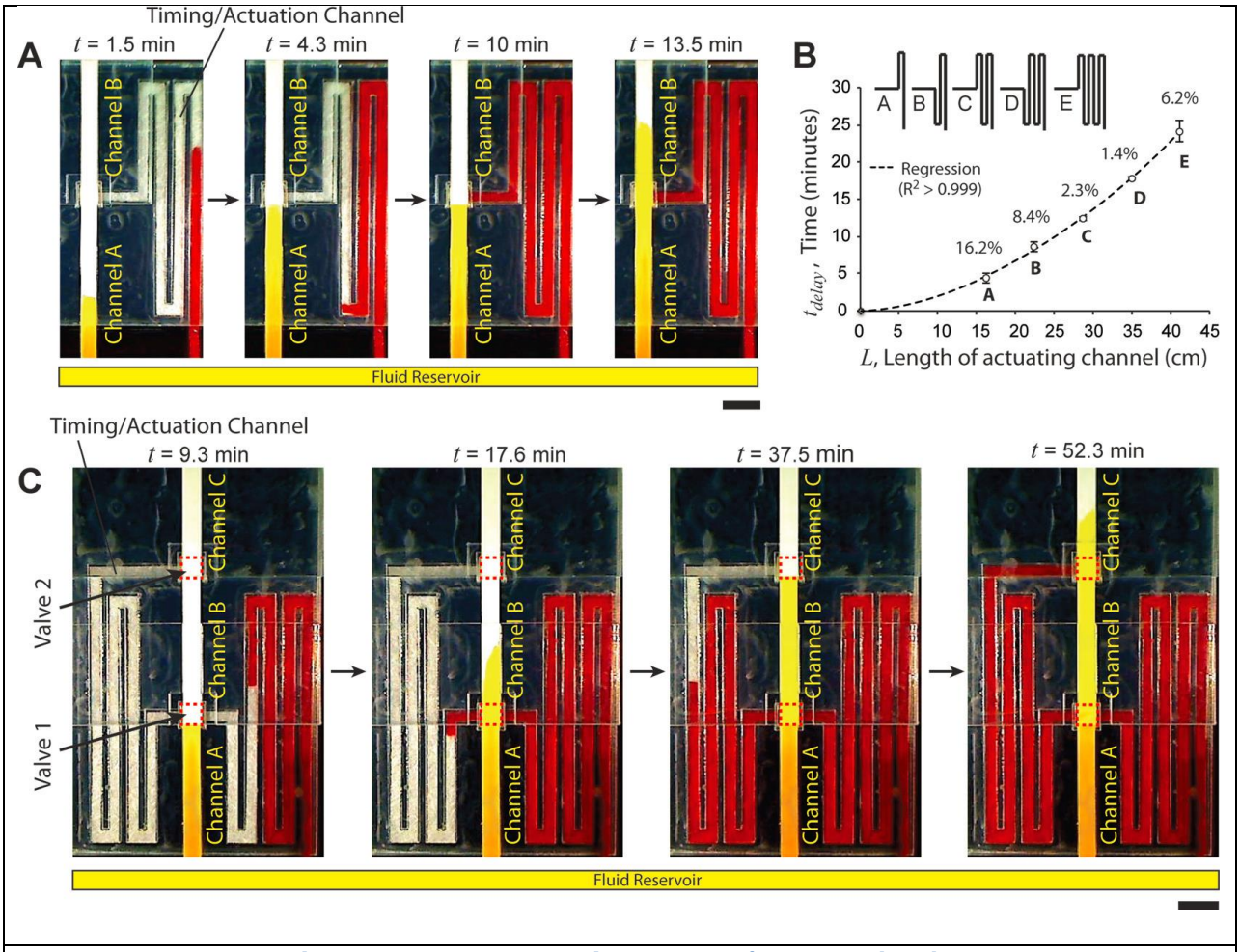

Figure 98: Programming valve actuation time. A. Time-lapse images of an on-switch with a serpentine actuation channel that times valve actuation. Channel A and the actuation channel were connected to a common fluid reservoir. Yellow fluid was added in the reservoir at time, t = 0. The fluid reached the end of channel A at 4.3 min. Fluid in the timing/actuation channel reached the actuator at 10 minutes and actuated the valve. Note that the fluid appears darker in the actuation channel because it is thicker than channels A and B. B. Time required for fluid to traverse the length of different lengths of serpentine glass fiber channels. Percent values are coefficients of variation (N = 6). C. Time-lapse images of a device consisting of two on-switches (valve 1 and valve 2; dotted red squares) that actuate sequentially by a common timing/actuation channel. Valves actuated when fluid in the timing channel reached the corresponding actuators.

This strategy of timing valve actuation can also be used to actuate multiple valves on a device sequentially. Figure 98C shows a device with two on-switches actuated sequentially. It consists of three nitrocellulose flow channels, A, B, and C, placed at three different levels. On-switches lie between channel A and channel B (valve 1; dotted rectangle; Figure 98C), and between channel B and channel C (valve 2; dotted rectangle; Figure 98C). Because channel B

makes contact with channel A placed below it and channel C placed above it, it was made of unbacked nitrocellulose. A 2.9 mm wide serpentine glass fiber actuation channel originated at the fluid reservoir, passed through valve 1, and terminated at valve 2 (Figure 98C). Channel A and the actuation channel were inserted into a common fluid reservoir, which was filled with a yellow fluid at time, t = 0. Figure 98C shows time-lapse images of the device in operation. At 9.3 minutes, the process fluid had reached the end of channel A but actuation fluid had not reached valve 1. Valve 1 actuated at 15 minutes. At 17.6 minutes, actuation fluid had crossed valve 1 and the process fluid front was in channel B. At 37.5 minutes, process fluid had reached the end of channel B, but the actuating fluid had not reached valve 2. Valve 2 actuated at 50.5 minutes. At 52.3 minutes, the process fluid front can be seen in channel C. This demonstrates controlled incubation and subsequent movement of fluid into different zones of a paper microfluidic device. This method can also be used to implement sequential delivery of fluids over a detection zone, as demonstrated in a protein detection assay below. This could be the basis of conducting automated multi-step biochemical assays in paper microfluidic devices.

15.3.4 Volume-metered valves

Volume-metered valves are useful for any washing operation where the important parameter is wash volume as opposed to reaction time. In such cases, these methods eliminate the need for using timing wicks. The particular application for which we developed these valves was in the context of a sample purification method in which the components of interest from a fixed sample volume are captured over a zone upstream from the valve, followed by elution of the captured components and their transport downstream from the valve, where they can be used for analysis. The sample fluid from which the components are captured is routed to a waste pad (the metering pad), which becomes disconnected from the system after valve actuation. Two types of volume-metered diversion switches are presented. The design of the first type of volume-metered switch

(branch B1; Figure 96) is similar to the time-metered switches presented above, *i.e.*, it consists of two flow channels, A and B, placed at different heights (Figure 99A). The valve actuates when one end of channel A is lifted up by the expansion of the actuator and makes contact with channel B (Figure 99A). The primary difference compared to time metered valves is that as opposed to using fluid in a separate actuating channel, volume-metered valves divert the process fluid towards the actuator. A metering pad in between the flow channel and the actuator is used to meter the volume for valve actuation. Specifically, channel A makes contact with a metering pad placed under it near one end (Figure 99A). The channel extends over the metering pad and connects to an impermeable fluid barrier, attached on top of a cavity containing the actuator (Figure 99A). The bottom surfaces of the metering pad and the actuator are connected with a connector pad (Figure 99A). Fluid introduced in channel A flows into the metering pad, then into the connector pad, and then into the actuator. Expansion of the actuator disconnects channel A from the metering pad and connects it with channel B (Figure 99A; right panel).

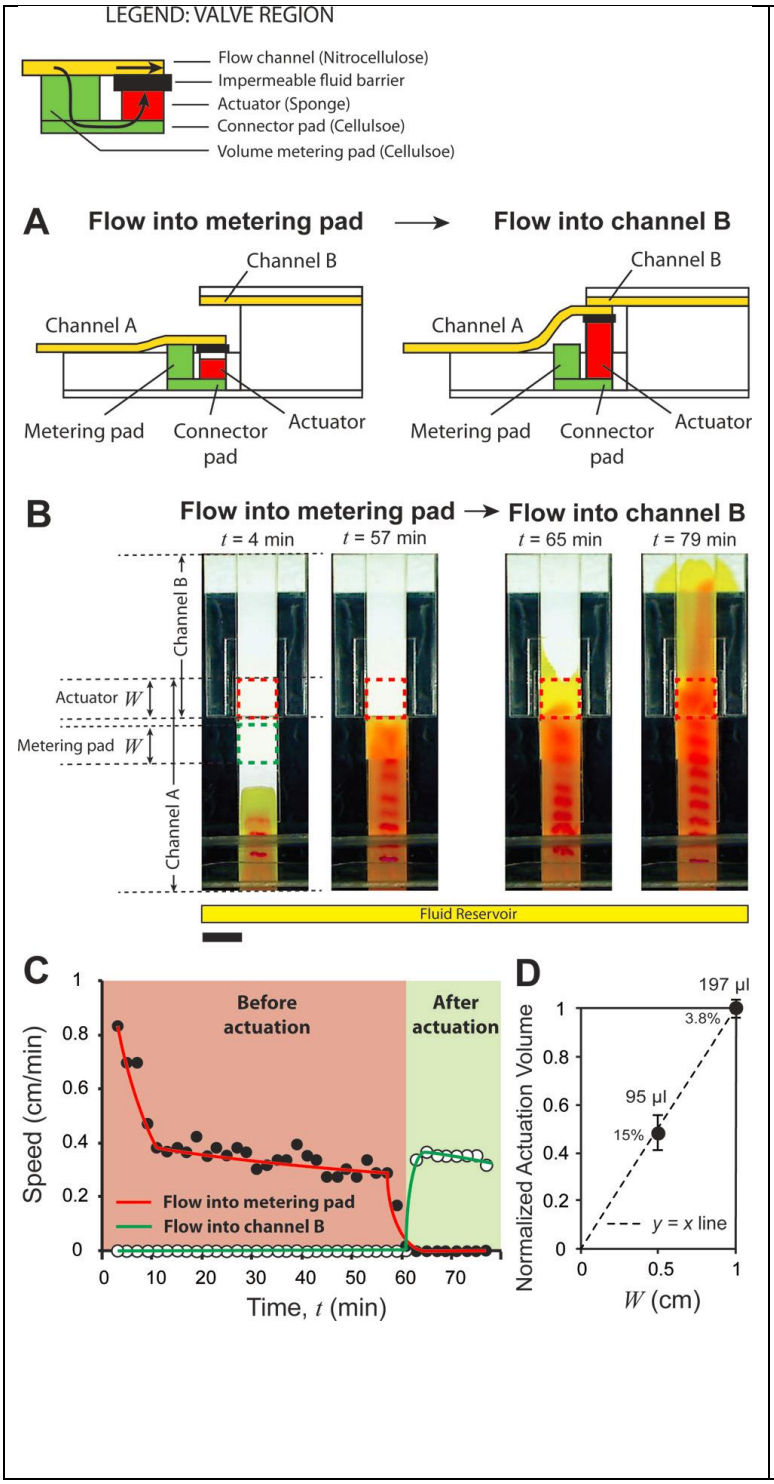

Figure 99: Volume-metered valve with a cantilever channel. A. Schematic of a volume-metered flow-diversion switch. It consists of two channels, A and B, placed at two different heights. Channel A connects to a metering pad placed under it, which delivers fluid to an actuator, through a connector pad. After the passage of a certain volume of fluid, the actuator expands, disconnects channel A from the metering pad and connects it to channel B. B. Time-lapse images of the valve. The length of the metering pad and actuator, W, was 1 cm for this design. Before actuation (4 and 57 min), fluid in channel A flowed into the metering pad. After actuation (65 and 79 min), fluid was diverted into channel B. Scale bar is 1 cm. C. Linear velocity as a function of time for the device shown in B showed a steady flow into the metering pad (solid circles; red line) before actuation. During actuation, the velocity into the metering pad decreased to zero, and after actuation, velocity into channel B (hollow circles; green line) increased from zero to a positive value. Curves are added to guide the eye. D. Normalized mean volumes of fluid flow before valves actuated, as a function of W. Percent values are coefficients of variation. Mean volumes of actuation are provided next to the data points (N = 5 for W = 1 cm and N = 4 for W = 0.5 cm).

A specific implementation of a volume-metered diversion switch with 1 cm wide nitrocellulose channels is presented here (Figure 99B; Movie S5 in ESI[154]). Channel A was made of unbacked nitrocellulose because it must make contact with the metering pad and

channel B placed on either sides. Channel B was made of plastic-backed nitrocellulose, and placed 2 mm above channel A. The metering pad and connector pads were 1 cm wide and made of cellulose. One of the requirements of this design is that the metering pad must be thick enough to protrude above the surface to contact channel A (Figure 99A; left panel). The protrusion should be approximately equal to the thickness of the impermeable fluid barrier to ensure good contact with channel A (Figure 99A; left panel). To attain the appropriate height, here, the thickness of the metering pad was adjusted by stacking 2.70 mm and 0.87 mm thick layers of cellulose. The actuator was made of 1 cm wide, 2.3 mm thick compressed cellulose sponge. The width, W, of the metering pad and the actuator (Figure 99B) was used as a parameter to tune actuation volume. Two designs with W = 0.5 and 1 cm were fabricated. Time-lapse images of the valve with W = 1 cm are shown in Figure 99B. Channel A was inserted into a fluid reservoir where a yellow fluid was added at time t = 0. The electrochemical band marking setup was used to track fluid velocity. At t = 4 and 57 minutes, respectively, fluid flowed into channel A and into the metering pad (Figure 99B). The valve actuated at t = 60 minutes. At t = 65 and 79 minutes, channel A had disconnected from the metering pad and fluid flowed into channel B and the cellulose wicking pad attached to it (Figure 99B). The velocity through channel A for this valve was tracked as a function of time, t. After the initial decreases in velocity during wet out ($t < 10$ min), a nearly constant velocity was maintained in channel A while fluid flowed into the metering pad (Figure 99C; pink zone). During actuation, the velocity into the metering pad decreased to zero over 4 minutes (Figure 99C; rightmost region of pink zone). After actuation, flow entered channel B and a nearly constant velocity was maintained in the device (Figure 99C; green zone). Finally, reproducibility and volume tunability of this valve are demonstrated. Volume before actuation was measured as area under the speed-time curve (Figure 99C; pink

zone). When W was changed from 1 cm to 0.5 cm, the volume required for valve actuation decreased to very close to half (Figure 99D). For W = 1 and 0.5 cm, the mean actuation volumes were 197 μL (N = 4) and 95 μL (N = 5) with standard deviations of 7 and 14 μL, respectively.

The second type of volume-metered switch (branch B2; Figure 96) is based on the displacement of metering pads and has fixed paper channels. The basic idea is shown schematically in a transverse view of this valve (Figure 100A; left column). A metering pad with embedded expanding actuators is placed on top of a flow channel. The actuators extend out below the metering pad and are inserted in cavities on the surface. For this design, the properties of the metering pad relative to the flow channel must be such that the process fluid directly under the pad preferentially flows into the pad; there should be no flow in the channel downstream of where the pad contacts it. This occurs when the capillary forces generated by the wicking pad, Fpad, are considerably higher than those generated by the channel, Fchannel. For a detailed discussion of fluid flow in such assemblies, refer to Toley *et al.*[156] If this condition is satisfied, after a certain volume of fluid accumulates in the metering pad, it reaches the actuators, which expand and lift the metering pad (Figure 100A; left bottom panel), allowing fluid to flow downstream of the valve region. Flow diversion can thus occur using a single flow channel and one metering pad. When the flow channel is composed of nitrocellulose, a common material used in paper microfluidics, a modification to this basic design is necessary. Nitrocellulose generates large capillary forces and the necessary condition, Fpad > Fchannel, is not satisfied for most combinations of pad materials and nitrocellulose. However, this problem can be resolved by inserting an adapter channel between two nitrocellulose channels, A and B, as shown in the lateral view of the schematic (Figure 100A; right column). The adapter channel is made of glass fiber, generates lower capillary forces than nitrocellulose, and preferentially delivers fluid to a

cellulose metering pad with little leakage downstream. Before valve actuation, fluid introduced into the nitrocellulose channel A flows into the metering pad through the adapter channel (Figure 100A; top right panel). After actuation, fluid in channel A flows into channel B (Figure 100A; bottom right panel).

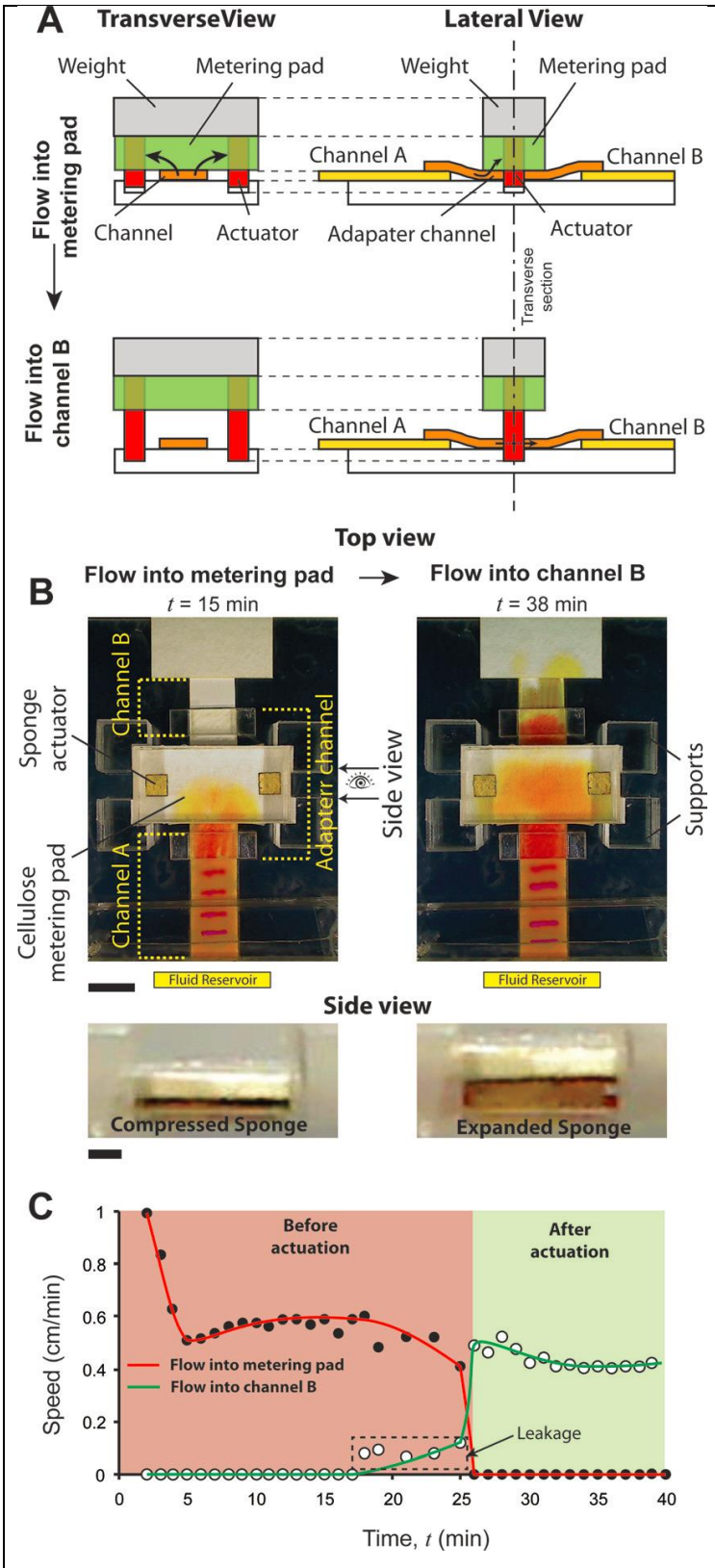

Figure 100: Volume-metered valve with a moveable metering pad. A. Schematic of the volume-metered flow-diversion switch showing transverse and lateral views. It consists of a metering pad with actuators inserted in it, resting on top of a flow channel. Actuators extend out of the metering pad into cavities on the surface. Firm contact between the flow channel and metering pad is ensured by a weight attached on top of the pad. Fluid in the channel flows into the metering pad initially, until actuators expand and lift the pad off. After actuation, fluid flows downstream the valve in the flow channel. The lateral view shows the schematic of this valve with two flow channels, A and B, with an adapter channel in between. B. Top and side views of the valve before (t = 15 min) and after (t = 38 min) actuation. Fluid flowed into the metering pad before actuation (t = 15 min; top view) and into channel B after actuation (t = 38 min; top view). Scale bar is 1 cm. Side view shows the sponge actuator before (t = 15 min) and after (t = 38 min) actuation. Scale bar is 1 mm. C. Flow rates (linear velocity) of fluid flowing into the metering pad (solid circles; red line) and channel B (hollow circles; green line) as a function of time. Graphs show steady flow into the metering pad and channel B, before and after actuation, respectively. There was slight leakage of fluid into channel B before actuation, between t = 18 and 25 min (dotted rectangle).

A specific implementation of this volume-metered switch is shown in Figure 100B (Movie S6 in ESI[154]). It consists of two 1 cm wide plastic-backed nitrocellulose channels, A and B, connected with a 1 cm wide glass fiber adapter channel. The metering pad was a 3 cm × 1.5 cm, 0.87 mm thick cellulose pad and had two 2.3 mm thick square sponge actuators of side 4.5 mm inserted within it (Figure 100B). An adhesive Mylar layer was placed on top of the metering pad to hold the assembly together. A transparent block of poly (methyl methacrylate) (PMMA) was attached on top of this as weight to ensure good contact between the metering pad and the adapter channel. Four PMMA support posts were built around the metering pad to constrain its horizontal motion during valve actuation. Channel A was connected to a fluid reservoir, in which yellow fluid was added at time, t = 0. At t = 15 min, fluid had flowed into the metering pad, through channel A and the adapter channel, but had not reached the sponge actuators (Figure 100B). At t = 38 min, fluid had reached the actuators, the metering pad had lifted off, and fluid had flowed into channel B (Figure 100B). Side view shows the compressed sponge before actuation and expanded sponge after actuation (Figure 100B). Note that there was a darker fluid front downstream from the valve after actuation (Figure 100B; t = 38 min; top view). We believe that this is a result of a) chromatographic separation caused by the adapter channel, and b) an increase in pH of the phenol red solution in the adapter channel (alternate adapter channel materials may eliminate this effect, but we have not tested other materials in this work). Flow rates (linear velocities) were measured in channel A (vA) using the electrochemical band marking system and in channel B (vB) by tracking the yellow fluid front. The flow rate into the metering pad, vpad, was determined as vpad = vA − vB. A plot of flow speed as a function of time shows initial reduction during wet out (t < 5 min; Figure 100C) followed by sustained flow into the metering pad. Close to t = 18 min, flow rate into the metering pad started decreasing and

flow rate in channel B started increasing slowly (Figure 100C). At t > 26 min, flow rate into the metering pad became zero and flow rate in channel B increased to a steady rate (Figure 100C; green zone). The mean volume that flowed into the metering pad before the valve actuated was 145 μL with a standard deviation of 12 μL (CV = 8.3%; N = 3). The time between t = 18–26 minutes can be designated as the actuation period of this valve. Compared to volume-metered valves using cantilever channels (Figure 99C), the actuation of this valve was less sharp and there was slight leakage into channel B before valve actuation was complete (dotted rectangle; Figure 100C). However, for applications where slight leakage can be tolerated, this valve provides a simpler design for volume metering because the flow channels are fixed. The PMMA weight may be replaced by a spring or a similar tension mount assembly, which will make the design more compact. The actuation volume of this valve could be tuned by changing the geometry of the metering pad, the location of the actuators within the pad, and/or by stacking multiple metering pads on top of each other. Note that for volume metering valves, sample viscosity may affect the time at which valves actuate, but the volume for actuation is governed by the size of the metering pads and should be less sensitive to sample viscosity.

15.3.5 Demonstration of a protein detection assay

We demonstrate the use of sponge-based valves in a portable device for the detection of the malaria protein, *Plasmodium falciparum* histidine rich protein 2 (*Pf HRP2*), using a signal amplified ELISA based on sequential delivery of reagents to a detection zone. The device has a footprint of 7.5 cm × 5.2 cm, smaller than a credit card, and is 2 cm tall at its highest point. All assay reagents are stored dry on the device. A top view of the device is shown in Figure 101A. The base of the device is a 1.1 cm acrylic block with a fluid reservoir near one end. The test strip is made of 4 mm-wide plastic-backed nitrocellulose, porous side facing down. It is attached to a cellulose wicking pad at one end and to a sample inlet port on the other. Three on-switches,

VON,1, VON,2, and VON,3, when actuated, connect dry reagent-containing glass fiber legs 1, 2, and 3, respectively, to the test strip. Dried reagents on these legs are rehydrated by a glass fiber feeder channel that is connected to the fluid reservoir. An off-switch, VOFF, when actuated, disconnects the feeder channel from the three legs, converting them into limited volume fluid sources. A 2.5 mm-wide glass fiber timing wick, connected to the fluid reservoir, times the actuation of the 4 switches on the device. The shape of the wick is shown in Figure 101B. The wick splits at the point indicated by a green asterisk (*; Figure 101B); one branch carries fluid to VOFF and the other branch carries fluid to the three on-switches that are actuated in the order: VON,1, VON,2, and VON,3. Each on-switch actuation connects one leg to the test strip and delivers a reagent to the detection zone. The sequential actuation of valves results in sequential delivery of reagents. The user initiates the test simply by introducing 30 μL sample into the sample port, and 2 mL water into the fluid reservoir (Figure 101C). All subsequent operations happen automatically, and a test result appears in the detection zone of the device after ~20 minutes (Figure 101C).

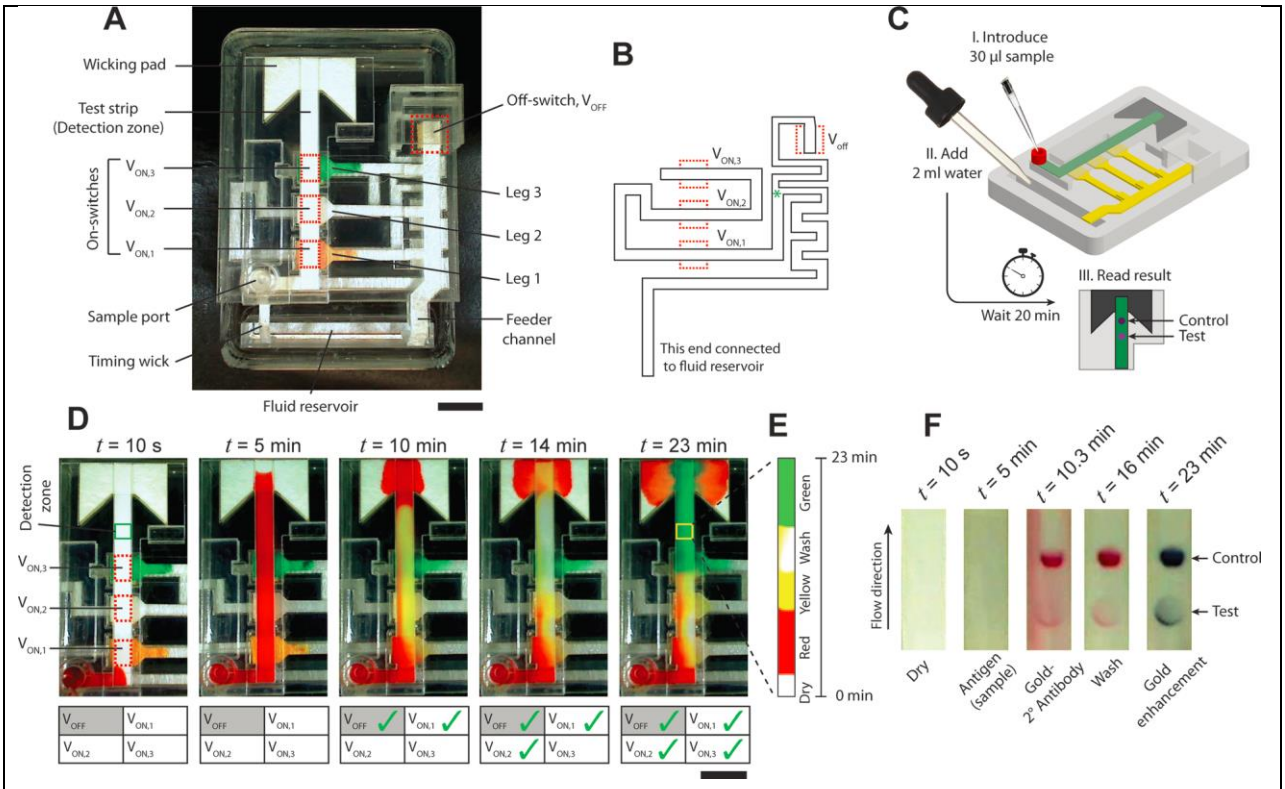

Figure 101: Protein detection device. A. Top view of the device showing important parts. The device consists of one nitrocellulose test strip, and three source legs, one feeder channel, and one timing wick, all made of glass fiber. There are three on-switches, VON,1, VON,2, VON,3, between the test strip and source legs 1, 2, and 3, respectively, and an off-switch, VOFF, that, when actuated, disconnects the feeder channel from all three source legs. Scale bar is 1 cm. B. The shape of the glass fiber timing wick and the location of the four valves. The wick splits at the point indicated by the green asterisk – one branch actuates VOFF and the other actuates the three on-switches sequentially. C. Schematic of a step-by-step procedure of conducting the protein detection test. The test is initiated by adding 30 µL sample in the sample inlet port and 2 mL water in the fluid reservoir. No further user steps are required and the result can be read in the detection zone after 20 minutes. D. The operation of the device is demonstrated using colored fluids. Time-lapse images show the sequential flow over the detection zone of i) red fluid introduced through the sample port (t = 5 min), ii) yellow fluid (t = 10 min), iii) a wash fluid (t = 14 min), and iv) green fluid (t = 23 min), rehydrated from legs 1, 2, and 3, respectively. The status of valves is tabulated at each time point; a green check indicates an actuated valve. Scale bar is 1 cm. E. Montage of time-lapse images over a square region indicated by the yellow box (t = 23 min) in the detection zone. F. Time-lapse images of the detection zone of the device that was used to conduct a *PfHRP2* protein detection assay. The two spots represent test result (bottom) and control (top). The sample flows over the detection zone first (t = 5 min), followed by the labeling antibody (t = 10.3 min), wash buffer (t = 16 min), and gold enhancement reagents (t = 23 min).

The operation of this device is first demonstrated using colored dyes (Movie S7 in ESI[154]). 30 µL solutions of yellow food color with 4% trehalose and 0.1% BSA, TBST (Tris

buffered saline with 0.1% tween 20), and green food color with 4% trehalose and 0.1% BSA, were dried on legs 1, 2, and 3 respectively (Figure 101A). Time-lapse images of the device in operation are shown in Figure 101D with the status of valves tabulated at each time point. Check marks indicate actuated valves. At time, t = 0, a 30 μL solution of red food color was introduced into the sample port (Figure 101D; t = 10 s). Immediately after this, 2 mL DI water was added into the fluid reservoir (not shown in figure). Addition of water engaged the feeder channel and the timing wick. The feeder channel delivered water to the three legs and rehydrated the dried reagents while red fluid from the sample port continued to flow through the detection strip into the detection zone and the wicking pad (Figure 101D; t = 5 min). None of the four valves had actuated at this point. Valves VON,1 and VOFF actuated at 5.17 and 5.67 min, respectively. Actuation of VON,1 delivered yellow fluid to the detection zone (Figure 101D; t = 10 min). Valves VON,2 and VON,3 actuated at 10 and 15.5 min, delivering wash solution and green fluid, respectively, to the detection zone (Figure 101D; t = 14 and 23 min). A montage of time-lapse images of a rectangular region, approximately 4 mm × 4 mm (highlighted by a yellow rectangle in Figure 101D; t = 23 min), shows sequential delivery of four fluids over the detection zone (Figure 101E) over 23 minutes.

Finally, we demonstrate a signal amplified ELISA test for *Pf HRP2* on this device. A detailed description of this assay is provided in Fu *et al.*[93] and in ESI section V[154]. The assay follows a standard sandwich format. A murine antibody to *Pf HRP2* was spotted in the detection zone as a capture agent. Another murine antibody to *PfHRP2* conjugated to gold nanoparticles was used as the labeling agent and dried in leg 1. An anti-mouse antibody was spotted downstream of the capture spot as a control spot. A solution of TBST wash buffer was dried in leg 2 and gold signal enhancement reagents were dried in leg 3. The test was initiated by

introducing a 30 μL solution of 5 μg mL− 1 *PfHRP2* (150 ng total) in fetal bovine serum to the sample port, followed by adding 2 mL DI water to the fluid reservoir. Figure 101F shows time-lapse images of the detection zone with different reagents flowing over it – no reagent/dry (t = 10 s), sample (t = 5 min), labeling antibody conjugated to gold nanoparticles (t = 10.3 min), wash buffer (t = 16 min), and gold enhancement reagents (t = 23 min). A standard lateral flow assay would have only provided the test result shown at t = 10.3 min (Figure 101F). This device enables subsequent delivery of wash fluid and gold enhancement reagents, which improves the sensitivity of the assay[93].

There are several advantages of using this device for conducting sequential delivery-based assays. First, the number of pipetting steps is minimized, making it simple for operation by untrained users. The number of user steps in this device is equal to or less than several FDA approved home test kits, *e.g.* BinaxNOW® Malaria (Alere, Waltham, MA). Further, the number of fluids delivered sequentially can be increased by increasing the number of legs, without increasing the number of pipetting steps. Second, the volumes delivered through each leg are fully customizable. The same test strip geometry can be used to deliver different volumes of fluids through the legs by changing the size of the legs and the shape of the timing wick. Finally, the performance of this device is robust and reproducible. In the last 6 runs, the CV's in valve actuation time of the four valves on the device were <10% and sequential delivery of the four fluids was successful on all the devices.

The valving toolkit presented here is comprehensive and enables multiple types of automated fluidic operations. One of the salient features of these valves is that they do not introduce any chemicals in the flow path and thus will not affect chemical compatibility of paper microfluidic devices. The use of mechanical actuators and moving paper channels makes these

designs more complex compared to paper devices without moving parts. However, fluidic capabilities increase considerably with these valves; capabilities comparable to those achievable in micromachined or PDMS microfluidic devices are imparted to paper microfluidic devices. Even though they may be more complex, they are reasonably easy to construct and involve simply stacking layers of adhesive-backed plastic, PMMA slabs, and paper. Sponge actuators are extremely low cost – the volume amount of sponge required for a 4.5 × 4.5 mm2 actuator was purchased at a retail cost of ~$0.003 US. Retail cost of all materials and reagents used for the PfHRP2 test device was ~$6.8 US, out of which, $4.7 US was the cost of plastic (see ESI section VI[154] for a detailed cost analysis). The only machine required to fabricate these parts was a CO_2 laser cutter, which are rapidly becoming cheaper and more accessible. If manufactured in large scale using injection molding, the cost of plastic parts will reduce to well under a dollar, using a conservative estimate. Thus a device for conducting a multistep ELISA assay can be fabricated for under $3 US. Compared to conventional microfluidic devices, the critical cost saving associated with paper microfluidic devices is the operational cost. Such a paper-based device would not require electricity, batteries, permanent instruments, maintenance, or trained personnel for operation.

Sponge actuators do not spontaneously compress when dried; actuation is irreversible, so these are single-use valves. For most biochemical assays that involve either sequential delivery of fluids to a detection zone, or the controlled movement and incubation of a plug of fluid into different zones of a device, single-use valves work well. The volume of actuating fluid required by these valves can be high. Even though the volume required to expand the actuators is only ~30 μL for time-metered switches, the volume required to wet the glass fiber timing channels is ~500 μL for the longest channel (design E; Figure 98B). However, as demonstrated in the protein

assay device, such large volumes can easily be accommodated in portable test devices. If desired, this volume can be reduced by timing channels made of thinner materials or slower-wetting materials. Before proceeding, it must be ensured that the alternate materials have reproducible flow and a sufficient rate of fluid delivery to the sponge actuators. Another possibility is to use alternate actuators that are not based on fluid absorption. A variety of such alternate strategies may be utilized – the end result should be mechanical motion triggered by the arrival of fluid. Because actuation of these valves is coupled with the arrival of fluid at actuators, they can be used as 'logic gates' in paper microfluidic circuits and lay the ground for development of highly integrated paper microfluidic systems.

15.4 Experimental

15.4.1 Paper materials

Plastic-backed and unbacked channels were made of nitrocellulose FF80HP and AE100, respectively (GE Healthcare; Waukesha, WI). Test strip used in the protein detection assay was made of nitrocellulose HF120 (Millipore, Billerica, MA). The adapter channel for volume-metered valves with displaceable metering pads was made of glass fiber grade 691 (VWR, Radnor, PA). All cellulose pads were made of 0.87 mm thick CFSP223000 (Millipore, Billerica, MA), except a 2.7 mm thick cellulose 320 (Ahlstrom, Helsinki, Finland) pad that was used for the volume metering valve with cantilever channel. Glass fiber actuation channels and all glass channels in the protein assay device were made of GR8964 (Ahlstrom). Actuators were made of 2.3 mm thick compressed cellulose sponge #43CC (Sponge Producers Company, St. Louis, MO). All thicknesses reported here are of dry materials.

15.4.2 Device fabrication

Devices were constructed by stacking layers of 10 mil thick adhesive-backed Mylar (Fralock, Valencia, CA), slabs of poly (methyl methacrylate) (PMMA; McMaster-Carr, Elmhurst, IL), and paper channels. Designs were drawn using DraftSight (Dassault Systemes HQ, France) and all parts were cut using a 42 W CO_2 laser cutter (M360, Universal Laser Systems, Scottsdale, AZ). Individual layers of plastic and paper were cut to desired shapes before stacking. The detailed procedure for cutting nitrocellulose channels was described previously[386]. Compressed sponges were also laser cut to the desired dimensions. The actuator cavity was laser cut in a 2.5 mm thick PMMA layer. Height difference between flow channels was maintained by a 1.5 or 2 mm thick PMMA layer. To create a cantilever channel, laminate protecting the adhesive on a Mylar layer was selectively removed from under one end of the channel by laser cutting; the other end was not adhered to the surface and was free to move. This movable end of the channel was attached to an impermeable fluid barrier, which was a flap made of 10 mil thick double adhesive backed Mylar. The channel adhered to this flap on its top surface and the bottom surface of the flap adhered over the cavity containing the actuator. There was no adhesive on the bottom surface of the sponge actuator or on the glass fiber actuation channel; good contact between the actuator and the actuation channel was maintained by reducing the width of the actuation channel under the actuator to half, in order to expose the adhesive on the surrounding Mylar. Actuators were adhered on top of actuating channels in this way. Schematics of part by part assembly of a device and geometric details of various parts around the actuator are provided in ESI section III[154]. Unbacked nitrocellulose channels tended to warp when wet, which resulted in improper contact. To avoid this, unbacked channels were laminated with adhesive-backed 4 mil thick Mylar films at places where they did not make contact with other channels from both sides. For volume-metered valves with displaceable metering pads, the weight and

support posts were constructed by stacking three 3.8 mm thick PMMA parts after laser cutting to desired shape.

15.4.3 Experimental setup, image acquisition and analysis

All devices (except the protein detection device) were set on a 19.1 mm thick black PMMA block with a fluid reservoir etched near one edge. Channel A and timing/actuator channels of all devices extended out into the fluid reservoir. Some valves used different fluids in the actuation and flow channels. For these, the actuation channels extended into a separate cylindrical fluid reservoir attached to the side of the block. The electrode for the electrochemical band marking system that created pink bands in the yellow fluid (phenol red solution; described by Kauffman *et al*.[95]) resided on top of channel A just downstream the fluid reservoir. A custom made humidity chamber with multiple sources of water was used to raise the relative humidity to 75% before addition of fluids into the devices. Images were acquired at intervals of 10 or 15 seconds using a Logitech Pro 9000 (Logitech, Newark, CA) webcam operated using HandyAvi (AZcendant, Tempe, AZ). The location of fluid fronts and pink bands were tracked over time using ImageJ (NIH Research Services Branch). Speed (cm min^{-1}) at any instant, t (min), was calculated by measuring the distance (cm) traveled by fluid fronts or bands between t to t + 1 min. Volume (μL) passed until time, t, was calculated as area under the speed–time curve (cm) from 0 to t, multiplied by the width (cm) of the channel and absorption capacity (μL cm^{-2}) of the channel material. Area under the curve was approximated by the trapezoidal rule. Absorption capacity of nitrocellulose materials was experimentally determined26 to be 10 μL cm^{-2}. The protein detection device was run on a tabletop at ambient temperature and humidity to demonstrate its standalone operation.

15.4.4 Protein detection assay

See ESI section V[154].

15.5 Conclusion

We have, for the first time, demonstrated functional mechanically actuated valves that can be programmed to actuate automatically in paper microfluidics. We also demonstrated the use of these valves in designing portable devices that can be operated by untrained users to conduct complex detection chemistries. These valves are enabling for the two ongoing projects in our laboratory aimed at developing paper-based diagnostic devices for conducting nucleic acid amplification or protein binding assays. Broadly, this valving and automation toolkit will enable researchers to conduct complex multistep fluidic operations in paper microfluidic devices while maintaining their fundamental advantage, *i.e.*, fluid flow without pumps and electricity.

15.6 Acknowledgements

The work presented in this paper was carried out with support of two grants to PI Paul Yager at the University of Washington: one from DARPA DSO (grant number HR0011-11-2-0007), and one from the National Institute of Allergy and Infectious Disease of the National Institutes of Health (Award Number R01AI096184). We wish to acknowledge helpful communications with collaborators on these grants at UW, Seattle Children's, PATH, GE Global Research, and ELITechGroup North America Inc. Molecular Diagnostics (previously Epoch Biosciences). We would like to thank Tinny Liang, Sujatha Ramachandran, Koji Abe, and Shichu Huang for help with protein assays, and Peter Kauffman for the design of the electrochemical band marking setup. The information in this manuscript does not necessarily reflect the position or policy of the government, and no official endorsement should be inferred. The content is solely the responsibility of the authors and does not necessarily represent the official views of the National Institutes of Health.

16 Appendix: Design of a New Type of Compact Chemical Heater for Isothermal Nucleic Acid Amplification

Kamal G. Shah, Dylan Guelig, Steven Diesburg, Joshua Buser, Robert Burton, Paul LaBarre, Rebecca Richards-Kortum, Bernhard Weigl

This appendix section is taken in a largely unmodified form from the manuscript[209]. I would like to thank primary author Kamal Shah, and my other coauthors, for involving me in the project.

16.1 Abstract

Previous chemical heater designs for isothermal nucleic acid amplification have been based on solid-liquid phase transition, but using this approach, developers have identified design challenges *en route* to developing a low-cost, disposable device. Here, we demonstrate the feasibility of a new heater configuration suitable for isothermal amplification in which one reactant of an exothermic reaction is a liquid-gas phase-change material, thereby eliminating the need for a separate phase-change compartment. This design offers potentially enhanced performance and energy density compared to other chemical and electric heaters.

16.2 Introduction

Nucleic acid based diagnostic tests enable earlier diagnosis for some infectious diseases compared to antibody tests[387]. Amplification of extremely low sample concentrations of RNA and DNA provide comparably high sensitivity and specificity[388]. Although PCR is typically used in laboratories in developed countries to amplify nucleic acids, the need for complex equipment, staff training, electricity, and precisely-timed thermal cycling limit its applicability to low-resource settings[329]. In response, isothermal amplification techniques such as loop-mediated amplification (LAMP), helicase-dependent amplification (HDA), cross priming amplification (CPA), and recombinase polymerase amplification (RPA) have been developed to

amplify DNA to detectable concentrations in 15–60 minutes[389], [390]. When combined with electricity free isothermal chemical heaters that utilize an exothermic reaction with a phase-change material that melts at an appropriate temperature (55–65°C for LAMP and 15–37°C for RPA), these amplification techniques enable accurate diagnosis in low-resource settings where electricity is unreliable[162], [389], [391].

Given the large heat output of the reaction of magnesium metal with water to produce magnesium hydroxide and hydrogen gas as shown in Equation 16[392], several devices have been developed based on this galvanic corrosion including ready-to-eat meals for soldiers and several isothermal chemical heaters, such as those developed by the PATH team and the Liu laboratory[114], [148], [175].

$Mg_s + 2H_2O_{(l)} \rightarrow Mg(OH)_{2(s)} + H_{2(g)}$ $\Delta H_r = -14.6 \frac{kJ}{g\ Mg}$	Equation 16

When the reaction temperature is moderated only by the boiling point of water, the resultant heat applied to the assay is too great; thus this reaction must also be coupled with a solid liquid phase-change material (PCM) with an appropriate melting point, such as palmitic acid for LAMP (Tf = 61.9°C) to maintain an appropriate isothermal sample temperature[175], [393]. The additional presence of a PCM separate from the exothermic reaction increases device size, thus creating a design challenge to simultaneously minimize the ramp-up time to reach optimal LAMP temperatures, maximize the holdover time at optimal LAMP temperatures, and minimize device size. Up until now, electricity-free nucleic acid amplification temperature modulation has only been demonstrated with solid phase change materials separate from the

exothermic reactants. In this work, we utilize the analogous exothermic magnesium reaction with methanol functioning as both reactant and PCM, thereby eliminating the need for having a separate PCM since methanol boils at 64.7°C (Equation 17)[394]:

$Mg_{(s)} + 2CH_3OH_{(l)} \rightarrow Mg(CH_3O)_{2(s)} + H_{2(g)}$	Equation 17

The use of liquid-vapor phase change in lieu of the typical solid-liquid phase change used in isothermal chemical heaters may increase the ambient temperature operating range since the reaction temperature is capped by the boiling of the PCM. Additionally, enthalpy of vaporization is typically much higher than the enthalpy of fusion at a particular temperature, thus increasing energy density and allowing for a smaller device[114], [148], [175], [393], [394].

Due to the reduced thermal load of the system, the latter reaction may also enable a reduction in the ramp-up time and a potential increase in holdover time. Similarly, both reactions in Equation 16 and Equation 17 are accelerated in the presence of chloride ions[392]. Furthermore, since the holdover time is inversely related to the rate of reaction, combining the slow simmer reaction in Equation 17 with a kinetically fast reaction that brings the system to boiling may serve to reduce ramp-up time and potentially extend holdover time. Indeed, copper (II) chloride reacts exothermically at a rate 10 orders of magnitude faster than the chloride ion catalysed magnesium-water reaction in accordance with Equation 18[162], [392]:

$Mg_{(s)} + CuCl_{2(aq)} \rightarrow Mg^{2+} + Cl^{-}_{(aq)} + Cu_{(s)}$ $\Delta H_r = -24.0 \frac{kJ}{g\ Mg}$	Equation 18

Therefore, we explored the impact of chloride ion and copper (II) chloride concentration on the ramp-up and holdover time of a proof-of-concept liquid-vapor PCM isothermal chemical heater that is compatible with LAMP.

16.3 Materials and Methods

Design criteria encompassing desirable performance and form factor were established in accordance with the requirements of LAMP, such as for foot-and-mouth disease, and of laboratories in developing countries. Given the challenges of transporting materials in resource-limited settings, the reusable components of the proof-of-concept prototype were designed for fabrication solely using materials that would be locally available in a low resource setting and using common laboratory equipment with no reliance on additional custom molded or printed components. An average ramp-up time to 57°C of less than 5 minutes and a holdover time of 15 minutes for temperatures between 57 and 62°C was defined a priori to characterize a successful prototype.

In light of these design specifications, six identical proof-of-concept prototypes were constructed as shown in Figure 102 by drilling a 9/16” diameter, 60 mm hole in a 28.5 mm x 28.5 mm x 70 mm reusable PVC foam block (Item 85925K352, McMaster-Carr). A standard 5 mL centrifuge tube (Eppendorf North America Biotools) was pressed into the cavity and used as a disposable reaction chamber, and a pressure-equalizing hole was drilled into the cap with a 0.067” diameter drill bit. A 20 mm x 32 mm fuel pack was constructed by heat-sealing muslin (Item 10011, Muslinbag) that contained 400–450 μm particle diameter, 500 ± 2 mg, mechanically alloyed magnesium-iron (Luxfer Magtech Inc, USA) and 0, 10, 25, 50, 75 or 100 ± 2 mg sodium chloride (Item S7653, Sigma-Aldrich). In a second set of experiments, with 50 mg of sodium chloride mixed into the fuel pack, 0, 10, 20, 30, 40, 50 or 60 ± 2 mg anhydrous copper (II) chloride (Item 22011, Sigma-Aldrich) was added to the reaction chamber to prevent premature corrosion (50 mg of copper (II) chloride is needed to bring the system to boiling). An

open-cell annular foam PCR tube holder was placed at an angle at a fixed height in the centrifuge tube to ensure that a 100 µL PCR tube was consistently positioned in all tests.

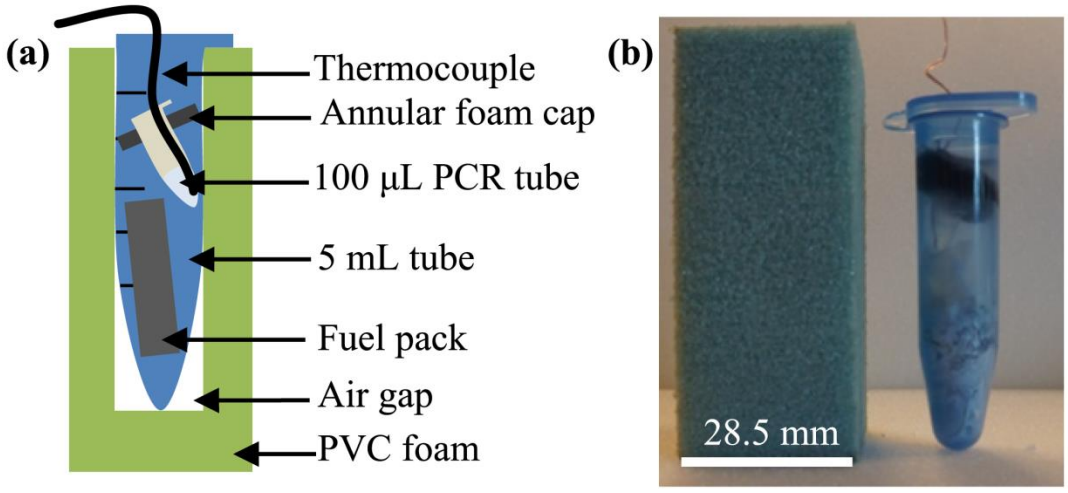

Figure 102: Device design. (a) Labeled vertical cross-section and (b) photograph of used, proof-of-concept, direct liquid-vapor phase change, and isothermal chemical heater. The exothermic reaction occurs in a standard laboratory 5 mL tube and is initiated by the addition of methanol to the tube.

In all performed tests, the PCR tube contained 50 µL of tap water and was instrumented with a T-type thermocouple sampled continuously at 1 Hz with a custom LabVIEW virtual instrument via a NI cDAQ–9172 and NI–9211 (National Instruments). The isothermal heater was initiated by injecting a 3 g bolus of methanol to the reaction chamber at an ambient temperature of 23°C. To simulate use at the point-of-care, device performance was evaluated with 50 mg of sodium chloride in an environmental chamber (BTL–433, ESPEC, Hudsonville, Michigan) at an ambient temperature set to 22 or 45°C. All quantities are reported as a mean ± standard deviation (X ± s) unless otherwise indicated. Statistical analysis was performed by comparing the ramp-up and holdover times in each experimental group to a negative control via an unpaired, one-tailed t-test with unequal variance.

16.4 Experimental Results

The six identical proof-of-concept prototypes successfully met the requirements for LAMP with holdover times of 19.0 ± 5.0 minutes when the fuel pack was mixed with 50 mg of sodium chloride. However, the ramp-up time was slightly longer than the 5 minutes targeted, and was 7.9 ± 1.9 minutes.

Figure 103 shows characteristic temperature-time profiles for the chemical heaters at varying levels of sodium chloride. As expected and shown in Figure 104a, there is a statistically-significant decrease in ramp-up time from 25.0 ± 5.6 minutes to 8.9 ± 1.5 minutes when comparing the negative sodium chloride control to all tested sodium chloride concentrations ($p = 0.018$). No statistically significant difference in holdover time was observed with the addition of sodium chloride ($p = 0.32$), and was 12.7 ± 3.4 minutes. Temperatures exceeding the 62°C upper threshold by up to 0.1°C were observed when 75 or 100 mg of sodium chloride was added.

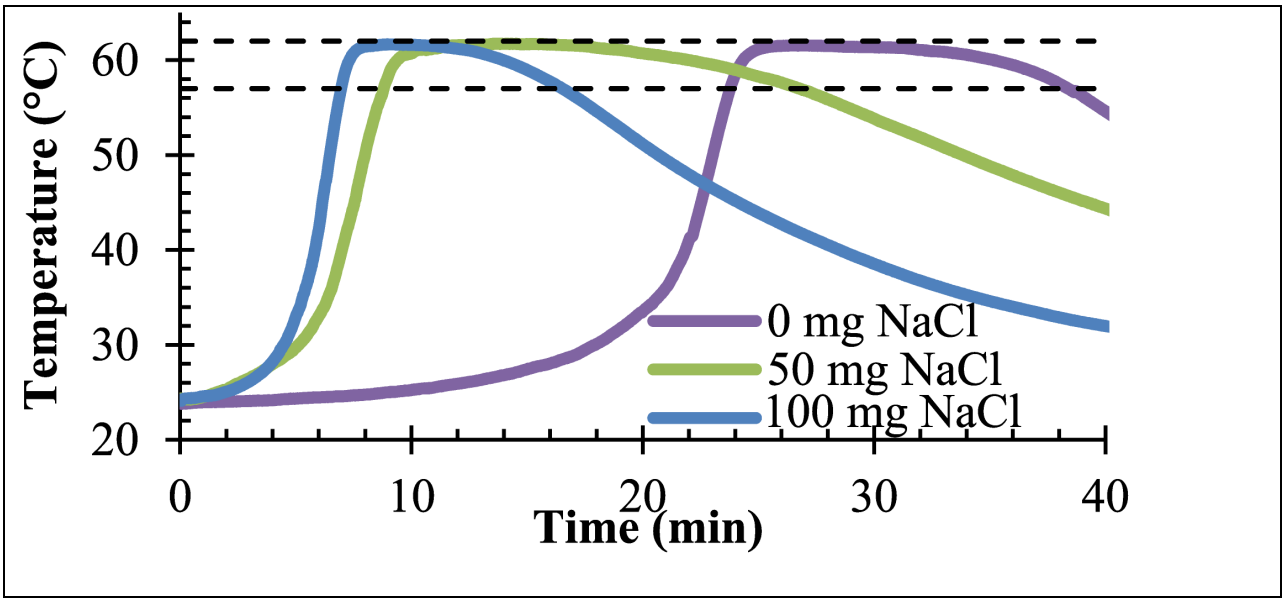

Figure 103: Representative temperature-time curves. The isothermal chemical heater shows relatively flat temperature-time profiles between 57°C and 62°C (dashed lines).

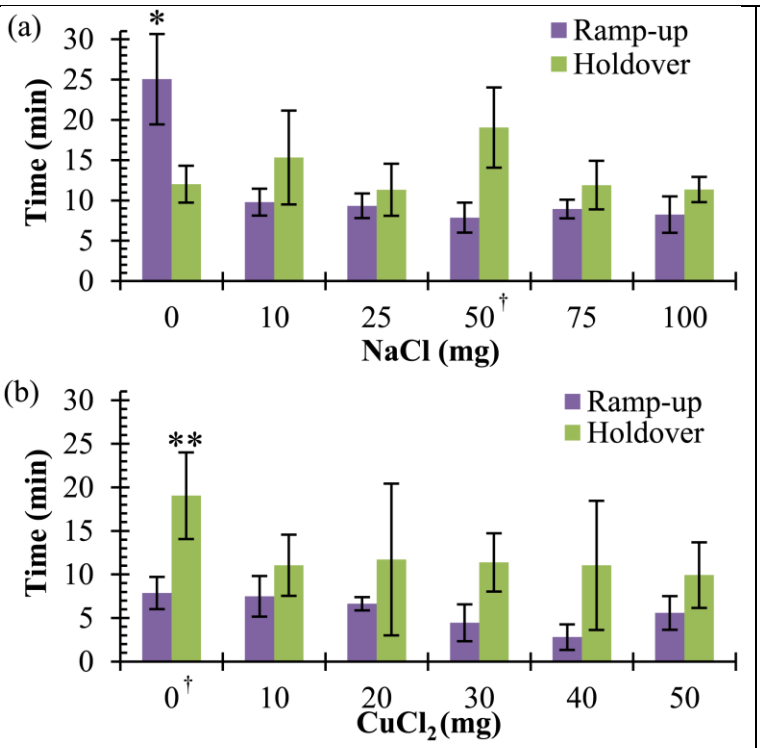

Figure 104: Ramp-up and holdover times. (a) Ramp-up times (X± s) are reduced (*p = 0.018) and holdover times (X± s) show no change with the addition of sodium chloride to the magnesium-iron fuel pack. (n = 3) (b) In contrast, the addition of copper (II) chloride does not significantly affect ramp-up, but significantly reduces holdover (**p = 0.005). (n = 3) † indicates identical data points.

In contrast, the addition of copper (II) chloride resulted in no statistically-significant difference in ramp-up time compared to the negative control as shown in Figure 104b ($p = 0.06$). Upon addition of copper (II) chloride, holdover time decreased from 19.0 ± 5.0 minutes to 10.6 ± 4.7 minutes ($p = 0.005$). Overheating by up to 0.9°C was observed when 30 mg or greater of copper (II) chloride was added.

As shown in Figure 105, increasing the ambient temperature from 22 to 45°C led to a statistically significant, though small, decrease in ramp-up time from 7.1 ± 0.3 minutes to 5.7 ± 0.4 minutes ($p = 0.006$). The holdover time increased from 10.9 ± 1.2 minutes to 18.1 ± 4.0 minutes ($p = 0.038$).

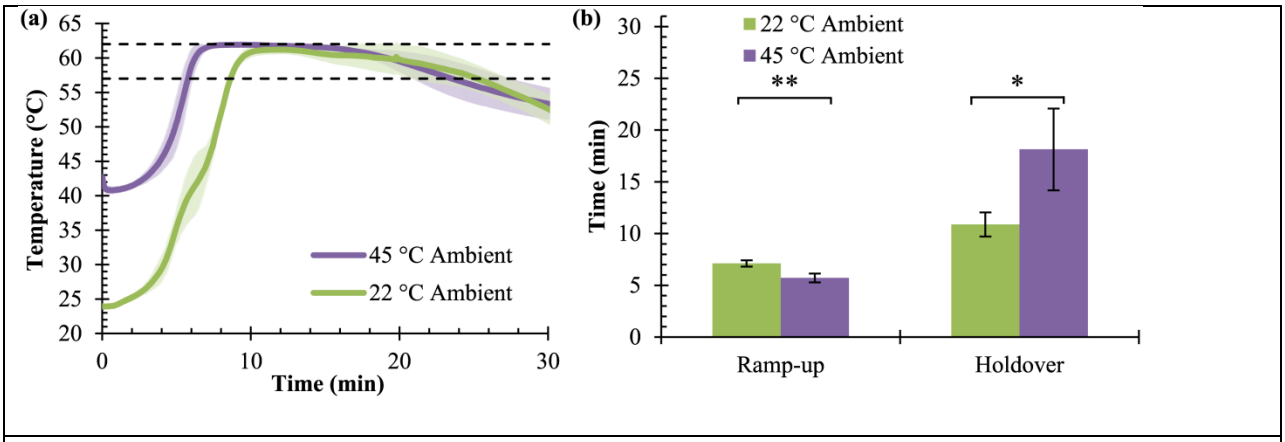

Figure 105: Performance at elevated temperatures. (a) The temperature-time curve (X± s) shows smoother ramp-up and extended holdover between 57°C and 62°C (dashed lines) at a 45°C ambient temperature compared to 22°C. (n = 3) (b) Ramp-up time decreases by 1 minute (**p = 0.006) and holdover time increases by 60% compared to room temperature (*p = 0.04). (n = 3).

The device is also compatible with non-methanol liquid-vapor PCM such as water, but ramp-up (to 90°C) and holdover time (between 90 and 95°C) is reduced to 29 seconds and 117 seconds, respectively (data not shown).

16.5 Discussion

Isothermal nucleic acid amplification shows significant promise to enable early diagnosis compared to antibody-based tests in the developing world. However, current compact solid-liquid phase change material-based systems may be impractical to design to operate at large ambient temperature ranges. Although the Liu chemical heater is operable between 20 and 40°C, the single-use device is complex and only compatible with sample volumes up to 15 μL, which may be impractical for larger sample volumes such as when diagnosing HIV[148], [261]. A disposable, solid-liquid phase-change, isothermal heater developed by LaBarre *et al.* occupies a 85 cm^3 volume but is only operable over a 14°C ambient temperature range[114].

In contrast, a liquid-vapor PCM also used as reactant would enable use at ambient temperatures of up to the boiling point, thereby increasing the feasibility of designing a device

suitable for the developing world. The heater described in this work occupies a volume of 57 cm^3, weighs about 15 g, requires only a drill to manufacture, and is compatible with samples up to 100 μL. The external foam housing is reusable and the device costs just $1.61 for the housing and $0.41 per use at low manufacturing volumes. In comparison, an alkaline D-cell battery alone occupies a volume of 56.5 cm^3, weighs 135 g, and costs $0.55 (McMaster-Carr).

One potential concern for using liquid-vapor PCM is the altitude-dependence of the boiling point. For example, water boils at 92°C in Addis Ababa, Ethiopia (elevation of 2360 meters). However, this apparent limitation may instead enable precise control of the temperature profile if pressure-dependent valves are incorporated into future liquid-vapor PCM devices. By operating at a precisely controlled pressure, a liquid-vapor PCM device may improve holdover time by taking advantage of the increase in temperature when a gas is pressurized.

An additional benefit of liquid-vapor PCM heaters may be their adaptability to a variety of operating temperatures for further use for sample lysis, DNA denaturation, reagent reconstitution, organism culture or other diagnostic applications. In a solid-liquid PCM device, the entire device may have to be re-engineered to be compatible with a new PCM in order to supply a different target temperature. The fuel mass would also need to be adjusted to ensure that the latent heat absorption of the PCM is sufficient to absorb the heat emitted by the exothermic reaction. In contrast, since the liquid-vapor PCM reacts directly with the magnesium fuel in a two to one molar ratio, alcohols with higher boiling points, such as ethanol (Tb = 78°C), may be directly substituted in lieu of methanol with no change to device geometry or manufacturing. However, holdover time is reduced when water is substituted for methanol, which may limit the usefulness of direct alcohol substitution. Liquid-vapor systems may be somewhat limited by

these appropriate material constraints but utilizing azeotropes or dilutions may offer a level of adjustability to the systems.

Since we did not observe substantial gains to system performance when adding more than 10 mg (0.28% by mass) of sodium chloride, there appears to be a saturation of reaction rate after a critical threshold of sodium chloride is reached. Given the toxicity of copper (II) chloride, the reduction in holdover time, and the tendency to overheat, copper (II) chloride may not be appropriate to include in the chemical heater for use in the developing world. We have therefore demonstrated the efficacy of a sodium chloride-catalyzed, isothermal, exothermic chemical heater based on the methanol-water reaction at temperatures compatible with LAMP and potentially with other isothermal methods such as HDA and CPA, which uses the Bst polymerase and are most efficient in the range 60–65°C[390].

Despite the challenges present in developing a liquid-vapor PCM, isothermal heater, there is significant potential for such a device to improve access to diagnostics in the developing world. Unlike other isothermal chemical heaters, the proposed device has great potential to simplify device design and manufacturability by eliminating the need for a separate PCM; alleviate ambient temperature range concerns with a liquid-vapor PCM; and increase the likelihood of successful uptake by lowering barriers to materials access and precise machining requirements[114].

16.6 Conclusions

We have demonstrated that a low-cost, liquid-vapor PCM exothermic isothermal heater may be designed for use with isothermal amplification at temperatures required for LAMP, HDA, and CPA. Such a device may be suitable for use in developing countries by being simple and reduce

device volume and mass compared to previous chemical or electric heaters, while expanding the ambient temperature operating range.

16.7 Acknowledgments

We have no nonfinancial acknowledgements to disclose.

16.8 Author Contributions

Conceived and designed the experiments: KGS DG SD. Performed the experiments: KGS. Analyzed the data: KGS. Contributed reagents/materials/analysis tools: KGS DG SD. Wrote the paper: KGS DG SD JB RB PL RRK BW.

16.9 Funding

Funding was provided by the National Institutes of Health to support this work (NIAID R01 AI097038). Partial salary support to Shah was provided by a grant to Rice University from the Howard Hughes Medical Institute through the Precollege and Undergraduate Science Education program (52006938) and the Arnold and Mabel Beckman Foundation through the Beckman Scholars Program. Salary support was provided to Buser from a Defense Advanced Research Projects Agency grant to Paul Yager (who is not an author on this paper) at the University of Washington (HR0011-11-2-0007), and partial salary support to Shah, Guelig, Diesburg, and Weigl was provided via a subcontract from that grant to PATH. The funders had no role in study design, data collection and analysis, decision to publish, or preparation of the manuscript.

17 Appendix Swab Sample Transfer for Point-Of-Care Diagnostics: Characterization of Swab Types and Manual Agitation Methods

Nuttada Panpradist, Bhushan J. Toley, Xiaohong Zhang, Samantha Byrnes, Joshua R. Buser, Janet A. Englund, Barry R. Lutz

This appendix section is taken in a largely unmodified form from the manuscript[155]. I would like to thank primary author Nuttada Panpradist along with my other coauthors for involving me in the project.

17.1 Abstract

Background: The global need for disease detection and control has increased effort to engineer point-of-care (POC) tests that are simple, robust, affordable, and non-instrumented. In many POC tests, sample collection involves swabbing the site (*e.g.*, nose, skin), agitating the swab in a fluid to release the sample, and transferring the fluid to a device for analysis. Poor performance in sample transfer can reduce sensitivity and reproducibility.

Methods: In this study, we compared bacterial release efficiency of seven swab types using manual-agitation methods typical of POC devices. Transfer efficiency was measured using quantitative PCR (qPCR) for *Staphylococcus aureus* under conditions representing a range of sampling scenarios: 1) spiking low-volume samples onto the swab, 2) submerging the swab in excess-volume samples, and 3) swabbing dried sample from a surface.

Results: Excess-volume samples gave the expected recovery for most swabs (based on tip fluid capacity); a polyurethane swab showed enhanced recovery, suggesting an ability to accumulate organisms during sampling. Dry samples led to recovery of ~20–30% for all swabs tested, suggesting that swab structure and volume is less important when organisms are applied to the outer swab surface. Low-volume samples led to the widest range of transfer efficiencies between swab types. Rayon swabs (63 μL capacity) performed well for excess-volume samples, but showed poor recovery for low-volume samples. Nylon (100 μL) and polyester swabs (27 μL) showed intermediate recovery for low-volume and excess-volume samples. Polyurethane swabs (16 μL) showed excellent recovery for all sample types. This work demonstrates that swab transfer efficiency can be affected by swab material, structure, and fluid capacity and details of the sample. Results and quantitative analysis methods from this study will assist POC assay developers in selecting appropriate swab types and transfer methods.

17.2 Introduction

Diagnostics for non-blood-associated pathogens often use swabs as a specimen-collecting tool. For example, swabs are used to collect throat specimens for Group A *Streptococcus*[395]; nasal and nasopharyngeal specimens for *Staphylococcus aureus*[396], [397], *Bordetella pertussis*, influenza virus[398], [399], and respiratory syncytial virus (RSV)[400], [401]; female endocervical or male urethral specimens for *Neisseria gonorrhea*[402] and *Chlamydia trachomatis*[403]; and fecal swabs for viral gastroenteritis[404]. Depending on the source of collection, swabs should have shaft properties (flexibility, length) and tip size/shape appropriate for the sampling site, and the swab tip material and microstructure should provide efficient sample capture and target release in the presence of sample matrix components (*e.g.*, human cells, body fluids, and other contaminants). Commercially available swabs are currently utilized

with a variety of swab tip materials (*e.g.*, nylon, rayon, cotton, polyester, polyurethane, and alginate polymer) and microstructures (*e.g.*, tightly wound, knitted, flocked fiber, and reticulated). In laboratory settings, swabs are typically agitated by vortex mixing to release organisms into a transfer fluid[405]–[409] that is analyzed by culture, immunoassays (ELISA), or nucleic acid tests (PCR).

Swab sampling and fluid transfer are also used in lateral flow tests (LFTs) intended for point-of-care (POC) testing in non-laboratory settings. Commercial LFTs that are being used with swabs worldwide include rapid streptococcal antigen assays, respiratory syncytial virus (RSV) assays: BinaxNOW RSV Lateral Flow (Alere Inc., Waltham, MA), RSV Respi-Strip (Coris Bioconcept, Namur, Belgium); and influenza detection tests: BinaxNOW Influenza A&B Card (Alere Inc., Waltham, MA), QuickVue Influenza Test (Quidel Corp., San Diego, CA). Typical instructions require the user to dip the swab into transfer fluid (,0.7 mL to 1 mL), manually agitate the swab for a specified time[410], and transfer a fraction of the fluid (~100 μL) to the device[411]. The low fluid capacity of LFTs results in most of the sample being discarded, and manual agitation may be less effective than vigorous vortex mixing used in laboratory settings. Since the sensitivity of LFTs is typically lower than laboratory-based tests, there is a need to maximize transfer of sample from the swab to the device. Studies evaluating swab transfer use widely varied definitions of transfer efficiency, often focus on a specific clinical application, and typically rely on qualitative analysis techniques. Thus, we built on previous work to develop quantitative analysis methods and definitions for swab transfer efficiency that can be applied to a variety of swab types, sampling applications, and transfer methods. We present methods to quantify swab transfer efficiency, discuss potential pitfalls that could bias quantitative analysis, and evaluate transfer efficiency for a range of swab types, sample properties, and manual

agitation methods that meet the unique needs for POC applications. The results and discussion can aid researchers or test developers in rational selection of swabs and transfer methods for diagnostics development in both POC and laboratory settings.

17.3 Materials and Methods

17.3.1 Model organism (*Staphylococcus aureus*)

A single colony of *S. aureus* (ATCC 25923) was inoculated in tryptic soy broth (TSB) (Fisher B11768) and shaken overnight (250 rpm, 37°C). The overnight culture was further diluted 1:100 in TSB and incubated (250 , 37°C) for 3 hours until the OD600 reached 260.2, corresponding to a concentration of ,10^9 CFU/ mL. *S. aureus* bacteria were then harvested and resuspended in one of two buffers: 1X Tris-EDTA buffer at pH 8.0 (TE: 10 mM Tris-HCl +1 mM EDTA) or TE buffer with in-house human simulated nasal matrix (SNM: 110 mM NaCl, 1% w/v mucin from porcine stomach Type III (Sigma, M1778-10G) and 10 μg/ mL w/v human genomic DNA (Promega G3041)) at 90% v/v of TE/SNM.

17.3.2 Swabs and agitation methods

Seven different commercially-available swabs were tested: rayon (Copan Diagnostics Inc., 170KS0, Murrieta, CA), cotton (Puritan Medical Products Co., LLC, 25–806, Guilford, ME), midturbinate (MT) flocked nylon (Copan Diagnostics Inc, 56380CS01, Murrieta, CA), regular-tip flocked nylon (Copan Diagnostics Inc., 502CS01, Murrieta, CA), polyester (PES) (Contec Inc., 19059209, Spartanburg, SC), polyurethane (PUR) (Foamtec International, 19304613, Oceanside, CA), and calcium alginate (Puritan Medical Products Co., LLC, 25-806-2PA, Guilford, ME).

Vortexing is commonly used in the laboratory to maximize release of organisms from swabs, but it is likely not available in low resource settings. Agitation methods for POC tests are

normally specified in units of time, without definition of the method. For consistency across experiments, we defined a base case method for translating the submerged swab along a circular path against the side of the tube at a rate of 1 cycle per second (1 Hz) for a specified time (*e.g.*, ‘‘10 second 1 Hz side twirl’’). The swab agitation was done by hand but using the timer as a reference for manual control of the twirling rate. The potential errors introduced by the users were not excluded in the data. The impact of these variations was tested (below in the section titled ‘‘Robustness to user variations in manual agitation’’).

After the sample was applied to swabs, swabs were agitated in 128 µL of transfer fluid. This volume was chosen to be compatible with the fluid capacity of typical POC devices (~100 µL for LFT) to enable complete utilization of the sample fluid.

17.3.2.1 Volume recovery experiments

To quantify fluid release volume, 15 µL TE buffer was pipetted onto the tip of a dry swab. The swab was then dipped into pre-weighed 128 µL TE buffer (or 1% w/v sodium citrate solution for calcium alginate swab) and agitated (10 second 1 Hz side twirl). The swab was removed, and the fluid left in the tube was weighed. The volume left in tube was calculated (Equation 19) and compared to a control (Equation 20). As the control, 15 µL TE buffer was pipetted into 128 µL of pre-weighed TE buffer, and the fluid in the tube was weighed. The % Volume Recovery was calculated using Equation 21.

$$Vol\ avail.for\ analysis\ (test) = V_{initial} - V_{losttoswab}$$ $$= V_{initial} - \frac{(W_1, test - W_2 test)}{density\ of\ fluid}$$	Equation 19

$Vol.avail.for\ analysis\ (control) = V_{initial} - V_{added}$	Equation 20

$\%Vol.avail.for\ analysis\ (\%\ Vol.Recovery) = \frac{Vol.avail.for\ analysis\ (test)}{Vol.avail.for\ analysis\ (control)}$	Equation 21

where $W_{1,\ test}$ = initial weight of test tube containing 128 µL TE buffer

$W_{2,\ test}$ = weight of test tube after swab transfer and removal

$W_{1,\ control}$ = initial weight of control tube containing 128 µL TE buffer

$W_{2,\ control}$ = weight of control tube after 15 µL TE buffer was added

V_{added} = added volume of TE (either onto swab or onto control tube), 15 µL

$V_{initial}$ = initial volume of TE in test or control tube, 128 µL

$\frac{W_2,control - W_1,control}{V_{added}} = density\ of\ fluid$, used to convert weight change of fluid in the test tube ($W_{2,test} - W_{1,test}$) into volume change. ($W_{2,test} - W_{1,test}$) is negative when the swab absorbed more fluid from the tube than it released. Adding

$$\frac{(W_2, test - W_1, test)\ x\ V_{added}}{(W_2, control - W_1, control)}$$

to $V_{initial}$ would provide the recovered volume in the test tube (Volume available for analysis (test)). A transfer volume of 128 µL was selected because this volume allowed at least 20 µL to be recovered after the swab transfer step for all swab types for further testing by qPCR (as described in the next section); it also represents an appropriate volume for LFTs.

17.3.2.2 Organism recovery experiments.

Bacteria from swabs and control samples were lysed using a method modified from Patel *et al* [412], and lysed samples were analyzed by quantitative PCR (qPCR). Regular-tip nylon, MT nylon, and rayon swabs were obtained in sterile packaging, and PES and PUR swabs and other materials were autoclaved prior to use. All swabs and materials were tested for bacteria and DNA bacteria contamination. In all experiments, bacteria were transferred from the swab to 128 µL of 3 U/µL achromopeptidase (ACP) (Sigma #A3547) in TE to lyse the bacteria. Lysis continued for 2 minutes at room temperature. Following lysis, ACP was deactivated by heating (10 minutes, 95°C), and the sample tube was placed in ice immediately. Bacterial lysate was filtered through a centrifuge tube filter (0.2 mm pore size) to remove debris. 9 µL of the filtered lysate was analyzed by a MRSA/SA ELITe MGB qPCR assay (Elitech Group Molecular Diagnostics, formerly Epoch Biosciences, #M800346). This assay detects a single open reading frame encoding *S. aureus* specific lactate-dehydrogenase-1 (*ldh1*). The concentration of *ldh1* copies in each sample (copies/µL) was estimated based on a standard curve (80 to $8x10^8$ *ldh1* copies). To verify that swabs were not contaminated during experiments, negative control samples (15 µL of TE buffer (N =3) and swabs with no added bacteria (N = 3)) were transferred to 128 µL of lysis buffer and analyzed by the same procedures as other samples.

S. aureus was applied to swab tips using one of the three methods described in the following sections and eluted into 128 µL of pre-weighed lysis buffer. In the control case, *S. aureus* was introduced directly to 128 µL of pre-weighed lysis buffer. Both test and control tubes were weighed and set aside to allow for the lysis to complete. Filtered lysate then underwent qPCR for quantitation of *ldh1* concentration (copies/µL). The limit of detection (LoD) of qPCR was less than 5 *ldh1* copies per reaction, corresponding to about 1 CFU per reaction (Fig.

S1[155]). Weights of test and control tubes were used to calculate volumes left in the tubes (Equation 19 and Equation 20, respectively). The number of *ldh1* copies left in tube in each case was calculated using Equation 22, and the % Organism Recovery was calculated using Equation 23.

$$ldh1\ copies\ (control\ or\ test) = ldh1\ concentration\ \left(\frac{copies}{\mu L}\right) x\ Volume\ (\mu L)(control\ or\ test)$$

Equation 22

$$\%Organism\ Recovery = \frac{ldh1\ copies\ (test)}{ldh1\ copies\ (control)}\ x\ 100$$

Equation 23

Further details on how *S. aureus* was introduced to swabs in each method are described below.

17.3.3 Low-volume fluid sample (less than swab saturation)

15 µL *S. aureus*/TE (100, 10^4, and 10^6 CFU) was pipetted onto a swab tip. The amount of bacteria input exceeded the LoD of the qPCR assay (Fig. S1[155]). The swab was then dipped into lysis buffer, manually agitated (as described above or 10 second 1 Hz side twirl), and removed. The number of *ldh1* copies was measured and compared to a control case in which *S. aureus*/TE solution was directly pipetted into pre-weighed lysis buffer (with no submergence of pipette tip to avoid introducing bacteria from the outside surface of the tip). A fresh pipette tip was then used for mixing.

17.3.4 Excess-volume fluid sample (beyond swab saturation)

A dry or a pre-wet (by dipping into TE) swab was dipped into 1 mL of *S. aureus*/TE solution (10^6 CFU/mL) and manually agitated (10 second 1 Hz side twirl) to load sample into the swab.

Swabs were transferred into pre-weighed lysis buffer, manually agitated, and removed. The number of *ldh1* copies in the lysis tube was measured and reported.

17.3.5 Sample dried on a surface

Dried bacterial samples were prepared by pipetting 15 µL of *S. aureus*/TSB (10^4 CFU) onto sterilized 25/46-inch diameter polydimethylsiloxane (PDMS) punches and left in a desiccator for 30 minutes. PDMS was chosen as the surface since it is known to not adhere to *S. aureus* organisms[413], and we attempted to remove effects of collection efficiency by using a very vigorous swabbing procedure (goal of 100% collection). A dry or a pre-wet swab was rubbed across the PDMS surface 10 times to pick up organisms (Fig. S2[155]), transferred into the pre-weighed lysis buffer (128 µl), manually agitated, and removed. The number of *ldh1* copies in the lysis tube was measured and compared to a control. In the control, the eluate was derived from placing the PDMS punch with dried bacteria directly in lysis buffer and vortexing for 10 seconds.

17.3.6 Robustness to user variations in manual agitation

15 µL of *S. aureus*/TE solution (10^4 CFU) was pipetted onto a dry swab, and the swab was dipped into lysis buffer. Different manual-twirling methods were used to release bacteria. ‘‘Side twirl’’ refers moving the swab tip around the interior side of the tube in a circular motion. ‘‘Bottom twirl’’ refers to placing the swab tip at the bottom of the tube and rotating the shaft.

17.3.7 Engineering for improved recovery

A forced-flow method using a syringe was developed as an alternative to manual agitation to improve organism recovery. In the test case, 15 µL of S. aureus/TE (10^4 CFU) was introduced onto a dry swab, and the swab was dipped into the lysis buffer tube, the bottom of which was connected to a syringe. The plunger of the syringe was then pushed and pulled 5 times. At the

end, the swab remained in the tube whereas the eluate was contained within the syringe piston and could be purged through an opening in the side of the syringe.

17.3.8 Bench-top gold standard method

Swabs (N =5) were tested for organism recovery using a laboratory protocol: vortexing for 10 seconds at the maximum speed. In the test case, 15 µL of *S. aureus*/TE (10^4 CFU) was introduced onto a dry swab, and the swab was dipped into lysis buffer prior to vortexing.

17.3.9 Data Analysis

Statistical analysis was performed using MATLAB (MathWorks, Natick, MA). Analysis of variance (ANOVA) was used to test for significant differences among means. In the case that ANOVA indicated significant differences ($p<0.05$), post-hoc comparisons (Tukey-Kramer procedure, adjusted for multiple comparisons) were used to determine which means were significantly different from one another. The data and analysis underlying the findings are fully available on request.

17.4 Results

A variety of swab types were evaluated under different conditions, as illustrated in Figure 107. We selected a set of commercially-available swabs representing a range of materials, microstructure, and size: low absorbent foam (reticulated polyurethane swab – PUR and knitted-pattern PES swabs – PES), low absorbent fiber (MT nylon flocked swabs – MT nylon, and regular-tip nylon flocked swabs), high absorbent fiber (tightly wound cotton and rayon swabs), and dissolvable swabs (calcium alginate swabs). Figure 106 shows scanning electron microscopy images of the nylon (flocked), PUR (reticulated), PES (knitted), and rayon (wound) swab tips; this set exhibits a wide variety of material structures and pore sizes.

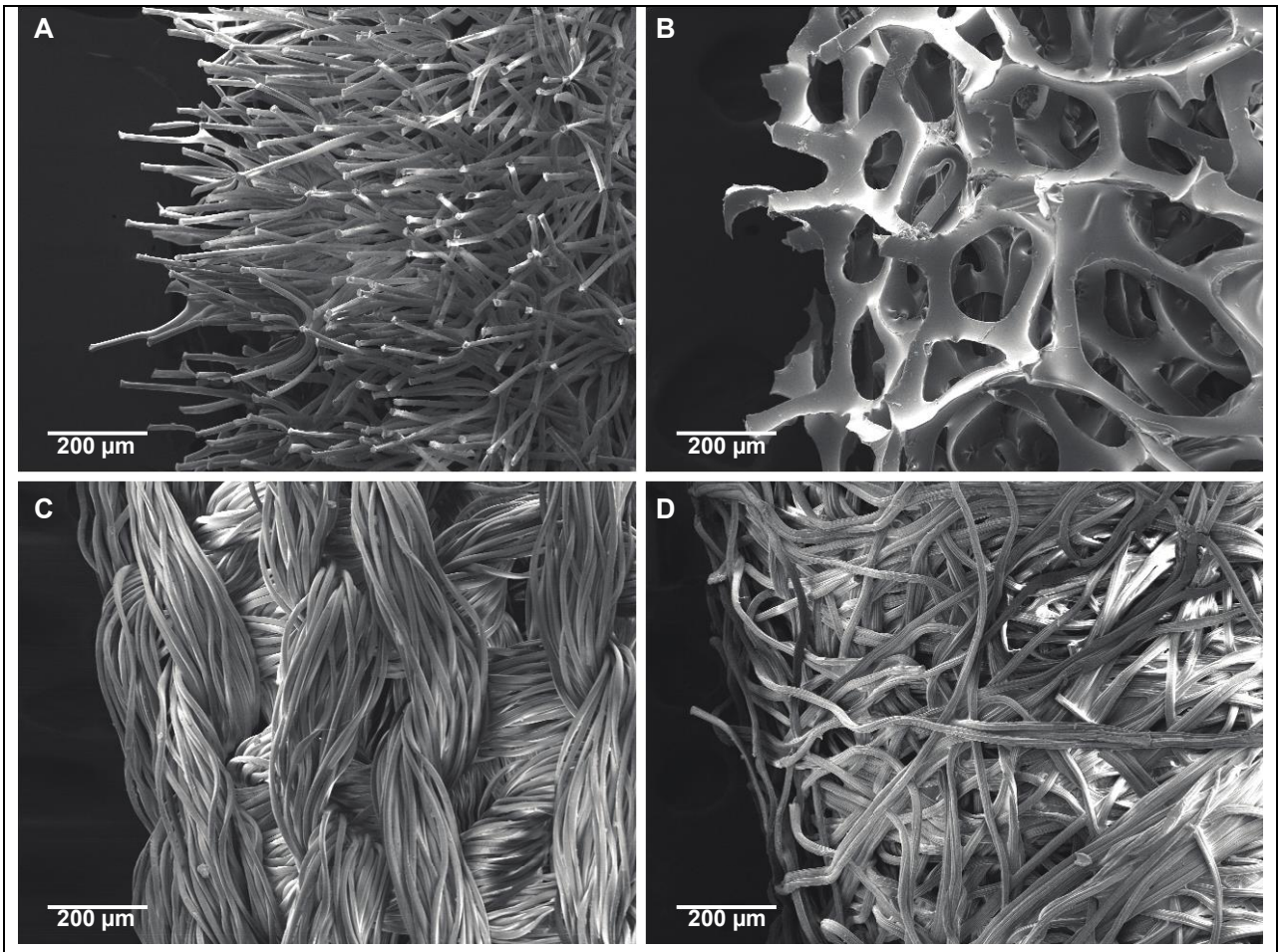

Figure 106: Scanning electron micrographs of swab tips: (A) mid-turbinate Nylon (B) polyurethane (C) polyester (D) Rayon. Scanning electron micrographs were obtained using an FEI Sirion scanning electron microscope. Samples were sputtered with an 11 nm Au/Pd coating prior to imaging (SPI Module Control, Structure Probe, Inc., West Chester, PA, USA.) SEM imaging and sputter coating work was performed at the University of Washington Nanotech User Facility (NTUF), a member of the NSF-sponsored National Nanotechnology Infrastructure Network (NNIN).

We focused on the manual ‘‘insert and twirl’’ agitation method common for LFTs and used a reduced fluid transfer volume (~100 µL) appropriate for typical LFTs. Swabs were evaluated in a series of tests, with subsets of swabs chosen for each test to illustrate key differences and analysis methods. Swabs were first tested for fluid retention (loss of fluid sample to the swab), and swabs with low retention volume were carried forward to test organism recovery. We used *Staphylococcus aureus* as a model system, with recovery quantified by

quantitative polymerase chain reaction (qPCR). Organisms were applied to swabs under various conditions to represent a range of sampling conditions from dry to wet: a) low-volume fluid sample (less than swab saturation), b) high-volume fluid sample (beyond swab saturation), and c) sample dried on a surface. For the low-volume sample condition, recovery was tested for a wide range of concentrations (100 to 10^6 organisms)[414], and a simulated human nasal matrix was used as an example of a complex sample. Pre-wet swabs were compared to dry swabs for the cases of excess sample volume and dry sample collection. We also tested variations on manual agitation to identify sensitivity to user operation, and demonstrated an engineered manual agitation method to improve recovery for swab-sample combinations that performed poorly. The data from all experiments are summarized in Tables S1 and S2[155].

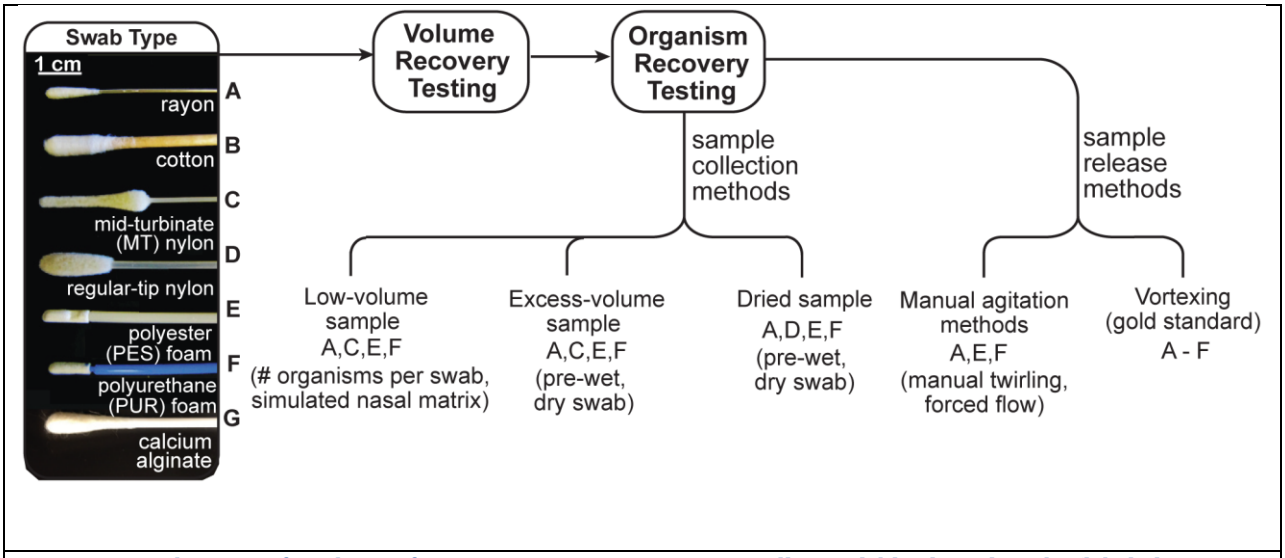

Figure 107: Schematic of swab transfer experiments. Seven commercially-available clinical swabs (labeled A, B, C, D, E, F, and G) were tested for volume recovery and organism recovery. Organisms were applied to swabs in three ways: pipetting a low-volume sample onto the swab, dipping the swab into excess-volume sample, or rubbing the swab across dried sample on a surface. Selected cases included variation in sample concentration, addition of simulated nasal matrix, and comparison of dry and pre-wet swabs. Different manual swab agitation methods, manual twirling and forced flow, were tested for their effects on swab transfer efficiency compared to vortexing (gold standard method). doi:10.1371/journal.pone.0105786.g001

17.4.1 Volume recovery

Fluid volume retention for seven commercially-available swabs is shown in Figure 108. Swabs with 15 µL of added fluid were inserted into tubes containing 128 µL of fluid and removed, and the fluid remaining in the tube was used to calculate fluid volume lost to the swab (Figure 108A). Figure 108B shows the fluid volume lost to each swab, and Figure 108C shows the percent volume available for analysis (% volume recovery) for a starting volume of 128 µL. PUR and PES yielded the highest volume recovery (PUR: mean± SE = 89±0.4%; PES: 81±0.3%). Conversely, cotton and regular-tip nylon swabs retained more fluid resulting in the poorest volume recovery (cotton: 8±0.6%; regular-tip nylon: 30±3.4%). The remaining swabs, rayon and MT nylon, had intermediate volume recovery (rayon: 56±2.5%; MT nylon: 70±0.8%). All data points in Figure 108B and C have 5 replicates. A one-way ANOVA indicated that volume recovery differed significantly across swab types ($p<0.0001$). Post-hoc comparisons indicated that PUR had a significantly higher volume recovery than other swab types ($p<0.05$). Additionally, we tested dissolvable calcium alginate swabs in the recommended dissolution buffer (sodium citrate). The recommended procedure uses a buffer volume that is too large for LFTs (15 mL), and using the small volume (128 µL) resulted in a glue-like gel that would not flow through an LFT (Fig. S4[155]).

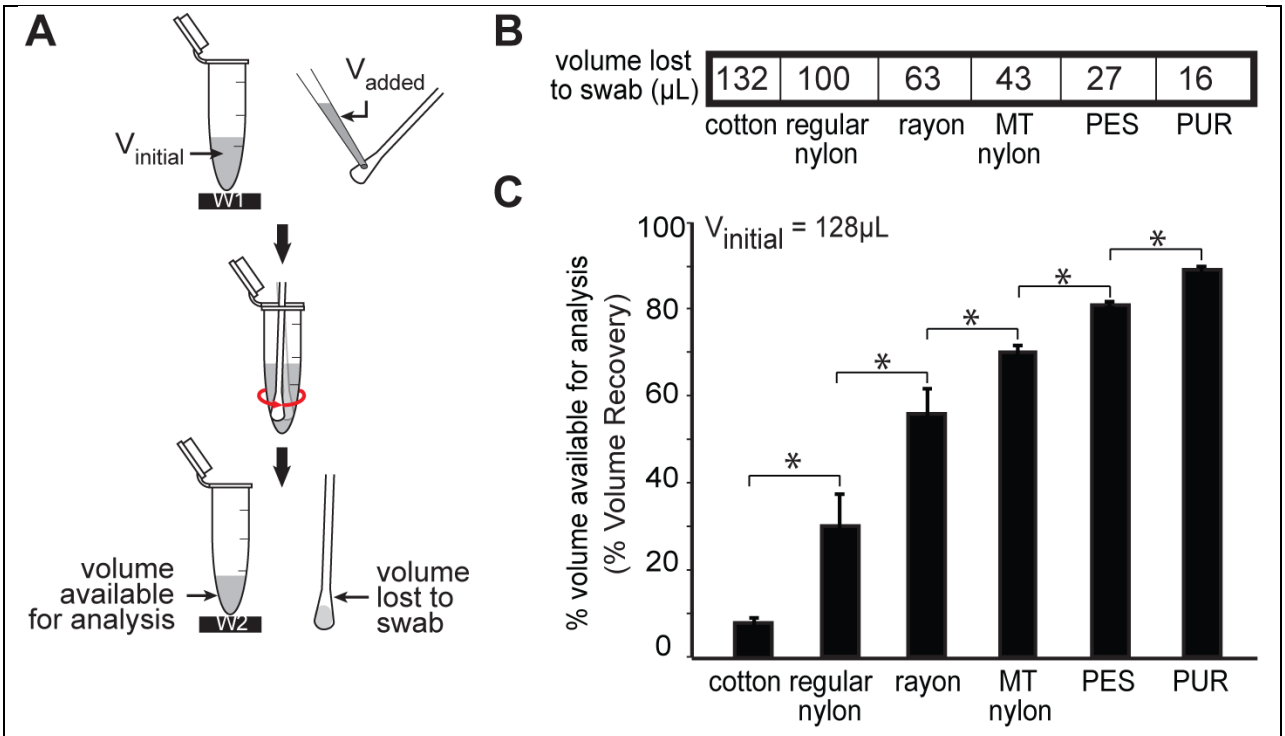

Figure 108: Volume recovery testing. (A) Schematic of the experimental setup. The tube containing 128 µL TE was weighed (W1), and 15 µL TE was pipetted onto the swab, which was then transferred into the tube using 10 second 1 Hz side twirl, and removed. The tube containing the leftover buffer (eluate) was weighed (W2). The % volume available for analysis (% Volume Recovery) was calculated using Equation 21 in the text. (B) Mean TE volume (µL) absorbed by each type of swab (N = 5). (C) Comparison of the % Volume Recovery (mean ± SE; N= 5) from each swab. Calcium alginate swabs were resuspended in 1% w/v sodium citrate buffer to dissolve fibrous tip materials, the % Volume Recovery was not reported here due to density change of the buffer during (A). * indicates significant differences (Tukey-Kramer, α = 0.05). doi:10.1371/journal.pone.0105786.g002

17.4.2 Organism recovery

We determined that our modified ACP lysis method gave the same amount of amplifiable DNA as the original method by Patel *et al*[412] (Fig. S5[155]) . Eluate recovered from swabs was devoid of bacteria or bacterial DNA (Fig. S6[155]) and did not interfere with qPCR or ACP lysis (Fig. S7[155]). The qPCR assay reported 3–6 genomic copies per CFU across all experiments; along with each experiment result we report the sample CFU for reference, but recovery values reported in this paper are based on copies measured by qPCR. Results are reported as absolute

organisms recovered (Equation 22) or as % organism recovery based on a control sample analyzed by the same method (Equation 23).

17.4.2.1Low-volume fluid samples

Swabs were tested with a sample volume that was less than the fluid capacity for all swabs (15 µL). Four dry swab types (PUR foam, knitted PES, rayon, and MT flocked nylon swabs (N = 5)) were tested for organism recovery using low-volume samples (Figure 109A). When bacterial solution was pipetted onto the swab tip, fluid absorption behaved differently among swab types. For PUR swabs, the fluid beaded up on the surface without absorbing. For PES and nylon swabs,

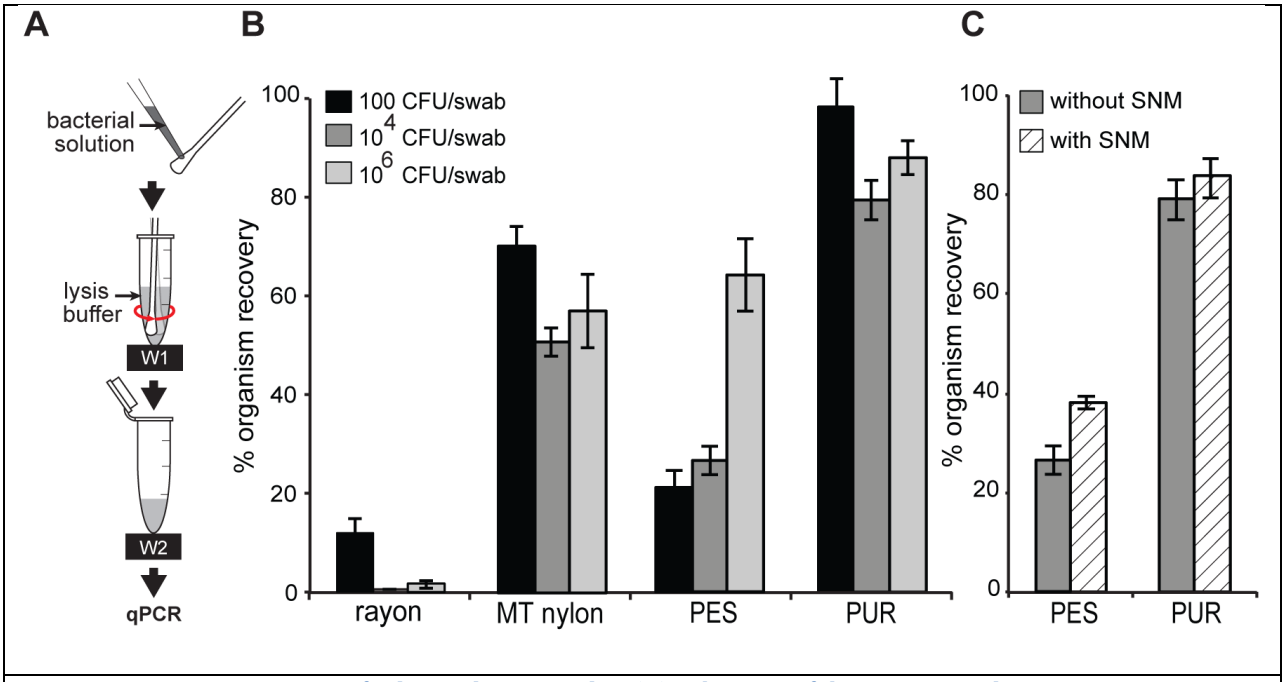

Figure 109: Organism recovery for low-volume samples. (A) Schematic of the experimental set up. 15 µL *S. aureus*/TE (~100,~10^4, or ~10^6 CFU, equivalent to 500, 6x10^4, or 4x10^6 *ldh1* copies, respectively, as measured by qPCR) was spiked onto the swab, which was then agitated in 128 µL lysis buffer using 10 second 1 Hz side twirl, and removed. (B) Comparison of the % Organism Recovery in four swabs at three different organism input numbers (mean± SE, N= 5), which was calculated using Equation 23 in the text. (C) Comparison of the % Organism Recovery (mean± SE; N= 5) using ~10^4 CFU/swab of *S. aureus* in the presence and absence of simulated nasal matrix (SNM). doi:10.1371/journal.pone.0105786.g003

the bacterial fluid formed a thin film around swab tip but did not bead up. For rayon swabs, fluid was completely absorbed into swab tips.

The percent organism recovery of each swab using low-volume samples is shown in Figure 109B. Regardless of the number of organisms added, PUR foam yielded the highest organism recovery of 79%–98%. MT nylon and PES had intermediate organism recovery of 51–70% and 21–65%, respectively. Rayon provided the lowest organism recovery of 1–12%. A two-way ANOVA indicated significant effects of swab type and numbers of organisms applied to swab, and a significant interaction (every $p < 0.05$). Post-hoc comparisons showed that organism recovery of PUR was significantly higher than other swabs (followed by MT nylon, PES, and rayon).

Figure 109C compares % organism recovery of PES (N =5) and PUR (N = 5) for bacterial samples in the presence and absence of simulated nasal matrix (SNM). We verified that SNM did not interfere with qPCR and ACP lysis (Fig. S8[155]). Despite the presence of SNM, PUR swabs still yielded significantly higher organism recovery than PES swabs; mean±SE was 84±4% for PUR and 38±2% for PES (two-way ANOVA, effect of swab type, $p<0.0001$). SNM significantly increased % organism recovery ($p = 0.03$).

17.4.2.2 Excess-volume fluid sample (beyond swab saturation)

Four swabs (rayon, PES, PUR, and MT nylon (N = 5)) were tested using excess-volume samples (1 mL). As the swab was submerged into 1 mL bacterial solution and twirled (Figure 110A), dry rayon, PUR and PES swabs released air bubbles and allowed solution to flow into the interior of the swab tip. Figure 110B reports the number of organisms released from the swab into lysis buffer. A two-way ANOVA showed a significant effect of swab type on the number of

organisms recovered (p= 0.0001) and prewetting the swab (p= 0.001). No significant interaction was found (p = 0.63). Post-hoc analysis indicated that PES swabs yielded significantly fewer organisms recovered than rayon, MT nylon and PUR. Wetting the swab reduced number of organisms recovered. The number of organisms recovered from each swab was then normalized by the product of its volume capacity and the concentration of organisms in the bacterial sample solution (Figure 110C). Two-way ANOVA indicated significant effect of swab type (p<0.0001) and pre-wetting the swab (p = 0.009). Post-hoc analysis reported that PUR swabs had significantly higher normalized organism recovery than other swabs.

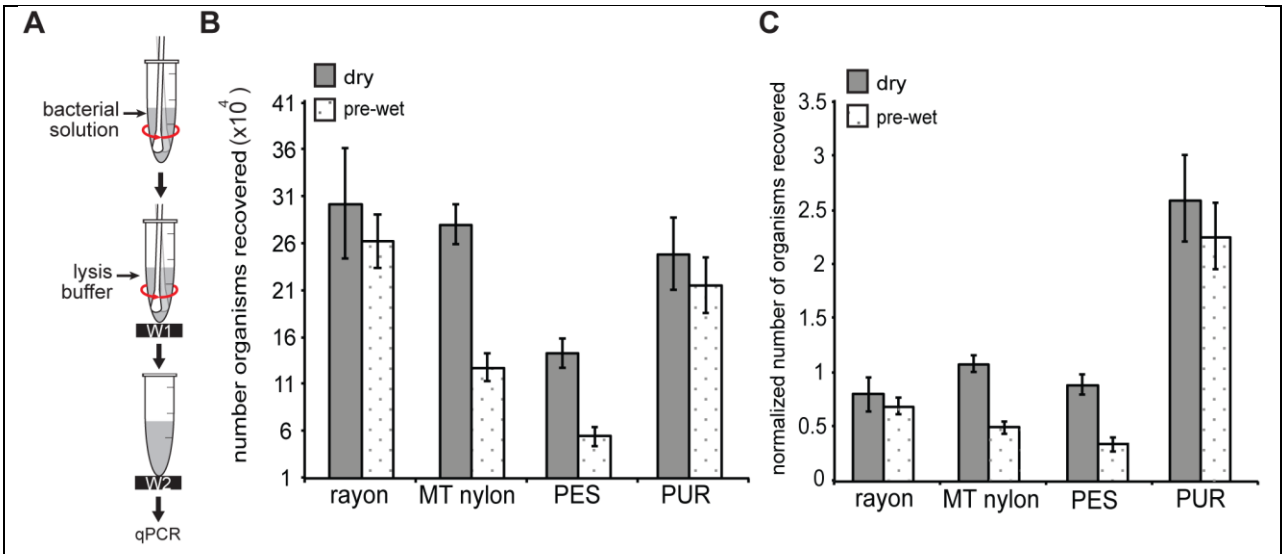

Figure 110: Organism recovery for high-volume samples. (A) Schematic of the experimental set up. Either a dry or pre-wet swab was dipped into 1 mL ,10^6 CFU/mL *S. aureus* solution (equivalent to 6x10^6 *ldh1* copies/mL, as measured by qPCR) and agitated by 10 second 1 Hz side twirl. The swab was then inserted into 128 µL lysis buffer, agitated by 10 second 1 Hz side twirl, and removed. (B) Comparison of the absolute number of organisms recovered for dry and pre-wet swabs. Absolute organism recovery was reported (rather than %) since the uptake of sample volume was different for each swab; absolute recovery was calculated using Equation 22 in the text. In all cases, recovery was larger than would be expected based on swab volume and sample concentration by colony counts due to presence of multiple target copies per CFU. (C) The number of organisms recovered from each swab from panel (B) normalized by the number of organisms expected based solely on the sample concentration and volume capacity of the swab (estimated number of organisms collected by the swab = swab volume capacity (µL) x bacterial stock concentration (copies/µL from qPCR)). doi:10.1371/journal.pone.0105786.g004

17.4.2.3 Sample dried on a surface

Four swabs (PUR, PES, rayon, and regular-tip flocked nylon swabs (N = 5)) were tested for organism recovery using a dried bacterial sample (Figure 111A). Swabs were dry or pre-wet (by dipping into TE buffer). To ensure that a swab was able to pick up the dried sample effectively, the swab was rubbed vigorously on the surface of PDMS (Fig. S2[155]). Figure 111B shows % organism recovery for dried samples. A two-way ANOVA indicated % organism recovery was affected by swab type ($p = 0.0004$) and wet/dry swab pre-conditions ($p = 0.02$) with no significant interaction ($p = 0.4$). Post-hoc comparisons showed rayon had significantly lower % organism recovery than other swabs.

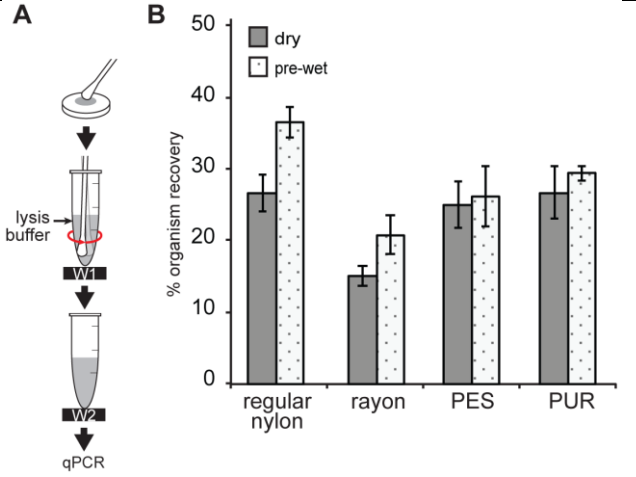

Figure 111: Organism recovery for dried samples. (A) Schematic of the experimental set up. 15 µL of *S. aureus* solution (~10^4 CFU, equivalent to 6x10^4 *ldh1* copies, as measured by qPCR) was spotted on a 25/64-inch diameter PDMS punch and left to dry. A dry or pre-wet swab was rubbed on the PDMS surface (10 times), agitated in 128 µL lysis buffer using 10 second 1 Hz side twirl, and removed. (B) Comparison of % organism recovery for pre-wet and dry swabs based on a control sample and an assumption of 100% collection efficiency. doi:10.1371/journal.pone.0105786.g005

17.4.2.4 Robustness to user variations in manual agitation.

Three dry swab types (PUR, PES, and rayon (N = 5)) were tested for variations in manual agitation to release organisms into the lysis buffer (Figure 112A). All manual twirl methods yielded comparable % organism recovery from PUR swabs (Figure 112B); the low variation in PUR swabs was likely due to lack of sample absorption into the hydrophobic swab tip, which allowed sample release without agitation. Greater variation was observed in PES and rayon swabs (Figure 112D), which represented more realistic sampling conditions. Coefficients of

variation of organism recovery of all manual twirling methods were 7% for PUR, 23% for PES and 40% for rayon swabs.

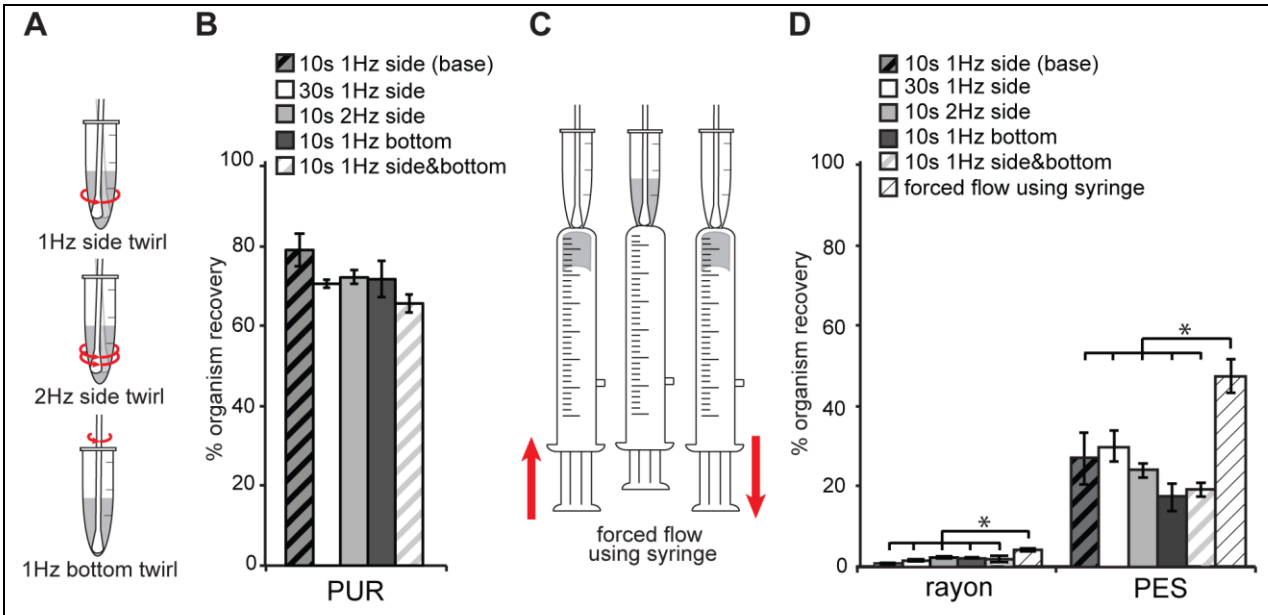

Figure 112: Comparison of manual agitation methods for swab transfer. (A) Schematic of action performed over a period of 1 second for different manual twirling methods. (B) Comparison of % organism recovery of PUR swabs using different twirling methods, which was calculated using Equation 23 in the text. (C) Schematic of the new forced flow syringe method. (D) Comparison of % organism recovery for PES and rayon swabs, using different twirling methods and the forced flow syringe method. * indicates statistically significant differences (Tukey-Kramer, α = 0.05). doi:10.1371/journal.pone.0105786.g006

17.4.2.5 Engineering for improved recovery.

A new manual agitation method, forced fluid flow using a syringe, was developed to increase organism recovery (Figure 112C). In order to test effectiveness of this method in improving organism recovery, intermediate-performing swabs (rayon and PES; Figure 109D) were selected. We compared % organism recovery derived from the forced-flow using the syringe method to other agitation methods (Figure 112D). A one-way ANOVA rejected the hypothesis that there was no difference among the six agitation methods. Post-hoc comparison (Tukey-Kramer, α

=0.05) indicated that the forced flow using the syringe method yielded significantly higher organism recovery than the other five methods. This was true for both swab types.

17.4.2.6 Bench-top gold standard method.

Six swabs (PUR, PES, MT nylon, regular-tip nylon, cotton, and rayon) were tested for their organism recovery when 10 seconds of vortexing was applied. Organism recovery of cotton swabs could not be reported, since they absorbed all of the sample fluid. For the rest of swab types, a one-way ANOVA rejected the hypothesis that there was no difference among swab types. Post-hoc comparison (Tukey- Kramer, $\alpha = 0.05$) indicated that PUR, PES, and MT nylon yielded significantly higher organism recovery than rayon and regular-tip nylon (Fig. S9[155]). In comparing the efficiency of vortexing and 1 Hz side twirl, vortexing offered a significant improvement over 1 Hz side twirl methods for PES, MT nylon, and rayon ($p<0.001$ in all cases). However, vortexing did not significantly increase organism recovery in PUR ($p>0.05$). Additionally, vortexing yielded a significantly higher organism recovery for PES and rayon compared to forced flow using syringe method ($p<0.001$ in both cases).

17.5 Discussion

In this study, we characterized several important properties of swabs currently utilized world-wide in many POC diagnostic tests. The experimental design had three overall aims: 1) to provide quantitative analysis and definitions of swab transfer efficiency that can be used to evaluate swabs and transfer methods, 2) to identify differences in swab transfer efficiency for a selection of common swabs and sample conditions, and 3) to identify commercially available swabs that perform well for sample conditions and manual agitation methods typical of POC testing. The results demonstrate that the choice of swab type for POC testing may be critical to achieving a sensitive and reliable test.

We built on previous work to develop analysis methods and definitions for quantitative evaluation of swab transfer efficiency. Some studies have assumed that the volume absorbed is an accurate representation of organisms picked up by the swab[408], [415], [416]. This assumption applies only when organism densities are the same inside and outside the swab; it will be inaccurate if organisms accumulate in the swab during agitation or if organisms do not flow freely into the swab. Our results show that swab transfer efficiency cannot be predicted based on fluid volume recovery alone, rather it requires analysis of organism recovery. The method for measuring the number of organisms in a sample also varies across studies. For bacteria, common measures include optical density at 600 nm (OD600), colony counts (as colony forming units, CFU)[408], [417]–[419], and quantitative polymerase chain reaction (qPCR). However, OD is only applicable to high organism density. In colony counting, the transfer procedure itself can affect organism vitality (*e.g.*, due to fluid composition, physical damage by vortexing or agitation)[420]. For clustering or biofilm forming organisms[421], such as *S. aureus*, fragmentation during the transfer procedure can artificially increase the apparent recovery[420]. Thus, colony counting can bias results when comparing transfer methods or using a control to calculate percent organism recovery since each sample experiences different conditions. In contrast, qPCR provides consistent results independent of cell viability or clustering[422], [423], and it allows calculation of transfer efficiency by normalizing organism recovery to an input control sample analyzed by the same method. Our results demonstrate that qPCR and input controls allow quantitative measurement of swab transfer efficiency that can be applied across studies.

The scenario of low-volume samples showed the largest difference between swab types. For example, the sample beaded on the hydrophobic tip of the PUR foam swab and was

promptly released into the lysis buffer; this scenario is not a realistic sampling case since the swab resists collection of the small fluid volume, and the high recovery should be interpreted with caution (although we note that PUR swabs also gave high recovery for high-volume samples and dry samples). In less hydrophobic materials such as PES and MT nylon, a thin film coating of bacterial solution was created surrounding the swab tip resulting in intermediate recovery. The hydrophilic tip of the rayon swab[408] fully absorbed the small sample solution, and absorption of transfer fluid may have further driven sample into the swab interior resulting in poor recovery during agitation. Thus, the wettability of the swab itself may impact specimen recovery.

Intuitively, swabs with larger volume capacity will collect more organisms when excess fluid sample is available. We hypothesized that, in addition to the swab volume capacity, swab chemical composition and structure can impact organism pick up and release. To investigate this, we normalized the number of organisms recovered by the estimated number of organisms that would have been picked up if there were no impact of material composition and structure. The nylon, PES, and rayon swabs all transferred near the expected number of organisms based on their volume capacity, but the normalized organism recovery for the PUR swab was more than 2.5 fold higher than the other swabs (Figure 110C). This result suggests that swabs may accumulate organisms during agitation. Surprisingly, the PUR and rayon swabs maintained their recovery under pre-wet conditions. For the PUR swab, the large open pore structure may have allowed effective exchange of pre-wetting fluid with sample during collection. For the rayon swab, the large tip and dense structure may have prevented access to sample in the swab interior (as in Figure 109) for both dry and pre-wet conditions; the good recovery would then imply that rayon also accumulated organisms on its outer surfaces during collection. The results suggest

that swab composition and structure can have a significant impact on collection and release efficiency and should be evaluated for the specific organism and sample type.

Swabs can be used to collect samples from dry surfaces, such as for environmental testing and sampling from skin or dry nasal passages, and pre-wet swabs are sometimes used to increase collection efficiency for dry samples[418]. The improved performance of rayon swabs with dry samples (Figure 111B) compared to the low-volume case (Figure 109B) suggests that organisms collected from a dry surface were more accessible to manual agitation. This would be expected since dry collection deposits sample on the exterior surface of the swab, whereas liquid samples wick into the swab interior where they may be inaccessible by manual agitation. Similarly, the effect of pre-wetting was more pronounced for rayon and regular nylon (Figure 111B), which have relatively high volume absorption compared to PES and PUR (Figure 108B). The pre-wetting step filled the interior volume of swabs prior to sampling, and presumably this allowed dried sample to remain on the exterior surface of swabs where they were more effectively released during manual agitation.

Biological fluids found in clinical specimens can affect organism recovery. Complex matrices can affect physical properties (*e.g.*, viscosity) or chemical properties (*e.g.*, binding to swab materials or passivating swab surfaces). For example, mucin has been found to reduce non-specific binding of protein and has been used to coat biomaterials to create non-fouling surfaces[424] and repel other negatively charged molecules[328] (*e.g.*, DNA). However, the increased viscosity of complex matrices may reduce the effectiveness of agitation. As an example of a sample matrix, we measured recovery in the presence of simulated nasal matrix (SNM) and found that it had little effect on organism recovery (Figure 109C). The effect of sample matrix will be highly dependent on the sample type and should be evaluated for each

application; the experimental design used here for SNM can be applied to quantitatively measure the effects of sample matrix on swab transfer efficiency.

User variations in swab transfer procedure could affect test sensitivity and reproducibility. Commercial LFTs typically include instructions to agitate the swab for a given time but do not specify the method. Our results with selected swabs showed that variations in agitation method and time had modest impact on organism recovery for the case of low-volume samples. Robustness to user variation will be especially important to maintain sensitivity and reproducibility for POC tests performed by untrained users and should be tested for all applications.

We demonstrated that an engineered swab transfer method can increase recovery from poorly performing swabs. However, the improved organism recovery was still significantly lower compared to vortexing (gold standard). Other engineered methods could include buffer-filled swab shafts that push fluid from the swab interior or methods that compress the swab to remove absorbed fluid. This finding has direct application to future developments in POC testing.

The PUR swab was the best performing swab across all sample conditions. This may be of clinical interest as similar PUR swabs have been found to be sensitive for the detection of respiratory viruses in immunocompetent and immunocompromised human subjects[425]. In addition, smaller swab size may be applicable to clinical use in subjects of diverse size and in sampling of diverse structure. The small volume of the PUR swab and reproducible recovery for variations in agitation methods also make it well suited for application in POC devices.

Limitations of this work included the use of analytical samples instead of clinical samples, and the use of a single organism, *Staphyloccocus aureus*, as a model due to its relevance as a human pathogen. However, these choices allowed us to create replicable cultured samples with known numbers of organisms and to create various sample types representative of swab collection sites (from dry to wet samples, in the presence or absence of other biological components). Other limitations of this work include the evaluation of a limited number of swab types, although they represent some of the most common commercially-available swab types used in clinical testing today. Finally, although the number of organisms transferred from swabs involves both collection and release, swab collection efficiency is highly dependent on the target pathogen and details of the sampling site; our work only focused on swab transfer release efficiency.

17.6 Conclusions

We have built on previous work to develop a quantitative method to evaluate and compare swab transfer performance. We evaluated a variety of swabs under manual agitation conditions appropriate for POC testing. By selecting a set of commercially available swabs representing a variety of tip sizes, shapes, and materials, and utilizing qPCR as a direct measure of target quantity, we were able to quantitatively measure the transfer efficiency of a model organism. Our data show that swab size, structure, or composition affects swab release performance under different sampling conditions (low-volume, excess volume, or dry samples). Variations in manual agitation method and time had modest impact on swab transfer efficiency for three swabs tested, which is encouraging considering the likelihood of user variation in POC tests. For cases when a test is constrained to a swab with poor transfer efficiency, we demonstrated how forced-flow transfer methods could be used to improve transfer efficiency.

The results and discussion presented here highlight key factors that should be considered in selecting swabs for POC applications. The quantitative evaluation methods developed here can be applied to other swab types in the future, both for POC applications or laboratory tests.

17.7 Acknowledgments

We thank our colleagues Paula Ladd and Erin Heiniger at the University of Washington, who provided useful discussions on experimental design and analytical methods. We thank collaborators Nic Vermeulen, Boris Alabyev and Karina Stepaniants from ElitechGroup North America Inc. Molecular Diagnostics (previously Epoch Biosciences) for input on swab selection, simulated nasal matrix, and experimental design and for supply of the qPCR assay; and David Moore, Erik Kvam, Andrew Burns, Bing Li, Frank Mondello, Scott Duthie and Matt Misner from GE Global Research for discussions on swab materials and experimental design. We thank our colleagues Paul Yager and Elain Fu and members of the Yager Lab, Fu Lab, and Lutz Lab at the University of Washington. SEM imaging and sputter coating work was performed at the University of Washington Nanotech User Facility (NTUF), a member of the NSF-sponsored National Nanotechnology Infrastructure Network (NNIN).

17.8 Author Contributions

Conceived and designed the experiments: NP BJT XZ SB JRB JAE BRL. Performed the experiments: NP BJT XZ SB JRB. Analyzed the data: NP BJT XZ SB JRB JAE BRL. Contributed reagents/materials/analysis tools: NP BJT XZ SB JRB. Contributed to the writing of the manuscript: NP BJT XZ SB JRB JAE BRL.

18 Appendix: Tunable-Delay Shunts for Paper Microfluidic Devices

Bhushan J. Toley, Brittney McKenzie, Tinny Liang, Joshua R. Buser, Paul Yager, and Elain Fu

This appendix section is taken in a largely unmodified form from the manuscript[156]. I would like to thank primary author Dr. Bhushan Toley along with my other coauthors for involving me with the project.

18.1 Abstract

We demonstrate a novel method for controlling fluid flow in paper-based devices. The method delays fluid progress through a porous channel by diverting fluid into an absorbent pad based shunt placed into contact with the channel. Parameters to control the delay include the length and the thickness of the shunt. Using this method, reproducible delays ranging from 3 to 20 min were achieved. A simple electrical circuit model was presented and used to predict the delays in a system. Results from the model showed good agreement with experimental observations. Finally, the shunts were used for the sequential delivery of fluids to a detection zone in a point-of-care compatible folding card device using biochemical reagents for the amplified detection of the malaria protein *Pf HRP2.*

18.2 Introduction

The current standard diagnostic test format for low resource settings is the lateral flow test (LFT). Though LFTs fulfill many of the ASSURED criteria[426], *i.e.*, affordable, user-friendly, rapid, and equipment-free, they have been criticized for both their inability to assay for multiple

analytes from a single biosample and their poor sensitivity for some analytes of clinical importance[71]. Addressing either of these issues in a simple paper-based test format could have great utility, especially for applications in low-resource settings. (Here the term “paper” is used to broadly refer to porous materials including nitrocellulose used in conventional lateral flow tests.)

In 2008, the Whitesides group introduced microfluidic paper based analytical devices (μPADS), two and three-dimensional paper-based structures that enable multiplexed colorimetric assays (*e.g.,* for detection of glucose and protein)[77], [79]. Subsequent work in the area of paper-based assay development has included demonstrating alternate fabrication methods[427], [428], implementing multiplexed assays for the detection of additional biomarkers using one-step colorimetric reactions (*e.g.,* nitrite, uric acid, and lactate)[120], [429], or performing the simultaneous analysis of multiple controls for on-device calibration[430]. More recently, two dimensional paper networks (2DPNs) for automated multistep sample processing have been introduced. A key feature of the 2DPN assay is the configuration of the network, composed of multiple inlets per detection region, which functions as a program for the timed delivery of multiple reagent volumes within the network. 2DPNs have the ability to expand testing capability over LFTs to achieve improved test performance, *e.g.*, a higher sensitivity. For example, 2DPNs that perform the processes of signal amplification[91]–[93], sample dilution and mixing[94], and small molecule extraction[94] have been demonstrated.

Critical to the operation of multistep paper-based assays is a set of paper fluidic tools (*i.e.*, analogs to the pump controls and valves of conventional microfluidics) to manipulate fluids within the network for the precise timing of reagent delivery and metering of reagent volumes. (Here the term “valve” is used to broadly refer to a tool whose function is to regulate or control

fluid flow in a channel.) A number of paper fluidic tools have been demonstrated. Channel geometry has been used to vary the flow velocity of fluids within the channel[88], [89], [95]. In a related effort, the geometry of the downstream wick, *e.g.*, a fan shape, was used to produce quasi-steady flow in the channel upstream[129]. Several tools for switching-off fluid flow have been demonstrated. These include source pads of varying fluid capacity that release a well-defined volume of fluid into the channel[91], [92] or inlets that are submerged by varying distances into a common well that disconnect from the well after a well-defined volume of fluid has passed. Complementary to this, several tools for switching on fluid flow to a downstream location at a specific time have been demonstrated. One method uses a dissolvable sugar barrier to create delays of up to an hour[219]. Another method relies on modification of the wetting properties of the channel through application of wax[218] or use of surfactant to bridge a hydrophobic region to create a diode valve[220]. Additional tools for switching on flow rely on simple user-activated mechanical means[80], [375], [431]. Most recently, several active methods for the switching on of flows have been developed, including electrowetting of a dielectric in a porous channel19 and the use of magnetically actuated valves[376].

Our goal was to create a tool to complement existing methods. Like the other methods of switching on flows, it should be compatible with use in paper microfluidic devices and be easy to fabricate. In addition, a tool that requires no user intervention, does not involve the release of chemicals, and does not require any equipment to operate would have value for certain applications. In the current report, we demonstrate a novel system of tunable delays for use in paper microfluidic devices that meets these criteria. We demonstrate the operation of this valving method, “shunts” in which fluid flow transiently follows two parallel paths, and the capability to produce a range of delays from 3 min to nearly 20 min. Control is achieved by varying

parameters including the dimensions of the shunt material. Further, we present a simple electrical circuit model for the system and show how the model can be used to inform the design of a shunt with a desired delay. We characterize the shunts in a compact card format that is compatible with point of care use and demonstrate their operation through the sequential delivery of fluids.

18.3 Materials and methods

"Paper" strips for all experiments were made from nitrocellulose membranes (FF80HP, GE Healthcare; Waukesha, WI). Absorbent pad-based shunts were made from cellulose CFSP223000 (Millipore, Billerica, MA) or cellulose 320 (Ahlstrom, Helsinki, Finland). Fluid source pads were made from glass fiber 8964 (Ahlstrom). All designs were drawn using the CAD program DraftSight (Dassault Systemes HQ, France) and parts were cut using a 42-W CO2 laser cutter (Universal Laser Systems, Scottsdale, AZ). Some material properties can be found in the Supporting Information Section I[156].

A benchtop system was built for characterizing the range and reproducibility of the absorbent pad-based shunts (shown schematically in Figure 114A). Nitrocellulose strips and cellulose pad shunts were attached to two separate transparent poly(methyl methacrylate) (PMMA) slabs using double adhesive backed 4-mil Mylar sheets (Fralock, Valencia, CA). The strips and pads were so arranged that when the PMMA slabs were placed together, the cellulose pads made contact with the nitrocellulose strips at the desired locations. Screws were used to hold the assembly together. Each device contained one control strip without a pad and four strips with pads. The nitrocellulose strips were 108 mm long and 4.6 mm wide and the cellulose pads were 7.6 mm, 15.2 mm, 22.9 mm, or 30.5 mm long and 4.6 mm wide. A 19.1 mm thick black PMMA block with a fluid reservoir etched into the top surface served as a base for the assembly. Specifically, the assembly was placed onto the base such that the inlets of the nitrocellulose

strips extending out from one edge of the assembly were submerged in the fluid reservoir. A 1-mg/mL solution of phenol red, adjusted to pH 7.0, was added to the reservoir and used to visualize the transport of the fluid front. Using a custom designed humidity chamber, a device, surrounded by multiple sources of water, was equilibrated to a relative humidity of 75% before introduction of any fluids into the device.

The absorbent pad-based shunts were also incorporated into folding cards, a format appropriate for POC use (one version is shown schematically in Figure 115A). The cards were fabricated from adhesive backed 10-mil Mylar (Fralock, Valencia, CA). Nitrocellulose strips and cellulose pads, a single layer of 15.2 mm long CFSP223000, were attached to adjacent sides of the card. The lengths and widths of the nitrocellulose and cellulose were otherwise equal to those in the benchtop system. On folding, the cards sealed closed as a result of the adhesion of regions between the strips and around the edges of the card. For characterization of the delays in the card format, a control strip and four nitrocellulose strips with identical pads were incorporated within a single card. The inlets of the nitrocellulose strips, extending out from one edge of the card, were dipped into a fluid reservoir prior to imaging. Humidity was controlled in these experiments as described above.

For the sequential delivery of fluids in the card format, nitrocellulose strips were completely contained within the folding card and glass fiber was used to create source pads. Cards with two folding flaps were fabricated, cellulose pads were attached to one flap and source pads were attached to the second flap. Different volumes of fluids to be sequentially delivered to a detection zone were pipetted onto the source pads before folding. The flap containing the cellulose pads was folded first to establish contact between the cellulose pads and the nitrocellulose. The second flap, containing the source pads, was folded to initiate the

simultaneous flow of fluids into the nitrocellulose. A cellulose wicking pad was placed downstream of the detection zone to collect the fluids. Colored fluids, red and yellow food coloring (The Kroger Co., Cincinnati, OH) and a solution of phenol red (Sigma-Aldrich, St. Louis, MO), were used to visualize the timing and uniformity of sequential fluid delivery to the detection zone. Rough estimates of the fluid volumes delivered were made as follows. The lengths of the red regions in the montages were assumed to correspond to the total volumes of the red fluid delivered in each case,12 μL for the device with shunts and 8 μL for the device without shunts. Approximate volumes of the yellow and pink fluids that flowed over the detection zone were accordingly estimated by measuring the lengths of the yellow and pink regions in the respective montages. The same device design was then used to demonstrate the compatibility of the shunts with biochemical reagents. Details of the reagent list (*Pf HRP2* antigen detection) have previously been published[92], [93]; see the Supporting Information Section II[156] for the specifics of the protocol used in this study.

Images of flow through a device were acquired using a Logitech Pro 9000 (Logitech, Newark, CA) webcam operated using HandyAvi (AZcendant, Tempe, AZ) software. The position of the fluid front as a function of time was measured using ImageJ (NIH Research Services Branch). The fluid fronts had V-shaped profiles with two leading regions along the edges and a lagging region along the center. For consistency, in this study the location of the fluid front was taken to be at the lagging region. The error bars on the experimental data represent 1 standard deviation. Statistical comparisons were made using a two-tailed Student's t test in Microsoft Excel (Microsoft, Redmond, WA). For the sequential delivery experiments, images were acquired every 2 s. A time series montage of a 2.3 mm × 3.0 mm region (scaled 0.02× in one dimension) slightly upstream of the wicking pad was created using ImageJ.

Electrical circuit equations were solved in MATLAB (Mathworks, Natick, MA). The circuit model consisted of a system of algebraic-integral equations with time-dependent resistances and voltages (see the Supporting Information Section III[156]) and was solved to calculate electrical currents as a function of time. The equations were discretized in time and the integral terms were approximated using the trapezoidal rule to yield a system of algebraic equations. An intrinsic method was utilized to avoid numerical instability. The resulting system of nonlinear equations was solved at each time step using the MATLAB *fsolve* function. For the estimation of error in the calculation of the delay by the model for a given combination of channel and shunt materials, the errors in the measurement of material properties, absorption capacity, permeability (inversely related to the fluidic resistance), and capillary pressure, were taken into account. Specifically, upper and lower limits of delay predictions by the model were obtained by inputting lower and upper limits of these parameters into the model; these errors were then plotted as error bars on the model results.

18.4 Results and discussion

18.4.1 Shunts Using Absorbent Pads.

Fluid introduced at one end of a strip of a porous material, such as nitrocellulose, flows into the strip as a result of capillary forces exerted at the liquid− air−solid interface along the fluid front (Figure 113A). The rate of fluid flow through the material of the main channel, in this case nitrocellulose, may be altered by placing a shunt made out of an absorbent material, in this case cellulose, into contact with the main channel (Figure 113B). Specifically, a portion of the fluid from the main channel is diverted into the shunt material, producing a delay in the progress of the fluid front to downstream locations of the main channel. In the absence of the shunt, the distance traveled by the fluid front will follow the Washburn equation[88], [127] and is

represented by a straight line on a distance vs square root of time plot (ab; schematic of Figure 113C). In the presence of the shunt, the fluid front follows this same trajectory before reaching the shunt (ac; Figure 113C). After reaching the shunt, the absorption of fluid by the shunt material slows down the progress of the fluid front in the channel (cd; Figure 113C). In time, the fluid front transits the shunt and its velocity increases again (de; Figure 113C). The presence of the shunt causes a net delay, Δt, in the time required for the fluid front to reach the end of the main channel, represented by be (Figure 113C).

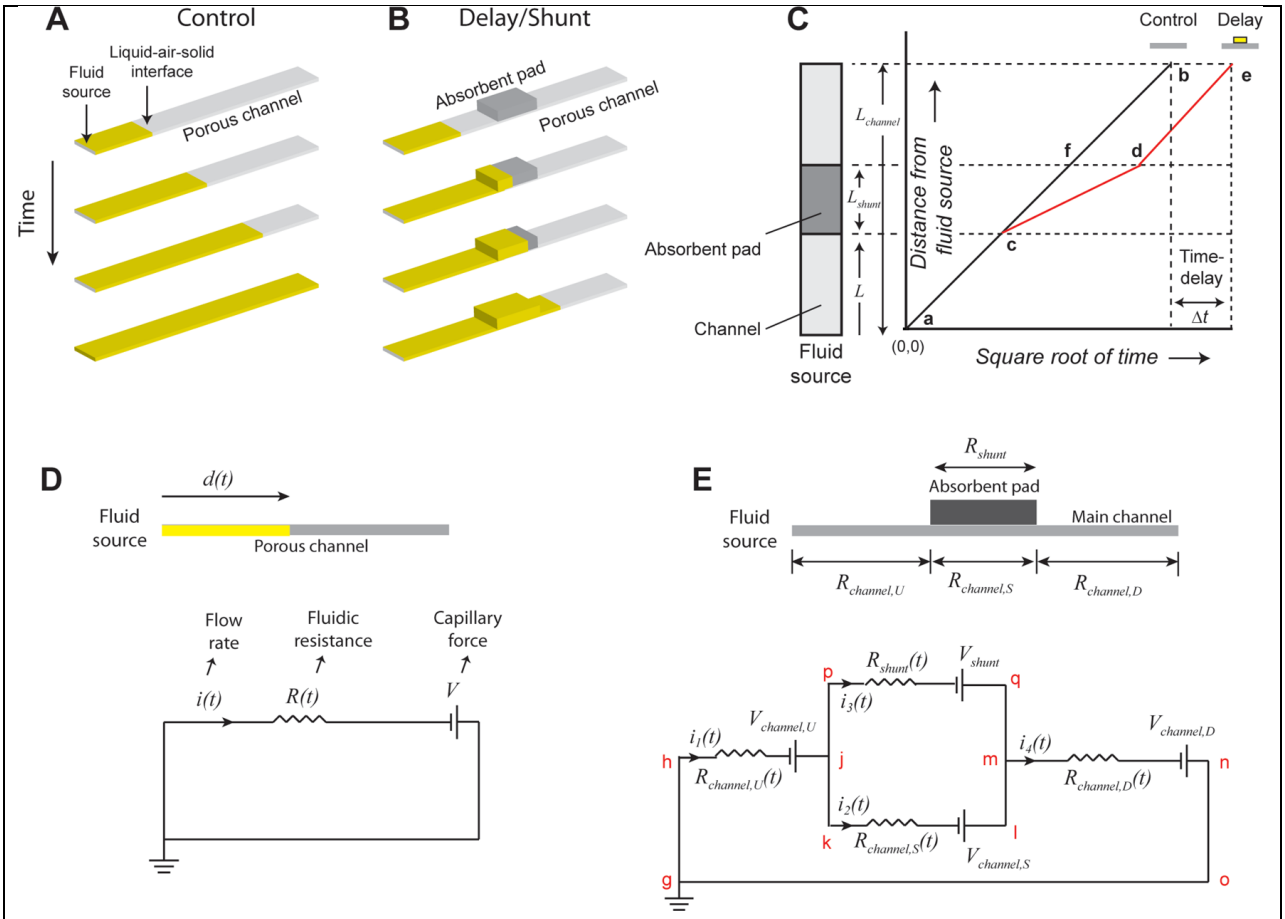

Figure 113: Delays using absorbent pads as shunts: concept and electrical circuit analogy: (A,B) flow of fluid through a channel of a porous membrane in the absence (control; A) and in the presence (B) of a shunt. (C) Schematic showing an idealized plot of the distance traveled by the fluid front as a function of square root of time. For the control with no shunt, fluid progression follows a straight line, as predicted by the Washburn equation. When a shunt is present, fluid progression deviates from Washburn flow, and there is a net delay, Δt, in the progress of the fluid front compared to the control. Depending on the net fluidic resistance offered by the assembly of the shunt placed over the main channel, compared to the channel of porous material alone, de may be either parallel to fb (approximately equal net resistance, when the resistance of the absorbent shunt material is much greater than the resistance of the main channel material) or may have a greater slope (lower net resistance) compared to fb. (D) The electrical circuit analogy of fluid flow through a porous channel. (E) The electrical circuit analogy of fluid flow through an assembly of an absorbent pad-based shunt in contact with a porous main channel. See the Supporting Information Section III[156] for a detailed description of this circuit.

The flow of fluid through a porous material is analogous to the flow of electrons in an electrical circuit[88], [157]. For example, a length of dry porous material with a fluid source at one end may be represented by an electrical circuit, where the voltage V is analogous to the

capillary force generated by the porous material, the electrical resistance, R(t), is analogous to the fluidic resistance of the material at time t after the fluid source is introduced, and the current, i(t), is analogous to the flow rate of fluid through the porous material (Figure 113D). An analytical solution of the electrical circuit equations produces the linear relationship between distance traveled and the square root of time that is observed experimentally as Washburn flow, indicating that the model accurately predicts the progress of fluid through a porous material channel (see the Supporting Information Section IV[156]). The electrical circuit analogy can be extended to the shunt system composed of a porous material main channel in contact with a different porous material shunt (circuit of Figure 113E). The assembly can be represented by two parallel branches of the circuit with different voltage sources and resistances for the shunt and the main channel. The values of the voltages in this circuit depend on the location of the fluid front. Specifically, a fully wetted section has no ability to imbibe fluid and is represented by a zero voltage, while any section that has a capacity for imbibition is represented by a nonzero voltage. Similarly, the resistance of each branch in the circuit is proportional to the amount of fluid that has passed through that branch, until the section becomes fully wet. A step-by-step progression of fluid through this system and its equivalent electrical circuit at each stage is provided in the Supporting Information Section III[156].

18.4.2 Tuning Delays

The delays of the shunts can be tuned by changing the dimensions of the shunts, length or thickness, of a given material. First, delays produced using nitrocellulose (FF80HP) as the main channel and different lengths of cellulose (CFSP223000) shunts were measured using the benchtop system (Figure 114A). A delay was defined as the difference in time required for the fluid front to reach the end of a nitrocellulose channel containing a cellulose shunt compared to a control, the nitrocellulose channel only. The image series shows that increasing the length of the

shunt increased the delay (Figure 114B). A plot of the progress of the fluid fronts though the material indicates the behavior described above (Figure 114C). Specifically, after reaching the cellulose shunt, progress of the fluid front deviated from the initial Washburn behavior in the nitrocellulose with significantly slowed progress, *i.e.*, decreased slope relative to the initial slope of the distance vs square root of time plot. Then, once the fluid front was in the nitrocellulose downstream of the shunt, the slope increased to near the initial slope. The resulting delay increased as the length of the shunt was increased (Figure 114D). Distinct delays, between 200 and 750 s ($*$; $P < 10^{-4}$; $N = 4$), were demonstrated by changing the shunt length in 7.6 mm increments. For each shunt length, the delays were reproducible with coefficients of variation (CV) ranging from 3.8% to 8.0%.

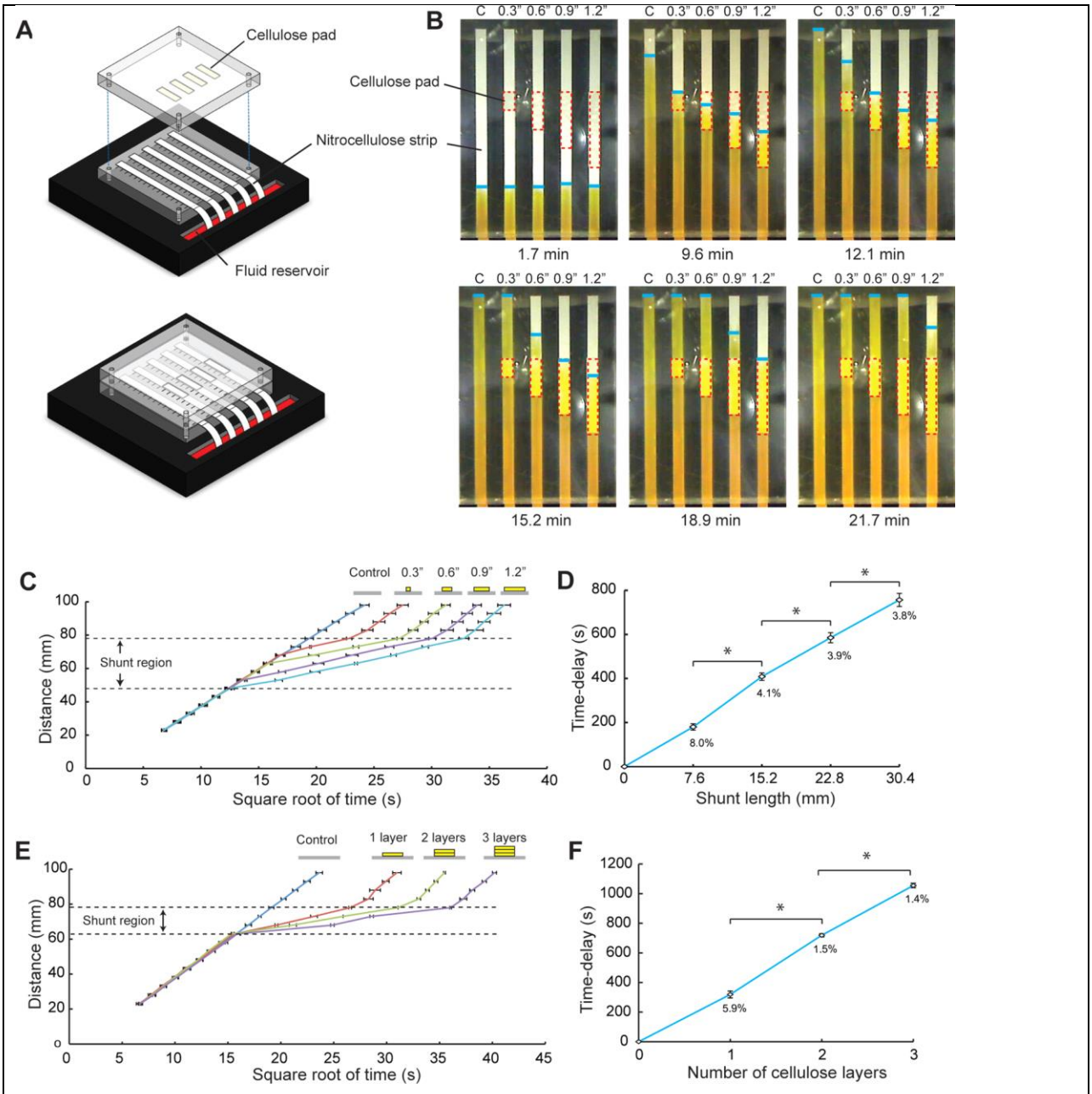

Figure 114: Effect of shunt length and thickness on the magnitude of the delay: (A) schematic of the benchtop system used for measuring delays and (B) time-lapse images of the flow of fluid through nitrocellulose strips in the absence of (control) and in contact with 7.6 mm, 15.2 mm, 22.9 mm, and 30.5 mm shunts of cellulose CFSP223000. Dotted red lines indicate the location of the cellulose shunts and the blue lines mark the fluid fronts. Longer shunts produced longer delays. (C,E) Plots of the distance traveled by the fluid front as a function of the square root of time for a nitrocellulose strip in contact with cellulose CFSP223000 shunts of different lengths (N = 4) (C) and multiple layers of cellulose of length 15.2 mm (N = 4) (E). (D,F) Plots of the delays produced by cellulose shunts as a function of shunt length (D) and number of layers in the shunt (F). Percent values represent the coefficient of variation.

The delay can also be varied by changing the thickness of a shunt while maintaining constant length. The benchtop system was used to measure the delays produced by implementing shunts formed from one, two, and three layers of 15.2 mm long cellulose (CFSP223000) (Figure 114E,F). Distinct delays, ranging from 319 to 1055 s ($*$; $P < 10^{-6}$; $N = 4$), were obtained by varying the number of cellulose layers between one and three. For these delays, the CVs were between 1.4% and 5.9%. Note that alternate materials may also be chosen to increase the delays further if desired. However, producing very long delays may not be desirable in the context of minimizing assay time to result.

18.4.3 Incorporation of Shunts in Folding Cards for POC Use

The shunts were demonstrated in a folding card format compatible with POC use (Figure 115A), and the reproducibility of the delays was characterized. For three runs of a card with 10-mil thick spacers, the normalized delays produced by the 15.2 mm long shunts were consistent across all runs at each strip position (Figure 115C). In order to vary the magnitude of the delay, the length or thickness of the shunt may be adjusted, as was demonstrated in the benchtop system. The delay can also be varied by changing the thickness of the spacer in the card (see the Supporting Information Section V[156]).

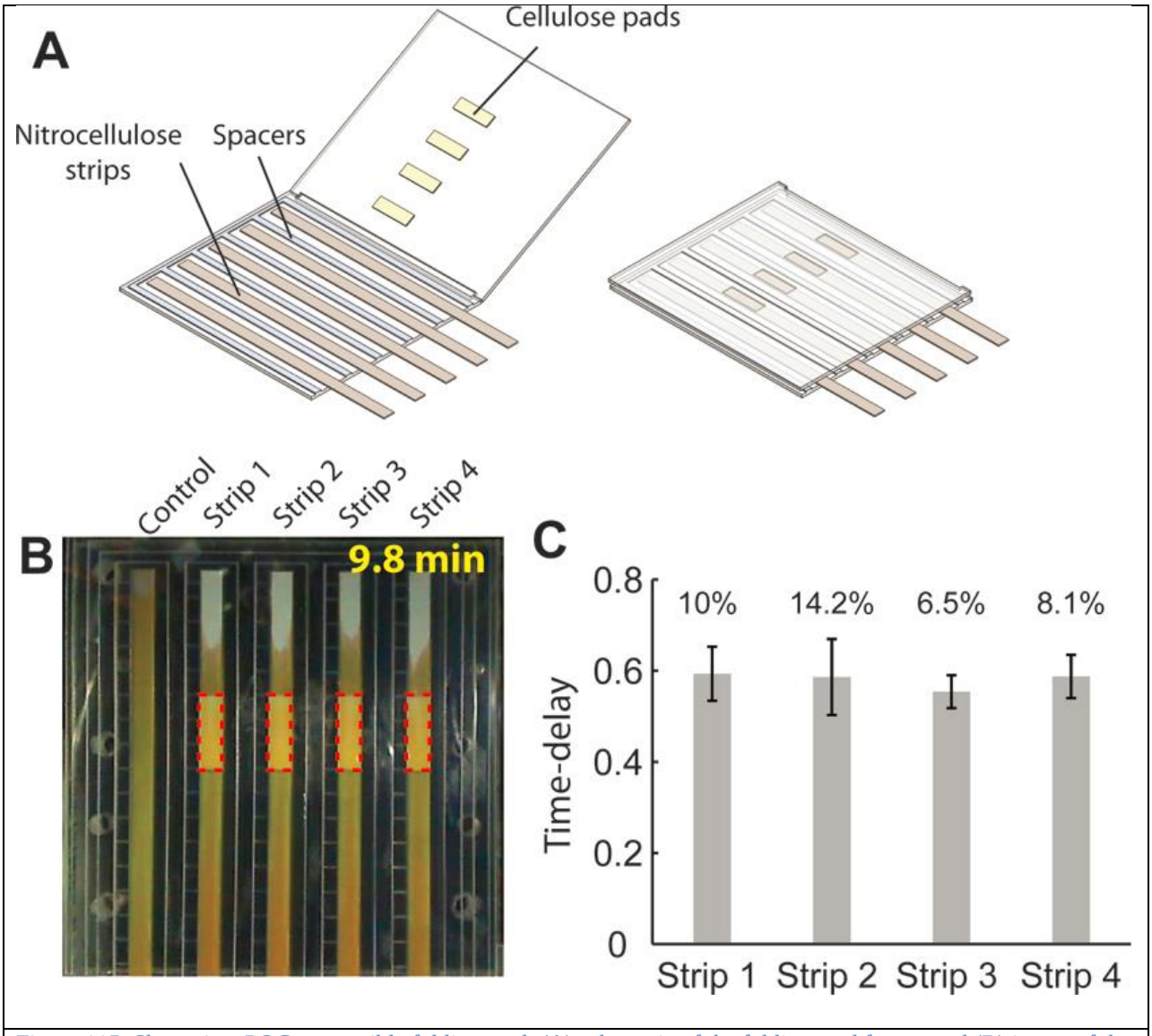

Figure 115: Shunts in a POC-compatible folding card: (A) schematic of the folding card format and (B) image of the progress of fluid through nitrocellulose strips in the absence of (control) and in contact with 15.2 mm long cellulose CFSP223000 shunts. Fluid flow in the nitrocellulose channel was delayed by the presence of a cellulose shunt. (C) Delays obtained at different strip locations within the cards. The mean delay is plotted at each location across multiple cards (N = 3). The error bar is the standard deviation and percent values represent coefficients of variation.

18.4.4 Model Predictions and Comparison with Experimental Results

The electrical circuit model was used to predict the locations of the fluid fronts in a system of a nitrocellulose (FF80HP) channel and a cellulose CFSP223000 shunt as a function of time (Figure 116A). The cellulose shunt in this model had a 2.5-fold greater absorption capacity, a 0.5-fold greater fluidic resistance, and a 1.1-fold greater capillary force than the nitrocellulose channel.

These model input parameters were consistent with the experimentally measured values for the permeability, capillary pressure, wicking rate, and absorption capacity of the nitrocellulose and cellulose (Table S1 in the Supporting Information[156] and the discussion following it). The model predictions (Figure 116A) agreed well qualitatively with the experimental results for the system (Figure 116B, see Supporting Information Section VI[156] for a description of the experiment). First, the model predicted the experimentally observed decrease in velocity of the fluid fronts in cellulose and nitrocellulose within the shunt region. Second, the model predicted the faster progress of the fluid front through the cellulose as compared to the nitrocellulose. And third, the model predicted the increase in velocity of the fluid front in nitrocellulose after the cellulose shunt was saturated.

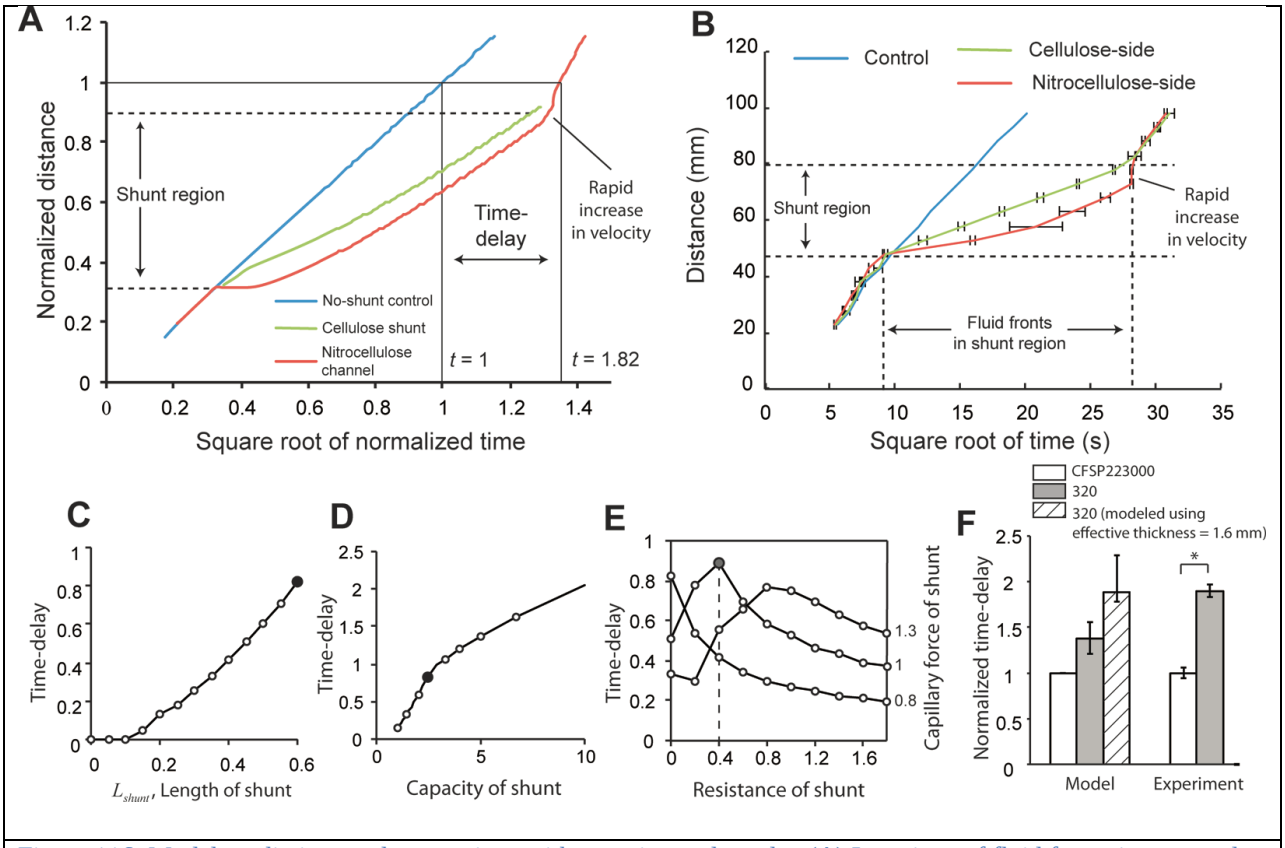

Figure 116: Model predictions and comparison with experimental results. (A) Locations of fluid fronts in a control of nitrocellulose channel only (blue line), a nitrocellulose channel in contact with a 33.0 mm cellulose shunt (red line), and a cellulose shunt (green line) that is in contact with a nitrocellulose channel, as a function of square root of time, as predicted by the electrical circuit model. (B) Experimental results of the locations of fluid fronts plotted as a function of the square root of time for a control and the two opposite-facing assemblies. In the shunt region, the fluid front in nitrocellulose lagged the fluid front in the cellulose. There was a rapid increase in the velocity of the fluid front in the nitrocellulose after the cellulose was fully wetted. There was good agreement between model predictions (A) and experimental observations (B). (C) The model predicts that increasing the length of the cellulose increases the delay as experimentally observed (Figure 114D). (D) The model predicts that increasing the capacity of the cellulose increases the delay as experimentally observed (Figure 114F). The solid data points represent the nominal case. (E) Resistance-voltage map for predicting delays. Each point on this map corresponds to a combination of these two properties and predicts the values of the properties for maximizing the delays (solid data point). (F) Comparison of model and experimental results for the delays generated by 15.2 mm long cellulose CFSP223000 and cellulose 320.

The model was used to predict the delay dependence for different lengths and number of layers in the cellulose CFSP223000 shunt. In each case, a single model parameter was varied from the nominal value described above (used for the solution of Figure 116A). The predicted

delays corresponding to the nominal case are highlighted as dark circles (Figure 116C,D). The model predicted that as the length of the shunt is increased, the delay produced increases (Figure 116C), in qualitative agreement with the experimental results of Figure 114D. Similarly, the model showed that as the capacity, or thickness, of the shunt is increased, the delay produced increased (Figure 116D). This trend was also experimentally observed in measurements of the delays produced by stacking multiple layers of absorbent material to create the shunts (Figure 114F).

The electrical circuit model was also used to qualitatively predict the effect of material properties on the resulting delays. The capillary force and fluidic resistance of a porous material are interrelated in that changing the pore structure of a material changes both of these parameters for a given fluid. The combined effect of the variation of the capillary force and fluidic resistance on delays can be represented by a map as shown in Figure 116E (see Supporting Information Section VII[156] for model predictions on the delay for each of these independently). Each point on this map corresponds to a particular combination of capillary force and fluidic resistance that may be associated with a given set of materials and fluid. The map shows that for a shunt having a 2.5-fold higher absorption capacity than the channel material, the maximum delay would be achieved with a shunt material that generates an equal capillary force as the channel material but with a 0.4-fold smaller fluidic resistance than the channel material (gray circle; Figure 116E).

The electrical circuit model can be used as a design tool to obtain qualitative predictions on the delay for a different shunt material. For example, the model can be used to predict how the delay will change from the case of the cellulose CFSP223000 shunt with the nitrocellulose channel (fluid is water), when an alternate cellulose material with a higher absorption capacity such as cellulose 320, is used for the shunt. The model parameters were the same as for the

nominal case (Figure 116A), except the material properties of the shunt were adjusted to reflect the experimentally measured properties for cellulose 320 (Table S1 in the Supporting Information[156]). Specifically, model parameters for cellulose 320 were estimated by scaling the corresponding model parameters for cellulose CFSP223000 using the ratio of measured properties as scaling factors. The model predicted that the delay would increase (left white vs gray bars; Figure 116F) for cellulose 320 as compared to cellulose CFSP223000. This agreed qualitatively with experimental results (right white vs gray bars; Figure 116F), (∗; $P < 0.05$; $N = 4$; Figure 116F). However, the model underestimated the increase in the delay compared to the experimentally observed increase in the delay. A reason for this may be that the physical thickness used as an input for the model overestimated the cross-sectional area used for wicking, and thus the model prediction for the increase in the delay is low. The model prediction can be made to match the increase observed in the experimental results (left white vs hashed bar; Figure 116F) when an effective thickness of 1.6 mm (compared to the measured thickness of 2.7 mm; Table S1 in the Supporting Information[156]) is used to estimate the capillary force. The errors bars in the estimation of delay by the model represent the uncertainty in the measurement of the material properties input into the model.

18.4.5 Sequential Fluid Delivery in Folding Cards

Sequential delivery of fluids to a detection zone using cellulose (CFSP223000) shunts was demonstrated, first for a system of three colored fluids and second in an immunoassay for the detection of the malaria protein *Pf HRP2*. The device had three legs, each connected to a different fluid source. The first leg did not contain a shunt. The second and third legs contained 5.1 mm and 20.3 mm long shunts (dotted green lines; Figure 117A). A double folding card format was used in which the first fold established contact between the cellulose shunts and nitrocellulose channels, and the second fold established contact between the source pads and the

channels. In the example here, 12 μL of red, 20 μL of yellow, and 80 μL of pink colored fluid were automatically delivered to the detection zone. The image series, at 0, 0.2, 4.2, and 10.7 min after completing the double fold, shows the introduction of fluids into the device inlets and the arrival of red fluid, yellow fluid, and pink fluid to the detection zone (Figure 117A). A montage of time-lapse images of the detection zone shows the timing and the relative volumes of the three fluids delivered up to a time of 19.3 min (Figure 117B). Note that in this design, the sequential delivery of fluids to the detection zone was enabled both by the shunts and the geometry of the inlet legs, *i.e.*, different lengths of the input legs. Though sequential delivery can be achieved using geometry only[89], [93], a significant advantage of using the absorbent pad-based shunts is the capability to deliver larger volumes of fluids using the same device footprint. Specifically, in a device with the same footprint but without shunts, only smaller volumes of the red (8 μL) and yellow (15 μL) fluids could be delivered sequentially (and a larger volume of pink fluid in the same time of 19.3 min, Figure 117C vs Figure 117B). An attempt to load larger volumes led to premature delivery of fluids from legs 2 and 3 to the detection zone.

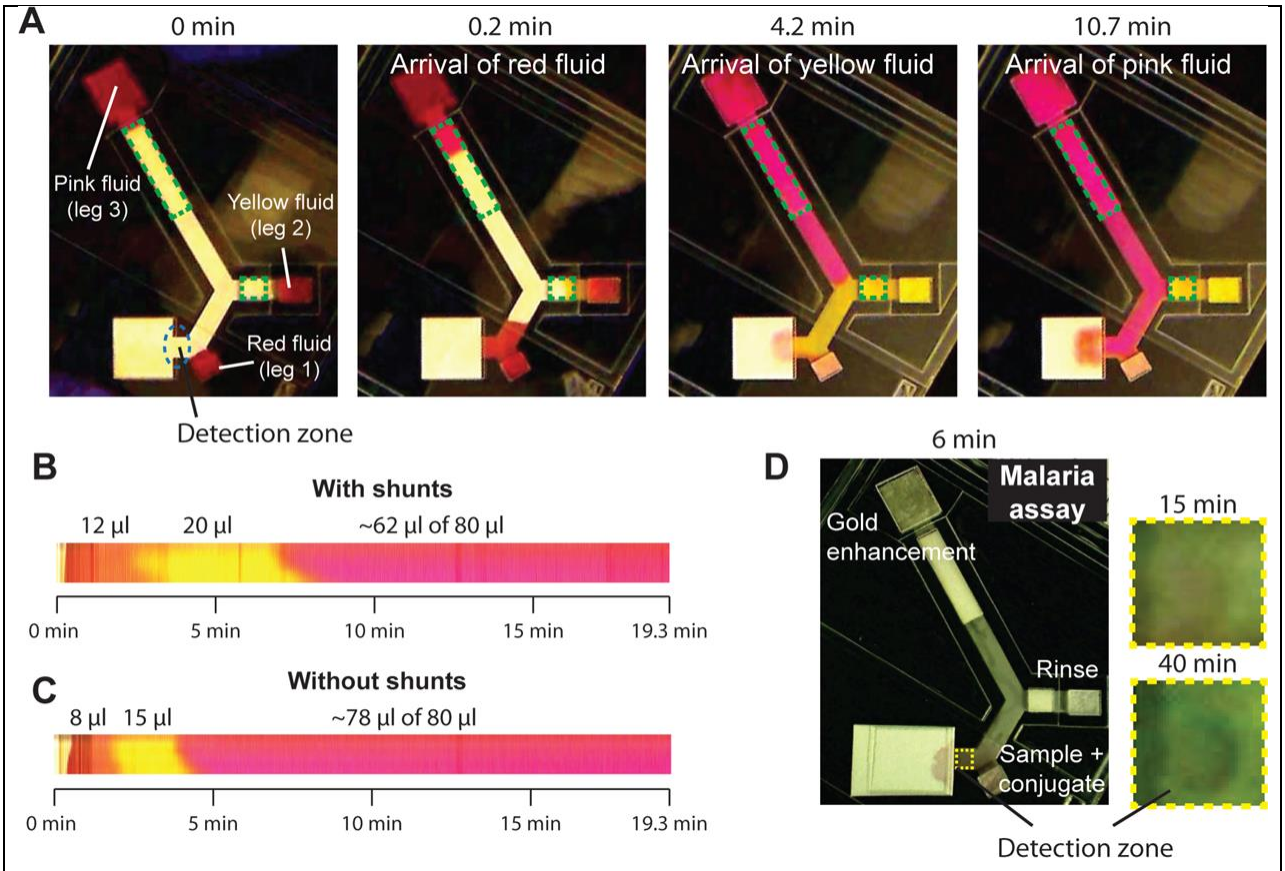

Figure 117: Sequential delivery of fluids using shunts. (A) Time-lapse images of a folding-card device for the sequential delivery of red, yellow, and pink fluids to a detection zone. Legs 2 and 3 of the device contained cellulose CFSP223000 shunts, outlined by the dotted green lines, of length 5.1 mm and 20.3 mm, respectively. All legs were 4.6 mm wide. (B,C) Montages of a portion of the detection zone, a sub-region within the dotted blue lines, of a device containing shunts (B) and not containing shunts (C). The shunts enabled delivery of larger volumes of fluid to the detection zone. (D) Folding-card device for the feasibility demonstration of amplified detection of the malaria protein *Pf HRP2*. Antigen plus gold-antibody conjugate, a rinse solution, and a gold enhancement solution were sequentially delivered to the detection zone. The original pink signal obtained at 15 min was amplified to a blue-black signal by 40 min.

The compatibility of the shunts with biochemical reagents from a signal amplified assay for *Pf HRP2* was then demonstrated. The same device design was used to sequentially deliver 12 µL of sample plus a gold nanoparticle-antibody conjugate, 20 µL of a rinse solution, and 80 µL of a gold enhancement solution to a detection zone (Figure 117D). A light pink signal could be seen in the detection zone 15 min after the passage of the conjugate (leg 1) and rinse (leg 2) solutions (Figure 117D); this is analogous to the signal obtained from the steps in a conventional

lateral flow test. This signal was then amplified by the delivery of the gold enhancement solution from the third leg of the device, producing a dark blue-black signal at 40 min (Figure 117D).

These absorbent pad-based shunts have several potential advantages over previously developed valving methods. These shunts can reduce the device footprint compared to devices that use geometry only (*e.g.*, varying the path lengths from the sources to the detection zone to deliver fluids sequentially). In contrast to dissolvable barriers or hydrophobic barriers, there are no chemicals applied to the porous substrate that might then have a negative impact on downstream device processes. Though these shunts introduce additional volume into the fluid path, in the folding card device of Figure 117, in which small fluid volumes in source pads feed into the network and the cellulose wicking pad is significantly larger in fluid capacity than the cellulose shunts, the fluid volume retained in the network is expected to be small. Moreover, when storing reagents dry on the device for rehydration at the time of use, the dry reagents may be incorporated downstream of any cellulose shunts, so that waste of potentially expensive reagents is not an issue. Future work includes demonstration of the utility of the shunts in an assay, as well as quantification of the effects of varying environmental conditions, *i.e.*, humidity levels and temperature on device operation.

18.5 Conclusion

We have demonstrated a novel tunable shunt for use in paper microfluidic devices. Such shunts are capable of producing delays, ranging from 3 min to close to 20 min, using control parameters such as the dimensions of the absorbent material of the shunt. We have also presented a simple electrical circuit model that can be used as a design tool for creating absorbent pad-based shunts with the desired properties for a given application. These shunts are compatible with a compact

card format suitable for point-of-care use and were demonstrated to perform sequential delivery in the context of amplified detection of a malaria antigen.

18.6 Associated content

Supporting information Table of material properties; an experimental protocol for the demonstration of shunt compatibility with biochemical reagents in the context of *Pf HRP2* detection; details of an electrical circuit model of an absorbent pad-based shunt on a porous channel; an analytical solution for fluid progress through a porous material using Ohm's Law; both experimental and model results on the effect of spacer thickness on delay time in the folding card format; an experimental description of tracking fluid fronts in a system of cellulose and nitrocellulose; and additional model predictions on the effect of shunt material. This material is available free of charge via the Internet at http://pubs.acs.org.

18.7 Acknowledgements

We would like to thank Barry Lutz, Ryan Gallagher, Josh Bishop, Luke Allpress, and Nuttada Panpradist for stimulating discussions and technical assistance throughout the course of this work. The research reported in this publication was supported by the Defense Advanced Research Projects Agency under Grant Number HR0011-11-2-0007 and the National Institute of Allergy and Infectious Disease of the National Institutes of Health under Award Number R01AI096184. B.M. acknowledges the Washington NASA Space Grant Consortium, the University of Washington Department of Bioengineering, the Mary Gates Endowment, the Pacific Northwest LSAMP, and the University of Washington GenOM Project (National Institutes of Health under Award Number HG02360-12, Genentech Foundation, Washington Research Foundation) for their support. T.L. acknowledges support from the National Science Foundation Graduate Research Fellowship under Grant Number DGE-1256082. The content is

solely the responsibility of the authors and does not necessarily represent the official views of the National Institutes of Health.

19 Appendix: Programming paper networks for point of care diagnostics

Shivani Dharmaraja, Lisa Lafleur, Samantha Byrnes, Peter Kauffman, Josh Buser, Bhushan Toley, Elain Fu, Paul Yager, Barry Lutz

This appendix section is taken in a largely unmodified form from the manuscript[157]. I would like to thank the primary author Shivani Dharmaraja and my coauthors for involving me with the work.

19.1 Abstract

Lateral flow tests (LFTs) are well-suited for rapid point-of-care testing in low resource settings. The wicking action of the paper strip moves the sample and reagents through the device without a need for pumps, but LFTs are typically limited to tests that can be carried out in a single fluidic step. The materials from LFTs can be reconfigured to create paper networks that automatically carry out multi-step fluidic operations, while retaining the same easy-to-use format as a conventional LFT. Here, we describe basic principles of wicking and system-level behavior of paper networks by analogy to electrical circuits. We describe key design principles for a previously-developed 2D paper network (2DPN) and introduce an alternative linear paper network (Pseudo-1DPN) that takes advantage of system-level behavior to perform clean sequential fluid delivery while reducing device running time.

19.2 Introduction

Lateral flow strip tests have been identified as a diagnostic technology well suited for point-of-care (POC) use in low resource settings[2], [66]. With fluid transport occurring due to the capillary pressure of the strip material (rather than through the use of pumps), lateral flow strip tests are entirely disposable, rapid, user-friendly, and affordable[63], [432], [433] (Figure 118). Numerous lateral flow strip tests have already been developed and successfully used in limited-resource settings, with applications including pregnancy testing and disease diagnosis. The basic function of a lateral flow device is to mix sample with a visible label (*e.g.*, antibody conjugated to gold nanoparticles) and capture the analyte-label complex at a detection line via an immobilized capture molecule (*e.g.*, antibody). While the simplicity of these strip tests makes them ideal for use as a POC tool, it has generally limited them to performing tests that can be carried out in a single chemical step. Using lateral flow tests (LFTs) as clinically relevant diagnostic tools is sometimes limited to targets with high(er) concentrations because of the limited analytical sensitivity of the LFT format. Recently, many research groups have been rethinking the advantages and limitations of LFTs and creating new devices with similar simplicity but added features, such as multiple assays in a single device[63], [66], [77], [79], [217], [218], [428], [434].

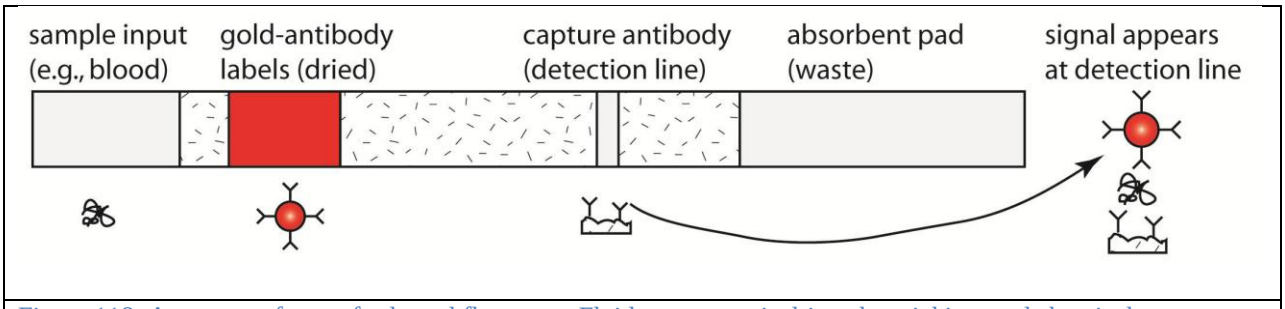

Figure 118: A common format for lateral flow tests. Fluid movement is driven by wicking, and chemical reagents are stored on the device. Most LFTs perform single-step sandwich immunoassays by binding a label to the analyte, then capturing the analyte-label complex at a detection line. In a LFT, these two reactions are carried out in a single fluidic step. LFTs typically cannot perform chemistries that require multiple steps (*e.g.*, amplification, sample preparation).

In recent years, the Fu/Lutz/Yager group at UW has worked to increase the functionality of disposable tests by patterning the membrane into two-dimensional paper networks (2DPNs)[88]–[94], [102]. Utilizing non-linear geometries of a wicking membrane makes it possible to perform automated multi-step assays without greatly increasing the device complexity from a user standpoint. Figure 119 shows an early demonstration of a 2DPN designed to deliver three fluids to a detection zone in a timed sequence. The three-legged device was contacted with three fluid droplets to initiate flow. The fluids initially wicked into the strip and met at the midway point between legs (Figure 119A), followed by wicking of fluids toward the detection region on the right of the strip (Figure 119B). Delivery from each leg stopped when its source fluid became depleted. The result was treatment of the detection zone with three fluids in a timed sequence (Figure 119C). The preliminary design, in this case, led to the undesired co-arrival of two fluids at the detection zone (most evident in the parallel yellow and clear fluids at 9 minutes); prevention of this type of problem will be addressed in this paper.

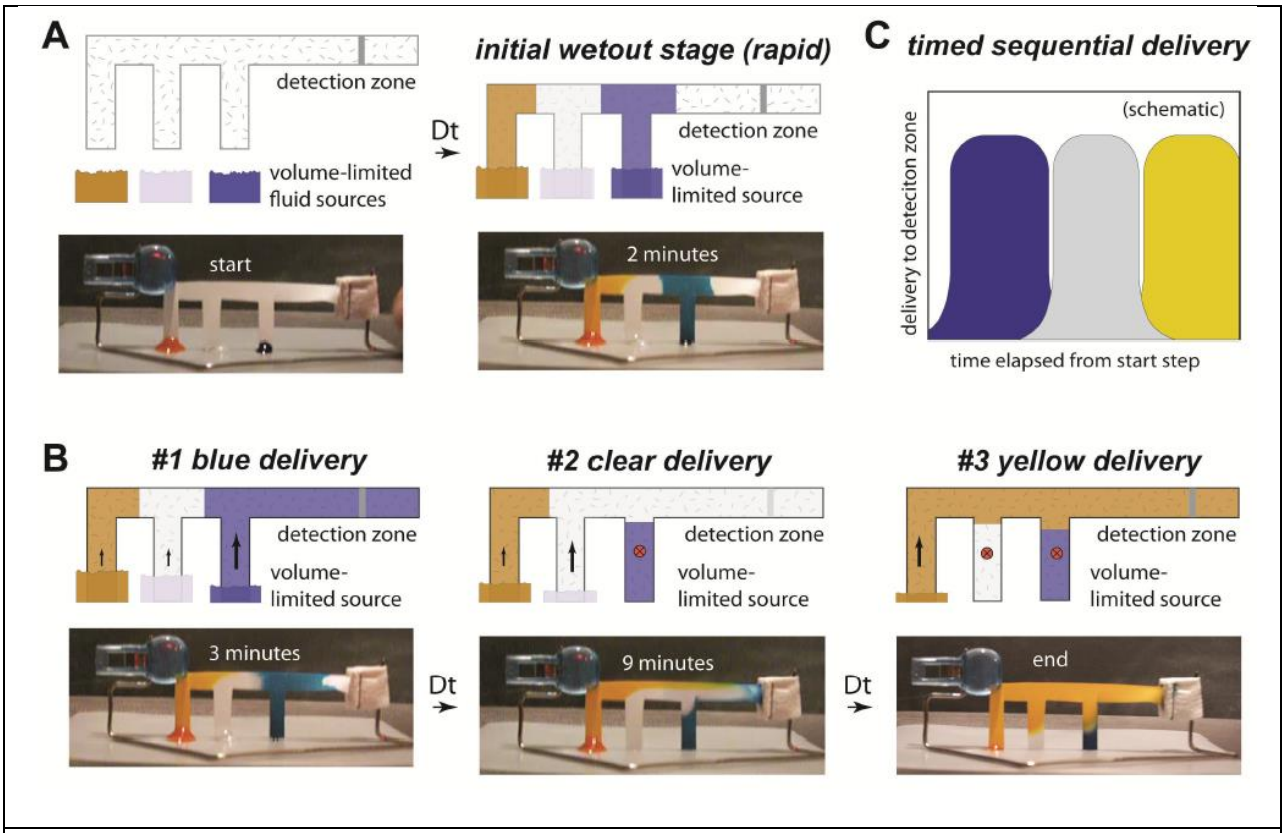

Figure 119: Early concept and demonstration of a 2-dimensional paper network (2DPN) for automated sequential fluid delivery. The device was fabricated from a porous nylon membrane cut by scissors, an absorbent pad (paper towel stapled to the membrane), and support stand (bent paper clip). Three drops of source fluid (water with food coloring) were pipetted onto a table, and flow was initiated by contacting the legs with droplets. Imperfections in sequential delivery (parallel flows of yellow and colorless fluids) can be seen in the images. The width of the main channel in the device was approximately 6 mm, and total time was about 9 minutes.

Sequential delivery in 2DPNs is controlled by two principles: 1) arrival time of each fluid at a detection zone is controlled by the length of the path followed by that fluid, and 2) fluid sources of finite volume are "shut off" by their depletion. Thus, 2DPNs represent a form of fluidic programming that depends on wicking properties of the materials and the system-level behavior of paper networks.

Since the initial concept demonstration (*circa* 2008), we have developed devices that automatically perform multi-step immunoassays using enzyme-based signal amplification (ELISA chemistry) and electroless gold deposition onto gold detection labels for signal

enhancement[91]–[93]. Design variations have included card-like formats that used porous pads as fluid sources[91]–[93] and a cartridge format that used a single fluid well as the source for all legs[90]. Figure 120 shows a previous example of a 2DPN that used porous (glass fiber) pads as the fluid sources[91]. The image sequences at left show delivery of colored fluids, and those at right show the same device performing a multi-step signal enhancement. Glass fiber pads were chosen because they release nearly all fluid, but as we find in this paper, what appeared to be an ideal source actually is not. Successful fluidic sequencing depends not only on the paper network design but also on the release properties of the fluid sources.

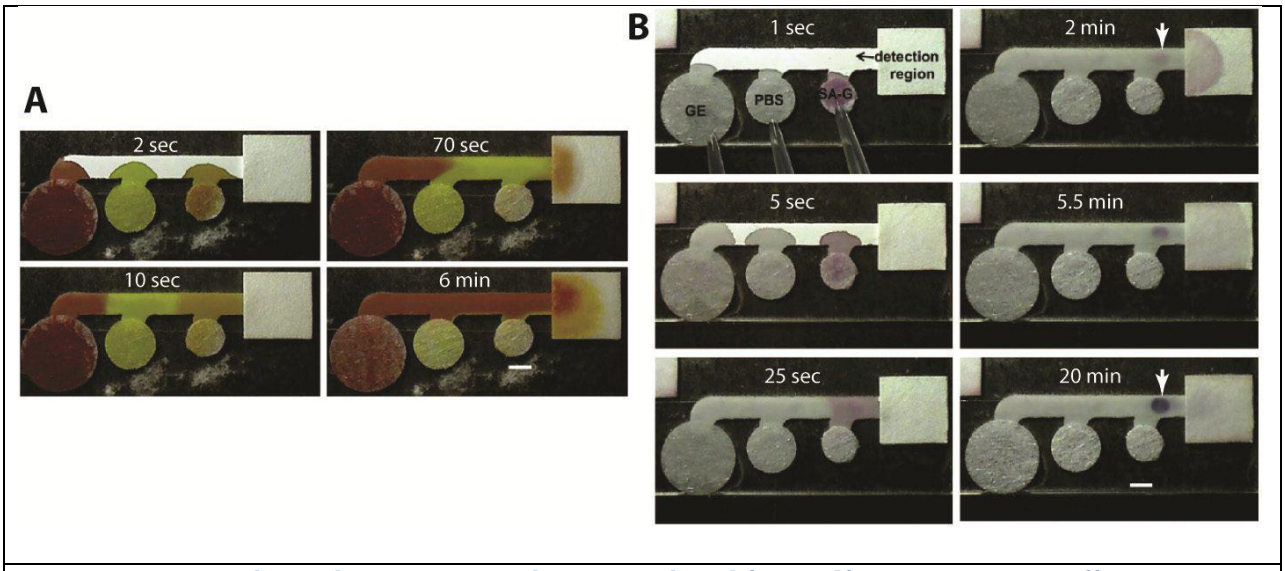

Figure 120: A 2DPN designed to automate a multi-step signal amplification [figure source: Fu, Kauffman, Lutz, Yager, "Chemical signal amplification in two-dimensional paper networks," Sensors & Actuators B 149 (2010) 325–328]. Porous (glass fiber) pads were used to hold finite volumes of source fluids. A) Image sequence of delivery of three fluids to a common leg in a timed sequence (orange, yellow, red). B) Image sequence for a sandwich immunoassay using a multi-step signal amplification process (SA-G: streptavidin-gold; PBS: phosphate-buffered saline; GE: gold enhancement reagent). The upper right image shows a faint gold spot (end point of a typical LFT), and the lower right image shows the darkened spot after enhancement. The device carried out all delivery steps without intervention. The width of the main channel was 3 mm.

It is possible to develop a functional 2DPN by an "estimate and check" method. However, this method generally requires multiple iterations to achieve sequential delivery with

minimal overlap in the delivery of fluids. Our goal is efficient, rational design of 2DPN devices. This requires an understanding of the physical properties, namely the capillary pressure and the fluid resistances, of the multiple materials within the paper network. For example, even the simple lateral flow strip contains at least four connected materials whose physical properties affect fluid flow in the device. We note that Mendez, *et al* provided an excellent description of wicking principles and manipulated material shape to control fluid flow rates in strips[129]. In addition, the Delamarche group has done excellent work on capillary-driven flow control in microfluidic channels[435]–[437], and the channel-based format shares many principles with the porous material system discussed here.

In this manuscript, we apply simple electrical circuit models to paper networks to identify design principles for capillary driven sequential fluid delivery in paper networks. We introduce basic concepts of wicking and how electrical models can be constructed for simple cases, and we show how fluid sources can affect the extent and speed of fluid delivery into a strip. Finally, we use electrical models to identify design principles in paper networks and show that a linear paper network (Pseudo-1DPN) provides clean sequential delivery in a simple format.

19.3 Experimental

19.3.1 Characterization of alternative fluidic sources

Tested materials included thick glass fiber (8964; Millipore, Billerica, MA), cellulose (CFSP223; Millipore, Billerica, MA), and nitrocellulose (HF135; Millipore, Billerica, MA). A nitrocellulose (HF135) wicking membrane was used for each case. Materials were housed on adhesive Mylar (10 mil T- 5501 Mylar core with 1 mil adhesive on each side; Fraylock, San Carlos, CA) cards. All materials were cut using a CO_2 laser cutting system (Universal Laser Systems, Scottsdale, AZ).

19.3.2 Fabrication of sequential delivery devices

All sequential delivery devices were fabricated from nitrocellulose and adhesive Mylar. Fluid sources used were either wells (CV2024; VitroCom, Mountain Lakes, NJ) or thick glass fiber pads. Wells were held in place using a stand fabricated from thick cellulose (Grade 320; Ahlstrom, Helsinki, Finland).

19.3.3 General experimental protocols

Fluids used in any experiments were either deionized water or commercially available food dyes diluted in deionized water. Sequential delivery using well sources was performed in the ambient environment. All other experiments were conducted in a humidity-controlled environment (70% - 80% humidity). A web camera was used to perform all imaging (Logitech, Fremont, CA).

19.3.4 Computational modeling

All computational simulations were performed using MATLAB R2012a. Equations for the flow rates through each leg of a device (later denoted as Q1, Q2) were derived using mesh and nodal analysis of the analogous electrical circuit. Models were implemented only after initial wet-out occurred; initial conditions were defined by setting the position of the fluid fronts (known to be mid-way between spacer regions) and appropriately depleting the sources (based on membrane capacity). A time step of 0.2 seconds was used to track source depletion/saturation, source backpressures, the position of each fluid front, and fluid flow rates. As a note, this model has not yet been thoroughly validated and will only be used for qualitative purposes in this manuscript.

19.4 Physical principles and modeling approach

19.4.1 Electrical circuit analogues

Capillary-driven flow in porous media can be described conceptually by analogy to simple electrical circuits (Table 14). Pressure (P) created by capillary force or gravity is represented as voltage (V), fluid flow rate (Q) is represented as current (I), and viscous resistance ($R=\mu L/\kappa WH$)

is related to properties of the fluid (fluid dynamic viscosity μ) and the permeability (κ) and dimensions of the porous material (cross-sectional area W*H, wetted length L). Atmospheric pressure acts on fluid-air interfaces and is represented as electrical ground at inlets and outlets. The 1D form of Darcy's Law relates the fluid flow rate to the driving pressure and viscous resistance; it is the equivalent of Ohm's Law in electrical circuits[88], [94], [129].

Table 14: Electrical analogy for capillary-driven flow in porous media

Electrical	**Fluidic**
Voltage, V	Pressure, P (capillary, gravity)
Current, I	Fluid Flow Rate, Q
Resistance, R	Resistance, R = μL/κWH
Ground (V=0)	Atmospheric Pressure (P=0)
Ohm's Law, V = IR	Darcy's Law, P = QR

Figure 121A illustrates a simple case of fluid wicking from a finite fluid source into a straight, initially dry strip. The rate at which fluid wicks through a porous membrane is affected by two opposing forces: 1) the capillary pressure of the material (P_p) that pulls fluid into the strip, and 2) the viscous resistance (R) that opposes fluid flow through the pores. As more fluid is taken up by the material, the length of the fluid column increases as a function of time (L(t)), and the viscous resistance increases (R=μL(t)/κWH). Figure 121B shows the electrical circuit model describing this time-dependent wicking, where an ideal fluid source is represented as ground (P_s=0). Evaluating this circuit, we find that:

$$Q(t) = \varepsilon WH\frac{dL(t)}{dt} = \frac{P_p}{R} = \frac{\kappa WHP_p}{\mu L(t)}$$ Equation 24

and

$$L^2 = \frac{2P_p\kappa}{\mu\varepsilon}t$$ Equation 25

where ε is the void volume of the porous material. Figure 121C illustrates Equation 25 for wicking of fluid into a strip from a finite fluid source. The combination of a constant capillary pressure and the rising resistance during wet out causes the fluid front to slow down over time (following L^2~t) until the fluid source is depleted. The scaling found in Equation 25 (L^2~t) matches exactly with the classic Lucas-Washburn expression describing 1D capillary-driven wet-out[127], [383]. Thus, electrical analogies can be useful for understanding basic concepts of capillary-driven flow in porous materials[88], [94].

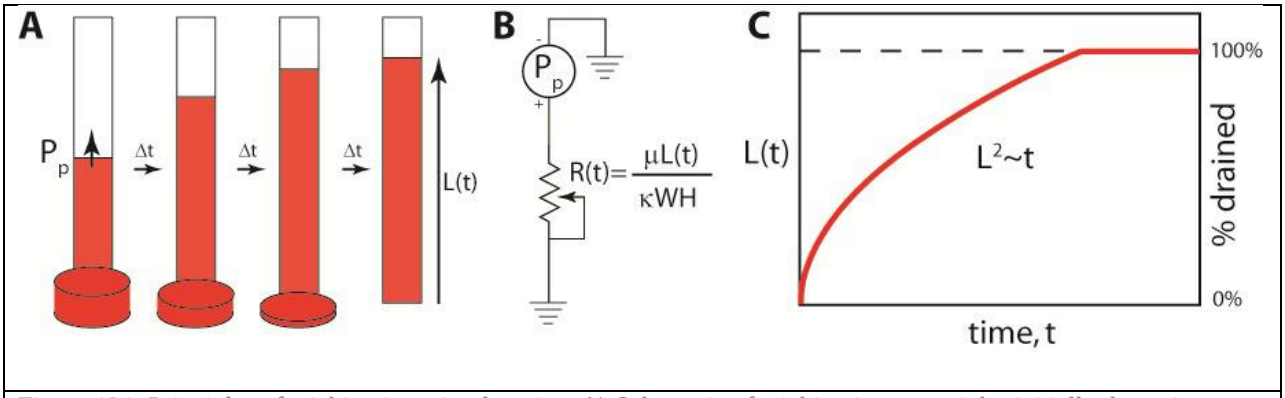

Figure 121: Principles of wicking into simple strips. A) Schematic of wicking into a straight, initially dry strip. Wicking is driven by capillary pressure (Pp) and opposed by viscous resistance to flow through pores that increases as wicking proceeds; the result is a slowing of wicking rate over time. B) An electrical circuit model for wicking into a strip. C) Illustration of migration of the fluid front as a function of time following Equation 25 for a finite fluid source.

19.4.2 Non-ideal fluid sources: backpressure effects

The previous derivations assumed ideal fluid sources that apply negligible backpressure on the strip during release (a condition inherently achieved using well sources). While this simplification offered by wells makes them a well-characterized fluid delivery system, alternative fluid source materials may be better suited for POC settings. For example, LFTs commonly use a sample pad as a fluid source, and we have used glass fiber pads in 2DPNs to hold defined volumes of each source fluid (*e.g.*, Figure 120).

Figure 122A shows the result of wicking fluid into strips from different source materials; images were taken after wicking had ceased. Each source material was sized to hold the same volume of fluid, and nitrocellulose was used as the wicking strip in all cases. The well case represents perfect delivery; the length of wicking into the strip is a measure of the volume released. Glass fiber completely released its fluidic content, while both cellulose and nitrocellulose source pads retained a large percentage of the fluid.

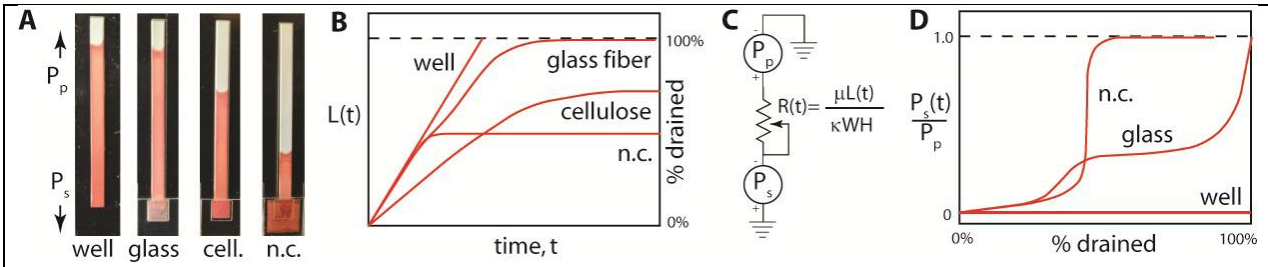

Figure 122: Effects of fluid source materials on capillary-driven fluid delivery into strips. A) Wicking of fluid from different source materials into nitrocellulose strips. Each source was sized to hold the same fluid volume, and images were taken after wicking ceased. The well source can provide complete delivery (100% drained); some materials did not deliver all fluid. B) Migration of the fluid front during wicking from different source materials as illustrations derived from experiments. The well case followed the L2 versus t scaling from Equation 25, while other sources deviated to varying degrees. The % drained was calculated from L(t) based on the fluid capacity of the nitrocellulose. C) Circuit model for wicking into a strip from a non-ideal fluid source. D) Backpressure profiles during release for different source materials. Profiles were determined from plots in C based on Equation 28 and presented here as illustrations. The backpressure applied by the source ($P_S(t)$) was normalized to the capillary pressure of the nitrocellulose strip (P_p), such that capillary flow stops when this ratio is one.

Figure 122B shows wicking profiles derived from data (not shown) for different fluid source materials. The source material affects not only the total amount of fluid released into the membrane, but also the rate at which fluid is released. While glass fiber fully drained, the release rate was slowed in comparison to the ideal case (well). When nitrocellulose was used as both a fluid source and wicking membrane, well-like delivery occurred until the source became ~50% depleted, at which point delivery quickly halted. In contrast to both materials, cellulose delivered an intermediate amount but showed a much slower release. The release profiles shown in Figure

122B suggest that the pressure applied on the membrane by the source pad can change as fluid is drained.

Following the electrical analogy, these fluid sources will function as a voltage source (rather than the previously used 'ground') that opposes the capillary pressure of the wicking membrane (Figure 122C). The circuit models for ideal and non-ideal sources can be used to derive the time-dependent pressure applied by a given material based on experimentally obtainable values.

$$Well\ source: Q^{well} = \epsilon WH \frac{dL^{well}}{dt} = \frac{P_p}{R} = \frac{\kappa WHP_p}{\mu L_{well}}$$	Equation 26
$$Nonideal\ source: Q^{pad} = \varepsilon WH \frac{dL^{pad}}{dt} = \frac{P_p - P_s(t)}{R} = \frac{\kappa WH[P_p - P_s(t)]}{\mu L^{pad}}$$	Equation 27

Taking the ratio of these two equations gives the time dependent applied pressure of a non-ideal fluid source ($P_S(t)$):

$$\frac{P_s(t)}{P_p} = 1 - \frac{L(t)^{pad} \frac{dL(t)^{pad}}{dt}}{L(t)^{well} \frac{dL(t)^{well}}{dt}}$$	Equation 28

As suggested by the experiments, we again see that the capillary pressure of the nitrocellulose and the backpressure exerted by the source material affect both the distance and rate at which fluid travels through the membrane (L(t) and dL(t)/dt, respectively).

Figure 122D plots the backpressure profile during release for selected materials (curve derived from experimental data, not shown); it shows how drastically the pressure applied by a non-ideal source may deviate from the ideal case. In contrast to the constant, negligible backpressure exerted by a well, glass fiber and nitrocellulose sources had complex pressure

functions that varied as they were drained. In the initial stages of delivery, the glass fiber pad behaved similar to an ideal well source and applied a very low backpressure. However, this pressure drastically increased as more fluid was released. This matches the wicking behavior observed in Figure 122B where release from glass fiber pad increasingly deviated from the well case over time. Release from nitrocellulose initially occurred with little backpressure until reaching a critical depletion level (~50%), at which point the capillary pressure of the membrane and the backpressure applied by the source equalized. This pressure equilibration eliminated the driving force for flow and as a result, the nitrocellulose pad retained the remainder of its fluid (as seen in Figure 122B).

Since many potential source materials have a non-uniform pore distribution, it is not surprising that the backpressure applied by the source changes during drainage. For example, a material composed of small and large pores may apply a bimodal backpressure. The pressure may first be low as the large pores drain but then increase when only the small pores remain filled. Glass fiber, cellulose, and nitrocellulose (all common lateral flow materials) all have non-uniform pore distributions. In the following sections, we describe the impact of ideal and non-ideal fluid sources on paper network behavior. In some cases, backpressure profiles from Figure 122D data were used in calculations.

19.4.3 Basic principles in 2D paper network (2DPN) design

Figure 123 illustrates the network behavior for sequential fluid delivery in a 2DPN. For simplicity, we show a device with two legs of equal length and ideal fluid sources of finite volume. Figure 123A (left) shows the state after an initial wet-out period in which the two fluids meet in the spacer region mid-way between the two legs. After this point, both sources continue to deliver fluid, but at different rates. A “leakage” flow (Q2) causes migration of the blue fluid

front, and successful sequential delivery requires that the first fluid (red) is completely drained before arrival of the blue-red fluid front. Unsuccessful design results in both fluids flowing into the detection leg in parallel (*e.g.*, yellow and clear fluids in Figure 119). Figure 123A (right) shows the state after complete drainage of the first (red) fluid for a condition of successful delivery.

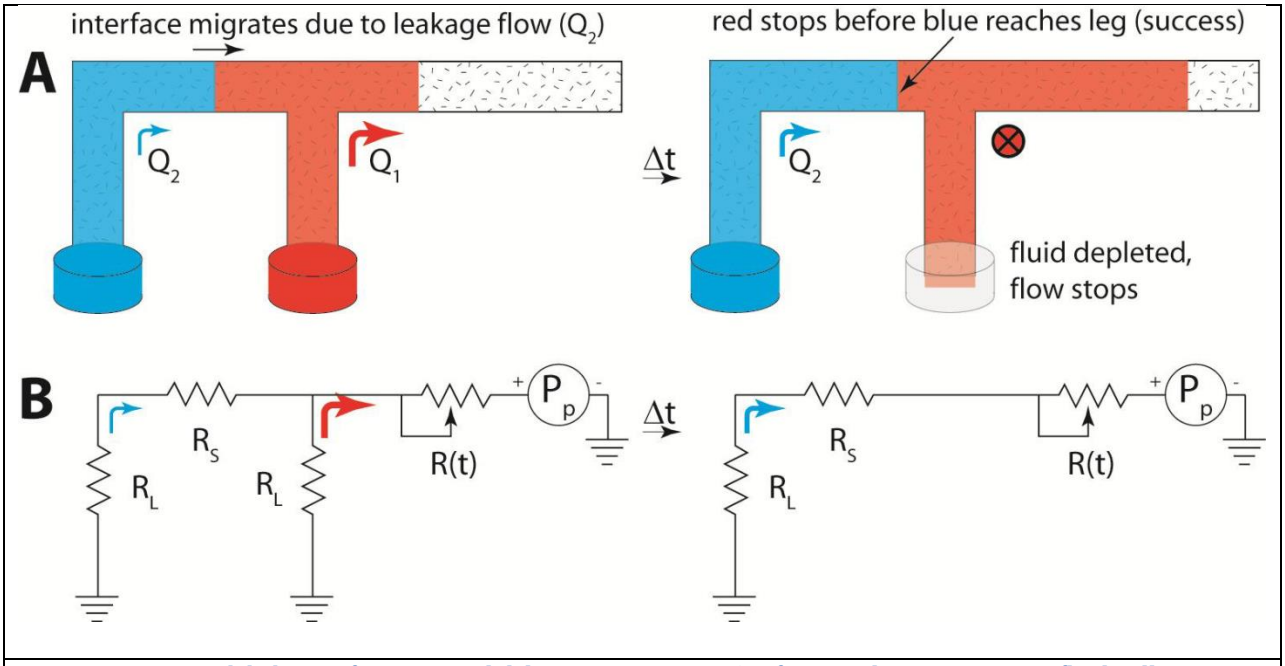

Figure 123: Network behavior for sequential delivery in a 2DPN. A) After initial wet-out occurs, fluid will continue to flow through both legs, which causes the fluid interface to migrate. Successful sequential delivery occurs if the red fluid drains completely before the blue fluid reaches its leg. B) Circuit model for the two stages of delivery in the 2DPN.

Figure 123B shows circuit diagrams for the two stages of sequential delivery in the 2DPN. The ratio of flow rates delivered by each leg is a critical parameter in achieving device success; we find that it can be determined solely by the resistances in the network:

$$\frac{Q_2}{Q_1} = \frac{1}{1 + {R_s}/{R_L}}$$ Equation 29

Ideally, this flow ratio would be zero in the first stage of delivery, with no fluid release occurring from the left source (blue, Q_2) as the right source (red, Q_1) drains. Conceptually, delivery is clean if the time for depletion of the first fluid (T_{drain}) is shorter than the time for migration of the leakage front (T_{mig}). A quantitative criterion for success must also consider the volumetric capacity of the spacer region (*i.e.*, the region that can be filled by the flow Q_2 before failure, not shown). While the 2DPN is incapable of eliminating leakage flow, the leakage flow can be mitigated by increasing the spacer resistance (R_S, *e.g.*, by increasing length or decreasing width) or by decreasing the leg resistance (R_L, *e.g.*, by decreasing length or increasing width). Non-ideal sources further increase the leakage flow (equations not shown). The simple analysis shows the most critical concept – eliminating legs should improve sequential delivery.

19.4.4 A linear paper network (Pseudo-1DPN): basic principles

Prior to developing the network models presented here, some of our authors (Lafleur, Kauffman, Byrnes) created a linear strip using wells as fluid sources. Their design provided clean sequential delivery for three fluids (shown later). Here, we develop the circuit model that explains this behavior and describe the effects when non-ideal fluid sources are used. Figure 124 illustrates sequential delivery in a linear paper network (Pseudo-1DPN) with ideal and non-ideal fluid sources.

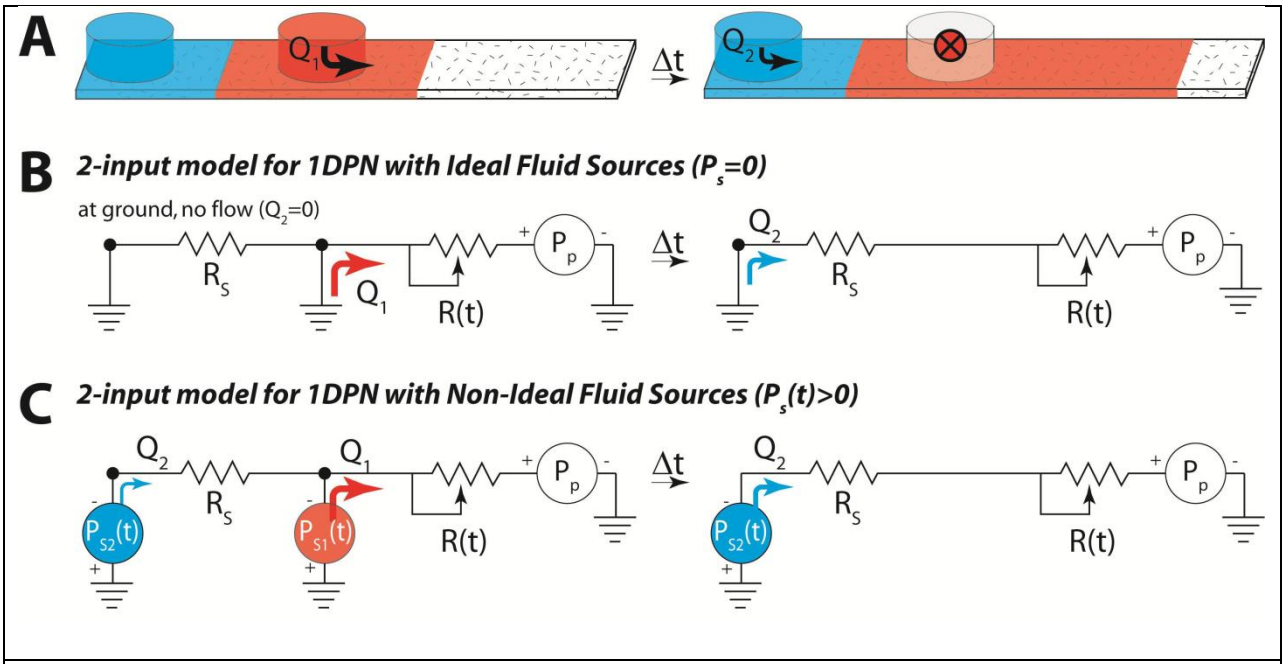

Figure 124: Network behavior of sequential delivery in a Pseudo-1DPN using ideal and non-ideal fluid sources. A) If ideal sources are used, the fluid front of the left fluid (blue) will remain stationary until the right source (red) is completely drained. Only then will the left source (blue) release its contents. B) A circuit model for sequential delivery in a Pseudo-1DPN that uses ideal fluid sources. C) A circuit model for sequential delivery in a Pseudo-1DPN that uses non-ideal fluid sources. Fluid will be released from both sources simultaneously, allowing a potential for leakage to occur (similar to the 2DPN device).

For the initial stage of sequential delivery, the case of non-ideal fluid sources is described by:

$$Q_2 = \frac{P_{S1} - P_{S2}}{R_s}; \quad Q1 = \frac{P_p - P_{S1}}{R(t)}; \quad \frac{Q_2}{Q_1} = \frac{R(t)[P_{S1} - P_{S2}]}{R_s[P_p - P_{S1}]}$$

Equation 30

From these equations, we see that initially, the flow rate of fluid from the left source is not necessarily zero, but a function of the pressure differential between the two sources (Figure 124C) and the spacer resistance (R_S). Thus, the potential for leakage to occur will depend on the backpressure applied by the source material and how it changes as fluid is drained (see Figure 122). As with the 2DPN above, leakage caused by non-ideal fluid sources can be mitigated by increasing the spacing resistance (R_S).

For the case of ideal sources (P_{S1}=P_{S2}=0), the leakage flow is zero, by definition, since there is no pressure difference acting between the fluid sources (if we ignore the force of gravity acting on the fluid columns, both are at "ground", Figure 124B). Thus, ideal sources are expected to give clean sequential delivery even for small spacing between fluid sources. Below, we explore the behavior of both cases in more complex 3-source devices.

19.4.5 Sequential delivery in Pseudo-1DPNs with ideal fluid sources

Figure 125 describes sequential delivery in a Pseudo-1DPN with ideal fluid sources. Figure 125A shows a mathematical simulation of a well-based device case using the previously defined circuit equations. The ideal sources provide perfect sequential delivery since there is no driving pressure for the leakage flow (as shown for the two-leg model in Figure 124B).

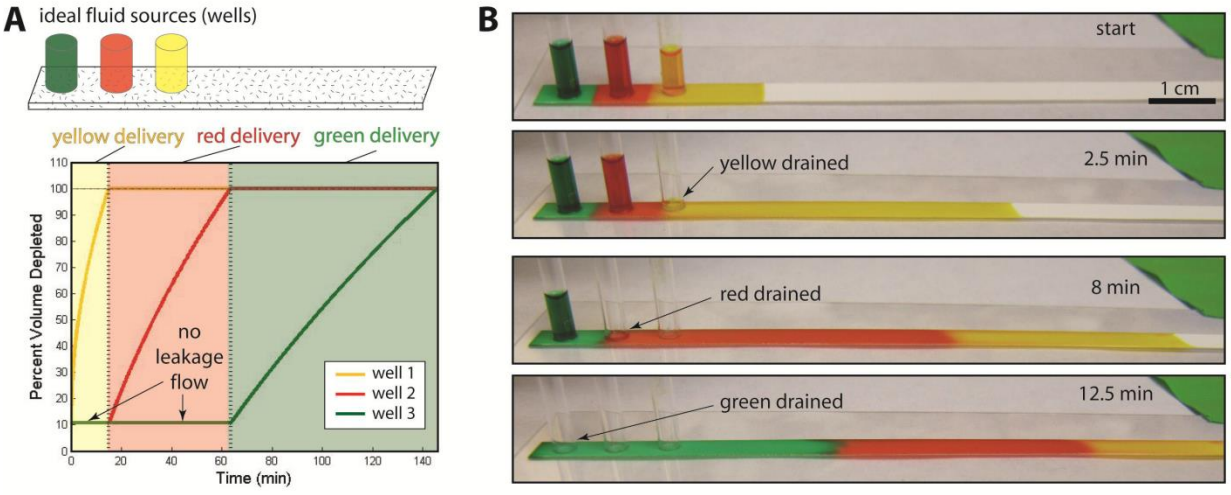

Figure 125: Model behavior and experiments for a Pseudo-1DPN with ideal fluid sources (wells, but in this case sitting above the nitrocellulose membrane). A) Schematic of the Pseudo-1DPN with ideal fluid sources, and model results showing sequential delivery of three fluids. Unlike the 2DPN, wells drain in a perfect sequence with no leakage flow. B) Experimental results for Pseudo-1DPN with ideal sources. Large diameter tubes (wells) serve as ideal sources – they apply a negligible backpressure compared to nitrocellulose capillary pressure (P_S=0.13 kPa, P_P=12 kPa); similarly, the height of fluid in the well is small, so pressure due to gravity is also negligible (P=0.065 kPa). After tubes were contacted with the strips, fluid from each source was delivered in a timed sequence through the strip. Images show the device a few seconds after contact ('start') and at the moments when each tube became depleted (yellow: 2.5 min, red: 8 min, green: 12.5 min). Each well delivered 20 microliters (60 microliters total for three wells).

Experiments confirm that clean sequential delivery can be achieved using a well-based Pseudo-1DPN. Time-lapse images of fluid delivery show that the fluid from one source of the device is released only after the previous source has been completely drained (Figure 125B). The position of the green and red fluid fronts and the levels of fluid in the wells did not significantly change until the fluid in the well to its right was completely drained. As a note, the discrepancy in the time scale of fluid delivery between our model predictions (~140 minutes) and our experimental results (~12.5 minutes) may be due to inaccurate membrane parameter values used in the model (*e.g.*, permeability, void volume).

Using well sources in our Pseudo-1DPN allows us to achieve ideal flow behavior – fluids are released sequentially (and with no leakage) over a time scale appropriate for a potential POC device. Also, the model suggests that a Pseudo-1DPN with ideal fluid sources should provide perfect sequential delivery even when fluid volumes are changed, without the need to alter design. By contrast, the 2DPN format must be redesigned to accommodate any volume changes. Further, the model suggests that fluid sources can be placed close together without impacting behavior; this reduces the total time for delivery since the device can be short. Incorporating these sources into a usable POC test, however, may be a challenge, since they require a user to fill them with the correct volume and they may not be suitable as a storage medium for dried assay reagents.

19.4.6 Sequential delivery in Pseudo-1DPNs with non-ideal sources

Though glass fiber is a widely used source material in LFTs, the changing backpressure it applies on the nitrocellulose membrane during drainage has the potential to cause issues of premature flow and leakage in this Pseudo-1DPN. Figure 126 describes sequential delivery in a Pseudo-1DPN with non-ideal, glass fiber pad fluid sources (Figure 126A). Initial simulations involving

three-step sequential delivery matched our expectation that premature flow will occur between the pads (Figure 126B). While fluid from the right-most pad (clear) was being released, fluid drained from all other sources. The left-most pad (red) released nearly all of its fluid (~90%) before the yellow pad was drained, demonstrating that this leakage flow may not be trivial.

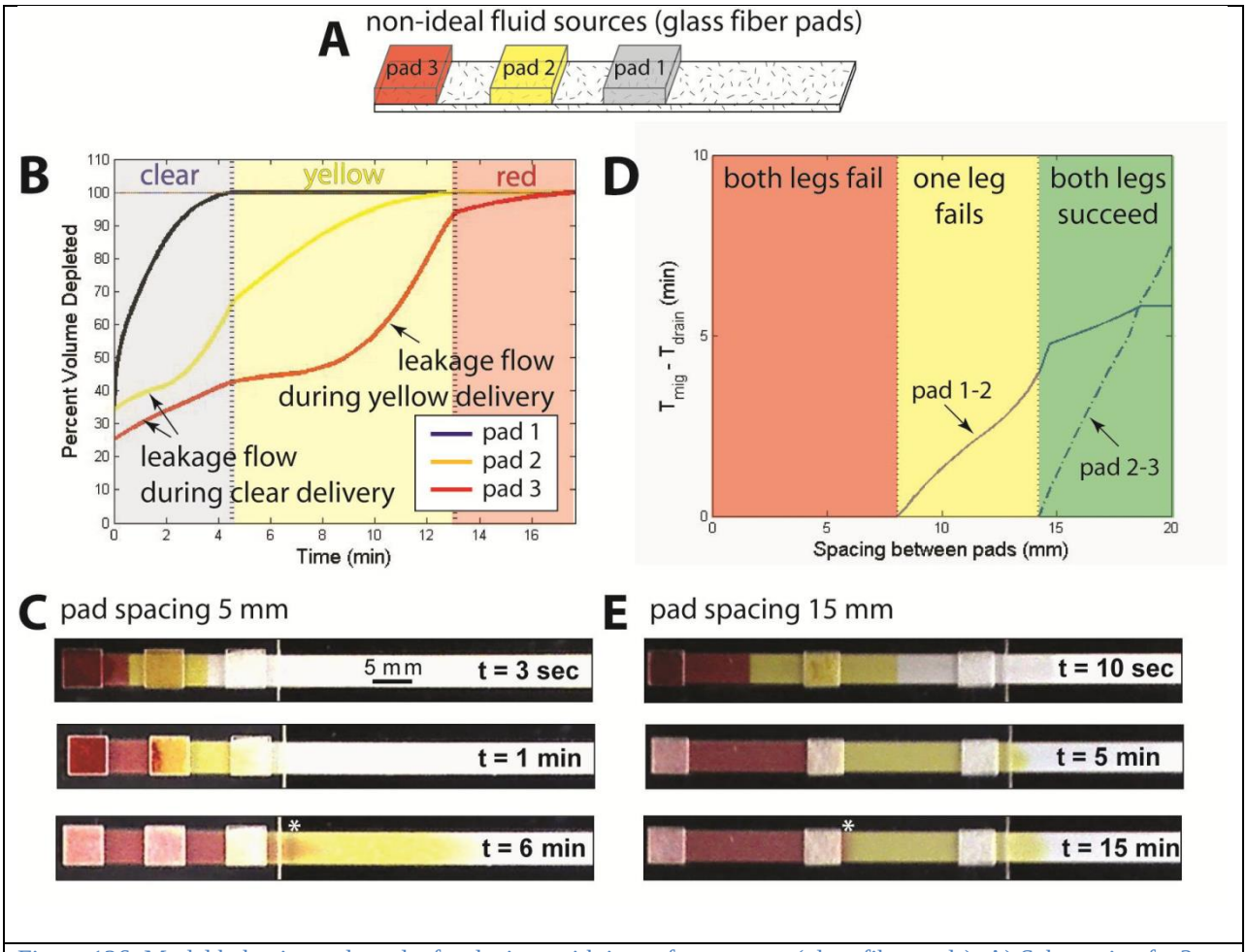

Figure 126: Model behavior and results for devices with imperfect sources (glass fiber pads). A) Schematic of a 3-source Pseudo-1DPN that uses glass fiber pads to deliver clear, yellow, and red fluids. B) A computational model of this scenario predicts that both the yellow and red fluids will be prematurely released. C) Time-lapse images of failed sequential delivery. High leakage flow (due to small spacer resistances (L=5 mm)) resulted in mixing and non-uniform fluid interfaces. D) A computational model was used to illustrate the effect of spacer resistance on failure and success. E) Time-lapse images of successful sequential delivery. Increased spacer resistances (L=15 mm) accommodate fluid leakage so that clean delivery is still achieved. No mixing occurs in the glass fiber pads and similar to the ideal Pseudo-1DPN case, there is a distinct interface between the different fluids. Each pad delivered 10 microliters (30 microliters total for three wells).

Figure 126C shows time-lapse images of a failed device, with pads spaced 5 mm apart. Initial wet-out occurred soon after device activation. However, after wet-out, fluids from the yellow and red pads continued to migrate, reaching the next pad before it was completely drained. This caused unwanted mixing to occur in both the glass fiber pad (noticeably seen at t = 1 min) and the nitrocellulose membrane (exhibited by the long red fluid front seen at t = 6 min, marked by *).

As was the case of the 2DPN, issues caused by this leakage flow can be avoided with appropriate device design. Figure 126D shows a computational model that predicts device behavior given a specific spacing distance/resistance. The times T_{mig} and T_{drain} are used to determine device success. In the model, T_{mig} is the time it takes for fluid from one pad to migrate from the middle of the spacer region (where initial wet-out has terminated) to the left boundary of the subsequent pad. T_{drain} corresponds to the time required for this 'subsequent pad' to release all of its fluid. A successful device will have non-negative $T_{mig} - T_{drain}$ values for all pairs of pads. For example, relating this to Figure 126A, T_{mig} (yellow) – T_{drain} (clear) and T_{mig} (red) – T_{drain} (yellow) must both be greater than or equal to zero for the device to be successful. The plot generated by our model is broken into three distinct regions: red (no clean delivery), yellow (clean delivery between the first and second pad), and green (clean delivery between all pads). As predicted by the circuit model, increasing spacer resistance decreases the flow ratio between sources and improves the likelihood of device success.

Figure 126E shows time-lapse images of a Pseudo-1DPN predicted to achieve clean delivery (with a pad spacing distance of 15 mm). No obvious mixing of fluids occurred in either the pads or at the fluid boundaries. While the fluid front of the red fluid stopped somewhat

beneath Pad 2, there still appeared to be a relatively clear distinction between the red and yellow fluids (marked by *).

In previous work, we chose to use glass fiber pads as fluid sources (*e.g.*, Figure 120) based on their use as dry reagent storage media in lateral flow tests, their ability to self-fill to a fixed volume by wicking (potentially eliminating the need for pipetting steps), and our observation that they release nearly all fluid into a nitrocellulose strip. However, here we found that changes in backpressure during release from glass fiber pads required compensation by increasing the spacer length between fluid sources (and thus increasing total device run time). In contrast, experiments with ideal fluid sources (wells, Figure 125) showed that the Pseudo-1DPN can provide clean sequential delivery even with closely-spaced fluid sources. Our overall goal of a simple user interface (no pipetting), on-device reagent storage, and clean sequential delivery with short total run times is highly-dependent on proper selection of fluid source materials. The analysis here provides a framework to guide that selection.

19.5 Conclusions

The lateral flow test is an ingenious device that performs basic immunoassays in a rapid and easy-to-use format. Paper networks use the same set of materials but reconfigure them to automatically carry out timing for multi-step processes. The behavior of both devices depends on the connectivity of multiple materials and their wicking properties. Here, we explored basic principles of wicking in simple devices and paper networks through use of electrical circuit models. We identified key design principles in a previously-developed sequential delivery device (2DPN) and described an alternative linear paper network (Pseudo-1DPN) that can provide remarkably clean sequential delivery in a very simple device. We showed that materials used as fluid sources can affect both the rate of fluid delivery into a strip and the fraction of fluid volume

released, and these fluid release properties are especially important for programming sequential delivery in paper networks. The analysis provides a framework for more rational design and material selection for paper networks and other capillary-driven diagnostic devices.

19.6 Acknowledgements

The work presented in this paper was carried out in part with support from DARPA DSO under a grant to the University of Washington (grant number HR0011-11-2-0007) with collaborators at PATH, GE Global Research, and Epoch Biosciences.

20 References

[1] J. R. Buser, C. A. Holstein, and P. Yager, “Microfluidic Diagnostics for Low-resource Settings: Improving Global Health without a Power Cord,” in *Microfluidics for Medical Applications*, 2014, pp. 151–190.

[2] P. Yager, T. Edwards, E. Fu, K. Helton, K. Nelson, M. R. Tam, and B. H. Weigl, “Microfluidic diagnostic technologies for global public health.,” *Nature*, vol. 442, no. 7101, pp. 412–8, Jul. 2006.

[3] P. Yager, G. J. Domingo, and J. Gerdes, “Point-of-care diagnostics for global health.,” *Annu. Rev. Biomed. Eng.*, vol. 10, pp. 107–44, Jan. 2008.

[4] The Lewin. Group, “The Value of Diagnostics Innovation, Adoption and Diffusion into Health Care,” July, 2005

[5] PATH, World Health Organization (WHO). Delivering Vaccines: A Cost Comparison of In-Country Vaccine Transport Container Options. Seattle: PATH, WHO; 2013.

[6] B. H. Weigl, D. S. Boyle, T. de los Santos, R. B. Peck, and M. S. Steele, “Simplicity of use: a critical feature for widespread adoption of diagnostic technologies in low-resource settings.,” *Expert Rev. Med. Devices*, vol. 6, no. 5, pp. 461–4, Sep. 2009.

[7] R. McNerney and P. Daley, “Towards a point-of-care test for active tuberculosis: obstacles and opportunities,” *Nat. Rev. Microbiol.*, vol. 9, no. 3, pp. 204–213, Mar. 2011.

[8] D. Mabey, R. W. Peeling, A. Ustianowski, and M. D. Perkins, “Diagnostics for the developing world.,” *Nat. Rev. Microbiol.*, vol. 2, no. 3, pp. 231–40, Mar. 2004.

[9] V. Gubala, L. F. Harris, A. J. Ricco, M. X. Tan, and D. E. Williams, “Point of care diagnostics: status and future.,” *Anal. Chem.*, vol. 84, no. 2, pp. 487–515, Jan. 2012.

[10] C. D. Chin, V. Linder, and S. K. Sia, “Lab-on-a-chip devices for global health: past studies and future opportunities.,” *Lab Chip*, vol. 7, no. 1, pp. 41–57, Jan. 2007.

[11] A. K. Yetisen, M. S. Akram, and C. R. Lowe, “Paper-based microfluidic point-of-care diagnostic devices.,” *Lab Chip*, vol. 13, no. 12, pp. 2210–51, Jun. 2013.

[12] The Institute for Health Metrics and Evaluation (IHME), “The Global Burden of Disease: Generating Evidence, Guiding Policy,” 2013.

[13] C. J. L. Murray, T. Vos, R. Lozano, M. Naghavi, A. D. Flaxman, C. Michaud, M. Ezzati, K. Shibuya, J. a Salomon, S. Abdalla, V. Aboyans, J. Abraham, I. Ackerman, R. Aggarwal, S. Y. Ahn, M. K. Ali, M. Alvarado, H. R. Anderson, L. M. Anderson, K. G. Andrews, C. Atkinson, L. M. Baddour, A. N. Bahalim, S. Barker-Collo, L. H. Barrero, D. H. Bartels, M.-G. Basáñez, A. Baxter, M. L. Bell, E. J. Benjamin, D. Bennett, E. Bernabé, K. Bhalla, B. Bhandari, B. Bikbov, A. Bin Abdulhak, G. Birbeck, J. a Black, H. Blencowe, J. D. Blore, F. Blyth, I. Bolliger, A. Bonaventure, S. Boufous, R. Bourne, M. Boussinesq, T. Braithwaite, C. Brayne, L. Bridgett, S. Brooker, P. Brooks, T. S. Brugha, C. Bryan-Hancock, C. Bucello, R. Buchbinder, G. Buckle, C. M. Budke, M. Burch, P. Burney, R. Burstein, B. Calabria, B. Campbell, C. E. Canter, H. Carabin, J. Carapetis, L. Carmona, C. Cella, F. Charlson, H. Chen, A. T.-A. Cheng, D. Chou, S. S. Chugh, L. E. Coffeng, S. D. Colan, S. Colquhoun, K. E. Colson, J. Condon, M. D. Connor, L. T. Cooper, M. Corriere, M. Cortinovis, K. C. de Vaccaro, W. Couser, B. C. Cowie, M. H. Criqui, M. Cross, K. C. Dabhadkar, M. Dahiya, N. Dahodwala, J. Damsere-Derry, G. Danaei, A. Davis, D. De Leo, L. Degenhardt, R. Dellavalle, A. Delossantos, J. Denenberg, S. Derrett, D. C. Des Jarlais, S. D. Dharmaratne, M. Dherani, C. Diaz-Torne, H. Dolk, E. R. Dorsey, T. Driscoll, H. Duber, B. Ebel, K. Edmond, A. Elbaz, S. E. Ali, H. Erskine, P. J. Erwin, P. Espindola, S. E. Ewoigbokhan, F. Farzadfar, V. Feigin, D. T. Felson, A. Ferrari, C. P. Ferri, E. M. Fèvre, M. M. Finucane, S. Flaxman, L. Flood, K. Foreman, M. H. Forouzanfar, F. G. R. Fowkes, M. Fransen, M. K. Freeman, B. J. Gabbe, S. E. Gabriel, E. Gakidou, H. a Ganatra, B. Garcia, F. Gaspari, R. F. Gillum, G. Gmel, D. Gonzalez-Medina, R. Gosselin, R. Grainger, B. Grant, J. Groeger, F. Guillemin, D. Gunnell, R. Gupta, J. Haagsma, H. Hagan, Y. a Halasa, W. Hall, D. Haring, J. M. Haro, J. E. Harrison, R. Havmoeller, R. J. Hay, H. Higashi, C. Hill, B. Hoen, H. Hoffman, P. J. Hotez, D. Hoy, J. J. Huang, S. E. Ibeanusi, K. H. Jacobsen, S. L. James, D. Jarvis, R. Jasrasaria, S. Jayaraman, N. Johns, J. B. Jonas, G. Karthikeyan, N. Kassebaum, N. Kawakami, A. Keren, J.-P. Khoo, C. H. King, L. M. Knowlton, O. Kobusingye, A. Koranteng, R. Krishnamurthi, F. Laden, R. Lalloo, L. L. Laslett, T. Lathlean, J. L. Leasher, Y. Y. Lee, J. Leigh, D. Levinson, S. S. Lim, E. Limb, J. K. Lin, M. Lipnick, S. E. Lipshultz, W. Liu, M. Loane, S. L. Ohno, R. Lyons, J. Mabweijano, M. F. MacIntyre, R. Malekzadeh, L. Mallinger, S. Manivannan, W. Marcenes, L. March, D. J. Margolis, G. B. Marks, R. Marks, A. Matsumori, R. Matzopoulos, B. M. Mayosi, J. H. McAnulty, M. M. McDermott, N. McGill, J. McGrath, M. E. Medina-Mora, M. Meltzer, G. a Mensah, T. R. Merriman, A.-C. Meyer, V. Miglioli, M. Miller, T. R. Miller, P. B. Mitchell, C. Mock, A. O. Mocumbi, T. E. Moffitt, A. a Mokdad, L. Monasta, M. Montico, M. Moradi-Lakeh, A. Moran, L. Morawska, R. Mori, M. E. Murdoch, M. K. Mwaniki, K. Naidoo, M. N. Nair, L. Naldi, K. M. V. Narayan, P. K. Nelson, R. G. Nelson, M. C. Nevitt, C. R. Newton, S. Nolte, P. Norman, R. Norman, M. O’Donnell, S. O’Hanlon, C. Olives, S. B. Omer, K. Ortblad, R. Osborne, D. Ozgediz, A. Page, B. Pahari, J. D. Pandian, A. P. Rivero, S. B. Patten, N. Pearce, R. P. Padilla, F. Perez-Ruiz, N. Perico, K. Pesudovs, D. Phillips, M. R. Phillips, K. Pierce, S. Pion, G. V Polanczyk, S. Polinder, C. A. Pope, S. Popova, E.

Porrini, F. Pourmalek, M. Prince, R. L. Pullan, K. D. Ramaiah, D. Ranganathan, H. Razavi, M. Regan, J. T. Rehm, D. B. Rein, G. Remuzzi, K. Richardson, F. P. Rivara, T. Roberts, C. Robinson, F. R. De Leòn, L. Ronfani, R. Room, L. C. Rosenfeld, L. Rushton, R. L. Sacco, S. Saha, U. Sampson, L. Sanchez-Riera, E. Sanman, D. C. Schwebel, J. G. Scott, M. Segui-Gomez, S. Shahraz, D. S. Shepard, H. Shin, R. Shivakoti, D. Singh, G. M. Singh, J. a Singh, J. Singleton, D. a Sleet, K. Sliwa, E. Smith, J. L. Smith, N. J. C. Stapelberg, A. Steer, T. Steiner, W. a Stolk, L. J. Stovner, C. Sudfeld, S. Syed, G. Tamburlini, M. Tavakkoli, H. R. Taylor, J. a Taylor, W. J. Taylor, B. Thomas, W. M. Thomson, G. D. Thurston, I. M. Tleyjeh, M. Tonelli, J. a Towbin, T. Truelsen, M. K. Tsilimbaris, C. Ubeda, E. a Undurraga, M. J. van der Werf, J. van Os, M. S. Vavilala, N. Venketasubramanian, M. Wang, W. Wang, K. Watt, D. J. Weatherall, M. a Weinstock, R. Weintraub, M. G. Weisskopf, M. M. Weissman, R. a White, H. Whiteford, N. Wiebe, S. T. Wiersma, J. D. Wilkinson, H. C. Williams, S. R. M. Williams, E. Witt, F. Wolfe, A. D. Woolf, S. Wulf, P.-H. Yeh, A. K. M. Zaidi, Z.-J. Zheng, D. Zonies, A. D. Lopez, M. a AlMazroa, and Z. a Memish, "Disability-adjusted life years (DALYs) for 291 diseases and injuries in 21 regions, 1990-2010: a systematic analysis for the Global Burden of Disease Study 2010.," *Lancet*, vol. 380, no. 9859, pp. 2197–223, Dec. 2012.

[14] C. H. Chew, Y. A. L. Lim, P. C. Lee, R. Mahmud, and K. H. Chua, "Hexaplex PCR detection system for identification of five human Plasmodium species with an internal control.," *J. Clin. Microbiol.*, vol. 50, no. 12, pp. 4012–9, Dec. 2012.

[15] F. S. Younai, "Thirty years of the human immunodeficiency virus epidemic and beyond.," *Int. J. Oral Sci.*, vol. 5, no. 4, pp. 191–9, Dec. 2013.

[16] J. M. Binley, T. Wrin, B. Korber, M. B. Zwick, M. Wang, C. Chappey, G. Stiegler, R. Kunert, S. Zolla-Pazner, H. Katinger, C. J. Petropoulos, and D. R. Burton, "Comprehensive cross-clade neutralization analysis of a panel of anti-human immunodeficiency virus type 1 monoclonal antibodies.," *J. Virol.*, vol. 78, no. 23, pp. 13232–52, Dec. 2004.

[17] World Health Organization, "Global tuberculosis report 2013," 2013.

[18] UNITAID, "Tuberculosis Diagnostic Technology Landscape," 2012.

[19] World Health Organization, "diabetes action now."

[20] World Health Organization, "Use of glycated haemoglobin (HbA1c) in the diagnosis of diabetes mellitus," *Diabetes Res. Clin. Pract.*, vol. 93, no. 3, pp. 299–309, Sep. 2011.

[21] B. H. Weigl, G. Zwisler, R. Peck, and E. Abu-Haydar, "Rapid screening test for

gestational diabetes: public health need, market requirement, initial product design, and experimental results," vol. 8615, p. 86150L, Mar. 2013.

[22] World Health Organization, "WHO methods and data sources for country-level causes of death 2000-2012," 2014.

[23] S. Brown and T. X. Brown, "Value of mobile monitoring for diabetes in developing countries," in *Proceedings of the Sixth International Conference on Information and Communication Technologies and Development Full Papers - ICTD '13 - volume 1*, 2013, pp. 267–273.

[24] D. M. Smith and R. T. Schooley, "Running with scissors: using antiretroviral therapy without monitoring viral load.," *Clin. Infect. Dis.*, vol. 46, no. 10, pp. 1598–600, May 2008.

[25] A. Calmy and N. Ford, "HIV viral load monitoring in resource-limited regions: optional or necessary?," *Clin. Infect. ...*, vol. 44, 2007.

[26] M. Usdin, M. Guillerm, and A. Calmy, "Patient needs and point-of-care requirements for HIV load testing in resource-limited settings.," *J. Infect. Dis.*, vol. 201 Suppl , no. Suppl 1, pp. S73–7, Apr. 2010.

[27] W. S. Stevens, L. E. Scott, and S. M. Crowe, "Quantifying HIV for monitoring antiretroviral therapy in resource-poor settings.," *J. Infect. Dis.*, vol. 201 Suppl , no. Suppl 1, pp. S16–26, Apr. 2010.

[28] HHS Panel on Antiretroviral Guidelines for Adults and Adolescents – A Working Group of the Office of AIDS Research Advisory Council (OARAC), "Guidelines for the use of antiretroviral agents in HIV-1-infected adults and adolescents," 2008.

[29] X. Wei, S. Ghosh, M. Taylor, and V. Johnson, "Viral dynamics in human immunodeficiency virus type 1 infection," *Nature*, 1995.

[30] UNAIDS, "UNAIDS report on the global AIDS epidemic," 2010.

[31] World Health Organization, "Antiretroviral therapy." [Online]. Available: http://www.who.int/hiv/topics/treatment/en/index.html. [Accessed: 24-Sep-2013].

[32] C.-C. Li, K. D. Seidel, R. W. Coombs, and L. M. Frenkel, "Detection and Quantification

of Human Immunodeficiency Virus Type 1 p24 Antigen in Dried Whole Blood and Plasma on Filter Paper Stored under Various Conditions," *J. Clin. Microbiol.*, vol. 43, no. 8, pp. 3901–3905, Aug. 2005.

[33] S. A. Fiscus, B. Cheng, S. M. Crowe, L. Demeter, C. Jennings, V. Miller, R. Respess, and W. Stevens, "HIV-1 Viral Load Assays for Resource-Limited Settings," *PLoS Med.*, vol. 3, no. 10, p. e417, Oct. 2006.

[34] S. Wang, F. Xu, and U. Demirci, "Advances in developing HIV-1 viral load assays for resource-limited settings.," *Biotechnol. Adv.*, vol. 28, no. 6, pp. 770–81, 2010.

[35] H. E. Rawizza, B. Chaplin, S. T. Meloni, G. Eisen, T. Rao, J.-L. Sankalé, A. Dieng-Sarr, O. Agbaji, D. I. Onwujekwe, W. Gashau, R. Nkado, E. Ekong, P. Okonkwo, R. L. Murphy, and P. J. Kanki, "Immunologic criteria are poor predictors of virologic outcome: implications for HIV treatment monitoring in resource-limited settings.," *Clin. Infect. Dis.*, vol. 53, no. 12, pp. 1283–90, Dec. 2011.

[36] World Health Organization, "Recommendations for a public health approach: 2010 revision," 2010.

[37] M. Badri, S. D. Lawn, and R. Wood, "Utility of CD4 cell counts for early prediction of virological failure during antiretroviral therapy in a resource-limited setting.," *BMC Infect. Dis.*, vol. 8, no. December 2006, p. 89, Jan. 2008.

[38] M. Piatak, M. Saag, L. Yang, and S. Clark, "High levels of HIV-1 in plasma during all stages of infection determined by competitive PCR," *Science (80-.).*, vol. 259, no. 5102, pp. 1749–1754, 1993.

[39] World Health Organization, "Medicines: spurious/falsely-labelled/ falsified/counterfeit (SFFC) medicines–Fact Sheet," 2012.

[40] A. A. Weaver, H. Reiser, T. Barstis, M. Benvenuti, D. Ghosh, M. Hunckler, B. Joy, L. Koenig, K. Raddell, and M. Lieberman, "Paper Analytical Devices for Fast Field Screening of Beta Lactam Antibiotics and Antituberculosis Pharmaceuticals," *Anal. Chem.*, vol. 85, no. 13, pp. 6453–6460, Jul. 2013.

[41] J. C. Jokerst, J. M. Emory, and C. S. Henry, "Advances in microfluidics for environmental analysis.," *Analyst*, vol. 137, no. 1, pp. 24–34, Jan. 2012.

[42] L. Romana, L. Vega, P. Plata, S. P. De Macoris, and M. Plata, “Pan American Health Organization (PAHO). Epidemiological update. Cholera.,” no. January, pp. 1–2, 2013.

[43] P. Farmer, C. P. Almazor, E. T. Bahnsen, D. Barry, J. Bazile, B. R. Bloom, N. Bose, T. Brewer, S. B. Calderwood, J. D. Clemens, A. Cravioto, E. Eustache, G. Jérôme, N. Gupta, J. B. Harris, H. H. Hiatt, C. Holstein, P. J. Hotez, L. C. Ivers, V. B. Kerry, S. P. Koenig, R. C. Larocque, F. Léandre, W. Lambert, E. Lyon, J. J. Mekalanos, J. S. Mukherjee, C. Oswald, J.-W. Pape, A. Gretchko Prosper, R. Rabinovich, M. Raymonville, J.-R. Réjouit, L. J. Ronan, M. L. Rosenberg, E. T. Ryan, J. D. Sachs, D. a Sack, C. Surena, A. a Suri, R. Ternier, M. K. Waldor, D. Walton, and J. L. Weigel, “Meeting cholera’s challenge to Haiti and the world: a joint statement on cholera prevention and care.,” *PLoS Negl. Trop. Dis.*, vol. 5, no. 5, p. e1145, Jan. 2011.

[44] G. Madico, W. Checkley, R. H. Gilman, N. Bravo, L. Cabrera, M. Calderon, and A. Ceballos, “Active surveillance for Vibrio cholerae O1 and vibriophages in sewage water as a potential tool to predict cholera outbreaks . Active Surveillance for Vibrio cholerae O1 and Vibriophages in Sewage Water as a Potential Tool To Predict Cholera Outbreaks,” *J. Clin. Microbiol.*, vol. 34, no. 12, pp. 2968–2972, 1996.

[45] S. Richardson and T. Ternes, “Water analysis: emerging contaminants and current issues,” *Anal. Chem.*, vol. 81, no. 12, pp. 4645–77, Jun. 2005.

[46] S. C. Terry, J. H. Jerman, and J. B. Angell, “A gas chromatographic air analyzer fabricated on a silicon wafer,” *IEEE Trans. Electron Devices*, vol. 26, no. 12, pp. 1880–1886, Dec. 1979.

[47] A. Manz, N. Graber, and H. M. Widmer, “Miniaturized total chemical analysis systems: A novel concept for chemical sensing,” *Sensors Actuators B Chem.*, vol. 1, no. 1–6, pp. 244–248, Jan. 1990.

[48] D. C. Duffy, J. C. McDonald, O. J. Schueller, and G. M. Whitesides, “Rapid Prototyping of Microfluidic Systems in Poly(dimethylsiloxane).,” *Anal. Chem.*, vol. 70, no. 23, pp. 4974–84, Dec. 1998.

[49] T. Thorsen, S. J. Maerkl, and S. R. Quake, “Microfluidic large-scale integration.,” *Science*, vol. 298, no. 5593, pp. 580–4, Oct. 2002.

[50] L. Lafleur, D. Stevens, K. McKenzie, S. Ramachandran, P. Spicar-Mihalic, M. Singhal, A. Arjyal, J. Osborn, P. Kauffman, P. Yager, and B. Lutz, “Progress toward multiplexed sample-to-result detection in low resource settings using microfluidic immunoassay cards.,” *Lab Chip*, vol. 12, no. 6, pp. 1119–27, Mar. 2012.

[51] S. Choi, M. Goryll, L. Y. M. Sin, P. K. Wong, and J. Chae, “Microfluidic-based biosensors toward point-of-care detection of nucleic acids and proteins,” *Microfluid. Nanofluidics*, vol. 10, no. 2, pp. 231–247, Jun. 2010.

[52] C. C. Boehme, M. P. Nicol, P. Nabeta, J. S. Michael, E. Gotuzzo, R. Tahirli, M. T. Gler, R. Blakemore, W. Worodria, C. Gray, L. Huang, T. Caceres, R. Mehdiyev, L. Raymond, A. Whitelaw, K. Sagadevan, H. Alexander, H. Albert, F. Cobelens, H. Cox, D. Alland, and M. D. Perkins, “Feasibility, diagnostic accuracy, and effectiveness of decentralised use of the Xpert MTB/RIF test for diagnosis of tuberculosis and multidrug resistance: a multicentre implementation study.,” *Lancet*, vol. 377, no. 9776, pp. 1495–505, Apr. 2011.

[53] Cepheid, “Xpert® MTB/RIF.” [Online]. Available: http://www.cepheid.com/us/cepheid-solutions/clinical-ivd-tests/critical-infectious-diseases/xpert-mtb-rif. [Accessed: 24-Sep-2013].

[54] A. Vassall, S. van Kampen, H. Sohn, J. S. Michael, K. R. John, S. den Boon, J. L. Davis, A. Whitelaw, M. P. Nicol, M. T. Gler, A. Khaliqov, C. Zamudio, M. D. Perkins, C. C. Boehme, and F. Cobelens, “Rapid diagnosis of tuberculosis with the Xpert MTB/RIF assay in high burden countries: a cost-effectiveness analysis.,” *PLoS Med.*, vol. 8, no. 11, p. e1001120, Nov. 2011.

[55] FIND, “Price for Xpert® MTB/RIF and FIND country list.” [Online]. Available: http://www.finddiagnostics.org/about/what_we_do/successes/find-negotiated-prices/xpert_mtb_rif.html. [Accessed: 24-Sep-2013].

[56] N. P. Pai, C. Vadnais, C. Denkinger, N. Engel, and M. Pai, “Point-of-care testing for infectious diseases: diversity, complexity, and barriers in low- and middle-income countries.,” *PLoS Med.*, vol. 9, no. 9, p. e1001306, Jan. 2012.

[57] A. Pantoja, C. Fitzpatrick, A. Vassall, K. Weyer, and K. Floyd, “Xpert MTB/RIF for diagnosis of tuberculosis and drug-resistant tuberculosis: a cost and affordability analysis.,” *Eur. Respir. J.*, vol. 42, no. 3, pp. 708–20, Sep. 2013.

[58] C. D. Chin, T. Laksanasopin, Y. K. Cheung, D. Steinmiller, V. Linder, H. Parsa, J. Wang, H. Moore, R. Rouse, G. Umviligihozo, E. Karita, L. Mwambarangwe, S. L. Braunstein, J. van de Wijgert, R. Sahabo, J. E. Justman, W. El-Sadr, and S. K. Sia, “Microfluidics-based diagnostics of infectious diseases in the developing world.,” *Nat. Med.*, vol. 17, no. 8, pp. 1015–9, Aug. 2011.

[59] I. R. Lauks, “Microfabricated Biosensors and Microanalytical Systems for Blood Analysis,” *Acc. Chem. Res.*, vol. 31, no. 5, pp. 317–324, May 1998.

[60] C. D. Chin, Y. K. Cheung, T. Laksanasopin, M. M. Modena, S. Y. Chin, A. a Sridhara, D. Steinmiller, V. Linder, J. Mushingantahe, G. Umviligihozo, E. Karita, L. Mwambarangwe, S. L. Braunstein, J. van de Wijgert, R. Sahabo, J. E. Justman, W. El-Sadr, and S. K. Sia, “Mobile device for disease diagnosis and data tracking in resource-limited settings.,” *Clin. Chem.*, vol. 59, no. 4, pp. 629–40, Apr. 2013.

[61] “Microfluidics 2.0.” [Online]. Available: http://www.mf20.org/. [Accessed: 24-Sep-2015].

[62] J. P. Rolland and D. a. Mourey, “Paper as a novel material platform for devices,” *MRS Bull.*, vol. 38, no. 04, pp. 299–305, Apr. 2013.

[63] X. Li, D. R. Ballerini, and W. Shen, “A perspective on paper-based microfluidics: Current status and future trends.,” *Biomicrofluidics*, vol. 6, no. 1, pp. 11301–1130113, Mar. 2012.

[64] B. O’Farrell, “Evolution in Lateral Flow–Based Immunoassay Systems,” R. Wong and H. Tse, Eds. Totowa, NJ: Humana Press, 2009, pp. 1–33.

[65] J. L. Osborn, “Novel Paper Networks for Point-of-Care Sample Preparation and Indirect IgM Detection,” University of Washington, 2011.

[66] A. W. Martinez, S. T. Phillips, G. M. Whitesides, and E. Carrilho, “Diagnostics for the developing world: microfluidic paper-based analytical devices.,” *Anal. Chem.*, vol. 82, no. 1, pp. 3–10, Jan. 2010.

[67] S. Rosen, “Market Trends in Lateral Flow Immunoassays,” in *Lateral Flow Immunoassay*, 2009, pp. 35–49.

[68] G. E. Fridley, C. a. Holstein, S. B. Oza, and P. Yager, “The evolution of nitrocellulose as a material for bioassays,” *MRS Bull.*, vol. 38, no. 04, pp. 326–330, Apr. 2013.

[69] T. Chard, “Pregnancy test: a review,” *Hum. Reprod.*, vol. 7, no. 5, pp. 701–710, 1992.

[70] A. B. Bonner, K. W. Monroe, L. I. Talley, A. E. Klasner, and D. W. Kimberlin, “Making and Patient Management in the Pediatric Emergency Department :,” vol. 112, no. 2, 2015.

[71] G. A. Posthuma-Trumpie, J. Korf, and A. van Amerongen, “Lateral flow (immuno)assay: its strengths, weaknesses, opportunities and threats. A literature survey,” *Anal. Bioanal. Chem.*, vol. 393, no. 2, pp. 569–582, Jan. 2009.

[72] M. H. Craig, B. L. Bredenkamp, C. H. V. Williams, E. J. Rossouw, V. J. Kelly, I. Kleinschmidt, A. Martineau, and G. F. J. Henry, “tests comparative evaluation of ten rapid malaria diagnostic,” pp. 258–265, 2002.

[73] CDC, “Morbidity and mortality weekly report,” vol. 61, pp. 873–876, 2012.

[74] S. D. Blacksell, J. A. Doust, P. N. Newton, S. J. Peacock, N. P. J. Day, and A. M. Dondorp, “A systematic review and meta-analysis of the diagnostic accuracy of rapid immunochromatographic assays for the detection of dengue virus IgM antibodies during acute infection,” *Trans. R. Soc. Trop. Med. Hyg.*, vol. 100, no. 8, pp. 775–784, Aug. 2006.

[75] “OraQuick ADVANCE® Rapid HIV-1/2 Antibody Test.” [Online]. Available: http://www.orasure.com/products-infectious/products-infectious-oraquick.asp. [Accessed: 24-Sep-2013].

[76] A. Carballo-Diéguez, T. Frasca, I. Balan, M. Ibitoye, and C. Dolezal, “Use of a rapid HIV home test prevents HIV exposure in a high risk sample of men who have sex with men.,” *AIDS Behav.*, vol. 16, no. 7, pp. 1753–60, Oct. 2012.

[77] A. W. Martinez, S. T. Phillips, M. J. Butte, and G. M. Whitesides, “Patterned paper as a platform for inexpensive, low-volume, portable bioassays.,” *Angew. Chem. Int. Ed. Engl.*, vol. 46, no. 8, pp. 1318–20, Jan. 2007.

[78] E. Carrilho, A. W. Martinez, and G. M. Whitesides, “Understanding wax printing: a simple micropatterning process for paper-based microfluidics.,” *Anal. Chem.*, vol. 81, no. 16, pp. 7091–5, Aug. 2009.

[79] A. W. Martinez, S. T. Phillips, and G. M. Whitesides, “Three-dimensional microfluidic devices fabricated in layered paper and tape.,” *Proc. Natl. Acad. Sci. U. S. A.*, vol. 105, no. 50, pp. 19606–11, Dec. 2008.

[80] A. W. Martinez, S. T. Phillips, Z. Nie, C.-M. Cheng, E. Carrilho, B. J. Wiley, and G. M. Whitesides, “Programmable diagnostic devices made from paper and tape.,” *Lab Chip*, vol. 10, no. 19, pp. 2499–504, Oct. 2010.

[81] K. M. Schilling, D. Jauregui, and A. W. Martinez, “Paper and toner three-dimensional fluidic devices: programming fluid flow to improve point-of-care diagnostics.,” *Lab Chip*, vol. 13, no. 4, pp. 628–31, Feb. 2013.

[82] N. K. Thom, K. Yeung, M. B. Pillion, and S. T. Phillips, “‘Fluidic batteries’ as low-cost sources of power in paper-based microfluidic devices.,” *Lab Chip*, vol. 12, no. 10, pp. 1768–70, Apr. 2012.

[83] M. M. Mentele, J. Cunningham, K. Koehler, J. Volckens, and C. S. Henry, “Microfluidic paper-based analytical device for particulate metals.,” *Anal. Chem.*, vol. 84, no. 10, pp. 4474–80, May 2012.

[84] N. R. Pollock, J. P. Rolland, S. Kumar, P. D. Beattie, S. Jain, F. Noubary, V. L. Wong, R. a Pohlmann, U. S. Ryan, and G. M. Whitesides, “A paper-based multiplexed transaminase test for low-cost, point-of-care liver function testing.,” *Sci. Transl. Med.*, vol. 4, no. 152, p. 152ra129, Sep. 2012.

[85] Diagnostics For All, “Liver Function.” [Online]. Available: http://www.dfa.org/projects/liver-function.php. [Accessed: 24-Sep-2013]

[86] S. T. Phillips and G. G. Lewis, “Advances in materials that enable quantitative point-of-care assays,” *MRS Bull.*, vol. 38, no. 04, pp. 315–319, Apr. 2013.

[87] E. J. Maxwell, A. D. Mazzeo, and G. M. Whitesides, “Paper-based electroanalytical devices for accessible diagnostic testing,” *MRS Bull.*, vol. 38, no. 04, pp. 309–314, Apr. 2013.

[88] E. Fu, S. A. Ramsey, P. Kauffman, B. Lutz, and P. Yager, “Transport in two-dimensional paper networks.,” *Microfluid. Nanofluidics*, vol. 10, no. 1, pp. 29–35, Jan. 2011.

[89] E. Fu, B. Lutz, P. Kauffman, and P. Yager, “Controlled reagent transport in disposable 2D paper networks.,” *Lab Chip*, vol. 10, no. 7, pp. 918–20, Apr. 2010.

[90] B. R. Lutz, P. Trinh, C. Ball, E. Fu, and P. Yager, “Two-dimensional paper networks: programmable fluidic disconnects for multi-step processes in shaped paper.,” *Lab Chip*, vol. 11, no. 24, pp. 4274–8, Dec. 2011.

[91] E. Fu, P. Kauffman, B. Lutz, and P. Yager, “Chemical signal amplification in two-dimensional paper networks.,” *Sens. Actuators. B. Chem.*, vol. 149, no. 1, pp. 325–328,

Aug. 2010.

[92] E. Fu, T. Liang, J. Houghtaling, S. Ramachandran, S. A. Ramsey, B. Lutz, and P. Yager, "Enhanced sensitivity of lateral flow tests using a two-dimensional paper network format.," *Anal. Chem.*, vol. 83, no. 20, pp. 7941–6, Oct. 2011.

[93] E. Fu, T. Liang, P. Spicar-Mihalic, J. Houghtaling, S. Ramachandran, and P. Yager, "Two-dimensional paper network format that enables simple multistep assays for use in low-resource settings in the context of malaria antigen detection.," *Anal. Chem.*, vol. 84, no. 10, pp. 4574–9, May 2012.

[94] J. L. Osborn, B. Lutz, E. Fu, P. Kauffman, D. Y. Stevens, and P. Yager, "Microfluidics without pumps: reinventing the T-sensor and H-filter in paper networks.," *Lab Chip*, vol. 10, no. 20, pp. 2659–65, Oct. 2010.

[95] P. Kauffman, E. Fu, B. Lutz, and P. Yager, "Visualization and measurement of flow in two-dimensional paper networks.," *Lab Chip*, vol. 10, no. 19, pp. 2614–7, Oct. 2010.

[96] B. a Rohrman and R. R. Richards-Kortum, "A paper and plastic device for performing recombinase polymerase amplification of HIV DNA.," *Lab Chip*, vol. 12, no. 17, pp. 3082–8, Sep. 2012.

[97] A. Apilux, Y. Ukita, M. Chikae, O. Chailapakul, and Y. Takamura, "Development of automated paper-based devices for sequential multistep sandwich enzyme-linked immunosorbent assays using inkjet printing.," *Lab Chip*, vol. 13, no. 1, pp. 126–35, Jan. 2013.

[98] M. Funes-Huacca, A. Wu, E. Szepesvari, P. Rajendran, N. Kwan-Wong, A. Razgulin, Y. Shen, J. Kagira, R. Campbell, and R. Derda, "Portable self-contained cultures for phage and bacteria made of paper and tape.," *Lab Chip*, vol. 12, no. 21, pp. 4269–78, Nov. 2012.

[99] C. D. Chin, V. Linder, and S. K. Sia, "Commercialization of microfluidic point-of-care diagnostic devices.," *Lab Chip*, vol. 12, no. 12, pp. 2118–34, Jun. 2012.

[100] Y. Thakker and S. Woods, "Storage of vaccines in the community: weak link in the cold chain?," *BMJ*, vol. 304, no. 6829, pp. 756–8, Mar. 1992.

[101] D. Y. Stevens, C. R. Petri, J. L. Osborn, P. Spicar-Mihalic, K. G. McKenzie, and P. Yager, "Enabling a microfluidic immunoassay for the developing world by integration of on-card

dry reagent storage.," *Lab Chip*, vol. 8, no. 12, pp. 2038–45, Dec. 2008.

[102] G. E. Fridley, H. Q. Le, E. Fu, and P. Yager, "Controlled release of dry reagents in porous media for tunable temporal and spatial distribution upon rehydration.," *Lab Chip*, vol. 12, no. 21, pp. 4321–7, Nov. 2012.

[103] N. J. Cira, J. Y. Ho, M. E. Dueck, and D. B. Weibel, "A self-loading microfluidic device for determining the minimum inhibitory concentration of antibiotics.," *Lab Chip*, vol. 12, no. 6, pp. 1052–9, Mar. 2012.

[104] S. Begolo, F. Shen, and R. F. Ismagilov, "A microfluidic device for dry sample preservation in remote settings.," *Lab Chip*, vol. 13, no. 22, pp. 4331–42, Oct. 2013.

[105] W. Du, L. Li, K. P. Nichols, and R. F. Ismagilov, "SlipChip.," *Lab Chip*, vol. 9, no. 16, pp. 2286–92, Aug. 2009.

[106] F. Shen, B. Sun, J. E. Kreutz, E. K. Davydova, W. Du, P. L. Reddy, L. J. Joseph, and R. F. Ismagilov, "Multiplexed quantification of nucleic acids with large dynamic range using multivolume digital RT-PCR on a rotational SlipChip tested with HIV and hepatitis C viral load.," *J. Am. Chem. Soc.*, vol. 133, no. 44, pp. 17705–12, Nov. 2011.

[107] K. G. McKenzie, L. K. Lafleur, B. R. Lutz, and P. Yager, "Rapid protein depletion from complex samples using a bead-based microfluidic device for the point of care.," *Lab Chip*, vol. 9, no. 24, pp. 3543–8, Dec. 2009.

[108] L. A. Marshall, L. L. Wu, S. Babikian, M. Bachman, and J. G. Santiago, "Integrated printed circuit board device for cell lysis and nucleic acid extraction.," *Anal. Chem.*, vol. 84, no. 21, pp. 9640–5, Nov. 2012.

[109] M. Mahalanabis, H. Al-Muayad, M. D. Kulinski, D. Altman, and C. M. Klapperich, "Cell lysis and DNA extraction of gram-positive and gram-negative bacteria from whole blood in a disposable microfluidic chip.," *Lab Chip*, vol. 9, no. 19, pp. 2811–7, Oct. 2009.

[110] J. Siegrist, R. Gorkin, M. Bastien, G. Stewart, R. Peytavi, H. Kido, M. Bergeron, and M. Madou, "Validation of a centrifugal microfluidic sample lysis and homogenization platform for nucleic acid extraction with clinical samples.," *Lab Chip*, vol. 10, no. 3, pp. 363–71, Feb. 2010.

[111] P. E. Vandeventer, K. M. Weigel, J. Salazar, B. Erwin, B. Irvine, R. Doebler, A. Nadim,

G. a Cangelosi, and A. Niemz, “Mechanical disruption of lysis-resistant bacterial cells by use of a miniature, low-power, disposable device.,” *J. Clin. Microbiol.*, vol. 49, no. 7, pp. 2533–9, Jul. 2011.

[112] “OmniLyse® Ultra-Rapid Cell Lysis Kits.” [Online]. Available: http://www.claremontbio.com/OmniLyse_Cell_Lysis_Kits_s/56.htm. [Accessed: 24-Sep-2013].

[113] R. Kubota, P. Labarre, J. Singleton, A. Beddoe, B. H. Weigl, A. M. Alvarez, and D. M. Jenkins, “Non-Instrumented Nucleic Acid Amplification (NINA) for Rapid Detection of Ralstonia solanacearum Race 3 Biovar 2,” *Biol. Eng. Trans.*, vol. 4, no. 2, pp. 69–80, 2011.

[114] P. LaBarre, K. R. Hawkins, J. Gerlach, J. Wilmoth, A. Beddoe, J. Singleton, D. Boyle, and B. Weigl, “A Simple , Inexpensive Device for Nucleic Acid Amplification without Electricity — Toward Instrument- Free Molecular Diagnostics in Low-Resource Settings,” *PLoS One*, vol. 6, no. 5, p. e19738, 2011.

[115] J. Singleton, C. Zentner, J. Buser, P. Yager, P. LaBarre, and B. H. Weigl, “Instrument-free exothermic heating with phase change temperature control for paper microfluidic devices,” *Proc. SPIE*, vol. 8615, p. 86150R, Mar. 2013.

[116] C. Liu, E. Geva, M. Mauk, X. Qiu, W. R. Abrams, D. Malamud, K. Curtis, S. M. Owen, and H. H. Bau, “An isothermal amplification reactor with an integrated isolation membrane for point-of-care detection of infectious diseases.,” *Analyst*, vol. 136, no. 10, pp. 2069–76, May 2011.

[117] J. P. Esquivel, M. Castellarnau, T. Senn, B. Löchel, J. Samitier, and N. Sabaté, “Fuel cell-powered microfluidic platform for lab-on-a-chip applications.,” *Lab Chip*, vol. 12, no. 1, pp. 74–9, Jan. 2012.

[118] P. Chun, “Colloidal Gold and Other Labels for Lateral Flow Immunoassays,” in *Lateral Flow Immunoassay*, 2009, pp. 75–93.

[119] K. Faulstich, R. Gruler, M. Eberhard, D. Lentzsch, and K. Haberstroh, “Handheld and Portable Reader Devices for Lateral Flow Immunoassays,” in *Lateral Flow Immunoassay*, 2009, pp. 157–183.

[120] W. Dungchai, O. Chailapakul, and C. S. Henry, “Use of multiple colorimetric indicators for paper-based microfluidic devices.,” *Anal. Chim. Acta*, vol. 674, no. 2, pp. 227–33,

Aug. 2010.

[121] G. G. Lewis, M. J. DiTucci, and S. T. Phillips, “Quantifying analytes in paper-based microfluidic devices without using external electronic readers.,” *Angew. Chem. Int. Ed. Engl.*, vol. 51, no. 51, pp. 12707–10, Dec. 2012.

[122] D. J. You, T. S. Park, and J.-Y. Yoon, “Cell-phone-based measurement of TSH using Mie scatter optimized lateral flow assays.,” *Biosens. Bioelectron.*, vol. 40, no. 1, pp. 180–185, Jul. 2012.

[123] O. Mudanyali, S. Dimitrov, U. Sikora, S. Padmanabhan, I. Navruz, and A. Ozcan, “Integrated rapid-diagnostic-test reader platform on a cellphone.,” *Lab Chip*, vol. 12, no. 15, pp. 2678–86, Aug. 2012.

[124] A. W. Martinez, S. T. Phillips, E. Carrilho, S. W. Thomas, H. Sindi, and G. M. Whitesides, “Simple telemedicine for developing regions: camera phones and paper-based microfluidic devices for real-time, off-site diagnosis.,” *Anal. Chem.*, vol. 80, no. 10, pp. 3699–707, May 2008.

[125] N. Dell, N. Breit, T. Chaluco, J. Crawford, and G. Borriello, “Digitizing paper forms with mobile imaging technologies,” *Proc. 2nd ACM Symp. Comput. Dev. - ACM DEV ’12*, p. 1, 2012.

[126] J. R. Buser, S. Diesburg, J. Singleton, D. Guelig, J. D. Bishop, C. Zentner, R. Burton, P. LaBarre, P. Yager, and B. H. Weigl, “Precision chemical heating for diagnostic devices,” *Lab Chip*, vol. 15, pp. 4423–4432, 2015.

[127] E. W. Washburn, “The Dynamics of Capillary Flow,” *Phys. Rev.*, vol. 17, no. 3, pp. 273–283, Mar. 1921.

[128] W. K. T. Coltro, D. P. de Jesus, J. A. F. da Silva, C. L. do Lago, and E. Carrilho, “Toner and paper-based fabrication techniques for microfluidic applications.,” *Electrophoresis*, vol. 31, no. 15, pp. 2487–98, Aug. 2010.

[129] S. Mendez, E. M. Fenton, G. R. Gallegos, D. N. Petsev, S. S. Sibbett, H. a Stone, Y. Zhang, and G. P. López, “Imbibition in porous membranes of complex shape: quasi-stationary flow in thin rectangular segments.,” *Langmuir*, vol. 26, no. 2, pp. 1380–5, Jan. 2010.

[130] Millipore, “Rapid Lateral Flow Test Strips. Considerations for Product Development”, 2008.

[131] A. Jena and K. Gupta, “Recent Advances in Techniques for Porosity Characterization of Membranes Pore Diameter , Distribution and Permeability of Membranes,” Porous Materials Inc.

[132] T. N. Narasimhan, “Central Ideas of Buckingham (1907): A Century Later,” *Vadose Zo. J.*, vol. 6, no. 4, p. 687, 2007.

[133] L. A. Richards, “Capillary conduction of liquids through porous mediums,” *J. Appl. Phys.*, vol. 1, no. 5, pp. 318–333, 1931.

[134] F. Zhang, “Soil Water Retention and Relative Permeability for Full Range of Saturation,” report for the Pacific Northwest National Laboratory. September, 2010.

[135] K. Kosugi, “Lognnormal Distribution Model for Unsaturated Soil Hydraulic Properties,” *Water Resour. Res.*, vol. 32, no. 9, pp. 2697–2703, 1996.

[136] R. H. Brooks and a T. Corey, “Hydraulic properties of porous media,” *Hydrol Pap Fort Collins CO Colo State Univ*, vol. 3, no. 3, p. 27, 1964.

[137] M. T. van Genuchten, *A Closed-form Equation for Predicting the Hydraulic Conductivity of Unsaturated Soils*, vol. 44, no. 5. 1980, p. 892.

[138] ASTM, *Standard Test Methods for Determination of the Soil Water Characteristic Curve for Desorption Using Hanging Column , Pressure Extractor , Chilled Mirror Hygrometer , or Centrifuge 1*, vol. 02, no. Reapproved 2008. 2015, pp. 1–22.

[139] K. Seki, “SWRC fit – a nonlinear fitting program with a water retention curve for soils having unimodal and bimodal pore structure,” *Hydrol. Earth Syst. Sci. Discuss.*, vol. 4, no. 1, pp. 407–437, 2007.

[140] H. Darcy, *Les fontaines publiques de la ville de Dijon*. 1856.

[141] K. H. Head, *Manual of Soil Laboratory Testing*, 2nd ed. Pentech Press Limited, 1994.

[142] C. Parolo, M. Medina-Sánchez, A. de la Escosura-Muñiz, and A. Merkoçi, “Simple paper

architecture modifications lead to enhanced sensitivity in nanoparticle based lateral flow immunoassays," *Lab Chip*, vol. 13, no. 3, pp. 386–390, Feb. 2013.

[143] M. A. Dineva, L. Mahilum-Tapay, and H. Lee, "Sample preparation: a challenge in the development of point-of-care nucleic acid-based assays for resource-limited settings," *Analyst*, vol. 132, no. 12, p. 1193, 2007.

[144] A. Niemz, T. M. Ferguson, and D. S. Boyle, "Point-of-care nucleic acid testing for infectious diseases.," *Trends Biotechnol.*, vol. 29, no. 5, pp. 240–50, May 2011.

[145] P. K. Drain, E. P. Hyle, F. Noubary, K. a Freedberg, D. Wilson, W. R. Bishai, W. Rodriguez, and I. V Bassett, "Diagnostic point-of-care tests in resource-limited settings.," *Lancet. Infect. Dis.*, vol. 14, no. 3, pp. 239–49, Mar. 2014.

[146] J. C. Linnes, A. Fan, N. M. Rodriguez, B. Lemieux, H. Kong, and C. M. Klapperich, "Paper-based molecular diagnostic for Chlamydia trachomatis.," *RSC Adv.*, vol. 4, no. 80, pp. 42245–42251, Jan. 2014.

[147] S. Huang, J. Do, M. Mahalanabis, A. Fan, L. Zhao, L. Jepeal, S. K. Singh, and C. M. Klapperich, "Low cost extraction and isothermal amplification of DNA for infectious diarrhea diagnosis.," *PLoS One*, vol. 8, no. 3, p. e60059, Jan. 2013.

[148] C. Liu, M. G. Mauk, R. Hart, X. Qiu, and H. H. Bau, "A self-heating cartridge for molecular diagnostics.," *Lab Chip*, vol. 11, no. 16, pp. 2686–92, Aug. 2011.

[149] B. Hatano, T. Maki, T. Obara, H. Fukumoto, K. Hagisawa, Y. Matsushita, A. Okutani, B. Bazartseren, S. Inoue, T. Sata, and H. Katano, "LAMP using a disposable pocket warmer for anthrax detection, a highly mobile and reliable method for anti-bioterrorism.," *Jpn. J. Infect. Dis.*, vol. 63, no. 1, pp. 36–40, Jan. 2010.

[150] UNICEF, "Innovative HIV Point-of-care (POC) CD4 , EID and Viral Load Equipment Project: Early Infant Diagnosis (EID) and Viral Load (VL) POC Technology 2015," 2015.

[151] mini PCR, "mini PCR home page," 2015. [Online]. Available: http://www.minipcr.com/. [Accessed: 24-Sep-2015].

[152] Ahram Biosystems, "http://www.ahrambio.com/," 2015. [Online]. Available: http://www.ahrambio.com/. [Accessed: 20-May-2006].

[153] J. J. Lowe, S. G. Gibbs, S. S. Schwedhelm, J. Nguyen, and P. W. Smith, “Nebraska Biocontainment Unit perspective on disposal of Ebola medical waste.,” *Am. J. Infect. Control*, vol. 42, no. 12, pp. 1256–7, Dec. 2014.

[154] B. J. Toley, J. a Wang, M. Gupta, J. R. Buser, L. K. Lafleur, B. R. Lutz, E. Fu, and P. Yager, “A versatile valving toolkit for automating fluidic operations in paper microfluidic devices.,” *Lab Chip*, vol. 15, no. 6, pp. 1432–44, Mar. 2015.

[155] N. Panpradist, B. J. Toley, X. Zhang, S. Byrnes, J. R. Buser, J. a Englund, and B. R. Lutz, “Swab sample transfer for point-of-care diagnostics: characterization of swab types and manual agitation methods.,” *PLoS One*, vol. 9, no. 9, p. e105786, Jan. 2014.

[156] B. J. Toley, B. McKenzie, T. Liang, J. R. Buser, P. Yager, and E. Fu, “Tunable-delay shunts for paper microfluidic devices.,” *Anal. Chem.*, vol. 85, no. 23, pp. 11545–52, Dec. 2013.

[157] S. Dharmaraja, L. Lafleur, S. Byrnes, P. Kauffman, J. Buser, B. Toley, E. Fu, P. Yager, and B. Lutz, “Programming paper networks for point of care diagnostics,” vol. 8615, no. 206, p. 86150X–86150X–11, Mar. 2013.

[158] J. R. Buser, A. Wollen, E. K. Heiniger, S. Byrnes, P. C. Kauffman, P. D. Ladd, and P. Yager, “Electromechanical cell lysis using a portable audio device: enabling challenging sample preparation at the point-of-care,” *Lab Chip*, vol. 15, pp. 1994–97, 2015.

[159] S. A. Byrnes, J. D. Bishop, L. Lafleur, J. R. Buser, B. Lutz, and P. Yager, “One-step purification and concentration of DNA in porous membranes for point-of-care applications.,” *Lab Chip*, vol. 15, no. 12, pp. 2647–59, Jun. 2015.

[160] B. J. Toley, I. Covelli, Y. Belousov, S. Ramachandran, E. Kline, N. Scarr, N. Vermeulen, W. Mahoney, B. R. Lutz, and P. Yager, “Isothermal Strand Displacement Amplification (iSDA): A Rapid and Sensitive Method of Nucleic Acid Amplification for Point-Of-Care Diagnosis,” *Submitted*, 2015.

[161] Y. S. Belousov, B. Alabeyev, and N. Scarr, “Methods for true isothermal strand displacement amplification,” US20140255928 A12014.

[162] L. Lillis, D. Lehman, M. C. Singhal, J. Cantera, J. Singleton, P. Labarre, A. Toyama, O. Piepenburg, M. Parker, R. Wood, J. Overbaugh, and D. S. Boyle, “Non-instrumented

incubation of a recombinase polymerase amplification assay for the rapid and sensitive detection of proviral HIV-1 DNA.," *PLoS One*, vol. 9, no. 9, p. e108189, Jan. 2014.

[163] J. Singleton, D. Guelig, J. Buser, R. Burton, O. Edeh, K. Hawkins, B. Weigl, and P. LaBarre, "Advancing electricity-free molecular diagnostics at the point-of-care: Optimizing the NINA platform for a malaria LAMP assay," in *IEEE Global Humanitarian Technology Conference (GHTC 2014)*, 2014, pp. 721–725.

[164] M. Mehrali, S. T. Latibari, M. Mehrali, H. S. C. Metselaar, and M. Silakhori, "Shape-stabilized phase change materials with high thermal conductivity based on paraffin/graphene oxide composite," *Energy Convers. Manag.*, vol. 67, pp. 275–282, Mar. 2013.

[165] F. Yavari, H. R. Fard, K. Pashayi, M. A. Rafiee, A. Zamiri, Z. Yu, R. Ozisik, T. Borca-Tasciuc, and N. Koratkar, "Enhanced Thermal Conductivity in a Nanostructured Phase Change Composite due to Low Concentration Graphene Additives," *J. Phys. Chem. C*, vol. 115, no. 17, pp. 8753–8758, May 2011.

[166] R. J. Warzoha and A. S. Fleischer, "Improved heat recovery from paraffin-based phase change materials due to the presence of percolating graphene networks," *Int. J. Heat Mass Transf.*, vol. 79, pp. 314–323, Dec. 2014.

[167] L. Fan and J. M. Khodadadi, "Thermal conductivity enhancement of phase change materials for thermal energy storage: A review," *Renew. Sustain. Energy Rev.*, vol. 15, no. 1, pp. 24–46, Jan. 2011.

[168] V. D. Bhatt, K. Gohil, and A. Mishra, "Thermal Energy Storage Capacity of some Phase changing Materials and Ionic Liquids," *Int. J. ChemTech Res.*, vol. 2, no. 3, pp. 1771–1779, 2010.

[169] N. Ukrainczyk, S. Kurajica, and J. Šipušiæ, "Thermophysical Comparison of Five Commercial Paraffin Waxes as Latent Heat Storage Materials," *Chem. Biochem. Eng. Q.*, vol. 24, no. 2, pp. 129–137, 2010.

[170] M. C. Costa, M. P. Rolemberg, L. a. D. Boros, M. a. Krähenbühl, M. G. de Oliveira, and A. J. a. Meirelles, "Solid−Liquid Equilibrium of Binary Fatty Acid Mixtures," *J. Chem. Eng. Data*, vol. 52, no. 1, pp. 30–36, Jan. 2007.

[171] Entropy Solutions. [Online]. Available: http://www.puretemp.com. [Accessed: 24-Sep-2015].

[172] Rubitherm Technologies. [Online]. Available: http://www.rubitherm.de. [Accessed: 24-Sep-2015].

[173] PCM Products Ltd. [Online]. Available: http://www.pcmproducts.net. [Accessed: 24-Sep-2015].

[174] A. Sarı, "Thermal reliability test of some fatty acids as PCMs used for solar thermal latent heat storage applications," *Energy Convers. Manag.*, vol. 44, no. 14, pp. 2277–2287, Aug. 2003.

[175] J. Singleton, J. L. Osborn, L. Lillis, K. Hawkins, D. Guelig, W. Price, R. Johns, K. Ebels, D. Boyle, B. Weigl, and P. LaBarre, "Electricity-free amplification and detection for molecular point-of-care diagnosis of HIV-1.," *PLoS One*, vol. 9, no. 11, p. e113693, Jan. 2014.

[176] J. R. Buser, X. Zhang, S. A. Byrnes, P. D. Ladd, E. K. Heiniger, M. D. Wheeler, J. D. Bishop, J. A. Englund, B. R. Lutz, B. H. Weigl, and P. Yager, "A disposable chemical heater and dry enzyme preparation for lysis and extraction of DNA and RNA from microorganisms," *Anal. Methods*, vol. 8, no. 14, pp. 2880–2886, 2016.

[177] R. Mariella, "Sample preparation: the weak link in microfluidics-based biodetection.," *Biomed. Microdevices*, vol. 10, no. 6, pp. 777–84, Dec. 2008.

[178] P. Wood and D. Sinton, "Portable audio electronics for impedance-based measurements in microfluidics," *J. Micromechanics Microengineering*, vol. 20, no. 8, p. 087001, 2010.

[179] H. Kaneko, T. Kawana, E. Fukushima, and T. Suzutani, "Tolerance of loop-mediated isothermal amplification to a culture medium and biological substances.," *J. Biochem. Biophys. Methods*, vol. 70, no. 3, pp. 499–501, Apr. 2007.

[180] BioSpec, "Mini-beadbeater-8." [Online]. Available: http://www.biospec.com/instructions/minibeadbeater_8/. [Accessed: 24-Sep-2015].

[181] D. Hughes, "A press for disrupting bacteria and other micro-organisms," *Br. J. Exp. Pathol.*, 1951.

[182] E. M. B. Laboratory, "Protein purification: Extraction and Clarification Preparation of cell lysates from E.coli." [Online]. Available:

https://www.embl.de/pepcore/pepcore_services/protein_purification/extraction_clarification/cell_lysates_ecoli/. [Accessed: 24-Sep-2015].

[183] N. S. Lawrence, C. S. French, and N. Series, "Colloidal Dispersion of Chloroplast Materiall," vol. 111, no. 2893, pp. 633–634, 2015.

[184] H. Lange, P. Taillandier, and J.-P. Riba, "Effect of high shear stress on microbial viability," *J. Chem. Technol. Biotechnol.*, vol. 76, no. 5, pp. 501–505, May 2001.

[185] G. Seltmann and O. Holst, *The bacterial cell wall*. 2002.

[186] D. White, *The Physiology and Biochemistry of Prokaryotes*, 2nd ed. New York: Oxford University Press, 1995.

[187] J. Jacobs, M. Rhodes, B. Sturgis, and B. Wood, "Influence of environmental gradients on the abundance and distribution of Mycobacterium spp. in a coastal lagoon estuary.," *Appl. Environ. Microbiol.*, vol. 75, no. 23, pp. 7378–84, Dec. 2009.

[188] J. Ashmore, C. del Pino, and T. Mullin, "Cavitation in a Lubrication Flow between a Moving Sphere and a Boundary," *Phys. Rev. Lett.*, vol. 94, no. 12, p. 124501, Mar. 2005.

[189] Acroname, "Back-EMF Motion Feedback." [Online]. Available: http://acroname.com/articles/back-emf-motion-feedback. [Accessed: 24-Sep-2015].

[190] R. Lozano, M. Naghavi, K. Foreman, S. Lim, K. Shibuya, V. Aboyans, J. Abraham, T. Adair, R. Aggarwal, S. Y. Ahn, M. Alvarado, H. R. Anderson, L. M. Anderson, K. G. Andrews, C. Atkinson, L. M. Baddour, S. Barker-Collo, D. H. Bartels, M. L. Bell, E. J. Benjamin, D. Bennett, K. Bhalla, B. Bikbov, A. Bin Abdulhak, G. Birbeck, F. Blyth, I. Bolliger, S. Boufous, C. Bucello, M. Burch, P. Burney, J. Carapetis, H. Chen, D. Chou, S. S. Chugh, L. E. Coffeng, S. D. Colan, S. Colquhoun, K. E. Colson, J. Condon, M. D. Connor, L. T. Cooper, M. Corriere, M. Cortinovis, K. C. de Vaccaro, W. Couser, B. C. Cowie, M. H. Criqui, M. Cross, K. C. Dabhadkar, N. Dahodwala, D. De Leo, L. Degenhardt, A. Delossantos, J. Denenberg, D. C. Des Jarlais, S. D. Dharmaratne, E. R. Dorsey, T. Driscoll, H. Duber, B. Ebel, P. J. Erwin, P. Espindola, M. Ezzati, V. Feigin, A. D. Flaxman, M. H. Forouzanfar, F. G. R. Fowkes, R. Franklin, M. Fransen, M. K. Freeman, S. E. Gabriel, E. Gakidou, F. Gaspari, R. F. Gillum, D. Gonzalez-Medina, Y. a Halasa, D. Haring, J. E. Harrison, R. Havmoeller, R. J. Hay, B. Hoen, P. J. Hotez, D. Hoy, K. H. Jacobsen, S. L. James, R. Jasrasaria, S. Jayaraman, N. Johns, G. Karthikeyan, N. Kassebaum, A. Keren, J.-P. Khoo, L. M. Knowlton, O. Kobusingye, A. Koranteng, R. Krishnamurthi, M. Lipnick, S. E. Lipshultz, S. L. Ohno, J. Mabweijano, M. F. MacIntyre, L. Mallinger, L. March, G. B. Marks, R. Marks, A. Matsumori, R. Matzopoulos, B. M.

Mayosi, J. H. McAnulty, M. M. McDermott, J. McGrath, G. a Mensah, T. R. Merriman, C. Michaud, M. Miller, T. R. Miller, C. Mock, A. O. Mocumbi, A. a Mokdad, A. Moran, K. Mulholland, M. N. Nair, L. Naldi, K. M. V. Narayan, K. Nasseri, P. Norman, M. O'Donnell, S. B. Omer, K. Ortblad, R. Osborne, D. Ozgediz, B. Pahari, J. D. Pandian, A. P. Rivero, R. P. Padilla, F. Perez-Ruiz, N. Perico, D. Phillips, K. Pierce, C. A. Pope, E. Porrini, F. Pourmalek, M. Raju, D. Ranganathan, J. T. Rehm, D. B. Rein, G. Remuzzi, F. P. Rivara, T. Roberts, F. R. De León, L. C. Rosenfeld, L. Rushton, R. L. Sacco, J. a Salomon, U. Sampson, E. Sanman, D. C. Schwebel, M. Segui-Gomez, D. S. Shepard, D. Singh, J. Singleton, K. Sliwa, E. Smith, A. Steer, J. a Taylor, B. Thomas, I. M. Tleyjeh, J. a Towbin, T. Truelsen, E. a Undurraga, N. Venketasubramanian, L. Vijayakumar, T. Vos, G. R. Wagner, M. Wang, W. Wang, K. Watt, M. a Weinstock, R. Weintraub, J. D. Wilkinson, A. D. Woolf, S. Wulf, P.-H. Yeh, P. Yip, A. Zabetian, Z.-J. Zheng, A. D. Lopez, and C. J. L. Murray, "Global and regional mortality from 235 causes of death for 20 age groups in 1990 and 2010: a systematic analysis for the Global Burden of Disease Study 2010.," *Lancet*, vol. 380, no. 9859, pp. 2095–128, Dec. 2013.

[191] H. Wang, L. Dwyer-Lindgren, K. T. Lofgren, J. K. Rajaratnam, J. R. Marcus, A. Levin-Rector, C. E. Levitz, A. D. Lopez, and C. J. L. Murray, "Age-specific and sex-specific mortality in 187 countries, 1970-2010: a systematic analysis for the Global Burden of Disease Study 2010.," *Lancet*, vol. 380, no. 9859, pp. 2071–94, Dec. 2012.

[192] R. W. Peeling, D. Mabey, A. Herring, and E. W. Hook, "Why do we need quality-assured diagnostic tests for sexually transmitted infections?," *Nat. Rev. Microbiol.*, vol. 4, no. 12 Suppl, pp. S7–19, Dec. 2006.

[193] D. Litaker, S. M. Koroukian, and T. E. Love, "Looking Beyond the Individual," *Med. Care*, vol. 43, no. 6, pp. 531–540, 2005.

[194] S. Ramani and G. Kang, "Viruses causing childhood diarrhoea in the developing world.," *Curr. Opin. Infect. Dis.*, vol. 22, no. 5, pp. 477–482, 2009.

[195] D. R. Hill and N. J. Beeching, "Travelers' diarrhea.," *Curr. Opin. Infect. Dis.*, vol. 23, no. 5, pp. 481–487, 2010.

[196] Mayo Clinic, "Diarrhea Causes" [Online]. Available: http://www.mayoclinic.org/symptoms/diarrhea/basics/causes/sym-20050926, [Accessed: 24-Sep-2015]

[197] K. Hodges and R. Gill, "Infectious diarrhea," *Gut Microbes*, vol. 1, no. 1, pp. 4–21, Jan. 2010.

[198] World Health Organization “Antimicrobial Resistance Fact Sheet,” 2015.

[199] M. Z. David and R. S. Daum, “Community-associated methicillin-resistant Staphylococcus aureus: epidemiology and clinical consequences of an emerging epidemic.,” *Clin. Microbiol. Rev.*, vol. 23, no. 3, pp. 616–87, Jul. 2010.

[200] M. A. Borg, M. de Kraker, E. Scicluna, N. van de Sande-Bruinsma, E. Tiemersma, J. Monen, and H. Grundmann, “Prevalence of methicillin-resistant *Staphylococcus aureus* (MRSA) in invasive isolates from southern and eastern Mediterranean countries.,” *J. Antimicrob. Chemother.*, vol. 60, no. 6, pp. 1310–5, Dec. 2007.

[201] C. M. Kusuma, J. F. Kokai-kun, and S. a Sam, “Comparison of Four Methods for Determining Lysostaphin Susceptibility of Various Strains of *Staphylococcus aureus*,” *Society*, vol. 49, no. 8, pp. 3256–3263, 2005.

[202] D. Voet, J. G. Voet, and C. W. Pratt, *Fundamentals of Biochemistry*, Third Edit. John Wiley & Sons, Inc., 2008.

[203] O. Salazar and J. a. Asenjo, “Enzymatic lysis of microbial cells,” *Biotechnol. Lett.*, vol. 29, no. 7, pp. 985–994, 2007.

[204] T. Masaki and K. Nakamura, “A new proteolytic enzyme from *Achromobacter lyticus* M497-1,” *Agric. Biol. Chem.*, vol. 42, no. 7, pp. 1443–1445, 1978.

[205] S. M. Paule, D. M. Hacek, B. Kufner, K. Truchon, R. B. Thomson, K. L. Kaul, A. Robicsek, and L. R. Peterson, “Performance of the BD GeneOhm methicillin-resistant *Staphylococcus aureus* test before and during high-volume clinical use.,” *J. Clin. Microbiol.*, vol. 45, no. 9, pp. 2993–8, Sep. 2007.

[206] N. Kobayashi, H. Wu, K. Kojima, K. Taniguchi, S. Urasawa, N. Uehara, Y. Omizu, Y. Kishi, A. Yagihashi, and I. Kurokawa, “Detection of mecA, femA, and femB genes in clinical strains of *staphylococci* using polymerase chain reaction,” *Epidemiol. Infect.*, vol. 113, no. 02, p. 259, May 2009.

[207] N. M. Rodriguez, J. C. Linnes, A. Fan, C. K. Ellenson, N. R. Pollock, and C. M. Klapperich, “Paper-based RNA extraction, in situ isothermal amplification, and lateral flow detection for low-cost, rapid diagnosis of Influenza A (H1N1) from clinical specimens.,” *Anal. Chem.*, Jun. 2015.

[208] J. R. Choi, J. Hu, R. Tang, Y. Gong, S. Feng, H. Ren, T. Wen, X. Li, W. A. B. Wan Abas, B. Pingguan-Murphy, and F. Xu, "An integrated paper-based sample-to-answer biosensor for nucleic acid testing at the point of care," *Lab Chip*, vol. 16, no. 3, pp. 611–621, 2016.

[209] K. G. Shah, D. Guelig, S. Diesburg, J. Buser, R. Burton, P. LaBarre, R. Richards-Kortum, and B. Weigl, "Design of a New Type of Compact Chemical Heater for Isothermal Nucleic Acid Amplification.," *PLoS One*, vol. 10, no. 10, p. e0139449, Jan. 2015.

[210] "MREInfo.com - Home." [Online]. Available: http://www.mreinfo.com. [Accessed: 24-Sep-2015].

[211] J. Kuypers, N. Wright, and R. Morrow, "Evaluation of quantitative and type-specific real-time RT-PCR assays for detection of respiratory syncytial virus in respiratory specimens from children.," *J. Clin. Virol.*, vol. 31, no. 2, pp. 123–9, Oct. 2004.

[212] V. M. Cowton, D. R. McGivern, and R. Fearns, "Unravelling the complexities of respiratory syncytial virus RNA synthesis.," *J. Gen. Virol.*, vol. 87, no. Pt 7, pp. 1805–21, Jul. 2006.

[213] N. Casali and A. Preston, *E. coli plasmid vectors: Methods and applications*. 2003.

[214] J. Schüpbach and J. Böni, "Quantitative and sensitive detection of immune-complexed and free HIV antigen after boiling of serum," *J. Virol. Methods*, vol. 43, no. 2, pp. 247–256, Jul. 1993.

[215] J. Kim, M. Johnson, P. Hill, and B. K. Gale, "Microfluidic sample preparation: cell lysis and nucleic acid purification.," *Integr. Biol. (Camb).*, vol. 1, no. 10, pp. 574–86, Oct. 2009.

[216] W. A. Al-Soud and P. Rådström, "Purification and characterization of PCR-inhibitory components in blood cells," *J. Clin. Microbiol.*, vol. 39, no. 2, pp. 485–493, 2001.

[217] H. Noh and S. T. Phillips, "Fluidic timers for time-dependent, point-of-care assays on paper," *Anal. Chem.*, vol. 82, no. 19, pp. 8071–8078, 2010.

[218] H. Noh and S. T. Phillips, "Metering the capillary-driven flow of fluids in paper-based microfluidic devices.," *Anal. Chem.*, vol. 82, no. 10, pp. 4181–7, May 2010.

[219] B. Lutz, T. Liang, E. Fu, S. Ramachandran, P. Kauffman, and P. Yager, "Dissolvable

fluidic time delays for programming multi-step assays in instrument-free paper diagnostics.," *Lab Chip*, vol. 13, no. 14, pp. 2840–7, 2013.

[220] H. Chen, J. Cogswell, C. Anagnostopoulos, and M. Faghri, "A fluidic diode, valves, and a sequential-loading circuit fabricated on layered paper.," *Lab Chip*, vol. 12, no. 16, pp. 2909–13, Aug. 2012.

[221] S. F. An and K. A. Fleming, "Removal of inhibitor(s) of the polymerase chain reaction from formalin fixed, paraffin wax embedded tissues.," *J. Clin. Pathol.*, vol. 44, no. 11, pp. 924–927, 1991.

[222] W. A. Al-soud and P. Rådström, "Purification and Characterization of PCR-Inhibitory Components in Blood Cells Purification and Characterization of PCR-Inhibitory Components in Blood Cells," *J. Clin. Microbiol.*, vol. 39, no. 2, pp. 485–493, 2001.

[223] C. Schrader, a. Schielke, L. Ellerbroek, and R. Johne, "PCR inhibitors - occurrence, properties and removal," *J. Appl. Microbiol.*, vol. 113, pp. 1014–1026, 2012.

[224] B. Srinivasan and S. Tung, "Development and Applications of Portable Biosensors," *J. Lab. Autom.*, vol. 20, no. 4, pp. 365–389, 2015.

[225] S. Ahmed, M. P. N. Bui, and A. Abbas, "Paper-based chemical and biological sensors: Engineering aspects," *Biosens. Bioelectron.*, vol. 77, pp. 249–263, 2016.

[226] Y. He, Y. Wu, J. Z. Fu, and W. B. Wu, "Fabrication of paper-based microfluidic analysis devices: a review," *Rsc Adv.*, vol. 5, no. 95, pp. 78109–78127, 2015.

[227] M. Chernesky, D. Jang, S. Chong, J. Sellors, and J. Mahony, "Impact of urine collection order on the ability of assays to identify Chlamydia trachomatis infections in men.," *Sex. Transm. Dis.*, vol. 30, no. 4, pp. 345–7, 2003.

[228] A. Rogacs, L. a. Marshall, and J. G. Santiago, "Purification of nucleic acids using isotachophoresis," *J. Chromatogr. A*, vol. 1335, pp. 105–120, 2014.

[229] M. D. Borysiak, K. W. Kimura, and J. D. Posner, "NAIL: Nucleic Acid detection using Isotachophoresis and Loop-mediated isothermal amplification," *Lab Chip*, vol. 15, no. 7, pp. 1697–1707, 2015.

[230] B. Y. Moghadam, K. T. Connelly, and J. D. Posner, "Isotachophoretic Preconcenetration

on Paper-Based Microfluidic Devices," *Anal. Chem.*, vol. 86, no. 12, pp. 5829-5837, 2014.

[231] M. Bercovici, G. V Kaigala, J. C. Liao, and J. G. Santiago, "Rapid and high sensitivity detection of urinary tract infections using isotachophoresis," *14th Int. Conf. Miniaturized Syst. Chem. Life Sci. 2010, MicroTAS 2010*, vol. 2, pp. 797–799, 2010.

[232] J. Noiphung, K. Talalak, I. Hongwarittorrn, N. Pupinyo, P. Thirabowonkitphithan, and W. Laiwattanapaisal, "A novel paper-based assay for the simultaneous determination of Rh typing and forward and reverse ABO blood groups," *Biosens. Bioelectron.*, vol. 67, pp. 485–489, 2015.

[233] T. Songjaroen and W. Laiwattanapaisal, "Simultaneous forward and reverse ABO blood group typing using a paper-based device and barcode-like interpretation," *Anal. Chim. Acta*, vol. 921, pp. 67-76, 2015.

[234] R Core Development Team and R Core Team, "R: A language and environment for statistical computing," vol. 5, 2106.

[235] S. Danielsen, K. M. Vårum, and B. T. Stokke, "Structural analysis of chitosan mediated DNA condensation by AFM: influence of chitosan molecular parameters.," *Biomacromolecules*, vol. 5, no. 3, pp. 928–36, 2004.

[236] G. Maurstad, S. Danielsen, and B. T. Stokke, "The influence of charge density of chitosan in the compaction of the polyanions DNA and xanthan.," *Biomacromolecules*, vol. 8, no. 4, pp. 1124–30, Apr. 2007.

[237] J. P. Esquivel, J. R. Buser, F. J. del Campo, S. Rojas, P. Yager, and N. Sabate, "Disposable hydrogen fuel cells for powering next-generation lateral flow devices," in *2015 Transducers - 2015 18th International Conference on Solid-State Sensors, Actuators and Microsystems (TRANSDUCERS)*, 2015, pp. 66–69.

[238] "Clearblue digital pregnancy test instructions." [Online]. Available: http://uk.clearblue.com/sites/default/files/cb9row_leaflet.pdf. [Accessed: 24-Sep-2015].

[239] "What's accepted -- Seattle Public Utilities." [Online]. Available: http://www.seattle.gov/util/MyServices/Garbage/HouseResidentsGarbage/WhatsAcceptedasGarbage/index.htm. [Accessed: 24-Sep-2015].

[240] L. Nyholm, G. Nyström, A. Mihranyan, and M. Strømme, “Toward flexible polymer and paper-based energy storage devices.,” *Adv. Mater.*, vol. 23, no. 33, pp. 3751–69, Sep. 2011.

[241] L. Hu, H. Wu, and Y. Cui, “Printed energy storage devices by integration of electrodes and separators into single sheets of paper,” *Appl. Phys. Lett.*, vol. 96, no. 18, p. 183502, 2010.

[242] Y. Koo, J. Sankar, and Y. Yun, “High performance magnesium anode in paper-based microfluidic battery, powering on-chip fluorescence assay.,” *Biomicrofluidics*, vol. 8, no. 5, p. 054104, Sep. 2014.

[243] J. P. Esquivel, F. J. Del Campo, J. L. Gómez de la Fuente, S. Rojas, and N. Sabaté, “Microfluidic fuel cells on paper: meeting the power needs of next generation lateral flow devices,” *Energy Environ. Sci.*, vol. 7, no. 5, p. 1744, 2014.

[244] C. W. Narváez Villarrubia, C. Lau, G. P. M. K. Ciniciato, S. O. Garcia, S. S. Sibbett, D. N. Petsev, S. Babanova, G. Gupta, and P. Atanassov, “Practical electricity generation from a paper based biofuel cell powered by glucose in ubiquitous liquids,” *Electrochem. commun.*, vol. 45, pp. 44–47, Aug. 2014.

[245] F. R. Brushett, M. S. Naughton, J. W. D. Ng, L. Yin, and P. J. a. Kenis, “Analysis of Pt/C electrode performance in a flowing-electrolyte alkaline fuel cell,” *Int. J. Hydrogen Energy*, vol. 37, no. 3, pp. 2559–2570, Feb. 2012.

[246] Alfa Aesar, “45041 Platinum, nominally 70% on high surface area advanced carbon support, HiSPEC^{TM} 13100.” [Online]. Available: http://www.alfa.com/en/catalog/45041. [Accessed: 24-Sep-2015].

[247] L. K. Lafleur, J. D. Bishop, E. K. Heiniger, R. P. Gallagher, M. D. Wheeler, P. C. Kauffman, X. Zhang, E. C. Kline, J. R. Buser, S. Ramachandran, S. A. Byrnes, N. M. J. Vermeulen, N. K. Scarr, Y. Belousov, W. Mahoney, B. J. Toley, P. D. Ladd, B. R. Lutz, P. Yager, S. Kumar, S. A. Byrnes, N. M. J. Vermeulen, N. K. Scarr, Y. Belousov, W. Mahoney, B. J. Toley, P. D. Ladd, B. R. Lutz, and P. Yager, “A rapid, instrument-free, sample-to-result nucleic acid amplification test,” *Lab Chip*, vol. 52, no. 19, pp. 3377–3383, 2016.

[248] A. V. Ritchie, I. Ushiro-Lumb, D. Edemaga, H. A. Joshi, A. De Ruiter, E. Szumilin, I. Jendrulek, M. McGuire, N. Goel, P. I. Sharma, J. P. Allain, and H. H. Lee, “SAMBA HIV semiquantitative test, a new point-of-care viral-load-monitoring assay for resource-limited settings,” *J. Clin. Microbiol.*, vol. 52, no. 9, pp. 3377–3383, 2014.

[249] M. J. Binnicker, M. J. Espy, C. L. Irish, and E. A. Vetter, “Direct Detection of Influenza A and B Viruses in Less Than 20 Minutes Using a Commercially Available Rapid PCR Assay.,” *J. Clin. Microbiol.*, vol. 53, no. 7, pp. 2353–4, 2015.

[250] D. M. Cohen, M. E. Russo, P. Jaggi, J. Kline, W. Gluckman, and A. Parekh, “Multicenter clinical evaluation of the novel Alere i Strep A isothermal nucleic acid amplification test,” *J. Clin. Microbiol.*, vol. 53, no. 7, pp. 2258–2261, 2015.

[251] R. Fang, X. Li, L. Hu, Q. You, J. Li, J. Wu, P. Xu, H. Zhong, Y. Luo, J. Mei, and Q. Gao, “Cross-priming amplification for rapid detection of Mycobacterium tuberculosis in sputum specimens,” *J. Clin. Microbiol.*, vol. 47, no. 3, pp. 845–847, 2009.

[252] World Health Organization “Laboratory Procurement” [Online]. Available: http://www.who.int/diagnostics_laboratory/procurement. [Accessed: 01-Apr-2016].

[253] M. Sajid, A. N. Kawde, and M. Daud, “Designs, formats and applications of lateral flow assay: A literature review,” *J. Saudi Chem. Soc.*, vol. 19, no. 6, pp. 689–705, 2015.

[254] A V Govindarajan, S. Ramachandran, G. D. Vigil, P. Yager, and K. F. Böhringer, “A low cost point-of-care viscous sample preparation device for molecular diagnosis in the developing world; an example of microfluidic origami.,” *Lab Chip*, vol. 12, no. 1, pp. 174–81, Jan. 2012.

[255] J. T. Connelly, J. P. Rolland, and G. M. Whitesides, “‘Paper Machine’ for Molecular Diagnostics,” *Anal. Chem.*, vol. 87, no. 15, pp. 7595–7601, 2015.

[256] P. B. Allen, S. A Arshad, B. Li, X. Chen, and A. D. Ellington, “DNA circuits as amplifiers for the detection of nucleic acids on a paperfluidic platform.,” *Lab Chip*, vol. 12, no. 16, pp. 2951–8, 2012.

[257] K. Pardee, A. A. Green, M. K. Takahashi, D. Braff, G. Lambert, J. W. Lee, T. Ferrante, D. Ma, N. Donghia, M. Fan, N. M. Daringer, I. Bosch, D. M. Dudley, D. H. O’Connor, L. Gehrke, and J. J. Collins, “Rapid, low-cost detection of Zika virus using programmable biomolecular components,” *Cell*, vol. 165, no. 5, pp. 1–12, 2016.

[258] K. Roskos, A. I. Hickerson, H. W. Lu, T. M. Ferguson, D. N. Shinde, Y. Klaue, and A. Niemz, “Simple System for Isothermal DNA Amplification Coupled to Lateral Flow Detection,” *PLoS One*, vol. 8, no. 7, 2013.

[259] J. Song, M. G. Mauk, B. A. Hackett, S. Cherry, H. H. Bau, and C. Liu, “Instrument-Free Point-of-Care Molecular Detection of Zika Virus,” *Anal. Chem.*, p. acs.analchem.6b01632, 2016.

[260] B. Sun, F. Shen, S. E. McCalla, J. E. Kreutz, M. A. Karymov, and R. F. Ismagilov, “Mechanistic evaluation of the pros and cons of digital RT-LAMP for HIV-1 viral load quantification on a microfluidic device and improved efficiency via a two-step digital protocol,” *Anal. Chem.*, vol. 85, no. 3, pp. 1540–1546, 2013.

[261] K. A. Curtis, D. L. Rudolph, I. Nejad, J. Singleton, A. Beddoe, B. Weigl, P. LaBarre, and S. M. Owen, “Isothermal amplification using a chemical heating device for point-of-care detection of HIV-1,” *PLoS One*, vol. 7, no. 2, pp. 1–6, 2012.

[262] A. R. Richardson, S. J. Libby, and F. C. Fang, “A nitric oxide-inducible lactate dehydrogenase enables Staphylococcus aureus to resist innate immunity,” *Sci. (New York, NY)*, vol. 319, no. 5870, pp. 1672–1676, 2008.

[263] J. Eigner, H. Boedtker, and G. Michaels, “The thermal degradation of nucleic acids.,” *Biochim. Biophys. Acta*, vol. 51, pp. 165–168, 1961.

[264] J. Hoorfar, B. Malorny, a Abdulmawjood, N. Cook, P. Fach, and M. Wagner, “Practical Considerations in Design of Internal Amplification Controls for Diagnostic PCR Assays MINIREVIEW Practical Considerations in Design of Internal Amplification Controls for Diagnostic PCR Assays,” *J. Clin. Microbiol.*, vol. 42, no. 5, pp. 1863–8, 2004.

[265] E. K. Heiniger, J. R. Buser, L. Mireles, X. Zhang, P. D. Ladd, B. R. Lutz, and P. Yager, “Comparison of point-of-care-compatible lysis methods for bacteria and viruses,” *J. Microbiol. Methods*, vol. 128, pp. 80–87, 2016.

[266] S. Ehses, J. Ackermann, and J. S. McCaskill, “Optimization and design of oligonucleotide setup for strand displacement amplification,” *J. Biochem. Biophys. Methods*, vol. 63, no. 3, pp. 170–186, 2005.

[267] L. A. Mermel, S. J. Eells, M. K. Acharya, J. M. Cartony, D. Dacus, S. Fadem, E. A. Gay, S. Gordon, J. R. Lonks, T. M. Perl, L. K. McDougal, J. E. McGowan, G. Maxey, D. Morse, and F. C. Tenover, “Quantitative Analysis and Molecular Fingerprinting of Methicillin-Resistant *Staphylococcus aureus* Nasal Colonization in Different Patient Populations: A Prospective, Multicenter Study,” *Infect. Control Hosp. Epidemiol.*, vol. 31, no. 6, pp. 592–597, 2010.

[268] S. Li, S. Norioka, and F. Sakiyama, “Bacteriolytic activity and specificity of Achromobacter beta-lytic protease.,” *J. Biochem.*, vol. 124, no. 2, pp. 332–339, 1998.

[269] G. M. Hogg, J. P. McKenna, and G. Ong, “Rapid detection of methicillin-susceptible and methicillin-resistant Staphylococcus aureus directly from positive BacT/Alert® blood culture bottles using real-time polymerase chain reaction: evaluation and comparison of 4 DNA extraction methods,” *Diagn. Microbiol. Infect. Dis.*, vol. 61, no. 4, pp. 446–452, Aug. 2008.

[270] S. S. Atshan, M. N. Shamsudin, L. T. T. Lung, K. H. Ling, Z. Sekawi, C. P. Pei, and E. Ghaznavi-Rad, “Improved method for the isolation of RNA from bacteria refractory to disruption, including S. aureus producing biofilm,” *Gene*, vol. 494, no. 2, pp. 219–224, 2012.

[271] K. Becker, I. Pagnier, B. Schuhen, F. Wenzelburger, A. W. Friedrich, F. Kipp, G. Peters, and C. Von Eiff, “Does nasal cocolonization by methicillin-resistant coagulase-negative staphylococci and methicillin-susceptible Staphylococcus aureus strains occur frequently enough to represent a risk of false-positive methicillin-resistant S. aureus determinations by m,” *J. Clin. Microbiol.*, vol. 44, no. 1, pp. 229–231, 2006.

[272] World Health Organization “Procurement of HIV diagnostics.” [Online]. Available: http://www. who.int/diagnostics_laboratory/procurement/hiv/en/. [Accessed: 01-Apr-2016].

[273] R. Boom, C. J. Sol, M. M. Salimans, C. L. Jansen, P. M. Wertheim-van Dillen, and J. van der Noordaa, “Rapid and simple method for purification of nucleic acids.,” *J. Clin. Microbiol.*, vol. 28, no. 3, pp. 495–503, Mar. 1990.

[274] P. Chomczynski, “Single-Step Method of RNA Isolation by Acid Guanidinium Extraction,” *Anal. Biochem.*, vol. 159, no. 1, pp. 156–159, 1987.

[275] G. M. Whitesides, “The origins and the future of microfluidics.,” *Nature*, vol. 442, no. 7101, pp. 368–73, Jul. 2006.

[276] C. W. Price, D. C. Leslie, and J. P. Landers, “Nucleic acid extraction techniques and application to the microchip.,” *Lab Chip*, vol. 9, no. 17, pp. 2484–94, Sep. 2009.

[277] B. C. Giordano, D. S. Burgi, S. J. Hart, and A. Terray, “On-line sample pre-concentration

in microfluidic devices: a review.," *Anal. Chim. Acta*, vol. 718, pp. 11–24, Mar. 2012.

[278] A Bhattacharyya and C. M. Klapperich, "Design and testing of a disposable microfluidic chemiluminescent immunoassay for disease biomarkers in human serum samples.," *Biomed. Microdevices*, vol. 9, no. 2, pp. 245–51, Apr. 2007.

[279] X. Qiu, J. a Thompson, Z. Chen, C. Liu, D. Chen, S. Ramprasad, M. G. Mauk, S. Ongagna, C. Barber, W. R. Abrams, D. Malamud, P. L. a M. Corstjens, and H. H. Bau, "Finger-actuated, self-contained immunoassay cassettes.," *Biomed. Microdevices*, vol. 11, no. 6, pp. 1175–86, Dec. 2009.

[280] A. Bange, H. B. Halsall, and W. R. Heineman, "Microfluidic immunosensor systems.," *Biosens. Bioelectron.*, vol. 20, no. 12, pp. 2488–503, Jun. 2005.

[281] C. Liu, M. G. Mauk, and H. H. Bau, "A disposable , integrated loop-mediated isothermal amplification cassette with thermally actuated valves," *Microfluid. Nanofluidics*, vol. 11, pp. 209–220, 2011.

[282] A. K. White, M. VanInsberghe, O. I. Petriv, M. Hamidi, D. Sikorski, M. a Marra, J. Piret, S. Aparicio, and C. L. Hansen, "High-throughput microfluidic single-cell RT-qPCR.," *Proc. Natl. Acad. Sci. U. S. A.*, vol. 108, no. 34, pp. 13999–4004, Aug. 2011.

[283] M. C. Breadmore, K. a Wolfe, I. G. Arcibal, W. K. Leung, D. Dickson, B. C. Giordano, M. E. Power, J. P. Ferrance, S. H. Feldman, P. M. Norris, and J. P. Landers, "Microchip-based purification of DNA from biological samples.," *Anal. Chem.*, vol. 75, no. 8, pp. 1880–6, Apr. 2003.

[284] Q. Wu, J. M. Bienvenue, B. J. Hassan, Y. C. Kwok, B. C. Giordano, P. M. Norris, J. P. Landers, and J. P. Ferrance, "Microchip-based macroporous silica sol-gel monolith for efficient isolation of DNA from clinical samples.," *Anal. Chem.*, vol. 78, no. 16, pp. 5704–10, Aug. 2006.

[285] H. Tian, a F. Hühmer, and J. P. Landers, "Evaluation of silica resins for direct and efficient extraction of DNA from complex biological matrices in a miniaturized format.," *Anal. Biochem.*, vol. 283, no. 2, pp. 175–91, Aug. 2000.

[286] J. Wen, C. Guillo, J. P. Ferrance, and J. P. Landers, "DNA extraction using a tetramethyl orthosilicate-grafted photopolymerized monolithic solid phase.," *Anal. Chem.*, vol. 78, no. 5, pp. 1673–81, Mar. 2006.

[287] Q. Cao, M. Mahalanabis, J. Chang, B. Carey, C. Hsieh, A. Stanley, C. a Odell, P. Mitchell, J. Feldman, N. R. Pollock, and C. M. Klapperich, "Microfluidic chip for molecular amplification of influenza A RNA in human respiratory specimens.," *PLoS One*, vol. 7, no. 3, p. e33176, Jan. 2012.

[288] A. Bhattacharyya and C. M. Klapperich, "Thermoplastic microfluidic device for on-chip purification of nucleic acids for disposable diagnostics.," *Anal. Chem.*, vol. 78, no. 3, pp. 788–92, Feb. 2006.

[289] Q. Cao, M.-C. Kim, and C. M. Klapperich, "Plastic Microfluidic Chip for Continuous-Flow Polymerase Chain Reaction: Simulations and Experiments," *Biotechnol. J.*, vol. 6, no. 2, pp. 177–184, 2012.

[290] D. Chen, M. Mauk, X. Qiu, C. Liu, J. Kim, S. Ramprasad, S. Ongagna, W. R. Abrams, D. Malamud, P. L. a M. Corstjens, and H. H. Bau, "An integrated, self-contained microfluidic cassette for isolation, amplification, and detection of nucleic acids.," *Biomed. Microdevices*, vol. 12, no. 4, pp. 705–19, Aug. 2010.

[291] J. Wang, K. Morabito, J. X. Tang, and A. Tripathi, "Microfluidic platform for isolating nucleic acid targets using sequence specific hybridization," *Biomicrofluidics*, vol. 7, no. 4, p. 044107, 2013.

[292] P. Liu, X. Li, S. a Greenspoon, J. R. Scherer, and R. a Mathies, "Integrated DNA purification, PCR, sample cleanup, and capillary electrophoresis microchip for forensic human identification.," *Lab Chip*, vol. 11, no. 6, pp. 1041–8, Mar. 2011.

[293] S. W. Yeung and I.-M. Hsing, "Manipulation and extraction of genomic DNA from cell lysate by functionalized magnetic particles for lab on a chip applications.," *Biosens. Bioelectron.*, vol. 21, no. 7, pp. 989–97, Jan. 2006.

[294] R. C. den Dulk, K. a Schmidt, G. Sabatté, S. Liébana, and M. W. J. Prins, "Magneto-capillary valve for integrated purification and enrichment of nucleic acids and proteins.," *Lab Chip*, vol. 13, no. 1, pp. 106–18, Jan. 2013.

[295] X. Liu, D. Erickson, D. Li, and U. J. Krull, "Cationic polymer coatings for design of electroosmotic flow and control of DNA adsorption," *Anal. Chim. Acta*, vol. 507, no. 1, pp. 55–62, Apr. 2004.

[296] T. Nakagawa, R. Hashimoto, K. Maruyama, and T. Tanaka, "Capture and Release of DNA Using Aminosilane-Modified Bacterial Magnetic Particles for Automated Detection

System of Single Nucleotide Polymorphisms," 2006.

[297] M. a Witek, M. L. Hupert, D. S.-W. Park, K. Fears, M. C. Murphy, and S. a Soper, "96-well polycarbonate-based microfluidic titer plate for high-throughput purification of DNA and RNA.," *Anal. Chem.*, vol. 80, no. 9, pp. 3483–91, May 2008.

[298] C. Tarmann and A. Jungbauer, "Adsorption of plasmid DNA on anion exchange chromatography media," *J. Sep. Sci.*, vol. 31, pp. 2605–2618, 2008.

[299] S. M. Kenyon, M. M. Meighan, and M. a Hayes, "Recent developments in electrophoretic separations on microfluidic devices.," *Electrophoresis*, vol. 32, no. 5, pp. 482–93, Feb. 2011.

[300] C. R. Reedy, K. a Hagan, B. C. Strachan, J. J. Higginson, J. M. Bienvenue, S. A. Greenspoon, J. P. Ferrance, and J. P. Landers, "Dual-domain microchip-based process for volume reduction solid phase extraction of nucleic acids from dilute, large volume biological samples.," *Anal. Chem.*, vol. 82, no. 13, pp. 5669–5678, Jul. 2010.

[301] W. Cao, C. J. Easley, J. P. Ferrance, and J. P. Landers, "Chitosan as a Polymer for pH-Induced DNA Capture in a Totally Aqueous System," *Anal. Chem.*, vol. 78, no. 20, pp. 7222–7228, 2006.

[302] K. A. Hagan, W. L. Meier, J. P. Ferrance, and J. P. Landers, "Chitosan-Coated Silica as a Solid Phase for RNA Purification in a Microfluidic Device," *Anal. Chem.*, vol. 81, no. 13, pp. 8453–8460, Jul. 2009.

[303] K. A. Hagan, C. R. Reedy, M. L. Uchimoto, D. Basu, D. a Engel, and J. P. Landers, "An integrated, valveless system for microfluidic purification and reverse transcription-PCR amplification of RNA for detection of infectious agents.," *Lab Chip*, vol. 11, no. 5, pp. 957–61, Mar. 2011.

[304] M. Alatorre-meda, P. Taboada, F. Hartl, T. Wagner, M. Freis, and J. R. Rodríguez, "Colloids and Surfaces B : Biointerfaces The influence of chitosan valence on the complexation and transfection of DNA : The weaker the DNA – chitosan binding the higher the transfection efficiency," *Colloids Surfaces B Biointerfaces*, vol. 82, pp. 54–62, 2011.

[305] L. E. Prevette, T. E. Kodger, T. M. Reineke, and M. L. Lynch, "Deciphering the role of hydrogen bonding in enhancing pDNA-polycation interactions.," *Langmuir*, vol. 23, no. 19, pp. 9773–84, Sep. 2007.

[306] H. Yagoda, “Applications of Confined Spot Tests in Analytical Chemistrv,” pp. 79–82, 1937.

[307] R. H. Muller, A. N. D. D. L. Clegg, and N. York, “Automatic Paper Chromatography,” pp. 1123–1125.

[308] R. Consden, A. H. Gordon, and J. P. Martin, “Qualitative Analysis of Proteins : a Partition Chromatographic,” *Biochem. J.*, vol. 38, pp. 224–232, 1944.

[309] U. K. Banik, M. A. Hirsch, D. S. Irvine, J. Krupey, A. Hurwitz, K. Singh, J. Wetsel, and M. L. Givner, “A Simple and Sensitive Nonradioactive Method for the Detection of Urinary Human Chorionic Gonadotropin and Diagnosis of Early Human Pregnancy II Single Unit Test,” *Fertil. Steril.*, vol. 32, no. 4, pp. 426–432, 1979.

[310] “EPT Do-It-Yourself Early-Pregnancy Test,” *Med. Lett. Drugs Ther.*, vol. 20, no. 8, pp. 30–40, 1978.

[311] S. Arora and S. Tyagl, “Detection of Early Pregnancy,” *Clinician (Goa).*, vol. 42, no. 5, pp. 179–183, 1978.

[312] S. Byrnes, G. Thiessen, and E. Fu, “Progress in the development of paper-based diagnostics for low-resource point-of-care settings.,” *Bioanalysis*, vol. 5, no. 22, pp. 2821–36, Nov. 2013.

[313] S. R. Jangam, D. H. Yamada, S. M. McFall, and D. M. Kelso, “Rapid, point-of-care extraction of human immunodeficiency virus type 1 proviral DNA from whole blood for detection by real-time PCR.,” *J. Clin. Microbiol.*, vol. 47, no. 8, pp. 2363–8, Aug. 2009.

[314] G. Decher, “Fuzzy Nanoassemblies: Toward Layered Polymeric Multicomposites,” *Science (80-.).*, vol. 277, no. 5330, pp. 1232–1237, 1997.

[315] A. Díez-Pascual and P. Shuttleworth, “Layer-by-Layer Assembly of Biopolyelectrolytes onto Thermo/pH-Responsive Micro/Nano-Gels,” *Materials (Basel).*, vol. 7, pp. 7472–7512, 2014.

[316] J. Bishop, J. Buser, S. Byrnes, S. Dharmaraja, E. S. Fu, J. Houghtaling, P. C. Kauffman, S. Kumar, L. Lafleur, T. Liang, B. Lutz, B. Toley, M. Wheeler, P. Yager, and X. Zhang, “Sequential Delivery of Fluid Volumes and Associated Devices, Systems and Methods,”

PCT/US2014/0126182014.

[317] C. Eckerskorn and F. Lottspeich, “Structural characterization of blotting membranes and the influence of membrane parameters for electroblotting and subsequent amino acid sequence analysis of proteins.” pp. 831–838, 1993.

[318] A. Edelstein, N. Amodaj, K. Hoover, R. Vale, and N. Stuurman, “Computer control of microscopes using μManager.,” *Curr. Protoc. Mol. Biol.*, Chapter 14, Unit14.20, 2010.

[319] M. D. Abràmoff, I. Hospitals, P. J. Magalhães and M. Abràmoff, “Image Processing with ImageJ”, *Biophotonics International*, vol. 11, pp. 36–42, 2004.

[320] A Akane, K. Matsubara, H. Nakamura, S. Takahashi, and K. Kimura, “Identification of the heme compound copurified with deoxyribonucleic acid (DNA) from bloodstains, a major inhibitor of polymerase chain reaction (PCR) amplification.,” *J. Forensic Sci.*, vol. 39, no. 2, pp. 362–72, Mar. 1994.

[321] P. L. Ma, M. Lavertu, F. M. Winnik, and M. D. Buschmann, “New insights into chitosan-DNA interactions using isothermal titration microcalorimetry.,” *Biomacromolecules*, vol. 10, no. 6, pp. 1490–9, Jun. 2009.

[322] M. D. Buschmann, A. Merzouki, M. Lavertu, M. Thibault, M. Jean, and V. Darras, “Chitosans for delivery of nucleic acids.,” *Adv. Drug Deliv. Rev.*, vol. 65, no. 9, pp. 1234–70, Aug. 2013.

[323] R. Moriyama, N. Shimada, A. Kano, and A. Maruyama, “DNA assembly and re-assembly activated by cationic comb-type copolymer.,” *Biomaterials*, vol. 32, no. 9, pp. 2351–8, Mar. 2011.

[324] Y. Wang, J. Wang, F. Yang, and X. Yang, “Probing biomolecular interactions with dual polarization interferometry: real-time and label-free coralyne detection by use of homoadenine DNA oligonucleotide.,” *Anal. Chem.*, vol. 84, no. 2, pp. 924–30, Jan. 2012.

[325] M. E. Blocker, R. G. Krysiak, F. Behets, M. S. Cohen, M. M. Hobbs, C. Hill, and N. Carolina, “Quantification of Chlamydia trachomatis Elementary Bodies in Urine by Ligase Chain Reaction,” *J. Clin. Microbiol.*, vol. 40, no. 10, pp. 3631–3634, 2002.

[326] J. S. Towner, P. E. Rollin, D. G. Bausch, A. Sanchez, S. M. Crary, M. Vincent, F. Lee, C. F. Spiropoulou, T. G. Ksiazek, M. Lukwiya, F. Kaducu, R. Downing, T. Nichol, W. F.

Lee, and S. T. Nichol, “Rapid Diagnosis of Ebola Hemorrhagic Fever by Reverse Transcription-PCR in an Outbreak Setting and Assessment of Patient Viral Load as a Predictor of Outcome Rapid Diagnosis of Ebola Hemorrhagic Fever by Reverse Transcription-PCR in an Outbreak Setting an,” *J. Virol.*, vol. 78, no. 8, pp. 4330–4341, 2004.

[327] P. F. Wright, G. Neumann, and Y. Kawaoka, “Orthomyxoviruses,” in *Fields Virology*, 1985, pp. 1692–1740.

[328] M. A. Hollingsworth and B. J. Swanson, “Mucins in cancer: protection and control of the cell surface.,” *Nat. Rev. Cancer*, vol. 4, no. 1, pp. 45–60, Jan. 2004.

[329] B. a Rohrman, V. Leautaud, E. Molyneux, and R. R. Richards-Kortum, “A lateral flow assay for quantitative detection of amplified HIV-1 RNA.,” *PLoS One*, vol. 7, no. 9, p. e45611, Jan. 2012.

[330] D. Mabey, R. W. Peeling, A. Ustianowski, and M. D. Perkins, “Tropical infectious diseases: Diagnostics for the developing world,” *Nat Rev Micro*, vol. 2, no. 3, pp. 231–240, 2004.

[331] L. K. Archibald and L. B. Reller, “Clinical microbiology in developing countries.,” *Emerg. Infect. Dis.*, vol. 7, no. 2, pp. 302–305, 2001.

[332] P. Rådström, R. Knutsson, P. Wolffs, M. Lövenklev, and C. Löfström, “Pre-PCR Processing,” vol. 26, 2004.

[333] G. Biswas and M. Sakai, “Loop-mediated isothermal amplification (LAMP) assays for detection and identification of aquaculture pathogens: Current state and perspectives,” *Appl. Microbiol. Biotechnol.*, vol. 98, no. 7, pp. 2881–2895, 2014.

[334] F. Teles and L. Fonseca, “Nucleic-Acid Testing, New Platforms and Nanotechnology for Point-of-Decision Diagnosis of Animal Pathogens,” in *Veterinary Infection Biology: Molecular Diagnostics and High-Throughput Strategies*, V. M. Cunha and J. Inácio, Eds. New York, NY: Springer New York, 2015, pp. 253–283.

[335] I. A. N. G. Wilson, “Inhibition and Facilitation of Nucleic Acid Amplification,” vol. 63, no. 10, pp. 3741–3751, 1997.

[336] K. A. Eckert and T. A. Kunkel, “High fidelity DNA synthesis by the *Thermus aquaticus*

DNA polymerase," *Nucleic Acids Res.*, vol. 18, no. 13, p. 3739, 1990.

[337] P. Chomczynski and M. Rymaszewski, "Alkaline polyethylene glycol-based method for direct PCR from bacteria, eukaryotic tissue samples, and whole blood," *Biotechniques*, vol. 40, no. 4, pp. 454–458, 2006.

[338] K. Sung, S. a. Khan, M. S. Nawaz, and A. a. Khan, "A simple and efficient Triton X-100 boiling and chloroform extraction method of RNA isolation from Gram-positive and Gram-negative bacteria," *FEMS Microbiol. Lett.*, vol. 229, no. 1, pp. 97–101, 2003.

[339] J. P. Bearinger, L. C. Dugan, B. R. Baker, S. B. Hall, K. Ebert, V. Mioulet, M. Madi, and D. P. King, "Development and initial results of a low cost, disposable, point-of-care testing device for pathogen detection.," *IEEE Trans. Biomed. Eng.*, vol. 58, no. 3, pp. 805–8, Mar. 2011.

[340] D. Rajendram, R. Ayenza, F. M. Holder, B. Moran, T. Long, and H. N. Shah, "Long-term storage and safe retrieval of DNA from microorganisms for molecular analysis using FTA matrix cards," *J. Microbiol. Methods*, vol. 67, no. 3, pp. 582–592, 2006.

[341] R. de Boer, R. Peters, S. Gierveld, T. Schuurman, M. Kooistra-Smid, and P. Savelkoul, "Improved detection of microbial DNA after bead-beating before DNA isolation," *J. Microbiol. Methods*, vol. 80, no. 2, pp. 209–211, 2010.

[342] A. Bera, S. Herbert, A. Jakob, W. Vollmer, and F. Götz, "Why are pathogenic staphylococci so lysozyme resistant? The peptidoglycan O-acetyltransferase OatA is the major determinant for lysozyme resistance of Staphylococcus aureus," *Mol. Microbiol.*, vol. 55, no. 3, pp. 778–787, 2005.

[343] S. Li, S. Norioka, and F. Sakiyama, "Purification, staphylolytic activity, and cleavage sites of alpha-lytic protease from Achromobacter lyticus," *J. Biochem.*, vol. 122, no. 4, pp. 772–778, Oct. 1997.

[344] T. Masaki, T. Fujihashi, K. Nakamura, and M. Soejima, "Studies on a new proteolytic enzyme from *Achromobacter lyticus* M497-1. II. specificity and inhibition studies of *Achromobacter* protease I," *Biochim. Biophys. Acta*, vol. 660, no. 1, pp. 51–55, Jul. 1981.

[345] F. D. Lowy, "*Staphylococcus aureus* infections," *N. Engl. J. Med.*, vol. 339, no. 8, pp. 520–532, Aug. 1998.

[346] S. E. Cosgrove, G. Sakoulas, E. N. Perencevich, M. J. Schwaber, A. W. Karchmer, and Y. Carmeli, “Comparison of mortality associated with methicillin-resistant and methicillin-susceptible *Staphylococcus aureus* bacteremia: a meta-analysis,” *Clin. Infect. Dis.*, vol. 36, no. 1, pp. 53–59, Jan. 2003.

[347] K. M. Tatti and M. L. Tondella, “Utilization of multiple real-time PCR assays for the diagnosis of *Bordetella* spp. in clinical specimens,” *Methods Mol. Biol.*, vol. 943, pp. 135–147, 2013.

[348] T. Spilker, A. L. Leber, M. J. Marcon, D. W. Newton, R. Darrah, P. Vandamme, and J. J. LiPuma, “A simplified sequence-based identification scheme for *Bordetella* reveals several putative novel species,” *J. Clin. Microbiol.*, vol. 52, no. 2, pp. 674–677, 2014.

[349] P. J. Brennan and H. Nikaido, “The envelope of *mycobacteria*.,” *Annu. Rev. Biochem.*, vol. 64, pp. 29–63, 1995.

[350] T. Niwa, Y. Kawamura, Y. Katagiri, and T. Ezaki, “Lytic enzyme, labiase for a broad range of Gram-positive bacteria and its application to analyze functional DNA/RNA,” *J. Microbiol. Methods*, vol. 61, no. 2, pp. 251–260, 2005.

[351] C. L. Cosma, L. E. Swaim, H. Volkman, L. Ramakrishnan, and J. Davis, “Zebrafish and Frog Models of *Mycobacterium marinum* Infection,” in *Current Protocols in Microbiology*, 2006, pp. 10B.2.1–10B.2.33.

[352] L.-Y. Gao and J. Manoranjan, “Laboratory Maintenance of *Mycobacterium marinum*,” in *Current Protocols in Microbiology*, 2005, pp. 10B.1.1–10B.1.8.

[353] B. N. Kreiswirth, S. Lofdahl, M. J. Betley, M. O’Reilly, P. M. Shlievert, M. S. Bergdoll, and R. P. Novick, “The toxic shock syndrome exotoxin structural gene is not detectably transmitted by a prophage,” *Nature*, vol. 305, no. 5936, pp. 709–12, 1983.

[354] R. R. Hulbert and P. A. Cotter, “Laboratory Maintenance of *Bordetella pertussis*,” *Curr. Protoc. Microbiol.*, vol. Chapter 4, p. Unit 4B.1, Nov. 2009.

[355] S. B. Munro, J. Kuypers, and K. R. Jerome, “Comparison of a multiplex real-time PCR assay with a multiplex luminex assay for influenza virus detection,” *J. Clin. Microbiol.*, vol. 51, no. 4, pp. 1124–1129, 2013.

[356] J. Amita, T. Vandana, R. S. Guleria, and R. K. Verma, “Qualitative evaluation of

mycobacterial DNA extraction protocols for polymerase chain reaction," *Mol. Biol. Today*, vol. 3, no. 4, pp. 43–50, 2002.

[357] S. Fleige and M. W. Pfaffl, "RNA integrity and the effect on the real-time qRT-PCR performance," *Mol. Aspects Med.*, vol. 27, no. 2–3, pp. 126–139, 2006.

[358] J. Sambrook, F. EF, and T. Maniatis, *Molecular cloning: A laboratory manual 2nd ed*. 1989.

[359] S. E. Zale and a M. Klibanov, "Why does ribonuclease irreversibly inactivate at high temperatures?," *Biochemistry*, vol. 25, no. 19, pp. 5432–5444, 1986.

[360] T. Poeckh, S. Lopez, A. O. Fuller, M. J. Solomon, and R. G. Larson, "Adsorption and elution characteristics of nucleic acids on silica surfaces and their use in designing a miniaturized purification unit," *Anal. Biochem.*, vol. 373, no. 2, pp. 253–262, 2008.

[361] B. Li, W. Zhang, L. Chen, and B. Lin, "A fast and low-cost spray method for prototyping and depositing surface-enhanced Raman scattering arrays on microfluidic paper based device," *Electrophoresis*, vol. 34, no. 15, pp. 2162–2168, 2013.

[362] P. Rattanarat, W. Dungchai, D. Cate, J. Volckens, O. Chailapakul, and C. S. Henry, "Multilayer paper-based device for colorimetric and electrochemical quantification of metals," *Anal. Chem.*, vol. 86, no. 7, pp. 3555–3562, 2014.

[363] S. A. Bhakta, R. Borba, M. Taba, C. D. Garcia, and E. Carrilho, "Determination of nitrite in saliva using microfluidic paper-based analytical devices," *Anal. Chim. Acta*, vol. 809, pp. 117–122, 2014.

[364] Y. Zhang and D. Rochefort, "Fast and effective paper based sensor for self-diagnosis of bacterial vaginosis," *Anal. Chim. Acta*, vol. 800, pp. 87–94, 2013.

[365] B. Li, L. Fu, W. Zhang, W. Feng, and L. Chen, "Portable paper-based device for quantitative colorimetric assays relying on light reflectance principle," *Electrophoresis*, vol. 35, no. 8, pp. 1152–1159, 2014.

[366] L. He, T. Nan, Y. Cui, S. Guo, W. Zhang, R. Zhang, G. Tan, B. Wang, and L. Cui, "Development of a colloidal gold-based lateral flow dipstick immunoassay for rapid qualitative and semi-quantitative analysis of artesunate and dihydroartemisinin.," *Malar. J.*, vol. 13, no. 127, pp. 1–10, 2014.

[367] D. Z. Hung, J. H. Lin, J. F. Mo, C. F. Huang, and M. Y. Liau, “Rapid diagnosis of *Naja atra* snakebites,” *Clin. Toxicol.*, vol. 52, no. 3, pp. 187–191, 2014.

[368] Y. K. Oh, H.-A. Joung, S. Kim, and M.-G. Kim, “Vertical flow immunoassay (VFA) biosensor for a rapid one-step immunoassay.,” *Lab Chip*, vol. 13, no. 5, pp. 768–72, 2013.

[369] Z. Fang, C. Ge, W. Zhang, P. Lie, and L. Zeng, “A lateral flow biosensor for rapid detection of DNA-binding protein c-jun,” *Biosens. Bioelectron.*, vol. 27, no. 1, pp. 192–196, 2011.

[370] B. E. Fu, P. Yager, P. N. Floriano, N. Christodoulides, and J. T. McDevitt, “Challenges in Evolving Chips-in-a-Lab to a True Lab-on-a-Chip,” *IEEE Pulse*, Nov. 2011.

[371] J. Houghtaling, T. Liang, G. Thiessen, and E. Fu, “Dissolvable Bridges for Manipulating Fluid Volumes in Paper Networks.,” *Anal. Chem.*, Nov. 2013.

[372] S. Jahanshahi-Anbuhi, A. Henry, V. Leung, C. Sicard, K. Pennings, R. Pelton, J. D. Brennan, and C. D. M. Filipe, “Paper-based microfluidics with an erodible polymeric bridge giving controlled release and timed flow shutoff.,” *Lab Chip*, vol. 14, no. 1, pp. 229–36, Jan. 2014.

[373] R. Gerbers, W. Foellscher, H. Chen, C. Anagnostopoulos, and M. Faghri, “A new paper-based platform technology for point-of-care diagnostics.,” *Lab Chip*, vol. 14, no. 20, pp. 4042–9, 2014.

[374] C. K. W. Koo, F. He, and S. R. Nugen, “An inkjet-printed electrowetting valve for paper-fluidic sensors.,” *Analyst*, vol. 138, no. 17, pp. 4998–5004, Sep. 2013.

[375] X. Li, J. Tian, T. Nguyen, and W. Shen, “Paper-Based Microfluidic Devices by Plasma Treatment,” *Anal. Chem.*, vol. 80, no. 23, pp. 9131–9134, Dec. 2008.

[376] X. Li, P. Zwanenburg, and X. Liu, “Magnetic timing valves for fluid control in paper-based microfluidics,” *Lab Chip*, vol. 13, no. 13, p. 2609, 2013.

[377] A. C. Glavan, R. V Martinez, E. J. Maxwell, A. B. Subramaniam, R. M. D. Nunes, S. Soh, and G. M. Whitesides, “Rapid fabrication of pressure-driven open-channel microfluidic devices in omniphobic R(F) paper.,” *Lab Chip*, vol. 13, no. 15, pp. 2922–2930, 2013.

[378] N. Kurn, R. D. Patel, M. Becker, and E. F. Ullman, “Device and method for interrupting capillary flow,” 51048121992.

[379] R. D. Patel, N. Kurn, M. Becker, and E. F. Ullman, “Device and method for completing a fluidic circuit which employs a liquid expandabe piece of bibulous material,” 51358731992.

[380] R. A. Bunce, G. H. G. H. Thorpe, J. E. C. Gibbons, L. J. Keen, and M. R. Walker, “Liquid Transfer Devices,” 51981931993.

[381] D. J. Beebe, J. S. Moore, J. M. Bauer, Q. Yu, R. H. Liu, C. Devadoss, and B.-H. Jo, “Functional hydrogel structures for autonomous flow control inside microfluidic channels” *Nature*, vol. 404, no. 6778, pp. 588–590, 2000.

[382] D. T. Eddington and D. J. Beebe, “Flow control with hydrogels,” *Adv. Drug Deliv. Rev.*, vol. 56, no. 2, pp. 199–210, 2004.

[383] R. Lucas, “Rate of capillary ascension of liquids,” *Kolloid Z*, 1918.

[384] J. M. Bell and F. K. Cameron, “The flow of liquids through capillary spaces,” *J. Phys. Chem.*, vol. 50, no. 30, pp. 658–674, 1906.

[385] J. Li and J. Macdonald, “Advances in isothermal amplification: Novel strategies inspired by biological processes,” *Biosens. Bioelectron.*, vol. 64, pp. 196–211, 2014.

[386] P. Spicar-Mihalic, B. Toley, J. Houghtaling, T. Liang, P. Yager, and E. Fu, “CO 2 laser cutting and ablative etching for the fabrication of paper-based devices,” *J. Micromechanics Microengineering*, vol. 23, no. 6, p. 067003, Jun. 2013.

[387] P. Patel, B. Bennett, T. Sullivan, M. M. Parker, J. D. Heffelfinger, and P. S. Sullivan, “Rapid HIV screening: Missed opportunities for HIV diagnosis and prevention,” *J. Clin. Virol.*, vol. 54, no. 1, pp. 42–47, 2012.

[388] A. Hadgu, N. Dendukuri, and J. Hilden, “Evaluation of nucleic acid amplification tests in the absence of a perfect gold-standard test: a review of the statistical and epidemiologic issues.,” *Epidemiology*, vol. 16, no. 5, pp. 604–612, 2005.

[389] L. M. Zanoli and G. Spoto, “Isothermal amplification methods for the detection of nucleic acids in microfluidic devices,” *Biosensors*, vol. 3, no. 1, pp. 18–43, 2013.

[390] G. Xu, L. Hu, H. Zhong, H. Wang, S.-I. Yusa, T. C. Weiss, P. J. Romaniuk, S. Pickerill, and Q. You, “Cross priming amplification: mechanism and optimization for isothermal DNA amplification.,” *Sci. Rep.*, vol. 2, p. 246, 2012.

[391] R. A. Waters, V. L. Fowler, B. Armson, N. Nelson, J. Gloster, D. J. Paton, and D. P. King, “Preliminary validation of direct detection of foot-and-mouth disease virus within clinical samples using reverse transcription Loop-mediated isothermal amplification coupled with a simple lateral flow device for detection,” *PLoS One*, vol. 9, no. 8, pp. 1–10, 2014.

[392] I. A. Taub, W. Roberts, S. Lagambina, and K. Kustin, “Mechanism of Dihydrogen Formation in the Magnesium - Water Reaction ⊥,” pp. 8070–8078, 2002.

[393] N-hexadecanoic Acid Phase Change Data; 2011. Database: NIST Chemistry Webbook [online]. Available: http://webbook.nist.gov/cgi/cbook.cgi?Name = palmitic+acid&Units=SI&cTP=on. [Accessed: 01-Jan-2016].

[394] Methyl Alcohol Phase Change Data; 2011. Database: NIST Chemistry Webbook [online]. Available: http://webbook.nist.gov/cgi/cbook.cgi?Name = methyl+alcohol&Units=SI&cTP=on. [Accessed: 01-Jan-2016].

[395] R. D. Sheeler, M. S. Houston, S. Radke, J. C. Dale, and S. C. Adamson, “Accuracy of rapid strep testing in patients who have had recent *streptococcal* pharyngitis.,” *J. Am. Board Fam. Pract.*, vol. 15, no. 4, pp. 261–5, 2001.

[396] L. R. Peterson, O. Liesenfeld, C. W. Woods, S. D. Allen, D. Pombo, P. A. Patel, M. S. Mehta, B. Nicholson, D. Fuller, and A. Onderdonk, “Multicenter evaluation of the lightcycler methicillin-resistant *Staphylococcus aureus* (MRSA) advanced test as a rapid method for detection of MRSA in nasal surveillance swabs,” *J. Clin. Microbiol.*, vol. 48, no. 5, pp. 1661–1666, 2010.

[397] W. C. Yam, G. K. H. Siu, P. L. Ho, T. K. Ng, T. L. Que, K. T. Yip, C. P. K. Fok, J. H. K. Chen, V. C. C. Cheng, and K. Y. Yuen, “Evaluation of the lightcycler methicillin-resistant *Staphylococcus aureus* (MRSA) advanced test for detection of MRSA nasal colonization,” *J. Clin. Microbiol.*, vol. 51, no. 9, pp. 2869–2874, 2013.

[398] C. K. Goodell, J. Prickett, A. Kittawornrat, F. Zhou, R. Rauh, W. Nelson, C. O’Connell, A. Burrell, C. Wang, K. J. Yoon, and J. J. Zimmerman, “Probability of detecting influenza A virus subtypes H1N1 and H3N2 in individual pig nasal swabs and pen-based oral fluid specimens over time,” *Vet. Microbiol.*, vol. 166, no. 3–4, pp. 450–460, 2013.

[399] L. T. Wu, I. Thomas, M. D. Curran, J. S. Ellis, S. Parmar, N. Goel, P. I. Sharma, J. P. Allain, and H. H. Lee, “Duplex molecular assay intended for point-of-care diagnosis of influenza A/B virus infection,” *J. Clin. Microbiol.*, vol. 51, no. 9, pp. 3031–3038, 2013.

[400] M. E. Waris, T. Heikkinen, R. Osterback, T. Jartti, and O. Ruuskanen, “Nasal swabs for detection of respiratory syncytial virus RNA.,” *Arch. Dis. Child.*, vol. 92, no. 11, pp. 1046–7, 2007.

[401] I. S. Spyridaki, I. Christodoulou, L. de Beer, V. Hovland, M. Kurowski, A. Olszewska-Ziaber, K. H. Carlsen, K. Lødrup-Carlsen, C. M. van Drunen, M. L. Kowalski, R. Molenkamp, and N. G. Papadopoulos, “Comparison of four nasal sampling methods for the detection of viral pathogens by RT-PCR-A GA2LEN project,” *J. Virol. Methods*, vol. 156, no. 1–2, pp. 102–106, 2009.

[402] P. Hassanzadeh, J. Mardaneh, and M. Motamedifar, “Conventional Agar-Based Culture Method, and Nucleic Acid Amplification Test (NAAT) of the cppB Gene for Detection of *Neisseria gonorrhea* in Pregnant Women Endocervical Swab Specimens.,” *Iran. Red Crescent Med. J.*, vol. 15, no. 3, pp. 207–11, 2013.

[403] L. Ostergaard, T. Agner, E. Krarup, U. B. Johansen, K. Weismann, and E. Gutschik, “PCR for detection of *Chlamydia trachomatis* in endocervical, urethral, rectal, and pharyngeal swab samples obtained from patients attending an STD clinic.,” *Genitourin. Med.*, vol. 73, no. 6, pp. 493–7, 1997.

[404] L. Gustavsson, J. Westin, L. M. Andersson, and M. Lindh, “Rectal swabs can be used for diagnosis of viral gastroenteritis with a multiple real-time PCR assay,” *J. Clin. Virol.*, vol. 51, no. 4, pp. 275–278, 2011.

[405] C. V. Van Der Schee, A. Van Belkum, L. Zwijgers, E. V. Van Der Brugge, E. L. O’Neill, A. Luijendijk, T. Van Rijsoort-Vos, W. I. Van Der Meijden, H. Verbrugh, and H. J. F. Sluiters, “Improved diagnosis of *Trichomonas vaginalis* infection by PCR using vaginal swabs and urine specimens compared to diagnosis by wet mount microscopy, culture, and fluorescent staining,” *J. Clin. Microbiol.*, vol. 37, no. 12, pp. 4127–4130, 1999.

[406] L. Mikalová, P. Pospíšilová, V. Woznicová, I. Kuklová, H. Zákoucká, and D. Smajs, “Comparison of CDC and sequence-based molecular typing of *syphilis treponemes*: tpr and arp loci are variable in multiple samples from the same patient.,” *BMC Microbiol.*, vol. 13, no. 1, p. 178, 2013.

[407] R. C. Jerris, D. K. Jarrett, W. Cherney, and A. Atlanta, “Comparison of StarSwab II with BD CultureSwab Max V (+) Transport Systems for Preservation of Bacterial Pathogens Important in Pediatric Medicine ; *Hemophilus influenza* , *Streptococcus pneumoniae* , and *Neisseria meningitidis*,” *Clin. Lab.*, no. June, pp. 1–4, 2005.

[408] J. Turner, K. Harry, D. Lofland, and K. Madhusudhan, “The Characterization of the Absorption and Release Properties of Various Clinical Swabs,” in *26th Clinical Virology Symposium, Florida, USA.*, 2010.

[409] X. Gao, X. S. Chen, Y. P. Yin, M. Y. Zhong, M. Q. Shi, W. H. Wei, Q. Chen, R. W. Peeling, and D. Mabey, “Distribution study of Chlamydia trachomatis serovars among high-risk women in china performed using PCR-restriction fragment length polymorphism genotyping,” *J. Clin. Microbiol.*, vol. 45, no. 4, pp. 1185–1189, 2007.

[410] I. Technologies, “IStrep Instruction – Clinical Diagnostic Products,” 2011. [Online]. Available: http://www.tryi.com/products/clinical/istrep/instructions.php. [Accessed: 01-Jan-2011].

[411] A. Scarborough, “Alere BinaxNOW RSV Card package insert.” Maine USA, 2012.

[412] P. A. Patel, N. A. Ledeboer, C. C. Ginocchio, S. Condon, S. Bouchard, P. Qin, T. Karchmer, and L. R. Peterson, “Performance of the BD GeneOhm MRSA achromopeptidase assay for real-time PCR detection of methicillin-resistant Staphylococcus aureus in nasal specimens,” *J. Clin. Microbiol.*, vol. 49, no. 6, pp. 2266–2268, 2011.

[413] A. Komaromy, R. I. Boysen, H. Zhang, M. T. W. Hearn, and D. V. Nicolau, “Effect of various artificial surfaces on the colonization and viability of,” *Proc. SPIE*, vol. 6799, p. 67990J–67990J–10, 2007.

[414] P. Verhoeven, F. Grattard, A. Carricajo, B. Pozzetto, and P. Berthelot, “Better detection of Staphylococcus aureus nasal carriage by use of nylon flocked swabs,” *J. Clin. Microbiol.*, vol. 48, no. 11, pp. 4242–4244, 2010.

[415] A. S. Rossney, C. M. Herra, G. I. G. I. Brennan, P. M. Morgan, and B. O’Connell, “Evaluation of the Xpert methicillin-resistant Staphylococcus aureus (MRSA) assay using the GeneXpert real-time PCR platform for rapid detection of MRSA from screening specimens.,” *J. Clin. Microbiol.*, vol. 46, no. 10, pp. 3285–90, Oct. 2008.

[416] K. H. Harry, J. C. Turner, and K. T. Madhusudhan, “Comparison of physical

characteristics and collection and elution performance of clinical swabs," *Aftrican J. Microbiol. Res.*, vol. 7, no. 31, pp. 4039–4048, 2013.

[417] L. G. Rubin, A. Rizvi, and A. Baer, "Effect of swab composition and use of swabs versus swab-containing skim milk-tryptone-glucose-glycerol (STGG) on culture- or PCR-based detection of Streptococcus pneumoniae in simulated and clinical respiratory specimens in STGG transport medium," *J. Clin. Microbiol.*, vol. 46, no. 8, pp. 2635–2640, 2008.

[418] T. F. Landers, A. Hoet, and T. E. Wittum, "Swab type, moistening, and preenrichment for Staphylococcus aureus on environmental surfaces," *J. Clin. Microbiol.*, vol. 48, no. 6, pp. 2235–2236, 2010.

[419] A. Matheson, P. Christie, T. Stari, K. Kavanagh, I. M. Gould, R. Masterton, and J. S. Reilly, "Nasal swab screening for methicillin-resistant Staphylococcus aureus—how well does it perform? A cross-sectional study.," *Infect. Control Hosp. Epidemiol.*, vol. 33, no. 8, pp. 803–808, 2012.

[420] P. D. Sparham, D. I. Lobban, and D. C. Speller, "Isolation of *Staphylococcus aureus* from sputum in cystic fibrosis.," *J. Clin. Pathol.*, vol. 31, no. 10, pp. 913–8, 1978.

[421] A. I. Freitas, C. Vasconcelos, M. Vilanova, and N. Cerca, "Optimization of an automatic counting system for the quantification of *Staphylococcus epidermidis* cells in biofilms," *J. Basic Microbiol.*, vol. 54, no. 7, pp. 750–757, 2014.

[422] D. Jonas, M. Speck, F. D. Daschner, and H. Grundmann, "Rapid PCR-Based Identi cation of Methicillin-Resistant *Staphylococcus aureus* from Screening Swabs" *J. Clin. Microbiol.*, vol. 40, no. 5, pp. 1821–1823, 2002.

[423] S. M. Paule, M. Mehta, D. M. Hacek, T. M. Gonzalzles, A. Robicsek, and L. R. Peterson, "Chromogenic media vs real-time pcr for nasal surveillance of methicillin-resistant staphylococcus aureus impact on detection of mrsa-positive persons," *Am. J. Clin. Pathol.*, vol. 131, no. 4, pp. 532–539, 2009.

[424] B. Ratner, A. Hoffman, and F. Schoen, "Biomedical Engineering e-Mega Reference: Academic Press," 2009, pp. 305–347.

[425] A. P. Campbell, J. Kuypers, J. A. Englund, K. A. Guthrie, L. Corey, and M. Boeckh, "Self-collection of foam nasal swabs for respiratory virus detection by PCR among immunocompetent subjects and hematopoietic cell transplant recipients," *J. Clin. Microbiol.*, vol. 51, no. 1, pp. 324–327, 2013.

[426] H. Kettler, K. White, and S. Hawkes, “Mapping the landscape of diagnostics for sexually transmitted infections: Key findings and recommandations,” pp. 1–44, 2004.

[427] K. Abe, K. Suzuki, and D. Citterio, “Inkjet-printed microfluidic multianalyte chemical sensing paper.,” *Anal. Chem.*, vol. 80, no. 18, pp. 6928–34, Sep. 2008.

[428] E. M. Fenton, M. R. Mascarenas, G. P. Lopez, and S. S. Sibbett, “Multiplex lateral-flow test strips fabricated by two-dimensional shaping,” *ACS Appl. Mater. Interfaces*, vol. 1, no. 1, pp. 124–129, 2009.

[429] X. Li, J. Tian, and W. Shen, “Quantitative biomarker assay with microfluidic paper-based analytical devices,” *Anal. Bioanal. Chem.*, vol. 396, no. 1, pp. 495–501, 2010.

[430] W. Wang, W. Y. Wu, W. Wang, and J. J. Zhu, “Tree-shaped paper strip for semiquantitative colorimetric detection of protein with self-calibration,” *J. Chromatogr. A*, vol. 1217, no. 24, pp. 3896–3899, 2010.

[431] H. Liu, X. Li, and R. M. Crooks, “Paper-based SlipPAD for high-throughput chemical sensing,” *Anal. Chem.*, vol. 85, no. 9, pp. 4263–4267, 2013.

[432] B. Ngom, Y. Guo, X. Wang, and D. Bi, “Development and application of lateral flow test strip technology for detection of infectious agents and chemical contaminants: A review,” *Anal. Bioanal. Chem.*, vol. 397, no. 3, pp. 1113–1135, 2010.

[433] B. Weigl, G. Domingo, P. LaBarre, and J. Gerlach, “Towards non-and minimally instrumented, microfluidics-based diagnostic devices,” *Lab Chip*, vol. 8, no. 12, pp. 1999–2014, 2008.

[434] D. R. Ballerini, X. Li, and W. Shen, “Patterned paper and alternative materials as substrates for low-cost microfluidic diagnostics,” *Microfluidics and Nanofluidics*, vol. 13, no. 5. pp. 769–787, 2012.

[435] L. Gervais, M. Hitzbleck, and E. Delamarche, “Capillary-driven multiparametric microfluidic chips for one-step immunoassays,” *Biosens. Bioelectron.*, vol. 27, no. 1, pp. 64–70, 2011.

[436] M. Zimmermann, P. Hunziker, and E. Delamarche, “Autonomous capillary system for one-step immunoassays,” *Biomed. Microdevices*, vol. 11, no. 1, pp. 1–8, 2009.

[437] L. Gervais and E. Delamarche, “Toward one-step point-of-care immunodiagnostics using capillary-driven microfluidics and PDMS substrates.,” *Lab Chip*, vol. 9, no. 23, pp. 3330–7, Dec. 2009.